COPY I

TEMPERATURE AND STRUCTURAL CHANGES DURING HOT ROLLING

BY

RICHARD ANTHONY HARDING M.Met.

A thesis submitted for the degree of Doctor of Philosophy

University of Sheffield
Department of Metallurgy
November 1976.

TEMPERATURE AND STRUCTURAL CHANGES DURING HOT ROLLING

R.A. HARDING

SUMMARY

The published literature on strength, structural and thermal aspects of hot working has been reviewed with particular reference to their application to the hot rolling of stainless steel.

Mild and stainless steel slabs have been hot rolled on a mill instrumentated to measure load, torque and speed. Internal temperatures have been measured during rolling using embedded thermocouples whose outputs have been recorded on a U.V. recorder coupled with an automatic back-off system.

As-rolled stainless steel slabs recrystallised very slowly relative to the rate found by previous workers for simpler austenitic stainless steels. Additionally, slabs exhibited retarded recrystallisation at the surface compared with the centre whereas theoretical analysis predicts the reverse. These phenomena have been explained by rapid precipitation at temperatures $\lesssim 950^{\circ}C$ and limited electron microscopical evidence has been obtained to support this. Precipitation also increased the flow stresses at lower rolling temperatures and masked any effects that different substructures were expected to have on the hot strength.

A finite difference computer programme has been developed to predict the temperature changes that occur through a two dimensional transverse section of a slab during a hot rolling schedule. The air cooling and roll contact heat transfer coefficients have been derived by comparison of measured and computed temperature-time curves. This programme enabled a mean pass temperature to be derived from measured temperatures which then resulted in good agreement between hot strengths derived from rolling and torsion tests on stainless steel.

The programme has been simplified to a one dimensional

model for simulating temperature changes over central regions of wide sections during industrial hot rolling. Data have been presented to enable mean temperatures to be derived from measured surface temperatures and to illustrate the effects of various parameters on the heat loss during a pass.

CONTENTS

CHAPTER 8 RESULTS

CHAPTER 9 DISCUSSION OF RESULTS

CHAPTER ONE

BACKGROUND TO THE PRESENT RESEARCH

1.1 Hot Working

Hot workability is traditionally defined as the ability to deform a material under conditions of high temperature (greater than 0.6 of the absolute melting temperature) and relatively high strain rates (10^{-1} to 10^{4} sec^{-1}). The hot workability of a material is characterised by its hot strength (i.e. its resistance to plastic deformation) and its hot ductility (i.e. its ability to be deformed without cracking). Since the present work has not been concerned with hot ductility and as it has been reviewed elsewhere (e.g. Sellars and Tegart 1972, Harding 1973) this aspect will receive little further attention.

As will be shown in Chapter 2, much effort has been concentrated on the measurement of hot strengths which essentially govern the loads encountered in hot working processes. Much effort has also been directed towards quantitatively understanding the structural changes that occur during hot working, as will be shown in Chapter 3. Since the structure during working affects the hot strength and since both strength and structure are strongly temperature dependent, it may be concluded that a knowledge of temperatures during hot working operations is of vital importance to a full understanding of the subject. However until recently it has received little attention, and Chapter 4 will describe the progress that has been made in this area.

As the following literature review will show, much of the strength and structural data have been obtained on

laboratory simulative tests (especially tension, compression and torsion tests) and whereas such tests are capable of isolating the numerous variables that occur in practice, their value is limited unless the data are applicable to industrial processing operations. Hence in both the literature review and the description of the present research, emphasis will be placed on the methods and models available for the application of laboratory data to industrial hot working. The present research has involved the use of a small scale rolling mill and much of the following review will be biased towards the aspects of hot working directly relevant to hot rolling.

1.2 Industrial Hot Rolling

Rolling is the oldest metal working process after forging and today is the most commonly used method of deforming as-cast metals into shapes suitable for fabricating into a wide range of products. Although still primarily thought of as a shaping process, hot rolling has recently become more sophisticated because of the possibility of improving the mechanical properties of the final product by controlling the grain size. The advent of controlled rolling has therefore been largely dependent on a fuller understanding of the structural changes that occur during hot working and although controlled rolling will not be considered per se, the applicability of the principles derived from studies on a wide range of alloys will be apparent. In addition, the introduction of computer controlled rolling mills has created a demand for greater knowledge regarding the variables inherent in hot rolling. As an example, let us consider a few applications of a knowledge of hot strength. One aspect of computer control lies in the

prediction of hot rolling loads (Chapter 2) which are used to

(a) ensure that a particular pass will not overload the mill,

(b) enable the effect of mill spring to be allowed for so that products of close tolerance can be produced

and (c) enable the effect of roll distortion along its length to be corrected to give products of good shape.

In addition knowledge of roll loads is important during the design stage of a new mill and for designing suitable rolling schedules.

Although plant design and material variables differ greatly between different mills, a typical example of a rolling schedule is given in Fig.1. Also shown are typical examples of strain-time behaviour encountered in extrusion and planetary rolling. It can be seen that whereas the latter two processes are one-step processes, hot rolling consists of a series of non-isothermal, low incremental strains at a variety of strain rates. Thus it can be seen that, even neglecting the problems that can arise due to limited ductility, any investigation of hot rolling necessitates the study of the complex interactions of strain, strain rate, time, temperature, strength, structure and material variables. Fig.2 schematically shows the interactions for any particular material, assuming there are no limiting factors (e.g. the maximum strain is not limited by the temperature, strength etc.)

CHAPTER TWO

STRENGTH DURING HOT WORKING

2.1 Introduction

Over the past 20 years 4 main hot workability tests have been developed to study the strength and ductility of materials under hot working conditions. Moore (1968) has defined the information that is ideally required from such tests. Firstly it is important to know the stress required to deform the material under known conditions of temperature, strain rate and strain in order that the working equipment may be adequately designed. Secondly, it is necessary to determine the amount of deformation a material can stand under given conditions without fracturing. Thirdly, the chosen test method should ideally be able to simulate the interrupted deformation cycles that occur in practice. Finally, in order to be able to study the high temperature structure, it is necessary that the chosen test method allows the rapid cooling of specimens following a test.

Disregarding ductility measurements, which are not of direct relevance to the present study, hot working tests essentially provide stress-strain data (as a function of such variables as structure, temperature and strain rate) which, when used with a suitable theory, can be used to predict the loads developed during, and the power required for, industrial hot working processes.

2.2 Hot Workability Tests

2.2.1 Scaled Down Tests

The most reliable test is to process the material under plant conditions where variables inherent in the material (composition, size, shape and structure) and variables inherent in the working process (strain rate, stress system, temperature, friction effects)are covered. For obvious reasons such tests are expensive and as an alternative, scaled down tests in the laboratory are sometimes used. Simulation of extrusion by the use of a small scale extrusion press is a particularly good example since die face angle and lubrication can be satisfactorily simulated. Regarding rolling, Moore (1968) considers that only processes such as cogging, slabbing and plate rolling can be satisfactorily reproduced on single stand laboratory mills but Walker (1970) considers that, in spite of the disadvantages, laboratory rolling remains the best method to simulate high speed strip mills. The main problem with results from laboratory rolling is that it is difficult to scale up the effects of friction and temperature but this is because knowledge is limited about such parameters. In spite of these disadvantages laboratory rolling is a widely used testing method. Although rolling is commonly used simply for obtaining data on strength and power requirements, other workers have considered metal flow during rolling. Crane and Alexander (1963) hot rolled longitudinal grids while Orowan (1943) and Gleave and Modlen (1968) simulated rolling by using plasticene which is considered to be equivalent to a non-hardening isotropic metal.

2.2.2 Mechanical Tests

The inherent problems in scaled down tests have led other workers to develop available mechanical tests, such as tension, compression and torsion, into high temperature tests. Such tests will only be considered briefly as they have been widely reviewed elsewhere (e.g. Moore 1968, Whittaker 1973, Harding 1973, Barraclough 1974).

Hot tensile tests suffer from the onset of necking at fairly low true strains (~ 0.4) although this effect can be corrected for. Although high strain rate machines have been developed to give strain rates up to 10^3 sec^{-1} the true strain rate decreases slightly during the initial stages of the test unless this is corrected for by the use of logarithmic cams (Rossard and Blain 1959).

Hot torsion testing, in which a twisting moment is applied to a solid or tubular sample, has found world wide acceptance since high strains (up to 20), constant true strain rates (10^{-3} to 10^2 sec^{-1}) and multipass simulation are all easily obtainable (Rossard 1962, 1967, 1968, Barraclough 1974, Gittins et al 1974B).

Hot compression testing has been developed since the majority of hot working operations involve compression. Axisymmetric compression tests, in which a cylindrical specimen is compressed between flat platens, and plane strain compression tests, in which a strip sample is compressed between narrow platens, are available. Frictional effects are the main limitations in both tests (Moore 1968). Logarithmically shaped cams have to be used to obtain constant true strain rates and double acting cam plastometers allow the simulation

of double deformation sequences (Dunstan and Evans 1969). More recently, servo hydraulic systems have been used to obtain constant true strain rates (Djaic and Jonas 1972) and a computer controlled servo hydraulic plane strain compression testing machine has been installed in the Sheffield University Metallurgy Department. This allows simulation of multipass rolling schedules and additionally, simulation of the constantly varying strain rate which occurs during any particular rolling pass (Sellars 1976).

The important fact to note about these tests is that when the stress-strain data are converted to uniaxial stress-true strain curves the results are comparable (Jonas et al 1969). This conclusion has been confirmed by Sah (1976) who has obtained excellent agreement between the data obtained from tension, torsion, plane strain and axisymmetric compression of lead.

2.3 Stress-Strain Behaviour

Typical flow curves obtained by the above test methods are given in Fig.3 for an 18-8 stainless steel. It can be seen that, with increasing strain ε, the equivalent tensile stress $\bar{\sigma}$ increases during the initial work hardening stage to a maximum value and then falls to a steady state flow stress. This behaviour is found in a wide range of metals and single phase alloys (Sellars and Tegart 1972). The stress at a given strain and the strain to the peak stress increase with increasing strain rate and decreasing temperature.

There have been many attempts to fit empirical equations to both the work hardening and steady state regions of the curve. Typical equations amongst those listed by Sellars and Tegart (1972) and Barraclough (1974) for the work hardening region are

$$\sigma = K\varepsilon^{m} \tag{2.1}$$

$$\sigma = \sigma_o + B\varepsilon^{m} \tag{2.2}$$

$$\sigma = \sigma_o + B\left[1 - \exp(-C\varepsilon)\right]^{m} \tag{2.3}$$

$$\sigma = A\left[1 - \exp.(-C\varepsilon^{mn})\right]^{1/n} \tag{2.4}$$

where A, B, C, K, m, n, σ_o are strain rate and temperature dependent constants. Such relationships can also be written in terms of the temperature compensated strain rate or Zener-Holloman parameter Z.

$$Z = \dot{\varepsilon} \exp \frac{Q}{RT} \tag{2.5}$$

where $\dot{\varepsilon}$ is the strain rate

Q is the activation energy for deformation

R is the gas constant

T is the absolute temperature

The use of this parameter leads to a reasonable superimposition of torsion curves at equivalent Z values, as shown in Fig.4. Sellars and Tegart (1972) suggested equations of the form

$$\sigma = (BZ)^{1/n}\ \varepsilon^{m} \tag{2.6}$$

$$\sigma = \frac{\varepsilon^{m}}{\beta}\ \ln\ BZ \tag{2.7}$$

$$\sigma = \frac{\varepsilon^{m}}{\alpha}\ \sinh^{-1}\ (BZ)^{1/n} \tag{2.8}$$

and commented that the purpose of such equations was to allow experimental data to be used in hot working calculations even

though the data were not originally obtained for the exact deformation conditions of interest. Whittaker et al (1971) fitted an empirical relation by regression analysis:

$$\sigma = A + B \ln \varepsilon + T (C + D \ln \varepsilon + E \ln \dot{\varepsilon} + F \ln \varepsilon \ln \dot{\varepsilon}) \quad (2.9)$$

Regarding the steady state region of the curve Sellars and Tegart (1966) showed that the following empirical relationship applied to high temperature data over 10 orders of magnitude of strain rate:

$$Z = \dot{\varepsilon} \exp \frac{Q}{RT} = A (\sinh \alpha \sigma)^n \quad (2.10)$$

where A, n, α are temperature independent constants, whose values could be obtained from the limiting forms of the equation at low and high stress values.

Barraclough (1974) and Barraclough and Sellars (1974) have recently carried out extensive torsion testing on a low alloy steel and an 18-8 stainless steel (type AISI 304/EN 58E), the results of which will be covered in detail since the present research has been a continuation of this work. For the stainless steel they came to the following conclusions:

(i) The work hardening range extended to strains of between 0.5 and 0.7 (over 6 orders of magnitude of Z). Since these strains are above those usually found in typical rolling passes, it may be concluded that steady state strains are rarely achieved.

(ii) The peak stress was related to Z by a power law relationship with a stress exponent (n) of 5.75 when the stress was below 100 N mm^{-2}. Above this level an exponential relationship applied with β as 0.047, Fig.5.

No significant changes in n and β were found if the stress to a constant strain, rather than the peak stress, was used.

(iii) The activation energy was found to be 410 kJ/mole (compared with 414 kJ/mole (Rossard and Blain 1958, Nair 1969) and 402 kJ/mole (Muller 1967)) and independent of restoration mechanism and strain.

The effect of changing deformation conditions (i.e. changing Z during a test) was also investigated: this is relevant to rolling since the strain rate changes during a pass (Section 2.4.6). The following conclusions were drawn:

(i) An instantaneous change in Z produced a strain lag $\Delta\varepsilon$ before the stress predicted from the equation of state is attained, Fig.6, the strain to return to equilibrium being greater when the strain rate was increased.

(ii) The lag $\Delta\varepsilon$ was a function of the strain, the magnitude of the change in Z and the final value of Z.

(iii) Under conditions of continually changing Z, the equation of state is limited to a maximum value of $dZ/d\varepsilon$ and when this is exceeded, a 'history' effect (i.e. a cumulative error in stress prediction) should occur. When this limit is not exceeded an equation of state can successfully predict σ- ε curves in cases of continually changing Z or of partially recrystallised structures.

(iv) On application to typical hot rolling passes, an equation of state should be applicable most of the

time, (e.g. at least 90% of a 0.3 strain pass) but beyond this a cumulative history effect should develop resulting in a final flow stress significantly higher than the value predicted by the equation of state. It was pointed out that this would affect the structure of the material on exit from the rolls and possibly the subsequent static recrystallisation kinetics.

2.4 Application of Hot Strength Data

2.4.1 Introduction

Having obtained the hot strength data for any particular material they are then applicable to the prediction of working forces and power requirements for particular hot working processes. Theories have been developed to predict these parameters for the majority of processes but rolling has received the most attention. The following sections will consider the development of rolling theories from the simple approach of von Kármán (1925) through to the more comprehensive approach of Orowan (1943) and its subsequent simplifications by several authors to make it suitable for rapid on-plant calculation and, more recently, for computer control of rolling mills.

Although the general principles are the same in hot and cold rolling theories the latter will not be considered here as good reviews have been given by Ford (1963) and Foster and Marshall (1975). It should also be noted that no attempt will be made to consider triaxial strain theories or the empirical formulae that are applicable for shapes other than

flats as Economopoulos (1975) has recently listed these.

2.4.2 Analogy with Plane Strain Compression

A commonly used starting point for discussing rolling theory is to consider the analogy of plane strain compression of a slab since this, in a simple manner, introduces the concepts of friction and inhomogeneous deformation during rolling. If perfectly frictionless conditions are present between slab and platens then uniform (i.e. homogeneous) deformation occurs and compression occurs under a uniform pressure equal to the yield stress in plane strain, S. Using von Mises distortion energy criterion for yielding,

$$S = 2k = \frac{2}{\sqrt{3}} Y = 1.155Y \qquad (2.11)$$

where k is the yield stress in pure shear and Y is the yield stress in uniaxial tension.

However when friction occurs between platens and slab, zones of material are created which are unable to deform freely, i.e. inhomogeneous deformation occurs. In this case, Dieter (1961) shows that consideration of the equilibrium of forces on any element, gives a pressure distribution as

$$p = 1.15Y \exp\left[\frac{2\mu(a-x)}{h}\right] \qquad (2.12)$$

which is shown in Fig.7. The shaded portion of the pressure diagram, known as the friction hill, is a measure of the additional work necessary due to friction. In this case Coulomb's law of sliding friction was used i.e. shear stress at slab/platen interface was given by the product of the friction coefficient and the normal stress. Dieter (1961) also considers the case of plane strain forging with sticking

friction (i.e. the shear stress at the interface is constant and equal to the shear strength of the metal in plane strain) and shows that a linear relationship results

$$p = 1.155Y \left(1 + \frac{a-x}{h}\right) \qquad (2.13)$$

These equations can be integrated to give the total compressive load and, by analogy, an approximate value of the rolling load can be obtained if the slab width in compression (2a) is made equal to the projected length of arc of contact in rolling.

2.4.3 Friction in Rolling

Considering the velocity conditions in the roll gap, Fig.8, at the entry plane the material is moving slower than the rolls and frictional forces (F) try to drag the material into the roll gap and on exit, the converse situation is true. There is thus a neutral plane within the roll gap where the velocities of rolls and material are equal and by analogy with compression there are zones of non-uniformly deformed material and a friction hill.

In cold rolling, which is usually carried out with lubricated, polished rolls on material which usually has a fairly high yield stress in shear, it is commonly accepted that slipping friction takes place (Orowan 1943). However, in hot rolling, which is usually carried out with rough unlubricated rolls on a relatively plastic material, it is commonly assumed that the frictional forces are high enough, and the shear yield stress low enough, to produce sticking friction. Crane and Alexander (1963) showed that during hot

rolling of a grid, the vertical lines curved round in the direction of rolling and became tangential to the surface under entry conditions and that a reversal of curvature occurred on exit. Although this demonstrated the presence of sticking friction it did not prove that it was present throughout the roll gap and the present general opinion (e.g. Denton and Crane 1972) is that partial slipping does occur, particularly at entry and exit.

El-Kalay and Sparling (1968) have noted the possible methods of friction measurement but cast doubts on the validity of such methods. It is reasonable to conclude that, along with temperature, friction remains one of the unknown quantities in the roll gap.

2.4.4 Rolling Theories

As a result of the complexity of the situation in the roll gap, the early rolling theories, starting with those of Siebel (1924, 1925) and von Kármán (1925) made the following assumptions:

(i) No elastic deformation of the rolls i.e. a circular arc of contact.

(ii) No lateral spread i.e. plane strain deformation.

(iii) Plane sections remained plane i.e. homogeneous deformation.

(iv) A constant yield stress during the pass: this requires that, in cold rolling, there is no strain hardening and that, in hot rolling, there is no effect of strain rate on yield stress.

(v) Negligible elastic deformation in the stock; this coupled with assumption (iv) implies a rigid-perfectly plastic material.

(vi) Von Mises plastic yielding criterion holds.

(vii) Many authors assumed slipping friction and all detailed calculations assumed dry friction although Nadai (1939) considered the alternatives of purely viscous friction and of a constant frictional drag.

By considering the pressures acting on a small element in the roll gap, von Kármán (1925) derived equations to describe the distribution of the vertical pressure from which the roll load could be obtained by integration. As Dieter (1961) states, the mathematics are "rather formidable" but Trinks (1937) provided a graphical solution by assuming a constant yield stress and a parabolic arc of contact. This solution and others are discussed in detail by Underwood (1952). In the introduction to his paper, Orowan (1943) mentions the work of Siebel and Lueg (1933) who measured the roll pressure distribution through the roll gap and comments that in cases of poor agreement with theory it was not clear which of the simplifying assumptions was incorrect and even cases of good agreement may be due to the simplifications cancelling out. Ekelund (1933) allowed for the influence of strain rate on the mean yield stress and allowed for friction by assuming slipping on the entry side and sticking on the exit side although this is far from the truth. Ekelund presented empirical equations for the 'viscosity' of the steel, the coefficient of friction and the 'static' yield stress and Rowe (1965) comments that it is a generally useful equation.

Having criticised most of the previous work, Orowan (1943) set out to produce a rolling theory devoid of mathematical and physical approximations which, as he realised, was too complex to use in rolling mill practice but which he hoped would be a 'yardstick' against which other theories could be judged. He deduced a numerical or graphical method for computing the pressure distribution and hence the roll load, torque and power consumption. His method allows for any variation in yield stress and coefficient of friction to be taken into account. He allowed for inhomogeneous deformation by simplifying the problem to one of compression between inclined platens and used the treatment of Nadai (1939) and Prandtle (1923) for both sticking and slipping friction. Orowan's theory was little used until Hockett (1960) used a computer for its solution and he concluded that, allowing for roll flattening, Orowan's equations gave very accurate results compared with measured results for uranium sheet.

The accurate equations were later modified by Orowan and Pascoe (1946) who assumed sticking friction throughout the roll gap. They considered that such an assumption introduces only a small error except in the case of hot rolling of thin strip or sheet. They showed that, when the initial stock width W is not less than 6 times the initial stock thickness h_1, the load P is given by

$$P = S\,W\,\sqrt{R\,\Delta h}\left(\frac{\pi}{4} + \frac{\sqrt{R\,\Delta h}}{4h_1}\right) \qquad (2.14)$$

where S is the plane strain compressive yield stress, R the roll radius and Δh the draft, i.e. $\Delta h = h_1 - h_2$.

For cases where the width is between 2 and 6 times the thickness, they showed that

$$P = S\,\bar{W}\,\sqrt{R\Delta h}\left[0.8 + 0.5g - \frac{\bar{h}}{3\,\bar{W}g}\,(g - 0.2)^3\right] \qquad (2.15)$$

where $\bar{W}$ = mean width = $\dfrac{2\,W_2 + W_1}{3}$

W_1, W_2 = initial and final widths

g = relative length of arc of contact = $\sqrt{\dfrac{R\,\Delta h}{2h_1}}$

$\bar{h}$ = mean stock thickness = $(2h_1 + h_2)/3$

Finally if the width was less than twice the thickness they showed that

$$P = S\,\bar{W}\,\sqrt{R\,\Delta h} \qquad (2.16)$$

Equations were also given for the roll torque.

Sims (1954) later combined elements of von Kármán's and Orowan's approaches to produce a theory that was much simpler to apply. Sims used von Kármán's equilibrium of forces equation which gives

$$p_n\,(\tan\theta \pm \mu)\,R'd\theta - \frac{1}{2}\,d\,(th) = 0 \qquad (2.17)$$

where θ = angular co-ordinate from the plane of exit, Fig.9

t = horizontal stress

p_n = normal roll pressure

h = thickness at any point

R' = elastically deformed roll radius

μ = coefficient of friction

+,- refer to conditions near the exit/entry plane.

Sims then assumed sticking friction over the whole contact area so that

$$\mu p_n = S/2 \tag{2.18}$$

where S is the plane strain yield stress.

By substitution and by use of the small angle approximation ($\theta = \sin\theta = \tan\theta$), equation 2.17 becomes

$$\frac{d\,T}{d\,\theta} = 2\,R'\,p_n\theta \pm R'\,S \tag{2.19}$$

where T is the horizontal force per unit width acting over the element and is given by Orowan (1943) as

$$T = h\left(p_n - \frac{\pi}{4}S\right) \tag{2.20}$$

Sims (1954) then showed that the equations

$$\frac{p_n^+}{S} = \frac{\pi}{4}\left(1 + \ln\frac{h}{h_2}\right) + \sqrt{\frac{R'}{h_2}}\,\tan^{-1}\left[\sqrt{\frac{R'}{h_2}}\,\theta\right] \tag{2.21}$$

$$\frac{p_n^-}{S} = \frac{\pi}{4}\left(1 + \ln\frac{h}{h_1}\right) + \sqrt{\frac{R'}{h_2}}\,\tan^{-1}\left(\alpha\sqrt{\frac{R'}{h_2}}\right) - \tan^{-1}\left(\theta\sqrt{\frac{R'}{h_2}}\right) \tag{2.22}$$

hold near the exit and entry respectively where α is the contact angle (radians). The co-ordinates of the neutral point (h_n, ϕ) can be found by equating these expressions. By assuming that the vertical pressure equalled the normal roll pressure and by integration over the arc of contact Sims obtained an expression for the roll force as

$$P = S\,W\,\sqrt{R'\,\Delta h}\;\;Q_p \tag{2.23}$$

where Q_p, the function that allows for the contribution of friction and inhomogeneous deformation, is given by

$$Q_p = \left[\frac{\pi}{2}\sqrt{\frac{1-r}{r}}\tan^{-1}\sqrt{\frac{r}{1-r}} - \frac{\pi}{4} - \sqrt{\frac{1-r}{r}}\sqrt{\frac{R'}{h_2}}\ln\frac{h_n}{h_2} + \frac{1}{2}\sqrt{\frac{1-r}{r}}\sqrt{\frac{R'}{h_2}}\ln\left(\frac{1}{1-r}\right)\right] \tag{2.24}$$

Sims also gave an expression for the torque as

$$G = 2\ W\ R\ R'\ S\ \ Q_g \qquad (2.25)$$

where $Q_g = \frac{\alpha}{2} - \phi$

Sims calculated values of Q_p and Q_g for a wide range of rolling conditions but Larke (1963) provided corrected values. Sims assumed that, for the load calculation, the mean yield stress used could be given by

$$S = \bar{S}_p = \frac{1}{\alpha} \int_0^{\alpha} S.d\theta \qquad (2.26)$$

whereas for the torque calculation

$$S = \bar{S}_g = \frac{1}{r} \int_0^{r} S.de \qquad (2.27)$$

where e is the fractional reduction at any point $= \frac{h_1 - h}{h_2}$

Cook and McCrum (1958) modified Sims' method to make it suitable for rapid calculation by rewriting his equations as

$$P = WR'\ J_p\ C_p \text{ and } G = 2\ RR'W\ J_g\ C_g \qquad (2.28)$$

where $$J_p = \sqrt{\left(\frac{1+r}{1-r}\right)}\ \bar{S}_p\ ,\ C_p = \sqrt{\frac{h_2 r}{R'(1+r)}}\ \ Q_p \qquad (2.29)$$

$$J_g = \sqrt{\left(\frac{1+r}{1-r}\right)}\ \bar{S}_g\ ,\ C_g = \sqrt{\frac{1-r}{1+r}}\ \ Q_g \qquad (2.30)$$

It can be seen that C_p and C_g are purely geometrical factors. Cook and McCrum presented values of J_p and J_g for a wide variety of steels as a function of reduction, strain rate and temperature using results obtained by Cook (1957) on a cam plastometer. Their equations and data are probably the most widely used of the rolling theories since they are the optimum balance between accuracy and speed of computation.

Tarokh and Seredynski (1970) have also modified Sims' equations to make them more easy to use but no less accurate. In addition they gave the following mathematical expression for the yield stress in which the constants a_o, a_1 etc. were found by multiple regression on a large volume of data:

$$S = a_o + \frac{a_1}{T^2} + a_2\sqrt{r} + a_3\frac{\sqrt{r}}{T} + a_4\sqrt{r}\,\log\dot{\varepsilon} \qquad (2.31)$$

With the exception of the development of slip line field theories (see following section) the recent trend has been towards semi-empirical equations. Typical of these is that due to Izzo (1974) who calculated the load from the product of the projected contact area and the mean roll pressure. The latter term consisted of the yield strength (fn.(h_2/R, % redn.)) and 4 other terms, all functions of T and h_2/R. These equations were designed for rapid computer/graphical calculations and considered to be accurate to within 10%. A few examples of empirical expressions for computer controlled rolling mills are given in Section 2.4.11.

Finally, mention should be made of a popular method of calculating roll torque. It can be quickly calculated from the product of the mean load and the lever arm i.e. the distance from the line of action of the mean load to the line joining the roll centres. The lever arm ratio (lever arm : projected arc of contact) can be taken as 0.5 for a rough calculation. Full details of the method are given by Larke (1963) who also derives equations for calculating the energy consumed, and Wright and Hope (1975) have given experimentally measured values of the lever arm ratio.

2.4.4.1 Slip Line Field Theories

Owing to the simplifying assumptions and resultant inaccuracies in traditional rolling theories, attempts have been made to apply slip line field theory to hot rolling. Green and Wallace (1962) developed a shear plane theory which is based on localised deformation during the rolling process. They presented accurate and simplified forms of their equations but, most usefully gave functions equivalent to the C_p and C_g functions of Cook and McCrum (1958).

Ford and Alexander (1964) extended the slip line theory field solution of Alexander (1955) and showed that

$$P = W\bar{k}\, L \left[\frac{\pi}{2} + \frac{L}{h_1 + h_2}\right] \qquad (2.32)$$

$$\text{and } G = W\bar{k}\, L^2 \left[\frac{\pi}{2} + \frac{2}{3} L \frac{(h_1 + 2h_2)}{(h_1 + h_2)^2}\right] \qquad (2.33)$$

where L is the arc of contact and $\bar{k}$ the mean shear yield stress. The theory is based on plane strain deformation of a plastic-rigid material (i.e. infinite elastic modulus and zero work hardening) and essentially consists of satisfying the velocity and stress boundary conditions within the roll gap. Renouard (1972) used a similar approach and derived comparable equations for different ranges of mean height to length of arc of contact ratios.

El-Kalay and Sparling (1968) developed a model which allowed for slipping friction near the entry and exit planes and sticking friction near the neutral plane. Denton and Crane (1972) analysed the available slip line fields and the theory of Sims (1954) and came to the conclusion that they all gave similar results. Hence it is not clear what advantages

there are in the considerably complex slip line field theories. Nevertheless a computer solution has been developed by Sparling (1976) who is at present computing results for the whole range of rolling and hopes to produce easily applicable functions similar to the ones developed by Cook and McCrum (1958).

2.4.5 Deformation of the Rolls

In many of the above equations mention has been made of the elastically deformed roll radius R'. The most popular method used to calculate this is due to Hitchcock (1935) who replaced the actual roll pressure distribution with an elliptical distribution giving the same total load. He proposed an equation

$$R' = R\left(1 + 2\frac{cP}{\Delta h w}\right) \qquad (2.34)$$

where c is a constant (0.0223 mm^2/kN for cast iron rolls, 0.0108 mm^2/kN for steel rolls, 0.0123 mm^2/kN for chill cast iron rolls). This equation is used by successively redetermining the load and roll radius until the required degree of accuracy is obtained as described by Larke (1963). High speed photography by Kobasu and Schultz (1968) suggested that, in cold rolling, the deformed arc of contact was longer than that given by Hitchcock's equation. Many workers neglect the correction during hot rolling although others (e.g. Gupta and Ford 1967, Ford and Alexander 1964) consider it to be important, especially at the lower temperature end of hot working.

2.4.6 Strain Rate during Rolling

Section 2.3 has demonstrated the dependence of hot strength on the strain rate and several equations are available for calculating the latter. Larke (1963) has shown that the instantaneous strain rate at any point is given by

$$\dot{E}_{st} = \frac{2V \sin\theta}{h_2 + 2R\,(1-\cos\theta)} \qquad (2.35)$$

for sticking friction and

$$\dot{E}_{sl} = \frac{2Vh_n \cos\phi \tan\theta}{\left[h_2 + 2R\,(1-\cos\theta)\right]^2} \qquad (2.36)$$

for slipping friction. Here V is the peripheral roll velocity and other quantities as defined in Fig.9 (angles in degrees). These expressions show that the strain rate is a maximum at entry and falls to zero on exit.

It is common practice to employ a mean strain rate. For sticking friction

$$\bar{\dot{E}}_{st} = \frac{\ln\left(\frac{h_1}{h_2}\right) V}{\text{contact length}} = V \ln\left(\frac{h_1}{h_2}\right) \cdot \frac{360}{2\pi R\theta} \qquad (2.37)$$

where $$\theta(\text{degrees}) = \cos^{-1}\left(1 - \frac{\Delta h}{2R}\right) \qquad (2.38)$$

In practice this is often approximated to

$$\bar{\dot{E}}_{st} = V \sqrt{\frac{1}{R\,\Delta h}} \ln\left(\frac{h_1}{h_2}\right) \qquad (2.39)$$

In the case of slipping friction, Larke (1963) gives

$$\bar{\dot{E}}_{sl} = \frac{V h_n \cos\phi}{h_1 h_2} \sqrt{\frac{\Delta h}{R}} \qquad (2.40)$$

Orowan (1943) and Ford and Alexander (1964) have given other alternatives. Cornfield and Johnson (1971) have theoretically analysed the strain rate distributions for typical passes as described in the following section.

2.4.7 Effect of Temperature

Section 2.3 has shown the marked dependence of hot strength on temperature but no rolling theory has been proposed to allow for the varying temperature during hot rolling. This is partly due to the added complexity that this would entail and partly due to the lack of detailed knowledge regarding temperature distribution during rolling (see Chapter 4). Tarokh and Seredynski (1970) showed that the equivalent yield stress, S, of a slab of N geometrically identical layers but at different temperatures was given by

$$S = N\left[\sum_{i=1}^{N} \frac{1}{S_i}\right]^{-1} \qquad (2.41)$$

where S_i is the yield stress of the i^{th} layer (i = 1 to N). They calculated the equivalent yield stress for a slab composed of layers at 970, 975, 985 and 1000°C using data given by eqn.2.31 and found a yield stress of 15.3 kN/cm^2 compared to 16 kN/cm^2 for a slab with a uniform temperature equal to the above surface temperature. However they did not appear to allow for the temperature gradients that develop during the pass itself.

They assumed that the extent to which each layer deformed depended on its temperature. This is contrary to the findings of Arnold and Whitton (1959) who cold rolled a hard metal between two pieces of soft metal (analogous to rolling a slab with a step temperature change in it) and showed that the reduction was shared equally between both if the Vickers Hardness ratio of hard:soft was less than 3. Chelyshev et al (1971) rolled slabs with a through thickness

temperature gradient and related the measured strain ratio of the hot and cold side ($\varepsilon_h/\varepsilon_c$) with the flow stress ratio (S_f^h/S_f^c). They showed that the relationship between these ratios became linear only at high reductions e.g. at 40% reduction

$$\frac{\varepsilon_h}{\varepsilon_c} = 1.85 - 0.85 \frac{S_f^h}{S_f^c} \qquad (2.42)$$

Cornfield and Johnson (1971) computed the theoretical strain, strain rate and hydrostatic stress distributions during hot rolling for slabs with (a) uniform temperatures (b) cold centre - hot surface (often produced by induction heating) (c) hot centre - cold surface (as occurs during normal air cooling). Their results, Fig.10, showed the different strain distributions especially between profiles (b) and (c), the former leading to very heavy shearing of the surface layers. Also shown in Fig.10 are the distributions of effective strain rate and as before, a slab with a cold centre shows the most inhomogeneous deformation.

2.4.8 Spread in Hot Rolling

Even though the foregoing rolling theories have assumed plane strain deformation it is well known that spread (i.e. deformation parallel to the roll axes) often occurs in practice. Equations have been developed to predict this and consist of empirical relationships fitted to measurements. The formulae of Wusatowski (1955), Hill (1950) and Sparling (1961) were considered to be progressively more accurate by Helmi and Alexander (1968) who proposed an equation:

$$\frac{\ln \frac{W_2}{W_1}}{\ln \frac{h_1}{h_2}} = 0.95 \left(\frac{W_1}{h_1}\right)^{-1.1} \exp\left(-0.707 \frac{W_1}{\sqrt{R \Delta h}} \left(\frac{W_1}{h_1}\right)^{0.971}\right) \qquad (2.43)$$

The earlier equations were essentially of the same form.

Beese (1972) found that the maximum spread could be obtained from

$$\frac{\ln \frac{W_2}{W_1}}{\ln \frac{h_1}{h_2}} = 0.61 \left(\frac{h_1}{W_1}\right)^{1.3} \exp\ -0.32\left(\frac{h_1}{\sqrt{R \Delta h}}\right) \qquad (2.44)$$

which was suitable for $W_1 : h_1$ ratios of between 3 and 16. In addition to the influence of W_1, h_1, R and % reduction, it might be expected that the flow stress and temperature gradients during a pass might affect the spread. Any such influences are probably hidden in the values of the constants in the above equations.

2.4.9 Measurement of Load and Torque

Rolling loads are usually measured by electric resistance strain gauges in the form of load cells inserted between the screwdown mechanism and top roll chocks (e.g. Stewartson 1954, Larke 1963, Bowler 1963). The recent development of (computer controlled) hydraulic screwdown mechanisms has enabled rolling loads to be deduced from the hydraulic pressure (Sparling 1976). Torque is conventionally measured from the twisting moment developed in the drive shafts by using strain gauges cemented to the shaft in a Wheatstone

bridge arrangement. The input and output currents can be made via slip rings (Ford 1946) or more recently, the output from strain gauges requiring no input voltage can be made via a short range telemetry system (Wright and Hope 1975). The torque meters can be calibrated in situ by applying a known moment using a lever arm inserted into the coupling joints (Ford 1946) or ex situ on a torsion machine (Bowler 1963). To obtain the pure rolling torque allowance has to be made for the frictional forces in the roll neck. This can be calculated if the friction coefficient is known (e.g. Underwood (1946) gives values for a wide range of bearings) or can be measured by screwing the rolls together and measuring the torque at constant load for different roll speeds (Bowler 1963).

2.4.10 Comparison Between Theory and Practice

Many authors have measured loads and torques on both laboratory and production mills as described above. Larke (1963) used available results and concluded that measured loads agreed with Sims' theory within ± 15% 90% of the time. A similar conclusion was drawn by Stewartson (1954). Gittins et al (1974A) concluded that, after allowing for temperature changes, their torsion and rolling results and the cam plastometer results of Cook and McCrum (1958) all gave equivalent results. Bleloch (1969) concluded that the equations due to Ford and Alexander (1964) gave the best values for wide stainless plate and strip

rolling. Helmi and Alexander (1968) considered their experimental results to agree best with the slip line field solutions of Ford and Alexander (1964) whereas Denton and Crane (1972) showed that, even allowing for temperature effects, perfect agreement between theory and practice required variable frictional conditions and a variable inhomogeneity factor and concluded that an adequate analytical theory was out of reach. Economopoulos (1975) concluded that all such comparisons were difficult to summarise and that none of the present theories was numerically accurate and their chief advantage lay in their ability to qualitatively predict the effect of various parameters.

2.4.11 Application of Theories to Computer Control

The advent of computer controlled rolling mills has encouraged the use of simple equations for predicting loads etc. Schultz et al (1965) used an equation of the form

$$\ln \text{pressure} = b_o + b_1 \ln \frac{R}{h_2} + b_2 \ln \frac{\Delta h}{h_2} + b_3 \ln \frac{\Delta h}{h_2} \ln \frac{R}{h_2} + b_4 \frac{T}{1000} + b_5 \frac{T}{1000} \ln \frac{\Delta h}{h_2} + b_6 \ln \frac{\Delta h}{h_1} \ln \frac{R^2}{h_1^2} + b_7 T^2 \qquad (2.45)$$

Buxton and Sutton (1969) have used a similar approach to fit equations to the data of Cook and McCrum (1958) for use in an on-line computer control programme. Comparison with laboratory rolling data showed errors which increased with temperature which they considered was due to the inadequacy

of Cook and McCrum's data and also the unknown temperature changes during rolling. Multiple regression analysis allowed the parameters to be adjusted. Wright and Hope (1975) exposed similar errors and put forward an empirical correction factor. Wilmotte et al (1973B) developed a simple model for both rolling load and power which was designed for on-line computer control and whose coefficients could be updated coil by coil. Other examples of theories for computer control have been given by Darnall (1968), Beadle et al (1970) and Muzalevskii et al (1970). Economopoulos (1975) has listed others.

CHAPTER THREE

STRUCTURE DURING HOT WORKING

3.1 Introduction

It has been shown in Chapter 2 that high temperature stress-strain curves are characterised by an initial work hardening stage followed by a constant or decreasing stress level. The latter steady state stage of deformation arises from the work hardening rate being balanced by the work softening rate, the latter being due to dynamic recovery or recrystallisation. It is well known that at high temperatures, restoration processes can also occur statically, that is, after a deformation or deformation sequence is complete. Table 1 classifies some common metals and alloys with regard to the softening processes that can occur during hot working and recent reviews (Jonas et al 1969, Sellars and Tegart 1972, Sellars and Whiteman 1974) have described the extensive work in this field and have shown how the interaction of dynamic and static restoration mechanisms control the final structure of hot worked products.

In this chapter it is proposed to summarise briefly some aspects of the restoration processes with particular regard to the data obtained for 18-8 stainless steel and its application to multipass rolling schedules.

3.2 Dynamic Restoration Processes

3.2.1 Dynamic Recovery

It is well established that during the cold working of pure cubic metals dislocation tangles are formed which link up into boundaries separating areas of low dislocation density. During high temperature deformation the ragged cell boundaries develop into regular subgrains within the deformed grains at strains below the peak stress. Recovery is therefore essentially a process of dislocation density reduction which can consist of a combination of annihilation of unlike dislocations, straightening of curved dislocations and sub-boundary formation (polygonisation). In addition there is the possibility of large angle grain boundary formation by subgrain growth. Such processes occur homogeneously throughout the material (Stüwe 1968). In the steady state region, the subgrains remain equiaxed and with a constant size (d) which is uniquely related to the applied stress σ, (Jonas et al 1969):

$$\sigma = \sigma_o + k\, d^{-m} \qquad (3.1)$$

where σ_o, k and m are constants. Their values and other possible relationships have been examined by Whittaker (1973), and Barraclough (1974) has cited the evidence which shows that the equilibrium subgrain size increases with increasing temperature and decreasing strain rate.

Since the subgrain size remains constant, the subgrain boundaries must be mobile and climb is necessary for this. Jonas et al (1969) suggest that large subgrains grow

at the expense of smaller ones and new boundaries form within the growing subgrains, thus setting up a dynamic equilibrium in which the rate of boundary annihilation is balanced by the rate of boundary formation. McQueen et al (1967) and others have suggested that a continuous repolygonisation process maintains an equiaxed structure at high strain rates since sub-boundary migration was not expected to be fast enough under these conditions. In this case they suggested that sub-boundaries are continuously disrupted by the dislocation flux and then reform at an equilibrium spacing governed by the applied stress. However, later work by Hartley (1972) showed that migration was fast enough to maintain an equiaxed substructure at high strain rates.

3.2.2 Dynamic Recrystallisation

Recrystallisation is usually defined as the replacement of an unstable strained grain structure by new strain free grains and as Stüwe (1968) points out this is usually a heterogeneous process. The presence of dynamic recrystallisation has long been accepted in creep but it has been a matter of controversy whether it can occur at the high strain rates encountered in hot working. The opposing arguments have been detailed by Barraclough (1974) and the main objection appears to be that static recrystallisation could occur between the end of the test and before, or during, quenching. However, torsion specimens quenched during deformation (McQueen and Bergerson 1972) showed a recrystallised structure and also showed that the statically recrystallised

grain size was approximately three times the dynamically recrystallised grain size. Glover (1969) and Sah (1970) also showed the presence of dynamic recrystallisation and that it begins shortly before the peak stress and is complete when the final steady state stress level is reached.

Dynamic recrystallisation is commonly associated with a low stacking fault energy and thus 18-8 austenitic stainless steel would be expected to dynamically recrystallise. This has been confirmed by Keown (1973) who showed a sequence of dislocation rearrangement, polygonisation, dynamic recrystallisation and repolygonisation with increasing temperature in a type 304 stainless steel. Dynamic recrystallisation was shown to occur at temperatures greater than 1200°C (at a strain rate > 6 sec^{-1}) whereas Ohtakara et al (1972A, 1972B) presented evidence for dynamic recrystallisation above $\sim 0.8\ T_m$ (1063°C). Other evidence has been presented by Müller (1967), Capeletti et al (1972), Pethen and Honeycombe (1973) and Barraclough (1974).

Only limited work has been carried out regarding the mechanism of dynamic recrystallisation. Richardson et al (1966) suggested nucleation by grain boundary bulging whereas Nicholson (1968) and Sah (1970) observed intragranular nucleation as well as boundary nucleation. Barraclough (1974) only observed grain boundary nucleation and growth along grain boundary regions and into grains in an 18-8 stainless steel.

The grain size has been found to be a function of the high temperature flow stress and independent of the temperature and Barraclough (1974) found a power law relationship

between grain size and peak stress with an exponent of -0.73.

Luton and Sellars (1969) have developed a model which predicts the stress-strain and recrystallisation behaviour in a dynamically recrystallising material. In their model the material work hardens until a critical strain (ε_c) is reached at which point the material begins to recrystallise. The form of the stress strain curve is determined by the relative values of ε_c and ε_x, the strain to a large % recrystallised. They showed, Fig.11, that when $\varepsilon_x < \varepsilon_c$, recrystallisation would be complete before the critical strain to initiate the next cycle of recrystallisation is reached and so discrete recrystallisation cycles and resultant stress cycles are observed. However, when $\varepsilon_x > \varepsilon_c$ then successive recrystallisation cycles are initiated before the previous cycle is complete which leads to a single peak after which the deformation appears uniform. Glover and Sellars (1973) refined this model and computer predicted stress-strain curves. Sah (1970) used a similar technique but allowed for heterogeneous recrystallisation along the gauge length of a torsion specimen by considering randomly arranged adjacent discs of recrystallised and unrecrystallised material.

In addition to structural evidence it is possible to demonstrate the transition from dynamic recovery to recrystallisation from the change in activation energy for hot working with strain rate. Sellars and Tegart (1966) examined the results of many workers and showed that

the activation energy for group A materials (Table 1) was constant over many orders of magnitude of strain rate whereas group B materials showed a significantly higher activation energy at higher strain rates. This was related to the activation energies for dynamic recovery and recrystallisation respectively.

To conclude this brief summary of dynamic recrystallisation it is important to stress that it does not begin until just before the peak stress and a consideration of stress-strain curves for 18-8 stainless steel (e.g. Fig.4) shows that during rolling it is unlikely to occur at reductions less than 30 to 40%. It is unlikely that such reductions would be achieved in a single rolling pass due to this steel's relatively high hot strength and low ductility but the necessary strains may be achieved in a multipass schedule where static recrystallisation is not complete between passes.

3.3 Static Restoration Processes

3.3.1 Static Recovery

Static recovery appears to have received relatively little attention compared with static recrystallisation. Table 1 shows that whereas group A materials statically recover and then recrystallise, group B materials (including 18-8 stainless steel) only undergo limited static recovery prior to recrystallisation. Static recovery can be demonstrated by the small decrease in room temperature hardness as the post-deformation holding time increases and is due to

the increased substructural perfection (e.g. Farag et al 1968). It should be noted that this method is only suitable where the specimens can be rapidly quenched and only for steels that show no transformation on cooling (Capeletti et al 1972). The latter problem can be overcome by a direct method involving the measurement of the changes in peak or yield stress that occur during interrupted annealing for different times between double deformation tests (Djaic and Jonas 1972, Whittaker 1973). Static recovery is shown by a small change in yield or peak stress on redeforming whereas the onset of static recrystallisation is shown by a much larger change, Fig.12.

Static recovery in 18-8 austenitic stainless steel is clearly shown by the hardness measurements of Kozasu and Shimizu (1971), Fig.13, especially at low temperatures and low strains where recrystallisation is discouraged. The results of Barraclough (1974) show a similar trend and he notes that recovery continues into the early stages of recrystallisation. There are few data on recovery rates but Fig.13 shows a slow linear decrease in hardness with log time. Capeletti et al (1972) found a relatively temperature independent recovery mode in type 304 stainless steel which produced a substantial amount of softening but little or no increase in subsequent ductility. They considered that dislocation rearrangement and annihilation and thermal microtwinning could account for this and acted to relieve the areas of highest strain energy.

3.3.2 Static Recrystallisation

Owing to the limited strain that can occur in a rolling pass, it may be concluded that, for 18-8 steel in particular, interpass recrystallisation behaviour is more important than dynamic recrystallisation in determining the structural development during a particular schedule. Although the present review is concerned with previous work carried out on recrystallisation following hot deformation, much of this is an extension of the early work which extensively explored the kinetics and mechanisms of recrystallisation following cold work.

3.3.2.1 Kinetics of Static Recrystallisation

Recrystallisation is a diffusion controlled process governed by nucleation and growth. After an incubation period during which nuclei are formed, recrystallisation starts slowly (due to the limited number of nuclei), accelerates to a maximum, and finally decreases due to the impingement of growing grains. Such behaviour results in a sigmoidal curve when the fraction recrystallised is plotted against time. Recrystallisation curves are usually shown by an Avrami plot of the form

$$X_v = 1 - \exp(-\beta t^k) \qquad (3.2)$$

where X_v is the fraction recrystallised

t is the time

β, k are constants at constant temperature and strain.

The value of k is obtained by plotting ln $(1/1-X_v)$ against ln t and Cahn (1956) showed that the value of k depended on whether nucleation occurred at grain boundary, grain edge or grain corner sites. Barraclough (1974) found $k \simeq 2$ (equivalent to a grain edge site) for 18-8 stainless steel which was in agreement with previous work. However for large initial grain sizes lower values were found (k=1 for 0.53 mm. grain size, k=1.5 for 0.23 mm grain size). Although the recrystallisation rate is theoretically governed by both the nucleation and growth rates, if intragranular nucleation is insignificant and sufficient new grains nucleate in each old grain early in the process, the recrystallisation rate becomes a function of the growth rate and independent of the nucleation rate (Cahn and Hagel 1962).

3.3.2.2 Nucleation

The proposed models to account for nucleation during annealing of cold worked materials are based on either subgrain growth or grain boundary migration. In the former it is assumed that dislocations form subgrains, some of which grow at the expense of others to attain boundary misorientations similar to grain boundaries and thereby act as nuclei. Cahn (1950) proposed polygonisation of regions having high dislocation densities of similar sign, the resultant subgrain growing by boundary migration at the expense of other subgrains. On the other hand, Hu (1962) proposed that subgrain coalescence occurred by annihilation of the boundaries by dislocation climb and glide. A grain boundary migration model has been proposed by Bailey and Hirsch (1962) who considered that local

differences in dislocation density across a grain boundary would provide a driving force for grain boundary bulging between pinning points. Such a model is advantageous in that it follows the experimentally observed grain boundary nucleation and also provides a mechanism for nucleation in low stacking fault energy materials where subgrain migration is difficult. Evidence (cited by Barraclough 1974) to support both models has been found applicable to a range of hot worked materials that have undergone prior dynamic recovery and/or dynamic recrystallisation. In addition, Glover (1969) found that dynamically recrystallising grains at the end of deformation could act as nuclei for static recrystallisation. Observations of a decreasing statically recrystallised grain size with increasing strain indicate a relatively strong dependence of nucleation rate on strain (Barraclough 1974). The time dependence of nucleation rate is not so clearly understood but Wusatowski (1966) showed a power relationship between the decrease in nucleation rate and time for an 18-8 steel.

3.3.2.3 Growth

The growth of nuclei results in the formation of strain free equiaxed grains by the migration of grain boundaries, the latter occurring by the transfer of single atoms across the boundary (Turnbull 1951). Such migration requires a driving force to overcome the activation energy

barrier and so the growth rate G is of an exponential form, a simple expression being

$$G = G_o \exp \frac{- Q_x}{RT} , \qquad (3.3)$$

where Q_x is an activation energy

R is the gas constant

T is the absolute temperature

G_o is a constant.

3.3.2.4 Effect of Material Variables

There is little evidence for the effect of material variables on static recrystallisation behaviour but it would be expected that the rate would be retarded by the presence of solutes since grain boundary migration would be slowed down by solute drag. The rather scant evidence of the effect of precipitates on recrystallisation after both hot and cold working appears to show that

(i) large particles tend to increase the recrystallisation rate by increasing the nucleation rate (English and Backofen 1964) probably due to the large dislocation densities produced around such particles during deformation

(ii) fine particles tend to retard recrystallisation e.g. NbC precipitation is used to control recrystallisation in controlled rolling (e.g. Sellars and Whiteman 1974). This may be due to the retardation/elimination of nucleation resulting from the effect of small, finely spaced particles on subgrain growth.

3.3.2.5 Effect of Initial Grain Size

It has been found (Wusatowski 1966, Barraclough 1974) that an increase in the initial grain size significantly decreases the recrystallisation rate and increases the final recrystallised grain size, this being especially so at small strains. The decreased recrystallisation rate is considered to be caused by the decreased number of nuclei (Wusatowski 1966) which results from the decreased grain boundary area (Barraclough 1974). Barraclough found that an initial grain size greater than 0.5 mm. promoted isolated intragranular nucleation and so reduced the above-mentioned effect and also noted that the deformation mode used to produce the initial grain size could affect the subsequent recrystallisation kinetics. No firm explanation was proposed for this. Wusatowski (1966) found that the influences of strain and strain rate were not modified by the initial grain size.

3.3.2.6 Effect of Texture

The effect of texture on static recrystallisation kinetics has not been widely studied but Whittaker (1973) showed that different initial textures altered the strain dependence of recrystallisation kinetics but only at low strains (prior to the peak stress). Since 18-8 steel has been shown to develop different textures during rolling (Jones and Walker 1974) this effect is of possible significance.

3.3.2.7 Effect of Temperature

All workers who have studied this parameter have shown that the growth rate increases with temperature in the manner described by the Arrhenius equation (3.3). Barraclough (1974) found the value of Q_x, the activation energy for recrystallisation, to be 426 kJ/mole which was independent of strain within experimental accuracy. Capeletti et al (1972) found values(for AISI 304 steel) of 196 kJ/mole for 35% deformation and 188 kJ/mole for 50% deformation but no attempt was made to separate recovery from recrystallisation or nucleation from growth. Kozasu and Shimizu (1971) found an apparent activation energy for grain boundary migration of 351 kJ/mole in 18-8 steel, and Rossard (1960) found 406 kJ/mole.

Glover (1969) showed that Q_x did not depend on the prior dynamic restoration process. Other workers (e.g. Grange 1964) have shown that an increased deformation temperature led to a decreased recrystallisation rate. This was considered to be due to the decreased stored energy and hence decreased driving force at higher deformation temperatures.

Whittaker (1973) proposed a temperature compensated time parameter $W_{0.5}$ for 50% recrystallisation

$$W_{0.5} = t_{0.5} \exp \frac{-Q_x}{RT} \qquad (3.4)$$

where $t_{0.5}$, the time to 50% recrystallisation, is commonly used because it can be more accurately measured than the times to any other fraction recrystallised. This parameter was satisfactorily related to the finishing stress in a similar

way that the Zener Holloman parameter, Z, is related to the finishing stress. For non-isothermal situations, such as interpass air cooling or annealing, Sellars and Whiteman (1974) have shown how a value of W (for full recrystallisation) can be obtained from

$$W = \sum_{o}^{t} \left(\exp \frac{-Q_x}{RT} \right) \delta t \qquad (3.5)$$

Hence by knowing the relevant cooling curve or thermal history the value of W can be obtained and then used to predict an equivalent time at a chosen isothermal annealing temperature for which the recrystallisation kinetics are known.

3.3.2.8 Effect of Strain

All workers have shown that recrystallisation rates increase with increasing strain in the work hardening region due to the increased driving force. Wusatowski (1966) rationalised the effect by producing empirical equations, applicable to 18-8 steel, for β and k in the Avrami equation (eqn.3.2).

$$k = 1 - 1.193\gamma \qquad (3.6)$$

$$\beta = (1.33 - 0.001T)\,\gamma^{(-0.013T + 14.9)} \qquad (3.7)$$

where $\gamma = h_2/h_1$

h_1, h_2 = initial, final thicknesses in rolling

T = temperature (^{o}C)

Barraclough (1974) showed that the time to 50% recrystallisation, $t_{0.5}$, could be related to the strain by

$$t_{0.5} = A\,\varepsilon^{-3.5} \qquad (3.8)$$

where A is a structural factor dependent on annealing

temperature, original grain size and finishing stress. This was valid at low strains (up to 0.3) for 18-8 steel.

In the steady state region the stress level is almost constant and so the subsequent static recrystallisation should be independent of strain. This has generally been found to be the case and it has been suggested that cases of disagreement could be explained by adiabatic heating (Jonas et al 1969). Glover (1969) studied the static recrystallisation rate after the peak stress and showed that, in the same material (α-Fe), it was greater in dynamically recovered structures than in dynamically recrystallised structures. This effect was related to the nucleation mechanism that was operative in each case. Further work by Djaic and Jonas (1972, 1973) on recrystallisation after strains to the steady state led them to propose a further mechanism of static restoration, namely metadynamic (or post dynamic) recrystallisation. Fig.14 shows the effect of increasing the strain at which double deformation tests were interrupted. Curve a is for a strain interruption prior to that for classical static recrystallisation, curves c to g for strain interruptions beyond the peak and curve h for an interruption well into the steady state region. The curves show that, after strains to the peak stress when dynamic recrystallisation is the only dynamic restoration mechanism, recrystallisation occurred without the usual incubation time. Djaic and Jonas also considered that some results of other authors could support their theory.

3.3.2.9 Effect of Strain Rate

An increased strain rate has been found to produce an increased recrystallisation rate (e.g. Barraclough 1974) due to the resultant higher stress levels and hence higher stored energy. Wusatowski (1966) showed that the increase in recrystallisation rate was not proportional to the increase in strain rate, but that it was strain dependent. Glover (1969) attempted to quantify this and related the growth rate G to the finishing stress σ by

$$G \propto \sigma^N \qquad (3.9)$$

where N was found to be constant (1.75) independent of temperature. Since σ is related to the temperature compensated strain rate, Z, this is equivalent to saying that the strain rate dependence was temperature independent. However Whittaker (1973) showed that the strain rate dependence increased with temperature and strain in the work hardening region.

3.3.2.10 Summary of the Effect of Variables on Static Recrystallisation

Disregarding the effect of material and textural variations, the above discussion may be summarised as follows:

(a) The recrystallisation rate is increased by:

(i) higher strains in the work hardening region (eqn.3.7),

(ii) higher annealing temperatures (eqn.3.3) but lower deformation temperatures,

(iii) higher strain rates,

and (iv) lower initial grain size.

(b) The final recrystallised grain size is increased by:

(i) lower strains in the work hardening region,

(ii) lower stresses in the steady state region,

(iii) higher initial grain sizes,

and (iv) higher deformation temperatures.

3.4 Application to Multipass Deformation Schedules

3.4.1 Structural Interactions

The previous sections have discussed the structural changes that can occur during and after a single deformation and such information is applicable to processes such as extrusion or planetary rolling. However, traditional hot rolling consists of a series of interrupted deformations of varying strain, strain rate and temperature, Fig.1. It follows from a consideration of interpass recrystallisation kinetics that recrystallisation may well be incomplete between successive passes, particularly in the final stages of plate and strip rolling where the temperature is dropping rapidly. Considering two passes of equal strain where the conditions are such that a mixed structure is present at the entry to the second pass, then on exit, the prior unrecrystallised portions will have received a total strain roughly twice that received by the recrystallised portion and would therefore subsequently recrystallise more rapidly.

The possible complex structure that could arise from several successive passes between which incomplete static recrystallisation occurs has been demonstrated by Sellars and Whiteman (1974) who considered the structural changes occurring

during a four pass isothermal sequence of constant strain (0.6) and constant interpass time (10 sec.). The basis from which they deduced the structural changes is shown in Fig.15 together with the progressively complex structural development. Clearly the effects when the temperature varies with time and through the thickness (as will be discussed in Chapter 4) would be expected to be even more complex.

3.4.2 Structural Dependence of Strength

The use of interrupted tests to study recrystallisation behaviour has already been discussed (section 3.3.1). Fig.12 illustrates that, following short interruptions during the plane strain compression of aluminium, the flow stress rises rapidly towards the stress level expected if the deformation had been continuous. However, after longer interruptions, as the material becomes more fully recrystallised, the flow stress behaviour more nearly approaches that of the initial material. It can be seen that, for any particular strain subsequent to interruption, the mean flow stress decreases with increasing restoration. Hence in idealised isothermal deformation sequences, the effect of long hold periods is to maintain the working loads for successive identical deformations at the same level. (This assumes no change in, or major effect of, grain size).

However during non-isothermal simulation the reverse has been found to be true. Nair (1971) found that the mean flow stresses for successive passes during the hot rolling of AISI 321 stainless steel were lower than those during rolling of material that had not been previously worked, as shown in

Table 2. In the multipass sequence the material was only partially recrystallised after the first pass and no recrystallisation took place after subsequent passes. The flow stress behaviour was explained by the dependence of flow stress on subgrain size (eqn.3.1). Thus the first pass produced a coarse subgrain size which was not destroyed in subsequent passes even though additional smaller subgrains were formed. The coarse subgrain size was considered to be responsible for the lowering of the resistance to deformation in successive passes.

This effect was also demonstrated by torsional simulation. Fig.16a shows the effect of a single isothermal deformation (at 900°C), curve A, compared with a two pass sequence starting at 1000°C, curve B, followed by incomplete recrystallisation and a further deformation at 900°C, curve B'. The flow stress is markedly lower. When complete recrystallisation occurs between passes, Fig.16b, curves D and D', then the second deformation at the lower temperature is identical to the isothermal simulation for that temperature.

Similar conclusions were reached by Farag et al (1968) during torsion testing of aluminium. Fig.17 shows that when recrystallisation is slow between passes (at $\sim$ 400°C) the presence of a substructure inherited from previous higher deformation temperatures results in a lower flow stress than that obtained by isothermal tests.

Glover (1969) deformed α-iron to strains into the steady state region and then measured stress-strain behaviour for subsequent continuously increasing or decreasing

temperatures. He showed that the stress at any temperature for a continuously cooled, or heated, specimen is lower, or higher, than the isothermal steady state value, Fig.18. If the temperature was controlled at any point it was shown that the stress continued to move towards the equilibrium value for that temperature. Whittaker (1973) carried out similar tests on 3% Si steel using only small strain increments, Fig.19, and found a smaller divergence than Glover (1969) especially during continuous heating. It was considered that the smaller divergence was due to the poorly developed substructure (due to the low strain increments used) which could easily adapt on further deformation.

CHAPTER FOUR

TEMPERATURES DURING HOT WORKING

4.1 Introduction

Chapter 2 has discussed the increasingly subtle theories proposed for the prediction of rolling loads and torques and Chapter 3 has discussed the dependence of structure on temperature. However, practical applications of such data to hot working are limited due to the lack of knowledge about the temperature distributions that occur therein and it is only within the last 10 years that any serious efforts have been made to measure or predict temperatures during hot rolling. The advent of rapid digital computers has encouraged the solution of the differential equations that govern heat flow and the wish to automate plant, coupled with the development of controlled rolling, has provided the justification.

In this chapter it is proposed to review the methods available for temperature measurement, the fundamental laws that govern heat flow and their application to hot rolling and to consider the results and uses of the ensuing mathematical models.

4.2 The Measurement of Temperatures during Hot Working

The methods of temperature measurement during hot working may be conveniently categorised into those which measure surface temperatures and those which measure internal temperatures.

4.2.1 Surface Temperature Measurements

In industrial hot working it is only possible to measure surface temperatures and radiation pyrometers are the most commonly used instruments for this. Coe (1971) has reviewed the different types of pyrometers available. Disappearing Filament Pyrometers (also called Visual Pyrometers), in which the power input to a filament is adjusted so that its colour matches that of the metal surface, can have an accuracy of $\pm$ 0.1°C although this would not be achieved in practice. Such instruments are useful for making rapid spot checks. Total Radiation Pyrometers, which measure the total radiated energy by means of a thermopile, are accurate to $\pm \frac{3}{4}\%$. The bolometer is gaining in popularity due to its greater robustness, reliability and sensitivity. Refinements have allowed temperatures as low as 50°C to be measured with an accuracy of $\pm$ 2°C. Partial Radiation Pyrometers, which measure the surface brightness using the short wavelength radiation of the visible spectrum, are more sensitive since the brightness is a stronger function of temperature than the total radiated energy. Silicon solar cells are commonly used as detectors since they have high sensitivity, stability and speed of response. The high sensitivity has allowed temperature measurement down to about 600°C and Beattie (1971) has described a PbS cell which, coupled with other refinements, has allowed reasonably accurate temperature measurements down to 100°C during the rolling of aluminium.

Ratio pyrometers, which measure the ratio of the energies emitted in two different wavebands, have been developed to minimise the effect of emissivity variations and partial target obscuration but are less temperature sensitive and also affected when the obscuring medium has a small particle size (e.g. smoke). The Chopped Radiation Pyrometer has been developed for low temperature measurement but Coe (1971) concludes that there are many disadvantages to it. The effect of emissivity variations has been minimised by the gold-plated hemisphere pyrometer which measures radiation under black body conditions but it can only be used for spot measurements. Finally, Beattie (1971) describes the contact probe pyrometer which consists of two sharpened spikes of alumel and chromel wire with the thermoelectric circuit being completed by the hot metal.

Coe (1971) concludes that the optimum system consists of a short wavelength partial radiation pyrometer with an integral amplifier and a peak holding device, the latter helping to eliminate the effect of scale. Nevertheless there are several drawbacks to the use of such pyrometers. Firstly, they have to be sited with great care to minimise the effect of smoke and steam. This is particularly true in hot rolling where there is steam in the vicinity of hydraulic descalers. Perhaps more serious is the dependence of the emissivity on the surface condition and so the varying scale thickness along a hot rolling line would be expected to affect the accuracy of surface temperature measurements.

Perhaps the biggest disadvantage of surface temperature measurements is that it is only when equilibrium coding is present that it is possible to accurately extrapolate from the surface temperature to obtain the internal temperature distribution. Whereas this condition is met during lengthy periods of air cooling it is often not met during hot rolling. Held et al (1970) and Bradley et al (1970) have shown that varying periods of time are required for the surface temperatures to recalesce after the chilling introduced by the rolls during a pass and for the equilibrium cooling rate to be re-established. It may be concluded that under many rolling conditions the measured surface temperatures are of little value unless the pyrometers are sited with due care. Modern mills usually have pyrometers located at the exit of the last roughing stand and at the entry and exit of the finishing train. Wilmotte et al (1973A) conclude that the only reliable temperature measurements are those made a certain distance from the end of the last roughing stand.

A further method lies in colour photography of the stock, the temperatures being obtained by comparison of the film optical densities with a reference. Mashinskii et al (1970) used a standard consisting of electrically heated nichrome strips (in situ) and Lee et al (1963) used a heated metal wedge, the latter authors claiming an accuracy of $\pm$ 20^{o}C.

4.2.2 Internal Temperature Measurements

The lack of accuracy inherent in surface temperature measurements has led other workers to attempt measurement of internal temperatures during hot working using embedded thermocouples. Bradley et al (1970) have used "Pyrotenax" metal sheathed, mineral insulated thermocouples during both hot rolling and extrusion trials on aluminium. McKensie and Young (1971) have used similar thermocouples during rolling and quenching of plate and Coldren et al (1970) have used them during the hot rolling of steel. The advantage of these thermocouples is that the highly compacted refractory powder insulation is maintained between the thermocouple wires and between them and the metal sheath up to considerable reductions. In addition a range of sizes is available, down to 1 mm. sheath diameter.

Held et al (1970) have also used embedded thermocouples during hot rolling but give no details of their construction. Hughes and Sellars (1972) have measured temperatures during upsetting in hot extrusion using standard thermocouples protected with thin walled stainless steel tube. Kozasu and Kubota (1968) have used PR13 thermocouples insulated with porcelain tubes and refractory cement and found that during rolling, at high reductions, even though the thermocouples were short-circuited by oxidation scale in the vicinity of the junction this had no effect on the temperature readings. Pozdeev et al (1972) have successfully measured temperatures during press upsetting with chromel-alumel thermocouples insulated with porcelain beads, asbestos cord and glass fibre.

Finally Dubinskii et al (1971) have cast doubts on both pyrometers and thermocouples due to their inertia and preferred to crop the end off billets and measure the temperature distributions by scanning with a photo-multiplier. This method would appear to be extremely doubtful due to such factors as chilling and deformation heating by the shear even though the authors considered this not to be so.

4.2.2.1 Effect of Deformation on Thermocouples

The main problem of using embedded thermocouples is that deformation may possibly affect the thermoelectric properties and there is considerable disagreement about this. Dutchak et al (1972) have constructed thermocouples from chromel, alumel and copel alloys deformed to various extents and compared their e.m.fs. with respect to a platinum electrode at temperatures between 0 and 700°C. They concluded that plastic deformation could have a considerable effect on the thermoelectric output of such alloys. Potts and McElroy (1962) have shown that 70% cold reduction of chromel-alumel thermocouples followed by 5 minutes annealing at 700°C leads to a 1% error. Dubinskii et al (1971) also cast doubts on the validity of results obtained with embedded thermocouples.

On the other hand, Bradley et al (1970) found no effect of deformation on their metal sheathed mineral insulated thermocouples. McKensie and Young (1971), using similar thermocouples, have shown that deformation (up to 64% reduction) in the temperature range where recrystallisation is rapid did not significantly affect the temperature reading.

Kinsie (1973) notes that chromel wire is in the fully disordered metastable state after cold working and at higher temperatures a drift of thermoelectric force occurs with time as short range ordering occurs. He quotes that times ranging from 40 weeks at 300°C to 1 minute at 450°C are required for the stable condition to be reached and that above 450°C almost instantaneous ordering occurs. Polishchuk (1974) found that the thermoelectric properties of chromel and alumel alloys were restored on annealing at above 500°C independent of the amount of prior deformation but also found a deviation of 500 μV at 600°C. Pozdeev et al (1972) found no effect of deformation.

It may be concluded that, although there are data to the contrary, the weight of evidence points to an insignificant effect of deformation at high temperatures.

4.3 Basis of Heat Transfer during Hot Working

The field of heat transfer is traditionally divided into 3 modes, namely radiation, conduction and convection. Thermal radiation is energy in the form of electromagnetic radiation emitted because of the absolute temperature of a body. Conduction refers to the kinetic and internal energy exchange between molecules and laws based on macroscopic models can be solved to give heat conduction rates as a function of the temperature gradients. Convection refers to the thermal energy transfer between a surface and a flowing medium (gas or liquid).

The heat transfer processes which occur during hot working are

(i) loss of heat by air cooling

(ii) heat gain due to deformation

and (iii) heat conduction both between the metal being worked and the tools and also within them.

The fundamental laws of heat transfer have been dealt with in great detail by many authors (including Dusinberre 1949, Carslaw and Jaeger 1959, Chapman 1967, Adams and Rogers 1973) and it is proposed to give only a brief summary here.

4.3.1 Laws of Heat Conduction within a body

If we consider a plate bounded by two parallel planes each of area A and a distance x apart, one plane being maintained at a uniform temperature T_1 and the other at T_2, then the rate of heat flow $\frac{dq}{dt}$ through the plate has been experimentally shown to be

$$\frac{dq}{dt} = k.A. \frac{(T_1 - T_2)}{x} \qquad (4.1)$$

where k is defined as the thermal conductivity. This observation leads to Fourier's First Law which states that the flux of heat conducted (energy per unit time per unit area) across a surface is proportional to the temperature gradient taken in a direction normal to the surface at the point in question, i.e.

$$\frac{d}{dA}\left(\frac{dq}{dt}\right) = - k \frac{dT}{dx} \qquad (4.2)$$

This equation also gives the direction of heat flow. Thus if the temperature increases with increasing positive x, the heat flows in the negative direction.

These equations lead to the general heat conduction equation for an isotropic solid with constant thermal conductivity:

$$\frac{\partial T}{\partial t} = \alpha\left(\frac{\partial^2 T}{\partial x^2} + \frac{\partial^2 T}{\partial y^2} + \frac{\partial^2 T}{\partial z^2}\right) \qquad (4.3)$$

where α = thermal diffusivity = $\frac{k}{s\rho}$.

s = specific heat,

ρ = density,

and x, y, z are three mutually perpendicular co-ordinate directions.

The solution of this differential equation may be obtained analytically for simple geometries and boundary conditions (Carslaw and Jaeger 1959). An alternative method lies in numerical analysis based on the finite difference method, this being commonly used since it is capable of handling more complex geometries and boundary conditions. The finite difference approximation involves the definition of selected discrete points within the body, the solution of the differential equation for each point, the result being numerical values of the temperature at each discrete point and at discrete time intervals. The finite difference equations are derived from the differential equation by a Taylor's expansion (Chapman 1967).

As an example, consider two-dimensional steady state conduction. 'Steady state' implies that the temperature is independent of time so that equation 4.3 reduces to

$$\frac{\partial^2 T}{\partial x^2} + \frac{\partial^2 T}{\partial y^2} = 0 \qquad (4.4)$$

A general body, Figure 20, is split into n elements of dimensions ∂x x ∂y x 1, the temperatures at the nodes (centres of each finite element) being T_a, T_b etc. The finite difference solution then gives

$$\frac{T_b - 2T_a + T_c}{(\partial x)^2} + \frac{T_d - 2T_a + T_e}{(\partial y)^2} = 0 \qquad (4.5)$$

When non steady state conduction is considered, the derivative $\frac{\partial T}{\partial x}$ in equation 4.3 is approximated to

$$\frac{\partial T}{\partial t} = \frac{T'_a - T_a}{\Delta t} \qquad (4.6)$$

where T'_a is the future temperature of the node and T_a its current temperature. The choice between an explicit or implicit solution is then available. The explicit solution gives the future temperature of a particular node in terms of the current temperatures of the node and its neighbours. The implicit solution gives the future temperature of the node in terms of its current temperature and the future temperatures of its neighbours. Hence, for the explicit case

$$\frac{T'_a - T_a}{\Delta t} = \alpha\left(\frac{T_b - 2T_a + T_c}{(\partial x)^2} + \frac{T_d - 2T_a + T_e}{(\partial y)^2}\right) \qquad (4.7)$$

and for the implicit case

$$\frac{T'_a - T_a}{\Delta t} = \alpha\left(\frac{T'_b - 2T'_a + T'_c}{(\partial x)^2} + \frac{T'_d - 2T'_a + T'_e}{(\partial y)^2}\right) \qquad (4.8)$$

In general the explicit case is preferred but since the time step Δt is restricted by the values of ∂x and ∂y more calculation may be involved. The calculations may be carried out by hand or by use of a digital computer.

In addition, there is an analogy between the finite difference formulation and an electrical network and solutions may be obtained from electrical analogues.

4.3.2 Heat Conduction Between Two Bodies

In the present context we are interested in the conduction of heat between a hot workpiece and the tools used to deform it. In the case of hot extrusion, heat is conducted from the billet to the container, ram and die, and in the case of hot rolling, from the slab to the work rolls and the roll tables. The theoretical approaches are the same in both cases and are limited to considering the heat flow between two bodies, both initially at different uniform temperatures, which are brought together with either perfect or imperfect contact.

Considering the case, Fig.21, where

(i) there is no thermal contact resistance,

(ii) the thermal properties of the two bodies are identical,

(iii) the region of the body $-a < x < a$ is initially at T_o,

and (iv) the region $|x| > a$ is infinite and initially at zero temperature,

then Carslaw and Jaeger (1959) have shown that the temperature distribution at time t after contact is given by

$$T = \frac{1}{2} T_o \left\{ \operatorname{erf} \frac{a - x}{2\sqrt{\alpha t}} + \operatorname{erf} \frac{a + x}{2\sqrt{\alpha t}} \right\} \text{ for } -\infty < x < \infty \quad (4.9)$$

Carslaw and Jaeger (1959) have also derived the solution for heat conduction between two bodies of different compositions, Fig.22. Assuming

(i) there is no thermal contact resistance,

(ii) the region $x > o$ is composed of a substance of diffusivity α_1, conductivity k_1 with a uniform initial temperature T_o

and (iii) the region $x < o$ is composed of a substance of diffusivity α_2, conductivity k_2 and a uniform initial zero temperature,

then in body 1 at $t > o$,

$$T_1 = \frac{T_o}{1 + \frac{k_2}{k_1}\sqrt{\frac{\alpha_1}{\alpha_2}}} \left\{ 1 + \frac{k_2}{k_1}\sqrt{\frac{\alpha_1}{\alpha_2}} \ \text{erf} \ \frac{x}{2\sqrt{\alpha_1 t}} \right\} \qquad (4.10)$$

and in body 2,

$$T_2 = \frac{T_o}{1 + \frac{k_2}{k_1}\sqrt{\frac{\alpha_1}{\alpha_2}}} \cdot \text{erfc} \ \frac{|x|}{2\sqrt{\alpha_2 t}} \qquad (4.11)$$

where erfc X = 1 - erf X.

Bradley et al (1970) have reached a similar solution but with the co-ordinate system reversed.

Carslaw and Jaeger (1959) have extended the above to provide a solution when a contact resistance exists and have shown that, in body 1 at $t > o$

$$T_1 = \frac{T_o}{1 + A}\left\{1 + A\left[\text{erf} \ \frac{x}{2B_1} + \exp h_1\left(x + h_1 B_1^{\,2}\right)\text{erfc}\left(\frac{x}{2B_1} + h_1 B_1\right)\right]\right\} \qquad (4.12)$$

and in body 2

$$T_2 = \frac{T_o}{1 + A}\left\{\text{erfc} \ \frac{|x|}{2B_2} - \exp h_2\left(x + h_2 B_2^{\,2}\right)\text{erfc}\left(\frac{|x|}{2B_2} + h_2 B_2\right)\right\} \qquad (4.13)$$

where $A = \frac{k_2}{k_1}\sqrt{\frac{\alpha_1}{\alpha_2}}$

$B_1 = \sqrt{\alpha_1 t}$, $\quad B_2 = \sqrt{\alpha_2 t}$

$h_1 = \frac{H}{k_1}\left(1 + \frac{1}{A}\right)$

$h_2 = \frac{H}{k_2}\left(1 + A\right)$

where H is the coefficient of surface heat transfer and is defined as the amount of heat transferred across the surface/unit area/unit time/unit temperature difference. In the case of an oxide film of conductivity k_{ox} and thickness d, $H = \frac{k_{ox}}{d}$.

4.3.3 Heat Loss during Air Cooling

In any hot working operation a certain amount of heat is lost by cooling in air, radiation and convection being jointly responsible for this. The rate of heat loss by radiation, $\frac{dq_r}{dt}$, from a body of surface area A, emissivity ε and surface temperature T_s (K) to ambient surroundings at T_o (K) is given by

$$\frac{dq_r}{dt} = \sigma A \varepsilon\left(T_s^4 - T_o^4\right), \qquad (4.14)$$

where σ is the Stefan Boltzmann coefficient (5.6699×10^{-12} $W/cm^2 K^4$). Equation 4.14 is sometimes rewritten (Chapman 1967) as

$$\frac{dq_r}{dt} = A h_r (T_s - T_o), \qquad (4.15)$$

where h_r is denoted as a "radiation coefficient". The latter approach is simpler to solve but h_r is only valid over a small temperature range.

Similarly the rate of convective heat loss, $\frac{dq_c}{dt}$, from the medium is given by Newton's law of cooling,

$$\frac{dq_c}{dt} = A\, h_c\, (T_s - T_o) \qquad (4.16)$$

where h_c is a "convection coefficient".

Equations 4.17 and 4.16 are sometimes added together to give the total rate of heat loss during air cooling,

$$\frac{dq}{dt} = A\, h_{cr}\, (T_s - T_o) \qquad (4.17)$$

where $h_{cr} = h_c + h_r$.

4.4 Application of Theory to Practice

When applying the above fundamental laws to hot rolling it should be noted that two approaches are possible. Firstly, the simplified approach assumes that the workpiece has a uniform temperature through its thickness, the temperature varying with time as described by the laws of radiation, convection and conduction. This is clearly an approximation but can provide sufficiently accurate answers for some applications. The second approach considers the evolution of a temperature distribution through the metal thickness as described by the law for heat conduction within a body (eqn.4.3) coupled with boundary conditions based on the laws of radiation, convection and conduction between two bodies. This approach is usually based on the subdivision of the body into regular cells as discussed previously. Dusinberre (1949) and Shenck (1963) have given general accounts of such methods.

Hollander (1970) and Wilmotte et al (1973A) used uniformly spaced networks but Bradley et al (1970) used a non uniform node spacing with more nodes near the surface due to the larger temperature gradients there. Price and Slack (1952) and Eyres et al (1946) have given details of the conditions necessary for a stable solution. It should be noted that one dimensional heat flow is only considered in the literature, the heat flow through the sides and ends of the workpiece being sufficiently small to be negligible.

4.4.1 Cooling Outside the Stands

The heat losses that occur outside the stands may be categorised into air cooling by radiation and convection, conduction to the roll tables and to other parts of the strip during coiling and water cooling.

4.4.1.1 Air Cooling by Radiation and Convection

These modes of heat loss outside the stands are the most important and often the only ones considered. The fundamental differential equations (section 4.3.3) are usually simplified by taking the finite difference approximation so that, for example, the Stefan Boltzmann radiation equation gives

$$\Delta \bar{T}_{rad} = \frac{q_r}{m\,s} = \frac{q_r}{V \rho\, s} = \frac{\sigma A \varepsilon (T_s^4 - T_o^4)\ \Delta t}{V s \rho} \qquad (4.18)$$

where $\Delta \bar{T}_{rad}$ is the temperature drop due to radiation in time Δt for a body of volume V, mass m, specific heat s and density ρ. The convection equation can be treated in a similar way.

The equations show that the relative contributions of radiation and convection to the total heat loss are temperature dependent. Thus Bradley et al (1970) considered just convection to the air and rolling emulsion during the hot rolling of aluminium. During the hot rolling of steel, Hollander (1970) considered convection to be 4-6% of the radiation loss, Zheleznov et al (1968) considered it to be 1-5% of the radiation loss, Pawelski (1969A) considered it to be less than 10% and Sims and Wright (1963) considered convection to be 5-7% of the total heat loss. Lee et al (1963) state that the convection contribution is only important when the product of the Grashof and Prandtle numbers exceeds 10^9 (when turbulent conditions apply) and took convection to be 7% of the total. In general convection is disregarded and at best it is included in the radiation equation by changing the value of the emissivity.

A further simplification of the basic equation is to neglect ambient temperature (e.g. Lee et al 1963, Wright and Hope 1975) which is reasonable since $T_s^4 >>> T_o^4$ when $T_s >> T_o$. A practical problem in applying the radiation equation is to choose a value for the emissivity ε which varies with temperature and surface condition. Seredynski (1973) used an average value of 0.8 for EN3 steel and presented an equation

$$\varepsilon = \frac{(T - 273)}{1000} \left(0.125 \left(\frac{T - 273}{1000} \right) - 0.38 \right) + 1.1 \quad (4.19)$$

Hollander (1970) measured it to be between 0.75 and 0.85 and also quoted a value of 0.68 for a very thin oxide skin and 0.82 for heavily oxidised surfaces. Lee et al (1963)

found 0.77, Hughes and Sellars (1972) found 0.84 for mild steel and Sarjant and Slack (1954) presented a graph showing a gradual change from 0.76 at 400°C to 0.9 at 1000°C.

A further sophistication was introduced by Hollander (1970) who allowed free radiation from the upper surface of strip and reradiation from the roller table for the bottom surface. Zheleznov et al (1968) allowed 10% less radiation from the lower surface and convection only from the upper surface.

A different approach has been used by Wilmotte et al (1973A) who considered the temperature gradient at the surface of the strip to be proportional to the difference in strip surface and ambient temperatures, the constant of proportionality being determined from the temperature measurements of more than 1000 coils.

4.4.1.2 Conduction Outside Stands

It is clear that some heat conduction will occur to the roller tables but no reference was found for its calculation, so it is presumed to be of negligible importance. Muzalevskii et al (1970) concluded that there were no data available to allow for it. Conductive heat transfer also occurs during coiling but no reference was found for it although mathematical models have been developed to study heat transfer during annealing of coils following cold rolling (e.g. Rosier 1970, Stikker 1970).

4.4.1.3 Water Cooling

Water is present during hot rolling due to roll coolant systems, hydraulic descalers and cooling banks on the run out tables. Roll coolant systems, which effectively act as a spray on the slab surface, are used to control the thermal history of the rolls and thereby limit surface deterioration due to thermal fatigue (Stevens et al 1971). Hydraulic descalers, consisting of high pressure jets, are used to remove scale from the metal surface which would otherwise be damaged. Water cooling banks on the run out table are gaining importance for controlling the final mechanical properties of the strip by grain size control.

Sigalla (1957) concluded that a water spray was only effective during its initial moment of application because a steam layer is formed which insulates the strip from the coolant. However, high pressure jets provided a continuous supply of coolant at the surface because the steam layer was not allowed to form. Both cases are theoretically governed by Newton's convection law (eqn.4.16), the difference lying in the value of the heat transfer coefficient. This has not been found for water sprays because the necessary data cannot be obtained (Minařík 1972). However, Hollander (1970), Seredynski (1973), Sigalla (1957) and Muzalevskii et al (1970) have derived equations for determining the temperature drop due to high pressure jets in terms of the water flow rate, jet nozzle diameter etc. Minařík (1972) quotes a heat transfer coefficient of 10^7-10^8 kcal/m^2 hr (1.16×10^7 - 1.16×10^8 J/m^2 sec), Gurkov (1968) quotes a

temperature drop of ~ 21°C for 23 mm thick strip and Muzalevskii et al (1970) found a 2-6°C drop in the roughing descalers and ~ 20-35°C drop in the finishing descalers. Wilmotte et al (1973A) used data from more than 1000 coils to deduce the heat transfer coefficients during descaling etc.

In a somewhat different but nevertheless related field Davis (1972) has used a finite difference method and a surface heat transfer coefficient (4.2 J/m^2 °C sec) to predict temperature distributions in a steel slab during water quenching. Reasonable agreement with measured results was obtained except for positions close to the surface.

4.4.2 Heat Transfer during a Pass

Although heat is lost by radiation and convection from the sides of the workpiece during a pass, this is negligible compared to the other heat transfer mechanisms, namely the heat gain due to deformation and the heat loss due to conduction to the rolls.

4.4.2.1 Heat Produced by Deformation

It is a direct consequence of the first law of thermodynamics that deformation of a material produces a temperature rise and in rolling this is usually estimated from the measured work done. Wilmotte et al (1973A) considered the mechanical work to consist of two components:

(i) The work done to overcome friction at the stock/roll interface but since sticking friction is commonly assumed, this component is negligible. Bradley et al (1970) comment that its presence would be very difficult to detect since the greatest roll chilling occurs at the surface.

(ii) The work done to deform the stock, most of this work being transformed to heat and the remainder (approximately 2% (Zheleznov et al 1968)) being stored in the deformed structure. However, recrystallisation can regenerate some of this energy as heat (Hollander 1970).

It is generally assumed that all the rolling power is transformed to heat.

The work done per unit volume (W) to deform a metal is given by

$$W = \int_0^{\varepsilon} \sigma \, d\varepsilon \qquad (4.20)$$

and can be found from the area under the stress-strain curve. The temperature rise, ΔT_{def}, is then found from the equation

$$V.W = m\ s\ \Delta T_{def} = V \rho\ s\ \Delta T_{def} \qquad (4.21)$$

Wilmotte et al (1973A) have allowed for cases when the material is not perfectly plastic.

Of more practical use, Gittins et al (1974A) calculated the temperature rise from

$$\Delta T_{def} = \frac{E}{\rho\ s\ V} \qquad (4.22)$$

where E/V is the energy to deform the material per unit

volume and is found from

$$E/V = G/R\sqrt{h_1 h_2} \qquad (4.23)$$

where R is the roll radius, h_1 and h_2 the initial and final thicknesses of the stock and G the total roll torque per unit width. The torque can be found from measured values, assuming instrumentation is available and allowance is made for the frictional torques in the roll necks, or from the standard rolling theories. Hollander (1970) comments that the latter do not give good results and preferred to calculate the temperature rise from the measured electrical power supply to the mill. In this case

$$\Delta T_{def} = \frac{Qr}{\rho s h} \qquad (4.24)$$

where h is the section thickness and Qr the developed rolling power per unit surface area and is given by

$$Qr = \eta \frac{E.I}{W.v} \qquad (4.25)$$

where E is the voltage, I the current, W the stock width, v the rolling speed and η is the electrical and transmission efficiency. Lee et al (1963) found η = 0.75, Bradley et al (1970) guessed at 0.8 and Minařík (1972) quotes 0.5 to 0.9.

Other workers have calculated the temperature rise from a mean yield stress, $\bar{S}$. Seredynski (1973) used Pavlov's equation:

$$\Delta T_{def} = \frac{\text{work done}}{\rho s V} = \frac{\bar{S}}{\rho s} \ln \frac{h_1}{h_2} \qquad (4.26)$$

Similar equations are given by Muzalevskii et al (1970), and Zheleznov et al (1968). These approaches assume homogeneous deformation.

Johnson and Kudo (1960) used the work done from the slip line field solution of rolling to give the temperature rise due to deformation but did not consider any of the other modes of heat transfer.

Lee et al (1963) also considered the kinetic energy transfer from the rolls to the strip and found that it was 0.1% of the total energy input.

In all the theories examined, the authors considered the heat gained to be evenly distributed throughout the stock thickness.

4.4.2.2 Heat Conduction to the Rolls

This is the most complex area of heat flow during rolling because the boundary conditions and dimensions are constantly changing and analytical theory (section 4.3.2) does not allow for initial temperature gradients in either the workpiece or the roll.

The simplest approach is to assume perfect contact between workpiece and rolls i.e. an infinite heat transfer coefficient. It can then be seen (Portevin and Blain 1967, Zheleznov et al 1968, Hollander 1970, Denton and Crane 1972) that this boundary condition, coupled with the one dimensional form of the general heat conduction equation (eqn.4.3) gives

$$\text{Rate of heat loss} = k\,\mathbf{A}\,(T_s - T_c)\sqrt{\frac{\rho s}{\pi\, k\, t_c}} \qquad (4.27)$$

where **A** is the contact area, t_c the contact time, T_s the initial slab temperature and T_c the instantaneous contact temperature. Integrating this equation with respect to time

gives the total heat lost, Δq_{cond}, as

$$\Delta q_{cond} = 2A\,(T_s - T_c)\sqrt{\frac{\rho s\, k\, t_c}{\pi}} \qquad (4.28)$$

The temperature drop ΔT_{cond} is then obtained from

$$\Delta T_{cond} = \frac{\Delta q_{cond}}{V \rho\, s} \qquad (4.29)$$

where V is the volume of the metal in the roll gap.

Wright and Hope (1975) assumed that T_c could be obtained from the mean of the initial strip and roll temperatures i.e.

$$T_c = \frac{1}{2}\left(T_s^o + T_r^o\right) \qquad (4.30)$$

whereas Zheleznov et al (1968) assumed the correct solution

$$T_c = \frac{T_s^o \sqrt{k_s\, S_s \rho_s} + T_r^o \sqrt{k_r\, S_r \rho_r}}{\sqrt{k_s\, S_s \rho_s} + \sqrt{k_r\, S_r \rho_r}} \qquad (4.31)$$

where the subscripts s and r refer to slab/strip and roll respectively. Hollander (1970) used the latter approach and calculated the contact temperatures and heat losses separately for the upper and lower sides of the strip. He also noted that the actual amount of heat lost was only 0.6 of the theoretical heat loss, thus reflecting the inaccuracy of assuming a zero contact resistance.

Seredynski (1973) and Minařík (1972) have used a different approach and considered that the heat loss is proportional to the product of the contact area, contact time and difference in initial temperatures of roll and ingot. The constant of proportionality is the heat transfer coefficient which Seredynski quoted as 44 kJ/m^2 sec.K.

Denton and Crane (1972) used the simplest Carslaw and Jaeger analysis (eqn.4.9) and from the theoretical temperature distribution obtained an average drop in temperature $\Delta\bar{T}$ for a contact time t_c assuming a mean strip thickness $\sqrt{h_o h_1}$. By converting t_c to terms involving the reduction ratio r and the mean strain rate $\bar{\dot{\varepsilon}}$ they obtained

$$\Delta\bar{T} = 1.1284\ T_s^o \sqrt{\frac{\alpha}{h_o h_1 \bar{\dot{\varepsilon}}}}\ (0.67-0.17r) \sqrt{\frac{r}{1-r}} \qquad (4.32)$$

Bradley et al (1970) used the Carslaw and Jaeger solution (eqns.4.10 and 4.11) for two bodies of different composition to determine the heat lost during the hot rolling of aluminium. Possibly the most interesting aspect of their work was their solution for cases when the initial slab temperature distribution was not uniform, Fig.23. shows an initial temperature distribution AB and the analytical solution CD for a uniform initial temperature AD. The final discrete solution CB is obtained by depressing each of the points on AB by the amount that the analytical solution lies below AD. Although there would appear to be no theoretical basis for this approach, Bradley et al considered that it gave a very good estimate of the chilling effect and since the whole contact period is considered in one step, the calculation is much faster.

Wilmotte et al (1973A) have used the final Carslaw and Jaeger approach (eqns.4.12 and 4.13) by assuming an oxide layer whose thickness is known on exit from the descaler. They present an equation for the scale growth outside the stands, assume that the scale undergoes the same reduction as the strip during a pass and use the mean oxide thickness in

the analytical solution. Preisendanz et al (1967) have also used this solution and have computed temperature distributions for a wide variety of heat transfer coefficients, contact times and initial slab and roll temperatures. They also quote a typical oxide thickness of 0.1 mm and oxide thermal conductivity of 1.8 kcal/m hr ^{o}C (2.09 J/m sec ^{o}C) rising to 2.4 kcal/m hr ^{o}C (2.79 J/m sec ^{o}C) due to the high pressure during a pass. Allowing for 30% compression of the oxide they calculate that typical heat transfer coefficients lie between 26 and 34 Mcal/m^2 hr ^{o}C (30.2 to 39.5 kJ/m^2 sec ^{o}C).

Taylor and Elliot (1962) have used a similar approach but in reverse, i.e. they considered the conduction of heat from a heated roll to cold strip. In addition they used a finite difference approach so that at the strip roll interface they had the equations:

$$- k_s \frac{\partial T_s}{\partial x} = R\,(T_s - T_r) \qquad (4.33)$$

$$- k_r \frac{\partial T_r}{\partial x} = R\,(T_s - T_r) \qquad (4.34)$$

where the subscripts s and r refer to strip and roll respectively and R is the conductance of the interface. They used values of R given by Weills and Ryder (1949) and Brunot and Buckland (1949) who showed that R depended on the surface roughness and contact pressure.

Davis (1971) used a similar approach for hot rolling and assumed a heat transfer coefficient of 4.2×10^2 J/m^2 ^{o}C sec. Although no comparison was made with measured values, the author considered that this approach gave good agreement with the predicted results of Miller (1969) who simulated rolling by using a hydraulic analogue.

Pawelski (1969A) took a different approach by assuming that the rate of heat flow was proportional to the difference in 'core' temperatures of slab and roll, the constant of proportionality being called the heat transmission number. He showed that this depends on the contact time and defined the maximum and minimum values corresponding to zero and infinite scale thicknesses. Fig.24 shows calculated values for a 0.08% C steel. Pawelski (1969B) later applied this to a 6 stand mill and by allowing for other heat losses/gains concluded that the approach was correct.

Portevin and Blain (1967) have simulated heat conduction during rolling by pressing cold test pieces against hot metal plates and measuring the heat absorbed by calorimetry. The results were presented in terms of heat gained, no attempt being made to deduce a heat transfer coefficient. They also noted that for short contact times the heat gain was proportional to the time, whereas at > 0.15 sec, the heat gain was more nearly dependent on the (theoretical) square root of time.

4.5 Agreement Between Theory and Practice

In spite of the detailed mathematical models put forward, relatively few comparisons have been made between measured and calculated temperatures. Bradley et al (1970) have presented comparisons for single pass (Fig.25) and multipass (Fig.26) aluminium rolling schedules and as can be seen, the agreement is excellent. Hollander (1970) has

calculated temperature distributions through a complete rolling schedule, Fig.27a, and has compared measured and calculated surface temperatures, Fig.27b. He also presented other results which showed that the worst discrepancy throughout a schedule occurred during roughing (20°C) where the scale thickness is likely to have its largest effect and that the largest error in the final temperature was 9°C. Seredynski (1973) has compared measured surface temperatures with those obtained by three different computational methods, Fig.28. Method A, which allowed for radiation only, and Method T, which was based on the rigorous solution of the heat conduction equation and assumed that heat losses were balanced by heat gains during a pass, were shown to be more inaccurate than Method C which considered all modes of heat transfer. Wilmotte et al (1973A) developed a simple algebraic model from their complete model and by updating the coefficients of the simple model have obtained results with a standard deviation of 8.4°C. Typical results are shown in Fig.29 for the finishing train of a hot strip mill.

4.6 Application of Mathematical Models

Hollander (1970) has used his model to optimise mill performance and to assist the choice between different designs for a new mill. Bradley et al (1970) developed their model to aid interpretation of different hot rolled structures. The model of Muzalevskii et al (1970), coupled

with data for rolling loads etc, was developed into an algorithm to optimise rolling schedules on a continuous wide strip mill. Wright and Hope (1975) used their mean temperature model to optimise the hot rolling of 18-8 strip on a mill designed for mild steel and Buxton and Sutton (1969) have used a similar approach as part of an on-line computer control model. The model of Wilmotte et al (1973A) was simplified to allow it to be used for on-line calculations and also allowed the calculation of the varying scale thickness through a mill. The simple model of Denton and Crane (1972) was used to adjust the yield stress during rolling to allow for roll quenching. Other examples of the applications of simple temperature models to computer controlled rolling mills have been given by Schultz and Smith (1965), Darnall (1968), Takano (1968), Polukhin et al (1972B).

4.7 Work in Related Areas

Other workers have been concerned with the temperature changes occurring in the rolls in an attempt to understand the thermal fatigue of roll surfaces. Polukhin et al (1972A) have used contact transducers just after the arc of contact whereas Stevens et al (1971) have fitted full-scale work rolls with thermocouples, including surface thermocouples. Niiyama et al (1967) have also used a similar technique. Kannel and Dow (1974) have described the use of vapour deposited transducers on the roll surface

to measure both pressure and temperature changes during cold rolling but make no comment as to their suitability for hot rolling. Theoretical predictions of temperature changes in rolls have been given by Peck et al (1954), Cerni et al (1963), Stevens et al (1971).

Other workers have proposed mathematical models which, if desired, could predict initial temperature distributions for ingots at the start of the hot rolling process. For example, Sevrin (1970) has considered conventional casting, Peel and Pengelly (1970) and Gautier et al (1970) have considered continuous casting, Sarjant and Slack (1954) and Massey et al (1973) have considered soaking/reheating of ingots. Cornfield and Johnson (1971) have used a finite difference technique to predict heating curves for conventionally and induction heated slabs. Even details such as the influence of skid design have been modelled (e.g. Howells et al 1972).

Finally mention should be made of work carried out in hot extrusion since the fundamental heat transfer laws are identical. Bradley et al (1970) have measured and predicted temperature changes during the hot extrusion of aluminium and Hughes and Sellars (1972) and Hughes et al (1974) have done likewise for the hot extrusion of steel.

CHAPTER FIVE

EXPERIMENTAL TECHNIQUES

5.1 The Aims of the Present Research

The preceding literature review has exposed various areas of the hot working field where knowledge is at present limited. The aims of the present research are to deepen the quantitative understanding of such areas and may be categorised as follows:

(i) It has been shown that one of the main parameters that is least understood is the temperature changes and the development of temperature gradients within the workpiece. The primary aim of the present research has therefore been to investigate more fully this parameter for the case of hot rolling. In particular it was decided to develop a method of accurately measuring and recording the temperature changes in a slab during a laboratory hot rolling schedule and to develop a computer programme which could furnish full details of such gradients from limited measurements and which could be used to predict the temperature changes which occur during typical industrial hot rolling operations.

(ii) Having achieved the above, the secondary aim was to investigate the interrelation between temperature, strength, structure and rolling variables in laboratory hot rolling schedules and to be able to relate such findings to those already established by simulative mechanical tests. It was thereby hoped to understand more fully such commercially important factors as the strength and power requirements for, and the structural changes occurring during, industrial hot rolling operations.

It was decided to carry out the proposed research on a commercial 18-8 steel partly because considerable hot working data were available on similar steels and partly because such a steel should allow relatively easy metallography since it remains austenitic at all temperatures.

5.2 Hot Rolling

5.2.1 The Rolling Mill

The hot rolling experiments were carried out on a fully instrumentated Hille 50 rolling mill, Fig.30. This mill can either be used as a 2-high or a 4-high mill and in the latter case either the work rolls or the back-up rolls can be driven. The mill was used in the 2-high, reversible configuration in the present work. The drive is supplied by a 20 H.P. (14.92 kW) motor through gearing to the work rolls. The speed of the rolls can be varied continuously between 2 and 63 r.p.m. and is indicated on a scale graduated between 0 and 10. The mill has a maximum capacity of 50 tons (498 kN) roll separating force. The roll screwdown may be done either manually or electrically, the latter enabling the roll gap to be changed at a speed of 50 mm/min. The roll gap setting is indicated on a scale graduated in increments of 0.2 mm and it is possible to set the roll gap to an accuracy of 0.1 mm $\pm$ 0.05 mm. Three roll changes were made in the course of the experimental work as detailed in Table 3.

The mill is fully instrumentated to measure and record

(i) rolling load by means of load cells inserted between the ends of the screwdown and the chocks of the top roll,

(ii) rolling torque by measuring the torsional strain on the surface of each drive shaft using strain gauges, and

(iii) roll speed, by means of a rotating disc-photocell arrangement.

Full details of the instrumentation, its calibration and the recording instrument are given in Appendix 1.

5.2.2 Temperature Measurement during Hot Rolling

The internal temperature of each slab during the hot rolling schedules was measured using an embedded 1.5 mm diameter "Pyrotenax" inconel sheathed, mineral insulated chromel-alumel thermocouple. The output was recorded on a U.V. recorder coupled with an automatic back-off system, the latter being developed during the course of the present research. Full details of the preliminary work carried out to establish the best method of temperature measurement and recording, and details of the method finally adopted are given in Appendix 2.

The majority of rolling experiments were carried out with the thermocouple located in a hole drilled so that the bead lay at the mid-length, mid-width and mid-thickness position. A limited number of runs were carried out with the thermocouple located closer to the top surface to investigate the effect of roll chilling. It was initially hoped to build up a temperature-time history for each point within a slab during rolling but the superimposition of curves from different runs was subsequently found to be impossible due to different interpass times and initial scale thicknesses.

This approach was later made unnecessary by the development of a computer programme which predicted the temperatures in a transverse section of a slab during rolling, given the temperature history of any particular point within the slab.

The initial position of non-central thermocouples was determined by measuring the distance of the centre of the locating hole from the surface with a travelling microscope. The final positions were measured likewise on a longitudinal section taken at the mid-width position.

A limited number of attempts were made to measure surface temperatures during rolling sequences. The optical pyrometer, as described in section 5.3, was mounted on one side of the mill and the temperatures recorded on a Telsec 700 recorder. Since the mill was reversed between passes, the surface temperatures could only be measured after the 1st and 3rd passes which, coupled with the difficulties of synchronising the two recorders and of ensuring that the temperatures read were those at the centre of the top face, meant that the results were of limited value.

5.2.3 Hot Rolling Schedules

5.2.3.1 Hot Rolling of Mild Steel

Preliminary hot rolling schedules were carried out on mild steel slabs with a view to gaining experience of operating the mill and developing a suitable temperature measurement method and a suitable schedule for hot rolling an 18-8 stainless steel. Mild steel was chosen as it was relatively cheap and considerable hot torsion data had been obtained by a previous worker (Hughes 1971). In addition,

data were available for comparing its hot strength with that of 18-8 steel. The mild steel, whose composition is given in Table 4, was received in the form of 3" (76 mm) diameter billets which were hot rolled at B.I.S.R.A. to slabs of nominal dimensions 0.725" (18.4 mm) thick and 1.5" (38.1 mm) wide. The actual width varied between 41.3 mm and 36.5 mm due to barrelling. Lengths between 6" and 8" (150-200 mm) were reheated to 1100 to 1150°C for 20-30 mins. and given a 10%, 20%, 30%, 40% pass sequence. The internal temperatures were measured by a variety of methods (Appendix 2) and the roll load and speed measured as described in Appendix 1. A small mobile furnace close to the mill ensured minimal heat loss prior to the first pass but the lack of a controlled atmosphere led to heavy scaling.

5.2.3.2 Hot Rolling of Stainless Steel

The composition of the commercial stainless steel used in the present research is given in Table 4. A comparison of the hot strengths of mild and austenitic stainless steels coupled with the preliminary results (Chapter 7) showed that the maximum initial slab width should be approximately 50 mm in order not to overload the mill. The initial thickness was chosen so that the width:thickness ratio approached plane strain conditions as closely as possible. In addition it was necessary to ensure that the rolls would 'bite' such a thickness and that during a 3 x 30% pass sequence the slab cooling rate was not excessive. These opposing considerations were optimised by having a nominal initial thickness of 20 mm.

The material was received in the form of 3" (76 mm) diameter billets. 18" (~460 mm) lengths were hot rolled at B.I.S.R.A. to nominally 20 mm x 50 mm flat slabs. Immediately following rolling the edges were drop forged to minimise the barrelling.

The experimental hot rolling schedule was initially standardised on a time basis. Thus after reheating, the specimens were given 30% passes at 10, 25 and 40 seconds from the time they passed over the furnace sill. The long interpass times were necessary to screwdown and reverse the mill. The schedule was later changed so that the passes occurred at 1140, 1000 and 890°C. This change was necessary because, on a time basis, the entry temperatures for the three passes were markedly affected by the time taken to remove the specimen from the reheating furnace and the surface condition of the slabs.

The reheating furnace was the same one as described above for the hot rolling of mild steel. A constant reheating temperature of 1180°C and constant reheating time of 20 mins. were chosen to give a minimum through-thickness temperature gradient and minimum scaling although the latter was not particularly a problem with stainless steel. The furnace temperature gradient was measured and an 'L' shaped refractory brick fashioned so that the slabs could be positioned in the furnace to give a reproducible minimum longitudinal temperature gradient. This gradient was not greater than 10°C over the 5" (127 mm) standard length slab.

Heat conduction to the tongs was minimised by modifying them (Fig.31) so that there was only point contact between them and the slab. The design also allowed the slabs

to be lifted easily from the run-in and run-out tables thus preventing excessive conduction to them and the development of an asymmetrical temperature gradient between passes.

Up to six measurements of the initial and final thicknesses and widths were made using a micrometer and calipers respectively. Attempts to measure these dimensions during interpass periods in multipass schedules did not prove very successful due to the limited time available.

The majority of rolling sequences were based on a 3 x 30% reduction schedule with a medium roll speed (approx. 200 mm/sec. peripheral roll speed). Different series of tests were carried out to investigate the structural changes that occurred during rolling and their subsequent effect on the hot strength. They can be summarised as follows:

(i) The structural changes that occurred during the standard schedule were investigated by giving slabs either 1, 2 or 3 passes and water quenching them at different times after the last pass.

(ii) The effect of interpass holds was investigated by interrupting a particular run and reheating the slab at the exit temperature (T_1', T_2', T_3') of the previous pass. After holding for varying times the slabs were either water quenched to investigate the structural changes or given a further pass to investigate the effect of structure on rolling load. In cases when the recrystallisation rate proved to be very slow the kinetics were investigated by rolling one slab, quenching, sectioning into $\sim$1 cm. cubes, reheating the latter and quenching after different hold times. In either case the temperature during reheating was monitored.

(iii) The effect of substructure on rolling load was investigated by designing rolling and reheating schedules to give different substructures prior to a further pass. For example, the hot strengths given by the standard T_1, T_2, T_3 sequence were compared with those given by a T_1, T_3, reheat at T_3', T_3 sequence. Full details of such schedules are given in Table 5.

Limited single pass runs were carried out giving 10% and 20% reductions at the medium roll speed and 30% reductions at the minimum and maximum available roll speeds. One run was carried out to investigate the uniformity of deformation through the thickness. A slab was sectioned longitudinally along its mid-width plane and a rectangular grid machined on one exposed face, Fig.32. The two halves were held together by passing stainless steel rods through holes drilled in the slabs and welding their ends to the slab edges.

5.3 Measurement of Temperatures During Air Cooling

A considerable amount of work was carried out to determine the temperature gradients that develop during air cooling. Initial work was carried out on mild steel slabs which were drilled to receive two standard chromel-alumel thermocouples (4 mm diameter), one located centrally and the other closer to the surface, the distance from the surface being varied in different experiments. It was hoped to superimpose the cooling curves from the different runs to obtain the temperature gradients at any particular time of cooling from a variety of reheating temperatures. However it was found that this was not possible because the scale

thickness, the exact reheating temperature and the time taken to remove the specimen from the reheating furnace were not reproducible.

Having noted the above, further experiments were carried out with the following aims:

(i) To measure the temperatures at five points within a cooling slab simultaneously to give direct values of the temperature gradient.

(ii) To use the cooling data to obtain a value of the heat transfer coefficient (i.e. the rate of heat loss per unit area) as a function of the surface temperature, which could then be used in a finite difference computer programme to give detailed knowledge of the gradients.

(iii) To investigate the effect of experimental variables (e.g. scale thickness) on the cooling rate.

The cooling curve determinations were carried out on both mild and stainless steel specimens since both were hot rolled in the present work. In addition to slabs, the cooling curves of round billets were also measured. This was to provide data for parallel work concerned with the development of temperature gradients in extrusion billets during air cooling. Such data were also useful in the present work since, unlike rectangular bars, the surface temperature is constant along the circumference of a round billet. Hence the relationship between the heat transfer coefficient and the surface temperature should be more easily established. Finally, by using such a relationship in finite difference computer programmes for both round billets and flat slabs it was hoped to show that it was applicable to specimens of any geometry and/or dimensions.

To obtain direct measurements of temperature gradients, five 'Pyrotenax' thermocouples with exposed hot junctions were inserted in a series of specimens. The thermocouples were distributed so that they could determine the steep gradients close to the surface. The slab specimens had nominally the same width and thickness dimensions as those used in the hot rolling experiments but were 232 mm long and the thermocouples were located over the central 75 mm with their beads on the mid-width plane. One cooling curve determination was carried out on an as-rolled stainless slab (mean dimensions 57 mm x 7.75 mm) to investigate the effect of different width:height ratios. The round billets were 73.7 mm or 76.2 mm diameter and 120 mm long with the thermocouples located at a depth of 60 mm.

The thermocouples were connected to a 'Solartron' data logger with a built-in cold junction. The data logger was set to read one thermocouple per second (i.e. each thermocouple every 5 seconds) and the temperature output was made on punch tape which was subsequently read on a 'Flexowriter'. Surface temperatures were simultaneously measured with a Land continuous reading optical pyrometer whose output was recorded on a Telsec 700 potentiometric recorder. Previous tests, in which the pyrometer was calibrated by comparing its reading with that given by a thermocouple welded to the surface, showed that a suitable mean value of the emissivity was 0.85 ($\pm$ 0.01) over the 800-1100°C range. During the cooling of slabs the pyrometer was positioned so that it read the surface temperature at the centre of the top face (target area 4.6 mm). During billet cooling tests the pyrometer was

positioned so that it read the surface temperatures at the same depth as the thermocouples.

Reheating was carried out in a 17 kW controlled atmosphere billet furnace with the reheating time standardised at 30 minutes which ensured minimum scaling with a minimum temperature gradient. Reheating temperatures between 700 and 1150°C were used. Several furnace power cycles were monitored to determine the optimum time to remove the specimen i.e. the time when the temperature gradient in the specimen was at its minimum. On removal from the furnace the slab specimens were supported on bricks at each end, Fig.34, and the billets supported on a 3 pronged stand, Fig.35. During removal from the furnace, note was made of the time the door was opened, the time the specimen was moved over the sill and the time it was placed on the stand.

The cooling curves of the slabs were recorded twice for each reheating temperature, once with the thermocouples close to the top surface and once with the slab inverted so that the thermocouples were close to the bottom surface. This was to check whether an asymmetrical temperature gradient developed through the thickness of the slab which could possibly result from reradiation between the lower surface of the slab and the floor and/or different convection conditions for the top and bottom surfaces. The effect of different convection conditions was also investigated by cooling a slab which was clamped vertically on removal from the furnace. The development of a longitudinal temperature gradient during air cooling was investigated by using a mild steel slab with thermocouples inserted in the mid-thickness plane but at different distances from the end of the bar. Hughes (1975) later measured the

cooling curve of a 508 mm long stainless billet whose ends were insulated with asbestos sheets to investigate the development of axial gradients in round billets.

The effect of scale thickness was investigated qualitatively by measuring the cooling curves of a mild steel slab that had been allowed to scale heavily in the furnace. This was for comparison with the standard cooling curve determinations for which the mild steel specimens were shot-blasted and remeasured prior to each run. The stainless steel specimens scaled sufficiently slowly to make this unnecessary.

Finally, one cooling curve determination was carried out using two Pt/Pt-13% Rh thermocouples (3 mm diameter) embedded in a stainless steel slab and reheated to 1320°C. This was to provide data at temperatures greater than those attainable using the 'Pyrotenax' thermocouples.

5.4 Hot Torsion Testing

The stainless steel used in the present research had a significantly different composition to that used by previous workers (e.g. Barraclough 1974, Cook 1957) so a limited number of hot torsion tests were carried out to obtain stress-strain data for comparison with both the results of the above workers and with the data obtained in hot rolling. A 76 mm diameter billet was hot extruded at 1150°C preheat temperature with a fuminite and molyslip lubricant to 19 mm diameter rod. Torsion specimens of dimensions as given in Fig.36 were machined from the rod and tested in the torsion machine shown in Fig.37. The test method differed little from that described by Whittaker (1973) and Barraclough (1974) and the torsion machine is that

described by Coward (1970) with later modifications by Cole (1976). Torsion tests were carried out at 800, 900, 1000 and 1100°C at nominal true uniaxial strain rates of 0.3 and 3 per sec.

Preliminary tests were carried out to establish the effect of the reheating history on the grain size and resultant stress-strain curves. As a result, the reheating practice adopted was to soak the furnace at the desired test temperature, slide the specimen (already screwed into the grips) into the hot zone and to soak the specimen for 5 minutes once it had reached the test temperature. Fixed end tests were carried out, the specimen being given 2 revs. or tested to the point at which the torque dropped rapidly, the latter indicating the imminent fracture of the specimen. The strain, torque and temperature were recorded in the standard way on a U.V. recorder using a fast chart speed so that the initial work hardening portion of the stress-strain curve was accurately recorded.

5.5 Metallography

5.5.1 Specimen Preparation

The as-rolled stainless steel bars were sectioned using a water cooled slitting wheel or mechanical hacksaw. Longitudinal sections were taken so that the face examined lay close to the mid-width of the slab ($\pm$ 2 mm) and were hot mounted in bakelite. Transverse sections were not mounted. Both sections were taken from the central 20 mm of the slab. The torsion specimens were sectioned in a similar way, the longitudinal section being taken such that one half exposed

the maximum radius. The specimens were ground and polished in the standard way to a $\frac{1}{4}$ μm finish. Chemical polishing was not attempted since it did not appear necessary and Barraclough (1974) found that it could lead to pitting.

Considerable difficulty was experienced in satisfactorily etching the polished specimens. Electrochemical etching was attempted using the methods described by Muller (1967), Barraclough (1974) and McTighe (1975). A stainless steel cathode was used with an oxalic acid electrolyte (both as a 10 weight % and a saturated aqueous solution) at both room temperature and cooled by ice. A wide range of cell voltages, cathode-anode separations and etching times was used but none gave a satisfactorily even or deep enough etch without pitting.

Hence a chemical etchant was adopted. Kalling's reagent which consists of

20 ml	HCl
15 ml	H_2O
65 ml	methyl alcohol
1 g.	$CuCl_2$

was found to give only a very light etch. Schafmeister's reagent consisting of

50 ml	HCl
5 ml	HNO_3
50 ml	H_2O

was found to give reasonable results especially if a piece of iron foil was dissolved in the solution prior to use.

The steel composition was such that small amounts of ferrite were present under most conditions. Its distribution was initially investigated by a magnetic method i.e. a few drops of a water based, fine particle size magnetite

suspension were applied to the specimen surface which was then covered with a cover glass and the specimen subjected to a magnetic field. The ferrite distribution was clearly shown by the magnetite particle distribution. It was then realised that the ferrite was delineated by Schafmeister's reagent but the standard time required for a deep etch of the austenite boundaries was such that the ferrite was etched out. Thus, when examining the ferrite phase Schafmeister's reagent was used, but the etching time reduced by half.

5.5.2 Quantitative Metallography

5.5.2.1 Fraction Recrystallised

The fraction recrystallised was obtained using a point counting technique which was carried out by either by using a microscope fitted with a travelling stage linked to a digital counter which moved the stage in 0.05 mm increments or by superimposing a grid on 2 or 3 enlarged photographs of each specimen. In each case at least 400 points were counted to give an accuracy of better than $\pm$ 10% (95% confidence limits) in the 20% to 80% recrystallised range. The measurements were made on longitudinal sections since these allowed maximum distinction between the elongated deformed grains and the equiaxed recrystallised grains.

For specimens in which the recrystallisation rate appeared to vary from centre to surface, the point counting traverses were made at different distances from, and parallel to, the surface. For specimens which clearly recrystallised evenly throughout the thickness (i.e. those specimens which were given isothermal holding treatments) the traverses were made at random positions within the specimen.

5.5.2.2 Hardness Measurements

The study of the progress of recrystallisation was aided by carrying out hardness measurements using both macro- and microhardness techniques. The former were carried out on a Vickers pyramidal hardness machine with a 30 kg load. Approximately 20 measurements were made on each specimen and the distance of the centre of each impression from the surface measured with a travelling microscope. Microhardness measurements were carried out using a Leitz microhardness indenter with a 100 g. load.

5.5.2.3 Grain Size Determination

The grain size of fully recrystallised specimens was measured in the standard way, i.e. by measuring the number of grains intercepted by a line of standard length. Both a straight line and circle were used to investigate if there was any structural anisotropy.

5.6 Electron Probe Microanalysis

As will be described later, it was found that during some isothermal holding treatments recrystallisation was retarded in regions immediately below the surface. To investigate whether this was a chemical effect a limited amount of electron probe microanalysis was carried out on a Cambridge Mark 5 microanalyser. One specimen which clearly showed this effect was mounted in Wood's metal and ground and polished in the usual way to $\frac{1}{4}$ μm. finish. Continuous scans to a depth of 300 μm. perpendicular to the surface of the specimen and shorter scans in the centre of the specimen were carried out. Scans were obtained for Cr, Ni and Mn but the C, N, O and Nb levels proved to be too low for quantitative analysis.

CHAPTER SIX

TEMPERATURE CALCULATIONS DURING HOT ROLLING

6.1 Introduction

The literature review has emphasised the importance of a knowledge of the temperature changes and distributions that occur during hot rolling and the preceding chapter has described the experimental work carried out to measure such changes. The recording equipment used could only measure the temperature at one point within a slab during hot rolling and attempts to superimpose the temperature curves from different runs to obtain temperature distributions were found impossible since the experimental variables (reheating temperature, interpass times, reduction per pass) could not be reproducibly controlled. Hence a computer programme was developed which could predict the temperature changes and distributions at discrete points within a slab during a hot rolling schedule. This chapter will describe the mathematical basis of the programme by considering the equations relevant for the air cooling and roll contact phases.

It will be appreciated that, as in most mathematical models of complex situations, numerous simplifying assumptions have to be made and in some cases it is not clear which assumption is best. Where this is the case the assumptions and equations used in the programme will be described under 'Method A' whereas the alternatives will be described under 'Method B'.

6.2 Air Cooling

6.2.1 Basis of Model

The model of heat conduction within a cooling slab was based on the well established finite difference method using Fourier's First Law (eqn.4.2). Thus if there are two planes of area **A** and a distance **D** apart at temperatures T_1 and T_2, then the rate of heat flow, $\frac{dQ}{dt}$, between them is given by

$$\frac{dQ}{dt} = \frac{(T_1 - T_2)\ k\ A}{D} \qquad (6.1)$$

where k is the conductivity.

The finite difference approximation essentially involves the division of the medium into a number of small elements as already discussed (section 4.3.1), the varying temperature through the volume occupied by each element being represented by a single temperature at the centre of each element. Thus a one-dimensional temperature gradient as shown in Fig.38 is represented by the discrete temperatures shown, T_1 to T_n.

This approximation approaches the true situation as the number of elements approaches infinity, but as will be shown, sufficiently accurate solutions are obtainable from relatively few elements. The finite difference approximation then allows the representation of the differential equation (eqn.6.1) by

$$Q = \frac{(T_1 - T_2)\ k\ A\ \delta t}{D} \qquad (6.2)$$

where **A** is the area of the heat conducting path and **D** the distance between the discrete elements.

6.2.2 Heat Conduction within a Flat Slab

For the particular case of the heat flow within a flat slab where the length is much greater than the height or width, the problem is simplified by ignoring the heat flow out of the end faces, i.e. two-dimensional heat conduction is considered between the elements of a transverse section, Fig.39. Furthermore, the assumption is made that the top and bottom faces are subjected to identical cooling conditions and likewise for the two side faces. This implies identical radiation and convection conditions for the top and bottom faces during air cooling and no contact with the run-in and run-out tables during rolling. This assumption allows, by symmetry, the consideration of only one quarter of the transverse slice. The position of this slice is shown in Fig.39 and its division into elemental sections in Fig.40. Thus the representative section of the slab consists of W rows (each of height D2) and V columns (each of width D1). Each element, of small finite length L, is represented using matrix notation as N, M, where N is the row number and M the column number and the temperature at each node is represented by $T_{N,M}$. Considering the heat flow between the N,M node and its 4 nearest surrounding nodes, Fig.41, equation 6.2 gives the amount of heat flowing between adjacent nodes in a small time interval δt as

$$Q1 = \frac{(T_{N,M} - T_{N+1,M})\ D1\ L\ k\ \delta t}{D2} \qquad (6.3)$$

$$Q2 = \frac{(T_{N,M} - T_{N,M+1})\ D2\ L\ k\ \delta t}{D1} \qquad (6.4)$$

$$Q3 = \frac{(T_{N-1,M} - T_{N,M})\ D1\ L\ k\ \delta t}{D2} \qquad (6.5)$$

$$Q4 = \frac{(T_{N,M-1} - T_{N,M})\ D2\ L\ k\ \delta t}{D1} \qquad (6.6)$$

The convention used is that heat flow from left to right and from top to bottom in Fig.41 is positive. Theoretically, the conductivity k should be calculated for the temperature at each boundary of the N,M element. This was written into an early computer programme and it was found that there was only a minimal difference ($< \pm 0.5^{\circ}C$) in the computed temperature gradients when k was calculated at the boundary of each element and when it was calculated at the mean temperature of the slab. Since the former involves considerably more computation, it was not adopted.

The net heat flow into the N,M element is then given by

$$\Sigma Q = - Q1 - Q2 + Q3 + Q4 \qquad (6.7)$$

However when

$$N = 1,\ M \neq V,\ \Sigma Q = Q4 - Q2 - Q1 \qquad (6.8)$$

$$M = 1,\ N \neq W,\ \Sigma Q = Q3 - Q1 - Q2 \qquad (6.9)$$

$$M = 1,\ N = 1,\ \Sigma Q = - Q1 - Q2 \qquad (6.10)$$

These conditions cover all non-radiating (i.e. non-surface) elements.

Since $dQ = m\ s\ dT$ (6.11)

where m = mass of element
$= D1\ D2\ L\rho$

ρ = density

s = specific heat

then the temperature change at N,M due to conduction from the surrounding elements is given by

$$\Delta T = \frac{\Sigma Q}{D1\ D2\ L\ \rho\ s} \qquad (6.12)$$

and hence the new temperature $T^{*}_{N,M}$ at the end of the interval is given by

$$T^{*}_{N,M} = T_{N,M} + \Delta T \qquad (6.13)$$

It should be noted that L is common to equations 6.3 to 6.6 and 6.12 and so may be omitted. When M=V and/or N=W it is necessary to consider the amount of heat lost by radiation and convection (in the case of air cooling) or conduction to the rolls (in the case of rolling).

6.2.3 Heat Loss during Air Cooling

The heat lost by radiation and convection during air cooling is governed by the heat transfer coefficient H which is a function of the surface temperature T_s:

$$H = b\,(T_s - T_o) + c\,(T_s^4 - T_o^4) \qquad (6.14)$$

where H = amount of heat lost/unit area/unit time

T_s, T_o = surface, ambient temperatures, ^oK

b, c are constants.

The T_o^4 term is negligible at elevated temperatures and so has been ignored and the constant c is a product of the emissivity ε and the Stefan Boltzmann coefficient (5.67×10^{-11} kW/m^2). Although ε is temperature dependent (section 4.4.1.1) a value of 0.84 was found suitable in the present work for the 800-1100°C range for stainless steel. Converting the above equation to ^oC, then

$$H = b\,(T_s - T_o) + c\,(T_s + 273)^4 \qquad (6.15)$$

As will be described, the air cooling data obtained in the present work were used to obtain values of b and c and the best fit of computed cooling curves to experimental cooling curves was obtained by:

$$H = -0.6875 + 0.01247\,T_s + 4.7628 \times 10^{-11}\,(T_s + 273)^4 \qquad (6.16)$$

where T_s is measured in ^oC and H in kW/m^2.

Since H represents the amount of heat lost per unit area per unit time, then the amount of heat lost Q in a small time interval δt by an elemental surface area A is given by

$$Q = \bar{H} A \delta t \qquad (6.17)$$

where $\bar{H}$ is strictly the mean rate of heat loss per unit area for the time interval under consideration. To obtain $\bar{H}$ it would be necessary to know the surface temperature, and thus the heat transfer rates, at both the start and end of the time interval. This would involve a time consuming iterative procedure which was not considered worth while for the relatively low values of $\bar{H}$ obtained during air cooling. Hence $\bar{H}$ was calculated using the surface temperatures at the start of the interval and its value will be denoted by H_o.

If Q5 and Q6 are the amounts of heat lost by the surface elements of the bottom and side edge respectively (Fig.42) then

$$Q5 = H_o \, D1 \, L \, \delta t \, 10^3 \qquad (6.18)$$

$$Q6 = H_o \, D2 \, L \, \delta t \, 10^3 \qquad (6.19)$$

where H_o is measured in kW/m^2.

For the surface elements, these heat losses are included in the ΣQ for conduction (as already discussed). Thus during air cooling the combinations of the heat losses are as follows (see Fig.42):

If N = 1 and

$$\begin{cases} M = 1 & \Sigma Q = (-Q1) - Q2 & (6.20) \\ M = 2 \text{ to } V-1 & \Sigma Q = (-Q1) + Q4 - Q2 & (6.21) \\ M = V & \Sigma Q = (-Q1) + Q4 - Q6 & (6.22) \end{cases}$$

If N = W and

$$\begin{cases} M = 1 & \Sigma Q = (Q3 - Q5) - Q2 & (6.23) \\ M = 2 \text{ to } V-1 & \Sigma Q = (Q3 - Q5) + Q4 - Q2 & (6.24) \\ M = V & \Sigma Q = (Q3 - Q5) + Q4 - Q6 & (6.25) \end{cases}$$

If N = 2 to W-1 and

$$\begin{cases} M = 1 & \Sigma Q = (Q3 - Q1) - Q2 & (6.26) \\ M = 2 \text{ to } V-1 & \Sigma Q = (Q3 - Q1) + Q4 - Q2 & (6.27) \\ M = V & \Sigma Q = (Q3 - Q1) + Q4 - Q6 & (6.28) \end{cases}$$

The brackets have been added to make the symmetrical combinations clear. Having found ΣQ for any particular element, the new temperature for that element is found from equations 6.12 and 6.13.

6.2.4 Surface Temperatures during Air Cooling

It is necessary to calculate the surface temperatures since they control the amount of heat lost by radiation and convection (or by conduction to the roll during a pass). The assumption is made that the surface temperature (T^*_S) and the temperature at the centre of the surface element ($T^*_{W,M}$) at the end of an interval, see Fig.43, belong to a parabola whose origin is at the centre of the slab and at an arbitrary temperature T_o. It is also assumed that the mean temperature of the surface element lies at the physical centre of that element.

It should be noted that the latter assumption is never strictly true for any element of a parabola or pseudo-parabola but the error introduced is negligible for

(a) conductive heat transfer between adjacent small elements, and (b) for the case of extrapolation from the mean temperature of the surface element to obtain the surface temperature during air cooling.

It should also be noted that poor estimates of the surface temperature are self-compensating i.e. if the drop in surface temperature is over estimated for one interval then the heat transfer coefficient is under estimated for the subsequent interval. This point will be considered more fully when considering the conductive heat transfer between roll and slab.

If T_o is an arbitrary temperature at the centre of the slab and T_x the temperature at a distance x from the centre, then it can be shown from a consideration of the heat fluxes across a small element that

$$T_x = T_o - ax^2 \qquad (6.29)$$

where a is a constant. Considering the M^{th} column of the slab, Fig.43, then this parabolic equation gives

$$\text{(i)} \quad T^*_{W,M} = T_o - a\,(W-\tfrac{1}{2})^2\,D2^2$$

$$\text{(ii)} \quad T^*_s = T_o - a\,W^2\,D2^2$$

so by subtraction,

$$T^*_s = T^*_{W,M} - a\,D2^2\,(W-\tfrac{1}{4})$$

In addition by differentiating equation 6.29

$$\left(\frac{dT}{dx}\right)_{surface} = -2a\,W\,D2$$

and from equation 6.1 it follows that

$$\left(\frac{dT}{dx}\right)_{surface} = \frac{-H_1}{k}$$

so

$$a = \frac{H_1}{2\;W\;D2\;k} \qquad (6.30)$$

where H_1 is strictly the rate of heat loss per unit area at the end of the interval. As the surface temperature is unknown at the end of the interval then so is the heat loss rate and unless an iterative procedure is adopted (as already

discussed) it is necessary to assume that $H_1 = H_o$. The errors introduced by such an assumption will again be self-compensating. Thus the temperature at the surface of the M^{th} column at the end of the interval is given by

$$T_s^* = T_{W,M}^* - \frac{H_o \, D2 \, (W-\frac{1}{4})}{2 \, W \, k} \qquad (6.31)$$

Similarly for the N^{th} row,

$$T_s^* = T_{N,V}^* - \frac{H_o \, D2 \, (V-\frac{1}{4})}{2 \, V \, k} \qquad (6.32)$$

6.2.5 Stability Criterion during Air Cooling

As mentioned briefly in section 4.3.1, the successful solution of explicit finite difference equations is dependent on the correct choice of the computational time interval δt. If δt is too large spurious temperature values are obtained and the solution of the heat flow equations becomes unstable. The condition for stability is that the temperature gradient (propagating inwards from the surface) reaches no further than the inside edge of the surface element in the chosen time interval. Additionally it is advantageous for it to reach at least half way into the element so that the extrapolated surface temperature is obtained as accurately as possible. Thus in Fig.44 the maximum allowable time interval t_{crit} is such that an initially uniform temperature gradient ($T_{W-\frac{1}{2},M} = T_{W,M} = T_s$) becomes a gradient $T^*_{W-\frac{1}{2},M}$, $T^*_{W,M}$, T^*_s.

6.2.5.1 Method A

The assumption is made that $T^*_{W-\frac{1}{2},M}$ and $T^*_{W,M}$ lie on a parabola whose origin is at an arbitrary temperature T_o at the centre of the bar (Fig.44). By using the equation for

a parabolic temperature gradient (eqn.6.29) the following equations are obtained:

$$\text{(i)} \quad T^{*}_{W-\frac{1}{2},M} = T_o - a\,(W-1)^2\,D2^2$$

$$\text{(ii)} \quad T^{*}_{W,M} = T_o - a\,(W-\tfrac{1}{2})^2\,D2^2$$

By subtraction and substitution for 'a',

$$T^{*}_{W-\frac{1}{2},M} = T^{*}_{W,M} - \frac{H_1\,D2}{2\,W\,k}\,(\tfrac{3}{4}-W) \qquad (6.33)$$

The heat lost from the surface element of area **A** in time δt is given by eqn.6.17 as

$$\Delta Q = \bar{H}\,\mathbf{A}\,\delta t$$

and since

$$\Delta Q = m\,s\,\Delta T$$

$$= \mathbf{A}\,D2\,\rho\,s\,(T_{W,M} - T^{*}_{W,M})$$

then

$$T_{W,M} = T^{*}_{W,M} + \frac{\bar{H}\,\delta t}{D2\,\rho\,s} \qquad (6.34)$$

The simultaneous solution of equations 6.33 and 6.34 assuming that $\bar{H} = H_o = H_1$ (as before) coupled with the limiting condition for stability gives

$$\delta t_{max} = \frac{D2^2\,(W-\frac{3}{4})\,\rho\,s}{2\,W\,k} \qquad (6.35)$$

This expression gives the maximum allowable value of the time interval to be used in the finite difference equations and represents the time taken for the temperature gradient to reach the inside edge of the surface element. If it is desired (for the reason outlined above) that the temperature gradient reaches at least half way into the element, then the minimum allowable time interval is a quarter of this value since $\delta t \propto (D2)^2$.

It should be noted that this equation is based on the elemental thickness (D2) being less than the elemental width (D1) as is applicable to slabs (assuming the use of

square matrices i.e. the same number of rows and columns). In the case of D1 < D2, then equation 6.35 needs to be changed to

$$t_{max} = \frac{D1^2 \, (V-\frac{3}{4}) \, \rho \, s}{2 \, V \, k} \qquad (6.36)$$

and if D2 = D1, then the stability criterion has to be based on the temperature changes occurring in the corner element.

6.2.5.2 Method B

A slightly different approach is based on assuming that the temperature gradient penetrates a distance X into the surface element, Fig.45. In this case it is assumed that the temperatures T_o^*, T_1^* and T_s^* form a parabola whose origin is at T_o^* (= T_o) and at a distance X from the surface. By considering the heat balance of the surface element for the start and end of the interval and making identical assumptions about the rate of heat loss as in 6.2.5.1 it can be shown that the time interval (δt) for penetration to a depth X is given by

$$\delta t = \frac{X^2 \, \rho \, s}{6 \, k} \qquad (6.37)$$

Thus the maximum allowable time interval is given when X = D2

$$\text{i.e. } \delta t_{max} = \frac{D2^2 \, \rho \, s}{6 \, k} \qquad (6.38)$$

6.2.5.3 Method A vs. Method B

Although of a similar form, the two criteria differ in that only one is dependent on the number of elements representing the slab.

Similar equations of both types were found in the literature for the case of cylindrical billets. The use of both equations in the computer programme showed that, for a

typical situation, method A gave a stable time of ~ 0.25 sec. compared with ~ 0.1 sec. for method B. Since both methods gave a stable solution, the former was chosen as it necessitated fewer calculations for a given air cooling period. The temperatures given by using the two criteria differed by less than $0.5^{\circ}C$ after 1 second of air cooling and less than $0.05^{\circ}C$ after 10 seconds air cooling of a 50 mm x 20 mm slab from $1180^{\circ}C$.

6.2.6 Summary of Solution for Air Cooling

The above equations form the essential basis of the finite difference method of computing the development of temperature gradients within a slab during air cooling. The flow chart shown in Fig.46 gives a brief summary of the logical application of these equations in a computer programme.

6.3 Hot Rolling

6.3.1 Introduction

The basic model for the heat flow within a slab during hot rolling is identical to that already discussed for air cooling. However during the roll contact phase, the side surface continues to air cool while the bottom surface chills by contact with the rolls and simultaneously the slab both changes in dimensions and gains heat due to deformation. Thus additional equations and computational routines had to be devised to accomplish the following:

(i) Division of each pass into a number of equal time intervals which satisfied the stability criteria for the dimensions of the elements at both the start and end of the pass. For the slab dimensions used in the

present work it was necessary to subdivide each row in the slab matrix into 3 new rows for reasons which will be discussed.

(ii) Definition of elements to represent the roll and equations to describe the heat transfer within the roll.

(iii) Equations to determine the amount of heat conducted from the slab to the roll.

(iv) Equations to determine the temperature rise in the slab due to deformation.

(v) A stepwise decrease in the slab element size in the thickness direction to represent deformation during rolling.

6.3.2 Subdivision of Matrix Prior to the Pass

The time interval applicable to the typical element and matrix dimensions was 0.25 seconds (using Method A) whereas the contact time was usually less than 0.2 seconds. Thus the maximum allowable stable time interval had to be reduced so that there were an integral number of time intervals per pass, the minimum number allowable being considered to be 5. This reduction was achieved by subdividing each row in the slab matrix into 3 new rows, thus decreasing the stable time by approximately 9. The definition of the temperatures for the centre of the new elements was carried out by parabolic interpolation as described in Appendix 3.

At the end of each pass it was no longer necessary to use the subdivided matrix and hence the original number of rows was returned to. This is also described in Appendix 3.

6.3.3 Stability Criterion During Rolling

The choice of the time interval δt to be used during the roll contact phase is complicated by the changing dimensions of the elements during a pass and the correct choice is crucial because the heat transfer rate is so great. Since there are 3W rows during a pass and the slab has initial and final dimensions h_1 and h_2 respectively, then the maximum value of the time interval relevant to the dimensions at the end of the pass is given by

$$\delta t_{max} = \frac{h_2^2 \, (3W - \frac{3}{4}) \, \rho s}{216 \, W^3 \, k} \qquad (6.39)$$

using the assumptions of section 6.2.5.1 (method A) and adapting eqn.6.36. The alternative assumptions (6.2.5.2) give

$$\delta t_{max} = \frac{h_2^2 \, \rho s}{216 \, k \, W^2} \qquad (6.40)$$

The choice is governed by identical principles as given in 6.2.5.3. Such equations satisfy the stability criterion for the end of the pass and therefore must do likewise for the larger element dimensions at the start of the pass. However, if it is wished to satisfy the other requirement that the gradient penetrates at least halfway into the surface element then an additional restriction is operative

$$\text{i.e.} \quad h_2^2 > \tfrac{1}{4} h_1^2 \qquad (6.41)$$

which imposes a maximum reduction of 50%.

6.3.4 Definition of Elements to Represent the Roll

The roll was represented by an array similar to that used for the slab with the same number of columns in the slab as in the roll and with the width of the columns being equal.

The number of rows in the roll matrix was made equal to the number of time intervals in the pass. This ensured that the temperature did not 'build up' at the innermost element of the roll and also prevented an excessive number of elements in the roll. It should be noted that only a limited surface region of the roll was considered since the gradient only penetrates to a depth of a few mm. The volume of each element in the roll was made equal and its value dictated by the stability criterion. It was only necessary to consider a small 'slice' of the roll of surface arc length $\delta 1$ as shown in Fig.47. Thus at time t a slice of slab of length 1 and elemental height D2 is in contact with the roll but at the start of the next time interval (i.e. at time $t + \delta t$) the elemental height is $D2^*$ and length 1^*. Since it is assumed that the temperature at the centre of each element is independent of the elemental length and since, for each time interval, the heat exchange is considered and then translated into new temperatures for the end of the interval, it is possible to consider a constant arc length on the surface of the roll.

Returning to the definition of the roll elemental volume it is first necessary to consider the stability criterion in the roll.

6.3.4.1 Stability Criterion for Roll

Using principles similar to those for Method A in the slab it is assumed that there is initially a uniform temperature in the roll, Fig.48, so that $R_s = R_1 = R_2$. It is assumed that the new temperatures at the end of the interval

are R_s^*, R_1^*, R_2^* where $R_2^* = R_2$ i.e. the gradient has penetrated to a depth of y_1. Assuming, as before, that R_1^* and R_2^* lie on a parabola whose origin is at the centre of the roll at an arbitrary temperature R_o then

$$R_1^* = R_o + b\, w_1^2 \tag{6.42}$$

and $$R_2^* = R_o + b\,(r - y_1)^2 \tag{6.43}$$

where r = roll radius

w_1 = distance of centre of surface element to centre of roll

$b = \dfrac{H_1}{2\,r\,k'}$ (cf. eqn.6.30)

H_1 = heat transfer rate per unit area during rolling

k' = thermal conductivity of roll.

Subtraction gives

$$R_2^* - R_1^* = \frac{H_1}{2rk'}\left[(r - y_1)^2 - w_1^2\right] \tag{6.44}$$

The heat gained by the surface element in the time interval δt is given by

$$\Delta J = \bar{H}\, D1\, \Delta l\, \delta t \tag{6.45}$$

and also $$\Delta J = v' s' \rho' (R_1^* - R_1) \tag{6.46}$$

where v' = elemental volume in roll

s', ρ' = specific heat, density of roll

Additionally

$$w_1^2 = \tfrac{1}{2}\left\{r^2 + (r - y_1)^2\right\} \tag{6.47}$$

Solving equations 6.44 to 6.47 and assuming $\bar{H} = H_1$

$$v' = \frac{4\,r\,k'\,D1\,\Delta l\,\delta t}{s'\rho'\left\{r^2 - (r - y_1)^2\right\}} \tag{6.48}$$

Additionally $$v' = \frac{\Delta l\, D1}{2r}\left\{r^2 - (r - y_1)^2\right\} \tag{6.49}$$

Solving 6.48 and 6.49 simultaneously gives the minimum volume of the roll surface element for the stability criterion to be valid as

$$v' = \sqrt{\frac{2k' D1^2 \Delta l^2 \delta t}{s' \rho'}} \qquad (6.50)$$

Using the principles of method B (section 6.2.5.2) (i.e. assuming that R_1^* lies on a parabola whose origin is at R_2^* and a distance y_1 from the surface) no solution could be found.

6.3.4.2 Dimensions of Elements in Roll

Having defined the volume of each roll element it is now possible to define the dimensions of each element. Fig.49 shows the dimensions of interest in the roll which is split into **X** rows, **X** being the number of time intervals during a pass. Let a particular row in the roll be the A^{th} row, the distance to the inside edge of this element being y_A from the surface and the distance from the centre of the element to the centre of the roll being w_A. Working in degrees

$$\theta = \frac{180\ \Delta l}{\pi\ r} \qquad (6.51)$$

and the area of each element (hatched in Fig.49) is given by

$$a' = \frac{v'}{D1} \qquad (6.52)$$

Since

$$a' = \frac{\theta\ \pi}{360} \left\{ (r - y_{A-1})^2 - (r - y_A)^2 \right\} \qquad (6.53)$$

by rearrangement it can be shown that

$$y_A = r - \sqrt{(r - y_{A-1})^2 - \frac{2\ r\ a'}{\Delta l}} \qquad (6.54)$$

Thus having found y_1, y_2 to y_x are defined.

$$y_1 = r - \sqrt{r^2 - \frac{2\ r\ a'}{\Delta l}} \qquad (6.55)$$

The values of w_A (A = 2 to X) are given by

$$w_A = \sqrt{\left\{(r - y_A)^2 + (r - y_{A-1})^2\right\}/2} \qquad (6.56)$$

and w_1 is given by

$$w_1 = \sqrt{\left\{(r - y_1)^2 + r^2\right\}/2} \qquad (6.57)$$

The other dimensions of interest are the lengths of the curved boundaries of the A^{th} element. Simple geometry gives the length of the inside curved boundary, a, as

$$a = \frac{\Delta l}{r}(r - y_A) \qquad (6.58)$$

and the length of the outside curved boundary as

$$b = \frac{\Delta l}{r}(r - y_{A-1}) \qquad (6.59)$$

6.3.5 Heat Conduction Within the Roll

The roll consists of V columns of width D1 (= width of element in slab) and X rows of variable dimensions as discussed, see Fig.50. Matrix notation is used as before with $R_{A,B}$ representing the temperature at the centre of the element belonging to the A^{th} row and B^{th} column. The heat transfer between the roll elements is based on identical principles to those for the slab. So referring to Fig.50, for the A,B element,

$$J1 = \frac{(R_{A-1,B} - R_{A,B})\ D1\ b\ k'\ \delta t}{W_{A-1} - W_A} \qquad (6.60)$$

$$J2 = \frac{(R_{A,B} - R_{A+1,B})\ D1\ a\ k'\ \delta t}{W_A - W_{A+1}} \qquad (6.61)$$

$$J3 = \frac{(R_{A,B-1} - R_{A,B})\ a'\ k'\ \delta t}{D1} \qquad (6.62)$$

$$J4 = \frac{(R_{A,B} - R_{A,B+1})\ a'\ k'\ \delta t}{D1} \qquad (6.63)$$

Where a and b are given by eqns.6.58 and 6.59, a' by eqns.6.50 and 6.52 and k' is the thermal conductivity of the roll.

The heat gained by the surface element of the roll by conduction from the slab is given by

$$J5 = \bar{H} \quad \Delta 1 \quad D1 \quad \delta t \tag{6.64}$$

where $\bar{H}$ is the mean rate of heat transfer per unit area between slab and roll for a particular interval and will be defined in section 6.3.6.1. The net amount of heat, ΣJ, flowing into any element is given by one of the following combinations:

If B = 1 and

$$\begin{cases} A = 1 & \Sigma J = (-J4) + J5 - J2 & (6.65) \\ A = 2 \text{ to } X-1 & \Sigma J = (-J4) - J2 + J1 & (6.66) \\ A = X & \Sigma J = (-J4) + J1 & (6.67) \end{cases}$$

If B = V and

$$\begin{cases} A = 1 & \Sigma J = (J3) - J2 + J5 & (6.68) \\ A = 2 \text{ to } X-1 & \Sigma J = (J3) - J2 + J1 & (6.69) \\ A = X & \Sigma J = (J3) + J1 & (6.70) \end{cases}$$

If B = 2 to V-1 and

$$\begin{cases} A = 1 & \Sigma J = (J3-J4) - J2 + J5 & (6.71) \\ A = 2 \text{ to } X-1 & \Sigma J = (J3-J4) - J2 + J1 & (6.72) \\ A = X & \Sigma J = (J3-J4) + J1 & (6.73) \end{cases}$$

Having found ΣJ for any element then the new temperature for that element at the end of the interval is given by

$$R^{*}_{A,B} = R_{A,B} + \frac{\Sigma J}{v' s' \rho'} \tag{6.74}$$

where v' = volume of roll element (eqn.6.50)

s', ρ' = specific heat, density of roll.

It should be noted that this analysis assumes that there is no heat flow in the roll in the axial direction beyond the point at which the corner of the slab is in contact with the roll. Furthermore it is assumed that there is no tangential heat flow, either in the slab or in the roll.

Finally it is assumed that the initial roll temperature is uniform for any pass. This requires that the length of rolled slab is less than the roll circumference for any pass and that the interpass time is long enough for the steep temperature gradients induced during a pass close to the roll surface to be dissipated. Although these requirements are realistically met during the laboratory rolling schedules, this is not necessarily true during industrial schedules.

6.3.6 Heat Conduction Between Slab and Roll

6.3.6.1 Basis of Model

The model of heat conduction between slab and roll is the essential feature of this work which distinguishes it from previous work. As discussed in Chapter 4, the majority of previous models have assumed zero contact resistance between slab and roll (i.e. an infinite heat transfer coefficient) and it is clear that this is far from the physical truth and this has been confirmed by the lack of agreement between measured values and the analytical solution. In the present model it is assumed that the rate of heat transfer per unit area between slab and roll is proportional to the difference in their surface temperatures

i.e. $$H = C\,(T_s - R_s) \qquad (6.75)$$

where T_s, R_s are the surface temperatures of slab and roll respectively

and C is a constant.

It is also clear that, since the values of T_s and R_s are constantly changing over any small time interval δt, it is necessary to make some assumptions about their values during the time interval. It is assumed that at the start of any

interval (time t) during a pass the slab elemental height is D2 (see Fig.51) and that at the end of the interval (time $t + \delta t$) the slab elemental height is $D2^*$. It is assumed that for the time interval δt, the conduction of heat between slab and roll is dependent on the mean slab elemental height ($\overline{D2}$) and on the mean heat transfer coefficient $\overline{H}$, where $\overline{H}$ is a suitable mean value of H_o and H_1, the heat transfer coefficients at the beginning and end of the interval respectively.

It is first necessary to derive equations for estimating the surface temperatures of roll and slab during their contact period.

6.3.6.2 Surface Temperature of Roll

Section 6.3.4 defined the volume, and hence the dimensions, of the roll elements in such a way that they led to a stable solution i.e. so that the temperature gradient in the roll did not penetrate any deeper than the inside edge of the first element in the first time interval. With such a roll element volume it was found that the roll and slab surface temperatures tended to fluctuate up and down especially during the first few intervals of a pass and it was thought that this arose for the following reason.

In the first time interval during a pass the roll surface temperature rises rapidly due to the large value of H. In the second time interval the heat flow from slab to roll would be relatively much smaller due to the large decrease in the difference between roll and slab surface temperatures.

However, in the same interval a relatively large amount of heat would be conducted from the roll surface element to its inner neighbour and hence the mean temperature of the roll surface element would fall for the second interval. The extension of this argument can explain the observed damped fluctuations in the surface element and surface temperatures of both slab and roll. Although this effect did not lead to instability as such, it was felt that such fluctuations were undesirable. The fluctuations were removed by increasing the roll elemental volume by an empirical factor i.e.

$$v' = n\, v' \qquad (6.76)$$

A value of n of 1.4 was found suitable. On reflection it seems more likely that this effect may have originated from poor estimates of the surface temperatures and/or mean values of the heat transfer coefficient. Additionally, there is the problem that, whereas the roll elemental volume is based on the thermal data for the initial roll temperature, the mean roll temperature (and hence the thermal diffusivity) rises during a pass. This means that the distance penetrated by a gradient from the surface increases with time during a pass and hence introduces the possibility of instability after the initial contact between roll and slab. Which of these explanations is correct is not clear and the effect was not investigated further once it was found that the empirical increase in volume solved the problem.

Having redefined the dimensions of the elements in the roll it was considered necessary to ensure that the estimate of the roll surface temperature was as realistic as possible. It was assumed that the temperature gradient

penetrated to a distance $\sqrt{2\ r_W^2 - r^2}$ from the centre of the roll as shown in Fig.52, where r_W is the distance of the new temperature for the surface element from the centre of the roll. Using the assumptions of Method A (6.2.5.1) it is assumed that R^*_W and $R^*_{1,B}$ lie on a parabola whose origin lies at the centre of the roll at an arbitrary temperature R_o. Using the standard parabolic equation it can be shown that

$$R^*_{1,B} = R^*_W + b\ (r^2 - r_W^2) \tag{6.77}$$

and since $b = \dfrac{H_1}{2\ r\ k'}$ and $R^*_W = R_W = R_{1,B}$

then $$R^*_{1,B} = R_{1,B} + \frac{H_1\ (r^2 - r_W^2)}{2\ r\ k'} \tag{6.78}$$

The heat gained by the surface element is given by

$$\Delta Q = \bar{H}\ D1\ \Delta l\ \delta t \tag{6.79}$$

and since $$\Delta Q = v'\ \rho'\ s'\ (R^*_{1,B} - R_{1,B}) \tag{6.80}$$

then 6.78 to 6.80 give

$$r_W = \sqrt{r^2 - \frac{2\ r\ k'\ \bar{H}\ \Delta l\ D1\ \delta t}{v'\ s'\ \rho'\ H_1}} \tag{6.81}$$

When this equation was used it was assumed that $\bar{H} = H_1$. The use of the Method B principles (section 6.2.5.2) to derive r_W was not investigated.

The roll surface temperature is then obtained from the parabola whose origin is at the centre of the roll and a temperature R_o and which includes $R^*_{1,B}$ and R^*_s. It can be easily shown that

$$R^*_s = R^*_{1,B} + \frac{H_1}{2\ r\ k'}\ (r^2 - r_W^2) \tag{6.82}$$

6.3.6.3 Slab Surface Temperature

The slab surface temperature during rolling is obtained in a similar way as during air cooling (section 6.2.4). However the situation is more complex during rolling since the slab thickness is changing in stepwise manner. Since the time interval used during the roll contact phase is based on the slab dimensions at the end of the pass, then the temperature gradient only penetrates to a distance D_x (see Fig.53) at the start of the pass. Thus the mean temperature of the surface element does not lie at $\overline{D2}/2$ (or more strictly $\overline{D2}/\sqrt{3}$) and such an assumption would lead to a low value of the surface temperature. It was considered that a better estimate of the surface temperature could be obtained by assuming that the mean temperature T_1^* of the surface element at the end of the interval lay at a distance $D_x/2$ from the surface.

The assumptions of Method A and the usual parabolic equations were used to derive a value of D_x as

$$D_x = \frac{2\,W\,\overline{D2}}{3} - \sqrt{\left(\frac{2\,W\,\overline{D2}}{3}\right)^2 - \frac{8\,W\,k\,\delta t}{3\,\rho\,s}} \qquad (6.83)$$

The use of Method B and eqn.6.37 used in reverse gives a considerably simpler expression:

$$D_x = \sqrt{\frac{6\,k\,\delta t}{\rho\,s}} \qquad (6.84)$$

As mentioned already, the heat transfer between slab and roll is based on $\overline{H}$ (a function of H_0 and H_1) and hence the surface temperatures of interest are those at the end of each interval. In the above equations D_x has been calculated using the mean slab dimensions ($\overline{D2}$) and it was assumed that the effective distance penetrated at the end of the interval

was $\frac{D_x\ D2^*}{\overline{D2}}$, see Fig.54. Hence in the parabolic extrapolation to obtain T_s^* from T_1^* it was assumed that T_1^* is a distance $\frac{D_x\ D2^*}{2\ \overline{D2}}$ from the surface. Manipulating the parabolic equation in the usual way, it can be shown that

$$T_s^* = T_1^* - \frac{H_1\ D2^*}{2\ W\ k}\left(2W - \frac{D_x}{2\ \overline{D2}}\right)\left(\frac{D_x}{2\ \overline{D2}}\right) \qquad (6.85)$$

It should be noted that when $D_x = D2$ and $\overline{D2} = D2 = D2^*$, the above equation reverts to that for surface temperatures during air cooling (equation 6.31).

The equations outlined above for estimating the surface temperatures of both roll and slab are thus dependent on extrapolation from a varying distance from the surface. The equations to obtain a value of this distance are based on a uniform initial temperature (which is never true) and are a mathematical simplification of a complex physical situation. Additionally, these equations were used for all intervals during a pass which, on reflection, may not be justified. However it was found that whichever equations were used to estimate this variable distance the final mean temperature was affected by less than 2%. This point is discussed further in section 6.3.6.5.

6.3.6.4 Details of Heat Transfer between Roll and Slab

As mentioned earlier the model assumes that the roll gains heat over an area $\Delta l\ D1$ whereas the slab loses heat over an area $\Delta l.\cos\beta_2.D1$ as shown in Fig.55 where β_2 is the angle of the roll from the vertical halfway through a particular interval. The heat transfer coefficient $\overline{H}$ is

defined as having a direction along the radius of the roll and thus is independent on the angular position of the roll. The heat transfer coefficient for the slab is therefore $\bar{H}/\cos\beta_2$ so that

(i) when the roll slice is vertical, the heat transfer coefficients are equal and

(ii) when the roll slice is horizontal (clearly a practical impossibility) the slab heat transfer coefficient needs to be infinite to obtain a finite heat transfer along the roll radius.

Since the amount of heat transferred is given by the product of the heat transfer coefficient, area and time interval, the heat gained by the roll is $\bar{H}\ \Delta 1\ D1\ \delta t$ and likewise the heat lost by the slab is given by $\left(\frac{\bar{H}}{\cos\beta_2}\right)\Delta 1\cos\beta_2\ D1\ \delta t$. As is correct, the amount of heat lost by the slab is equal to the amount gained by the roll. Since the slab elemental volume losing heat is $\overline{D2}\ D1\ \Delta 1\cos\beta_2$, the temperature drop in the slab is given by

$$\Delta T_{cond} = \frac{\bar{H}\ \Delta 1\ D1\ \delta t}{\overline{D2}\ D1\ \Delta 1\cos\beta_2 . s\rho} = \frac{\bar{H}\ \delta t}{\overline{D2}\cos\beta_2 . s\rho} \qquad (6.86)$$

The volume of the roll element gaining heat is v' (eqns.6.50 and 6.76) so that the temperature rise in the roll surface element is

$$\Delta R_{cond} = \frac{\bar{H}\ \Delta 1\ D1\ \delta t}{v'\ s'\ \rho'} \qquad (6.87)$$

The heat transfer coefficient is a rapidly changing function with time as shown in Fig.56 and it is necessary to average its value for any particular time interval. Since H is not simply related to time it was found impossible to

obtain the true value of $\bar{H}$ and it was estimated from

$$\bar{H} = \frac{n H_o + m H_1}{m + n} \qquad (6.88)$$

where m and n are empirical integers. Fig.56 also shows that when m = n = 1, $\bar{H}$ is overestimated by an amount dependent on time. The optimum values were found to be n = 1, m = 9.

Having obtained the above equations, the new temperature at the centre of the slab surface element at the end of a time interval δt is given by

$$T_1^* = T_1 + \frac{\Sigma Q}{D1\ D2\ s\ \rho} - \Delta T_{cond} \qquad (6.89)$$

where T_1 is the surface element temperature at the start of the interval, $\Sigma Q/(D1\ D2\ s\ \rho)$ is the temperature change due to conduction within the slab and ΔT_{cond} has been defined by eqn.6.86. Similarly, the temperature at the centre of the roll surface element at the end of the interval is given by

$$R_1^* = R_1 + \frac{\Sigma J}{v'\ s'\ \rho'} + \Delta R_{cond} \qquad (6.90)$$

where ΔR_{cond} has been defined by eqn.6.87. The surface temperatures of roll and slab at the end of the interval have been obtained in eqns.6.82 and 6.85 respectively. Defining the heat transfer coefficients for the start and end of an interval as

$$H_o = C\ (T_s - R_s) \qquad (6.91)$$

$$H_1 = C\ (T_s^* - R_s^*) \qquad (6.92)$$

and solving eqns.6.82, 6.85, 6.89 and 6.90 simultaneously and substituting for $\bar{H}$, H_o and H_1 using eqns.6.88, 6.91 and 6.92 it can be shown that

$$T_s^* - R_s^* = \frac{T_1^o - R_1^o + A1 - (T_s - R_s)\ A2}{1 + A3 + A4} \qquad (6.93)$$

where $$A1 = \frac{\Sigma Q}{D1\ D2\ \rho s} - \frac{\Sigma J}{v'\ s'\ \rho'} \qquad (6.94)$$

$$A2 = \left(\frac{n.C.\delta t}{n+m}\right)\left(\frac{1}{\overline{D2}\ s\ \rho \cos\beta_2} + \frac{\Delta 1\ D1}{v'\ s'\ \rho'}\right) \qquad (6.95)$$

$$A3 = \left(\frac{m\ C\ \delta t}{n+m}\right)\left(\frac{1}{\overline{D2}\ s\rho\ \cos\beta_2} + \frac{\Delta 1\ D1}{v'\ s'\ \rho'}\right) \qquad (6.96)$$

$$A4 = C\left\{\frac{D2^*\ D_x\ (2W - D_x/2.\overline{D2})}{4\ W\ k \cos\beta_3\ \overline{D2}} + \frac{(r^2 - r_W^2)}{2\ r\ k'}\right\} \qquad (6.97)$$

A consideration of these equations shows that the difference in surface temperatures of slab and roll is now known for the end of the interval in terms of known dimensional parameters and known temperatures at the start of the interval. Hence the heat transfer coefficient, H_1, is known for the end of the interval (eqn.6.92) and since it is known at the start of the interval (eqn.6.91), then the mean value, $\overline{H}$, is now known (eqn.6.88). Thus the surface temperatures at the end of the interval are known from eqns.6.82 and 6.85 and the surface element temperatures from eqns.6.89 and 6.90.

The above equations were initially solved by an iteration technique but its use was discontinued when it was found that the above simultaneous equations gave almost identical results in significantly shorter computation times.

6.3.6.5 Effect of Simplifying Assumptions

In the above sections several empirical assumptions have been made regarding the accurate estimation of roll and slab surface temperatures but regardless of their accuracy there remains the problem of obtaining an estimate of $\overline{H}$ from the initial and final values of H during an interval.

The effect of a poor estimate of $\bar{H}$ is shown in Fig.57. This shows the changing values of

(i) the mean temperature of the whole slab,

(ii) the temperature at the centre of the surface element of the innermost column, and

(iii) the surface temperature of the innermost column.

In one case $\bar{H}$ was obtained from $\frac{H_o + H_1}{2}$ and the surface temperatures extrapolated from a variable distance (D_x and r_w) for only the first interval. In the other case $\bar{H}$ was obtained from $\frac{H_o + 2H_1}{3}$ and the variable distance was used for all intervals. It can be seen that whereas the former approach overestimates the surface temperature drop, the latter gives 'smoother' temperature changes. The important fact to note is that both methods gave identical mean, centre of surface element and surface temperatures by the end of the pass. Similar effects were also noted in the roll. It was later found that this average was not suitable for higher values of C. Fig.58 shows the computed temperatures (as noted above) for C = 200 $kW/m^2\ ^oC$. It can be seen that the use of $\bar{H} = \frac{H_o + H_1}{2}$ leads to such a large overestimate of the heat loss in the first interval that the surface temperature is apparently higher than that at the centre of the surface element! The use of $\bar{H} = \frac{H_o + 2H_1}{3}$ prevented the latter but still caused an overestimation of the heat loss in the first interval. Finally $\bar{H} = \frac{H_o + 9H_1}{10}$ was adopted and it can be seen that the temperature changes are relatively smooth. As before, it can be seen that the method of averaging had only a minor effect on the temperatures on exit from the rolls.

This self-compensating effect appeared to counteract possible inaccuracies introduced by the simplifying assumptions, i.e.

different combinations of different equations for $\bar{H}$, T_s^*, R_s^*, D_x and r_w all gave very similar temperatures on exit from the pass. It was thus concluded that the equations adopted were suitable.

6.3.6.6 The Constant C

As has been noted, the constant C is partly dependent on the scale thickness and since the latter decreases during a pass it is necessary to increase C as the slab element size changes. It was assumed that the scale thickness underwent the same reduction as the slab so that

$$C_{current} = C_{init} \quad \frac{h_{init}}{h_{current}}$$

As will be discussed, this expression allowed the accurate prediction of temperatures for a three pass laboratory rolling schedule and different values of C were not necessary for each pass.

6.3.7 Change in Element Size During a Pass

The assumption of a stepwise decrease in the slab element height has already been introduced. In the time interval δt the roll slice moves through an angle $d\phi$ (see Fig.51) where

$$d\phi \text{ (deg)} = \frac{180\,\delta t\, v}{\pi\, r} \qquad (6.98)$$

where v is the peripheral roll speed and r the roll radius. At the beginning of the first interval during the pass the angle of the roll from the vertical (the contact angle) is β_1 and the element height D2 (equal to the element height prior

to the pass) where

$$\beta_1 = \cos^{-1}\left\{1 - \frac{(h_1 - h_2)}{2r}\right\} \qquad (6.99)$$

The mean element height for the first time interval depends on β_2 where

$$\beta_2 = \beta_1 - \frac{d\phi}{2} \qquad (6.100)$$

and is given by

$$\overline{D2} = \frac{r\,(1 - \cos\beta_2) + h_2/2}{W} \qquad (6.101)$$

Similarly, the element height for the end of the first time interval is given by

$$D2^* = \frac{r\,(1 - \cos\beta_3) + h_2/2}{W} \qquad (6.102)$$

where $$\beta_3 = \beta_1 - d\phi \qquad (6.103)$$

For succeeding time intervals the values of β_1, β_2, β_3 are all reduced by $d\phi$ and the above equations used with the new values. The stepwise change in element height is made at the end of each interval.

It should be noted that eqn.6.99 can be used to calculate the contact time since

$$\text{contact time} = \frac{\text{contact length}}{\text{peripheral roll velocity}}$$

This gives

$$t_{cont} = \frac{2\pi r}{360\,v}\cos^{-1}\left\{1 - \frac{(h_1 - h_2)}{2r}\right\} \qquad (6.104)$$

In this model it is assumed that no roll flattening takes place and that sticking friction is operative throughout the roll gap. It is also assumed that no spread occurs during the pass. If it wished to allow for the latter (the effect is minimal) a stepwise increase in element width is made at the end of the pass.

6.3.8 Temperature Rise due to Deformation

There are several ways of calculating the temperature rise in the slab due to deformation as reviewed in section 4.4.2.1. The fundamentally correct approach is to calculate the work done (and hence the temperature rise) for each element and for each interval during a pass from stress-strain curves for the temperatures and strain rates of interest. This method was not adopted because the stress-strain data were not available and it was felt that the extra computational time and extra memory necessary made this method unattractive.

Hence the temperature rise was calculated from values of the rolling torque. Gittins et al (1974A) have shown that

$$\Delta T_{def} = \frac{G}{r \sqrt{h_1 h_2}\ \rho s} \qquad (6.105)$$

where G is the torque per unit width. Rather than adding ΔT_{def} to the slab temperatures in one step it was decided to add $\Delta T'_{def}$ at the start of each interval where

$$\Delta T'_{def} = \frac{\Delta T_{def}}{\text{No. of intervals}} \qquad (6.106)$$

The torque values used were preferably those measured on the rolling mill after allowing for the frictional torques in the roll necks or, alternatively, those predicted from the rolling theories e.g. Cook and McCrum (1958). In this approach it was necessary to assume that the amount of deformational heating was independent of temperature and strain rate and that each element underwent an identical strain. The validity of the above approach was investigated as follows.

Firstly, the hot torsion data of Barraclough (1974) was used to predict the temperature rise due to deformation using the method discussed in Section 4.4.2.1 i.e. the work done per unit volume was found from the area under the stress-strain curve. This was converted to a temperature rise and plotted against the temperature compensated strain rate Z as shown in Fig.59. The computer programme was then used to give the typical temperature gradients occurring during the first pass of a three x 30% reduction schedule. The predicted temperatures (which had been found to agree with a typical run) of selected elements were then averaged to give a mean temperature for that element during the pass. A strain weighted average was used

$$\text{i.e. } \bar{T} = \frac{\sum_i \varepsilon_i \, T_i}{\sum_i \varepsilon_i}$$

where i was the number of intervals during the pass. The mean Z value was found for each element using the mean true strain rate and the temperature rise found from Fig.59 using linear interpolation between the lines for different strains. The resulting distribution of temperature rises is shown in Fig.60 and shows the rapid increase in ΔT_{def} near the surface where there is the large decrease in temperature due to conduction to the roll. The temperature rise at the centre was found to be 7.7°C and the mean temperature rise was 9.2°C. The measured temperature rise was 6-8°C and the rise predicted from the rolling torque (3800 N.m reduced to 2755 N.m after allowing for the frictional torque in the roll neck) was 9.9 °C. Hence within experimental accuracy and the limitations of the predictive method it may be concluded that, although the adopted method for calculating the temperature rise does not give the true distribution, the mean temperature rise is predicted satisfactorily.

6.4 Summary

The preceding sections have described the assumptions and methematical expressions to form the basis of a finite difference computer programme to predict the temperature changes in a flat slab during air cooling and hot rolling. Where appropriate, possible alternative assumptions and equations have been presented and their effects discussed. The model of heat conduction between slab and roll is fundamentally different from that used by previous workers and is based on the heat transfer rate being linearly dependent on the difference in surface temperatures of slab and roll.

The programme was written in BASIC and run on a Hewlett Packard 9830 computer. A line by line discussion of the programme together with programme listings and annotated typical print outs is given in Appendix 3. This programme for two dimensional heat flow was later adapted for one dimensional heat flow for simulation of typical industrial schedules; this is also discussed in Appendix 3.

CHAPTER SEVEN

RESULTS AND DISCUSSION OF PRELIMINARY WORK

The preliminary work carried out on mild steel, although primarily aimed at developing suitable methods and schedules for the subsequent rolling of stainless steel, also gave quantitative results which will now be presented and discussed.

7.1 Hot Strength Measurements

The mild steel rolling experiments were based on a 10, 20, 30, 40% reduction schedule, the nominal dimensions, strain rates etc. being given in Table 6. The torque meters were not operative for this part of the research programme and the load measurements may not be very accurate for reasons discussed in Appendix 1. The load cell outputs showed a maximum at entry to and exit from the rolls, this resulting from increased spread at the ends of the bar coupled with 'cold ends'. The rolling loads reported here were taken from the region of each load trace pertaining to the longitudinal position of the thermocouple. Only a few of the 21 preliminary experiments yielded both load and temperature data and these are shown in Fig.61. It should be noted that results for the first pass (10% reduction) have not been plotted as there was considerable uncertainty about the recorded temperatures since the thermocouples were not embedded tightly in the slabs. The temperatures plotted are those for the centre of the slab at the entry to the pass. The general

trend for increasing rolling load with decreasing temperature and increasing reduction and/or strain rate is clear. Also shown in Fig.61 are the rolling loads calculated from the data of Cook and McCrum (1958) for EN2 steel. During the preliminary work no careful measurements were made of the initial, intermediate or final dimensions and the calculated loads for each pass are based on the nominal reduction for that pass and estimates of the minimum and maximum values of the slab width. A mean width was used in the load calculation to allow for the initial barrelling and the spread that occurred during each pass.

Taking into account the above mentioned uncertainties, the agreement between measured and calculated values is good, especially for the 20% and 30% reductions.

The load measurements were converted to mean plane strain compressive yield stresses using the theory of Sims (1954), the latter having been discussed in detail in section 2.4.4. The mean true uniaxial yield stress $\bar{Y}$ was then obtained using von Mises criterion ($\bar{Y} = \frac{\bar{S}\sqrt{3}}{2}$) and the values presented as a function of temperature in Fig.62. This figure also shows the mean flow stresses for the strains and strain rates relevant to each pass calculated from the hot torsion results of Hughes (1971) for the same material. The latter flow stresses were estimated by calculating the area under the torsion curves (using the trapezoidal method) to the reduction of interest and dividing by the strain. The temperatures and strain rates used in rolling and torsion differed so the mean flow stresses from the latter were plotted as a function of the temperature compensated strain rate,

Z, using the reported value of the activation energy for hot working of 74.6 kcal/mole (312 kJ/mole). This plot is given in Fig.63 which shows the increasing mean flow stress with increasing reduction and Z. The scatter in such a plot is thought to be due to the lack of accuracy in the raw hot torsion data.

The comparison of the mean flow stresses from torsion and rolling, Fig.62, shows that there is a similar relationship with temperature for the three reductions, but that the mean flow stresses from rolling are always higher than those from torsion tests. It is thought that this was due to the fact that the temperatures for the rolling results are those at the centre of the slab at entry to the rolls and the present work clearly showed that

(i) the mean temperature of a slab was lower than the centre temperature at any time,

(ii) a net temperature drop of between 20 and 70°C occurred by conduction between slab and rolls.

Hence the mean flow stresses from rolling need to be shifted to a lower, mean temperature, the amount of shift necessary depending mainly on the % reduction and slab dimensions. This was not investigated for the mild steel results, but it was clear from the results obtained on stainless steel that the general order of magnitude of the shifts would be 30°C, 35°C, 40°C and 50°C for the 10%, 20%, 30% and 40% passes respectively.

It therefore appears that the effect of temperature gradients and changes could prove to be an important one and this was more thoroughly investigated for the stainless steel.

It is interesting to note that such an effect was not demonstrated, Fig.61, when the measured rolling loads are compared with those predicted by Cook and McCrum (1958). However, as Fig.63 shows, the mean flow stresses calculated from the data of Cook and McCrum (1958) are significantly higher than those calculated from the data of Hughes (1971) for any particular reduction and value of Z. The cause of this discrepancy is uncertain. A comparison of the two materials, Table 4, shows slight differences in chemical composition, but it is difficult to assess the effect of these.

7.2 Temperature Measurements

The temperatures during the hot rolling of mild steel were measured and recorded by a variety of methods which are discussed in Appendix 2. The important qualitative result of the preliminary work was the development of a suitable method for investigating experimentally the large temperature changes that occurred during contact between slab and rolls. Fig.64 shows the temperature changes as measured by thermocouples located at the centre and 6.8 mm (initially) from the centre of an 18.4 mm x 39 mm mild steel slab during a 10, 20, 30% reduction schedule. It can be seen that the centre of the slab undergoes a temperature rise on entry to the rolls due to deformational heating, the rise increasing with increasing strain and strain rate and/or decreasing temperature (details of schedule given in Table 6). At the same time, positions close to the surface undergo a much smaller temperature rise followed by a rapid drop due to the conduction of heat to the rolls.

On exit from the rolls there is thus a steep temperature gradient in the slab and heat flows rapidly from the centre to the surface of the slab to re-establish the equilibrium temperature distribution. This is shown in Fig.64 by a rapid decrease from the peak at the centre of the slab and a rapid recalescence to a maximum for positions close to the surface. The rate of temperature adjustment can be seen to increase with sequential passes. It was considered that the recalescence time would depend on the opposing factors of the mean temperature on exit, the exit thickness and the depth of penetration of the steep temperature gradient which would itself depend on the temperature and the contact time, the latter being a function of the initial thickness, reduction and rolling speed. Once the steep temperature gradient has been dissipated it can be seen that the two positions within the slab have essentially the same cooling rate until the start of the next pass.

Also shown in Fig.64 is the temperature record of a thermocouple located in a hole drilled at an angle so that it broke the slab surface at the centre of the top face. This run started from a different reheating temperature and had different interpass times and therefore is not directly comparable with the above results. However, it shows clearly the extremely rapid change in temperatures at the surface of the slab, the chilling effect increasing with sequential passes. It is considered that the increasing temperature drop recorded was probably a result of increasing contact time combined with deformation causing the thermocouple bead to be closer to, and in more intimate contact with, the surface.

The relatively slow response time of the potentiometric recorder used in the majority of the preliminary experiments meant that the temperature rise due to deformation could not be accurately measured. Hence no attempt was made to compare the measured temperature rises with those predicted from either the measured rolling loads or available hot torsion data.

The roll chilling effect was analysed to produce a heat transfer coefficient. Since the heat content, Q, of a bar is given by

$$Q = m\, s\, \bar{T}$$

where $\bar{T}$ is the mean temperature, then the heat lost by conduction to the rolls is given by

$$dQ = V \rho\, s\, \bar{T} - V^{*} \rho^{*} s^{*} \bar{T}^{*}$$

where the asterisk indicates values at the end of the pass. Since the slab volume is constant and since the product of the specific heat s and the density ρ is relatively temperature independent (4.98 $MJ/m^3\ ^{o}C$ at 1160°C and 4.91 $MJ/m^3\ ^{o}C$ at 800°C), then the amount of heat lost by conduction per unit area per unit time is given by

$$H = \frac{V \rho\, s\, (\bar{T}_{entry} - \bar{T}_{exit})}{A\, t_c} \qquad (7.1)$$

where t_c is the contact time

V, A are the volume and surface area of slab losing heat.

V was taken to be the volume of metal in the roll gap and A the contact area between slab and rolls. The volume to area ratio was found from

$$\frac{V}{A} = \frac{\frac{1}{2}(h_1+2R+h_2)\sqrt{R\,\Delta h - \frac{(\Delta h)^2}{4}} - \frac{\pi R^2}{180}\cos^{-1}\left(1 - \frac{\Delta h}{2R}\right)}{\frac{\pi R}{90}\cos^{-1}\left(1 - \frac{\Delta h}{2R}\right)} \qquad (7.2)$$

which follows from a consideration of the geometry of the roll gap. The heat transfer coefficient H in eqn.7.1 is found from the change in mean temperatures but these cannot be measured experimentally or deduced. However, to give an idea of the order of magnitude of the heat transfer coefficient the data provided by centrally located thermocouples was analysed to give values for this coefficient which would be relevant for the centre of the slab. The temperature drop for each pass was found by extrapolating the equilibrium coding curve after the pass backwards to the point at which the temperature started to rise due to deformation, as shown in Fig.65. The drops were used in eqns.7.1 and 7.2 to give values of H which are plotted against the slab surface temperature at entry to the rolls in Fig.66. The slab surface temperature is that at the centre of the top face and was estimated using the standard parabolic equation.

There were two main sources of error in this analysis. Firstly since detailed measurements of the initial and final slab dimensions were not made the values of the V/A ratio and the contact time could have had a large error, say 10%. The effect of the unknown thickness would also affect the estimation of the surface temperature but to a lesser extent. Secondly, since the heat transfer coefficient depends on the extrapolation of a cooling curve the latter needs to be as accurate as possible. It was considered that the extrapolation was no better than $\pm$ 2°C thus giving maximum accuracies of $\pm$ 10% and $\pm$ 2½% for temperature drops of 20°C and 80°C respectively (the range of

measured drops). Such an error also emphasised that increasing the interpass cooling rate by allowing the slab to cool by conduction to the run-out table could lead to serious errors.

Bearing these errors in mind it can be seen that the scatter in Fig.66 is not unreasonable for the 20%, 30% and 40% passes. It can be seen that H increases with temperature as expected but the results do not indicate whether the dependence is linear or more complex. The results for the first pass (10%) appear to lie below the general trend. It was considered that this indicated that the slab surface scale ($\sim$0.2 mm thick) prior to the first pass had a major effect on the amount of heat conducted to the roll. Since the scale was dislodged during the first pass, the heat transfer coefficient was higher for subsequent passes.

Experiments were carried out to investigate the development of temperature gradients during air cooling of mild steel slabs but suffered from the unreproducible effect of scale thickness. The results are presented in Chapter 8 together with the results of similar work carried out on the stainless steel.

7.3 Discussion of Results

In general the preliminary work was not extensive or accurate enough for a full quantitative analysis of the results. Regarding the hot strength results, the mean flow stresses derived from the measured loads were consistently higher than those predicted from the hot torsion data. This lack of agreement has been explained in terms of temperatures

and an estimate of the necessary correction given. The good agreement between measured loads and those predicted from Cook and McCrum is thought to be purely coincidental and to arise from the different hot strength characteristics of the two materials.

The rapidly changing temperatures during hot rolling were measured using limited recording equipment but nevertheless show good qualitative agreement with previous work, examples of which have been presented and discussed in Chapter 4. The quantitative analysis of the results gave a heat transfer coefficient for the conduction of heat from slab to rolls ranging from ~ 2 MJ/m^2 sec. at $\sim 700^{\circ}$C to ~ 7 MJ/m^2 sec. at $\sim 1100^{\circ}$C. Preisendanz et al (1967) quote a heat transfer coefficient of between 1.7 and 2.3 kJ/m^2 sec $^{\circ}$C thus giving a range of values of 1.2 to 2.5 MJ/m^2 sec over the 700°C to 1100°C range. Thus the present results indicate the same order of magnitude but a stronger temperature dependence. Preisendanz et al reached no conclusion regarding the temperature dependence. Seredynski (1973) assumed a roll heat conduction factor of 44 kJ/m^2 sec $^{\circ}$k, thus giving a range of between 43 and 60 MJ/m^2 sec for the heat transfer coefficient between 700°C and 1100°C. Thus the assumptions of Seredynski appear to overestimate the heat transfer coefficient by an order of magnitude. An example of the other extreme is given by Davis (1972) who assumed a heat transfer coefficient of 0.42 kJ/m^2 sec $^{\circ}$C thus giving values two orders of magnitude lower than Seredynski. Hence the present work gave results which lay within the large range of values assumed by previous workers. It was found that the

presence of a scale layer of ~0.2 mm thickness approximately halved the heat transfer coefficient compared with that for essentially scale free slabs. This indicates that the range of values for the heat transfer coefficient assumed in the literature is too wide.

The preliminary work emphasised that the following had to be achieved to obtain data as accurately as possible during the subsequent hot rolling experiments on stainless steel:

(i) The potentiometric recording system used in the preliminary work was too slow for the accurate recording of the rapid temperature changes during a pass and thus a U.V. recorder with an automatic back-off system was employed.

(ii) Since the accurate interpretation of the load and temperature results demands accurate values of the initial and final slab dimensions for each pass, data would have to be obtained regarding the mill spring and slab spread for use in multipass schedules where interpass measurements were not possible.

(iii) To be able to interrelate the mean flow stresses from rolling data and those from isothermal mechanical tests it would be necessary to estimate the mean slab temperatures during a pass. This could only be satisfactorily achieved by the use of a computer programme.

CHAPTER EIGHT

RESULTS

8.1 Temperatures During Air Cooling

Air cooling curve determinations were carried out on both flat slabs and round billets of mild and stainless steels and yielded both qualitative and quantitative results.

8.1.1 Qualitative Results

Although the mild steel specimens were shot blast prior to each run and reheating carried out in a controlled atmosphere, slight scaling was observed on the specimens on removal from the furnace. Additionally, scaling occurred during air cooling and, as expected, this was more serious for specimens cooled from the higher temperatures. Finally, in most cases the scale 'clinked' on cooling thus giving a non uniform scale thickness on any particular specimen. It was clear that these effects were not reproducible for sequential runs.

The effect of scale thickness is shown in Fig.67 which compares the cooling rates at the centre of the same mild steel slab following reheating firstly in a controlled atmosphere and secondly in air. The maximum room temperature oxide thicknesses were found to be 0.25 mm and 0.75 mm respectively with corresponding mean cooling rates of 2.94 and 2.24°C/sec. over the 1100°C to 800°C temperature range. The effect of oxide thickness was not investigated further since it was difficult to control and measure but it is clearly an important effect when considering the interpass air cooling of mild steel slabs during both laboratory and industrial hot rolling schedules. It was found that the stainless steel used in the present work developed only a fine powdery scale whose thickness did not measurably increase with temperature or reheating time (up to 4 hours at 1180°C and 30 mins. at 1300°C).

The mild steel cooling curves showed the γ to $\alpha+\gamma$ and $\alpha+\gamma$ to α phase transformations. The temperature of the former transformation was found to depend on the reheating temperature as the following tabulation shows:

Reheating Temperature °C	Transformation Temperature °C
1220	~ 740
1160	~ 754
1070	~ 774
850	~ 800

The decrease in transformation temperature with increasing reheating temperature was considered to be related to the increasing grain size and its effect on the nucleation rate of α in γ.

In view of the effects of scale thickness and phase transformation on the cooling rate it was decided to restrict the quantitative analysis of the cooling data to those obtained for the stainless steel. It was considered that, given similar oxide thicknesses and specimen dimensions, any quantitative data obtained for stainless steel could be satisfactorily applied to mild steel in the austenitic range. The justification for this is shown in Fig.68 which shows the experimental cooling curves for the centre of mild and stainless steel round billets of similar diameters (the origins have been shifted so that the curves almost coincide). It can be seen that, once equilibrium cooling is established, the cooling rates are similar in both billets.

As noted in section 5.3, the cooling curves of flat slabs were measured twice, once with the subsurface thermocouples close to the top surface and once close to the bottom surface. Comparison of the separate cooling curves showed no measurable difference in the cooling rates and it was therefore concluded that there was no development of an asymmetrical temperature gradient through the thickness of the slab. The symmetry of the temperature

gradient is important since it allows the finite difference computations to be carried out on a quarter section of the slab.

In both the quantitative analysis of the cooling data and in the computer model it was assumed that a transverse plane at the mid-length position underwent only two dimensional heat loss i.e. heat loss from the end faces was considered to be negligible. Data were obtained to determine under what conditions this assumption was true. Fig.69 shows the cooling curves of three positions in a 232 mm long mild steel slab. It should be noted that the three thermocouples indicated slightly different temperatures whilst the slab was still in the furnace and it was not clear whether this was due to the inherent temperature gradient of the furnace or inaccuracies of the thermocouples. After allowing for such differences it can be seen that thermocouple A (30 mm from end) deviates from thermocouple C (at centre) after approximately 10 seconds, while thermocouple B (98 mm from end) deviates after approximately 40 seconds. The onset of three dimensional cooling for the above two positions could be seen by a slight increase in slope in the original results. No such change could be seen for the central thermocouple which could imply that, even if the longitudinal temperature gradient reached the centre in, say, 60 seconds, the effect was minimal.

The air cooling curves for a stainless steel slab from 3 reheating temperatures are plotted in Fig.70 so that they almost coincide at low temperatures. The onset of three dimensional cooling was determined from the point at which the curve from a high reheating temperature became non-parallel with a curve from a lower reheating temperature, once two dimensional equilibrium cooling had been established in the latter. Although not capable of very high accuracy, this method showed that the longitudinal gradient reached the central transverse plane in ~80 seconds when cooling from 1100°C

and ~ 90 seconds when cooling from 1000°C. The computer programme for one dimensional heat flow later showed that the longitudinal gradient should reach the half-length plane in about 75 seconds air cooling from 1200°C thus agreeing reasonably well with the experimental results. Fig.70 also shows that even when three dimensional cooling is present the effect is negligible for up to ~150 seconds and hence it was ignored in all subsequent treatment of the air cooling data.

The development of an axial temperature gradient in the round billets is shown in Fig.68 where the cooling curve of a 120 mm long billet is compared with that of a 508 mm long billet with insulated ends. (The high temperature region of the latter has been omitted). It can be seen that the shorter billet took ~75 seconds to reach equilibrium cooling (i.e. when the curves are parallel) and then cooled more quickly after ~100 seconds. The latter divergence is an indication that the axial temperature gradient had reached the plane in which the thermocouples were located i.e. three dimensional heat loss was operative for the centre of the billet.

Considering the cooling curves of different positions within a stainless steel slab, Fig.71, two main points become clear. Firstly, there was up to 4°C random discrepancy between the different points in the slab whilst it was in the furnace, the origin of which was uncertain, as noted above. Secondly, considering the development of temperature gradients it can be seen that they appear 'sensible' (i.e. a progressive decrease in temperature from centre to surface) during the first 30 seconds but after this time the temperatures at 5.15 mm and 7.8 mm from the centre become indistinguishable. Such an effect may have arisen from either the longitudinal displacement of the thermocouples (the possible effects having been noted above) or from the original discrepancy in the thermocouples.

Similar effects were noted during most determinations. It was therefore considered that accurate values of the temperature gradient could not be obtained simply from such air cooling curve determinations. Additionally, the finite width of the thermocouple meant that there was considerable uncertainty concerning the exact position within the slab at which the temperatures were measured. There was a further uncertainty regarding the time at which true air cooling began because of the finite time to remove the specimen from the furnace. Finally, even if it was possible to measure the temperature gradients exactly, such measurements would need to be carried out for both the width and thickness directions and for a variety of dimensions and reheating temperatures if the mean temperature of the slab at entry to the rolls is to be determined.

To summarise the above briefly, the following main conclusions may be drawn:

(i) The cooling rate of mild steel depends on the scale thickness and is affected by transformation. Hence the cooling data were unsuitable for the present study.

(ii) During the air cooling of slabs, the through thickness temperature gradients are symmetrical about the centre and longitudinal gradients take a relatively long time to affect seriously the temperatures of a centrally located transverse section.

(iii) The measured through thickness temperature gradients could not be used directly to yield useful data regarding temperature distributions or mean temperatures during air cooling.

8.1.2 Quantitative Results

Having reached the above conclusions it was apparent that a full understanding of the development of temperature gradients during air cooling and hot rolling could only be gained from the combination of a mathematical model with suitable experimental data. The quantitative analysis of the air cooling data will now be considered. It is necessary to assume that, after a certain time of air cooling from the furnace, 'equilibrium' cooling exists in the body i.e. the cooling rate is identical at every point within the body. Clearly, at any point in time, the centre cools slightly faster than the surface so that a zero temperature gradient exists at room temperature. For all practical purposes the assumption is valid as can be seen in Fig.71 which compares the cooling rates of different positions within a slab. The assumption of 'equilibrium' cooling allows the use of a parabolic equation to describe the temperature gradient.

For a round billet, the surface temperature T_s is given by

$$T_s = T_a - \frac{s \rho \dot{T}}{4k} (r^2 - a^2) \qquad (8.1)$$

where T_a = temperature at a distance 'a' from the axis

$\dot{T}$ = cooling rate at 'a' from the axis

r = billet radius

s, ρ, k are the specific heat, density, conductivity.

Additionally, the heat content Q of the billet is given by

$$Q = m s T$$

$$\text{so} \quad \frac{dQ}{dt} = m s \dot{T}$$

where m is the mass of the billet and is given by

$$m = \pi r^2 l \rho$$

where l = length of billet

$$\text{so} \quad \frac{dQ}{dt} = \pi r^2 l \rho s \dot{T}$$

If it is assumed that heat is only lost radially then the heat transfer coefficient, H, is given by

$$H = \frac{dQ}{dt} \Big/ \text{unit area}$$

$$H = \frac{r \rho s \dot{T}}{2} \qquad (8.2)$$

The data used for the specific heat, thermal conductivity and density in the above and subsequent equations are given in Appendix 3.

Thus by measuring the temperature and cooling rate at any given point within a billet it is possible to relate H to T_s. The resulting relationship over a wide temperature range is shown in Fig.72 for a standard length billet (121 mm) and an 'infinite' billet (508 mm long with insulated ends). Considering the latter results first, a large amount of scatter and a stepwise increase of H with T_s is apparent. Both these effects are due to the accuracy of obtaining the cooling rate which was estimated from the difference in temperatures 10 seconds either side of a chosen temperature. Since the temperatures were only measured to $\pm$ 1°C this imposed an accuracy of $\pm$ 0.1°C/sec for the cooling rate. Such an error led to relatively large scatter bands for both H and T_s, an indication of these being given at selected points. Both curves show a maximum at high temperatures which indicates the onset of equilibrium cooling. Finally, considering the results for the short billet it can be seen that, although agreeing with those for the long billet within the experimental accuracy, the values of H are nevertheless consistently higher at any value of T_s except at high temperatures. This was taken to be an indication of axial heat flow in the short billet. This can be crudely corrected for by assuming that heat loss occurs equally from all faces of the short billet. Equation 8.2 then becomes

$$H = \frac{\rho s \dot{T} r l}{2 (l + r)} \qquad (8.3)$$

Substitution of the values of l and r showed that the values of H for the short billets should be decreased by a factor of 1.3 to give the true two dimensional heat transfer coefficient. Such a correction, although empirical, then gives good agreement between the results for the long and short billets after long cooling times (surface temperatures less than 850°C in Fig.72).

Similar principles were applied for the quantitative analysis of the slab cooling data. The parabolic equation in this case gives

$$T_s = T_x - \frac{s\rho}{2k} \dot{T} (a^2 - x^2) \qquad (8.4)$$

where T_x is the temperature at a distance x from the centre of the slab

$2a$ is the total thickness of the slab

T_s is the surface temperature at the centre of the top or bottom face.

The heat transfer coefficient is again given by

$$H = \frac{V\rho s \dot{T}}{A}$$

where V and A are the volume and surface area losing heat respectively. Assuming two dimensional heat loss then

$$\frac{V}{A} = \frac{a W}{2a + W}$$

where W is the slab width. Thus H is given by

$$H = \rho s \left(\frac{a W}{2a + W} \right) \dot{T} \qquad (8.5)$$

The results from 3 sets of cooling data are shown in Fig.73. Considering the data for the 19 x 52 mm and 7.75 mm x 57 mm slabs obtained with chromel-alumel thermocouples it can be seen that there is good agreement over the whole temperature range. The scatter in the results was considerably less than in those obtained for the round billets. This is because, although the error was the same in both cases, the cooling rate of the slabs was considerably higher. Also shown in Fig.73 are the results obtained at higher temperatures using Pt-Pt 13% Rh thermocouples. The error bars indicated on this plot arise from the

uncertainty regarding the true position at which the temperatures were measured due to the larger thermocouple diameter. It can be seen that the latter set of results is consistently higher than those obtained with chromel-alumel thermocouples. Although within the indicated errors, this difference could also arise from the higher inaccuracy of the chromel-alumel thermocouples.

Fig.73 also shows the mean curve of H vs. T_s obtained for the 'infinite' billet. It can be seen that, at any particular temperature, the heat transfer coefficient for the billet is higher than that for the slab. Furthermore, the difference increases with temperature. This is because the surface temperatures for the slabs are those at the centre of the top or bottom face, these being significantly higher than the mean slab surface temperature. Thus the curve for the slab needs to be shifted to lower temperatures, the shift increasing with temperature. Later computations showed that the shift varied from 24°C at 1000°C to 17°C at 800°C for the larger slab and from 25°C at 900°C to 15°C at 700°C for the thinner slab. This then allows good agreement between the curves for different geometries within the experimental accuracy.

The fitting of these data to a Stefan-Boltzmann equation has been briefly mentioned in section 6.2.3. Equation 6.15 gives

$$H = - b\ T_o + b\ T_s + c\ (T_s + 273)^4$$

where T_o, T_s are ambient, surface temperatures, °C

b is a constant

and $c = 5.67 \times 10^{-11} \times \varepsilon$ kW/m^2

Mean values of the data up to 1050°C in Fig.73 (the cooling data for an 'infinite' billet not being available at this time) were fitted to this equation by plotting $H - c\ (T_s + 273)^4$ against T_s to give a straight line of slope b and intercept $- b\ T_o$ as shown in Fig.74. A mean value of the emissivity ε over the temperature range of interest had been previously found to be 0.84. The best

fit appeared to be given by a line whose equation was

$$H = -0.376 + 0.01503\ T_s + 4.7628 \times 10^{-11}\ (T_s + 273)^4 \qquad (8.6)$$

where H is measured in kW/m^2, T_s in ^oC, and T_o was assumed to be 25^oC.

This equation was used in the finite difference computer programme to predict the temperature gradients and cooling rates of a flat slab. The predicted cooling rate was too high and it was considered that this was because the original values of H in Fig.73 had been plotted against the maximum surface temperature. This was corrected for by obtaining a plot of the mean surface temperature $\bar{T}_s$ against the maximum surface temperature from the computed results and then replotting H against $\bar{T}_s$. This did not prove very successful and a good fit was eventually obtained by empirically adjusting the convection term. The final equation was

$$H = -0.6875 + 0.01247\ T_s + 4.7628 \times 10^{-11}\ (T_s + 273)^4 \qquad (8.7)$$

This equation was found to give good agreement for the geometries investigated experimentally in which two-dimensional heat flow occurred. Fig.75 compares the experimental and computed cooling curves of a stainless steel slab. Accurate plotting of the results showed that the computed curve started 4^oC too low and coincided with the experimental curve after 100 seconds cooling at a temperature of $\sim 800^oC$. Hence the computed curve cooled too slowly by 4^oC in 300^oC (-1.3%). Comparison of measured and computed cooling curves for the thinner slab again showed good agreement and accurate plotting of the results showed that the computed curve over estimated the temperature drop by 5^oC in 450^oC ($\sim$80 seconds) i.e. an error of + 1.1%.

Equation 8.7 was also used in a finite difference programme developed by Whiteman (1975) to simulate the air cooling of the long billet with insulated ends. Again good agreement

was found and the equation underestimated the cooling rate by $\sim 2\%$. No attempt was made to simulate the air cooling of the short billets because, as already described, the axial gradient reached the centre in a relatively short time. It should be noted that in all these comparisons it was difficult to fit the computed curves to the initial stages of the measured curves. This was because of the finite time to remove specimens from the furnace, coupled with possible temperature gradients inherited from the furnace.

The computed gradients through the thickness and width of a flat slab are compared with the measured gradients (derived from Fig.71) in Fig.76. After allowing for the discrepancies in the temperatures as measured in the furnace and the uncertainty introduced by the thermocouple position ($\pm$ 0.75 mm) the agreement is reasonable. In retrospect it would have been beneficial to measure the transverse temperature gradients as well.

8.2 Temperatures During Hot Rolling

8.2.1 Temperature Measurements

The internal temperatures during the hot rolling of stainless steel slabs were measured and recorded as described in Section 5.2.2 and Appendix 2. A typical UV chart record for a centrally located thermocouple is reproduced in Fig.77 and clearly shows the temperature rise due to deformation of the slab followed by the rapid drop in temperature as the roll chilling effect penetrates inwards from the surface. A typical record for a subsurface thermocouple is presented and discussed in Appendix 2. The chart records were analysed as described in Appendix 2 to yield temperature-time curves for each rolling schedule, a typical example for a 3 x 30% schedule being given in Fig.78. It should be noted that these two curves were obtained from separate runs and slight differences in roll speed, initial dimensions, reduction per pass

and scale thickness means that the gradients should only be taken as an indication of the true gradients. The temperature changes can be seen to be similar to those presented and discussed for mild steel in Fig.64 and Section 7.2.

The effect of roll speed on the temperature changes can be seen by comparing the measured curves given in Fig.79 which show that the faster the roll speed, the greater the deformational heating and the smaller the chilling effect. These changes in behaviour are easily related to the changing strain rate and contact time respectively. Similarly, Fig.80 shows the increasing deformational heating and increasing roll chilling with increasing reduction at a constant roll speed, these changes being related to strain and contact time respectively.

All the available temperature-time curves were analysed to isolate the deformational heating and roll chilling effects. The former rise was found from the difference between the temperature at entry to the rolls and the peak temperature at exit. The latter was obtained by extrapolation so that the extra 'blip' (thought to arise from deformational heating of the thermocouple bead as discussed in Appendix 2) could be discounted. The extrapolation was of an empirical nature and although aided by the general shape of the computed curves, led to a possible error of $\pm$ 2°C for the first pass. The error increased for subsequent passes since the increased chilling rate made it more difficult to separate the 'blip' from the true temperature rise.

The temperature rises are given in Table 7 and presented as a function of temperature (at the centre of the slab at entry to the rolls) in Fig.81a. Allowing for the slight differences in strain and strain rate for each particular run and the above limitations of accuracy it can be seen that the temperature rise increases with decreasing temperature thus following the temperature

dependence of the mean flow stress. Additionally it would appear that the temperature rises for the first pass are lower than those for subsequent passes. Assuming that this does not result from experimental scatter it could arise from the increasing strain rate and increasingly deformed initial structures for passes subsequent to the first. This point is discussed further below. Fig.81a also includes the deformational temperature rises for 10% and 20% passes and for 30% passes at the minimum and maximum roll speeds. It can be seen that the lower strains led to the lowest temperature rises recorded. The temperature rises for the slow roll speed ($\bar{\dot{\varepsilon}} \sim 0.7\ \text{sec}^{-1}$) also lie consistently below the rises for the normal roll speed ($\bar{\dot{\varepsilon}} \sim 4\ \text{sec}^{-1}$) whereas the results for the maximum roll speed ($\bar{\dot{\varepsilon}} \sim 8\ \text{sec}^{-1}$) are not distinguishable from the general scatter. However the difference in strain rates in the latter case is not so great. Thus the limited results show a small decrease in the deformational heating effect with decreasing strain and strain rate.

The measured rolling loads were analysed to give a mean uniaxial flow stress ($\bar{\sigma}_p$) as described in Section 8.5.1 and are compared with the measureddeformational temperature rises in Fig.81b. A fair correlation can be seen, with the deformational temperature rise increasing with mean flow stress. Also shown in Fig.81b are the temperature rises calculated from the mean flow stresses as follows. The work done per unit volume is given by

$$\frac{W}{V} = \int_0^{\varepsilon} \sigma \, d\varepsilon = \bar{\sigma}.\bar{\varepsilon} \qquad (8.8)$$

$$\text{and} \quad \Delta T_{def} = \frac{1}{\rho s} \cdot \frac{W}{V} = \frac{\bar{\sigma}.\bar{\varepsilon}}{\rho s} \qquad (8.9)$$

Comparison with equations 2.26 and 2.27 shows that the mean flow stress to be used is $\bar{\sigma}_g$ whereas the rolling load gives $\bar{\sigma}_p$. Consideration of the Cook and McCrum data for 18-8 stainless steel showed that $\bar{\sigma}_p \simeq 1.06\ \bar{\sigma}_g$ for the ranges of strain, strain rate

and temperature used in the present work. By introducing this constant into equation 8.9, the correct relationship between ΔT_{def} and $\bar{\sigma}_p$ is obtained and this is presented graphically in Fig.81b. A constant value of ρs of 5 $MJ/m^3\ ^oC$ was used and values of ΔT_{def} are presented for strains equivalent to rolling reductions of 25 and 30% since this was the range of values obtained experimentally. Although showing reasonable agreement, this method of presentation does not allow the comparison of measured and predicted temperature rises for individual runs due to the varying strains involved.

The measured and predicted temperature rises are compared for individual runs in Fig.82. Good agreement can be seen, particularly for the second and third passes and reasons for the discrepancies for the first passes are considered in Chapter 9.

An alternative method for predicting the deformational heating effect is from the roll torques as proposed by Gittins et al (1974A), Section 4.4.2.1. Thus the rises were calculated using equations 4.22 and 4.23 after allowance had been made for the frictional torques developed in the roll necks, Section 8.5.1. A constant value of ρs was again assumed. The measured and predicted temperature rises are compared in Fig.83 and again show reasonable agreement with the worst discrepancy occurring for the first pass. The proposed equation is only strictly true for small contact angles and the effect of the simplification will be considered in Chapter 9.

The temperature drops due to conduction to the rolls were obtained using the same method of extrapolation as for mild steel, Section 7.2 and Fig.65. As with the mild steel results, the errors introduced by extrapolation were of the order $\pm 4^oC$. No attempts were made to analyse the results for slabs that had been allowed to cool excessively on the run out table or for slabs that had cooled for less than 10 seconds after the pass before quenching.

The temperatures at entry to the pass and the extrapolated exit temperatures are given in Table 7. Values marked with an asterisk are approximate values and arise because the above conditions were not fulfilled. They were not considered in the following analysis.

The temperature drops are presented as a function of the temperature at the centre of the slab on entry to the rolls in Fig.84. It is immediately clear that there is a large degree of scatter but nevertheless several effects can be seen:

(i) The effect of roll speed is very marked, the chilling effect increasing with contact time.

(ii) From the results for the first and second passes it would appear that the conductive temperature drop only increases slightly with increasing initial temperature.

(iii) The temperature drop appears to increase with sequential passes, this effect being due to the changing geometry and/or the decreasing scale thickness and slab surface roughness.

Attempts to convert the measured temperature drops at the centre of the slab into heat losses using the method adopted for mild steel results (Section 7.2) did not prove very successful and instead the analysis was based on mean temperatures. For each pass the entry and extrapolated exit temperatures were used, together with the relevant slab dimensions, to predict equivalent mean temperatures using the method described in Section 8.2.2 and the values are reported in Table 7. Consideration of the heat balance during the roll contact phase gives

$$\bar{T}_{exit} = \bar{T}_{entry} + \Delta\bar{T}_{def} - \Delta\bar{T}_{chill} \qquad (8.10)$$

The data were used to obtain $\Delta\bar{T}_{chill}$ for each pass using the values of $\Delta\bar{T}_{def}$ calculated from the mean flow stresses as described above. The values of $\Delta\bar{T}_{chill}$ were used to calculate

the mean heat loss per unit area, $\Delta\bar{h}_{chill}$, where

$$\Delta\bar{h}_{chill} = \frac{V \rho s \Delta\bar{T}_{chill}}{A} \qquad (8.11)$$

The use of the V/A ratio allows for the variable roll gap geometry as described previously in Section 7.2. The small observed effect of initial slab temperature was allowed for by dividing $\Delta\bar{h}_{chill}$ by the initial mean slab temperature to obtain $\Delta\bar{H}_{chill}$ ($J/m^2\ ^oC$), the corrected mean heat loss per unit area. Ideally a mean surface temperature, $\bar{T}_s$, should have been used but it was considered that the effect of temperature was sufficiently small, and that $\bar{T}_{entry}$ was sufficiently close to $\bar{T}_s$, to introduce a negligible error. Values of $\Delta\bar{H}_{chill}$ are presented as a function of contact time in Fig.85. The contact times were calculated from equation 6.104 and are presented in Table 8. It can be seen that there is a considerable scatter in the results but nevertheless the general trend of increasing heat loss with increasing contact time is clear. It is considered that part of the scatter is due to errors in estimating mean temperatures from measured temperatures. If an error of $\pm$ 2°C is allowed for in estimating both $\bar{T}_{entry}$ and $\bar{T}_{exit}$ from T^c_{entry} and T^c_{exit} and $\pm$ 2°C for estimating $\Delta\bar{T}_{def}$ from the mean flow stresses, then the final error in $\Delta\bar{H}_{chill}$ is as given in Fig.85. Other errors could arise from poor estimates of the slab dimensions during multipass schedules but it is considered that the method adopted (Section 8.5.3) would cause negligible errors in $\Delta\bar{H}_{chill}$.

Any remaining scatter is considered to arise from the varying scale thickness or slab surface condition and an attempt to understand this was made by superimposing values of $\Delta\bar{H}_{chill}$ computed for different values of C, the constant which controls the heat loss in the computer programme. It can be seen that most of the measured values fall in the range of C = 50 $kW/m^2\ ^oC$ to C = 1000 $kW/m^2\ ^oC$.

8.2.2 Temperature Calculations

Selected runs were simulated by use of the mathematical model described in Chapter 6. It has already been shown in Section 8.1.1 that the equation (8.7) derived to relate the heat transfer coefficient to the surface temperature could be used to satisfactorily predict the cooling rates and temperature gradients within a flat slab during air cooling. The simulation of practical rolling sequences necessitated fitting computed temperature curves to the measured curves by trial and error substitution of values of C, the unknown value of the constant which controls the heat transfer between slab and roll. It was considered that an agreement of $\pm$ 2°C between measured and computed curves was satisfactory, any further accuracy depending on the accuracy of the corrected torque values used to predict the mean deformational temperature rise.

An example of the excellent agreement between measured and predicted temperatures at the centre of a slab during a 3 x 30% pass sequence is shown in Fig.86. Simulations of this type of schedule showed that the use of an increasing C value (to allow for the decreasing scale thickness, Section 6.3.6.6) allowed good agreement for most three pass schedules without the need for a different initial C value for each pass. Also shown in Fig.86 are the computed temperature changes at the mid-width position, both at the surface and at a position initially 2.86 mm from the surface. Good qualitative agreement can be seen between the latter curves and the measured subsurface temperature curve given in Fig.78. It was not possible to simultaneously measure the temperature changes at the centre and subsurface positions so quantitative comparisons of measured and computed gradients could not be attempted.

Figs.87 and 88 show the good agreement between measured and computed temperature curves for a 30% pass at the maximum roll

speed and a 10% pass at the normal roll speed. The computed temperature changes at selected distances from the surface (at the mid width position) are also shown. Fig.87 shows poor agreement for the air cooling curves prior to the pass. This was a common problem and there are several possible explanations. Firstly, the presence of unknown temperature gradients in the slab whilst it was in the furnace would lead to anomalous cooling rates. Secondly, due to the finite time taken to remove the specimens from the furnace, the exact starting point for air cooling could not be determined. Finally, some slabs were allowed to cool on the run-in table prior to the pass, thus causing accelerated cooling rates. Hence the fitting of computed curves to measured curves was done on a temperature rather than time basis for cooling prior to the first pass. The cooling rates were generally found to show excellent agreement subsequent to the first pass.

Also shown in Figs.87 and 88 are two mean temperatures, namely that for the mid width line and that for the whole slab. It can be seen that the temperatures of the centre line become parallel both to each other and to the mean temperature of the centre line after a few seconds of air cooling, thus showing that an equilibrium through-thickness temperature gradient is soon established. However, the overall mean temperature is still divergent from the centre line temperatures at entry to the pass, this trend continuing until ~20 seconds after removal from the furnace. At this point it becomes parallel to the spectrum of temperatures for the centre line, this representing the onset of 'equilibrium' two dimensional cooling. The overall mean temperature also becomes lower than the centre line temperatures, thus showing that the width is relatively more important than the thickness in determining the overall mean temperature. This point is further illustrated in Fig.89 which shows the changing temperatures across the width at a

constant distance from the bottom surface for the same run as given in Fig.88. This illustrates clearly that several seconds are required before the transverse gradient reaches the centre line and that the gradient is still not fully established on entry to the rolls. Following the pass, the overall mean temperature retains a distinct curvature until $\sim$ 20 seconds after removal from the furnace after which the cooling rates of all points within the slab become essentially identical.

The temperature time curves presented above are not capable of showing the detailed development of temperature gradients during and immediately following a pass. The development of the through-thickness temperature gradient during the first pass of the 3 pass sequence given above is illustrated in Fig.90 and clearly shows the penetration of the steep temperature gradient inwards from the surface. The changing temperature gradient after the end of the pass is illustrated in Fig.91 and shows the rapid rise in temperatures close to the surface and, conversely, the rapid temperature drop at the centre. It can be seen that at intermediate distances from the centre the temperatures oscillate up and down and the dissipation of the steep gradient does not appear to be smooth. It is considered that this is an anomaly arising from the finite difference approximation and would be expected to disappear with an increased number of elements.

One reason for simulating practical rolling sequences was to enable the hot strength parameters to be related to a mean temperature during a pass. The changing overall mean temperature has been discussed above. Hence by fitting a computed curve to each measured curve the mean temperature of the slab cross section is automatically derived at each point in time. The mean temperature for a pass is then found from the average of the mean slab temperature at the start and end of the pass.

Ideally, the mean temperatures would be derived in this way for each practical sequence. However this proved impossible due to the computational time involved (about 3 hours on a Hewlett Packard 9830 per 3 pass sequence simulation, each sequence usually requiring at least 2 simulations). Thus the following short cut was adopted. Cooling curves were computed for a wide variety of slab dimensions and the difference between the temperature at the centre of the slab (T_c) and the mean temperature ($\bar{T}$) plotted against time, Fig.92, and against T_c, Fig.93. These plots show a rapid initial increase in $T_c - \bar{T}$ while the through-thickness temperature gradient is being established followed by a decelerating increase in $T_c - \bar{T}$ while the transverse gradient is being established. Finally, after going through a maximum, a gradual, non-linear relationship is established between $T_c - \bar{T}$ and T_c thus representing 'equilibrium' cooling. It can be seen that the time to reach the maximum is $\sim$20 seconds, thus reiterating the times necessary for the overall mean temperatures in Figs.87 and 88 to become parallel to the centre temperatures. The curves, which will be discussed more fully in Chapter 9 were used as follows:

(i) Fig.92 shows that $T_c - \bar{T}$ is strongly time dependent up to the peak (occurring at $\sim$ 20 seconds) so this plot was used for passes occurring at less than 20 seconds after the initial or intermediate reheating. Thus $T_c - \bar{T}$ was found in terms of the initial and final slab dimensions, reheating temperature and air cooling time from furnace to the start of the pass.

(ii) For all other passes it was assumed that equilibrium cooling was established so $T_c - \bar{T}$ was found from Fig.93 in terms of the initial and final dimensions and entry and extrapolated exit temperatures.

In this way, the mean temperatures were deduced for the start and finish of each pass and these are reported in Table 7.

Only a limited number of curves were computed in Figs.92 and 93 so interpolation was used to obtain $T_c - \bar{T}$ for intermediate cases. The accuracy was considered to be $\pm 2^{o}C$, this being supported by comparison of mean temperatures obtained this way with those obtained from computed simulations.

8.3 Results of Structural Studies

Selected stainless steel slab and torsion specimens were examined to produce information regarding the structural changes occurring during hot deformation sequences and yielded both qualitative and quantitative results.

8.3.1 Qualitative Results

8.3.1.1 General Observations

In general the microstructural examination of the stainless steel proved difficult due to problems in satisfactorily etching specimens. The final etchant adopted (Schafmeister's reagent) tended to give a non-uniform etch in spite of using a swabbing technique. It was often found necessary to over etch some areas to obtain a deep enough etch in other areas and this caused problems in high magnification observation.

Although the experimental material was nominally an 18-8 austenitic steel the composition (Table 4) was such that small amounts of ferrite were present in the steel under all conditions and, in some cases, sufficient to make the slabs weakly magnetic. Optical microscopy showed a second phase which appeared as 'stringers' in longitudinal slab and extruded bar sections e.g. Figs.94b,c and 102a,b respectively. Transverse sections showed that it was predominantly a grain boundary phase as Figs.99a,b and 102c to 102f show for slab and torsion specimens respectively. Using the early etchants the second phase was etched out and thus appeared black whereas later etchants combined with shorter etching

times showed the true existence of the second phase. It was found difficult to etch the specimens satisfactorily to show the second phase and simultaneously delineate the austenite grain boundaries.

The second phase was identified as ferrite by the use of a suspension of fine magnetite particles in water. When a drop of this suspension was applied to the specimen surface the particles took up a random distribution, but on application of a magnetic field they aligned themselves to give bands parallel to the rolling direction as shown in Fig.94d. These bands remained constant as the magnetic field was rotated. High magnifications showed that the majority of particles were attracted to the second phase and that each particle rotated as the applied magnetic field was rotated. Since the composition was such that the presence of ferrite might be expected from the phase diagram and since no other magnetic particles or phases would be expected in this steel, the second phase was presumed to be ferrite. A minority of the magnetite particles were found to cluster around points with no obvious structural features and it was presumed that sub-surface ferrite was responsible.

The ferrite stringers appeared to be heterogeneously distributed with a higher concentration at the centre of the as-received and rolled slabs. This is illustrated by comparison of Figs.94a and 94b. The ferrite distribution appeared relatively uniform over the gauge cross-sectional area of the torsion specimens but the ferrite concentration appeared to vary with reheating temperature. Figs.102a and 102c,e show longitudinal and transverse sections of the undeformed torsion specimen heads at 800°C and Figs.102b and 102d,f likewise at 1100°C. The transverse sections show a lower ferrite concentration at the higher reheating temperature and the longitudinal sections show the partial dissolution of ferrite to leave more isolated globules. The changes at intermediate temperatures were not clearly defined qualitatively.

The steel was heavily populated with inclusions, these appearing in a banded form. The most commonly occuring inclusions were hard, angular (often cuboidal) and orange-yellow in colour and were identified as titanium nitride. Some of the larger inclusions appeared to show a colour gradient as has been found for titanium cyano-nitride. These inclusions were not deformed during rolling as shown in Fig.100b. Among the other inclusions found were very fine, pink-mauve needles but, along with other inclusions, were too small and few in number to be readily identifiable.

8.3.1.2 Structural Changes During Rolling

The slabs were reheated at 1180°C (± 10°C) for 20 minutes prior to rolling and this led to a relatively uniform recrystallised structure, Figs.94a to 94c, which, as already described, consisted of an austenite matrix with ferrite stringers. It can be seen that the grain size was larger close to the surface which, as will be discussed, could be attributed to the lower ferrite concentration causing less impediment to grain growth.

Slabs were quenched at varying times after one of the three passes in the standard rolling schedule to study the progress of static recrystallisation during the interpass periods. Slabs quenched immediately following the first pass showed the as-rolled, deformed structure close to the surface, Fig.95a, the surface region becoming progressively more recrystallised as the delay time to quenching increased, Figs.95b to 95d. Regions in the centre of the slab showed a similar trend, Figs.96a to 96c. Since the depth of the unrecrystallised surface layer was found to be uniform along at least 25 mm of longitudinal sections and across the whole width of transverse sections, the position from which representative sections were taken was not particularly crucial.

Figs.95d and 96c therefore show incomplete and almost complete recrystallisation respectively at the surface and centre of

a slab quenched 20 seconds after the first pass. Since the second pass of the standard three pass schedule occurred at nominally 15 seconds after the first pass it can be assumed that the structure was mixed on entry to the second pass. No recrystallisation was found following the second pass, typical structures being given in Figs.97a to 97d. It can be seen that the surface regions show a heavily deformed structure and Fig.97b shows the characteristically deformed recrystallisation twins particularly well. The centre (Figs.97c and 97d) again shows a deformed structure, the general scale being much finer than for the surface. Thus the finer recrystallised grain size at entry to the second pass results in a finer deformed grain size on exit. The centre section (especially Fig.97c) shows occasional grains which are larger than average and this was taken to indicate incomplete static recrystallisation following the first pass.

Similarly, no static recrystallisation was found following the third pass of the standard sequence. A typical longitudinal section at the centre of the slab, Fig.98, shows a heavily deformed structure, and regions close to the surface were even more heavily deformed and coarser in a similar way to that noted above.

No structural changes were observed in the ferrite which became progressively compressed from a clearly defined grain shape (Fig.94c) to an essentially 'linear' phase (Fig.98) at which point it was often difficult to distinguish the austenite grain boundaries from the elongated ferrite stringers. The deformation of the ferrite phase was also shown clearly in transverse sections as exemplified by Figs.99a and 99b which show its location and shape following a single and three pass schedule respectively.

The important conclusion of the qualitative metallographic examination of recrystallisation during interpass periods is that it was very sluggish, leading to incomplete recrystallisation following

the first pass and zero recrystallisation following the second and third passes.

8.3.1.3 Structural Changes During Interpass Annealing

The above conclusion prompted the use of interpass reheating treatments to alter the structure that would normally be present prior to subsequent passes. Figs.100a and 100b show a longitudinal section at the centre of a slab that was given the standard sequence but reheated for 20 minutes at 1040°C following the first pass. Comparison of the structures following the third pass of the interrupted sequence with those of the standard sequence (Fig.98) showed no significant difference. However limited measurements of the aspect ratios of deformed grains close to the surface and at the centre of the slab following the third pass of the interrupted sequence indicated a more uniform structure than that produced by the standard 3 pass sequence. Thus it would appear that the interpass anneal promoted a more uniform recrystallised structure prior to the second pass. The gathering of such information was limited by the ability to etch the deformed grain boundaries (recrystallised grain boundaries always appeared to etch more easily) and, as already discussed, the difficulties of distinguishing between the grain boundaries and the deformed ferrite.

The relatively high rate of recrystallisation prior to the second pass of standard sequences meant that the structure could not be controlled sufficiently to investigate any effect it might have on the rolling load during the second pass. Thus it was decided to attempt to show any such effects by controlling the structure prior to, and thereby affecting the load during, the third pass. Hence the structural changes were investigated during annealing following two sequences, namely 30% at T_1, 30% at T_2 and 30% at T_1, 30% at T_3. Initial investigations were carried out by reheating slabs immediately after the second pass but it was again found that recrystallisation

was very sluggish. This enabled slabs to be rolled according to the two sequences and then quenched, sectioned into 1 cm cubes and the latter reheated to study the recrystallisation kinetics. Incidentally, this method had the advantage of ensuring that the structure prior to reheating was identical and that reheating was carried out at the same temperature for a particular series of specimens. Reheating was carried out at 900, 950 and 1000°C and in each case recrystallisation was so slow that 100% recrystallisation was not observed. Figs.101a to h show the structural changes that occurred at the centre and surface of a slab given a 30% at T_1, 30% at T_3 sequence followed by reheating at 1000°C. It can be seen that although recrystallisation has started after 600 seconds, it is still not complete after 19,200 seconds (5 hr 20 mins). Comparison of the ferrite concentrations at the centre of the specimens appears to show a decrease with increasing annealing time. These results will be discussed in conjunction with the limited quantitative results in Chapter 9.

8.3.1.4 Hot Torsion Specimens

The general structural features of the torsion specimens have already been described (8.3.1.1). Apart from the decreased ferrite content at 1100°C, Figs.102a and b also show that reheating to this temperature led to a more mixed structure, grain growth having occurred to a limited extent. This is also apparent in the transverse sections, Figs.101c and d. One specimen was heated to 1180°C before cooling to the test temperature of 900°C (to simulate the rolling practice more closely) and Fig.101g shows that this led to a higher dissolution of ferrite and a larger grain size variation. For these reasons this reheating practice was not adopted.

Examination of the deformed regions in the specimens showing poor ductility did not yield any conclusions regarding the

fracture mechanism. This was because the micro-cracks (penetrating inwards from the surface) were much larger than the austenite grain size or ferrite stringer width. The ferrite stringers appeared to be broken down in regions close to the specimen centre in longitudinal sections but this arose due to the helical nature of the deformation in relation to the sectioning plane.

8.3.1.5 Electron Microscopy

As will be discussed, some aspects of both the structural and strength studies appeared anomalous but could be explained in terms of precipitation under certain conditions. Evidence was sought to substantiate this possibility. 3 mm diameter rods were machined from the as-extruded bar and heat treated for 10 minutes at 800°C and 1100°C. Thin foils were prepared in the standard way and examined on the Phillips 301 electron microscope. Typical microstructures are shown in Fig.103.

Low magnification examination of the specimen treated at 800°C showed occasional large particles surrounded by a high density of dislocations, Fig.103a, but it is not clear whether these particles formed before or during annealing. At higher magnifications, many of the dislocations had a 'rippled' appearance and fine precipitates on the dislocations were just visible, Fig.103c. At the highest magnification, the dislocations were clearly seen to be 'decorated' by precipitates whose diameters were of the order of 200 Å, Fig.103e. The bowed nature of the dislocations could have arisen from either the strain induced by precipitation on the dislocations or from retardation of mobile dislocations during annealing.

Fig.103b shows the general structural features of the specimen treated at 1100°C and no large particles were found comparable to those observed following the lower temperature anneal. The high angle grain boundary in Fig.103b is shown in greater detail in Fig.103d and no precipitates were observed either on the dislocations

or in the grain boundary. The matrix dislocations are shown at a higher magnification in Fig.103f and, as in Fig.103d, no precipitates were observed.

Stacking faults were observed in both specimens as would be expected from the low stacking fault energy of austenitic materials. Fig.104a shows a stacking fault tetrahedron and this type of defect is only rarely observed. The more usual 'linear' type of stacking fault is illustrated in Fig.104b.

8.3.2 Quantitative Results

8.3.2.1 Initial Grain Size

The initial grain sizes of slab and torsion specimens were measured as described in Section 5.5.2.3 and the results are presented in Table 9. It can be seen that measurements are only given for one reheating treatment for the slab: this is because there was no method (i.e. hot shear) available for taking samples after reheating. However since all slabs were given the same reheating treatment it was considered that all would have essentially the same grain size.

The measurements made on torsion specimens showed a slight increase in grain size above 1000°C thus reflecting the qualitative observations. Although probably within experimental error, the grain sizes measured on transverse sections appear slightly lower than those measured on longitudinal sections. This may possibly arise from the ferrite restraining grain growth and will be discussed later.

8.3.2.2 Recrystallisation Kinetics

Attempts to measure the recrystallisation rates using both a point counting technique and superimposition of a grid on enlarged photographs proved to be difficult for several reasons. Firstly, as already noted, the adopted etchant often led to a non-uniform

etch on a macroscopic scale. Secondly, it was found difficult to differentiate consistently between recrystallised and unrecrystallised grains although the former were significantly smaller. In particular, some of the larger grains could be seen to have a faint, relatively equiaxed internal structure but because of the doubts regarding the evenness of the etch it was not clear whether this was recrystallised material or evidence of a substructure in deformed grains. Thus although Figs.101a to h show regions which are clearly either deformed or recrystallised, there remained many areas in which no definite decision could be made.

The point counting results for regions in the centre of specimens given a 30% at T_1, 30% at T_3 sequence followed by reheating at 950 and 1000°C are given in Fig.105. In each case timing was started when the specimen temperature had reached within 10°C of the furnace temperature and the latter fluctuated within $\pm$ 10°C of the nominal temperature during annealing. Additionally, the furnace temperature dropped by $\sim$10°C when specimens were removed and since the low capacity furnace took $\sim$100 secs. to regain the annealing temperature, later specimens in the same batch received a shorter true annealing time than that measured.

Bearing this in mind and, in addition, the errors in point counting (of the order of $\pm$ 5% for each % recrystallised), Fig.105 shows that, as expected, the time to any fraction recrystallised decreased with increasing annealing temperature. Extrapolation of the results show that $\sim 10^5$ seconds ($\sim$ 28 hours) annealing at 1000°C would be necessary to obtain a 90% recrystallised structure. The incubation time for the onset of recrystallisation can be seen to be of the order of 10^2 and 10^3 seconds at 1000°C and 950°C respectively. Fig.105 also includes selected recrystallisation data of Barraclough (1974). Although not for identical conditions, the present data show firstly an increased incubation time and secondly, a greatly

increased time ($\sim$ 2 orders of magnitude) to any fraction recrystallised.

As a result of the difficulties experienced in metallographic observation of the progress of recrystallisation, macrohardness testing was adopted. Such a method averages the hardnesses of the recrystallised and unrecrystallised areas to give an indication of the degree of restoration. The averages of at least 20 indentations on each specimen are plotted against log time in Fig.106 for two schedules (T_1, T_2 and T_1, T_3) and three annealing temperatures (900, 950 and 1000°C). It can be seen that there is a small decrease in hardness during the initial stages of annealing followed by a rapid drop leading finally to an essentially constant hardness level. The time to the onset of the rapid drop in hardness can be seen to decrease with increasing annealing temperature. The hardness of the as-rolled specimens can be seen to be higher for the slab given the T_1, T_3 schedule than for the slab given the T_1, T_2 schedule but the increased stored energy did not accelerate the restoration process.

The above hardness values were the average of values for the centre and close to the surface of the slab. For each series of specimens, the distances of the indentations from the surface were measured to give hardness profiles through the specimen thickness. A typical series of profiles is given in Fig.107 for a specimen annealed at 1000°C following a T_1, T_3 schedule. The broken lines indicate the areas outside which accurate hardness results could not be obtained because the surface was too close. (British Standard BS 427 Pt.1 (1961) limits the closest approach to 2.5 times the indentation diameter, typical values of the latter being 0.5 mm). Fig.107 shows a hardness gradient in the material immediately following rolling with the surface having the higher hardness. As the annealing time increases, both the gradient and average hardness decrease.

8.3.2.3 Electron Probe Microanalysis

Although not particularly noticeable in the micrographs presented in Fig.101, earlier annealing tests showed retarded recrystallisation in layers close to the surface. For example, Fig.108a shows large unrecrystallised grains at up to ~ 200 μm from the surface of a specimen annealed for 81900 seconds (22¾ hours) at 950°C following a T_1, T_3 schedule. The results of continuous microanalysis scans for chromium and nickel are shown in Figs.108b and 108c respectively. Surface depletion of chromium was found to a depth of ~50 μm after which the chromium content was found constant through the rest of the thickness to the centre of the specimen. Surface enrichment was found for nickel to a depth of ~80 μm, after which the nickel showed a gradually increasing concentration to a depth of 300 μm. From this depth to the centre of the specimen the nickel content remained constant.

8.4 Hot Torsion Tests

The hot torsion test results (torque vs. revolutions) were obtained as U.V. chart records which were analysed in the way described by Barraclough (1974). The shear flow stress, k, was obtained from the torque τ (N.mm.) using the relationship

$$k = \frac{3\tau}{2\pi a^3} \qquad (8.12)$$

where a is the initial specimen radius. The shear strain (γ) and strain rate ($\dot{\gamma}$) were calculated in terms of the effective radius (a_m) as described by Barraclough et al (1973):

$$\gamma = \frac{a_m \theta}{l} \qquad (8.13)$$

$$\dot{\gamma} = \frac{a_m \dot{\theta}}{l} \qquad (8.14)$$

where l is the gauge length,
θ is the angle of twist (radians),
$\dot{\theta}$ is the twisting speed,
and $a_m = 0.724a$ for solid specimens.

The gauge length and diameter were measured prior to each test using a travelling microscope ($\pm$ 0.05 mm) and a micrometer ($\pm$ 0.005 mm) respectively.

The stress and strain values were converted to uniaxial values using Von Mises criterion ($\sigma = \sqrt{3}k$, $\varepsilon = \gamma/\sqrt{3}$) and the stress-strain curves are presented in Fig.109. These show increasing ductility with increasing temperature and decreasing strain rate. Each curve shows the characteristic work hardening of the initial structure leading to a peak stress followed by a decrease to a steady state or decreasing stress level depending on the temperature. The curves show the well established increase in stress levels with increasing strain rate and decreasing temperature. All but one of the specimens were heated directly to the test temperature but it can be seen that soaking at 1180°C prior to testing at a lower temperature led to a slightly lower stress-strain curve in the work hardening region, a lower peak stress and increased ductility. Although the changes in work hardening and peak stress levels could arise from experimental scatter they nevertheless follow the trend expected from changing grain size. The increase in ductility with increasing grain size is not so easy to explain and will be returned to later.

The initial analysis of these data aimed to provide a value of the activation energy for hot working, Q. Thus, following the methods described by Whittaker (1973) and Barraclough (1974), the stress to a fixed strain was plotted as a function of strain rate at different temperatures, Fig.110a. Using the definition of the Zener Hollomon parameter (equation 2.5), then at a constant stress, the logarithm of the strain rate should be linearly related to the inverse of the absolute temperature with a constant slope of -Q/R. This is shown in Fig.110b. It can be seen that there is a distinct change in gradient between values obtained at 1000°C and 1100°C and those obtained at 1000°C and 900°C. The resultant activation energies were found to be 383 kJ/mole and 486 kJ/mole respectively.

Whether this range of values was due to experimental scatter or changing structural features will be discussed in Chapter 9.

To check the applicability of these values of Q, the flow stresses at two strains were plotted against Z, Fig.111. However, before doing so, the test temperatures were corrected to allow for the adiabatic temperature rise, ΔT_{def}. The latter was calculated from the area under the stress-strain curves (eqns.4.20, 4.21). The temperature rises were found to range from

$1.5^{\circ}C$ ($\varepsilon = 0.1$, $T = 1100^{\circ}C$, $\dot{\varepsilon} = 0.39\ sec^{-1}$) to

$23.7^{\circ}C$ ($\varepsilon = 0.4$, $T = 800^{\circ}C$, $\dot{\varepsilon} = 0.39\ sec^{-1}$).

Z was calculated using the two values of Q obtained above and also the value of Q obtained by Barraclough (1974) for an 18-10 steel (410 kJ/mole). Fig.111 shows that none of the values of Q allows a simple relationship between the flow stress and Z. It would appear that a low value of Q is suitable at high temperatures and a high value of Q at low temperatures.

Similar discontinuities were found when mean flow stresses to fixed strains (obtained as described below) were plotted against Z and it was concluded that the activation energy was not constant over the experimental range. Hence the data obtained at different strain rates were correlated by using an exponential relationship

$$\dot{\varepsilon} = A \exp \beta\sigma \qquad (8.15)$$

where A is a structural factor and β a temperature independent constant. Thus a plot of σ against $\ln \dot{\varepsilon}$ for different temperatures, Fig.110a, defines the value of β. This was found to be 0.051 ± 0.003. Hence if the flow stress is σ_1 at a strain rate of $\dot{\varepsilon}_1$, the equivalent flow stress is σ_2 at a strain rate of $\dot{\varepsilon}_2$ and is given by

$$\sigma_2 = \sigma_1 - \frac{1}{\beta} \ln \frac{\dot{\varepsilon}_1}{\dot{\varepsilon}_2} \qquad (8.16)$$

The use of this equation is illustrated below.

The second aim of the torsion testing was to obtain values of the mean flow stress for comparison with similar values obtained during hot rolling. The mean flow stresses were obtained from

$$\bar{\sigma} = \frac{1}{\varepsilon}\int_0^{\varepsilon} \sigma \, d\varepsilon \qquad (8.17)$$

and were found using a trapezoidal method to obtain the areas under the torsion curves. The mean flow stresses were calculated for strains equivalent to 10%, 20% and 30% rolling reductions for both strain rates used in torsion and the former then corrected to the average strain rate used in rolling (4 sec^{-1}) using eqn.8.16. The corrected mean flow stresses are presented as a function of test temperature (corrected for adiabatic heating) in Fig.112 and it can be seen that the use of the exponential relationship leads to a reasonable superimposition of data from different strain rates.

Also shown in Fig.112 are the mean flow stresses for a 30% rolling reduction calculated from the data of Barraclough (1974). The values (obtained at a strain rate of 1 sec^{-1}) were corrected to a strain rate of 4 sec^{-1} using the reported value of β of 0.047. Additionally, the nominal test temperatures were corrected to allow for adiabatic heating. It can be seen that the mean flow stresses are considerably lower than those found in the present work, particularly at lower temperatures.

It is worthy of note that Barraclough calculated β to be 0.047 from peak stress data whereas if his data of stress to a fixed strain is used instead (Fig.110a), β is increased to $\sim$ 0.07. This value lowers the mean flow stresses corrected to a strain rate of 4 sec^{-1}, Fig.112, thus increasing the difference between the present work and Barraclough's results. However, extrapolation of the stresses at fixed strains to a strain rate of 4 sec^{-1}, Fig.110a, does not show the same discrepancy. Hence there appears to be an inconsistency when comparing both the mean flow stresses and flow stresses to a fixed strain derived from the present work and that of Barraclough. The most likely explanation for this lies in errors in the stress-strain curves at low strains. Since the derivation of mean flow stresses counteracts such errors to a limited extent, it is presumed that the mean flow stress data, Fig.112, are more reliable

than the data of stresses to a fixed strain, Fig.110a. Reasons for the differences in mean flow stresses found in the present work compared with those derived from the results of Barraclough will be discussed in terms of structural differences in Chapter 9.

8.5 Results of Hot Rolling Experiments

8.5.1 Strengths During Hot Rolling

The rolling loads and torques were measured and recorded as described in Section 5.2.1 and Appendix 1. The typical U.V. chart record reproduced in Fig.77 shows the traces for the two load cells and for the top and bottom shaft torquemeters. The total roll loads and torques were obtained from the sum of the two separate measurements. It was occasionally found that one load cell gave a significantly higher load reading than the other; this arose when the slab was not rolled through the centre of the roll gap. The top and bottom shaft torquemeters rarely gave similar readings but since one was not consistently higher than the other it was presumed that the differences arose from different frictional conditions or different temperatures on the top and bottom slab surfaces rather than from calibration errors.

Both load and torque measurements showed a maximum at entry to and exit from the rolls. Additionally, the total load and torque generally showed a gradual increase or decrease during a pass, this presumably arising from a longitudinal temperature gradient. The load and torque measurements were therefore taken from the U.V. chart at the point where the thermocouple showed an increase in temperature due to deformation, see Fig.77. In this way the loads and torques could be directly related to the measured temperatures and the values are given in Table 7.

Initial consideration of the measured rolling loads showed that variation in the initial slab dimensions was an important factor. Thus the rolling loads were converted to mean flow stresses using the

hot rolling theory of Sims (1954), Section 2.4.4, eqns.2.23 and 2.24. Values of Sims' geometrical factor (Q_p) were calculated for the estimated dimensions for each pass and are given in Table 8. The derived mean plane strain flow stresses ($\bar{S}$) were converted to uniaxial stresses ($\bar{\sigma}$) using von Mises criterion and are given in Table 7.

The mean flow stresses are plotted against the mean slab temperature during the pass in Fig.113 (runs which involved 10% and 20% reductions and 30% reductions at the minimum and maximum roll speed have not been plotted). Considering the results for the first pass it can be seen that there is a scatter of $\sim \pm 15$ N/mm^2 in the values of the mean flow stresses around the mean values. Nevertheless the results show an increasing mean flow stress with decreasing rolling temperature. Part of the scatter was considered to be due to variations in the mean strain rate and this is considered below. The mean flow stresses for the second and third passes also show the same degree of scatter and appear indistinguishable from each other. However the general trend of higher mean flow stresses for the second and third passes compared with the first pass at the same temperature is clear.

A plot such as Fig.113 does not allow for the variation in strain rate for different passes and different runs and ideally the mean flow stresses should be plotted against Z. However, the hot torsion experiments did not give a unique value of the activation energy so this approach could not be adopted. Instead, the mean flow stresses were corrected to a constant strain rate (4 sec^{-1}) using the exponential relationship (eqn.8.16) with the experimentally determined value of β (0.051).

The corrected mean flow stresses for the first pass are plotted against the mean rolling temperature in Fig.114 which also includes the mean flow stresses for 30% reduction calculated from the

torsional stress-strain curves. Fig.114 distinguishes between single pass runs, which show only a small degree of scatter, and multipass runs which show higher scatter, probably as a result of greater uncertainty regarding the slab dimensions. It can be seen that the exponential relationship has allowed reasonable correlation of mean flow stresses obtained at low and high rolling strain rates. Comparison of the torsion and rolling results shows good agreement at low temperatures and poorer agreement at higher temperatures. However, as noted in Section 8.2.1, the area under the torsion curve gives $\bar{\sigma}_g$ whereas the rolling loads give $\bar{\sigma}_p$, the relationship between these being $\bar{\sigma}_p \simeq 1.06\ \bar{\sigma}_g$. Thus the torsional mean flow stresses have been increased by 6% (as indicated by the broken line) so that the torsion and rolling results are directly comparable. The rolling and torsion results then agree excellently at high temperatures and, although the agreement is better than $\pm$ 10% over the whole temperature range, there is an apparent crossover at $\sim 980^{\circ}C$. This crossover is considered to be real and to arise from structural differences as will be discussed in Chapter 9.

The mean flow stresses (corrected to a strain rate of 4 sec^{-1}) for the second and third passes are presented as a function of the mean rolling temperature in Fig.115 and distinction is made between the different interpass annealing treatments. Comparison of Figs.113 and 115 shows that correction of all the data to a common strain rate has not significantly reduced the scatter. The scatter in results for the second and third passes is less than $\pm$ 10%, this being equal to that found for the first pass. Fig.115 illustrates that the general trend of mean flow stresses for the second and third passes is significantly higher than that for the first pass, but the mean flow stresses for the second and third pass are not distinguishable from each other. These results, together with the effect of interpass annealing treatments, will be discussed in Chapter 9.

In the above derivation of mean flow stresses from rolling loads it was assumed that no elastic deformation of the rolls took place. The justification for this is now considered. Typical mean flow stresses were used to predict the nominal specific rolling load (using Sim's theory) and the latter used to calculate the deformed roll radius (R') using Hitchcock's equation (eqn.2.34). Then, using the procedure described by Larke (1963), the specific rolling load and deformed roll radius were successively redetermined until no further significant change was found in the roll load. Calculations were carried out for a roll radius of 68 mm, a roll bending coefficient of 0.01 mm^2/kN, and a 30% reduction. The following tabulation shows the results:

(i) h_1 = 20 mm, h_2 = 14 mm, mean plane strain yield stress = 200 N/mm^2

Roll radius, mm.	Specific Roll Load, N
68.0	4164.1
68.9439	4202.2
68.9525	4202.5

(ii) h_1 = 10 mm, h_2 = 7 mm, mean plane strain yield stress = 400 N/mm^2

Roll radius, mm.	Specific Roll Load, N
68.0	6657.0
71.0178	6861.3
71.1105	6867.6
71.1133	6867.8

Example (i), which corresponds roughly to the first pass of the normal 3 pass sequence, shows that deformation of the roll affects the prediction of the roll load from the flow stress (and hence vice versa as used in the present work) by less than 1%. Example (ii), corresponding roughly with the third pass, shows that the correction is ~3% at the higher stress levels. Thus the effect of roll deformation is seen to be small and no correction was made for it.

It was not considered worth while to analyse the torque data to produce mean flow stresses since the former were not so complete or so accurate as the load measurements. However, to

enable prediction of values of $\Delta\bar{T}_{def}$ from torque measurements it was necessary to correct the latter to allow for the frictional torques developed in the roll necks. The coefficient of friction was measured as described in Appendix 1 and gave an average value of μ of 0.055 $\pm$ 0.01. However, this analysis assumed that no energy is required to elastically deform the rolls when they are screwed together and rotated and so this method overestimates μ. The approach adopted was therefore to predict the pure rolling torque, G, from the rolling load. The equations (2.28 to 2.30) developed by Cook and McCrum (1958) give

$$G = \bar{W}\, 2\, R^2 \sqrt{\frac{1 + r}{1 - r}}\; C_g\, \bar{S}_g \qquad (8.18)$$

The factor $2\sqrt{\frac{1 + r}{1 - r}}\; C_g$ was calculated from the Cook and McCrum data at different % reductions for the R/h_2 ratios of interest. As noted above, $\bar{S}_g$ is not related simply to $\bar{S}_p$ but it was found that $\bar{S}_g \simeq \frac{\bar{S}_p}{1.06}$ was a sufficiently accurate conversion for the present work. Thus for each run, the mean plane strain flow stress ($\bar{S}_p$) was derived from the rolling load, corrected empirically to give $\bar{S}_g$, and the latter used in the above equation to give the predicted pure rolling torque. This was added to the roll neck frictional torque ($G_{frict} = \mu$ x roll load x roll neck diameter) to give the predicted total torque which was then compared with the measured total torque. It was necessary to try several values of μ before good agreement was found. Fig.116 shows that a value of μ of 0.03 gave a reasonable correlation. It is not clear whether the scatter is due to errors in measuring the loads and torques or an indication of a variable coefficient of friction. Fig.116 also differentiates between runs carried out before and after rewiring the mill at which point the rolls were also changed. The early results lie below the general trend but this could result from either a poor calibration of the torquemeters or a lower coefficient of friction.

Having established an average value of μ, it was used as noted above to deduce the frictional torque for each run and the true

rolling torque obtained by subtraction. Values of the latter are given in Table 7. As noted in Appendix 1, the torquemeters sometimes gave spurious results due to tarnishing of the silver plated slip rings: these values are marked with an asterisk in Table 7.

8.5.2 Deformation During Hot Rolling

The uniformity of deformation through the slab thickness during rolling was investigated primarily so that the position of non-central thermocouples during multipass sequences could be ascertained. In each of these runs, the initial and final distances (x_1, x_2) of the centre of the thermocouple from the centre of the slab were measured. The final position was calculated from x_1 using the overall % reduction of the slab and is compared with the measured x_2 in the following tabulation:

Run	x_1 (mm)	% Reduction	x_2 (mm) Calculated	x_2 (mm) Measured
4	4.3	46.96	2.28	2.35
7	6.9	46.62	3.68	3.90
8	7.3	62.84	2.71	2.7
10	4.4	62.59	1.65	1.75
31	4.0	30.66	2.77	2.85
32	5.35	30.56	3.71	4.40
33	3.4	30.49	2.36	2.45

Although the accuracy in measurement is $\pm$ 0.05 mm it can be seen that the calculated values of x_2 are consistently lower than the measured values. There are two possible explanations for this:

(i) non-uniform deformation of the slab, or

(ii) metal flow around the thermocouple.

The uniformity of deformation was investigated by giving a slab with an inscribed grid (Section 5.2.3.2, Fig.32) a single 30% pass at the normal first pass temperature. The deformed grid, Fig.33, shows that the deformation is constant through the slab thickness within the limitations of accuracy imposed by the inscribed line thickness. The deformed grid also shows the well established heavier shearing at distances close to the slab surface. Finally, careful examination of the deformed grid showed that, at the surface, there was a slight thickening and curvature of lines originally

perpendicular to the rolling direction. This was taken to be evidence of sticking friction during rolling.

The possibility of metal flow around the thermocouple was investigated by examining longitudinal sections of slabs with non-central thermocouples. The ferrite stringers could be seen to remain parallel to each other and to the slab surface in all regions except in the vicinity of the thermocouple, where they bent slightly outwards so that they became closer to the slab surface. This agrees with the tabulated results above and shows a small effect of deformation during rolling.

8.5.3 Dimensional Changes During Hot Rolling

The initial and final slab thicknesses and widths were measured for each schedule and are presented in Table 8. It should be noted that the widths are average values of the minimum and maximum widths found due to barrelling. Since the dimensions could not be accurately measured during multipass schedules it was necessary to analyse the data from single and double pass runs systematically so that a method for estimating these parameters could be established.

The initial and final thicknesses for the single 30% pass runs (neglecting runs 79 to 84 which were carried out at low temperatures) showed that there was random scatter between the % reduction obtained and the temperature at the centre of the slab at entry to the rolls. It was found that the reductions obtained ranged from 30.1% to 30.8% with an average of 30.46%. Thus in each case the reduction obtained was higher than that required, this being explicable by considering the thermal expansion of the slab. Taking a typical example of a slab whose thickness is 20.0 mm at room temperature, then the roll gap is set to 14.0 mm for a 30% reduction. Assuming a mean coefficient of linear expansion of $2 \times 10^{-5}/^{\circ}C$ over the $20^{\circ}C$ to $1100^{\circ}C$ range, the slab thickness becomes 20.43 mm at

1100°C. Assuming isothermal rolling and no mill spring, the exit thickness is 14.0 mm at 1100°C, which becomes 13.70 mm on cooling to room temperature. The apparent reduction at room temperature thus becomes 31.48% which is higher than the average measured values and therefore indicates a small amount of mill spring at 1100°C. It should be noted that all reported measurements are those at room temperature, no attempt being made to correct these for the rolling temperature of interest. The single pass runs at low temperatures gave reductions less than 30% due to increased mill spring but sufficient data were not obtained to give a satisfactorily confident relationship between the % reduction obtained and the rolling temperature. Thus it was assumed that all first pass runs of multipass schedules (in the 1100°C to 1160°C range) underwent a 30.5% reduction.

The data from two pass runs were used, together with the above assumption, to investigate how the % reduction obtained for the second pass depended on entry temperature. The results, Fig.117a, show a strong linear dependence of % reduction on temperature. Thus, for a 3 x 30% pass schedule, the first reduction was presumed to be 30.5%, the second reduction was found from Fig.117a in terms of the pass temperature and the third reduction presumed to be the remainder.

The changes in width were considered in a similar way. Fig.117b shows how the final width depends on the initial width as a function of the number of passes. Allowing for the indicated accuracy of measurement it can be seen that 3%, 8% and 10% (all ± 1%) spread on the original width hold for the first, second and third passes respectively. Thus an original width of 50 mm would be expected to spread to 51.5 mm, 54 mm and 55 mm during the first, second and third passes respectively. These spread values were used for all width estimations during multipass sequences. No attempt was made to correlate these data with the empirical equations given in Section 2.4.8 as it was considered that the present data were nei accurate enough or covered a wide enough w:h range.

CHAPTER NINE

DISCUSSION OF RESULTS

9.1 Temperature Changes During Hot Rolling

9.1.1 Qualitative Results

Typical experimentally measured temperature-time curves during hot rolling schedules have been presented in Figs.64 and 78 for mild and stainless steels respectively. Such curves show the following:

(i) The development of through thickness temperature gradients during normal air cooling, the gradients decreasing with decreasing slab thickness.

(ii) A temperature rise at the centre of the slab due to deformation during the roll contact period and, simultaneously, a rapid large temperature drop for positions close to the surface.

(iii) On exit from the rolls, heat is conducted outwards from the centre of the slab to give a rapid temperature drop at the centre and, conversely, a rapid recalescence at the surface.

(iv) A few seconds after exit from the rolls the surface temperature goes through a maximum and the slab subsequently undergoes normal air cooling.

It can be seen that the recalescence time decreases with decreasing slab thickness and that it can take up to 5 seconds for equilibrium cooling to be re-established on exit from the rolls. This is important for two reasons. Firstly, for schedules with short interpass times, equilibrium cooling may never be present so that the surface is always at a considerably lower temperature than the centre. This is of significance when considering structural changes such as recrystallisation and precipitation. Secondly, the accurate estimation of internal temperatures from surface temperatures depends on the presence of equilibrium cooling and thus temperature measurements must be made later than a certain minimum

time after exit from the rolls. This industrially important factor is considered further in Chapter 10.

The general shape of the measured curves is in good agreement with the limited information available in the literature. Thus the general behaviour is similar to that found by Bradley et al (1970), Figs.25 and 26, during the hot rolling of aluminium. Similar curves have been presented by Held et al (1970) and less explicit ones by Hollander (1970) and Wilmotte et al (1973A) for the hot rolling of steel.

9.1.2 Quantitative Results

Before discussing the quantitative results, the factors affecting the accuracy of the temperature measurements will be discussed briefly. Appendix 2 describes the calibration checks on the 'Pyrotenax' chromel-alumel thermocouples used in the present work and it has been shown that rewelding the thermocouple beads still retains the elevated temperature accuracy within the generally accepted standard ($\pm \frac{3}{4}\%$). It has been suggested that the magnesia insulation becomes slightly conducting at elevated temperatures (Birks 1975), but no evidence was found for this up to the reheating temperatures of interest. The limiting factor would appear to be the high temperature strength of the sheath material. The various tests devised to investigate the effect of deformation on a thermocouple (Appendix 2) have shown that any effect is negligible at elevated temperatures, thus agreeing with the balance of opinion in the literature (Section 4.2.2.1). The response time of the recording system used in the present work was superior to that of the thermocouple and thus was not a limiting factor. It was found that limited measurements of surface temperatures were both unreproducible and inconsistent with the temperatures measured at the centre of the slab. It is considered that this was due to:

(i) variations in the emissivity with temperature and surface condition,

(ii) inaccuracies in the optical pyrometer calibration and insufficiently sensitive recording equipment,

(iii) measurements being carried out at positions distant from the centre of the top face, particularly in view of the transverse temperature gradient,

and (iv) measurements being carried out with the incorrect separation between slab and pyrometer, this exaggerating the above problem.

It is now proposed to discuss quantitatively the results of measurements and computations during the interpass and roll contact periods.

9.1.2.1 Interpass Periods

The primary aim of the work carried out to measure the temperature gradients and cooling rates during air cooling was to provide data that would be applicable to the interpass periods during hot rolling schedules and will be discussed in this context. Section 8.1.1 has shown that both the oxide formation and phase transformation can have a marked effect on the cooling rate of mild steel and these would need to be investigated further before applying the present work to materials other than stainless steel. The varying scale thickness is difficult to simulate, partly because it is unlikely to be constant over a slab surface and partly because it is difficult to measure. In particular, the scale was found to break away during static air cooling, presumably due to thermal stresses. It would be of practical interest to quantify the effect of scale thickness by carrying out air cooling tests on materials with adherent oxide layers of different thicknesses. Such data were not available and since the present work was mainly concerned with stainless steel, detailed analysis of the mild steel data was not attempted.

An equation to relate the amount of heat lost/unit area/unit time to the surface temperature for the stainless steel has been derived in Section 8.1.2. The use of this equation in two dimensional finite difference computer models has shown that it

satisfactorily predicts the cooling rates of centrally located planes of flat slabs and long extrusion billets. Additionally, Fig.76 shows reasonable agreement between measured and computed through-thickness temperature gradients in a flat slab.

Much of the work carried out on air cooling proved to be superfluous and the following procedure is recommended for any further work in this field. Firstly, the heat transfer coefficient should be derived from cooling curves of round billets, the latter having as large a length:radius ratio as possible and insulated ends. This permits the assumption that all the heat is lost through the circumferential surface which will also be at a uniform temperature. The equation for the heat transfer coefficient should then be proved to be correct by comparison of the measured cooling curve with that predicted from a finite difference computer programme. Good agreement then allows the use of the equation in programmes for geometries where the surface temperature varies with position i.e. for sections other than rounds (such as ovals or rectangular slabs) as long as the representative section undergoes only two dimensional cooling.

The onset of three dimensional cooling at the mid-length position at long cooling times was found to affect the correlation of computed and measured curves, particularly for the standard length extrusion billets. The true solution for this would be the use of a three dimensional heat flow model but this would involve excessive computational time. Whiteman (1975) has allowed for the 'end effect' in short extrusion billets by the use of an empirical multiplying factor. For the slab lengths used in the rolling experiments, three dimensional cooling did not affect a centrally located plane prior to the normal first pass (10-15 seconds air cooling). Furthermore, since the length progressively increased during a schedule, it was assumed that two dimensional heat flow was operative for such a plane for the whole schedule. This is justified by the good agreement in the interpass air cooling rates throughout a 3 pass schedule, as exemplified by Fig.86.

As noted in Section 8.2.2 poor greeement was sometimes found between measured and computed air cooling curves prior to the first pass. Of the various explanations suggested, two are considered to be important. Firstly, there is no straightforward method to allow for the variable finite time taken to remove the specimens from the furnace apart from plotting the cooling curves to coincide at a fixed time after removal from the furnace. Secondly, cooling on the run-in table could be allowed for by the use of a suitable heat transfer coefficient for the bottom surface, as Hollander (1970) attempted when considering the industrial situation. However, this is a considerable complication of the situation, particularly in a two-dimensional model, and was avoided by ensuring minimal contact with the roll table.

The air cooling heat transfer equation derived in the present work combines the fundamental laws of radiation and convection (eqns.4.14 and 4.16), the unknown convection coefficient being found by analysis of the measured data. As noted in Section 4.4.1.1, the commonly adopted practice regarding air cooling is to ignore the convection term completely or, at best, to include it in the radiation term by changing the emissivity. Hence the present approach is more fundamental than that previously adopted in the hot working field and so it is difficult to compare the present results with previous work.

Consideration of eqn.8.7 shows that the contribution of convection to the total heat loss varies from $\sim 6\%$ at $1200^{\circ}C$ to $\sim 14\%$ at $800^{\circ}C$. This range is higher than that generally assumed by previous workers (Section 4.4.1.1) and illustrates that convection is a more important heat transfer mechanism than generally thought. The measured mean emissivity of 0.84 falls well within the wide range of values reported previously. Any further sophistication of the present work would necessitate knowledge of the temperature dependence of the emissivity in a similar way to that given by Seredynski (1973) eqn.4.19.

9.1.2.2 Roll Contact Period

The net temperature change during the roll contact period results from the combination of a heat input due to deformation and a heat loss due to conduction between slab and rolls. These effects will be discussed separately.

9.1.2.2.1 Heat Input due to Deformation

Isolation of the deformational temperature rises, ΔT_{def}, from the measured results demonstrated that the former increase with increasing strain, strain rate and decreasing temperature, Figs.81a,b. This effect is due to the dependence of the mean flow stress on these parameters and a reasonably good linear relationship between ΔT_{def} and mean flow stress was found for the three passes, Fig.81b. Measured values of ΔT_{def} have been compared with values predicted from mean flow stress (derived from rolling loads), Fig.82, and from roll torques, Fig.83. When considering the agreement, the following points should be noted:

(i) Accurate measurement of ΔT_{def} necessitates intimate contact between thermocouple bead and slab and extremely fast response times of both the thermocouple and the recording system. As already noted, the thermocouple response time was the limiting factor in the present work. Reduction of the thermocouple diameter to increase the response time leads to secondary problems (rewelding the thermocouple beads, mechanical strength of the thermocouple etc) and does not necessarily lead to increased contact between bead and slab. Good contact between bead and slab depends on

(a) a bead diameter similar to the diameter of the locating hole,

(b) ensuring that the bead protrudes from the end of the metal sheath, and

(c) inserting the thermocouple so that the bead lies at the bottom of the locating hole.

Even if these requirements are met it is possible that the

deformation in the vicinity of the thermocouple will differ from that elsewhere in the slab. All these factors are more important during the first pass and this partially explains why the predicted temperature rises are higher than the measured values in Figs.82 and 83. Better agreement was found for subsequent passes, particularly in Fig.82, and this is considered to arise from better contact between bead and slab.

(ii) Both the rolling load and torque predict a mean temperature rise, $\Delta\bar{T}_{def}$, which will be higher than that measured at the centre of a slab. This point has been discussed in Section 6.3.8 and illustrated by Fig.60. This factor can explain the consistently poor agreement found for runs carried out at the minimum roll speed. Thus with increasing contact time, the chilling effect penetrates further into the slab and so leads to higher loads and torques and correspondingly higher predicted values of $\Delta\bar{T}_{def}$. The discrepancy is exaggerated because the low strain rate also produces a lower ΔT_{def} at the centre of the slab.

Section 8.2.1 has described the fundamental approach for predicting $\Delta\bar{T}_{def}$ from the work done/unit volume, thus giving eqns.8.8 and 8.9. Although the mean flow stress can be obtained from simulative mechanical tests or from measured load or torque data, eqn.8.8 requires that the mean flow stress used is $\bar{\sigma}_g$. Hence it is more correct to predict $\Delta\bar{T}_{def}$ from measured torques than loads. However the equations (4.22, 4.23) used in the present work are based on simplifications of the roll gap geometry. Comparison with the fundamental equations showed that the simple equations always underestimate $\Delta\bar{T}_{def}$, particularly at high reductions and large contact angles (R/h_1 ratios <10). It was found that the values of $\Delta\bar{T}_{def}$ predicted from the simple equations should be increased by $\sim 6\frac{1}{2}\%$, $\sim 6\%$ and $\sim 5\%$ for the first, second and third passes respectively in the present work. Although the shift is small, correction

nevertheless moves the predicted points to the right in Fig.83 thereby increasing the discrepancy.

The overriding problem in predicting values of $\Delta\bar{T}_{def}$ from torque values is that the latter need to be corrected for the frictional torques developed in the roll necks. The method of estimating this correction has been described in Section 8.5.1 and an average value of the roll neck coefficient of friction μ found from a large volume of data. It is unlikely that μ will remain constant in practice and small changes in μ effectively change the angle of the equivalence line in Fig.83.

As noted in Section 8.2.1, mean flow stresses derived from rolling loads ($\bar{\sigma}_p$) need to be corrected to $\bar{\sigma}_g$ before being used to predict $\Delta\bar{T}_{def}$. The mathematical relationship between $\bar{\sigma}_p$ and $\bar{\sigma}_g$ appears to be very complex and instead, an empirical correction has been adopted and has been incorporated in Fig.82. Comparison of Figs.82 and 83 shows that the use of load rather than torque data is generally more successful in predicting values of $\Delta\bar{T}_{def}$. Fig.82 also shows better agreement between measured and predicted values of ΔT_{def} for the third pass compared with the second pass. It is considered that this is because the contact time is lower for the third pass so both the heat loss and the subsequent deviation of ΔT_{def} at the centre of the slab from $\Delta\bar{T}_{def}$ will be lower.

The use of corrected torque values in the computer programme therefore generally overestimates ΔT_{def} at the centre of the slab as illustrated in Figs.86 and 88. However, although not capable of being experimentally justified, it is considered that this predictive method allows the correct total amount of heat to be input, even though its distribution is incorrect. If the temperature rise distribution, coupled with the roll chilling effect (as discussed below), were incorrect to any significant amount, then equalisation of the steep temperature gradient on exit from the rolls would not be predicted satisfactorily. As Figs.86 to 88 show, good agreement

was found, thus supporting the assumptions used. In retrospect it would have perhaps been advisable to predict values of $\Delta\bar{T}_{def}$ from the rolling loads since, firstly, these were more accurately obtainable in the present work and, secondly, because no correction for roll neck friction would be necessary.

Regarding industrial practice, Section 4.4.2.1 has described a variety of methods adopted for the prediction of the deformational heating effect. It is only relatively recently that rolling mills have been more fully instrumentated and measurements on many of the older ones are limited to the power consumed by the drive motors. In this case, Lee et al (1963), amongst others, have produced data for the efficiency of the motor and bearings but it is difficult to envisage that these data are either accurate or applicable to other mills. Nevertheless, Hollander (1970) adopted this method in preference to others. The use of measured torque values, as proposed by Gittins et al (1974A) and discussed above, involves the correction for the frictional torques developed in the roll necks. In an industrial situation it might be expected that the coefficient of friction would vary more than in a laboratory mill due to the more frequent roll changes. The optimum method of predicting $\Delta\bar{T}_{def}$ industrially would appear to be from the roll loads which is essentially the method proposed by Seredynski (1973).

Finally it should be noted that the true distribution of the deformational temperature rise can only be obtained from a more sophisticated mathematical model. Such an approach could be based on the slip line field solutions as described by Johnson and Kudo (1960) and Sparling (1976) but it is perhaps doubtful whether the effort involved for the extra accuracy would be justifiable.

9.1.2.2.2 Heat Loss due to Conduction

Fig.84 has illustrated the marked effect of contact time on the net temperature drop measured at the centre of the slab and

smaller effects of roll gap geometry and initial temperature. Conversion of measured temperature changes into mean heat losses/ area/initial temperature difference, $\Delta\bar{H}_{chill}$, has shown that the latter are strongly dependent on contact time, Fig.85. Reasons for the scatter in Fig.85 have been discussed in Section 8.2.1 and, although this is large, it is considered that the results nevertheless show a marked effect of oxide thickness and/or surface roughness. This is allowed for in the mathematical model by varying the value of C (the constant that controls the heat transfer between slab and rolls) so that good agreement is obtained between measured and computed temperature curves, Figs.86 to 88. It is considered that these curves demonstrate that both the temperature gradient and heat loss during a pass have been correctly modelled. If the computed temperature gradient was significantly incorrect then, as noted above, the measured and computed curves immediately following a pass would not agree. Furthermore, if the value of C had been incorrectly chosen then the measured and predicted air cooling curves following a pass would be offset.

The effect of C on $\Delta\bar{H}_{chill}$ is illustrated in Fig.85 for the range of contact times used experimentally. It can be seen that the majority of measured values fall between C = 50 and 1000 $kW/m^2\ ^oC$. A plot such as this can do no more than give an indication of the C value to be tried in the mathematical model. Nevertheless Fig.85 gives a good idea of the range of values obtained experimentally on slabs that generally had a good surface finish and only a light oxide layer following reheating. Industrially, the situation is more varied and it is necessary to allow for variations in slab and roll surface finish and slab scale thickness.

Irregularities in the slab surface are likely to be removed by the first few roughing passes and hence are not particularly serious. The effect of scale on the air cooling rate has been

mentioned briefly above and it is clear that the scale thickness can vary significantly during a hot rolling schedule. Considering firstly the situation in the roll gap, the adherence and mechanical properties of the scale are important. For example, poorly adherent scales will flake off during a pass (e.g. mild steel) whereas adherent scales (e.g. stainless steel) will either thin down uniformly or form 'islands' depending on the scale ductility. Although rarely considered in the literature, the heat transfer rate will also be governed by the roll surface condition. Roll surfaces are often poor due to thermal fatigue ('fire-cracking') and are sometimes deliberately roughened to improve the 'bite', particularly during the roughing stands. In such cases a finite, rather than zero, contact resistance is clearly more realistic.

Scale is commonly removed both prior to, and during industrial rolling, either hydraulically or by means of a 'skin' pass. However the scale thickness may increase markedly during a rolling schedule, particularly for low alloy steel during the roughing stage where slabs are hottest and delays of several seconds can occur between passes. In such cases, it would be necessary to decrease C during interpass holds and a possible basis for this could be a scale growth equation of the form proposed by Wilmotte et al (1973A).

As described in Section 4.4.2.2 much of the previous work concerning the roll chilling effect has been based on the equations (4.9 to 4.11) derived by Carslaw and Jaeger (1959) which assume zero contact resistance. Hollander has quoted a factor of 0.6 to apply the theoretical solution to practice thus indicating the presence of a scale layer. Although other workers (e.g. Wilmotte et al, 1973A) have used a finite value of the heat transfer coefficient, data for the latter are generally restricted to empirical estimates which are usually derived from crude measurements of the oxide thickness. Additionally, all the previous work has assumed one dimensional heat

flow so it is unrealistic to compare the present results with previous work. However, the present mathematical model was adapted to a one dimensional model and the results will be presented in Chapter 10, at which time they will be discussed in relation to previous work.

9.1.2.3 Overall Temperature Model

The above has therefore discussed the results of temperature measurements and computations, the latter being based on a two dimensional heat transfer model whose distinguishing feature is that it allows a finite heat transfer rate between slab and rolls thereby closely simulating the practical situation. It has been shown that this model can satisfactorily simulate practical rolling schedules, therefore confirming that the approximating assumptions are reasonable. The model allows

(i) the study of the effects of strain, strain rate, interpass times, slab dimensions etc. on the temperature gradients and cooling rates, and

(ii) the acquisition of detailed knowledge regarding the severe temperature gradients developed during rolling, this being particularly useful for structural studies.

9.1.2.4 Empirical Temperature Model

As noted in Section 8.2.2, the fitting of computed curves to measured temperature curves is a time consuming operation and therefore not suitable for extensive use. Hence, to obtain reasonably good estimates of mean temperatures during rolling, a simplified method based on computed values of $T_c - \bar{T}$ during air cooling has been used. The mean temperature during a pass is taken as the average of the mean temperatures at the entry and exit planes, values of the latter being found from figures such as Figs.92 and 93. The use of these curves has been described in Section 8.2.2 and their general features will now be discussed briefly.

Fig.92 shows the variation in $T_c-\bar{T}$ with time for different slab dimensions and reheating temperatures. The maximum value of $T_c-\bar{T}$ was taken to be the onset of pseudo-equilibrium cooling and, as expected, this peak increases with slab thickness and reheating temperature. The time to reach the peak can be seen to

(i) increase with decreasing reheating temperature (for constant slab dimensions), thus following the temperature dependence of the diffusivity,

and (ii) increase with increasing slab thickness.

The latter conclusion was unexpected since the time to reach equilibrium should be determined by the value of the longest dimension (i.e. the width in this case). Since the thickness appears to have an effect, it is probable that it is the diagonal slab dimension (i.e. $\left[(\text{width})^2 + (\text{thickness})^2\right]^{\frac{1}{2}}$) which controls the time to reach equilibrium.

The plot of $T_c-\bar{T}$ as a function of T_c (Fig.93) shows that, even when the peak is reached, further cooling is necessary before the curves coincide with those showing true 'equilibrium' cooling. This is shown particularly well by comparing the cooling data for a 16 mm x 50 mm slab, but the explanation for the extra cooling before reaching the curve from the higher temperature is not clear. Fig.93 also shows that the relation between $T_c-\bar{T}$ and T_c is relatively independent of the slab width within the range used experimentally, thus simplifying the situation.

As noted in Section 8.2.2, when equilibrium cooling is not present it is necessary to know both the reheating temperature and cooling time before $\bar{T}$ can be estimated from measured values of T_c using a plot such as Fig.92. When equilibrium cooling is present, $\bar{T}$ depends only on the slab dimensions and T_c, Fig.93. Curves such as these therefore allow a relatively simple estimation of the mean temperature of a slab cross section during air cooling given temperatures measured at the centre of the slab. Hence the mean rolling

temperature can be determined simply from measured interpass air cooling curves. The accuracy is considered to be better than that of chromel-alumel thermocouples, assuming an extensive family of computed curves is available. This approach obviates the need for a complex mathematical model of temperatures during a pass if it is only wished to determine the mean temperatures. It is therefore suitable for correlating strength parameters with mean temperatures. which is of particular use when comparing mean flow stresses, loads etc. in hot rolling with those established by isothermal simulative mechanical tests. Industrially, only surface temperatures can be measured and the extension of this approach to cover this is considered in Chapter 10.

To conclude, the following recommendations are made concerning the measurement and prediction of temperatures during hot rolling with particular reference to laboratory investigations:

(i) Surface temperature measurements are not to be recommended (except as a general guide) unless the difficulties discussed in Section 9.1.2 can be overcome. In addition to these, it is necessary to be aware of the recalescence effect.

(ii) Embedded thermocouples should be located at the centre of the slab to avoid uncertainties regarding their position during multipass schedules and this additionally allows temperatures to be measured where the gradient is most shallow. Accurate temperature measurement is also aided by the use of a small diameter thermocouple. Location at the centre of the slab also allows the easiest possible correlation of measured and computed temperature changes.

(iii) If it is wished simply to know the mean pass temperature, this is available from computed and measured air cooling curves, thus avoiding the need for a complex computer programme and sophisticated temperature recording equipment.

(iv) To obtain detailed knowledge of temperature gradients in the roll gap, then the more complex mathematical model is required which, for reasonable accuracy, demands accurate recording of temperatures using equipment equivalent to that used in the present research.

9.2 Structural Changes During Hot Working

The metallography carried out aimed to investigate the structural development during hot rolling sequences and in particular, the recrystallisation occurring during interpass air cooling and interpass annealing treatments. However the stainless steel was found to contain both ferrite and banded inclusions and to exhibit precipitation under certain conditions. Since these second phase particles might be expected to influence the recrystallisation behaviour they will be considered first.

9.2.1 Effect of Second Phase Particles on Recrystallisation

In a recent review, Cotterill and Mould (1976) concluded that second phase particles may either accelerate or retard recrystallisation depending on the size and distribution of the second phase. With widely spaced incoherent particles, the localised strain at the matrix-particle interface leads to a higher nucleation rate than that for the single phase matrix. It is likely that this effect will be more pronounced when the second phase is less deformable than the matrix rather than vice versa. As the inter particle spacing decreases, nuclei formed at adjacent matrix-particle interfaces increasingly interact with each other until a point is reached where no stable nuclei are formed at these interfaces. In addition to its effect on the nucleation rate, the second phase may also affect the growth rate of the recrystallising grains. As the particle spacing decreases the migrating boundaries interact with an increasing number of second phase particles hence leading to a decreased growth rate.

9.2.1.1 Effect of Ferrite

The evidence for the undesired presence of ferrite in the austenitic stainless steel has been presented in Section 8.3.1.1. Examination of the Fe-Cr-Ni phase diagram (e.g. Bain and Aborn, 1939) indicated that the composition of the present steel (Table 4) lay close to the phase boundary line so, as pointed out by Muller (1967), ferrite might be expected solely on the grounds of segregation of Cr and Ni. In addition it is necessary to consider the other alloying elements and it is well known (Keown 1973) that Mo, W, V, Ti and Nb stabilise ferrite, the latter two acting by removing the γ stabilisers, N and C. The opposing effects of the different alloying elements have led some workers to derive empirical relationships to predict the ferrite content for a given composition. Such equations (e.g. Irvine et al (1959), Pryce and Andrews (1960)) predict a ferrite content of 5 to 7% for the present steel whereas random point counting indicated $\sim$10% ferrite. Stokowiec et al (1969) have pointed out that the ferrite content is both time and temperature dependant and it has been shown (e.g. Zidek, 1965) that hot working or prolonged heating at elevated temperatures can reduce or eliminate the ferrite, presumably as a result of a reduction of the microsegregation. The present work clearly showed a reduction in the ferrite content when specimens were reheated at 1100^{o}C prior to torsion testing, Figs. 102a,b.

Qualitative evidence has been presented (Figs.94a,b) to show an increased ferrite concentration at the centre of slabs compared with the surface. Limited electron probe microanalysis showed no macrosegregation of Cr or Ni (Figs.108b,c) over the distance that this effect was noticed and the concentrations of the other ferrite stabilisers were too low to be readily detectable. Stokowiec et al (1969) suggest that such a ferrite distribution originates from the variation in the cooling rates in the original casting, the lower rate at the centre leading to microsegregation and hence an increased likelihood of ferrite formation.

The slab specimens showed a coarser, more mixed structure at the surface following reheating, Figs.94a,b, and grain size measurements at the centre (Table 9) tend to show a larger grain size in the longitudinal direction. The latter conclusion can also be drawn from the grain size measurements of the torsion specimens. Transverse sections (e.g. Figs.102e,f) showed that the majority of ferrite particles lay in the grain boundaries and this can be taken to indicate that ferrite 'pins' the boundaries, thereby restricting grain growth. This explains why a coarser grain size was found at the surface of slab specimens. Additionally the grain size will be more mixed at higher temperatures (e.g. Fig.102g) partially due to the reduced ferrite content and partially due to the increased thermal energy available for the austenite grains to overcome the restraining effect of the ferrite. Finally, transverse and longitudinal sections of slab and torsion specimens showed that the ferrite consisted of long 'fibres' aligned with the rolling or extrusion direction and located in the grain boundaries. Hence the easiest direction for grain growth is parallel to the rolling or extrusion direction, thus explaining the grain size anisotropy noted above.

Following the principles outlined in Section 9.2.1, the ferrite in the as-rolled slabs would be expected to accelerate the nucleation rate of recrystallising grains but to have little effect on their growth rate since the recrystallised grain size was considerably smaller than the ferrite spacing (e.g. Figs.101a to h). It is clear from the evidence presented by Cotterill and Mould (1976) that the effect would only be marginal and it is likely that concurrent precipitation with recrystallisation (as discussed below) would mask any effect of ferrite.

9.2.1.2 Effect of Inclusions on Recrystallisation

A variety of different inclusions was found in the stainless steel and these occurred predominantly in a heavily banded form.

Following the general principles outlined in Section 9.2.1, it would be expected that the larger inclusions would accelerate the recrystallisation rate particularly since these inclusions appeared relatively undeformable. However accelerated recrystallisation would only be expected on the 'outside' of the bands and since there were relatively few bands, it may be concluded that the inclusions would have a relatively minor effect on the overall recrystallisation rate. No microstructural evidence was found for either acceleration or retardation of recrystallisation by inclusions.

9,2.1.3 Effect of Precipitation on Recrystallisation

The electron microscopy carried out in the present work was limited to examination of two specimens, these having been heat treated at 800°C and 1100°C. As has been described in Section 8.3.1.5, treatment at 1100°C led to a precipitate free structure whereas treatment at 800°C led to occasional, large precipitates and, more importantly, precipitation on the dislocations. In thelatter case, the precipitates were too fine to be identified by electron diffraction so it is only possible to hypothesise as to their composition.

Table 4 shows that the steel composition was complex and that there were several potential carbide and nitride formers. It can be seen that the Ti content is greater than 4 times the C content (the stoichiometric ratio of Ti:C in TiC). Hence it would be expected that all the C is tied up by the Ti on a thermodynamic basis. This then explains why large Ti(C,N) inclusions were readily observable. However under non-equilibrium conditions, the kinetics of the precipitation reactions have to be considered as well, and it is possible that the volume fraction of TiC will be reduced and that some chromium carbide ($Cr_{23}C_6$ or Cr_6C) will be present.

It is clear that considerable further work would be necessary before a full understanding could be gained of the precipitation reactions occurring in this steel. However it is clear that all slab

specimens should be precipitate free following reheating at 1180°C whereas torsion specimens reheated at the lower temperatures will contain some precipitates. No direct evidence was sought concerning precipitation following high temperature soaking but, as will be discussed, it is possible to infer from the strength and structural studies that this occurred rapidly in the 800°C-900°C range.

Considering the effects of precipitation on static recrystallisation, Section 3.3.2.2 has described briefly the nucleation models based on subgrain and grain boundary migration. In both cases, retarded recrystallisation would be expected in the presence of precipitates since these 'pin' the boundaries. However, as discussed by le Bon et al (1975) there is evidence that static recrystallisation is only retarded when Nb is in solution in the austenite before deformation and that when the Nb(C,N) precipitation reaction is complete prior to deformation, subsequent static recrystallisation is not retarded. This may be evidence for a 'solute-drag' mechanism of retardation as proposed by Cordea and Hook (1970). Thus in spite of considerable work in this field, knowledge is limited at present concerning the precise mechanisms controlling static and dynamic recrystallisation in steels where precipitation reactions can occur.

9.2.2 Restoration During Hot Working

The study of dynamic restoration processes did not form part of the present work but nevertheless certain information can be deduced from the mechanical behaviour. The torsional stress-strain curves (Fig.109) showed an increasing stress with strain up to strains of ~0.4 during which a poorly formed substructure is developed (Sellars and Whiteman, 1974). At higher strains, the stress drops which indicates the onset of dynamic recrystallisation in austenitic materials (Jonas et al, 1969). Since a 30% rolling pass is equivalent to a true strain of ~0.42 it may be inferred that dynamic recrystallisation did not occur during passes carried out on recrystallised material.

In addition, it may be concluded that if the temperatures were low enough to prevent static recrystallisation following a pass, then dynamic recrystallisation would not occur during the subsequent pass even though the material would have received a strain of $\sim$0.8 by the end of this pass. Hence dynamic recrystallisation was not of any importance during the hot rolling schedules.

9.2.2.1 Static Restoration During Hot Rolling

Section 8.3 has presented the qualitative and limited quantitative evidence that shows that full recrystallisation was not observed during any of the rolling schedules or interpass annealing treatments (except when the latter were carried out at $>1100^{\circ}C$).

Considering firstly the recrystallisation during interpass air cooling, it has been shown that recrystallisation is relatively rapid at the centre of the slab following the first pass (Fig.96), whereas recrystallisation is retarded at the surface (Fig.95). In particular Fig.95d shows that almost zero recrystallisation occurs to a depth of $\sim$ 0.5 mm. Previous work, reviewed in Section 3.2.2, has shown that the static recrystallisation rate depends on both the stored energy and the annealing temperature. During hot rolling, the stored energy increases from the centre to the surface of a slab as a result of the temperature gradient (both prior to, and introduced during, a pass). On the other hand, this gradient results in the thermal energy available for recrystallisation decreasing from centre to surface. The net effect of these opposing factors is complex and could only be investigated since the mathematical model gave detailed knowledge of the temperature gradients during and after a pass.

Whittaker (1973) and Sellars and Whiteman (1974) have described the use of a temperature compensated time parameter (eqns. 3.4, 3.5) for non-isothermal recrystallisation. Thus, if a point within a slab has a mean temperature T_1 (K) during a time interval δt, then the equivalent time (δt_{eq}) at a temperature T_2 (K) is given by

$$\delta t_{eq} = \delta t \exp\left\{ -\frac{Q}{R} \left(\frac{1}{T_1} - \frac{1}{T_2} \right) \right\} \qquad (9.1)$$

A simple sub routine based on this equation was added to the one-dimensional computer programme. Thus for each computational time interval following a pass, δt_{eq} was evaluated for each point within the slab and added to the cumulative total for that point.

The temperature changes following a typical 30% reduction of a 20 mm slab are shown in Fig.118a and the resultant values of the cumulative equivalent time for selected points shown as a function of time following exit from the rolls in Fig.118b. The equivalent times were calculated for a temperature of 1050°C, this being approximately equal to the mean slab temperature on exit from the rolls. It was assumed that the activation energy for recrystallisation was 426 kJ/mole as found by Barraclough (1974) for a fully austenitic 18-10 steel. The results, although not strictly comparable with the present work, serve to illustrate a point. Fig.118b shows that, at two seconds following exit, the equivalent time is an order of magnitude greater at the centre of the slab than at ~~exit~~ the surface. As the equilibrium temperature gradient becomes re-established, this difference decreases until it is only half an order of magnitude at 10 seconds from exit.

Sellars and Whiteman (1976) have recently derived the following empirical relationship between the time to a certain fraction recrystallised (t_x) and the structural factor (A), initial grain size (d_o), ε and Z:

$$t_x = A \, d_o^{2} \, \varepsilon^{-4} \, Z^{-0.375} \exp \frac{Q_{rex}}{RT} \qquad (9.2)$$

The recrystallisation curve for an 18-10 steel ($\varepsilon = 0.5$, $\dot{\varepsilon} = 1\ sec^{-1}$, $T = 1050°C$) is shown in Fig.118c, curve 1. The above equation shows that changing the values of ε, Z etc. displaces this curve sideways. The structural and grain size factors were ignored and the basic curve corrected to a strain equivalent to a 30% rolling reduction (curve 2, Fig.118c).

The first approach was to assume a uniform stored energy distribution through the slab thickness. A mean Z value for the pass was obtained from the mean strain rate and mean slab temperature using Barraclough's value of the activation energy for hot working (410 kJ/mole). This value was used with eqn.9.2 to derive the recrystallisation curve for the rolling conditions of interest (curve 3, Fig.118c). The combination of data given by Figs.118b,c then allowed the derivation of the fraction recrystallised at each point through the slab thickness at different times following the pass. This is shown in Fig.118d (broken line) at 10 seconds from exit. This approach therefore indicates a high recrystallisation rate at the slab centre decreasing to a low rate at the surface.

The second approach was to allow for the stored energy gradient in the slab. A mean temperature during the pass, and hence a mean Z value, was obtained for each finite element. Using the same approach as detailed above, the recrystallisation curve was obtained for each element and selected curves (corresponding to the temperature curves, Fig.118a) are shown in Fig.118c, curves a to e. The use of the latter curves with Fig.118b gave the fraction recrystallised through the slab thickness at different times from the end of the pass, Fig.118d (solid lines). The following features are clear:

(i) Recrystallisation is initially retarded at the surface due to the depressed temperatures but, once recalescence has occurred, the large amount of stored energy at the surface leads to rapid recrystallisation.

(ii) Recrystallisation starts more quickly at the centre due to the elevated temperatures but the rate then decreases due to the heat loss to the surface.

(iii) Intermediate regions do not lose heat while in contact with the roll so the stored energy is low. Additionally, such positions lose heat rapidly following exit from the rolls (e.g. curve d,

Fig.118a), so that the total equivalent time is also low compared with the slab centre.

Fig.118d therefore shows that the totally wrong impression is gained if the stored energy is assumed to be constant through the thickness. These calculations have assumed that the strain is uniform through the thickness and the heavy shearing that occurs close to the surface would tend to exaggerate the effect and cause even faster recrystallisation at the surface. Although no quantitative data appear to be available, previous workers (e.g. Richards, 1969) have noted the relatively slower recrystallisation rate at the centre of plates etc. (particularly during finishing) thus agreeing qualitatively with the above computations.

Although these computed results are not directly applicable to the present material, they illustrate that the experimentally observed unrecrystallised layer at the surface is an anomaly which cannot be explained in terms of the chilling effect introduced during a pass. It may also be noted that this layer is not a quenching artifact since it persists following passes subsequent to the first (Fig.97).

It has already been noted that the presence of ferrite would be expected to marginally increase the recrystallisation rate and that the ferrite concentration was higher at the centre of the slab. However it is extremely unlikely that the relatively small differences in ferrite concentrations would have a large enough effect to reverse the expected recrystallisation behaviour. The same conclusions can be drawn regarding the inclusion content.

Hence the remaining possibility for explaining the retarded recrystallisation at the surface lies in the precipitation behaviour. It has been shown that positions close to the surface undergo severe chilling during, or soon after, contact with the rolls and it is suggested that the times at these depressed temperatures are long enough for a limited amount of precipitation to occur. This effect

would be expected to be enhanced by the redundant shear strains close to the surface. It is considered that this deduced precipitation effect could be of commercial importance and needs to be investigated further using electron microscopy. When more detailed precipitation data become available, a mathematical model should allow their application to any rolling conditions.

Therefore on entry to the normal second pass, the majority of the slab cross section was 80% to 90% recrystallised with surface layers ~0.5 mm deep of unrecrystallised material. Slight variations in the fraction recrystallised would be expected from run to run due to differences in the strain, strain rate and temperatures during the first pass since these affect the amount of stored energy. The fraction recrystallised would also increase with increasing exit temperature and interpass cooling time. However it was found that air cooling to room temperature did not lead to 100% recrystallisation so all second passes (except for those following interpass annealing treatments) were carried out on slabs which did not have a fully recrystallised structure.

No recrystallisation was found following the second or third passes of the normal three pass schedule, Figs.97 and 98, and comparison with Barraclough's data showed that this was reasonable.

For reasons outlined in Section 8.3.1.3, some slabs (or sections from quenched slabs) were annealed isothermally following a pass. Fig.107 has shown that the slab had a hard surface-soft centre profile following a 30% at T_1, 30% at T_3 schedule and this could be attributed to any or all of the following reasons:

(i) The ferrite content was lower at the surface.

(ii) Precipitation occurred more heavily at the surface.

(iii) The surface layer was unrecrystallised following the first pass and therefore after the second pass had received double the strain to that received by the centre.

If either of the first two explanations are valid, then the hardness measurements do not give a true indication of the structural gradient in the austenite prior to reheating. During reheating at 1000°C, the hardness gradient firstly flattens out and secondly, the mean hardness progressively decreases with time. The disappearance of the gradient could be attributed to any of the following reasons:

(i) Reduction of the ferrite content at the centre of the slab although Fig.101 shows that this is only true at long annealing times.

(ii) Dissolution of precipitates at the surface at higher temperatures and precipitation at the centre at lower temperatures.

(iii) A higher restoration rate at the surface due to the higher stored energy. Fig.101 shows that recrystallisation did not occur significantly faster at the surface but it is possible that static recovery did.

The mean hardness measurements are presented as a function of time in Fig.106 for different schedules and annealing temperatures. The mean hardness drops only marginally during the initial stage of reheating and this may be taken to indicate limited static recovery. Similar hardness changes have been found by Barraclough (1974) and Kozasu and Shimizu (1971); results of the latter workers having been presented in Fig.13 and discussed in Section 3.3.1.

At the higher temperatures, this initial slow drop in hardness is followed by a rapid drop and metallographic examination, Figs.101a,b, showed that this indicates the onset of static recrystallisation. As expected, the onset of recrystallisation occurs at shorter times as the temperature increases.

An interesting point emerges when considering the effect of the rolling schedule on the subsequent isothermal restoration behaviour. Firstly the initial mean hardnesses ($\bar{H}_v$) of slabs given the T_1, T_2 and T_1, T_3 schedules and treated at 950°C do not agree with those for slabs

given similar schedules but treated at 1000°C. The explanation for this probably lies in slight differences in the schedules and errors in obtaining a mean hardness when there is a gradient present. However consideration of the results at a fixed annealing temperature shows that the T_1, T_2 schedule led to a lower initial $\bar{H}_v$ than the T_1, T_3 schedule and this is attributable to the lower stored energy introduced at the higher deformation temperatures. It would be expected that the slab given the T_1, T_3 schedule would start recrystallising first due to the increased stored energy. However the hardness measurements do not show this and it is considered that this is due to differences in the precipitation behaviour immediately following the two schedules.

It may be speculated that relatively coarser precipitation occurs after the pass given at T_2 than after the pass given at T_3. Thus following Cotterill and Mould (1976), greater retardation of recrystallisation would be expected following the pass at T_3. The experimental results suggest that this effect approximately balances the accelerating effect of the higher stored energy introduced by the pass at T_3.

The limited quantitative recrystallisation data are presented in Fig.105 in conjunction with typical recrystallisation curves found by Barraclough (1974). The former data were obtained for a T_1, T_3 schedule and allowance for differences in strain, strain rate, deformation temperature and grain size shifts Barraclough's curves significantly to shorter times. Thus these data again show that the present material had greatly increased incubation times and lower recrystallisation rates as a result of precipitation. Similar large differences have been reported by le Bon et al (1975) who showed that the time to any fraction recrystallised for a Nb HSLA steel was 2 orders of magnitude greater than for a plain C-Mn steel. They noted that the retardation of recrystallisation was very marked when the amount of deformation was 'low' (~30%).

In summary, it has been shown that recrystallisation was very sluggish compared with a simple austenitic stainless steel. This effect and the anomalous retarded recrystallisation at the slab surface, together with the limited electron microscopic evidence, strongly support the idea that precipitation at temperatures of $\sim 950^{o}C$ and below exerts a major influence on the recrystallisation kinetics of the present steel.

9.3 Strength During Hot Working

9.3.1 Hot Torsion Tests

The general form of the stress-strain curves obtained from the torsion tests, Fig.109, have already been noted in Section 8.4. It was not possible to compare directly these curves with those found by previous workers (e.g. Barraclough 1974) because of differences in test temperature and strain rate. Such a comparison would require the use of the Zener-Hollomon parameter but, as already noted, a constant activation energy for hot working could not be obtained in the present work. However, the general form of the curves is in good agreement with those found by previous workers for austenitic stainless steels (Fig.3). Thus, following the peak, the stress drops to a lower, steady state value (particularly at high temperatures) which is taken to indicate the occurrence of dynamic recrystallisation. As the temperature decreases, the plateau is not so clearly defined and this is considered to result from the net effect of the decreasing dynamic recrystallisation rate at lower temperatures coupled with a dropping stress level due to the imminent fracture of the specimens.

The hot ductility can be seen to decrease with decreasing temperature and increasing strain rate thus following the generally accepted trend (Sellars and Tegart, 1972). However the ductility proved to be inferior to that found by Barraclough (1974) for a simple 18-10 steel. This is considered to arise from the presence of ferrite and precipitates in the present material. It is interesting to note that the specimen heated to $1180^{o}C$ before testing at $900^{o}C$ (broken line,

Fig.109) showed an increased ductility compared with that heated directly to 900°C. It has been shown that heating to 1180°C reduces the ferrite content, increases the grain size and eliminates precipitates. The first two factors have an opposing influence on the hot ductility and their effects are considered to be sufficiently small to cancel each other out. It is likely that some reprecipitation occurred during the slow (furnace) cooling to 900°C and holding at 900°C. However it is unlikely that the coarse precipitates found at 800°C (Fig.103a) would be present after this treatment. Hence the increased ductility following overheating is considered to result from the elimination of coarse precipitates. No ductility problems were experienced during hot rolling so, for this steel, the deleterious effects of ferrite and precipitation were not of practical importance. This is not always the case, as is clear from examples quoted by Sellars and Tegart (1972).

It has been shown in Fig.110b that a constant activation energy for hot working, Q, could not be obtained and Fig.111 has shown that a low value (380 kJ/mole) is apparently suitable at high temperatures and a high value (490 kJ/mole) likewise at low temperatures. The changes in ferrite content and grain size over the temperature range are considered to be of negligible importance and the apparent change in Q is thought to arise from precipitation at the lower temperatures. It has been shown (Fig.103) that specimens reheated to 800°C exhibited precipitation on the dislocations whereas all precipitates were dissolved on reheating to 1100°C.

Hence the present results should only be comparable with previous work (where no precipitation has been found) at the higher temperatures. The reported activation energies range from 355 kJ/mole (Sellars and Tegart, 1966) and 338 to 347 kJ/mole (Muller, 1967) for a fully ferritic stainless steel to 410 kJ/mole (Barraclough, 1974) and 414 kJ/mole (Rossard and Blain, 1958) for a fully austenitic steel. The value of 380 kJ/mole found in the present work at high

temperatures not only falls well within this range but also agrees excellently with the value of 376 kJ/mole found by Muller (1967) for a 10% ferritic steel. The value of 490 kJ/mole found at the lower temperatures in the present work falls well outside this range and it may be concluded that this is an apparent value which has no meaning in terms of the rate controlling process and results from increasing precipitation with decreasing temperature.

Thus the structural changes were significant enough to prevent correlation of data using the Zener Hollomon parameter. Instead, results have been correlated using the exponential relationship (eqn.8.16) which only requires that the structure is independent of strain rate and is constant at a particular temperature. The temperature independent constant, β , was found to be 0.051 which compares excellently with the value of 0.047 reported by Barraclough (1974) for an 18-10 steel. The latter value was obtained from peak stress data and it has been noted that, if stresses at low strains are used instead, the value of β increases to ~ 0.07. The reasons for this discrepancy are not clear and meant that it was uncertain which value of β should be used when extrapolating Barraclough's results for comparison with the present work. However, either value leads to only small errors at a strain rate of 4 sec^{-1} assuming only Barraclough's data at the highest strain rate are used.

It has been shown that the exponential relationship allows good correlation of mean flow stresses obtained at the two strain rates as a function of temperature, Fig.112 (solid lines). These agree reasonably well with those of Barraclough (1974) for the same reduction (broken line, Fig.112) at high temperatures, but show an increasing discrepancy with decreasing temperature. This is considered to be a further effect of precipitation in the present steel at the lower temperatures and leads to $\sim$25% increase in mean flow stress at 800°C compared with Barraclough's steel. All precipitates are dissolved at 1100°C and the mean flow stresses for the

present material should lie below those for Barraclough's steel since the former contains ferrite. The reverse can be seen to be the case, and this can be taken to indicate solid solution strengthening in the present material. The analyses (Table 4) show that this is feasible.

It may be concluded that the torsion test results, although limited in number, indicate a marked effect of precipitation on the hot strength.

9.3.2 Hot Rolling Experiments

The experimental torque data were not analysed in depth for reasons outlined in Section 8.5.1. However the measured load and torque data have been used to deduce a value of 0.03 for the coefficient of friction in the roll necks, Fig.116. Although this agrees well with the range of values reported in the literature (e.g. Underwood, 1946) for phosphor bronze bearings it is likely that this value varies considerably in both laboratory and industrial rolling mills. The torque data were not analysed further. Section 8.5.1 has described the reasons for converting the measured rolling loads into mean flow stresses. The rolling theory used was that due to Sims (1954) as it appeared to be the most widely used and successful theory of the ones available (Section 2.4.4).

The plot of mean flow stress for 30% passes as a function of mean rolling temperature, Fig.113, did not allow for the variation in strain rate from pass to pass and run to run. The mean flow stresses could not be correlated with the Zener Hollomon parameter since the activation energy was not constant so they were corrected to a constant mean strain rate of 4 sec^{-1} using the exponential relationship. The results for the first pass are shown as a function of mean rolling temperature, Fig.114. Also shown are the mean flow stresses $\bar{\sigma}_g$ obtained from the torsion tests and these have been converted to $\bar{\sigma}_p$ by using a constant multiplying factor. The torsion and rolling results then agree well over the whole temperature range.

It is important to note that this agreement would not have been found if the measured rolling temperatures at the centre of the slab had not been converted to a mean temperature for each pass. Such a discrepancy was noted when comparing the torsion and rolling results for mild steel, Section 7.1 and Fig.62. It is apparent that many previous comparisons (e.g. Sims 1954, Stewartson 1954, Sims and Wright 1963) of loads or mean flow stresses from rolling and isothermal mechanical tests have not allowed for the large temperature changes that can occur during a pass and so it is not surprising that errors of $\pm$ 25% have been quoted (Stewartson, 1954). Only Gittins et al (1974A) appear to have allowed for the temperature changes during rolling and they found excellent agreement between mean flow stresses derived from rolling loads and torsion tests.

In spite of the good agreement between rolling and torsional flow stresses in Fig.114 it is considered that the cross-over at $\sim 980^{\circ}C$ is real and results from the changing precipitation behaviour with temperature. Since all slabs were reheated at $1180^{\circ}C$ for 20 minutes they were precipitate free at the higher rolling temperatures and it may be hypothesised that the slab cooling rates were sufficiently high to prevent significant precipitation prior to first passes carried out at the lower temperatures. However, as already discussed, the torsion specimens were only precipitate free at high temperatures. Hence the torsional mean flow stresses were higher than those derived from the rolling loads at low temperatures because of precipitation.

In addition to precipitation, it is necessary to consider the volume fraction of ferrite and previous discussion has shown that the latter is reduced at high soaking temperatures. Thus whereas the slabs should have a constant ferrite content, the torsion specimens have a relatively higher ferrite content at the lower temperatures. Although no attempt has been made to quantify this

effect, its outcome would be to lower the torsional flow stresses relative to the rolling flow stresses at the lower temperatures. This effect therefore partially masks the expected effect of precipitation.

Section 2.3 has reviewed work by Barraclough (1974) concerning the application of isothermal constant strain rate data to hot rolling. He showed that, under certain rolling conditions, the mean flow stresses predicted from an equation of state can be significantly lower than those obtained in practice. The differences in grain size and ferrite content in the torsion and slab specimens meant that this could not be investigated in the present work. However it should now be possible to study this effect in detail since the mathematical model allows the changing distribution of Z during a pass to be determined. Examples of such computations have been presented recently by Sellars and Whiteman (1976).

Also shown in Fig.114 are the mean flow stresses ($\bar{\sigma}_p$) derived from Barraclough's results. It can be seen that they lie essentially parallel to, but significantly below, the present rolling mean flow stresses. The displacement is considered to arise from differences in grain size and solid solution strengthening. Barraclough's mean grain size was 0.16 mm compared with the present mean slab grain size of 0.04 mm and Table 4 shows the significant increase in alloy content for the present material. The difference between the two curves appears to increase marginally at temperatures less than 950°C and this may indicate a small amount of precipitation during air cooling to the lower rolling temperatures. The compression data of Cook and McCrum (1958) for an 18-8 steel and the rolling and torsion data of Gittins et al (1974A) for a type 321 stainless steel lay between the curves for the present work and that for Barraclough's results.

The mean flow stresses (corrected to a strain rate of 4 sec^{-1}) for the second and third passes have been presented as a

function of the mean pass temperature in Fig.115. Although there appears to be a high degree of scatter, all points lie within a ± 10% scatter band and this is no worse than that found for the first pass. Fig.115 shows that, with few exceptions, the mean flow stresses for the second and third passes are significantly higher than those for the first pass which was carried out on fully recrystallised, precipitate free slabs.

The normal second pass was carried out on slabs that were ~ 80% recrystallised, the grain size being approximately a third of that prior to the first pass. In addition, the surface layer was unrecrystallised to a depth of ~½ mm due to heavy precipitation in this region. It may be speculated that a small amount of precipitation will also occur in other regions, particularly at the lower rolling temperatures and in unrecrystallised regions due to the higher dislocation density. Although the presence of a substructure in the unrecrystallised regions would be expected to decrease the mean flow stress relative to that for fully recrystallised slabs (as discussed below), the experimental results indicate that this is more than compensated for by the relative increases expected from the finer recrystallised grain size and the presence of precipitates.

Fig.115 shows that annealing slabs at 1040 or 1180°C prior to the second pass generally leads to mean flow stresses higher than those for the first pass but lower than those for the normal second pass. Both annealing treatments should lead to 100% recrystallisation, the grain size being finer than that following the initial reheating. Although some grain growth would be expected during annealing at 1180°C, its effect on the hot strength will be partly counteracted by further reduction of the ferrite content during this treatment. It may be concluded that the small observed differences in mean flow stresses for passes at T_2 on fully recrystallised slabs arise from differences in grain size.

When the second pass was delayed until T_3, metallography showed that the structure still consisted of ~ 80% recrystallised fine grains with surface layers of unrecrystallised material. The mean flow stresses of such slabs at T_3 could not be differentiated from those for the third pass of slabs given the normal 3 pass schedule. In the latter case zero recrystallisation occurred following the second pass. Thus the structure does not appear to have had any significant effect on the hot strength at the lower rolling temperatures. Similarly, no differences were found between the mean flow stresses for the third passes of T_1, T_2, T_3 and T_1, T_3, T_3 schedules. In both cases, an effect of substructure on mean flow stress was expected from previous work (reviewed in Section 3.4.2) as will now be discussed.

During isothermal hot working, the results of interrupted mechanical tests (e.g. Fig.12) show that the mean flow stresses for subsequent passes increase when zero static recrystallisation occurs between passes. However, Farag et al (1968), Fig.17, and Nair (1971), Figs.16a,b and Table 2, have shown that when a (coarse) substructure is inherited from a high deformation temperature during non-isothermal hot working, its effect is to lower the mean flow stress for subsequent passes relative to those that would be expected for fully recrystallised material. It is apparent that there will be a critical interpass temperature drop which will allow the mean flow stresses for subsequent passes during non-isothermal hot rolling to be maintained equal to those obtained for passes on recrystallised material. The effect of substructure on hot strength is not yet fully understood and further work needs to be carried out on this aspect as it is clearly of importance when applying laboratory data to practice.

Slabs should have distinct substructure prior to the third pass of the standard T_1, T_2, T_3 schedule (since zero recrystallisation followed T_2) whereas the substructure should almost be eliminated

prior to the second pass of the T_1, T_3 schedule. Additionally, since zero recrystallisation occurred in slabs given an interpass anneal at 930°C, the subgrain size before the third pass should be larger for a T_1, T_2, reheat, T_3 schedule than for a T_1, T_3, reheat, T_3 schedule. However, in both cases the experimental results indicate that the substructural differences had neither a significant nor reproducible effect on the mean flow stress for the pass at T_3. Although this may be evidence that the interpass temperature drop was in the critical range noted above, it is considered more likely that precipitation occurred very rapidly in all slabs at temperatures lower than $\sim 950^{\circ}C$ and therefore 'masked' any effects due to substructural differences. Support for the idea of rapid precipitation may be drawn from the fact that the overall mean flow stress-temperature curve for all passes follows closely that found by torsion tests.

CHAPTER TEN

APPLICATION OF MATHEMATICAL MODEL TO INDUSTRIAL HOT ROLLING

10.1 Introduction

Chapter 8 has demonstrated that the two dimensional heat flow model described in Chapter 6 is capable of accurately simulating the temperature changes during a laboratory rolling schedule. The aims of this chapter are:

(i) to present data for a wider range of conditions than that used experimentally so that the effects of the various parameters can be demonstrated, and

(ii) to present data which should allow a more realistic estimation of the temperature changes that occur during a pass of an industrial rolling sequence.

During the industrial hot rolling of rectangular sections, the width is generally much greater than the thickness so one dimensional heat flow will be operative over central regions of slabs, plate and strip. (Hereinafter all such sections will be referred to as 'plates'). Hence the computer programme was simplified so that it computed one dimensional heat flow as described in Appendix 3. Computations were carried out to simulate both the air cooling and roll contact periods and the results will be presented separately.

10.2 Air Cooling

In industrial hot rolling, it is only possible to measure the surface temperature; means for doing this have been reviewed in Section 4.2.1. One of the primary reasons for measuring temperatures during rolling is so that the loads and torques can be predicted either to ensure that the mill is not overloaded or for use in computer control of mills. In such cases it is necessary to know the mean rather than surface temperature of the plate, this being particularly so with increasing section thickness.

Computations were carried out to enable the measured surface temperature, T_s, to be related to a mean temperature, $\bar{T}$. Values of $\bar{T}-T_s$ are shown as a function of T_s in Fig.119 for a variety of section thicknesses and initial reheating temperatures. Considering firstly the solid lines (which represent the computed results) it can be seen that T_s drops more rapidly than $\bar{T}$ until an equilibrium gradient is established. At this point $\bar{T}-T_s$ goes through a maximum after which $\bar{T}$ depends solely on T_s for a particular thickness. Hence, once equilibrium cooling is established, measured values of T_s can be related uniquely to mean temperatures.

The computed results in Fig.119 have only been presented for a few values of section thickness but the standard parabolic equation predicts that $\bar{T}-T_s$ should be linearly dependent on section thickness. This was found to be so and thus linear interpolation is permissible in Fig.119 to obtain the equilibrium relationship between $\bar{T}-T_s$ and T_s for different section thicknesses. Such results are indicated by the broken lines in Fig.119 and they can be seen to be the envelope of the equilibrium portions of the curves from different reheating temperatures.

The effects of the initial reheating temperature and section thickness on the time to establish equilibrium cooling(t_{eq}) is illustrated by a plot of t_{eq} against thickness, Fig.120. This shows that the reheating temperature has only a small effect and equilibrium is reached more quickly when cooling from higher temperatures due to the temperature dependence of the diffusivity. Fig.120 shows that the section thickness has a much greater effect than temperature on the time to reach the peak value of $\bar{T}-T_s$. The relationship between log t_{eq} and log thickness is not linear, so t_{eq} is not simply related to thickness. For thin sections, the slope tends to a value of 2, i.e. $t_{eq} \propto (\text{thickness})^2$, but with increasing thickness the slope decreases to ~ 1.6. Since the cooling rate decreases with increasing section thickness, the mean

diffusivity is higher during a fixed cooling period. Hence the time to reach equilibrium decreases with increasing section thickness and so explains the changing slope in Fig.120.

Fig.119 illustrates that, even when the peak is reached, the curves of $\overline{T}-T_s$ against T_s do not immediately become coincident with the equilibrium curve (broken line). Hence the times indicated by Fig.120 should be taken as the absolute minimum if it is wished to estimate $\overline{T}$ with any degree of confidence. In cases where it is not possible to satisfy this minimum time requirement, mean temperatures should be obtained from a plot such as Fig.121. This shows how $\overline{T}-T_s$ varies with time for selected slab thicknesses and reheating temperatures. So, if surface temperatures are measured before equilibrium cooling is established, it is necessary to measure the time since removal from the furnace as well.

The primary assumption in this analysis is that the plate does not have a through thickness temperature gradient on exit from the furnace. It was found that initial temperature gradients changed the shape of the initial cooling curves and this therefore affects the accuracy of obtaining $\overline{T}$ from T_s prior to equilibrium cooling. This effect needs to be investigated further once measured data for such gradients become more readily available.

It will be appreciated that the material has the largest section thickness at the shortest cooling times from the furnace. Hence, when obtaining $\overline{T}$ from T_s, it will generally be necessary to use a plot such as Fig.121 at the start of a schedule and a plot such as Fig.119 towards the end of the schedule. Fig.120 indicates the minimum time for the change over from one approach to the other but strictly applies to air cooling of a constant plate thickness. In addition it is necessary to allow for the recalescence of the surface temperature following a pass and this is considered in Section 10.4.

10.3 Roll Contact Period

10.3.1 Heat Loss by Conduction

Computations were carried out to investigate the effects of the rolling variables on the heat loss during the roll contact period. In each case the deformational temperature rise was taken as $0^{o}C$ and the temperature drops reported are the differences in the mean section temperature at entry to and exit from the rolls.

10.3.1.1 Effect of Geometry of the Roll Gap

The roll gap geometry can be altered by changing the initial thickness (h_1), the rollradius (R) and the % reduction. Computations showed that changing each of these variables (but keeping all other parameters constant) significantly changed the conductive temperature drop $\Delta\bar{T}_{cond}$. Values of the latter were converted to mean heat losses/unit area by using the equation

$$\Delta\bar{h}_{cond} = \frac{V}{A} \rho s \quad \Delta\bar{T}_{cond} \qquad (10.1)$$

where V/A, the volume to surface area ratio in the roll gap, is given by eqn.7.2 and values can be obtained from Fig.122. The product $s\rho$ is relatively temperature independent and is 5.076 $MJ/m^3\ ^{o}C$ for 18-8 steel at $1140^{o}C$ (the mean plate temperature at entry to the rolls for the majority of computed results).

Values of $\Delta\bar{h}_{cond}$ then varied little with large changes in h_1 and R. $\Delta\bar{h}_{cond}$ increased with % reduction as shown in Fig.123 for a constant and a variable C. If eqn.10.1 allows perfect compensation for a variable roll gap geometry, then $\Delta\bar{h}_{cond}$ should remain constant with % reduction for a constant C. The discrepancy arises because eqn.10.1 is a simplification of

$$\Delta\bar{h}_{cond} = \sum_i \left(\frac{V}{A}\right)_i \rho_i s_i \quad \Delta\bar{T}_i \qquad (10.2)$$

where the subscript i indicates the value of each variable during a particular interval of the pass. Equation 10.2 only reduces to eqn.10.1 when $\left(\frac{V}{A}\right)_i$ is constant, but since this is not the case either in practice or in the computer programme, it is fundamentally incorrect to make this approximation.

However, the errors introduced by this simplification are small compared with the effects of C and contact time and so, in the absence of a suitable alternative method, all subsequent heat losses/unit area were calculated using eqn.10.1 with the V/A ratio given by eqn.7.2. As long as the same equations are used when converting backwards (i.e. from $\Delta\bar{h}_{cond}$ to $\Delta\bar{T}_{cond}$), the errors will be insignificant.

10.3.1.2 Effect of Initial Roll Temperature

The effect of the initial roll temperature is illustrated by Fig.124. This shows that $\Delta\bar{T}_{cond}$ increases linearly with increasing initial difference in plate and roll surface, ΔT_s^{init}, i.e.

$$\Delta\bar{T}_{cond} = k \quad \Delta T_s^{init}$$

$$\text{and so } \Delta\bar{h}_{cond} = k^* \quad \Delta T_s^{init} \qquad (10.3)$$

where k^* depends on C, contact time and roll gap geometry. It should be noted that the results in Fig.124 were obtained by varying the initial roll surface temperature but identical results were obtained when ΔT_s^{init} was changed by varying the initial plate surface temperature. Hence the heat loss depends only on the difference between the initial plate and roll surface temperatures and not on their absolute values.

All the subsequent results will be presented in terms of a heat loss/unit area/unit initial temperature difference, $\Delta\bar{H}_{cond}$, where

$$\Delta\bar{H}_{cond} = \frac{\Delta\bar{h}_{cond}}{\Delta T_s^{init}} \qquad (10.4)$$

This equation indicates that the heat loss is not particularly sensitive to poor estimates of ΔT_s^{init}. For example, with a slab surface temperature of 1200°C and an initial roll temperature of 200°C ± 50°C, ΔT_s^{init} is 1000°C ± 50°C. Hence an error of ± 25% in the initial roll temperature affects ΔT_s^{init} (and hence the heat loss) by ± 5%. This is an important conclusion for several reasons.

Firstly, it is difficult to measure roll temperatures unless instrumentated work rolls are used (Stevens et al, 1971). This is hardly a common industrial practice although the use of contact thermocouples (Polukhin et al, 1972A) might be more feasible. Secondly, although the roll circumference was greater than the rolled slab length in the experimental hot rolling, this is not true industrially and the middle and tail end sections of plates will be in contact with portions of the roll which will be at elevated temperatures. Industrially the situation is further complicated by the use of roll coolants. Finally, it is well known (e.g. Stevens et al, 1971) that the core and mean temperatures of the roll rise significantly during extended rolling operations.

Therefore although data are at present limited for roll temperatures during industrial rolling, this is not a serious barrier to the application of the present computations.

10.3.1.3 Effect of the Value of C

The experimental hot rolling showed that C, the heat transfer constant between plate and rolls, varied between 50 and 1000 $kW/m^2\ ^oC$. Industrially, it is likely that the range of C will generally be lower as discussed in Section 9.1.2.2.2. The effect of C on $\Delta\bar{T}_{cond}$ is shown in Fig.125 for two contact times. At long contact times it can be seen that the effect of C is very marked below C values of $\sim$100 $kW/m^2\ ^oC$ and above this value, large changes in C are necessary to have any significant effect on the value of $\Delta\bar{T}_{cond}$. This effect appears to be diminished at short contact times and $\Delta\bar{T}_{cond}$ changes more gradually with C. This arises because $\Delta\bar{H}_{cond}$ is effectively given by the sum of $C\left(T_s^{plate} - T_s^{roll}\right)\delta t$ over all the time intervals during a pass. At long contact times, the difference between T_s^{plate} and T_s^{roll} approaches zero relatively early during the contact period, and this occurs more rapidly with increasing C value. Thus the temperature difference between roll and plate tends to zero whatever

the value of C. However, at short contact times, the difference between T_s^{plate} and T_s^{roll} remains large for a relatively much greater proportion of the contact period. Hence a change in the value of C will have a relatively larger effect on the total heat loss as the contact time decreases.

10.3.1.4 Effect of Contact Time

The effect of contact time on $\Delta\bar{H}_{cond}$ is shown in Fig.126 for a variety of initial values of C, the latter being allowed to increase during the pass in proportion to the reduction. This illustrates clearly the increasing heat loss with contact time and C. All the values presented were obtained for a R/h_1 ratio of 10 and the majority for a 30% reduction so that any effect of roll gap geometry will be constant. Section 10.3.1.1 has indicated the small errors introduced by using the V/A ratio to correct for a variable roll gap geometry but comparison of these errors in relation to the effect of C and contact time showed that the former were negligible. Additionally, in order to maintain a sufficiently high number of computational time intervals during a pass, the results in Fig.126 were obtained on different initial section thicknesses. No discontinuities were found where these results overlapped, thus supporting the use of the V/A ratio as proposed above.

It has already been noted that allowing C to increase during a pass leads to a significant increase in $\Delta\bar{H}_{cond}$ with increasing reduction. This effect is indicated at selected points by error bars whose lower and upper limits represent 10% and 50% reductions respectively. The effect of the % reduction can be seen to be most marked when C is low and the contact time short. The explanation for this has been noted above.

As the contact time approaches infinity, the temperatures of plate and roll become uniform and equal to a temperature defined by equation 4.31 (assuming no heat is lost by radiation etc. from

plate or roll). Therefore there is only a finite amount of heat to be lost by the plate and so all curves have a common origin at a finite value of $\Delta\bar{H}_{cond}$ at an infinite contact time. Therefore the slopes must tend to zero at long contact times. Additionally, at zero contact time, zero heat is lost independent of C. Hence all curves must also have a common origin at $-\infty$, $-\infty$ in Fig.126. The following tabulation shows the slopes of the curves at long and short contact times (t_c) as a function of C.

	C kW/m^2 °C					
	12.5	25	50	100	200	1000
Long t_c	0.80	0.71	0.63	0.56	0.54	0.48
Short t_c	0.94	0.92	0.86	0.76	0.68	0.52

These results agree well with those of Portevin and Blain (1967) who found experimentally that the heat transfer between hot and cold bodies depended linearly on contact time at short contact times, whereas the heat transfer became more nearly dependent on the square root of contact time at times greater than 0.15 seconds.

The computed slopes can also be correlated with the analytical solution of the heat flow between two bodies (Sections 4.3.2, 4.4.2.2). It can be seen that the heat loss/unit area is proportional to the square root of contact time in all the different forms of the analytical equations (eqns.4.27, 4.28, 4.32). In the present model, as C and/or contact time increase, the analytical solution is approached more closely and hence the slopes in Fig.126 more closely approach 0.5.

Values of $\Delta\bar{H}_{cond}$ were calculated for a zero contact resistance using eqns.4.28 and 4.31 and are shown in Fig.126 by the broken line. It can be seen that this line (equivalent to a C value of infinity) coincides closely with the curve for C = 1000 kW/m^2 °C, lying above it at short contact times and below it at long contact times. However it would be expected that the line for zero contact resistance should lie above the curve for C = 1000 kW/m^2 °C at all contact times. This discrepancy is considered to result from errors

in the application of the analytical solution to the rolling situation as will now be discussed.

The analytical approach for calculating the heat flow between 2 bodies with a zero contact resistance (Section 4.3.2) results in equations describing the temperature as a function of distance and time, eqns.4.9 to 4.11. These equations are integrated with respect to time to obtain heat losses but since the dimensions change during rolling it is necessary to integrate these equations with respect to distance as well. This appears to be complex and previous workers have integrated the equations with respect to time and then assumed that all the heat is lost at a mean section thickness. Wright and Hope (1975), Zheleznov et al (1968) and Muzalevskii et al (1970) used the arithmetic mean of initial and final section thicknesses whereas Bradley et al (1970) and Denton and Crane (1972) have used the geometric mean. A more sensible approach would appear to be a mean height given by the V/A ratio. However, whichever mean height is used it is clearly an approximation and it is considered that this explains the discrepancy found when comparing the present work with the analytical solution.

10.3.1.5 Effect of Thermal Properties

The present computations were carried out with temperature dependent properties for the plate (18-8 steel) and constant thermal properties for the rolls (EN8 steel at room temperature). The values are given in Appendix 3. The heat flow across the plate-roll interface is governed partially by the diffusivities of the plate and roll and clearly many combinations of thermal properties can occur in practice. Although not investigated to any extent in the present work, this may be of significance and needs further study.

10.3.2 Heat Gain due to Deformation

The above results have assumed no heat input due to deformation. So, having calculated the temperature drop due to conduction, it is now necessary to add on the deformational temperature rise $\Delta\bar{T}_{def}$. The latter quantity can be calculated in several ways as reviewed in Section 4.4.2.1 and as discussed in Section 9.1.2.2.1. In the mathematical model $\Delta\bar{T}^{*}_{def}$ (= total $\Delta\bar{T}_{def}$/number of computational intervals) is added to the plate temperatures at the start of each interval thereby simulating the practical situation. However when $\Delta\bar{T}^{*}_{def}$ is added during a pass some of it will be conducted to the rolls and the heat conduction to the rolls will be marginally increased since the plate surface temperatures are increased prior to each interval of the pass. Hence when $\Delta\bar{T}_{def}$ is added at the end of the pass the deformational heat input is over estimated. Therefore when $\Delta\bar{T}_{def} < \Delta\bar{T}_{cond}$, the net mean temperature drop will be underestimated and when $\Delta\bar{T}_{def} > \Delta\bar{T}_{cond}$, the net mean temperature rise will be overestimated.

When the error was quantified it was found to be small numerically (even at high values of C and $\Delta\bar{T}_{def}$ and long contact times) and was insignificant compared with that introduced by the uncertainty of the value of C.

10.3.3 Application of Computed Data

It is suggested that the data presented above can be used in two ways. Firstly, $\Delta\bar{H}_{cond}$ can be obtained from Fig.126 in terms of the contact time assuming an estimate can be made of the value of C. The latter can be estimated from the ratio of the scale conductivity to its thickness if data for the former are available and measurements can be made of the latter. Alternatively, a value of C can be guessed - perhaps a value of C of 12.5 or 25 $kW/m^2\ ^oC$ rising to 100 $kW/m^2\ ^oC$ for the early stages of roughing and perhaps a value of 100 $kW/m^2\ ^oC$ rising to 1000 $kW/m^2\ ^oC$ during

the finishing stages of strip rolling. Although crude, such estimates allow a more realistic estimate of the amount of heat lost than the previously reported equations based on infinitely good contact between plate and roll.

Having found $\Delta\bar{H}_{cond}$, it is multiplied by ΔT_s^{init} to obtain $\Delta\bar{h}_{cond}$, the heat lost/unit area. The V/A ratio is then calculated or found from Fig.122 for the geometry of interest and a value of ρs obtained for the steel of interest. Hence the value of $\Delta\bar{T}_{cond}$ is arrived at. $\Delta\bar{T}_{def}$ is found using any suitable method and thus the net temperature change deduced. If the mean slab temperature is known at entry to or exit from the pass, the mean temperature for the pass can now be obtained.

The alternative approach is to measure portions of the air cooling curves before and after the pass and thereby deduce the mean temperatures at entry to and exit from the rolls. When attempting this, it is necessary to be aware particularly of the recalescence effect as discussed in Section 10.4. Then, by using the reverse of the procedure outlined above, it is possible to obtain a reasonable estimate of the value of C. This can then be used to estimate the through thickness temperature gradient at the exit plane as will now be discussed.

10.3.4 Temperature Gradients within Plate

The preceding results have illustrated that the presence of a finite contact resistance between plate and roll can markedly affect the heat loss during a pass, this effect being dependent on contact time, ΔT_s^{init} and C. Since this is so, then it would be expected that the temperature gradient on exit from the rolls would also be affected by these variables. Evidence will now be presented to illustrate this.

Fig.127 illustrates how the temperature gradient changes with contact time for a constant value of C. As the contact time

increases, the surface temperature drop increases, the gradient penetrates further into the plate and the temperature changes more gradually from surface to centre. As indicated in Section 4.3.2, equations for the temperature gradient are complex (particularly when there is a contact resistance present) and no attempt was made to fit equations of this type to the computed data. Instead it was considered that, by relating the distance penetrated and the drop in surface temperature to the rolling variables, the general shape of the gradient could then be deduced for any conditions of interest.

Considering firstly the distance penetrated by the gradient, it was found that this was independent of both ΔT_s^{init} and C and dependent only on contact time. The distance penetrated was found to increase linearly with the square root of contact time as illustrated in Fig.128 (solid line). Each point has an error bar associated with it indicating the dimension of the finite element. This plot is for an average initial plate temperature of 1140°C and the slope would be expected to decrease with temperature due to the decreasing diffusivity.

Incidentally, Fig.128 also illustrates an important point regarding operation of the programme. As already noted, three different plate thicknesses were used when computing heat losses, this being necessary to maintain a sufficiently high number of computational time intervals during a pass. This number is indicated adjacent to each point in Fig.128 and it can be seen that if the number of intervals per pass is too low (e.g. 10 mm initial thickness with a root contact time of 0.092 secs) then the distance penetrated is too low. Whenever possible, the number of intervals per pass was not allowed to be less than 10 and, if the contact time, initial thickness etc. are to be kept constant, this restriction is satisfied by changing the number of finite elements comprising the plate.

The drop in plate surface temperature between the entry and exit planes is illustrated in Fig.129 as a function of contact time for a wide range of values of C. This shows that, at high C values, the plate surface temperature drops almost instantaneously to a constant value, thus resembling the assumption made in the analytical solution for a zero contact resistance. As C decreases, it takes considerably longer for the temperature drop to reach an approximately constant value and, at the lowest values of C, a constant value is never approached. The temperature drops given in Fig.129 are for an initial surface temperature difference between plate and rolls of 1000°C. Computations showed that a higher or lower value of ΔT_s^{init} increased or decreased the temperature drop by simple proportion.

The data presented in Figs.128,129 therefore allow a reasonable estimate to be made of the magnitude of the gradient at the surface of the plate on exit from the rolls.

10.4 Recalescence following exit from Rolls

The experimental rolling clearly showed that a considerable time (up to ~ 5 seconds) was necessary before an equilibrium air cooling gradient was re-established in the slabs following a pass. It has been noted that this effect is important because only surface temperatures can be measured industrially. Thus considerable errors can occur when estimating mean temperatures from surface temperatures if the latter are measured too soon after the end of the pass. Computations were carried out to determine how the recalescence time (i.e. the time from the end of the pass necessary for the surface temperature to reach a peak) depended on the rolling variables.

Initial analysis of the data showed that, at constant thickness, the recalescence time increased with both C and contact time, i.e. with increasing heat loss. Hence the recalescence time was determined for different heat losses and plotted as a function

of the plate exit thickness, Fig.130. The error bars in this figure arise because the printouts were made at (different) multiples of a finite computational time interval. Fig.130 therefore demonstrates that there are two factors which control the recalescence time. Firstly, when only a small amount of heat is lost at the surface, an equilibrium gradient is re-established in relatively short times. With increasing heat loss, then a larger amount of heat has to be conducted from the centre to the surface, hence increasing the recalescence time. Secondly, the recalescence time increases with plate thickness, thus showing that the distance over which the heat has to be conducted is important. No simple relationship could be found between the recalescence time and section thickness.

Although data have been presented for only a limited range of section thicknesses, extrapolation allows estimates to be made of the recalescence time for thicker sections. Taking a heat loss of 1 $kJ/m^2\ ^oC$ as typical, then the recalescence time for a 50 mm slab is $\sim$10 seconds. Since further cooling is necessary following the surface temperature peak before a true equilibrium gradient is established, it will be appreciated that it is rarely possible to predict accurately the mean temperature from measured surface temperatures unless considerable delays occur between passes. Considering the other extreme of thickness, equilibrium is established rapidly (e.g. in less than $\sim$0.2 sec. for 2 mm strip) but finish rolling temperatures are measured with pyrometers which are usually sited only a short distance after the last stand. Taking a typical finish rolling speed of 10 m/sec. then as long as the pyrometer is situated $\sim$2 m. from the last stand, significant errors in surface temperature measurement are unlikely to occur. With increasing exit thickness and the trend for higher finishing speeds, this minimum distance will increase significantly.

It is clear that this important factor is not widely appreciated since only Wilmotte et al (1973A) mention it. They note that temperature measurements should be made at not less than 5 seconds following a pass but the present work shows that, in some cases, this is an unnecessary restriction and, in other cases, this time is not long enough.

CONCLUSIONS

Temperature Changes during Hot Rolling

1. Static air cooling tests on mild and stainless steel slabs and round billets have shown that:
   (a) The scale thickness and phase transformation in mild steel affect the cooling rate significantly.
   (b) Transverse sections at the centre of rectangular slabs of 130 mm length undergo only two dimensional cooling during the 3 x 30% rolling schedule used for stainless steel.
   (c) The through thickness temperature gradient is symmetrical about the slab centre.

2. Comparison of measured and computed air cooling curves showed that the rate of heat loss per unit area during air cooling of austenitic stainless steel sections is adequately represented by

$$H = -0.69 + 0.01247\ T_s + 4.7628 \times 10^{-11}\ (T_s + 273)^4\ kW/m^2$$

where T_s is the surface temperature (^oC).

3. (a) The internal temperatures of slabs during hot rolling can be measured successfully using embedded metal sheathed, mineral insulated thermocouples. Their outputs can be accurately recorded using a U.V. recorder combined with an automatic back-off system.
   (b) High temperature deformation does not measurably affect the accuracy of chromel-alumel thermocouples.

4. The temperature records showed that:
   (a) On entry to the rolls, the centre of slabs undergo a temperature rise due to deformation and, simultaneously, the surface regions undergo a severe chilling effect due to heat conduction to the rolls.
   (b) On exit from the rolls, up to 5 seconds was required for the steep temperature gradient introduced during a pass to be dissipated prior to equilibrium air cooling being re-established.

5. (a) The temperature rise due to deformation increases with increasing strain, strain rate and decreasing temperature and could be related satisfactorily to the dependence of the mean flow stress on these parameters.

(b) Computations showed that the deformational temperature rise is not uniform through the slab thickness and increases markedly at the slab surface.

(c) Both the measured roll loads and torques predict a mean temperature rise which may be significantly higher than that measured at the centre of a slab.

6. (a) The heat conducted to the rolls was greater than the heat input due to deformation.

(b) The chilling effect increases with increasing initial difference in slab and roll surface temperatures and with increasing contact time.

(c) After allowing for (b), considerable variations in the conductive temperature drop were observed and this is taken as evidence of the marked effect of the presence of a scale layer.

7. (a) A computer programme, based on a finite difference analysis of heat flow in a two dimensional slab cross-section, allows prediction of the changing temperatures and temperature distributions during the interpass and roll contact periods of hot rolling schedules.

(b) The correct choice of the finite heat transfer coefficient between slab and rolls (which is increased in proportion to the reduction) allows good agreement between measured and predicted temperature-time curves during a laboratory hot rolling schedule.

8. (a) The simplification of the above computer programme to a one dimensional model allows simulation of the temperature changes that occur in wide plate and strip during industrial hot rolling.

(b) Data have been presented to establish:

(i) The mean section temperature from measured surface temperatures during air cooling.

(ii) The conditions necessary for an equilibrium temperature gradient to be established both prior to and following a pass.

(iii) A realistic value of the temperature drop due to conduction.

Structural Changes during Hot Rolling

9. Metallography showed that the stainless steel contained ~ 10% ferrite under most hot working conditions but there was no evidence that this affected structural changes in the austenite.

10. (a) As-rolled slabs of the present stainless steel quenched at varying times during a 3 x 30% pass schedule have shown that recrystallisation is very sluggish in comparison with that expected from previous work on a simple austenitic stainless steel.

(b) Following the first pass, recrystallisation occurred rapidly at the centre of slabs but was retarded at the surface. This is the reverse of the theoretical behaviour.

(c) Recrystallisation occurred slowly after long incubation times during isothermal annealing at temperatures in the 900°C to 1000°C range.

11. (a) The retarded recrystallisation noted above is explicable in terms of dislocation pinning by precipitates.

(b) Limited electron microscopy has demonstrated the occurrence of precipitation under certain conditions thus supporting this hypothesis.

Strength during Hot Working

12. (a) Torsion tests on austenitic stainless steel showed the characteristic work hardening at low strains, leading to a peak stress which was followed by a decrease to a steady state or decreasing stress level.

(b) The activation energy for hot working was found to be 380 kJ/mole above 1000°C but increased anomalously to 490 kJ/mole at lower temperatures due to precipitation.

(c) Flow stresses during both rolling and torsion were satisfactorily related to strain rate by an exponential relationship with the exponent β as 0.051.

13. (a) A fully instrumentated rolling mill has been used to hot roll mild and stainless steel slabs and has enabled the measurement of roll loads, torques and speeds.

(b) In both cases, good agreement between rolling and torsional mean flow stresses is only found when the mean pass temperatures for the former are known.

(c) The mean flow stresses derived from torsion tests on stainless steel become significantly higher than those derived from roll loads at temperatures $\lesssim 950°C$: this has been attributed to heavier precipitation in the former.

14. When little or no recrystallisation occurred during hot rolling schedules carried out on stainless steel, the retained substructure had no effect on the hot strength for subsequent passes. This conclusion, which differs to that of previous workers, is attributed to the 'masking' effect of rapid precipitation at temperatures lower than $\sim 950°C$.

Recommendations for Further Work

The effect of substructure (inherited from high deformation temperatures during non-isothermal hot working) on hot strength is still not fully appreciated or understood and is worthy of further study. This should be carried out by hot rolling a simple stainless steel according to the schedules and techniques developed in the present work. Having obtained detailed information on how the present stainless steel behaves during hot rolling, it would be of interest to simulate the rolling schedules on the 'Servotest' computer-controlled plane strain compression machine. Due to the marked effects of precipitation, the present material should allow a critical evaluation of the machine's ability to simulate real hot rolling schedules.

Although the occurrence and mechanisms of precipitation during hot working are currently being investigated for HSLA steels, the acquisition and use of such data for other steels should not be overlooked in view of the marked influence of precipitation on hot strength and structure. Indeed, it is possible that the more fundamental aspects of precipitation may be elucidated more easily in the absence of phase transformations.

There are several possibilities for the further study of temperatures during hot rolling. The literature review has demonstrated the lack of knowledge regarding temperatures during industrial rolling. It is clear that there is an increasing demand for such knowledge and the present work has illustrated the factors which need to be considered for accurate temperature measurement. Two extensions of the present mathematical model have been presented briefly and are worthy of further investigation. Firstly, since it is now possible to provide a realistic estimate of the changing Z distribution during a pass, fundamental aspects of the application

of isothermal mechanical test strength data can now be studied. Secondly, knowledge of the temperature changes during and following a pass, coupled with recrystallisation and precipitation data, should now enable full investigation of the structural developments during hot rolling schedules. Such an approach should be of particular use when applied to the controlled rolling of HSLA steels.

Acknowledgements

The author wishes to extend his grateful thanks to his supervisor, Dr. C.M. Sellars, not only for providing an absorbing research topic, but also for his valuable help and advice.

Thanks are also gratefully due to many members of the academic and technical staff and fellow students for their help and interest. In particular, thanks are due to Mr. K.E. Hughes, Mr. R. Tyson and Mr. E. Shelton for their assistance with the hot rolling, to Mr. G.R. Smith for the design and construction of the automatic back-off unit, to Dr. S.R. Keown and Mr. N. Rogers for their assistance with the electron microscopy and to Dr. J.A. Whiteman for useful discussions regarding computer programming.

The author wishes to acknowledge the financial support from the Science Research Council, the Department of Metallurgy Research Fund and the D.H.S.S.

Finally, the author wishes to thank Mrs. E. Grant for her accurate typing and his family for further financial assistance and patient moral support.

REFERENCES

Adams J.A. and Rogers D.F., 1973, "Computer Aided Heat Transfer Analysis " McGraw-Hill.

Alexander J.M., 1955, Proc.Inst.Mech.Eng., 169, 1021.

Arnold R.R. and Whitton P.W., 1959, Proc.Inst.Mech.Eng., 173, 241.

Bailey J.E. and Hirsch P.B., 1962, Proc.Roy.Soc., London, A267, 11.

Bain E.C. and Aborn R.H., 1939, A.S.M. Metals Handbook, p.418.

Barraclough D.R., 1974, Ph.D. Thesis, Univ.of Sheffield.

Barraclough D.R. and Sellars C.M., 1974, Inst.Physics.Conf. Ser.No. 21, 111.

Beadle R.G., Lehr D.A. and Maxwell H.S., 1970, U.S. Patent No.3 332 263.

Beattie D.D., 1971, 'Process Instrumentation in the Metals Industry', Inst.of Meas. and Control, p.105.

Beese J.G., 1972, J.I.S.I., 210, 433.

Birks N., 1975, Priv.Comm., Univ. of Sheffield.

Bleloch W., 1969, South Afr.Mech.Eng., 19, 85.

Le Bon A., Rofes-Vernis J. and Rossard C., 1975, Met.Sci., 9, 36.

Bowler R.F., 1963, Sheet Met.Ind., 40, 329.

Bradley B.F., Cockett W.A. and Peel D.A., 1970, I.S.I. Special report 123, 79.

Brunot A.W., Buckland F.F., 1949, Trans.A.S.M.E., 71, 253.

Buxton S.A.E. and Sutton R.W., 1969, G.E.C.- A.E.I. J.Sci.Techn. 36, 19.

Cahn R.W., 1950, Proc.Phys.Soc., A63, 323.

Cahn R.W., 1956, Acta Met., 4, 449.

Cahn R.W. and Hagel W.C., 1962, 'Decomposition of Austenite by Diffusional Processes' Ed. V.F. Zackay, H.T. Aaronson, Inter-science, New York, p.131.

Capeletti T.L., Jackman L. and Childs W., 1972, Met.Trans., 3, 789.

Carslaw H.S. and Jaeger J.C., 1959, 'Conduction of heat in solids', Oxford, Clarendon Press.

Cerni S., Weinstein A.S. and Zorowski C.F., 1963, Iron and Steel Eng., 40, 165.

Chapman A.J., 1967, 'Heat Transfer', 2nd Ed., MacMillan Co.

Chelyshev N.A., Dadochkin N.V. and Medvedev V.A., 1971, Steel in U.S.S.R., 1, 131.

Coe C.D., 1971, ref. Beattie, p.170.

Coldren A.P., Cyderman R.L. and Semchyshen M., 1970, 'Strength and Impact Props. of Low C Steels containing Mo', Climax Moly. Co.

Cole A.T., 1976, Priv.Comm., Univ.of Sheffield.

Cook P.M., 1957, 'Conf. on Properties of Materials at High Rates of Strain, p.86, Inst.Mech.Eng.

Cook P.M., and McCrum A.W., 1958, 'The Calcn. of Load and Torque in Hot Flat Rolling', B.I.S.R.A.

Cordea J.M. and Hook R.E., 1970, Met.Trans., 1, 111.

Cornfield G.C. and Johnson R.H., 1971, E.C.R.C/M427; publ.as 1973, J.I.S.I., 211, 567.

Cotterill P. and Mould P.R., 1976, 'Recrystallisation and Grain Growth in Metals', Surrey Univ. Press.

Crane F.A.A. and Alexander J.M., 1963, J.Inst.Metals, 91, 188.

Darnall R.J., 1968, Iron and Steel Eng., 45, 128.

Davis W.B., 1972, J.I.S.I., 210, 437.

Denton B.K. and Crane F.A.A., 1972, J.I.S.I., 210, 606.

Dieter G.E., 1961, 'Mechanical Metallurgy', McGraw Hill Book Co. Ltd.

Djaic R.A.F. and Jonas J.J., 1972, J.I.S.I., 210, 256.

Djaic R.A.F. and Jonas J.J., 1973, Met.Trans., 4, 621.

Dubinskii B.E., Polukhin V.P. and Blaut-Blachev R.N., 1971, Steel in U.S.S.R., 1, 545.

Dunstan G.R. and Evans R.W., 1969, Metallurgia, 79, 96.

Dusinberre G.M., 1949, 'Numerical Analysis of Heat Flow', McGraw Hill Book Co. Inc.

Dutchak Y.A., Druk R.V., Slabkovskii I.S., Kits A.I., Lakh V.I., Polishchuk N.A. and Frenchko V.S., 1972, Sov.Mater.Sci., 8, 235.

Economopoulos M., 1975, I.S.I. Special Report 158, p.247.

Ekelund S., 1933, Steel, 93, 27; translated from 1927, Jerk.Ann., 111, 39.

El Kalay A.K.H.E.A., and Sparling L.G.M., 1968, J.I.S.I., 206, 152.

English A.T. and Backofen W.A., 1964, Trans.Met.Soc. A.I.M.E., 230, 396.

Eyres N.R., Hartree D.R., Ingham J., Jackson R., Sarjant R.J. and Wagstaff J.B., 1946, Phil.Trans., 240, Ser.A., p.1.

Farag M.M., Sellars C.M. and Tegart W.J.McG., 1968, I.S.I. Special Report 108, p.60.

Ford. H., 1946, I.S.I. Special Report 34, p.69.

Ford H., 1963, J.Inst.Metals, 91, 353.

Ford H. and Alexander J.M., 1964, J.Inst.Metals, 92, 397.

Foster M.A. and Marshall S.A., 1975, I.S.I. Special Report 158, p.308.

Gautier J.J., Morillon Y. and Dumont-Fillon J., 1970, I.S.I. Special Report 123, p.178.

Gittins A., Moller R.H. and Everett J.R., 1974A, B.H.P.Tech.Bull., 18, 2.

Gittins A., Moller R.H. and Tegart W.J.McG., 1974B, 'Strength of Steels in Hot Strip Rolling', Paper presented in Czechoslovakia.

Gleave M.C. and Modlen G.F., 1968, Iron and Steel, 41, 550.

Glover G., Ph.D. Thesis, Univ.of Sheffield, 1969.

Glover G. and Sellars C.M., 1973, Met.Trans., 4, 765.

Grange R.A., 1964, 'Fundamentals of Deformation Processing', Syracuse Univ. Press, p.299.

Green J.W. and Wallace J.F., 1962, J.Mech.Eng.Sci., 4, 136.

Gupta S. and Ford H., 1967, J.I.S.I., 205, 186.

Gurkov A.A., 1968, Stal in Eng., p.129.

Harding R.A., 1973, M.Met.Thesis, Univ.of Sheffield.

Hartley A.J., 1972, Ph.D.Thesis, Univ.of Sheffield.

Held J.F., Kruger H.J. and Bucher J.H., 1970, 'Mech.Working and Steel Processing VIII', Illinois.

Helmi A. and Alexander J.M., 1968, J.I.S.I., 206, 1110.

Hill R., 1950, Proc.Inst.Mech.Eng., 163, 135.

Hitchcock J.H., 1935, 'Roll Neck Bearings', A.S.M.E. Research Publication, Appendix 1.

Hockett J.E., 1960, Trans.A.S.M., 52, 675.

Hollander F., 1970, I.S.I. Special Report 123, p.46.

Howells R.L., Probert S.D. and Ward J., 1972, J.I.S.I. 210, 10.

Hu H., 1962, Trans.A.I.M.E., 224, 75.

Hughes K.E. and Sellars C.M., 1972, J.I.S.I. 210, 661.

Hughes K.E., Nair K.D. and Sellars C.M., 1974, Met.Tech., 1, 161.

Irvine K.J., Llewellyn D.T. and Pickering F.B., 1959, J.I.S.I. 192, 218.

Izzo H.F., 1974, Iron and Steel Int., 47, 45.

Johnson W. and Kudo H., 1960, Int.J.Mech.Sci., 1, 175.

Jonas J.J., Sellars C.M. and Tegart W.J.McG., 1969, Met.Rev. 130.

Jones A. and Walker B., 1974, Met.Sci., 8, 397.

Kannel J.W. and Dow T.A., 1974, A.S.M.E. Publn.No. 74-Lubs-7.

von Karman T., 1925, Z.angew.Math.u.Mech., 5, 139.

Keown S.R., 1973, Ph.D.Thesis, Univ.of Sheffield.

Kinsie P.A., 1973, 'Thermocouple Temp.Meas.', p.147, J.Wiley and Sons.

Kobasu D. and Schultz R.A., 1968, A.I.S.E. Yearly Proc., p.283.

Kozasu I. and Kubota H., 1968, Tetsuto Hagane, 54, 679.

Kozasu I. and Shimizu T., 1971, Trans.I.S.I.J., 11, 359.

Larke E.C., 1963, 'The Rolling of Strip, Sheet and Plate', Chapman and Hall Ltd., London.

Lee P.W., Sims R.B. and Wright H., 1963, J.I.S.I., 201, 270.

Luton M.J. and Sellars C.M., 1969, Acta Met., 17, 1033.

Mashinskii V.V., Bazhutin V.V., Tarnovskii I.Ya. and Vinokurov I.Ya., 1970, Stal in Eng., p.124.

Massey I.D., Robertson A.D., Sanders L.M. and Sheridan A.T., 1973, J.Inst.Fuel, 46, 373.

McKensie C.R. and Young R.W., 1971, J.I.S.I. 209, 918.

McQueen H.J., Wong W.A. and Jonas J.J., 1967, Acta Met., 15, 586.

McQueen H.J. and Bergerson S., 1972, Met.Sci.J., 6, 25.

McTighe J., 1975, Ph.D.Thesis, Univ.of Sheffield.

Miller J.S., 1969, J.I.S.I., 207, 1444.

Minarik J., 1972, Hutnik., 22, 213. (B.I.S.I.T. 11043).

Moore P., 1968, I.S.I. Special Report 108, 103.

Muller T.L.F., 1967, Ph.D.Thesis, Univ.of Sheffield.

Muzalevskii O.G., Burdin V.M., Kiryukhin V.E., Bukhvostov G.I., Voronin N.I. and Aravina L.V., 1970, Stal in Eng., p.220.

Nadai A., 1939, J.Appl.Mech., 6, p.A55.

Nair K.D., 1971, Metallography, 4, 375.

Nicholson A., 1968, I.S.I. Special Report 108, p.42.

Nicholson A., Smith D. and Shaw P., I.S.I. Special Report 108, p.161.

Niiyama E., Takami K., Mori R. and Hachisu M., 1967, Tetsu to Hagane, 53, 37.

Ohtakara Y., Nakamura T. and Sakui S., 1972A, I.S.I.J.Trans., 12, 207; 1972B., ibid, p.36.

Orowan E., 1943, Proc.Inst.Mech.Eng., 150, 140.

Orowan E. and Pascoe K.J., 1946, I.S.I. Special Report 34, p.124.

Pawelski O., 1969A, Arch.Eisen., 40, 821.

Pawelski O., 1969B, Stahl.Eisen., 89, 1146 (B.I.S.I.T. 7940).

Peck C.F., Bonetti J.M. and Mavis F.T., 1954, Iron and Steel Eng., 31, 45.

Peel D.A. and Pengelly A.E., 1970, I.S.I. Special Report p.186.

Pethen R.W. and Honeycombe R.W.K., 1973, Proc.Conf. 'Recrystallisation in the Control of Microstructure', Iron and Steel Inst/Inst.of Metals, London, paper 12.

Polishchuk M.O., 1974, Vestn.L'vov.Univ., pp.98, 132.

Polukhin P.I., Polukhin V.P., Terekhov V.N., Zinov'ev A.V., Nikolaev V.A. and Tereshko A.K., 1972A, Steel in U.S.S.R., 2, 304.

Polukhin V.P., Vasil'chenko A.G. and Podymov V.F., 1972B, Steel in U.S.S.R., 2, 643.

Portevin P.A. and Blain P., 1967, C.I.T., 2269 (B.I.S.I.T. 8401).

Potts J.F. and McElroy D.L., 1962, "Temperature - its Measurement and Control in Science and Industry", Pt.II, p.243, Reinhold, New York.

Pozdeev A.A., Karakina A.A., Ivanitskii A.V., Tarnovskii V.I. and Vinogradov V.I., 1972, Steel in U.S.S.R., 2, 986.

Prandtle L., 1923, Zeits.fur.ange.Math.und.Mech., 3, 401.

Preisendanz H., Schuler P. and Koschnitzke K., 1967, Arch.Eisen., 38, 905 (B.I.S.I.T. 6280)

Price P.H. and Slack M.R., 1952, Brit.J.Appl.Physics, 3, 379.

Pryce L. and Andrews K., 1960, J.I.S.I., 195, 415.

Renouard M., 1972, J.Inst.Metals, 100, 172.

Richards P.M., 1969, J.I.S.I., 207, 1333.

Richardson G.J., Sellars C.M. and Tegart W.J.McG., 1966, Acta Met., 14, 1225.

Rosier C., 1970, I.S.I. Special Report 123, p.93.

Rossard C. and Blain P., 1958, Rev.Mét., 55, 573.

Rossard C. and Blain P., 1959, Mem.Sci.Rev.Mét., 56, 285.

Rossard C., 1960, Met.Corros., 35, 140.

Rossard C., 1962, Centre.Doc.Sidér.Circ., 2199.

Rossard C., 1967, I.R.S.I.D. LA-160 (RE-43), p.1. (B.I.S.I.T.6037).

Rossard C., 1968, Rev.Mét., 65, 181 (B.I.S.I.T. 6438).

Rowe G.W., 1965, 'Introduction to the Principles of Metal Working, E. Arnold Ltd., London.

Sah J.P., 1970, Ph.D.Thesis, Univ.of Sheffield.

Sah J.P., 1976, Priv.Comm., Univ.of Sheffield.

Sarjant R.J. and Slack M.R., 1954, 177, 428(J.I.S.I.)

Schenck H., 1963, 'Fortran Methods in Heat Flow,' Ronald Press Co. New York.

Schultz R.G. and Smith A.W., 1965, Iron and Steel Eng., 42, 127.

Sellars C.M., 1976, Priv.Comm., Univ.of Sheffield.

Sellars C.M. and Tegart W.J.McG., 1966, Acta Met., 14, 1136.

Sellars C.M. and Tegart W.J.McG., 1972, Met.Rev. 158.

Sellars C.M. and Whiteman J.A., 1974, The Metallurgist and Materials Technologist, 4.

Sellars C.M. and Whiteman J.A., 1976, Proc.Conf. 'Controlled Processing of HSLA Steels, Univ.of York, paper 5.

Seredynski F., 1973, J.I.S.I., 211, 197.

Sevrin R., 1970, I.S.I. Special Report 123, p.147.

Siebel E., 1924, Berichte des Walz., Verein deutscher Eisen, No.37.

Siebel E., 1925, Stahl und Eisen, 45, 1563.

Siebel E. and Lueg W., 1933, Mitteilungen aus dem K.W.Inst.fur Eisenforschung, 15, p.1.

Sigalla A., 1957, J.I.S.I., 186, 90.

Sims R.B., 1954, Proc.Inst.Mech.Eng., 168, 191.

Sims R.B. and Wright H., 1963, J.I.S.I., 201, 261.

Sparling L.G.M., 1961, Proc.Inst.Mech.Eng., 175, 604.

Sparling L.G.M., 1976, Priv.Comm., Univ.of Sheffield.

Stevens P.G., Ivens K.P. and Harper P., 1971, J.I.S.I., 209, 1.

Stewartson R., 1954, Proc.Inst.Mech.Eng., 168, 201.

Stikker U.O., 1970, I.S.I. Special Report 123, p.104.

Stokowiec Z., Holland C.G., Dean A.H. and Everill A.C., 1969, I.S.I. Special Report 117, p.17.

Stuwe H.P., 1968, I.S.I. Special Report 108, p.1.

Takano H., Matsubara H. and Matsuda K., 1968, Iron and Steel Eng., 45, May, p.111.

Tarokh M. and Seredynski F., 1970, J.I.S.I., 208, 695.

Taylor H.L. and Elliot J.D., 1962, Met.Soc.Conf., 16, 85.

Trinks W., 1937, Blast Furnace and Steel Plant, 25, 617.

Turnbull D., 1951, Trans.A.I.M.M.E., 191, 661.

Underwood L.R., 1946, I.S.I. Special Report 34, p.5.

Underwood L.R., 1952, 'The Rolling of Metals', 1, Chapman and Hall.

Walker B., 1970, J.I.S.I., 208, 543.

Weills N.D. and Ryder E.A., 1949, Trans.A.S.M.E., 71, 259.

Whiteman J.A., 1975, Priv.Comm., Univ.of Sheffield.

Whittaker H.J., Walker B. and Adams M.A., 1971, Proc.Int.Conf.Sci. and Tech., Supp.Trans. I.S.I.J., 11, 662.

Whittaker H.J., 1973, Ph.D.Thesis, Univ.of Sheffield.

Wilmotte S., Mignon J. and Economopoulos M., 1973A, C.R.M. 36, 35.

Wilmotte S., Colin R., and Mignon J., 1973B, C.R.M. 36, 45.

Wright H. and Hope T., 1975, Met.Tech., 2, 565.

Wusatowski Z., 1955, Iron and Steel, 28, 49 and 89.

Wusatowski R., 1966, J.I.S.I., 204, 727.

Zheleznov Yu.D., Tsifrinovich B.A., Lyambalch R.V., Romashkevich L.F. and Savichev G.T., 1968, Stal' in Eng. p.854.

APPENDIX ONE

INSTRUMENTATION OF THE ROLLING MILL

1. Recording System

The outputs of the roll speed, load and torque measuring devices were recorded on separate channels of a 12-channel ultra-violet recorder (S.E.type 3006). A chart speed of 26 mm/sec was found to be the most useful in the present work. A variety of mirror galvanometers was used, the choice being governed essentially by the maximum output from the measuring device. The present work showed that two nominally identical galvanometers did not necessarily have the same characteristics i.e. the displacement per mV input varied from one particular galvanometer to another and in some cases even lay outside the manufacturer's quoted tolerance of $\pm$ 10%. This discrepancy could clearly affect the accuracy of the load and torque measurements and so calibrations and subsequent measurements were carried out using a particular galvanometer for a particular transducer.

2. Roll Speed Measurement

The roll speed was accurately recorded by means of an aluminium disc, with 8 equally spaced small holes drilled in it, which was fitted to the undriven end of the bottom roll with a light source on one side and a photo-cell on the other. During one revolution of the roll, 8 light pulses are received by the photocell, the output of which was recorded on one channel of the U.V. recorder (galvanometer type B160). This arrangement gives a series of 'blips' on the U.V. chart, Fig.77, the roll speed being given by $\frac{45\ s}{d}$ deg/sec, where s is the chart speed (mm/sec) and d the peak separation (mm). This is equivalent to a peripheral roll speed of $\frac{s \pi R}{4d}$ mm/sec, where R is the roll radius (mm).

3. Roll Load Measurement

The roll load was measured by two load cells, each of 25 ton (250 kN) capacity inserted between the ends of the screwdown and the chocks of the top roll. They were fed with a stabilised 6V. supply and their output fed to A.35 galvanometers in the U.V.recorder. The load cells were already fitted and calibrated at the start of this work but soon after the start of the research carried out on the stainless steel, they were removed from the mill and recalibrated on an Avery machine working in compression. The deflection of the U.V. galvanometers was recorded for loads between 0 and 250 kN in 25 kN steps using both increasing and decreasing loading cycles. No hysteresis was found.

The calibration emphasised the importance of loading the load cells centrally, during both calibration and use on the mill. Heavy scoring on the domed tops of the load cells and difficulties in locating them exactly centrally under the screwdown may have introduced a small unquantifiable error in the load measurements. Additionally it was found that the calibration changed slightly after the load cells had been taken once through their maximum allowable load cycle. The load and/or time dependence of such changes was not investigated since the phenomenon was not discovered until the end of the present work. It is clear that this effect could cause a small error and needs to be investigated further.

4. Roll Torque Measurement

Each torquemeter consists of four strain gauges (120Ω, gauge factor 2.08, type PL-15) cemented to the shaft using an epoxy resin specially formulated for strain gauge applications. The geometrical arrangement of the strain gauges compensates for any bending of the shaft that takes place. The strain gauges are wired in a Wheatstone Bridge circuit, Fig.131, with a variable resistor (R5) to balance the bridge initially. The strain gauges are fed with a stabilised 6V. supply and both input and output connections are made via slip ring units. The latter consist of silver plated rings fixed to the shaft with PVC insulation between the shaft and rings and 'Tufnol' spacers between adjacent rings. Electrical contact is effected by spring loaded, silver impregnated graphite brushes. It was found that the slip rings tarnished quickly and they were therefore polished at regular intervals with 'Duraglit' wadding silver polish.

Initial experiments showed that the torques developed during the hot rolling of stainless steel exceeded the full scale deflection of the available galvanometers (type B100). Additionally, the mill was reversed between passes and so the deflection of the galvanometers was also reversed. Hence with a chart width of 15 cm, the maximum allowable deflection of the galvanometers was $\pm$ 7.5 cm. These two limitations were overcome by attenuating the torque output by a series resistance. In addition, a parallel resistance was needed to match the impedance of the torquemeter and galvanometer to retain optimum damping of the latter. Their values were calculated using the method described in the galvanometer hand book.

The torquemeters were calibrated by applying known torques to the shafts. The torques were applied by inserting a 2.4 m bar into the coupling joints between rolls and shafts and hanging known weights on the end. To prevent the shafts from turning under the

applied torque they were secured by tightening a 'Stiltson' wrench onto the shafts and jamming the wrench against the mill bed. Nevertheless the shafts tended to slip and this, coupled with the bending of the lever under large applied loads, restricted the maximum applied torque to ~1200 Nm. Since the torque developed during rolling was ~ 4000 N.M, it was necessary to assume that the torquemeter output per unit applied torque was constant over the whole torque range. The torquemeters were calibrated in both the clockwise and anti-clockwise directions and no difference was detected.

Regardless of the accuracy of the torquemeters, allowance has to be made for the frictional torque developed in the roll necks. The coefficient of friction was measured by screwing the rolls together as tightly as possible (to give as large a load as possible) and measuring the torque developed during rotation of the rolls at the speed used in the majority of rolling schedules.

APPENDIX TWO

THE MEASUREMENT OF TEMPERATURES DURING HOT ROLLING

The successful measurement of the internal temperatures of a slab during hot rolling necessitated preliminary work to determine a suitable method of measurement and recording. In addition the effect of deformation of thermocouples was investigated.

1. Choice of Thermocouple

Initial trials were carried out by hot rolling mild steel slabs with standard chromel-alumel thermocouples inserted in them, the portion embedded in the slab being insulated with 'Refrasil' woven silica sleeving. This proved unsatisfactory for a number of reasons and 'Pyrotenax' metal sheathed, magnesia insulated, chromel-alumel thermocouples were adopted instead. Their design is such that high compressive reductions did not destroy the insulation between the thermocouple wires or between them and the sheath, Figs.132a,b. The metal sheathing allowed the thermocouples to be securely fixed in place by "pop-marking" the slab around the point of exit of the thermocouple. Both inconel and stainless steel sheathed thermocouples were evaluated and although the latter proved too brittle, the former could generally withstand three 30% passes.

A variety of thermocouple diameters are available: 1.5 mm diameter thermocouples were used in this present work. The thermocouples were supplied with either insulated (Fig.133a) or bonded (Fig.133b) hot junctions with a quoted response time of 0.24 sec. for the former and approximately half that for the latter. Since these thermocouples had to be used more than once, the hot junctions had to be rewelded. This was accomplished by burning off $\sim$1 cm. of the metal sheath with an oxy-acetylene welding torch and removing the insulation to expose the 0.3 mm. diameter thermocouple wires. The latter were twisted together and a bead welded using a reducing flame to produce an exposed hot junction, Fig.133c, whose response time would be expected to be better than that for the bonded junction. To counteract any hygroscopic tendencies of the magnesia insulation, the thermocouples were gently heated prior to use by slowly moving a welding torch from the 'cold end' to the hot junction.

Random calibration checks on rewelded thermocouples against a standard Pt/Pt-13% Rh thermocouple showed that they were within the standard accuracy of $\pm \frac{3}{4}\%$ for chromel-alumel thermocouples. In particular it was found that the discrepancy between the two types of thermocouple was temperature dependent as the following tabulation of typical results shows:

APPENDIX TWO (ii)

TEMPERATURE °C		ΔT °C
Chromel-Alumel	Pt/Pt-13% Rh	
1006	999	7
1026½	1019	7½
1102½	1097½	5
1145	1140	5
1160	1157	3
1166	1162	4
1178	1175	3

It can be seen that the two thermocouple readings approach each other as the temperature increases. It has been suggested (Birks 1975) that the magnesia insulation becomes slightly conducting at high temperatures thus leading to inaccurate readings. The above results show that this was not a problem in the present work since reheating was carried out at nominally 1180°C.

2. Recording System

Initially the thermocouple outputs were recorded on a Telsec 700 potentiometric chart recorder using a potentiometric back-off circuit for increased accuracy. This set up had two main disadvantages. Firstly, with a recorder response time of up to 0.5 seconds for full scale deflection, the rapid temperature changes that occur during rolling could not be recorded adequately. Secondly, when large temperature changes occurred the back-off voltage could not be changed quickly enough to keep the recorder pen within the chart limits..

The first problem was overcome by recording the temperatures on the U.V. recorder described in Appendix 1. The second problem was overcome by the development of an automatic back-off system. This system, whose components are shown schematically in Fig.134, is based around a differential amplifier, one input of which is the thermo electric output of the thermocouple. The amplifier output drives the U.V. recorder galvanometer and two voltage comparators which compare the output with a reference. The comparators sense when the amplifier output voltage exceeds that for full scale deflection of the galvanometer in either direction and their outputs control logic gates which steer pulses from a 500 Hz oscillator into the 'count up' or 'count down' inputs of a reversible counter.

The counter, by selecting an appropriate combination of resistors, controls the number of discrete 3 mV steps to be fed back to the other input of the differential amplifier. This combined back-off voltage is in such a sense to oppose the e.m.f. from the thermocouple to the nearest 3 mV step. The difference between this

opposing voltage and the thermocouple e.m.f. is fed to a high frequency galvanometer (type A1000; 1000 c.p.s.) in the U.V. recorder. The design of the system and the specifications of all the components are such that the overall response of the system is governed by the frequency of the oscillator. Thus the response time is 2 millisec. per step which is considerably faster than that of the thermocouple.

A second galvanometer was used to record the amplitude of the back-off voltage (i.e. the 'step' value) at all times.

The usefulness of this recording system is illustrated by Fig.135 which shows the rapidly changing mV. output of a thermocouple located close to the slab surface.

The input to the automatic back-off system was controlled by a 3 position switch which allowed:

(i) the calibration of the recording system prior to each run by feeding in known voltages from a potentiometer (0 to 3 mV in 0.1 mV steps and 0 to 57 mV in 3 mV steps),

(ii) the recording of the backed-off thermocouple output on the U.V. recorder, and

(iii) the reading of the thermocouple on the potentiometer and the short circuiting of the recording system. This was particularly useful since the thermocouples (especially those with exposed hot junctions) picked up mains leakage while the slabs were being reheated and this caused the automatic back-off system to continuously 'cycle'.

3. Effect of Deformation of the Thermocouple

In view of the opposing evidence for the effect of deformation on the accuracy of thermocouples (section 4.2.2.1), various tests were devised to investigate this effect further. The following results were obtained:

(i) Up to 60% cold working of a thermocouple affected the room temperature accuracy by ~3%. Although numerically small at room temperature, this inaccuracy becomes considerable at elevated temperatures.

(ii) A thermocouple, in both the deformed and undeformed states, was compared with a reference thermocouple inserted in a billet soaked thoroughly at ~1000°C. Seven repeat tests showed that deformation introduced a discrepancy of up to $\pm 2\frac{1}{2}$ °C. However, a delay of ~20 seconds was incurred in replacing the deformed thermocouple into the billet and so this test was not capable of determining instantaneous effects of deformation or subsequent restoration.

(iii) Undeformed and previously deformed thermocouples were inserted in a slab which was then hot rolled. The slight differences in the temperature records for the two thermocouples were insignificant compared with the differences expected for different scale thicknesses or different intimacies of contact between beads and slabs. This test was repeated several times, either holding the slabs at elevated temperatures or cooling them to room temperature prior to insertion of the undeformed thermocouple.

(iv) Evidence in the literature suggested that the undeformed thermoelectric properties would be restored to deformed thermocouples after short heating periods in the 450-500°C range. Two thermocouples were prepared and connected so that the output of one, and the differential output from both, could be recorded. One thermocouple was deformed heavily at room temperature and both thermocouples placed in holes drilled in a mild steel billet which was then heated in a furnace at 1100°C. A sharp peak in the differential output was found at ~450°C. However several repeat runs showed no change in the differential output apart from that attributable to internal gradients within the billet. The reasons for the lack of reproducibility of the effect are unclear.

(v) Further evidence for the effect of deformation on a thermocouple is given by the temperature records. Fig.77 shows a portion of a typical record for a centrally located thermocouple and it can be seen that, on entry to the mill, the temperature rises quickly to a peak due to the heat produced by deformation of the slab, drops rapidly, slows down and then falls again more rapidly until a steady air cooling rate is reattained. The temperature changes predicted from the computer programme are shown by the broken line i.e. there appears to be an additional 'blip' on top of the predicted heating and cooling effects. It is considered that this 'blip' arises from the heat produced by deformation of the thermocouple itself and its subsequent conduction to the slab. This hypothesis is supported by the observation that the rate of decay of the 'blip' decreased when thermocouples with insulated hot junctions were used i.e. the magnesia surrounding the hot junction reduced the rate of conductive heat transfer.

A similar effect was found for sub-surface thermocouples and Fig.135 clearly shows the small 'blip' prior to the rapid chilling. At positions very close to the surface, deformational heating in the slab is 'swamped' by the roll chilling effect and it was again concluded that the 'blip' arose from the deformational heating of the thermocouple.

It was concluded that high temperature deformation had no significant long term effect on the accuracy of chromel-alumel thermocouples.

APPENDIX THREE

DETAILS OF MATHEMATICAL MODEL

1. Introduction

This appendix examines some of the detailed aspects for translating the mathematical model of hot rolling into a computer programme. The programme was written in BASIC and run on a Hewlett Packard 9830A desk top computer with an 8K memory and facilities for matrix calculations. The symbols used in the programme are listed in section 2. Although the present programme is only for a three pass schedule, the matrix notation for many of the rolling variables should allow the programme to be extended easily to handle any number of passes.

The linking together of the different computational routines is illustrated by the overall flow chart, Fig.136. The programme is centred around the equations for heat transfer within the slab during air cooling and different subroutines are accessed on a time basis to calculate the slab dimensional changes, heat transfer between slab and roll etc. for the roll contact period. This flow chart should be consulted when considering the following discussion of the programme.

2. Notation for Two Dimensional Programme

A: Row number in roll matrices; varies from 1 to X.

A1,2,3,4: During input stage, represent number of time intervals during interpass stages. When programme is running, A1 to A3 represent (i) terms in eqns.6.93 to 6.97 (ii) the heat transfer coefficient at the start, middle and end of any pass interval.

A5: Area of roll slice defined by eqn.6.52.

A[N,M]: The temperature of the $(N,M)^{th}$ slab element at the start of any interval.

B: Column number in roll matrices; varies from 1 to V.

B1,2,3: Inclination of roll 'slice' from vertical at start, middle and end of any pass interval.

B4: Angular change of roll 'slice' per interval (eqn.6.98).

B[P]: Cosine of contact angle and then contact time for P^{th} pass.

C: Heat transfer constant between roll and slab.

C1: Initial value of C.

C2: Initial value of D2 for subdivided grid; used with C1 to increase C during a pass.

D1: Slab element width.

D2: Slab element height (mean element height during any pass interval).

D3: Slab element height at end of any pass interval.

D4: $D_x/D2$, see eqn.6.83.

D5: r_w^2, see eqn.6.81.

D[P]: % spread in width for P^{th} pass.

F: 'Counter' controlling print out frequency.

F A,B : Temperature of the $(A,B)^{th}$ roll element at end of interval.

G: If initial slab temperature distribution input, represents time of distribution.

G[N]: (i) Air cooling heat transfer coefficient of N^{th} row of slab matrix.
(ii) 'Transfer' matrix when slab matrix subdivided prior to pass and returned to original size at end of pass.

H: (i) Initial slab temperature (during input stage)
(ii) Air cooling heat transfer coefficient for M^{th} column of slab.

H1: Initial roll temperature.

I[P]: Number of time intervals to start of P^{th} pass.

J: Running total of heat conducted between roll elements.

K,K8: Thermal conductivity of slab, roll.

K[P]: Peripheral roll speed during P^{th} pass.

L[N]: Surface temperature of N^{th} row of slab.

M: Column number in slab; varies from 1 to V.

M[P]: Time of start of P^{th} pass.

N: Row number in slab matrices; varies from 1 to W (during air cooling) and from 1 to 3W (during pass).

N[P]: Total section thickness (2.W.D2) at start of P^{th} pass.

O[P]: Total roll torque for P^{th} pass.

P: (i) Used in input section to choose between uniform slab temperature or temperature distribution.
(ii) Pass number.

P[P]: Reduction ratio of P^{th} pass.

Q: Running total of heat conducted between slab elements.

Q[P]: Number of time intervals during P^{th} pass.

R: Roll radius.

R1,R8: Density of slab, roll.

R[A,B]: Temperature of $(A,B)^{th}$ roll element at start of interval.

S: Current value of S2, S3.

S1,S8: Specific heat of slab, roll.

S2,S3: Time intervals/print during air cooling and rolling.

S[B]: Surface temperature of B^{th} column of roll.

T4,5,6: Combinations of temperatures used when subdividing slab matrix.

T[N,M]: Temperature of (N,M)th slab element at end of interval.

U: 'Counter'; increased by 1 at the start of each time interval.

U[M]: Surface temperature of Mth column of slab.

V: Total number of columns in slab matrices.

V8: Volume of each roll element (eqn.6.50)

W: Total number of rows in slab matrices.

W[A]: Distance from centre of roll to centre of Ath element (eqns.6.56, 6.57).

X: (i) Constant during stable time calculations
(ii) Total number of rows in roll matrices.

Y: Current time.

Y[A]: Distance from surface of roll to inside edge of Ath roll element (eqns.6.54, 6.55).

Z: Current value of computational time interval.

Z1,Z3: Mean temperatures of slab, roll.

Z9: Deformational temperature rise in slab.

Z[P]: Time interval; Z [2P-1] is the time interval prior to Pth pass, Z [2P] likewise during Pth pass.

3. Programme Listing and Line by Line Discussion

The programme for computing two dimensional heat flow is listed in the following pages (left hand leaves). Simultaneously, a line by line discussion is given (right hand leaves).

Listing of Two Dimensional Computer Programme.

```
10 DIM A[15,5],T[16,7],L[15],U[5],G[15],Z[7],KS[3],PS[3],DS[3]
20 DIM N[4],M[4],OI[3],II[4],OI[3],Y[20],W[20],R[20,5],S[5],F[21,6]
30 DISP "WIDTH,HEIGHT IN M";
40 INPUT D1,D2
50 DISP "ROWS,COLS";
60 INPUT W,V
70 PRINT "D1="D1"D2="D2"W="W"V="V
80 DISP "ROLL.TEMP";
90 INPUT H1
100 REDIM A[W,V],T[W,V],U[V],L[W],G[W]
110 DISP "INPUT 1 FOR UNI.TEMP";
120 INPUT P
130 IF P=1 THEN 160
140 GOSUB 3590
150 GOTO 280
160 DISP "INGOT TEMP";
170 INPUT H
180 PRINT H;H1
190 FOR N=1 TO W
200 FOR M=1 TO V
210 A[N,M]=H
220 U[M]=H
230 L[N]=H
240 NEXT M
250 NEXT N
260 Z1=H
270 G=0
280 DISP "REDN.RATIOS";
290 INPUT P[1],P[2],P[3]
300 DISP "ROLL SPEEDS";
310 INPUT K[1],K[2],K[3]
320 DISP "ROLL RADIUS";
330 INPUT R
340 DISP "ROLLING H.T.C.";
350 INPUT C1
360 PRINT "SPEEDS:"K[1];K[2];K[3]"RATIOS:"P[1];P[2];P[3]"RAD="R"C1="C1
370 C1=C1*1E+03
380 C2=D2/3
390 DISP "%SPREAD,3PASSES";
400 INPUT D[1],D[2],D[3]
410 PRINT "%SPREAD"D[1];D[2];D[3]
420 N[1]=D2*2*W
430 N[2]=N[1]*(1-P[1])
440 N[3]=N[2]*(1-P[2])
450 N[4]=N[3]*(1-P[3])
460 S1=0.0677*(H-500)+622
470 R1=7950-0.5*(H-500)
480 K=0.01091*(H-500)+22.6
490 DEG
500 FOR P=1 TO 3
510 B[P]=1-(N[P]-N[P+1])/(2*R)
520 B[P]=R*PI/(180*K[P])*ATN(SQR(1-B[P]↑2)/B[P])
530 NEXT P
540 PRINT "CONT.TIMES:"B[1];B[2];B[3]
550 DISP "TIME OF PASSES&TOTAL RUN TIME";
560 INPUT N[1],M[2],M[3],M[4]
570 PRINT N[1];M[2];M[3];M[4]
580 X=S1*R1/(K*W↑3)
590 FOR P=1 TO 3
600 Z[2*P-1]=X*N[P]↑2*(W-3/4)/8
610 Z[2*P]=X*N[P+1]↑2*(3*W-3/4)/216
620 NEXT P
630 Z[7]=N[4]↑2*X*(W-3/4)/8
```

APPENDIX THREE (contd)

Line by Line Discussion of 2D Computer Programme

10 to 90: Lines 10 and 20 define the maximum allowable size of the matrices and allow a 5x5 slab matrix with an initial total thickness of ~20 mm to be given a 3x30% pass schedule with a peripheral roll velocity of ~200 mm/sec. If it is wished to increase the slab matrix to n x m then lines 10 and 20 need to be changed to:

10 DIM A[3n,m],T[3n+1,m+2],L[3n],U[m],G[3n] .....

20 DIM ..... R[20,m],S[m],F[21,m+1]

With different rolling speeds it may be necessary to alter the size of the roll matrices as discussed later. Lines 30 to 60 input the width and height of the slab elements(in metres) and the number of rows and columns in the slan matrix(minimum allowable is 3x3). The initial roll temperature (^{o}C) is input in lines 80 and 90.

100 to 270: Line 100 redefines the size of the slab matrices to save memory. Line 110 requires that a choice is made between a uniform initial slab temperature and an initial temperature distribution. If a temperature distribution is chosen(by inputting '1',line 120),then subroutine F is accessed(line3590). If a uniform initial temperature is chosen,this is input(^{o}C) by lines 160 and 170 and all slab temperatures made equal to it(lines 190 to 260). In the latter case,the time is set to zero(line 270).

280 to 410: Lines 280 to 320 input the reduction ratio and peripheral roll speed(metres/sec) for each of the three passes. The roll radius is assumed constant for each of the three passes(lines 320,330). The heat transfer coefficient between slab and rolls is input in kW/m^{2} ^{o}C (lines 340,350) and converted to the correct units(line 370). Line 380 defines the slab element height as it enters the first pass so that C can be increased during a schedule. Lines 390 to 410 input and print the %spread(which can be zero if desired)for each pass.

420 to 480: Line 420 calculates the initial total slab thickness and lines 430 to 450 likewise for subsequent passes. Lines 460 to 480 calculate the initial values of the specific heat,density and conductivity for the slab for subsequent critical time computation.

490 to 570: Line 510 calculates the cosine of the contact angle for each pass(eqn.6.99) and line 520 uses this to calculate the contact time (eqn.6.104).Lines 550 and 560 input the time(seconds) for the start of each pass and the total run time measured from the start of the programme. Thus if the first pass occurs at 15 seconds after reheating and the computed temperatures after 14 seconds of air cooling are input,the time input for the first pass is 1 second.

580 to 630: These lines calculate the maximum value of the time interval to be used prior to and during each pass. The critical time prior to each pass (Z[2P-1]) is given by eqn.6.35 and during each pass (Z[2P]) by eqn.6.39. Both equations contain the constant X and assume that the element width is greater than the height;section 6.2.5.1 should be consulted if the latter is not true. A separate line(630)is necessary for calculating the critical time interval following the last pass.

Two Dimensional Programme cont.(ii)

```
640 PRINT B[1]/Z[2];B[2]/Z[4];B[3]/Z[6]
650 DISP "ROUND UP TO INTEGERS";
660 INPUT Q[1],Q[2],Q[3]
670 PRINT M[1]/Z[1];(M[2]-M[1]-B[1])/Z[3]
680 DISP "ROUND UP TO INTEGERS";
690 INPUT A1,A2
700 PRINT (M[3]-M[2]-B[2])/Z[5];(M[4]-M[3]-B[3])/Z[7]
710 DISP "ROUND UP TO INTEGERS";
720 INPUT A3,A4
730 Z[1]=M[1]/A1
740 Z[3]=(M[2]-M[1]-B[1])/A2
750 Z[5]=(M[3]-M[2]-B[2])/A3
760 Z[7]=(M[4]-M[3]-B[3])/A4
770 DISP "TIME INT/PRINT/AC,ROLLING";
780 INPUT S2,S3
790 DISP "ROLL TORQUES";
800 INPUT O[1],O[2],O[3]
810 PRINT "TORQUES:"O[1];O[2];O[3]
820 Z=Z[1]
830 S=S2
840 I[1]=A1
850 I[2]=I[1]+Q[1]+A2
860 I[3]=I[2]+Q[2]+A3
870 I[4]=I[3]+Q[3]+A4
880 U=0
890 P=1
900 Y=0
910 F=1
920 Y=Y+Z
930 U=U+1
940 REDIM T[W,V]
950 K=0.01091*(Z1-500)+22.6
960 R1=7950-0.5*(Z1-500)
970 S1=0.0677*(Z1-500)+622
980 FOR M=1 TO V
990 FOR N=1 TO W
1000 Q=0
1010 IF M=1 THEN 1040
1020 Q=D2*K*Z*(A[N,M-1]-A[N,M])/D1
1030 IF M=V THEN 1060
1040 Q=Q-D2*K*Z*(A[N,M]-A[N,M+1])/D1
1050 GOTO 1080
1060 G[N]=-0.6875+0.01247*L[N]+4.7628*1E-11*(L[N]+273)↑4
1070 Q=Q-G[N]*D2*Z*1E+03
1080 IF N=1 THEN 1110
1090 Q=Q+D1*K*Z*(A[N-1,M]-A[N,M])/D2
1100 IF N=W THEN 1130
1110 Q=Q-D1*K*Z*(A[N,M]-A[N+1,M])/D2
1120 GOTO 1190
1130 IF U <= I[P] THEN 1170
1140 IF U>I[P]+Q[P] THEN 1170
1150 GOSUB 3040
1160 GOTO 1220
1170 H=-0.6875+0.01247*U[M]+4.7628*1E-11*(U[M]+273)↑4
1180 Q=Q-H*D1*Z*1E+03
1190 T[N,M]=Q/(S1*R1*D1*D2)+A[N,M]
1200 NEXT N
1210 U[M]=T[W,M]-H*1E+03*D2*(W-1/4)/(2*W*K)
1220 NEXT M
1230 FOR N=1 TO W
1240 L[N]=T[N,V]-G[N]*1E+03*D1*(V-1/4)/(2*V*K)
1250 NEXT N
1260 MAT A=T
```

640 to 760:These lines round down the maximum critical times calculated above. Lines 640 to 660 print the ratio of the contact time to the critical time for each pass. Rounded up values of these quotients are input and give the integral number of time intervals for each pass. Division of the contact time by the rounded up quotient later gives the rounded down critical time for each pass(line 2780). The minimum allowable value of the rounded up quotient is 3(and is preferably at least 5). Low values of the printed quotient indicate that the slab stable time is close to the contact time,the advised remedy being to increase the number of rows in the slab matrices. If the rounded up quotient is greater than 20,then either the number of rows in the slab matrices can be decreased or the roll matrix dimensions have to be increased(line 20). Lines 670 to 720 carry out similar computations for the air cooling periods.

770 to 810:The desired rate of printout is input for the air cooling and roll contact periods. Thus,if it is wished to print every tenth computation,the integer 10 is input. The total measured or calculated roll torques(N.m) for the whole slab width are input so that the deformational temperature rises can later be calculated.

820 to 910: The time interval is set to that for prior to the first pass (line 820)and the printout frequency set for air cooling(line 830).Lines 840 to 870 calculate the total number of time intervals from the programme start to the start of each pass and to the end of the programme. Lines 880 to 910 set the'counters'. U gives the total number of time intervals at any point in the computations(it is used in conjunction with I P). P,the pass counter,is set to 1. Y,the time,is set to zero. F controls the printout:it is set to 1 every time a slab printout is made;otherwise it is increased by 1 every time round the computing loop.

920 to 970: Line 920 marks the real start of the programme since this is the beginning of the overall loop. Lines 950 to 970 calculate the slab thermal properties as a function of the mean temperature at the end of the previous interval.

980 to 1260: These lines calculate the heat flow between each slab element in turn. The order of computation(which starts at the centre element) and the flow chart are given in Fig.46. Having calculated the net heat change for each element(eqns. 6.20 to 6.28),the new temperature for that element for the end of the interval is calculated(line 1190, eqns.6.12,6.13) Whenever the Wth.row(i.e.the bottom surface)is reached, then if lines 1130 or 1140 are true,the air cooling heat transfer equation is used and the surface temperature calculated(line 1210, eqn.6.31). Otherwise(i.e.during a pass) subroutine E is accessed to calculate the heat flow between slab and roll. When the side surface elements are reached(i.e. when M=V) the above decision does not have to made. Once the temperatures for each element for the end of the interval have been calculated,then line 1260 equates these temperatures to those for the beginning of the next interval.

Two Dimensional Programme cont.(iii)

```
1270 Z1=0
1280 FOR N=1 TO W
1290 FOR M=1 TO V
1300 Z1=Z1+T[N,M]
1310 NEXT M
1320 NEXT N
1330 Z1=Z1/(V*W)
1340 IF U#I[P] THEN 1380
1350 IF P=4 THEN 1380
1360 GOSUB 2240
1370 GOTO 1450
1380 IF P=1 THEN 1400
1390 IF M[P-1]+B[P-1]<Y AND Y<M[P-1]+B[P-1]+10*Z THEN 1450
1400 IF F=S THEN 1450
1410 IF P=4 THEN 1430
1420 IF U=I[P]+Q[P] THEN 1450
1430 F=F+1
1440 GOTO 1630
1450 REDIM T[W+1,V+2]
1460 FOR N=1 TO W
1470 FOR M=1 TO V
1480 T[N,M]=A[N,M]
1490 T[W+1,M]=U[M]
1500 T[N,V+1]=L[N]
1510 NEXT M
1520 NEXT N
1530 FOR N=1 TO W
1540 T[N,V+2]=(W-N+1/2)*D2*1E+03
1550 NEXT N
1560 T[W+1,V+2]=0
1570 T[W+1,V+1]=L[W]+U[V]-A[W,V]
1580 PRINT "TIME="Y"TRUE TIME="Y+G"D2="1000*D2"MEAN TEMP="Z1"Z="Z
1590 FIXED 2
1600 MAT PRINT T;
1610 STANDARD
1620 F=1
1630 IF U=I[4] THEN 3980
1640 IF U<I[P] THEN 920
1650 IF U=I[P] THEN 1710
1660 GOSUB 2100
1670 IF U=I[P]+Q[P] THEN 1690
1680 GOTO 920
1690 GOSUB 2820
1700 GOTO 920
1710 GOSUB 1750
1720 GOTO 920
1730 STOP
1740 REM SUB A TO DEF ROLL CONDS
1750 REDIM Y[X],W[X],R[X,V],S[V],F[X,V]
1760 FOR A=1 TO X
1770 FOR B=1 TO V
1780 R[A,B]=H1
1790 S[B]=H1
1800 NEXT B
1810 NEXT A
1820 Z3=H1
1830 S8=527.184
1840 R8=7790
1850 K8=46.4424
1860 A5=1.4*SQR(Z*2*1E-08*K8/(S8*R8))
1870 V8=A5*D1
1880 Y[1]=R-SQR(R↑2-A5*2*1E+04*R)
1890 W[1]=SQR((R↑2+(R-Y[1])↑2)/2)
1900 FOR A=2 TO X
1910 Y[A]=R-SQR((R-Y[A-1])↑2-A5*1E+04*2*R)
1920 W[A]=SQR(((R-Y[A])↑2+(R-Y[A-1])↑2)/2)
1930 NEXT A
```

1270 to 1330: These lines average the new slab temperatures so that the thermal properties for the subsequent interval can be determined.

1340 to 1440: These lines achieve the following:
(i) If it is the start of the pass,subroutine C is accessed(via line 1360) to subdivide the grid. On return from the subroutine the new temperature matrix is printed.
(ii) If less than 10 time intervals have elapsed from the end of the previous pass,the slab temperature matrix is printed:this is desirable because the slab temperatures change so rapidly on exit from the rolls.
(iii)If it is time to print(line 1400) or if is the last time interval during a pass and the temperatures have not been printed(line 1420), then this is carried out.
(iv)If it is not time to print(line 1430),the print counter is increased by 1 and the computation jumps to line 1630.

1450 to 1620: These lines are accessed when it is wished to print the slab temperatures. A matrix is redimensioned to accomodate the elemental and surface temperatures and the distance(in mm)from the bottom surface to the centre of each row element. Additionally,the slab corner temperature (point 16 in Fig.46) is estimated from the surrounding temperatures to complete the matrix(line 1570). The 'print counter' is returned to 1 following printing(line 1620).

1630 to 1730:These lines access many of the subroutines(see Fig.136) :
(i)If it is the end of the run,line 1630 halts the computations.
(ii) During interpass periods,line 1640 continues the computations at the start of the loop.
(iii)At the start of the pass,line 1650 accesses subroutine A(see below). On return,computations are continued at the start of the loop.
(iv)Having eliminated the foregoing possibilities,the time must lie within the roll contact period so line 1660 accesses subroutine B to change the slab element heights ready for the next interval. Additionally,if it is the end of the pass,line 1670 accesses subroutine D to reduce the number of rows in the slab to that prior to the pass. In both cases,computations are continued at the start of the loop.

Subroutine A (lines 1740 to 2080):accessed at the start of each pass.
1750 to 1930: Line 1750 redefines the roll matrices,the number of rows in each matrix being set equal to the number of time intervals during the pass. Lines 1760 to 1810 set each roll element temperature equal to the uniform initial temperature input in line 90. The thermal properties of the roll are defined(lines 1830 to 1850). Lines 1860,1870 define the volume of each roll element(eqn.6.50) and lines 1880 to 1920 define the dimensions of each roll element (eqns.6.54 to 6.57). The roll surface arc length was taken as 10^{-4} m.

```
1940 B4=180*K[P]*2/(PI*R)
1950 B1=1-(N[P]-N[P+1])/(2*R)
1960 B1=ATN(SQR(1-B1↑2)/B1)
1970 B2=B1-B4/2
1980 D2=(R*(1-COSB2)+N[P+1]/2)/W
1990 C=C1*C2/D2
2000 PRINT C
2010 B3=B1-B4
2020 D3=(R*(1-COSB3)+N[P+1]/2)/W
2030 PRINT B1,B2,B3,D2,D3
2040 Z9=Q[P]/(2*D1*V*R*R1*S1*Q[P]*SQR(N[P]*N[P+1]))
2050 GOSUB 3870
2060 PRINT "TDEF="Z9
2070 RETURN
2080 STOP
2090 REM SUB B TO CHANGE D2
2100 IF U=I[P]+Q[P] THEN 2170
2110 GOSUB 3870
2120 B2=B2-B4
2130 B3=B3-B4
2140 D3=(N[P+1]/2+(1-COSB3)*R)/W
2150 PRINT "D3="D3"B2="B2"B3="B3
2160 GOTO 2180
2170 B2=B2-B4/2
2180 D2=(N[P+1]/2+(1-COSB2)*R)/W
2190 C=C1*C2/D2
2200 PRINT "C="C
2210 RETURN
2220 STOP
2230 REM SUB C TO↑N0.OF ELEMENTS
2240 REDIM T[3*W,V],G[3*W]
2250 FOR M=1 TO V
2260 FOR N=1 TO W
2270 T[3*N-1,M]=A[N,M]
2280 IF N=1 THEN 2370
2290 IF N=W THEN 2420
2300 T4=2*A[N,M]-A[N-1,M]-A[N+1,M]
2310 T5=A[N+1,M]+3*A[N-1,M]-4*A[N,M]
2320 T[3*N-2,M]=A[N-1,M]+T5↑2/(8*T4)-T4/2*(T5/(2*T4)+2/3)↑2
2330 T[3*N,M]=A[N-1,M]+T5↑2/(8*T4)-T4/2*(T5/(2*T4)+4/3)↑2
2340 NEXT N
2350 NEXT M
2360 GOTO 2500
2370 T4=2*A[2,M]-A[1,M]-A[3,M]
2380 T5=A[3,M]+3*A[1,M]-4*A[2,M]
2390 T[1,M]=A[1,M]+T5↑2/(8*T4)-T4/2*(T5/(2*T4)-1/3)↑2
2400 T[3,M]=A[1,M]+T5↑2/(8*T4)-T4/2*(T5/(2*T4)+1/3)↑2
2410 GOTO 2340
2420 T4=2*A[W-1,M]-A[W-2,M]-A[W,M]
2430 T5=A[W,M]+3*A[W-2,M]-4*A[W-1,M]
2440 T6=A[W-2,M]+T5↑2/(8*T4)-T4/8*(T5/T4+3)↑2
2450 T4=2*A[W,M]-T6-U[M]
2460 T5=U[M]+3*T6-4*A[W,M]
2470 T[3*W-2,M]=T6+T5↑2/(8*T4)-2*T4*(T5/(4*T4)+1/6)↑2
2480 T[3*W,M]=T6+T5↑2/(8*T4)-2*T4*(T5/(4*T4)+5/6)↑2
2490 GOTO 2350
2500 FOR N=1 TO W
2510 G[3*N-1]=L[N]
2520 IF N=1 THEN 2590
2530 IF N=W THEN 2640
2540 T4=2*L[N]-L[N-1]-L[N+1]
2550 T5=L[N+1]+3*L[N-1]-4*L[N]
2560 G[3*N-2]=L[N-1]+T5↑2/(8*T4)-T4/2*(T5/(2*T4)+2/3)↑2
2570 G[3*N]=L[N-1]+T5↑2/(8*T4)-T4/2*(T5/(2*T4)+4/3)↑2
2580 NEXT N
2590 T4=2*L[2]-L[1]-L[3]
2600 T5=L[3]+3*L[1]-4*L[2]
```

1940 to 2210:Line 1940 defines the change in the angular position of the roll(eqn.6.98) and lines 1950 and 1960 derive the contact angle(eqn.6.99). Line 1970 defines the angle of the roll slice from the vertical for halfway through the first interval(eqn.6.100) and line 1980 defines the mean slab element height for the first interval(eqn.6.101). Line 1990 defines the value of C for the first interval. Lines 2010 and 2020 define the angle and element height for the end of the interval(eqns.6.102,6.103). Line 2040 calculates the deformational temperature rise for each interval (eqns.6.105,6.106) which is then added to the slab temperatures by accessing subroutine G.

Subroutine B(lines 2090 to 2220):Accessed at the end of each interval during a pass so that the slab element heights may be decreased. If it is any interval but the last,subroutine G is firstly accessed to add the deformational temperature rise to the slab temperatures. On return,the angle of the roll slice from the vertical is decreased by the set amount (line2120,2130) and the mean and final element heights calculated for the next interval(lines 2140,2180;see section 6.3.7). If it is the final interval during the pass,the mean angle is decreased by half the normal amount as was done at the start of the pass(which should give an angle of 0^{o}) and the exit elemental height calculated. In either case,the value of C is increased in proportion to the reduction of the original slab thickness (see section 6.3.6.6)

Subroutine C (lines 2230 to 2800): This subroutine is accessed immediately prior to each pass to subdivide the slab matrix (i.e. treble the number of rows).

2240 to 2600: These lines,together with lines 2610 to 2750 (next page), follow closely the parabolic interpolation equations discussed in the following section.

```
2610 G[1]=L[1]+T5↑2/(8*T4)-T4/2*(T5/(2*T4)-1/3)↑2
2620 G[3]=L[1]+T5↑2/(8*T4)-T4/2*(T5/(2*T4)+1/3)↑2
2630 GOTO 2580
2640 T4=2*L[N-1]-L[W-2]-L[W]
2650 T5=L[W]+3*L[W-2]-4*L[W-1]
2660 T6=L[W-2]+T5↑2/(8*T4)-T4/8*(T5/T4+3)↑2
2670 T4=L[W]-T6+A[W,V]-U[V]
2680 T5=3*T6-A[W,V]+U[V]-3*L[W]
2690 G[3*W-2]=T6+T5↑2/(8*T4)-2*T4*(T5/(4*T4)+1/6)↑2
2700 G[3*W]=T6+T5↑2/(8*T4)-2*T4*(T5/(4*T4)+5/6)↑2
2710 REDIM L[3*W],A[3*W,V]
2720 MAT A=T
2730 MAT L=G
2740 W=W*3
2750 D2=D2/3
2760 X=Q[P]
2770 S=S3
2780 Z=B[P]/Q[P]
2790 RETURN
2800 STOP
2810 REM SUB D TO 3*D2
2820 W=W/3
2830 REDIM A[W,V],G[W]
2840 FOR N=1 TO W
2850 FOR M=1 TO V
2860 A[N,M]=(T[3*N-2,M]+T[3*N-1,M]+T[3*N,M])/3
2870 NEXT M
2880 G[N]=(L[3*N-2]+L[3*N-1]+L[3*N])/3
2890 NEXT N
2900 REDIM L[W]
2910 MAT L=G
2920 REDIM T[W,V]
2930 MAT T=A
2940 D2=D2*3
2950 D1=D1*(1+D[P]/100)
2960 PRINT "NEW D1="D1
2970 S2=2*S2
2980 S=S2
2990 Z=Z[2*P+1]
3000 P=P+1
3010 RETURN
3020 STOP
3030 REM SUB E HEAT TO ROLL
3040 B=M
3050 FOR A=X TO 1 STEP -1
3060 J=0
3070 IF B=1 THEN 3100
3080 J=(R[A,B-1]-R[A,B])*A5*K8*Z/D1
3090 IF B=V THEN 3110
3100 J=J-(R[A,B]-R[A,B+1])*A5*K8*Z/D1
3110 IF A=1 THEN 3160
3120 J=J+(R[A-1,B]-R[A,B])*D1*1E-04*K8*Z*(R-Y[A-1])/(R*(W[A-1]-W[A]))
3130 IF A=X THEN 3310
3140 J=J-(R[A,B]-R[A+1,B])*D1*1E-04*K8*Z*(R-Y[A])/(R*(W[A]-W[A+1]))
3150 GOTO 3310
3160 J=J-(R[A,B]-R[A+1,B])*D1*1E-04*K8*Z*(R-Y[A])/(R*(W[A]-W[A+1]))
3170 D4=(2*W*D2/3-SQR(4/9*W↑2*D2↑2-8*W*K*Z/(3*S1*R1)))/D2
3180 D5=R↑2-2*R*K8*1E-04*D1*Z/(V8*S8*R8)
3190 A1=0/(D1*D2*S1*R1)-J/(V8*S8*R8)
3200 A2=C*Z/10*(1/(D2*R1*S1*COSB2)+D1*1E-04/(V8*S8*R8))
3210 A3=C/2*(D3*D4*(W-D4/4)/(W*K*COSB3)+(R↑2-D5)/(R*K8))
3220 A3=C*(A[W,M]-R[1,B]+A1-A2*(U[M]-S[B]))/(9*A2+A3+1)
3230 A1=C*(U[M]-S[B])
3240 A2=(A1+9*A3)/10
3250 T[W,M]=A[W,M]+Q/(D1*D2*S1*R1)-A2*Z/(D2*S1*R1*COSB2)
3260 U[M]=T[W,M]-A3*D3*D4*(W-D4/4)/(2*W*K*COSB3)
3270 F[1,B]=R[1,B]+(J+A2*D1*1E-04*Z)/(V8*S8*R8)
3280 S[B]=F[1,B]+A3*(R↑2-D5)/(2*R*K8)
```

2610 to 2730: Continuation of above discussion.

2740 to 2790: Line 2740 triples the number of rows in the slab matrices and line 2750 divides the slab element size by 3. Line 2760 sets the number of roll elements equal to the number of time intervals during a pass,line 2770 defines the printout rate during a pass and line 2780 defines the time interval to be used during a pass.

Subroutine D (lines 2810 to 3020): This subroutine,which is accessed at the end of each pass,accomplishes the reverse of subroutine C

2820 to 2940: Each group of three elements through the slab thickness is averaged to give the mean temperature for each new element.

2950 to 3010: Line 2950 increases the slab elemental width to allow for the spread that occurs during a pass. The printout rate during air cooling is arbitarily doubled(line 2970) since the computational time interval is considerably reduced following a pass. The time interval is set to that for air cooling for the new slab thickness (line 2990) and the 'pass counter' increased by 1 (line 3000).

Subroutine E (lines 3030 to 3570): This subroutine calculates the heat flow,both within the roll and between slab and roll,and is accessed whenever a surface element of a slab is reached during the roll contact period.

3040 to 3160: These lines calculate the heat flow between the elements comprising the roll column 'opposite' that of the slab,i.e.the order of computation is as shown in Fig.137. These lines represent eqns.6.60 to 6.63 and 6.65 to 6.73 combined in a compact form. For non-surface elements,having calculated the net heat flow,line 3110 is accessed to calculate the new temperature for that element.

3170 to 3280: Lines 3170 and 3180 calculate the variable distances used to obtain the slab and roll surface temperatures (eqns.6.83,6.81). Lines 3190 to 3280 calculate the heat flow between slab and roll as detailed in section 6.3.6.4. After each column is completed,computations continue in the main programme unless it is the last column.

```
3290 IF M=V THEN 3330
3300 GOTO 3560
3310 F[A,B]=R[A,B]+J/(V8*S8*R8)
3320 NEXT A
3330 MAT R=F
3340 Z3=0
3350 FOR B=1 TO V
3360 FOR A=1 TO X
3370 Z3=Z3+R[A,B]
3380 NEXT A
3390 NEXT B
3400 Z3=Z3/(X*V)
3410 IF F#S THEN 3560
3420 REDIM F[X+1,V+1]
3430 FOR B=1 TO V
3440 FOR A=1 TO X
3450 F[1,B]=S[B]
3460 F[A+1,B]=R[A,B]
3470 F[A+1,V+1]=W[A]*1000
3480 NEXT A
3490 NEXT B
3500 F[1,V+1]=R*1000
3510 PRINT "MEAN ROLL TEMP="Z3
3520 FIXED 2
3530 MAT PRINT F;
3540 STANDARD
3550 REDIM F[X,V]
3560 RETURN
3570 STOP
3580 REM SUB F INIT ING TEMPS
3590 REDIM T[W+1,V+1]
3600 FOR N=1 TO W
3610 FOR M=1 TO V
3620 DISP "A("N,M")";
3630 INPUT A[N,M]
3640 T[N,M]=A[N,M]
3650 IF M=V THEN 3670
3660 NEXT M
3670 DISP "L("N")";
3680 INPUT L[N]
3690 T[N,V+1]=L[N]
3700 NEXT N
3710 FOR M=1 TO V
3720 DISP "U("M")";
3730 INPUT U[M]
3740 T[W+1,M]=U[M]
3750 NEXT M
3760 T[W+1,V+1]=0
3770 DISP "MEAN TEMP";
3780 INPUT Z1
3790 H=Z1
3800 DISP "TIME OF DISTRIB";
3810 INPUT G
3820 PRINT "T.DIST.AT"G"SEC FROM FURNACE  MEAN TEMP="Z1"ROLL TEMP="H1
3830 MAT PRINT T;
3840 RETURN
3850 STOP
3860 REM SUB G(TDEF)
3870 FOR M=1 TO V
3880 FOR N=1 TO W
3890 A[N,M]=A[N,M]+Z9
3900 NEXT N
3910 U[M]=U[M]+Z9
3920 NEXT M
3930 FOR N=1 TO W
3940 L[N]=L[N]+Z9
3950 NEXT N
3960 Z1=Z1+Z9
3970 RETURN
3980 END
```

3290 to 3560: 3290,3300 continue the computations in the main programme unless it is the last column. In the latter case,line 3330 equates the temperatures for the start of the next interval to those for the end of the current interval. Lines 3340 to 3400 calculate the mean roll temperature and,if temperature dependent thermal properties are desired for the roll,they can be calculated here. A matrix is redefined to accomodate the roll surface temperatures and the distances in mm from the centre of the roll to the centre of each element. Finally,the roll temperatures are printed if it is time to do so.

Subroutine F (lines 3580 to 3850): This subroutine allows a slab temperature distribution to be input at the beginning of a programme run. Each row is considered in turn,the N,M value displayed and the temperature value input. At the end of each row,the side surface temperature is input and when the last row has been input,the bottom surface temperatures are input. Thus the order is the same as reading the slab temperature printout from left to right and from top to bottom. The mean roll temperature is input and,additionally,the relevant time for the slab temperature distribution.

Subroutine G (lines 3860 to 3970): This subroutine,which is accessed at the start of each interval during the roll contact period,adds the calculated deformational temperature rise to each slab temperature.

4. Subdivision of Slab Matrix

As noted in section 6.3.2, each row in the slab was subdivided to give 3 new rows prior to each pass, this being achieved by parabolic interpolation. Considering firstly a section of a temperature gradient, Fig.138a, it is only when equilibrium cooling is present that a true parabola of the form

$$T_y = T_o - a\,Y^2$$

describes the temperature gradient. In this case interpolation requires only two temperatures a known constant distance apart. In the case of a non-equilibrium gradient, it is necessary to assume that a parabola fits small sections of the gradient and, since the origin of the parabola is not necessarily at the centre of the slab, three temperatures a known distance apart are required to define the parabola. Using the notation given in Fig.138b and the above equation it can be shown that the parabola going through T1, T2 and T3 is given by

$$T_y = T1 + \frac{T5^2}{8T4} - \frac{T4}{2D^2}\left(\frac{D.T5}{2T4} + y\right)^2$$

where $T4 = 2T2 - T1 - T3$

$T5 = T3 + 3T1 - 4T2$

y = distance measured outwards from T1

Considering a through thickness temperature gradient in the slab, Fig.138b, each element prior to subdivision is denoted by A [N,M]. Each element is subdivided into 3 so that for the N^{th} element there are three temperatures, namely T [3N-2,M], T [3N-1,M] (= A [N,M]), T [3N,M]. The above equation was used to fit a parabola to A [N-1,M], A [N,M], A [N+1,M] from which T [3N-2,M] and T [3N,M] are found by substituting the relevant values of y. The resulting equations are simple but tedious and are not detailed here.

When N = 1, it is necessary to fit the parabola through A [1,M], A [2,M] and A [3,M]. It should be noted that if the interpolation is attempted before the gradient has reached the centre line, this method predicts spurious values for T [1,M] etc. When N = W, a similar treatment again gave a spurious temperature distribution, presumably due to the steeper temperature gradients at the surface. In this case A [W-2,M], A [W-1,M] and A [W,M] were used to predict T6, the temperature at the interface of the $(W-1)^{th}$ and W^{th} elements. T6 was then used in conjunction with A [W,M] and U [M] to obtain T [3W-2,M] and T [3W,M].

These interpolation procedures were applied, not only to each column in the slab but also to the side surface temperatures.

TYPICAL PRINTOUT FROM 2D PROGRAMME

Section A

(i) D1= 5.00000E-03 D2= 2.00000E-03 W= 3 V= 3

(ii) 1180 25

(iii) SPEEDS: 0.15 0.15 0.15 RATIOS: 0.3 0.3 0.3 RAD= 0.068

(iv) T1= 100

%SPREAD 2 3 4

CUMT. TIMES: 0.104538709 0.087405017 0.073094219

(v) 5 15 25 35

(vi) 6.184305452 10.55246882 18.00962490

(vii) 19.63283034 79.49823906

(viii) 62.52222201 332.1568432

(ix) TORQUES: 2800 3600 4200

Section B

(i) TIME= 2.5 TRUE TIME= 2.5 D2= 2 MEAN TEMP= 1155.691666 Z= 0.25

(ii)

1168.03	1165.07	1152.29	1136.66	5.00
1163.38	1160.46	1147.83	1132.38	3.00
1154.07	1151.21	1138.89	1123.79	1.00
1147.64	1144.83	1132.70	1117.61	0.00

Section C

(i) D3= 5.32168E-04 B2= 8.493693519 B3= 7.549949795

(ii) C= 121314.6777

MEAN ROLL TEMP= 87.51161235

(iii)

461.43	459.10	452.90	68.00
357.83	356.05	351.34	67.59
121.21	120.70	119.33	66.77
37.19	37.13	36.95	65.93
25.00	25.00	25.00	65.09
25.00	25.00	25.00	64.23
25.00	25.00	25.00	63.37
25.00	25.00	25.00	62.49

(iv) TIME= 5.044802304 TRUE TIME= 5.044802304 D2= 0.549535044

MEAN TEMP= 1090.042120 Z= 0.014934101

1160.18	1153.98	1137.26	1122.04	4.67
1159.68	1153.49	1136.79	1121.59	4.12
1158.67	1152.50	1135.84	1120.68	3.57
1157.17	1151.02	1134.42	1119.32	3.02
1155.16	1149.05	1132.54	1117.50	2.47
1152.67	1146.59	1130.18	1115.24	1.92
1134.74	1128.79	1112.72	1097.90	1.37
1035.80	1030.41	1015.86	1003.14	0.82
778.13	774.12	763.38	757.49	0.27
652.50	649.16	640.22	634.33	0.00

5. Annotated Printout:

Three sections of a printout are given opposite and are representative of the input, air cooling and roll contact periods. Each section has been annotated as follows:

Section A:Printout during Input Stage:
(i)The slab elemental width(D1) and height (D2) in metres;the number of rows (W) and columns (V) in the slab matrices.
(ii)The initial uniform slab and roll temperatures (^{o}C).
(iii)The peripheral roll speed for each of the three passes(metres/sec); the reduction ratios;the roll radius (metres).
(iv)The heat transfer coefficient between slab and rolls ($kW/m^2\ ^{o}C$)
(v)The times to the start of each pass and the total run time(seconds).
(vi)The values of the contact time/critical time for each pass. Their rounded up values are then input and divided into the contact time to give the rounded down stable time interval.
(vii),(viii) As (vi),except these refer to the air cooling periods.
(ix)The total roll torque for each pass(N.m).

Section B:Printout during Air Cooling:
(i)Time from start of programme run;time from removal from furnace;slab element height(mm);mean slab temperature;computational time interval.
(ii)Slab temperatures corresponding to Fig.46.i.e. top left hand corner is centre of slab. The right hand column consists of the distances(mm) from the bottom surface to the centre of each element.

Section C:Printout during Roll Contact Period:
(i) Slab elemental height(metres) at the end of the current time interval; angle between roll'slice' and vertical halfway through time interval; likewise at the end of the time interval.
(ii) Value of C for time interval($W/m^2\ ^{o}C$).
(iii)Roll temperatures corresponding to Fig.137. The right hand column indicates distance from centre of roll to centre of each element.
(iv) Slab temperatures as in section B(ii).

6. One Dimensional Programme

The two dimensional programme described above was adapted for computing one dimensional heat flow through the slab thickness for reasons given in section 10. The programme, which is listed overleaf, follows identical principles to those for the two dimensional programme and therefore will not be discussed at length. The essential difference is that all the two dimensional temperature matrices were replaced by single column matrices and this gave the following advantages:

(i) The programme was shorter and computation time considerably less than for the two dimensional programme.

(ii) The principle of finite difference was approached more closely i.e. whereas the two dimensional programme was generally limited to a 6 x 6 matrix for the slab, the one dimensional programme had sufficient memory available for computing slab matrices consisting of up to 40 elements. Thus, when using the one dimensional programme, a given section thickness could be represented by more elements than that permissible by the two dimensional programme. This was particularly useful when carrying out computations for very thick plates or for short contact times.

(iii) Further computational subroutines could be added easily due to the extra memory available. This facility was useful for calculating:

  (a) the distribution of the Zener Hollomon parameter during a pass, and

  (b) the theoretical static recrystallisation behaviour through the plate thickness.

LISTING OF ONE DIMENSIONAL COMPUTER PROGRAMME

```
10 DIM A[90],T[90],L[1,91],Z[7],K[3],PS[3]
20 DIM N[4],M[4],Q[3],I[4],O[3],Y[40],W[40],R[40],F[40]
30 DISP "HEIGHT IN M";
40 INPUT D2
50 DISP "ROWS";
60 INPUT W
70 PRINT "D2="D2"W="W"TOTAL THICKNESS="2*W*D2*1000"MM"
80 DISP "ROLL.TEMP";
90 INPUT H1
100 REDIM A[W],T[W]
110 DISP "INPUT 1 FOR UNI.TEMP";
120 INPUT P
130 IF P=1 THEN 160
140 GOSUB 2900
150 GOTO 250
160 DISP "INGOT TEMP";
170 INPUT H
180 PRINT H;H1
190 FOR N=1 TO W
200 A[N]=H
210 U1=H
220 NEXT N
230 Z1=H
240 G=0
250 DISP "REDN.RATIOS";
260 INPUT P[1],P[2],P[3]
270 DISP "ROLL SPEEDS";
280 INPUT K[1],K[2],K[3]
290 DISP "ROLL RADIUS";
300 INPUT R
310 DISP "ROLLING H.T.C.";
320 INPUT C1
330 PRINT "SPEEDS:"K[1];K[2];K[3]"RATIOS:"P[1];P[2];P[3]"RAD="R"C1="C1
340 C1=C1*1E+03
350 C2=D2/3
360 N[1]=D2*2*W
370 N[2]=N[1]*(1-P[1])
380 N[3]=N[2]*(1-P[2])
390 N[4]=N[3]*(1-P[3])
400 S1=0.0677*(H-500)+622
410 R1=7950-0.5*(H-500)
420 K=0.01091*(H-500)+22.6
430 DEG
440 FOR P=1 TO 3
450 B[P]=1-(N[P]-N[P+1])/(2*R)
460 B[P]=R*PI/(180*K[P])*ATN(SQR(1-B[P]↑2)/B[P])
470 NEXT P
480 PRINT "CONT.TIMES:"B[1];B[2];B[3]
490 DISP "TIME OF PASSES&TOTAL RUN TIME";
500 INPUT M[1],M[2],M[3],M[4]
510 PRINT M[1];M[2];M[3];M[4]
520 X=S1*R1/(K*W↑3)
530 FOR P=1 TO 3
540 Z[2*P-1]=X*N[P]↑2*(W-3/4)/8
550 Z[2*P]=X*N[P+1]↑2*(3*W-3/4)/216
560 NEXT P
570 Z[7]=N[4]↑2*X*(W-3/4)/8
580 PRINT B[1]/Z[2];B[2]/Z[4];B[3]/Z[6]
590 DISP "ROUND UP TO INTEGERS";
600 INPUT Q[1],Q[2],Q[3]
610 PRINT M[1]/Z[1];(M[2]-M[1]-B[1])/Z[3]
620 DISP "ROUND UP TO INTEGERS";
630 INPUT A1,A2
```

ONE DIMENSIONAL PROGRAMME cont.(ii)

```
640 PRINT (M[3]-M[2]-B[2])/Z[5];(M[4]-M[3]-B[3])/Z[7]
650 DISP "ROUND UP TO INTEGERS";
660 INPUT A3,A4
670 Z[1]=M[1]/A1
680 Z[3]=(M[2]-M[1]-B[1])/A2
690 Z[5]=(M[3]-M[2]-B[2])/A3
700 Z[7]=(M[4]-M[3]-B[3])/A4
710 DISP "TIME INT/PRINT/AC,ROLLING";
720 INPUT S2,S3
730 DISP "ROLL TORQUES";
740 INPUT Q[1],Q[2],Q[3]
750 PRINT "TORQUES:";Q[1];Q[2];Q[3]
760 Z=Z[1]
770 S=S2
780 I[1]=A1
790 I[2]=I[1]+Q[1]+S2
800 I[3]=I[2]+Q[2]+A3
810 I[4]=I[3]+Q[3]+A4
820 U=0
830 P=1
840 Y=0
850 F=1
860 Y=Y+Z
870 U=U+1
880 REDIM T[W]
890 K=0.01091*(Z1-500)+22.6
900 R1=7950-0.5*(Z1-500)
910 S1=0.0677*(Z1-500)+622
920 FOR N=1 TO W
930 Q=0
940 IF N=1 THEN 970
950 Q=Q+K*2*(A[N-1]-A[N])/D2
960 IF N=W THEN 990
970 Q=Q-K*2*(A[N]-A[N+1])/D2
980 GOTO 1050
990 IF U <= I[P] THEN 1030
1000 IF U>I[P]+Q[P] THEN 1020
1010 GOSUB 2480
1020 GOTO 1080
1030 H=-0.6875+0.01247*U1+4.7628*1E-11*(U1+273)↑4
1040 Q=Q-H*Z*1E+03
1050 T[N]=Q/(S1*R1*D2)+A[N]
1060 NEXT N
1070 U1=T[W]-H*1E+03*D2*(W-1/4)/(2*W*K)
1080 MAT A=T
1090 Z1=0
1100 FOR N=1 TO W
1110 Z1=Z1+T[N]
1120 NEXT N
1130 Z1=Z1/W
1140 IF U<I[P] THEN 1180
1150 IF P=4 THEN 1180
1160 GOSUB 2010
1170 GOTO 1250
1180 IF P=1 THEN 1200
1190 IF M[P-1]+B[P-1]<Y AND Y<M[P-1]+B[P-1]+10*Z THEN 1250
1200 IF F=S THEN 1250
1210 IF P=4 THEN 1230
1220 IF U=I[P]+Q[P] THEN 1250
1230 F=F+1
1240 GOTO 1350
1250 REDIM L[1,W+1]
1260 FOR N=1 TO W
1270 L[1,N]=A[N]
```

ONE DIMENSIONAL PROGRAMME cont.(iii)

```
1280 NEXT H
1290 L[1,H+1]=U1
1300 PRINT "TIME="Y"TRUE TIME="Y+G"D2="1000*D2"MM    MEAN TEMP="Z1"Z="Z
1310 FIXED 2
1320 MAT PRINT L
1330 STANDARD
1340 F=1
1350 IF U=I[4] THEN 3150
1360 IF U<I[P] THEN 860
1370 IF U=I[P] THEN 1430
1380 GOSUB 1870
1390 IF U=I[P]+Q[P] THEN 1410
1400 GOTO 860
1410 GOSUB 2330
1420 GOTO 860
1430 GOSUB 1470
1440 GOTO 860
1450 STOP
1460 REM SUB A TO DEF ROLL CONDS
1470 REDIM Y[X],W[X],R[X],F[X]
1480 FOR A=1 TO X
1490 R[A]=H1
1500 NEXT A
1510 S4=H1
1520 Z3=H1
1530 S8=481.3
1540 R8=7840
1550 K9=48.13
1560 A5=1.4*SQR(Z*2*1E-08*K8/(S8*R8))
1570 V8=A5
1580 Y[1]=R-SQR(R↑2-A5*2*1E+04*R)
1590 W[1]=SQR((R↑2+(R-Y[1])↑2)/2)
1600 FOR A=2 TO X
1610 Y[A]=R-SQR((R-Y[A-1])↑2-A5*1E+04*2*R)
1620 W[A]=SQR((R-Y[A])↑2+(R-Y[A-1])↑2)/2)
1630 NEXT A
1640 PRINT "DIST FROM SURFACE OF ROLL TO CENTRE OF ELEMENTS  MM."
1650 REDIM L[1,X+1]
1660 FOR A=1 TO X
1670 L[1,A+1]=1000*(R-W[A])
1680 NEXT A
1690 L[1,1]=0
1700 MAT PRINT L
1710 B4=180*K[P]*Z/(PI*R)
1720 B1=1-(N[P]-N[P+1])/(2*R)
1730 B1=ATN(SQR(1-B1↑2)/B1)
1740 B2=B1-B4/2
1750 D2=(R*(1-COSB2)+N[P+1]/2)/W
1760 C=C1*C2/D2
1770 PRINT C
1780 B3=B1-B4
1790 D3=(R*(1-COSB3)+N[P+1]/2)/W
1800 PRINT B1,B2,B3,D2,D3
1810 Z9=Q[P]/(2*R*R1*S1*Q[P]*SQR(N[P]*N[P+1]))
1820 GOSUB 3090
1830 PRINT "TDEF="Z9
1840 RETURN
1850 STOP
1860 REM SUB B TO CHANGE D2
1870 IF U=I[P]+Q[P] THEN 1940
1880 GOSUB 3090
1890 B2=B2-B4
1900 B3=B3-B4
1910 D3=(N[P+1]/2+(1-COSB3)*R)/W
1920 PRINT "D3="D3"B2="B2"B3="B3
1930 GOTO 1950
```

ONE DIMENSIONAL PROGRAMME cont.(iv)

```
1940 B2=B.C-04/2
1950 D2=(N[P+1]/2+(1-COSB2)*R)/W
1960 C=C1*C2/D2
1970 PRINT "C="C
1980 RETURN
1990 STOP
2000 REM SUB C TO↑N0.OF ELEMENTS
2010 REDIM T[3*W]
2020 FOR N=1 TO W
2030 T[3*N-1]=A[N]
2040 IF N=1 THEN 2110
2050 IF N=W THEN 2160
2060 T4=2*A[N]-A[N-1]-A[N+1]
2070 T5=A[N+1]+3*A[N-1]-4*A[N]
2080 T[3*N-2]=A[N-1]+T5↑2/(8*T4)-T4/2*(T5/(2*T4)+2/3)↑2
2090 T[3*N]=A[N-1]+T5↑2/(8*T4)-T4/2*(T5/(2*T4)+4/3)↑2
2100 NEXT N
2110 T4=2*A[2]-A[1]-A[3]
2120 T5=A[3]+3*A[1]-4*A[2]
2130 T[1]=A[1]+T5↑2/(8*T4)-T4/2*(T5/(2*T4)-1/3)↑2
2140 T[3]=A[1]+T5↑2/(8*T4)-T4/2*(T5/(2*T4)+1/3)↑2
2150 GOTO 2100
2160 T4=2*A[N-1]-A[N-2]-A[N]
2170 T5=A[N]+3*A[N-2]-4*A[N-1]
2180 T6=A[N-2]+T5↑2/(8*T4)-T4/8*(T5/T4+3)↑2
2190 T4=2*A[N]-T6-U1
2200 T5=U1+3*T6-4*A[N]
2210 T[3*N-2]=T6+T5↑2/(8*T4)-2*T4*(T5/(4*T4)+1/6)↑2
2220 T[3*N]=T6+T5↑2/(8*T4)-2*T4*(T5/(4*T4)-5/6)↑2
2230 REDIM A[3*N]
2240 MAT A=T
2250 N=N*3
2260 D2=D2/3
2270 K=Q[P]
2280 S=S3
2290 Z=B[P]/Q[P]
2300 RETURN
2310 STOP
2320 REM SUB D TO 3*D2
2330 N=N/3
2340 REDIM A[N]
2350 FOR N=1 TO N
2360 A[N]=(T[3*N-2]+T[3*N-1]+T[3*N])/3
2370 NEXT N
2380 REDIM T[N]
2390 MAT T=A
2400 D2=D2*3
2410 S2=2*S2
2420 S=S2
2430 Z=Z[2*P+1]
2440 P=P+1
2450 RETURN
2460 STOP
2470 REM SUB E HEAT TO ROLL
2480 FOR A=X TO 1 STEP -1
2490 J=0
2500 IF A=1 THEN 2550
2510 J=J+(R[A-1]-R[A])*1E-04*K8*Z*(R-Y[A-1])/(R*(W[A-1]-W[A]))
2520 IF A=X THEN 2690
2530 J=J-(R[A]-R[A+1])*1E-04*K8*Z*(R-Y[A])/(R*(W[A]-W[A+1]))
2540 GOTO 2690
2550 J=J-(R[A]-R[A+1])*1E-04*K8*Z*(R-Y[A])/(R*(W[A]-W[A+1]))
2560 D4=(2*N*D2/3-SQR(4/9*N↑2*D2↑2-8*N*K*Z/(3*S1*R1)))/D2
2570 D5=R↑2-2*R*K8*1E-04*Z/(V8*S8*R8)
2580 A1=0/(D2*S1*R1)-J/(V8*S8*R8)
2590 A2=C*Z/10*(1/(D2*R1*S1*COSB2)+1E-04/(V8*S8*R8))
```

```
2600 A3=C/2*(D3*D4*(W-D4/4)/(W*K*COSB3)+(R↑2-D5)/(R*K8))
2610 A3=C*(A[W]-R[1]+A1-A2*(U1-S4))/(9*A2+A3+1)
2620 A1=C*(U1-S4)
2630 A2=(A1+9*A3)/10
2640 T[W]=A[W]+Q/(D2*S1*R1)-A2*Z/(D2*S1*R1*COSB2)
2650 U1=T[W]-A3*D3*D4*(W-D4/4)/(2*W*K*COSB3)
2660 F[1]=R[1]+(J+A2*1E-04*Z)/(V8*S8*R8)
2670 S4=F[1]+A3*(R↑2-D5)/(2*R*K8)
2680 GOTO 2710
2690 F[A]=R[A]+J/(V8*S8*R8)
2700 NEXT A
2710 MAT R=F
2720 Z3=0
2730 FOR A=1 TO X
2740 Z3=Z3+R[A]
2750 NEXT A
2760 Z3=Z3/X
2770 IF F#S THEN 2870
2780 REDIM L[1,X+1]
2790 FOR A=1 TO X
2800 L[1,A+1]=R[A]
2810 NEXT A
2820 L[1,1]=S4
2830 PRINT "MEAN ROLL TEMP="Z3"TRUE TIME="Y+G
2840 FIXED 2
2850 MAT PRINT L;
2860 STANDARD
2870 RETURN
2880 STOP
2890 REM SUB F INIT ING TEMPS
2900 REDIM L[1,W+1]
2910 FOR N=1 TO W
2920 DISP "A("N")";
2930 INPUT A[N]
2940 L[1,N]=A[N]
2950 NEXT N
2960 DISP "SURFACE TEMP";
2970 INPUT U1
2980 L[1,W+1]=U1
2990 DISP "MEAN TEMP";
3000 INPUT Z1
3010 H=Z1
3020 DISP "TIME OF DISTRIB";
3030 INPUT G
3040 PRINT "T.DIST.AT"G"SEC FROM FURNACE  MEAN TEMP="Z1"ROLL TEMP="H1
3050 MAT PRINT L;
3060 RETURN
3070 STOP
3080 REM SUB G(TDEF)
3090 FOR N=1 TO W
3100 A[N]=A[N]+Z9
3110 NEXT N
3120 U1=U1+Z9
3130 Z1=Z1+Z9
3140 RETURN
3150 END
```

7. Thermal Properties

In both computer programmes and in other heat flow calculations the following thermal data were used:

(a) 18-8 stainless steel slabs: 500°C to 1200°C range:

$k = 22.6 + 10.91 \times 10^{-3} (T-500)$ W/m°C
$s = 622 + 0.0677 (T-500)$ J/kg°C
$\rho = 7950 - 0.5 (T-500)$ kg/m^3

(b) EN1 mild steel slabs: 500°C to 1200°C range:

$k = 22.0 + 10.91 \times 10^{-3} (T-500)$ W/m°C
$s = 622 + 0.0677 (T-500)$ J/kg°C
$\rho = 7800 - 0.5 (T-500)$ kg/m^3

N.B. Data extrapolated from austenitic range.

(c) EN8 rolls: 25°C to 200°C range:

$k = 48.13$ W/m°C
$s = 481.3$ J/kg°C
$\rho = 7840$ kg/m^3

All data were obtained by fitting the best lines to the data given in 'Physical Constants of some Commercial Steels in Elevated Temperatures', published by Butterworths Scientific Publications, 1953, London.

TABLE 1
(after Sellars and Tegart (1972))

Possible Softening Processes Associated with Hot Working

Group	Example	Dynamic	Static
A	Al, α-Fe, ferritic alloys	Recovery (all strains)	Recovery followed by recrystallisation
B	Cu, Ni, γ-Fe, austenitic alloys	Recovery (small strains) Recrystallisation (large strains)	Very limited recovery followed by recrystallisation

TABLE 2
(after Nair (1971))

Mean Plane Strain Flow Stresses during the Hot Rolling of AISI 321 Stainless Steel

Pass	Temp ^{o}C	Mean Flow Stress N/mm^2	
		Single Pass	Multipass
1	1040	159	157
2	892½	248	244
3	782½	372	341
4	712½	531	462

TABLE 3

Details of Rolls

(i) Preliminary work and stainless steel runs 1 to 12:
EN 8 (0.4% C, 0.2% Si, 0.69% Mn)
Average diameter: 136.5 mm.

(ii) Stainless steel runs 13 to 24:
As above but reground to 136.3 mm average diameter

(iii) Stainless steel runs 25 to 84:
5% Cr Die steel (0.4% C, 1.0% Si, 5.0% Cr, 1.4% Mo, 1.0% V) Average diameter: 139.7 mm.

In each case the roll neck diameter was 95 mm and the roll neck bearings were phosphor bronze.

TABLE 4

ANALYSES OF MATERIALS (Wt %)

(a) Mild Steel:

Material	C	Mn	Si	P	S	Ni
Present work	0.16	0.63	0.33	0.011	0.047	0.24
Cook and McCrum low C steel	0.15	0.68	0.12	0.025	0.034	-

(b) Stainless Steel:

Material	C	Mn	Si	P	S	Ni	Cr	Mo	W	V	Nb	Ti	Co	Cu	O_2	N_2 sol.
Present work	0.066	1.35	0.78	0.028	0.014	9.3	19.6	0.44	0.14	0.07	0.05	0.35	0.37	0.5	87 ppm	0.001
Specification (EN 58B)	0.15 max.	2.0 max.	0.2 min.	0.045 max.	0.045 max.	7.0*/ 10.0	17.0*/ 20.0	-	-	-	-	4x $C_{min.}$	-	-	-	-
Barraclough (1974)	0.05	0.92	0.11	-	-	11.3	18.2	<0.02	<0.02	<0.02	<0.02	<0.02	<0.02	-	-	0.086

* % Ni + % Cr must be greater than 25.0%

TABLE 5

STAINLESS STEEL ROLLING SCHEDULES

The bracketed details after each run give

(i) the interpass reheating treatment where applicable,
(ii) the cooling practice after the final pass.

Key: **AC**: air cooled to room temperature
QX: quenched X seconds after final pass.

(a) Single Pass Runs:

30% at T_1: 1 (Q6), 2 (Q2), 3 (Q20), 26 (Q42), 27 (Q25), 28 (Q25), 29 (Q40), 30 (Q21), 31 (AC), 32 (Q23), 33 (Q25), 38 (Grid, AC), 45 (Q12), 48 (Reheated for 20 mins at 1180°C after pass and quenched), 57 (Molyslip lubricant; AC), 58 (Molyslip lubricant; AC), 65 (AC), 66 (AC).

30% at T_1, minimum roll speed: 59 (Q18), 60 (Q15), 61 (Q9)

30% at T_1, maximum roll speed: 68 (Q8), 71 (16Q), 72 (2Q)

30% at $< T_1$: 79 (AC), 80 (AC), 81 (AC), 82 (AC), 83 (AC), 84 (AC)

20% at T_1: 16 (Q14)

10% at T_1: 17 (Q19)

(b) Two Pass Runs:

30% at T_1, 30% at T_2: 4 (Q1½), 5 (Q10), 6 (Q4), 7 (Q13), 11 (Q19), 54 (Q4), 56 (Q3), 62 (Q2), 64 (Q3)

30% at T_1, 30% at T_3:
43 (followed by 200 s. at 827°C, Q)
44 (" " 1000 s. " 840°C, Q)
46 (" " 2000 s. " 822°C, Q)
47 (" " 500 s. " 825°C, Q)
51 (Q4), 52 (Q4), 53 (Q4), 55 (Q3), 63 (Q3)

30% at T_1, Reheat, 30% at T_1:

39 (20 mins at 1180°C; AC)	Thermocouple in second pass only	To investigate effect of deformation on thermocouple
40 (" " " ")	" " "	" "
41 (" " " ")		
42 (" " " ")		

30% at T_1, Reheat, 30% at T_2:

34 (20 mins at 1000°C; AC)	Thermocouple in second pass only)	To investigate effect of deformation on thermocouple
35 (" " " ")	" " "	" "
36 (20 mins at 1032°C; AC)		
37 (" " " ")		

TABLE 5 (continued) (ii)

30% at T_1, Reheat 30% at T_3:

49 (20 mins at 1180°C; AC)
50 (" " " ; Q7)

20% at T_1, 20% at T_2:

25 (Q10)

(c) Three Pass Runs:

30% at T_1, 30% at T_2, 30% at T_3:

8 (Q6), 9 (Q17), 10 (Q19), 12 (AC), 13 (AC), 18 (AC), 19 (Q10), 21 (Initial soak: 30 mins at 1300°C, quench, 20 mins at 1180; AC), 23 (Q12), 24 (as 21), 73 (AC), 77 (AC), 78 (AC)

30% at T_1, Reheat, 30% at T_2, 30% at T_3:

14 (20 mins at 1040°C; AC), 22 (2 mins at 1155°C; Q4)

30% at T_1, 30% at T_2, Reheat, 30% at T_3:

15 (20 mins at 920°C; AC), 20 (25 mins at 920°C; Q6)
69 (20 mins at 950°C; AC), 70 (20 mins at 950°C; AC)
74 (20 mins at 935°C; AC)

30% at T_1, 30% at T_3, Reheat, 30% at T_3:

75 (20 mins at 930°C; AC), 76 (20 mins at 930°C; AC)

30% at T_1, Reheat, 30% at T_1, Reheat, 30% T_3:

67 (20 mins at 1180; 20 mins at 900; AC)

TABLE 6

NOMINAL SCHEDULE FOR THE HOT ROLLING OF MILD STEEL

Pass	% Redn.	Initial Thickness mm	Final Thickness mm	Mean Width mm	Uniaxial* Strain Rate sec-1	Uniaxial Strain	Contact* Time (sec)
1	10	18.4	16.6	39	0.90	0.12	0.13
2	20	16.6	13.3	40	1.44	0.26	0.18
3	30	13.3	9.3	41	2.09	0.41	0.20
4	40	9.3	5.6	44	3.09	0.59	0.19

* Assuming sticking friction and a constant peripheral roll speed of 84 mm/sec.

TABLE 7

TEMPERATURES AND STRENGTHS DURING THE HOT ROLLING OF STAINLESS STEEL

Key: NR : Not recorded
TCF: Thermocouple failure
* : Approximate value

All temperatures in ^{o}C

Load = total roll load, kN

Torque = total roll torque, N.m

Corrected torque = measured torque - frictional torque, N.m

$\bar{\sigma}$ = mean uniaxial flow stress calculated from rolling load, N/mm^2

TABLE 7 (i)

RUN	PASS	T^c_{entry}	$\overline{T}_{entry}$	T^c_{exit}	$\overline{T}_{exit}$	MEAN $\overline{T}$	ΔT_{def}	LOAD	TORQUE	CORRECTED TORQUE	$\overline{\sigma}$
1	1	1173	1152	-	-	-	-	143	NR	-	131
2	1	1173*	1152*	-	-	-	-	146	NR	-	131
3	1	1163	1139	-	-	-	-	159	NR	-	138
4	1	1135	1111	1084	1063	1087	6½	158	NR	-	133
	2	1001	980	925*	909	945	20	319	NR	-	287
5	1	1134*	1111*	1087*	1068*	1090*	-	156	NR	-	138
	2	1018*	996*	967*	949*	973*	-	282	NR	-	268
6	1	1143	1119	1095	1075	1097	5	165	NR	-	145
	2	1035	1012	950*	933*	973	16	260	NR	-	245
7	1	1134*	1112*	1085*	1063*	1088*	-	161	NR	-	144
	2	1015*	994*	938*	921*	958*	-	287	NR	-	274
8	1	1142*	1119*	1093*	1073*	1096*	-	187	NR	-	153
	2	1013*	992*	959*	942*	967*	-	284	NR	-	266
	3	903*	887*	842*	829*	858*	-	350	NR	-	372
9	1	1135	1110	1085	1066	1088	6	191	NR	-	142
	2	1009	988	954	937	963	18	334	NR	-	280
	3	894	879	845	832	856	27	378	NR	-	372
10	1	1135*	1111*	1083*	1063*	1087*	-	192	NR	-	157
	2	1010*	989*	959*	942*	966*	-	276	NR	-	256
	3	886*	871*	831*	819*	845*	-	353	NR	-	384
11	1	1133	1108	1072	1051	1080	8	219	NR	-	169
	2	1011	990	947	930	960	17½	284	NR	-	265
12	1	1127*	1102*	1041*	1020*	1061*	-	219	NR	-	177
	2	946*	927*	873*	858*	893*	-	285	NR	-	264
	3	821*	808*	785*	774*	791*	-	420	NR	-	442
13	1	1135	1111	1087	1066	1089	8½	203	3950	3371	164
	2	1011	990	972	954	972	21½	302	5330	4469	275
	3	TCF	-	-	-	-	-	430	6190	4965	427

TABLE 7 (continued) (ii)

RUN	PASS	T^c_{entry}	$\overline{T}_{entry}$	T^c_{exit}	$\overline{T}_{exit}$	MEAN $\overline{T}$	ΔT_{def}	LOAD	TORQUE	CORRECTED TORQUE	$\overline{\sigma}$
14	1	1150	1125	1093	1073	1099	8	195*	4160	3604	164
	2	1001	981	956	939	960	18	284*	4410	3601	271
	3	894	879	852	839	859	25	354*	5110	4101	372
15	1	1133	1107	1078	1058	1083	$8\frac{1}{2}$	206*	3860	3273	167
	2	1000	979	952	937	958	-	327*	5620	4688	300
	3	867	855	816	805	830	$27\frac{1}{2}$*	413*	5870	4693	422
16	1	1144	1120	1083	1062	1091	2	150	2790*	2363	148
17	1	1144	1120	1102	1080	1100	1	100	1420	1135	142
18	1	1144	1120	1091	1071	1096	5	192	3600	3053	156
	2	1012*	991*	TCF	-	-	-	306	5240	4368	286
	3	-	-	-	-	-	-	402	5660	4514	413
19	1	1126	1102	1078	1059	1081	$7\frac{1}{2}$	197	3710	3149	160
	2	1015	994	962	945	970	19	295	5190	4349	272
	3	893	878	836	823	851	$28\frac{1}{2}$	401	5530	4387	417
20	1	1125	1102	1065	1045	1074	7	205	3840	3256	163
	2	1002	981	950	933	957	$22\frac{1}{2}$	330	5720	4780	297
	3	880	869	832	823	846	28*	374	4900	3834	374
21	1	1138	1114	1091	1072	1093	6	NR	NR	-	-
	2	1010	990	959	942	966	20	NR	NR	-	-
	3	886	871	830	818	845	$32\frac{1}{2}$	NR	NR	-	-
22	1	1139	1116	1081	1062	1089	8	199	3790	3223	161
	2	1010	989	928	911	950	$17\frac{1}{2}$	282	4530	3726	259
	3	864	850	805	794	822	26*	423	5950	4744	433
23	1	1140	1116	1078	1058	1087	8	201	3820	3247	159
	2	1016	995	946	929	962	19	310	5230	4346	278
	3	879	864	817	805	835	$29\frac{1}{2}$	415	5630	4447	425
24	1	1142	1117	1077	1057	1087	$8\frac{1}{2}$	190	3610	3068	151
	2	1006	985	950	933	959	18	302	5060*	4199	274
	3	920*	904	854*	841	873	25*	357	4900	3882	370

TABLE 7 (continued) (iii)

RUN	PASS	T^c_{entry}	$\overline{T}_{entry}$	T^c_{exit}	$\overline{T}_{exit}$	MEAN $\overline{T}$	ΔT_{def}	LOAD	TORQUE	CORRECTED TORQUE	$\overline{\sigma}$
25	1	NR	-	NR	-	-	NR	164	-	-	172
	2	NR	-	NR	-	-	NR	243	-	-	282
26	1	1121	1098	1065	1045	1072	7	221	5190	4560	178
27	1	1139	1115	1086	1066	1091	7	207	4710	4120	166
28	1	1152	1128	1100	1081	1105	8	204	4620	4039	163
29	1	1156	1132	1108	1088	1110	-	194	4380	3827	156
30	1	1138	1115	1082	1063	1089	7	211	4710	4109	170
31	1	NR	-	-	-	-	-	202	-	-	160
32	1	1134*	1110*	1096*	1077*	1094*	-	202	4240	3664	161
33	1	1157*	1133*	1109*	1089*	1111*	-	199	4360	3793	162
34	1	1147	1123	1092	1073	1098	8	197	4160	3599	158
	2	974	959	911	897	928	-	282	5630	4826	258
35	1	NR	-	-	-	-	-	NR	NR	-	-
	2	NR	-	-	-	-	-	281	-	-	256
36	1	NR	-	-	-	-	NR	NR	NR	-	-
	2	988	972	933	919	946	17	290	5750	4924	276
37	1	1156	1132	1102	1083	1108	8	197	4130	3569	162
	2	977	961	931	917	939	18	287	5720	4902	268
38	1	1152	1128	1114	1093	1111	11	194	4660	4107	161
39	1	1158	1133	1096	1077	1105	4	202	4080	3504	171
	2	1131	1111	1068	1051	1081	12	198	3770	3206	181
40	1	NR	-	-	-	-	NR	NR	NR	-	-
	2	1132	1112	TCF	-	-	8	195	3190*	2634	176
41	1	NR	-	-	-	-	NR	NR	NR	-	-
	2	1128	1108	1073	1056	1082	11	204	3600	3019	179
42	1	NR	-	-	-	-	-	NR	NR	-	-
	2	1095	1076	TCF	-	-	-	223	3760	3124	202
43	1	1136	1109	1078	1055	1082	6	229	6320*	5667	175
	2	880	863	848	833	848	28	432	-	-	386

TABLE 7 (continued) (iv)

RUN	PASS	T^c_{entry}	$\overline{T}_{entry}$	T^c_{exit}	$\overline{T}_{exit}$	MEAN $\overline{T}$	ΔT_{def}	LOAD	TORQUE	CORRECTED TORQUE	$\overline{\sigma}$
44	1	1134	1107	1079	1056	1082	8	219	5730*	5106	167
	2	885	868	840	826	847	11½*	409	-	-	362
45	1	1132	1102	1078	1054	1078	8½	225	5670*	5029	171
46	1	1138	1112	1086	1065	1089	8	223	5340	4704	172
	2	884	867	847	834	851	26	420	-	-	376
47	1	1136	1109	1081	1058	1084	8	221	4970*	4340	171
	2	884	867	851	836	852	26	409	-	-	366
48	1	1132	1106	1020	997	1052	7	222	5400	4767	168
49	1	1136*	1107*	1086	1062	1085	9½	203	-	-	153
	2	888*	871*	TCF	-	-	-	366	-	-	320
50	1	1132	1107	1086	1065	1086	9	228	5340	4690	173
	2	885	869	847	833	851	23	379	7530	6449	335
51	1	1138	1113	1086*	1064	1089	6	228	5370	4720	173
	2	817	803	785*	773	788	29	482	-	-	432
52	1	1136	1109	1087*	1064*	1087*	8	223	-	-	169
	2	890	873	860*	845*	859*	29	432	-	-	380
53	1	1077	1050	1035	1012	1031	10	275	6550	5766	209
	2	898	880	860*	845*	863*	25	438	9440	8192	387
54	1	1154	1131	1102	1082	1107	6	215	5080	4467	164
	2	1032	1010	990*	970	990	15	286	7230	6415	245
55	1	1142	1114	1078	1054	1084	8	220	6000	5373	169
	2	899	882	870*	855*	869	23	391	8830*	7716	347
56	1	1142	1117	1089	1069	1093	6	224	6060	5422	171
	2	996	974	960*	942*	958	20	325	7200	6274	282
57	1	TCF	-	-	-	-	TCF	236	-	-	181
58	1	1146	1121	1089	1067	1094	7	204	5050*	4469	154
59	1	1116	1088	970	946	1017	4	213	4800*	4193	162
60	1	1120	1093	968	945	1019	3	212	4840*	4236	159
61	1	1138	1111	1010	988	1050	3	199	4310	3743	150

TABLE 7 (continued) (v)

RUN	PASS	T^c_{entry}	$\overline{T}_{entry}$	T^c_{exit}	$\overline{T}_{exit}$	MEAN $\overline{T}$	ΔT_{def}	LOAD	TORQUE	CORRECTED TORQUE	$\overline{\sigma}$
62	1	1128	1102	1084	1062	1082	6	235	-	-	180
	2	1024	1001	-	-	-	15	293	-	-	254
63	1	1148	1126	1108	1088	1107	9	218	-	-	166
	2	893	875	860*	845*	860	21	406	-	-	356
64	1	1140	1119	1098	1081	1100	8	212	5140	4536	163
	2	984	963	940*	922*	943	16	324	6340*	5418	282
65	1	1142	1119	1085	1065	1092	8	206	4960	4373	154
66	1	1139	1119	1098	1079	1099	$7\frac{1}{2}$	212	5010	4406	159
67	1	1134	1112	1083	1065	1089	$2\frac{1}{2}$	182	-	-	139
	2	1109*	1090	1060*	1038	1064	6	191	3720	3177	160
	3	892*	876*	TCF	-	-	-	341	5420	4449	323
68	1	1131	1109	1104	1085	1097	9	216	5340	4724	160
69	1	1142	1118	TCF	-	-	8	195	-	-	149
	2	-	-	-	-	-	-	291	-	-	248
70	1	1144	1121	1100	1080	1101	-	210	4880	4283	160
	2	1016	994	973	954	974	9	286	5720	4905	246
	3	TCF	-	TCF	-	-	-	401	-	-	369
71	1	1150	1129	1123	1105	1117	$10\frac{1}{2}$	222	5540	4907	166
72	1	1124	1100	1097*	1077*	1089*	8	230	5510	4855	173
73	1	1146	1122	1097	1077	1100	10	207	5200	4610	159
	2	1022	999	978	969	984	19	315	6200	5302	274
	3	923	905	872	858	882	23	369	6240	5188	351
74	1	1138	1116	1098	1079	1098	8	206	4880	4293	159
	2	992	970	953	935	953	14	318	6530	5624	278
	3	884	873	844	834	854	26	388	7470	6364	358
75	1	1144	1118	1070	1048	1083	6	204	4880	4299	155
	2	900	883	869	854	868	24	388	7900	6794	341
	3	891	881	851	842	862	28	396	6660	5532	362

TABLE 7 (continued) (vi)

RUN	PASS	T^c_{entry}	$\overline{T}_{entry}$	T^c_{exit}	$\overline{T}_{exit}$	MEAN $\overline{T}$	ΔT_{def}	LOAD	TORQUE	CORRECTED TORQUE	$\overline{\sigma}$
76	1	1142	1118	1096	1075	1097	8	206	4990	4403	156
	2	894	877	859	844	861	18	408	-	-	358
	3	889	878	850	841	860	21	391	-	-	353
77	1	1138	1111	1088	1065	1088	8	203	4880	4301	157
	2	984	963	947	929	946	20	323	7040*	6120	284
	3	861	846	820	808	827	31	405	-	-	377
78	1	1145	1118	1085	1064	1091	$7\frac{1}{2}$	205	5000	4416	155
	2	995	973	951	924	949	21	327	-	-	281
	3	896	881	840	828	855	$28\frac{1}{2}$	390	-	-	358
79	1	1041*	1015*	TCF	-	-	13	284	6690	5881	226
80	1	1059	1031	1030	1007	1019	$11\frac{1}{2}$	249	5710	4990	197
81	1	986	962	955	935	949	$14\frac{1}{2}$	302	6640	5779	244
82	1	977	954	948	928	941	16	320	7180	6268	255
83	1	953	931	922	904	918	14	331	7110	6168	265
84	1	904	885	880	864	875	20	364	8020	6983	293

TABLE 8

DIMENSIONAL PARAMETERS FOR STAINLESS STEEL HOT ROLLING SCHEDULES

Values of:

(1) Initial and final thickness and width for each pass (mm)

(2) Sims' geometrical factor, Qp

(3) Uniaxial strain, ε

(4) Peripheral roll speed, mm/sec.

(5) Mean uniaxial strain rate, $\dot{\bar{\varepsilon}}$, sec^{-1}

(6) Contact time, m.sec.

Key:

* : Approximate values
NR : Not recorded
\- : Underived because parameters not recorded.

TABLE 8

RUN	PASS	THICKNESS	WIDTH	Q_p	ε	ROLL SPEED mm/sec	$\dot{\varepsilon}$	CONTACT TIME m.sec.
1	1	19.12 14.24	50.5 52.0	1.016	0.340	216	4.0	85
2	1	19.00 14.12	51.0 52.5	1.018	0.343	216	4.0	85
3	1	18.95 14.05	52.7 54.2	1.020	0.345	200	3.8	85
4	1 2	19.10 13.93 10.16	52.8 54.4 57.0	1.024 1.077	0.364 0.364	197 197	3.8 4.5	96 82
5	1 2	19.10 13.91 10.13	50.0 51.5 54.0	1.025 1.078	0.366 0.366	197 197	3.8 4.5	96 82
6	1 2	19.03 13.91 10.16	50.7 52.2 54.8	1.024 1.077	0.362 0.363	197 197	3.8 4.4	95 82
7	1 2	19.03 13.90 10.16	50.0 51.5 54.0	1.024 1.077	0.363 0.362	197 197	3.8 4.4	95 82
8	1 2 3	18.95 13.18 9.48 7.04	50.4 52.0 54.5 56.2	1.043 1.094 1.142	0.419 0.380 0.344	197 197 197	4.1 4.7 5.2	101 81 66
9	1 2 3	19.05 13.25 9.45 7.06	55.5 57.1 59.9 61.2	1.042 1.097 1.139	0.419 0.390 0.337	197 197 197	4.1 4.8 5.2	101 82 65
10	1 2 3	19.06 13.25 9.49 7.13	50.4 52.0 54.5 56.2	1.042 1.095 1.134	0.420 0.385 0.330	197 197 197	4.1 4.7 5.1	102 82 65

TABLE 8 (continued) (i)

RUN	PASS	THICKNESS	WIDTH	Q_p	ε	ROLL SPEED mm/sec	$\dot{\varepsilon}$	CONTACT TIME m.sec.
11		19.00	53.0*					
	1	13.21	55.0*	1.042	0.420	197	4.1	101
	2	9.69	57.5	1.084	0.358	197	4.5	79
12		19.11	50.9					
	1	13.29	52.4	1.041	0.419	197	4.1	102
	2	9.57	55.0	1.092	0.379	197	4.7	81
	3	7.12	56.8	1.139	0.341	197	5.2	66
13		19.10	50.9					
	1	13.28	52.4	1.041	0.420	196	4.1	102
	2	9.47	55.0	1.097	0.390	196	4.7	82
	3	6.82	56.8	1.161	0.379	196	5.5	69
14		19.06	49.0					
	1	13.25	50.5	1.042	0.420	205	4.3	98
	2	9.46	52.4	1.096	0.389	205	4.9	79
	3	6.86	54.6	1.157	0.370	205	5.7	66
15		19.20	50.6					
	1	13.35	52.1	1.040	0.420	202	4.2	99
	2	9.53	54.6	1.095	0.389	202	4.9	80
	3	6.95	56.4	1.152	0.364	202	5.5	66
16		19.07	52.5					
	1	15.08	55.0	0.993	0.271	186	3.0	89
17		18.89	51.5					
	1	16.64	53.0	0.942	0.146	183	2.2	68
18		19.23	50.5					
	1	13.37*	52.0	1.040	0.420	183	3.8	109
	2	9.63*	54.5	1.091	0.379	183	4.3	87
	3	7.00	54.8	1.152	0.368	183	5.0	73
19		18.95	50.8					
	1	13.18	52.3	1.042	0.419	183	3.9	109
	2	9.40	54.3	1.098	0.390	183	4.4	88
	3	6.88	56.0	1.153	0.360	183	5.0	72

TABLE 8 (continued) (ii)

RUN	PASS	THICKNESS	WIDTH	Q_p	ε	ROLL SPEED mm/sec	$\dot{\bar{\varepsilon}}$	CONTACT TIME m.sec.
20	1	18.87	52.0	1.043	0.420	183	3.9	108
	2	13.12	53.6	1.098	0.389	183	4.4	87
	3	9.37	56.2	1.159	0.371	183	5.1	72
		6.80	56.8					
21	1	18.74	51.5	1.044	0.420	183	3.9	108
	2	13.03	52.8	1.100	0.389	183	4.5	87
	3	9.30	55.3	1.163	0.375	183	5.2	72
		6.72	56.6					
22	1	18.84	51.5	1.043	0.419	178	3.8	111
	2	13.10	52.5	1.099	0.389	178	4.3	90
	3	9.35	55.0	1.156	0.364	178	4.9	74
		6.82	56.3					
23	1	18.81	52.5	1.044	0.419	178	3.8	111
	2	13.08	53.5	1.100	0.391	178	4.4	90
	3	9.32	56.0	1.151	0.354	178	4.9	73
		6.86	57.4					
24	1	18.77	52.5	1.044	0.420	178	3.8	111
	2	13.05	53.3	1.099	0.389	178	4.3	90
	3	9.32	55.5	1.150	0.352	178	4.9	73
		6.87	56.9					
25	1	18.76*	50.5	0.993	0.258	NR	-	-
	2	15.00*	51.8	1.013	0.236	NR	-	-
		12.23	53.9					
26	1	19.13	49.9	1.045	0.418	204	4.2	99
		13.32	52.3					
27	1	19.22	50.1	1.045	0.422	204	4.2	100
		13.34	51.9					
28	1	19.08	49.9	1.047	0.423	204	4.2	99
		13.22	52.6					
29	1	19.13	49.8	1.046	0.423	204	4.3	99
		13.26	51.9					

TABLE 8 (continued) (iii)

RUN	PASS	THICKNESS	WIDTH	Q_p	ε	ROLL SPEED mm/sec	$\dot{\bar{\varepsilon}}$	CONTACT TIME m.sec.
30	1	19.13 13.32	49.8 52.5	1.045	0.418	204	4.2	99
31	1	19.11 13.25	50.1 53.2	1.046	0.423	204	4.3	99
32	1	19.10 13.26	50.4 52.8	1.046	0.421	204	4.2	99
33	1	19.12 13.29	49.3 51.4	1.045	0.420	204	4.2	99
34	1 2	18.97 13.13 9.33	49.8 52.1 53.2	1.048 1.105	0.425 0.394	198 198	4.1 4.8	103 83
35	1 2	NR 13.08 9.16	NR 51.2 52.0	- 1.113	- 0.411	203 203	- 5.0	- 82
36	1 2	18.86 13.11 9.34	48.6 49.6 52.0	1.048 1.104	0.420 0.391	199 199	4.2 4.8	101 82
37	1 2	18.88 13.14 9.38	49.1 51.2 52.6	1.047 1.103	0.419 0.390	199 199	4.1 4.8	101 82
38	1	18.85 13.15	49.5 50.5	1.046	0.415	208	4.3	96
39	1 2	18.85 13.20 9.19	48.9 49.9 51.9	1.045 1.114	0.411 0.418	207 214	4.3 5.3	96 79
40	1 2	NR 13.15 9.18	49.1 50.6 53.0	- 1.113	- 0.415	214 214	- 5.3	- 78
41	1 2	NR 13.16 9.17	50.6 52.1 53.9	- 1.114	- 0.417	217 217	- 5.4	- 77

TABLE 8 (continued) (iv)

RUN	PASS	THICKNESS	WIDTH	Q_p	ε	ROLL SPEED mm/sec	$\dot{\bar{\varepsilon}}$	CONTACT TIME m.sec.
42	1	NR	NR	-	-	226	-	-
	2	13.15	51.3	1.111	0.408	226	5.6	74
		9.24	52.8					
43	1	22.75	49.9	1.016	0.419	155	2.9	143
	2	15.82	51.4	1.059	0.364	155	3.3	112
		11.54	54.5					
44	1	22.79	50.1	1.016	0.420	159	3.0	140
	2	15.84	51.6	1.061	0.371	159	3.4	110
		11.49	54.1					
45	1	22.76	50.5	1.015	0.414	152	2.9	145
		15.91	52.0					
46	1	22.61	49.6	1.017	0.420	151	2.9	146
	2	15.72	51.1	1.062	0.369	151	3.2	115
		11.42	54.1					
47	1	22.56	49.5	1.018	0.420	158	3.0	139
	2	15.68	51.0	1.064	0.373	158	3.4	110
		11.35	53.8					
48	1	22.39	50.1	1.019	0.420	157	3.0	139
		15.56	52.7					
49	1	22.52	51.0	1.018	0.419	153	2.9	144
	2	15.66	52.5	1.064	0.374	163	3.5	107
		11.33	54.5					
50	1	22.51	50.6	1.018	0.420	208	4.0	106
	2	15.65	52.1	1.063	0.369	208	4.4	83
		11.37	54.4					
51	1	22.26	50.7	1.020	0.419	218	4.2	100
	2	15.48	52.2	1.061	0.360	218	4.6	78
		11.33	54.7					
52	1	22.44	50.5	1.019	0.420	212	4.1	104
	2	15.60	52.0	1.064	0.372	212	4.6	82
		11.30	54.8					

TABLE 8 (continued) (v)

RUN	PASS	THICKNESS	WIDTH	Q_p	ε	ROLL SPEED mm/sec	$\dot{\bar{\varepsilon}}$	CONTACT TIME m.sec.
53	1	22.43	50.5	1.019	0.419	206	3.9	106
	2	15.60	52.0	1.064	0.372	206	4.4	84
		11.30	54.3					
54	1	22.39	50.4	1.019	0.419	216	4.1	102
	2	15.57	51.9	1.072	0.391	216	4.8	82
		11.09	54.8					
55	1	22.22	50.1	1.020	0.420	214	4.1	102
	2	15.45	51.6	1.067	0.374	214	4.6	81
		11.18	54.3					
56	1	22.45	50.1	1.019	0.420	227	4.3	97
	2	15.61	51.6	1.069	0.386	227	5.0	78
		11.18	54.5					
57	1	22.29	49.7	1.019	0.418	201	3.8	109
		15.52	52.2					
58	1	22.22	50.4	1.019	0.418	205	3.9	107
		15.47	53.1					
59	1	22.20	49.9	1.020	0.419	37	0.7	596
		15.44	52.9					
60	1	22.33	50.4	1.020	0.424	39	0.8	561
		15.47	53.2					
61	1	22.36	50.1	1.021	0.425	37	0.7	602
		15.48	52.8					
62	1	22.45	50.0	1.019	0.420	217	4.2	101
	2	15.61	51.5	1.071	0.391	217	4.8	82
		11.12	53.9					
63	1	22.48	50.2	1.018	0.419	229	4.4	96
	2	15.64	51.7	1.066	0.378	229	5.0	76
		11.27	54.3					
64	1	22.24	50.1	1.020	0.419	256	4.9	85
	2	15.47	51.6	1.071	0.387	256	5.6	69
		11.06	54.3					

TABLE 8 (continued) (vi)

RUN	PASS	THICKNESS	WIDTH	Q_p	ε	ROLL/SPEED mm/sec	$\bar{\dot{\varepsilon}}$	CONTACT TIME m.sec.
65	1	22.68 15.58	49.9 52.8	1.020	0.434	NR	-	-
66	1	22.42 15.43	49.8 52.8	1.022	0.431	NR	-	-
67	1 2 3	22.48 15.63* 10.94* 7.87	50.1 51.6 54.1 55.9	1.018 1.079 1.136	0.420 0.412 0.380	217* 217* 217*	4.1 4.9 5.6	101 84 68
68	1	22.66 15.59	50.3 52.7	1.020	0.432	400	7.8	56
69	1 2	22.50 15.64 11.06	50.1 51.6 54.1	1.018 1.074	0.420 0.400	223 223	4.3 5.0	99 81
70	1 2 3	22.43 15.60 11.12 7.93	50.2* 51.7* 54.7 56.1	1.019 1.071 1.137	0.419 0.391 0.390	258* 258* 258*	4.9* 5.7* 6.7*	85* 69* 58*
71	1	22.52 15.51	49.9 52.8	1.021	0.431	408	7.9	55
72	1	22.40 15.45	50.0 52.6	1.021	0.429	411	8.0	54
73	1 2 3	22.70 15.78 11.24 8.11	49.6 51.1 53.6 55.5	1.017 1.069 1.129	0.420 0.392 0.377	204 204 204	3.9 4.5 5.2	108 88 73
74	1 2 3	22.57 15.70 11.23 7.96	49.7 51.2 53.7 55.3	1.018 1.069 1.139	0.419 0.387 0.397	195 195 195	3.7 4.3 5.1	113 91 78
75	1 2 3	23.31 15.52 11.24 7.99	50.7 52.2 54.8 55.8	1.019 1.065 1.137	0.419 0.373 0.394	202 202 202	3.9 4.3 5.3	108 86 75

TABLE 8 (continued) (vii)

RUN	PASS	THICKNESS	WIDTH	Q_p	ε	ROLL/SPEED mm/sec	$\dot{\varepsilon}$	CONTACT TIME m.sec.
76	1	22.48	50.5	1.018	0.419	202	3.9	109
	2	15.63	52.0	1.064	0.372	202	4.3	86
	3	11.33	55.1	1.136	0.396	202	5.3	75
		8.04	56.3					
77	1	22.53	49.6	1.018	0.419	197	3.8	112
	2	15.67	51.1	1.069	0.386	197	4.3	90
	3	11.22	53.6	1.136	0.392	197	5.1	76
		7.99	55.3					
78	1	22.74	50.4	1.016	0.419	197	3.7	112
	2	15.81	51.9	1.068	0.388	197	4.3	90
	3	11.30	54.4	1.134	0.390	197	5.1	76
		8.06	56.2					
79	1	23.13	48.2	1.010	0.404	132	2.4	166
		16.30	50.7					
80	1	23.33	48.5	1.008	0.402	206	3.8	106
		16.48	50.8					
81	1	23.06	47.4	1.008	0.397	208	3.8	105
		16.35	50.8					
82	1	23.11	48.5	1.009	0.399	213	3.9	102
		16.36	50.8					
83	1	23.36	48.3	1.007	0.397	205	3.7	107
		16.56	50.4					
84	1	23.28	48.4	1.005	0.391	210	3.8	103
		16.60	50.6					

TABLE 9

GRAIN SIZE MEASUREMENTS

(1) Slab: initial grain size after reheating for 20 minutes at 1180°C (measured on longitudinal sections)

(a) Linear, parallel to rolling direction:

Centre : 0.044 mm ± 0.004
Surface: 0.046 mm ± 0.004

(b) Circle: 0.036 mm ± 0.004

(2) Torsion Specimens: initial grain sizes (mm) after heating directly to temperature.

	TEMPERATURE °C			
	800	900	1000	1100
Longitudinal Section				
Linear:	0.018	0.020	0.021	0.024
Circle:	0.018	0.015	0.018	0.023
Transverse Section				
Linear:	0.015	0.015	0.016	0.020
Circle:	0.014	0.015	0.015	0.021

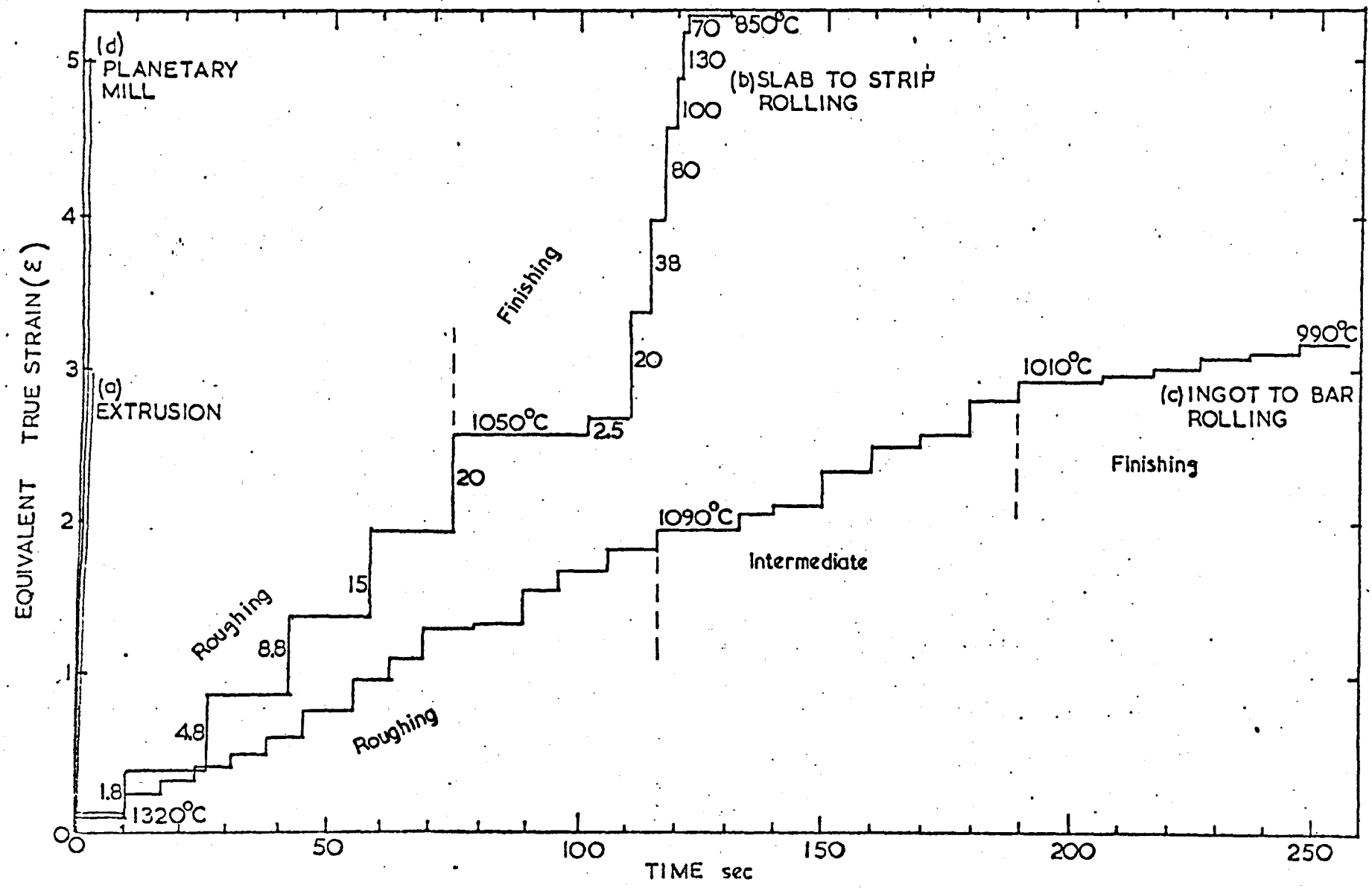

Fig.1 Typical deformation-time schedules for:(a)extrusion,(b)rolling 230mm.steel slab to strip (mean equivalent true strain rates given for each pass),(c)rolling 530x610 mm. ingot to 114 mm.square bar and (d)planetary rolling. (After Barraclough 1974).

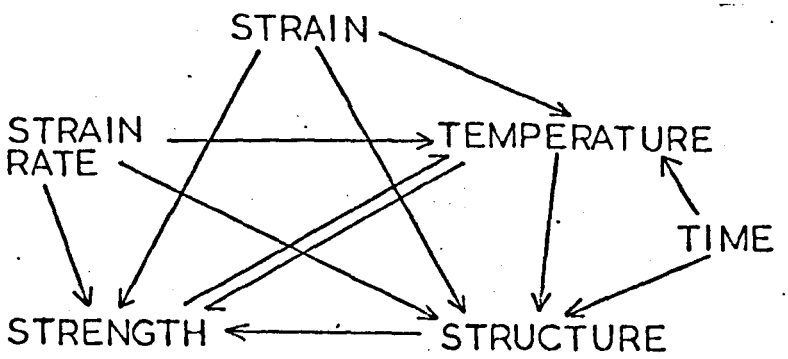

Fig.2 Interdependence of parameters during hot working.

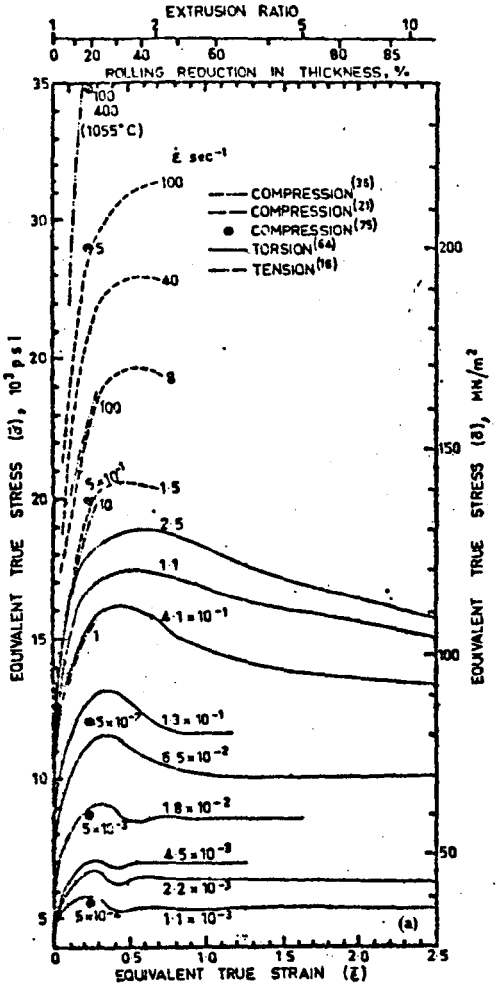

Fig.3 Stress-strain curves for 18/8 stainless steel. (After Sellars and Tegart 1972).

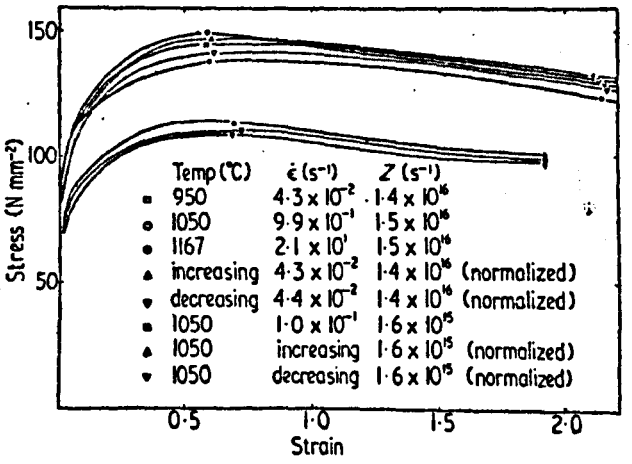

Fig.4 Stress–strain curves for stainless steel at two values of Z, including normalized curves from tests with varying conditions

(After Barraclough and Sellars 1974)

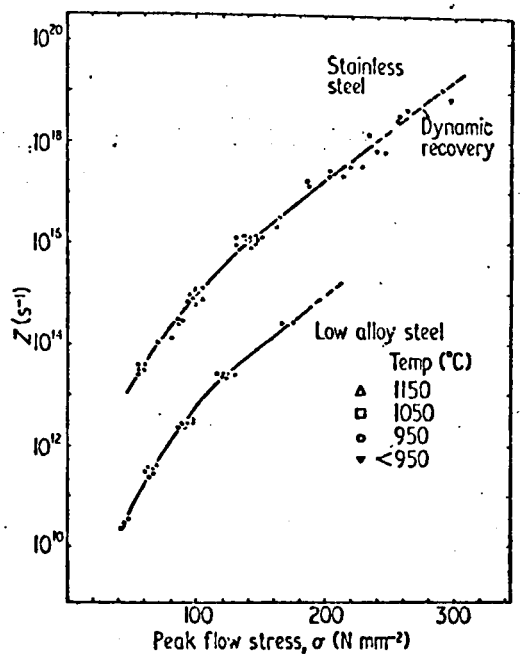

Figure 5 Dependence of peak flow stress on temperature-compensated strain rate (Z).

(After Barraclough and Sellars 1974)

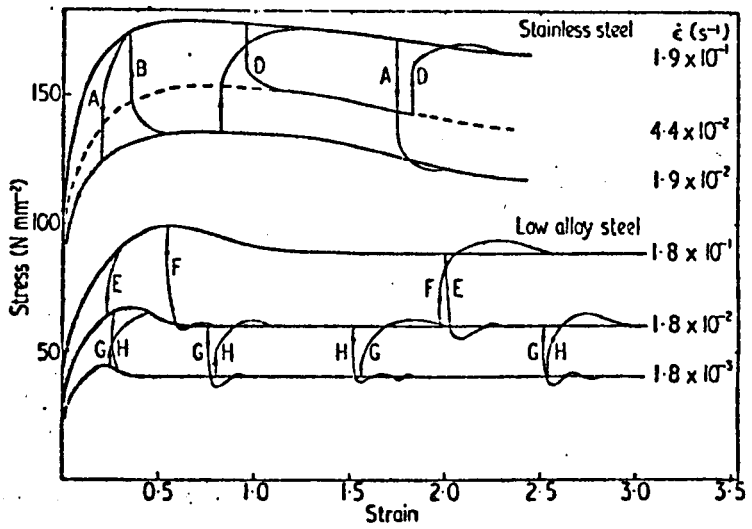

Figure 6. Typical stress-strain curves for tests involving instantaneous changes in strain rate for both stainless and low alloy steels.

(After Barraclough and Sellars 1974).

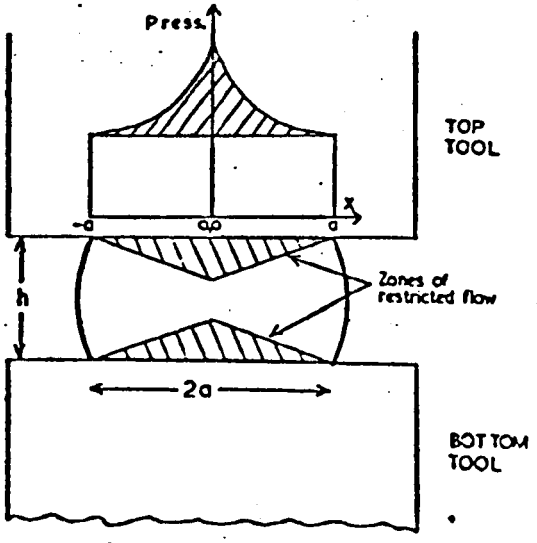

Fig.7 Inhomogeneous deformation and pressure distribution during compression (Adapted from Larke 1963).

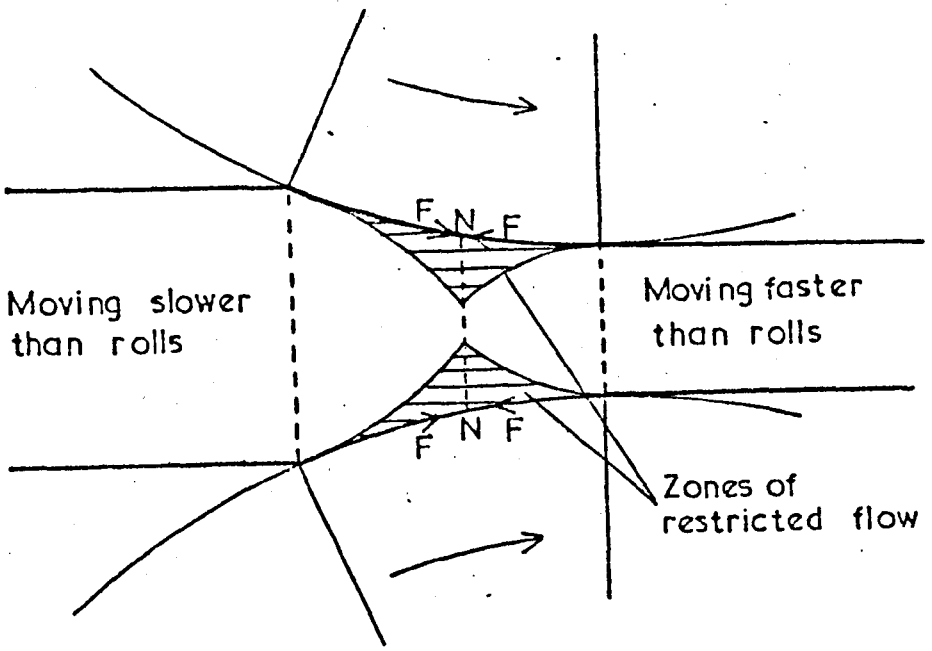

NN : Neutral plane
F : Frictional forces

Fig.8 Frictional conditions in the roll gap.

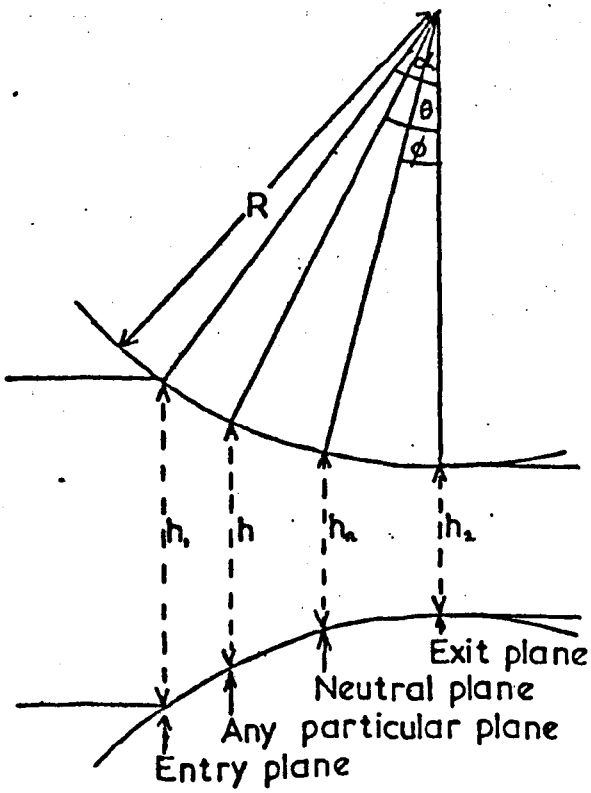

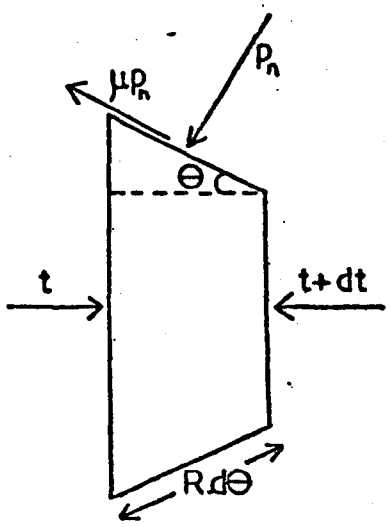

Fig.9 Notation for roll gap and equilibrium of forces on an elemental volume.

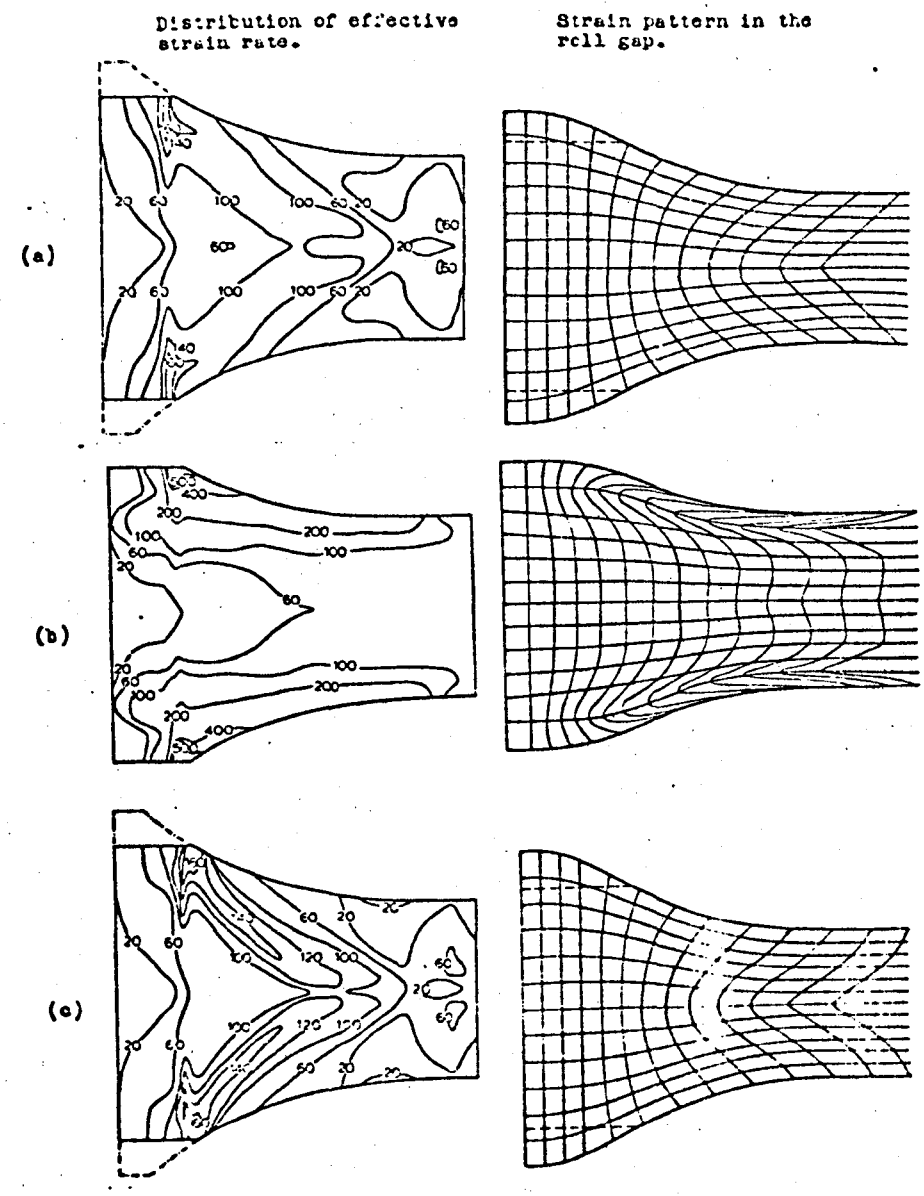

Fig.10 Effect of temperature profile on strain rate and strain distribution in roll gap: (a)Uniform temperature (b) Cold centre profile (c) Cold surface profile
(After Cornfield and Johnson 1971)

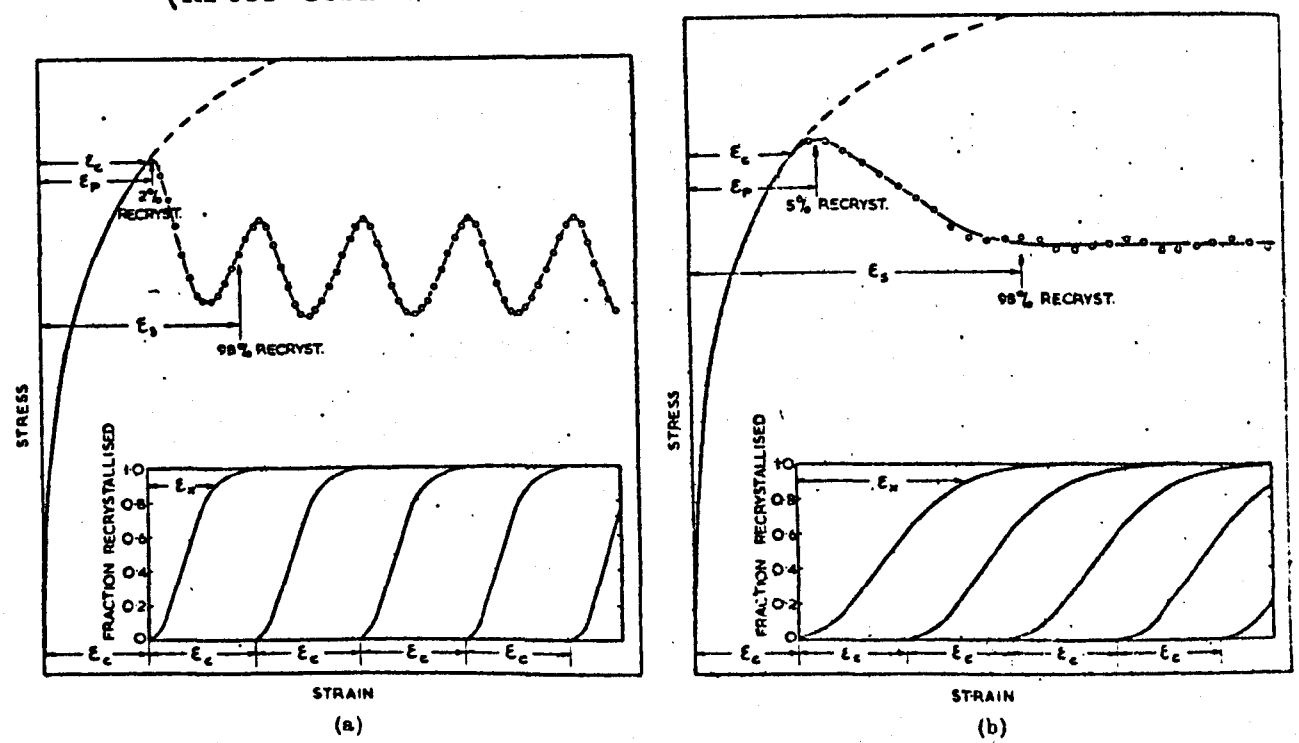

Fig.11 Predicted stress–strain curves for dynamic recrystallization (a) critical strain to initiate recrystallization, $\varepsilon_c > \varepsilon_p$, the strain occurring in the time for a large fraction of recrystallization. (b) $\varepsilon_c < \varepsilon_p$.

(After Luton and Sellars 1969).

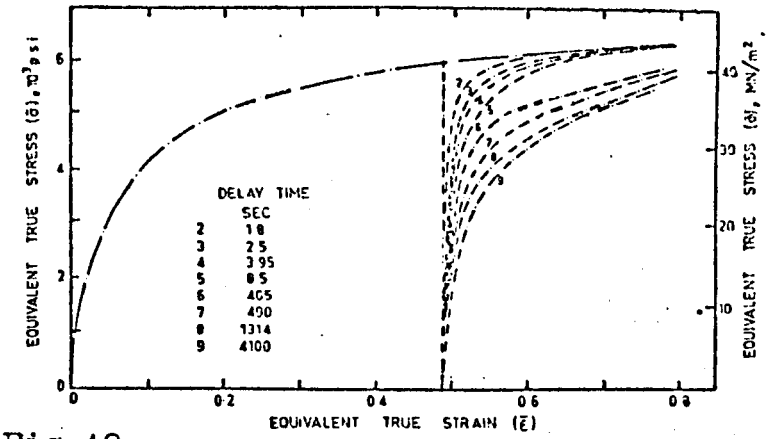

Fig.12 *Effect of delay time on stress/strain behaviour of commercial-purity aluminium deformed in plane-strain compression at an equivalent strain rate of 3·8 s^{-1} and at 410° C.*

(After Sellars and Tegart 1972)

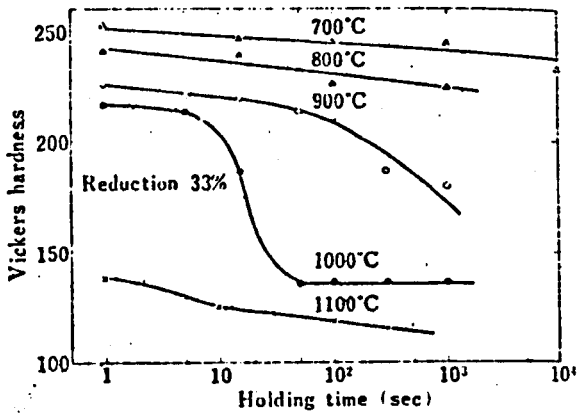

Fig.13a Change of Vickers hardness with holding time and temperature at 33% rolling reduction

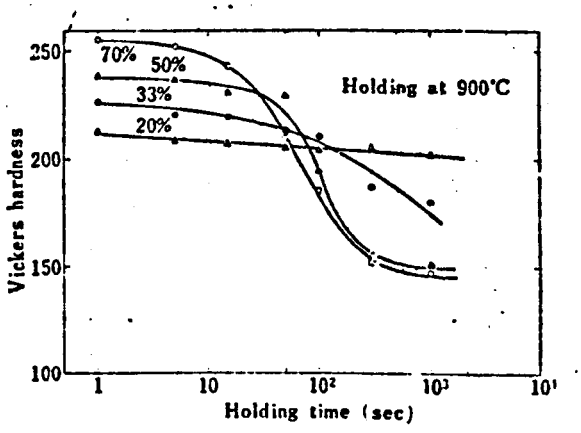

Fig.13b Change of Vickers hardness with holding time and rolling reduction at 900°C

(After Kozasu and Shimizu 1971)

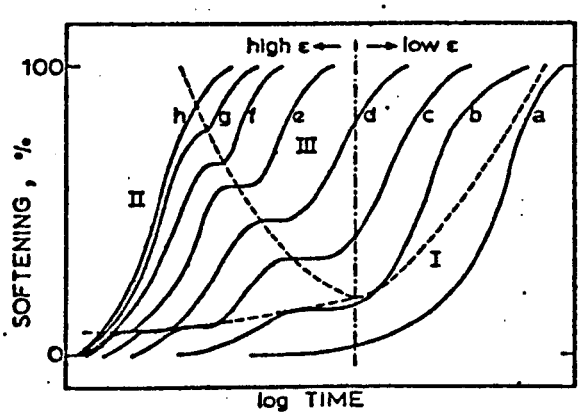

I static recovery; *II* metadynamic recrystallization; *III* classical recrystallization; curves *a–h* represent the effect of increasing interruption strains; the interruption strain associated with curve *a* is below the critical strain for classical recrystallization; curve *b* represents a strain just before the peak of the flow curve, and therefore the critical strain for dynamic and metadynamic recrystallization; curves *c–g* are for strains beyond the peak, but before steady state flow is achieved; curve *h* is for interruption in the steady state region

Schematic softening curves delineating the operating range of each of the three softening mechanisms

Fig.14 (After Djaic and Jonas 1972)

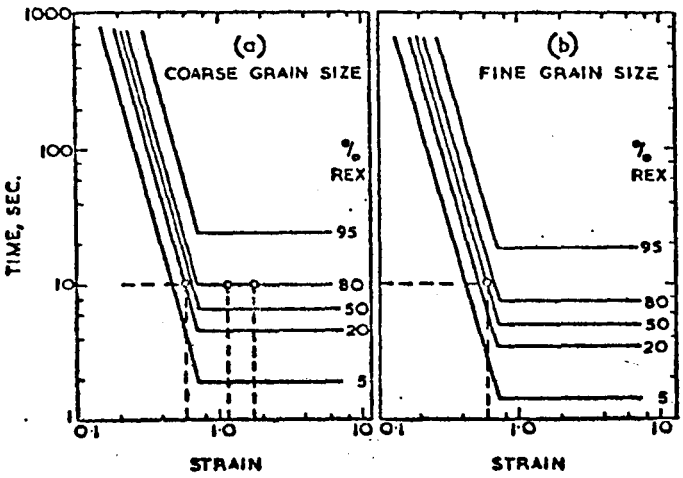

Fig.15—Strain and grain size dependence of static recrystallisation used in the derivation of Table α.

Table α. Change in structure during isothermal rolling schedule with passes of 0·6 strain and constant time intervals between passes.

After 1st Pass	100% Def. 0·6 (coarse)
Before 2nd Pass	25% Recrystallised (coarse) 75% Def. 0·6 (coarse)
After 2nd Pass	25% Def. 0·6 (coarse) 75% Def. 1·2 (coarse)*
Before 3rd Pass	25% × 25% Recryst. (coarse) = 6·3% × 75% Def. 0·6 (coarse) = 18·7% 75% × 80% Recryst. (fine) = 60·0% × 20% Def. 1·2 (coarse)* = 15·0%
After 3rd Pass	6·3% Def. 0·6 (coarse) 18·7% Def. 1·2 (coarse)* 60·0% Def. 0·6 (fine) 15·0% Def. 1·8 (coarse)*
Before 4th Pass	6·3% × 25% Recryst. (coarse) = 1·6% × 75% Def. 0·6 (coarse) = 4·7% 18·7% × 80% Recryst. (fine) = 15·0% × 20% Def. 1·2 (coarse)* = 3·7% 60·0% × 50% Recryst. (coarse) = 30·0% × 50% Def. 0·6 (fine) = 30·0% 15·0% × 80% Recryst. (fine) = 12·0% × 20% Def. 1·8 (coarse)* = 3·0%

*In materials in which dynamic recrystallisation can occur, the "coarse" structure after deformation to strains of 1·2 or more may be partially or completely replaced by a much finer dynamically recrystallised grain structure.

Fig.15 Structural development during isothermal rolling schedule (After Sellars and Whiteman 1974).

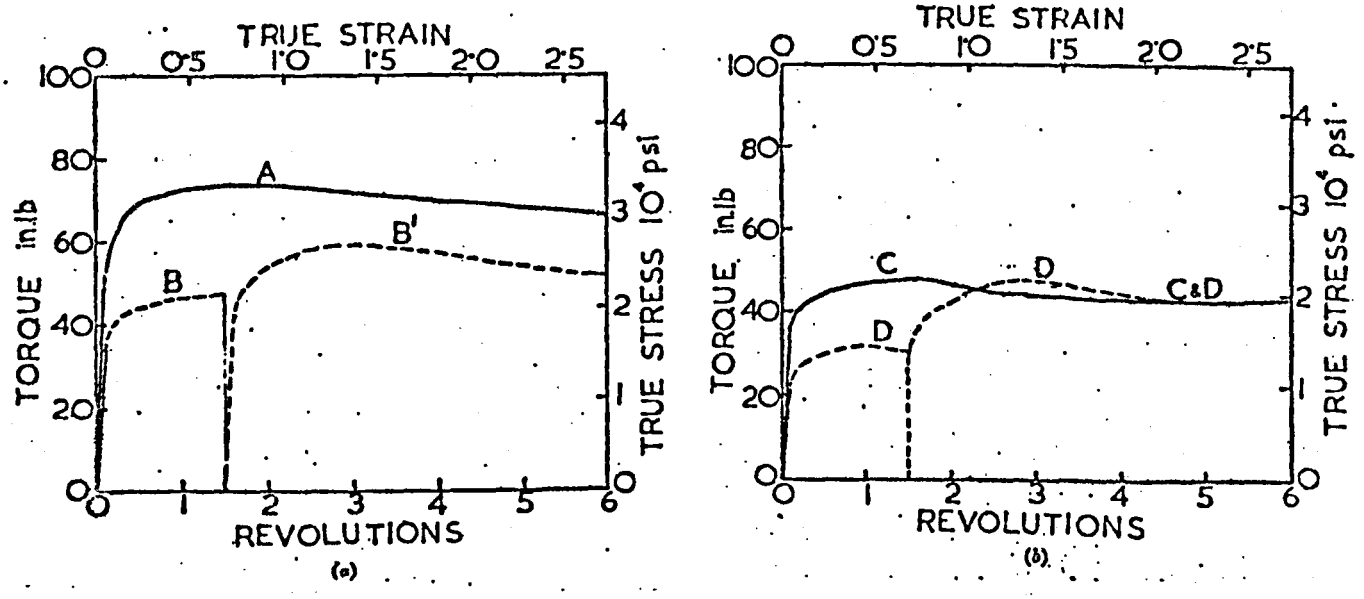

Fig.16 Effect of prestraining on the hot strength during restraining (a) Effect of incomplete recrystallisation (b) Effect of complete recrystallisation (After Nair 1971)

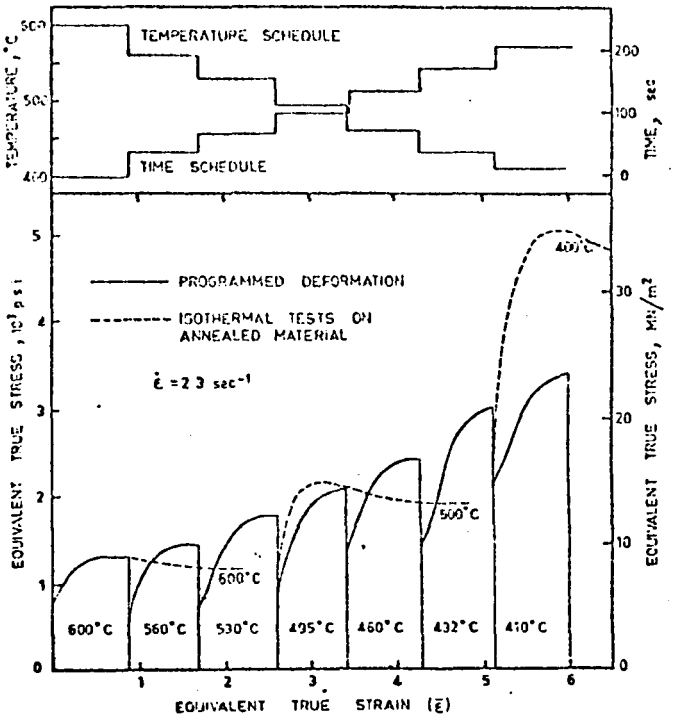

Deformation temperature/time schedule and resulting stress/strain behaviour of superpurity aluminium deformed in torsion at an equivalent strain rate of 2·3 s^{-1}.

Fig.17 Effect of inherited substructure on hot strength (After Farag et al 1968).

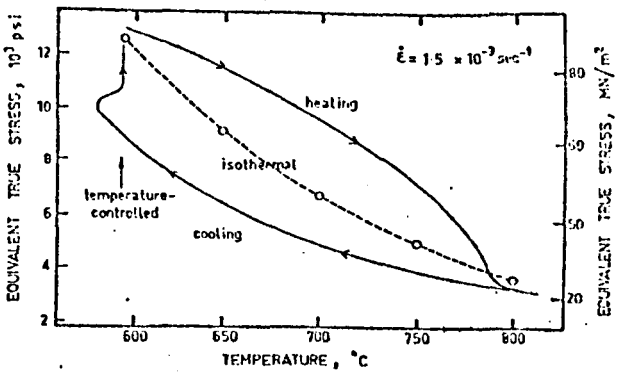

Effect of continuous heating or cooling on the steady-state flow stress of vacuum-melted iron deformed in torsion at an equivalent strain rate of 1·5 × 10^{-3} s^{-1}.

Fig.18 After Glover 1969

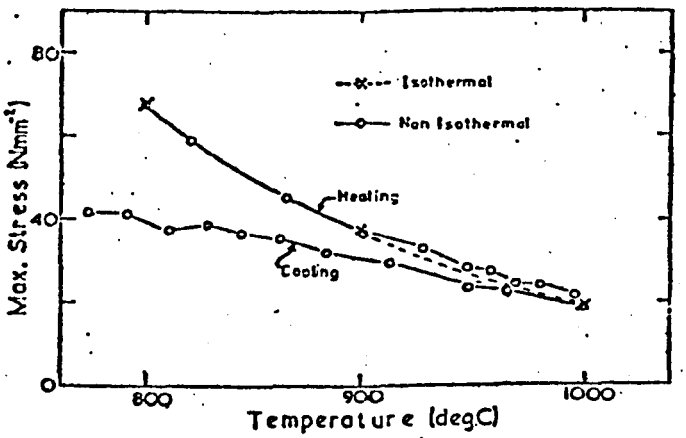

Fig.19 Effect of continuous heating or cooling on the stress to small strains for 3%Si steel (After Whittaker 1973)

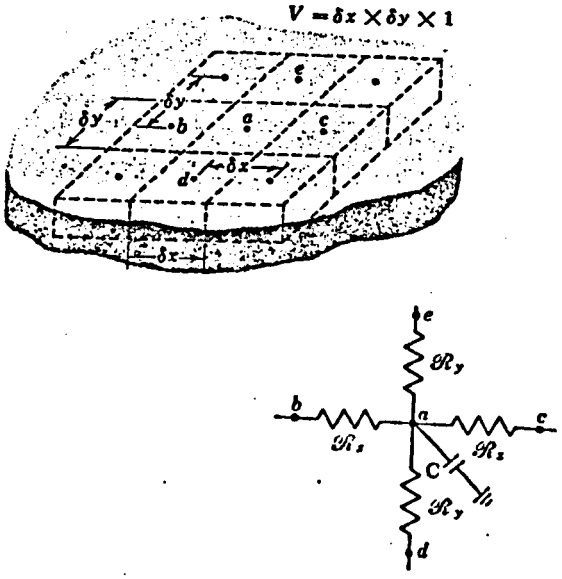

Fig.20 Nodal representation of two dimensional nonsteady conduction and electrical analogue.(After Chapman 1967)

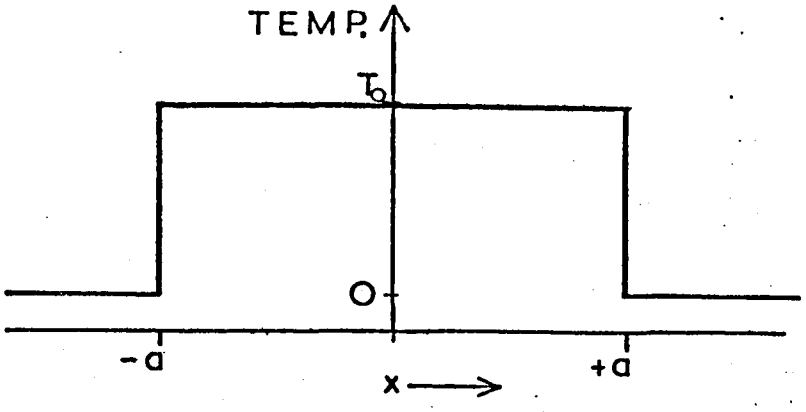

Fig.21 Basis of analytical solution of heat flow between two bodies with zero contact resistance and identical thermal properties.

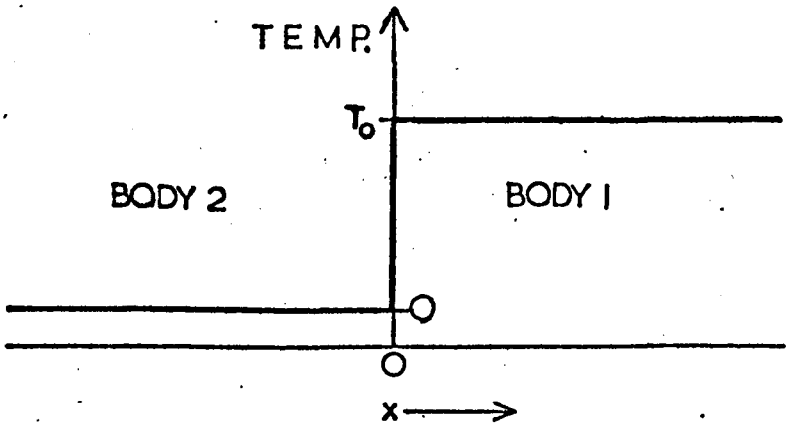

Fig.22 Basis of analytical solution of heat flow between two bodies with zero contact resistance and different thermal properties.

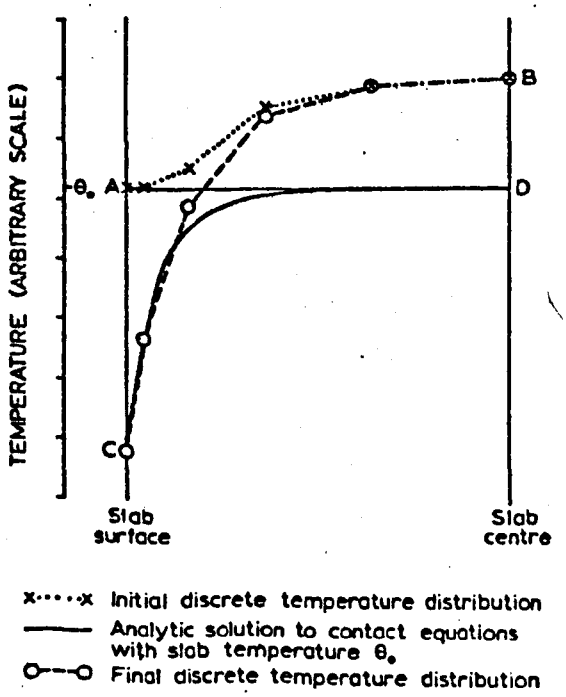

Fig.23 Heuristic method for heat flow between slab and roll (After Bradley et al 1970)

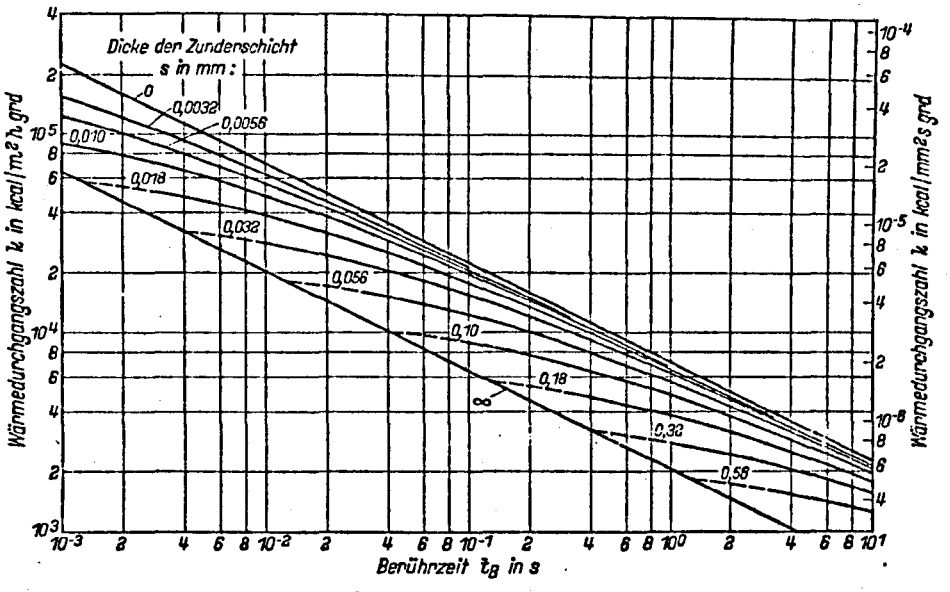

Fig.24 Heat conduction between slab and roll as a function of contact time. (After Pawelski 1969A).
Ordinate: Coefficient of heat transmission.
Abscissa: Contact time.
Dicke der Zunderschicht: Scale thickness.

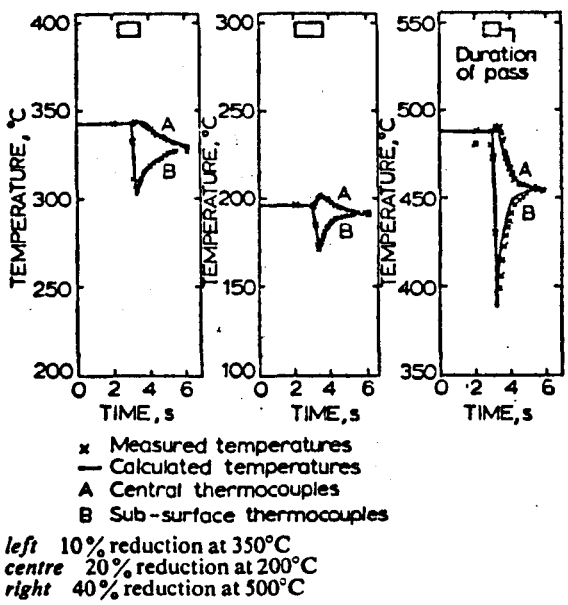

Fig.25 Comparison of temperatures during single pass rolling schedules for aluminium. (After Bradley et al 1970)

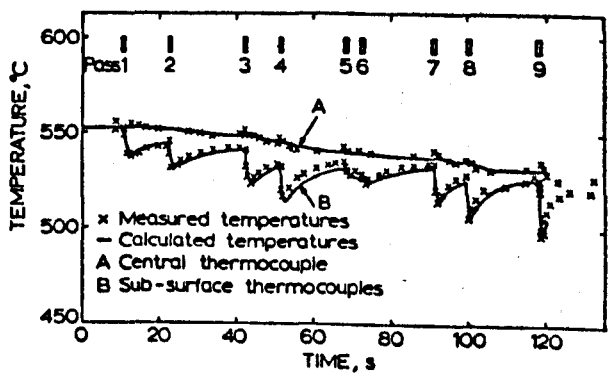

Fig.26 Comparison of temperatures during a multi-pass rolling schedule for aluminium. (After Bradley et al 1970)

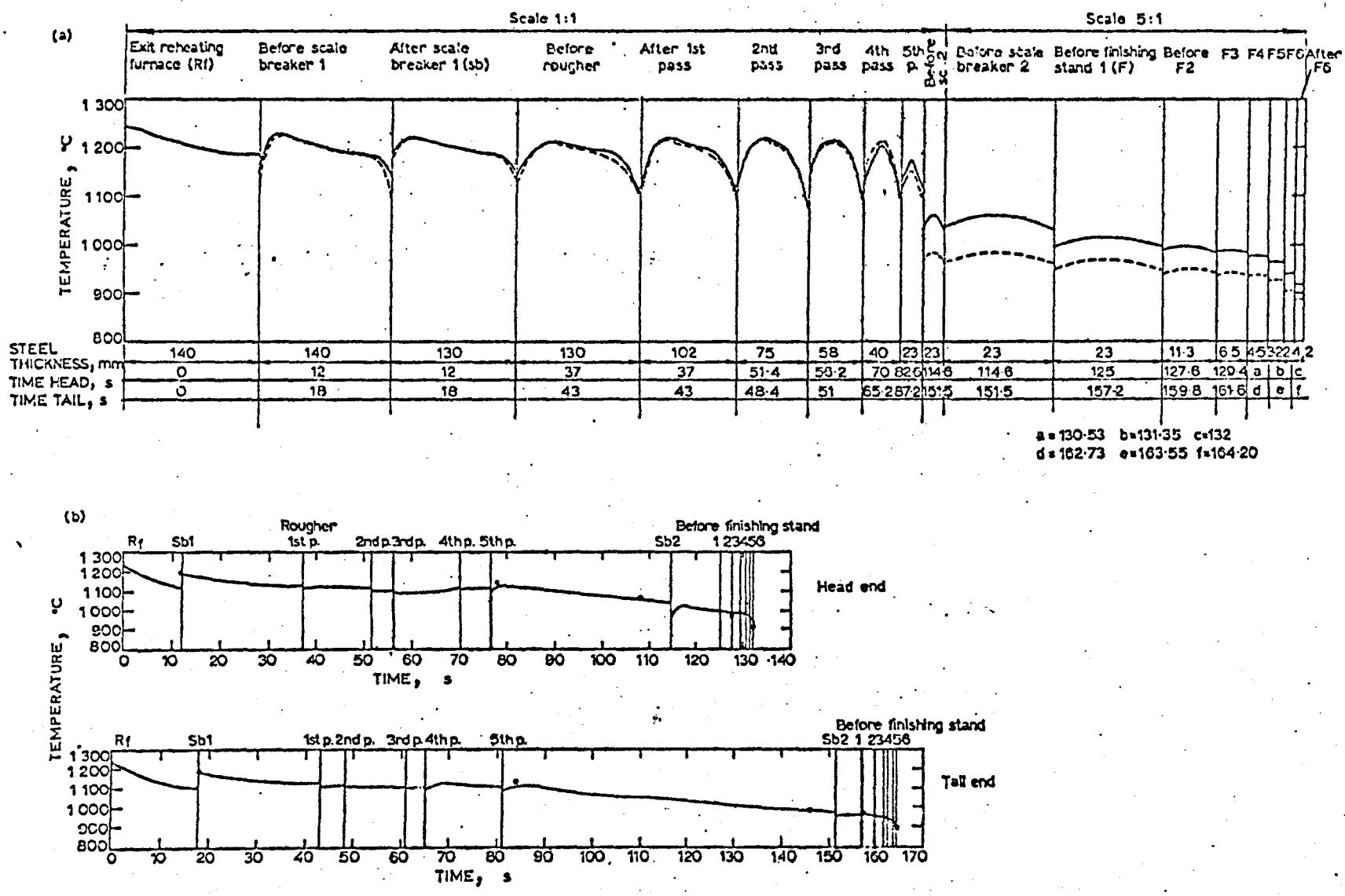

a survey of the calculated temperature distribution in head and tail of the slab for different phases in the process; left: upper side of the slab; right: lower side of slab; continuous line: temperature distribution in the head; dashed line: temperature distribution in the tail

b history of the surface temperature of the head and tail ends of the slab; ● measured temperature

Fig.27 Temperature distribution in a slab during a complete rolling schedule. (After Hollander 1970).

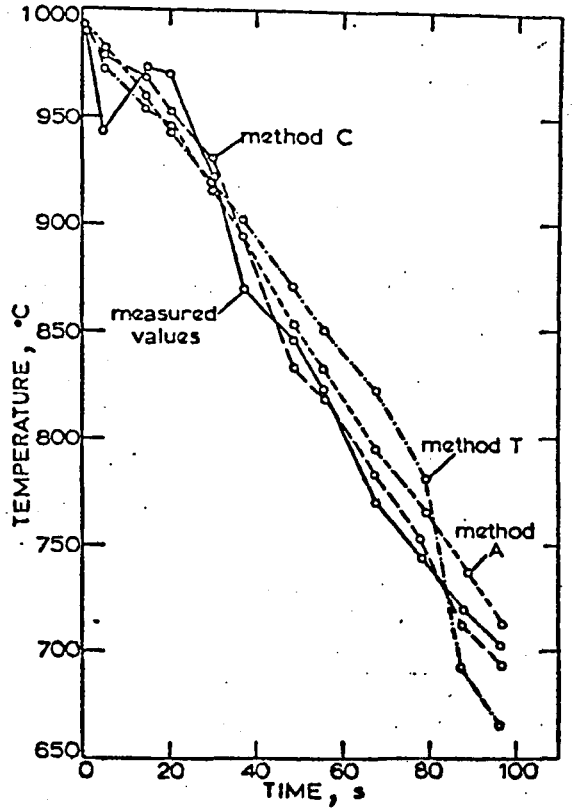

Fig.28 Comparison of measured and calculated temperatures during hot rolling (After Seredynski 1973).

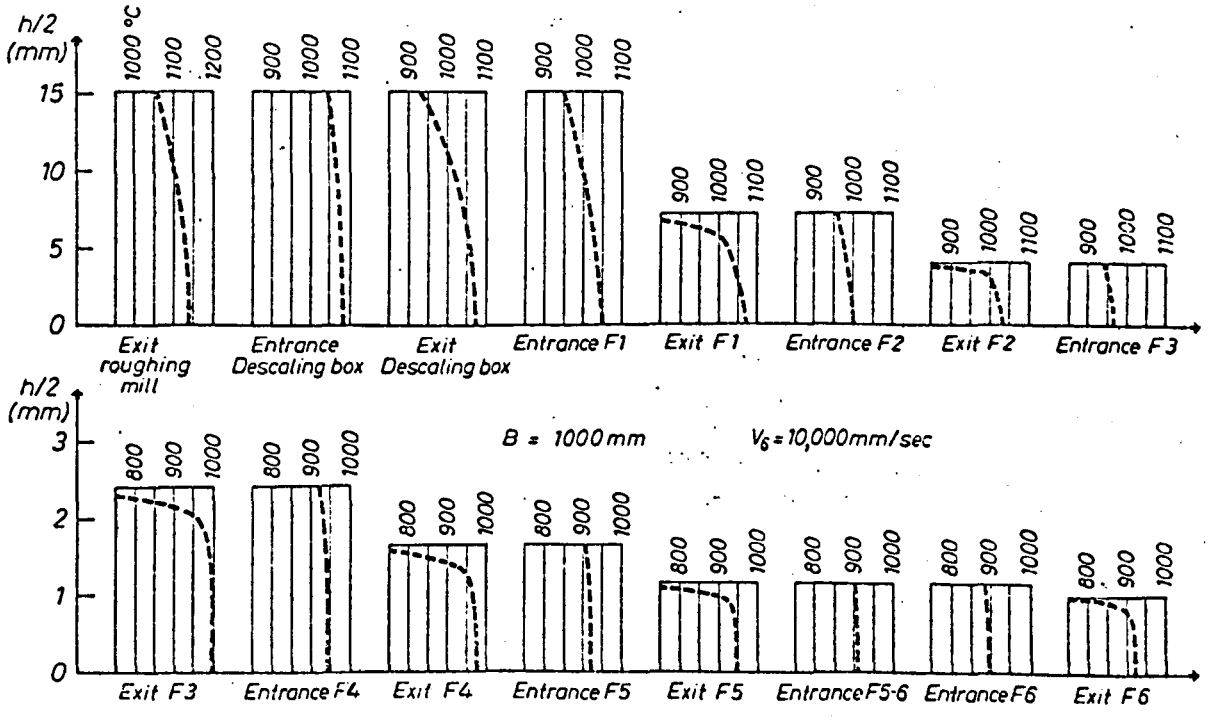

Fig.29 Predicted through thickness temperature distributions for the finishing train of a hot strip mill. (After Wilmotte et al 1973A).

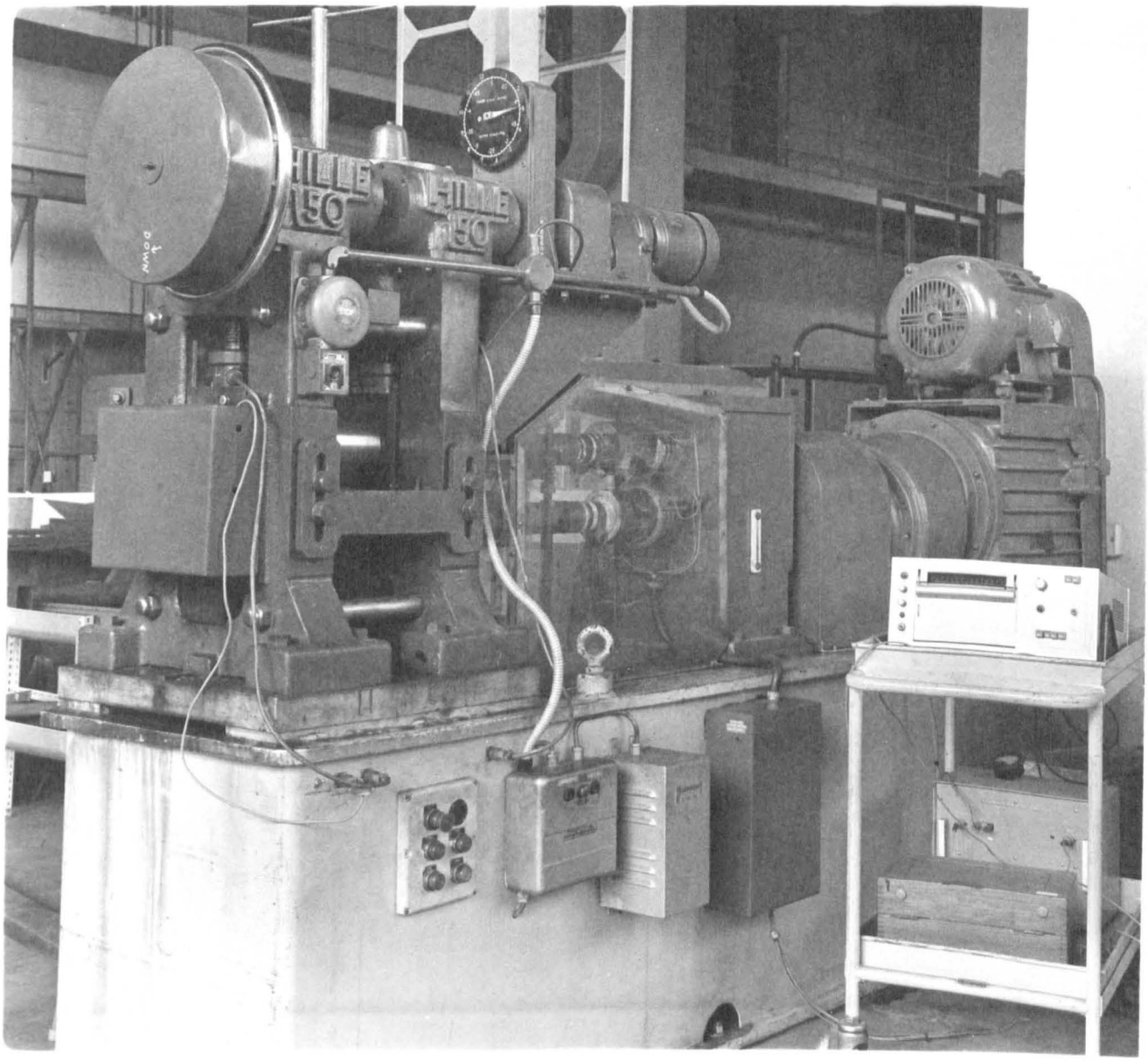

Fig.30 The fully instrumentated Hille 50 rolling mill.

Fig.31 The modified tongs used in the hot rolling experiments.

Fig.32 The grid machined onto the longitudinal section of a stainless steel slab (x 2)

Fig.33 The deformed grid following a 30% pass (x 3)

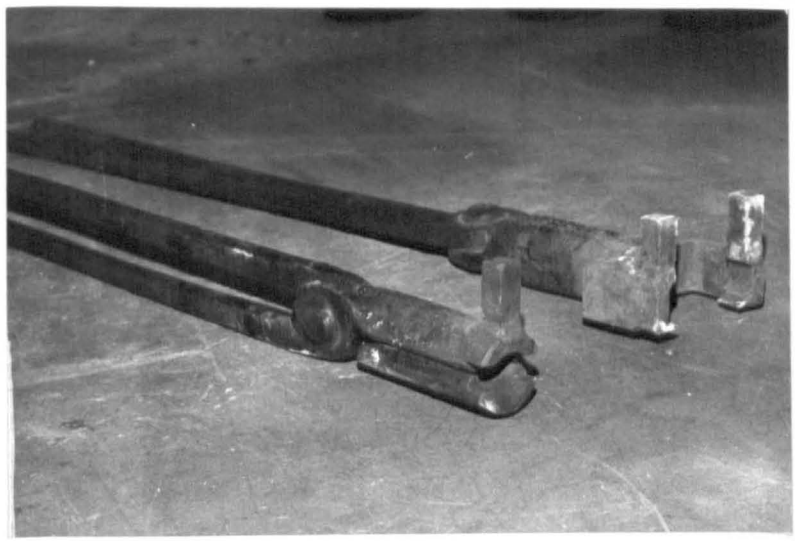

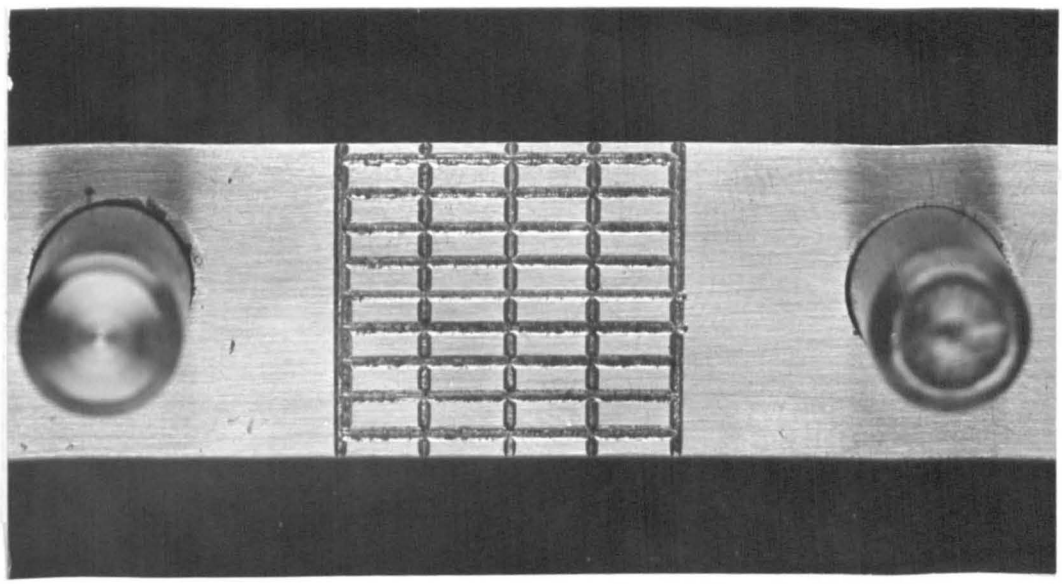

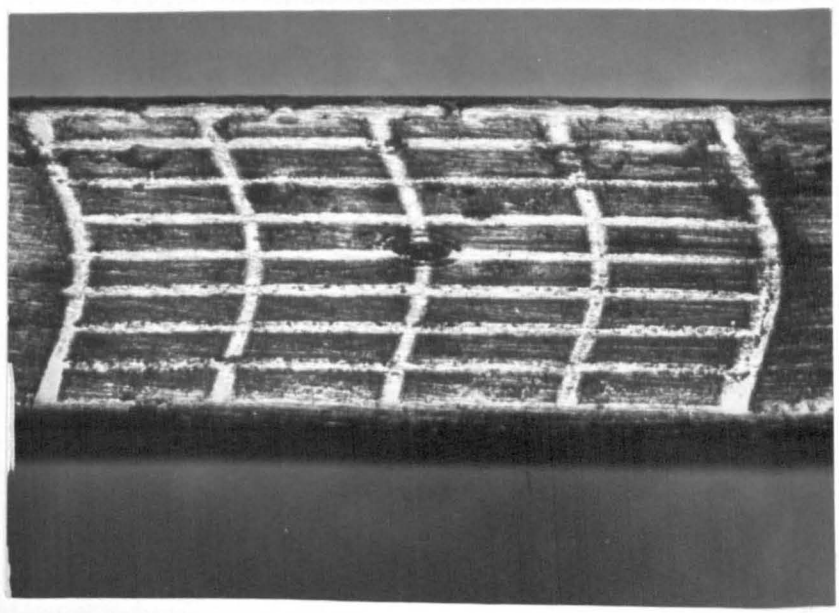

Fig.34 The experimental arrangement for air cooling tests on flat slabs.

Fig.35 The experimental arrangement for air cooling tests on round billets.

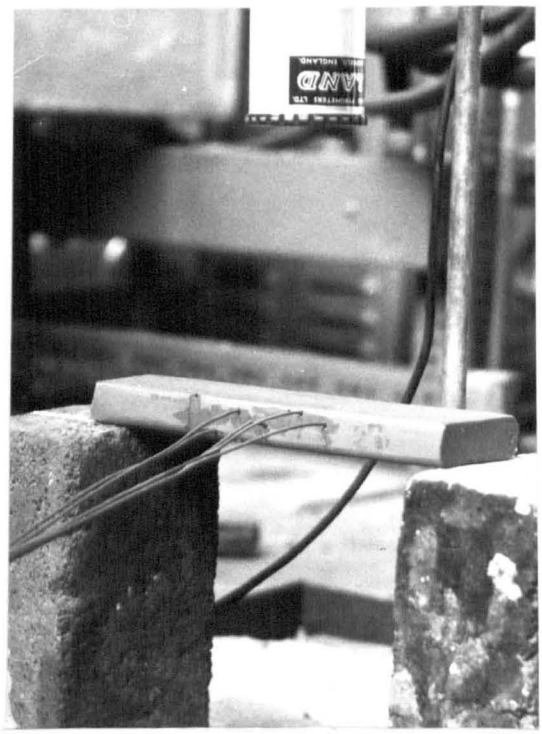

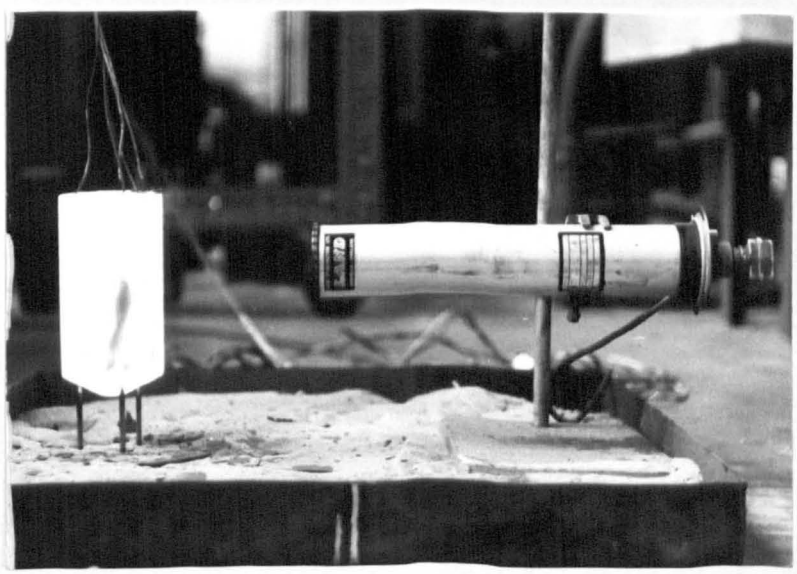

Fig.36 The torsion test specimen
(all dimensions in mm.)

Fig.37 The hot torsion machine

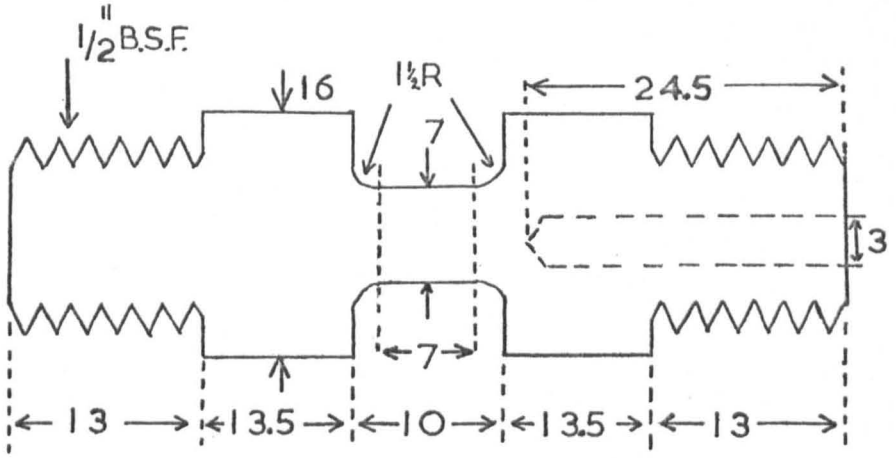
1/2" B.S.F.
16
1½R
24.5
7
3
7
13
13.5
10
13.5
13

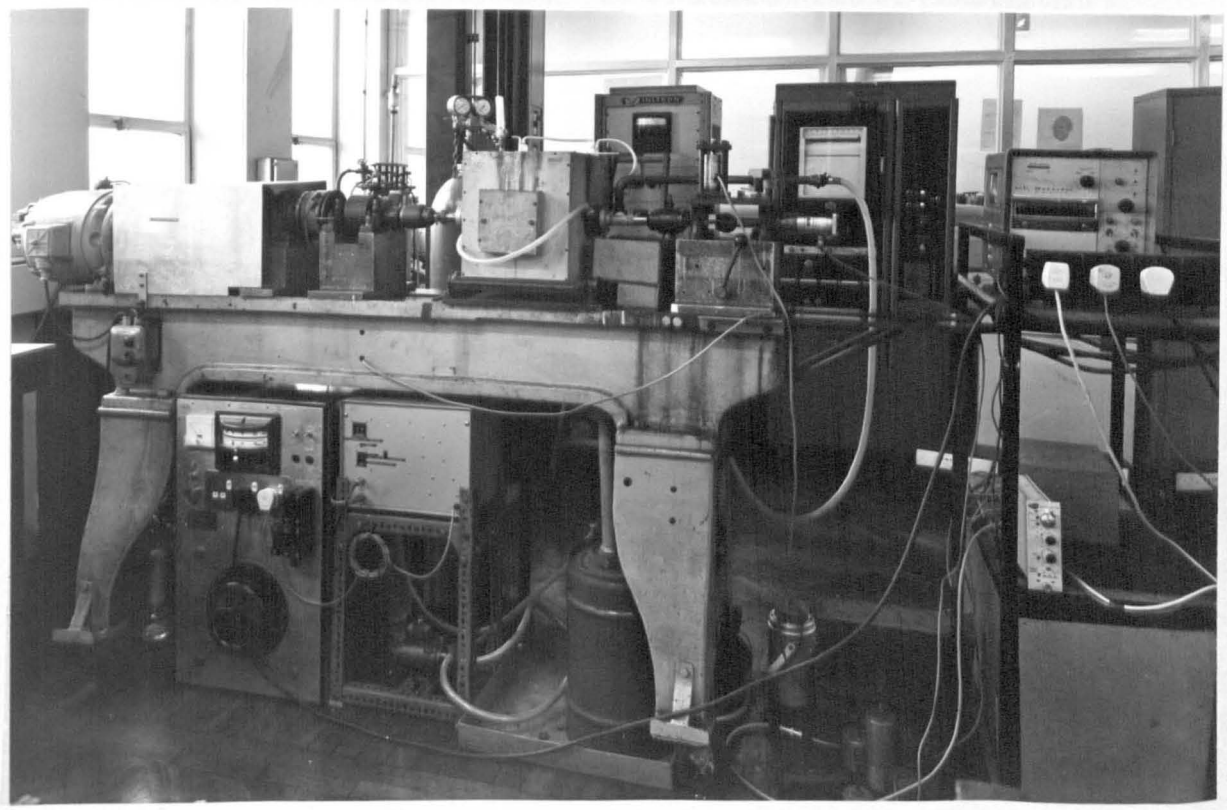

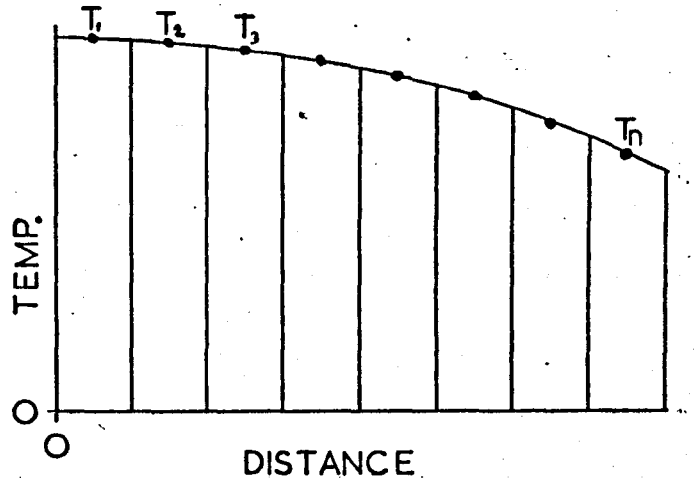

Fig.38 The finite difference approximation of a one dimensional temperature gradient.

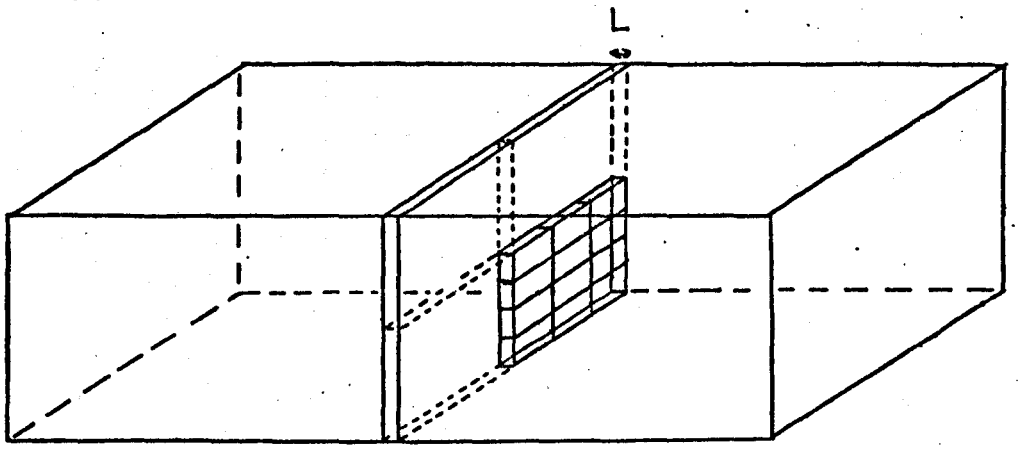

Fig.39 Subdivision of a slab into representative elements.

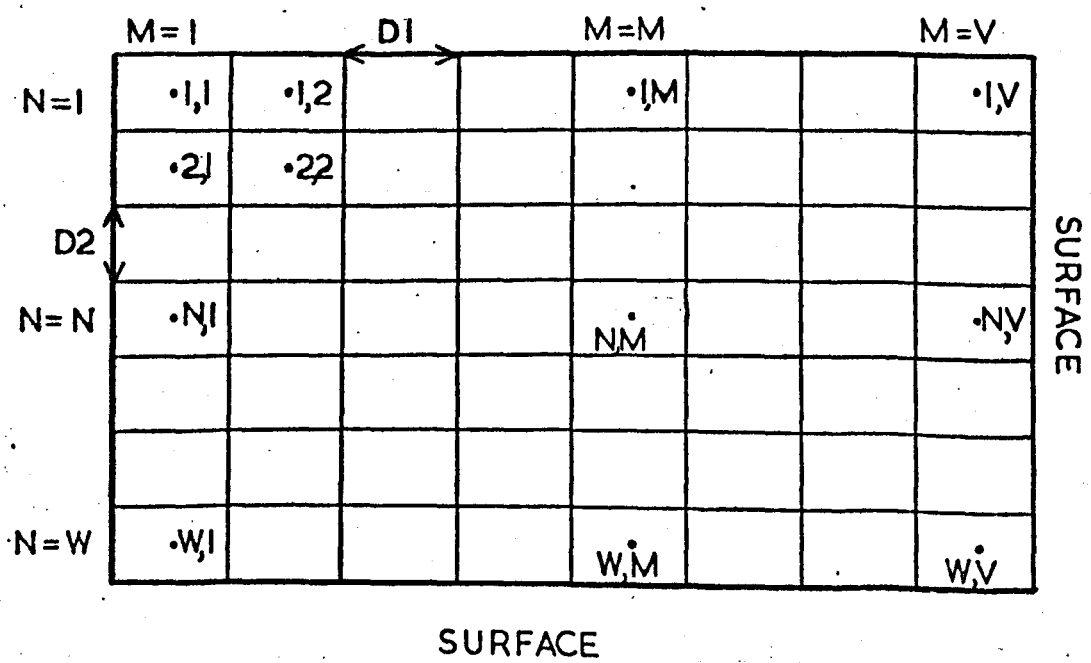

Fig.40 Matrix notation and dimensions of slab elements.

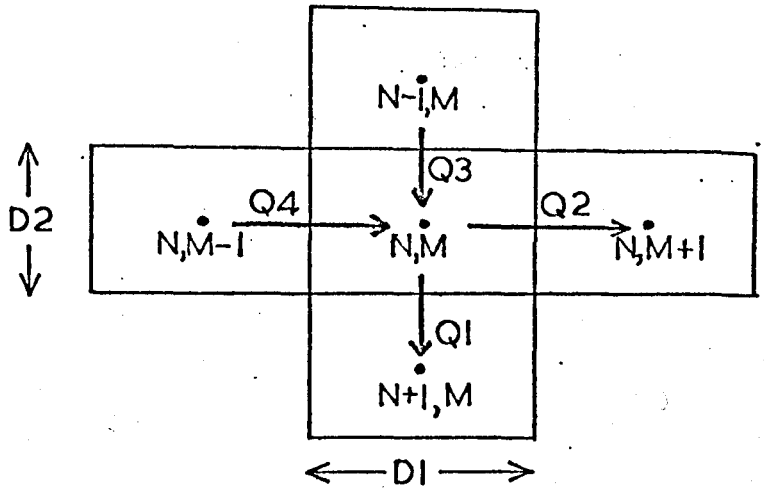

Fig.41 Heat flow between the N,M element and its four nearest neighbours. (Length of element perpendicular to paper= L).

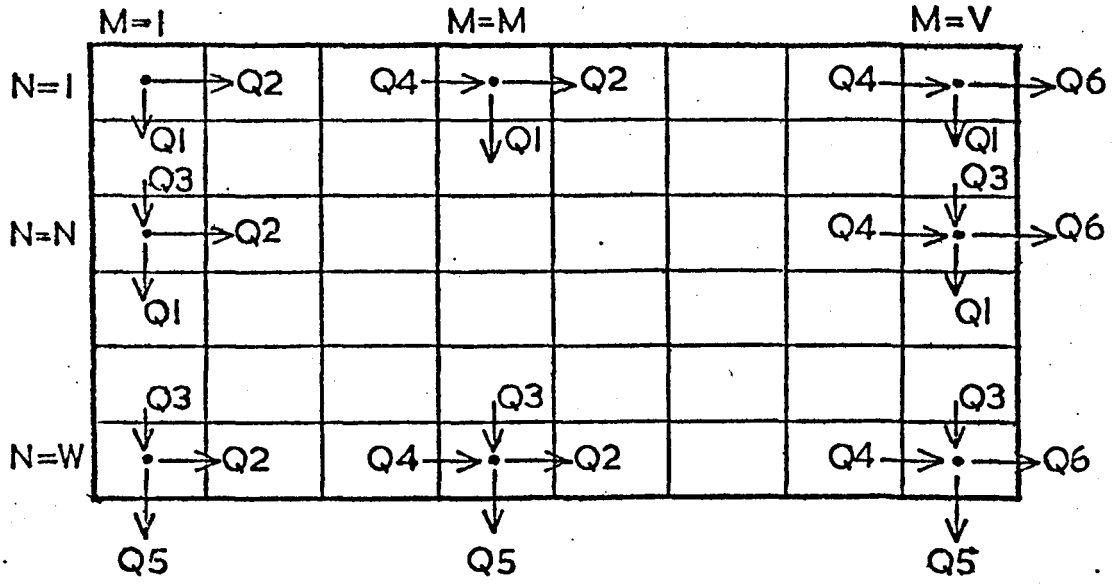

Fig.42 Values of $\sum Q$ for different slab elements.

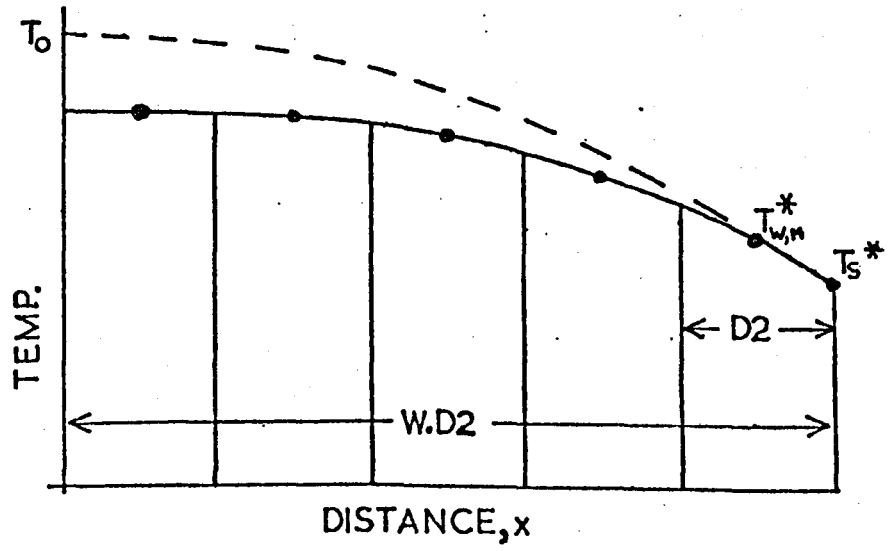

Fig.43 Extrapolation to obtain T_s^* from $T_{W,M}^*$ (Mth.column)

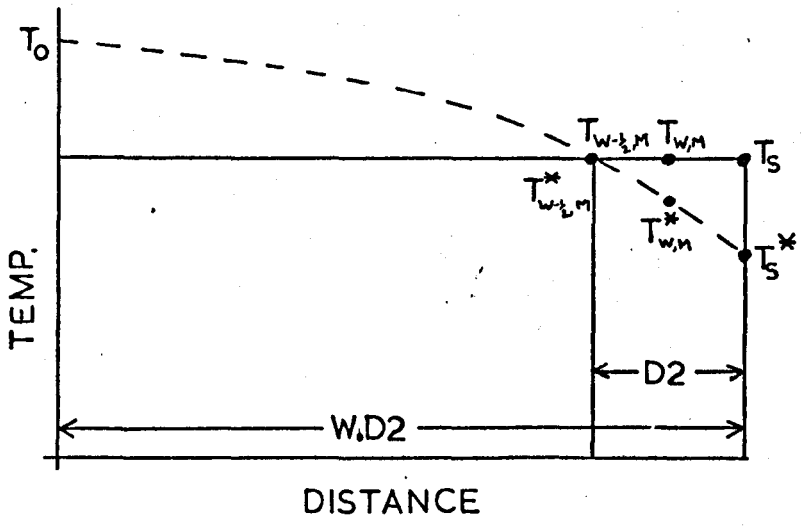

Fig.44 Basis of stability criterion during air cooling using assumptions of Method A.

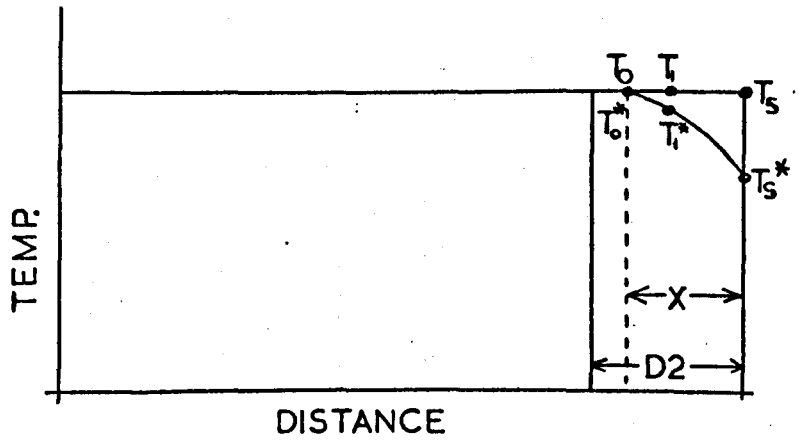

Fig.45 Basis of stability criterion using assumptions of Method B.

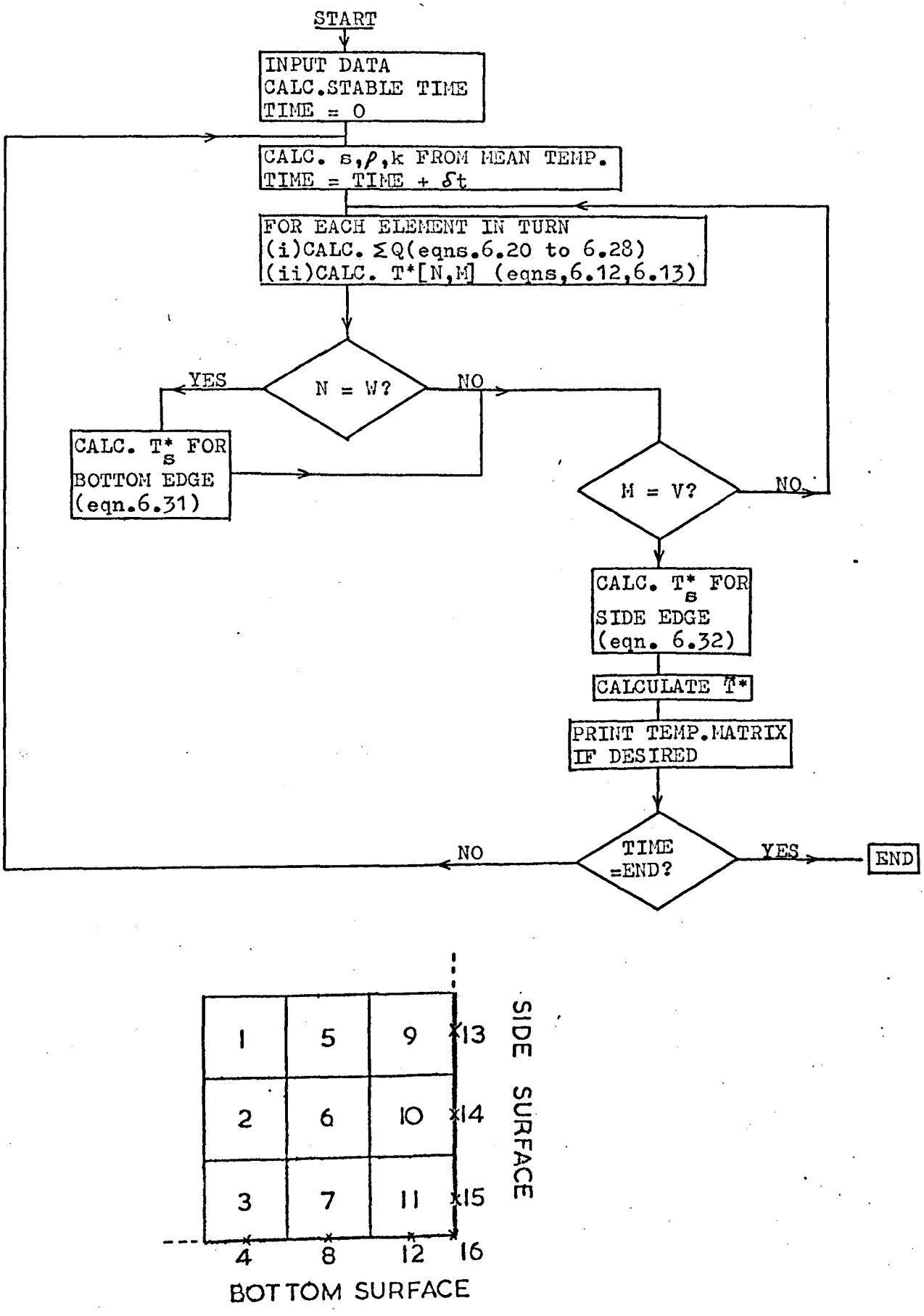

Fig.46 Flow chart and order of computation for a 3x3 matrix during air cooling.

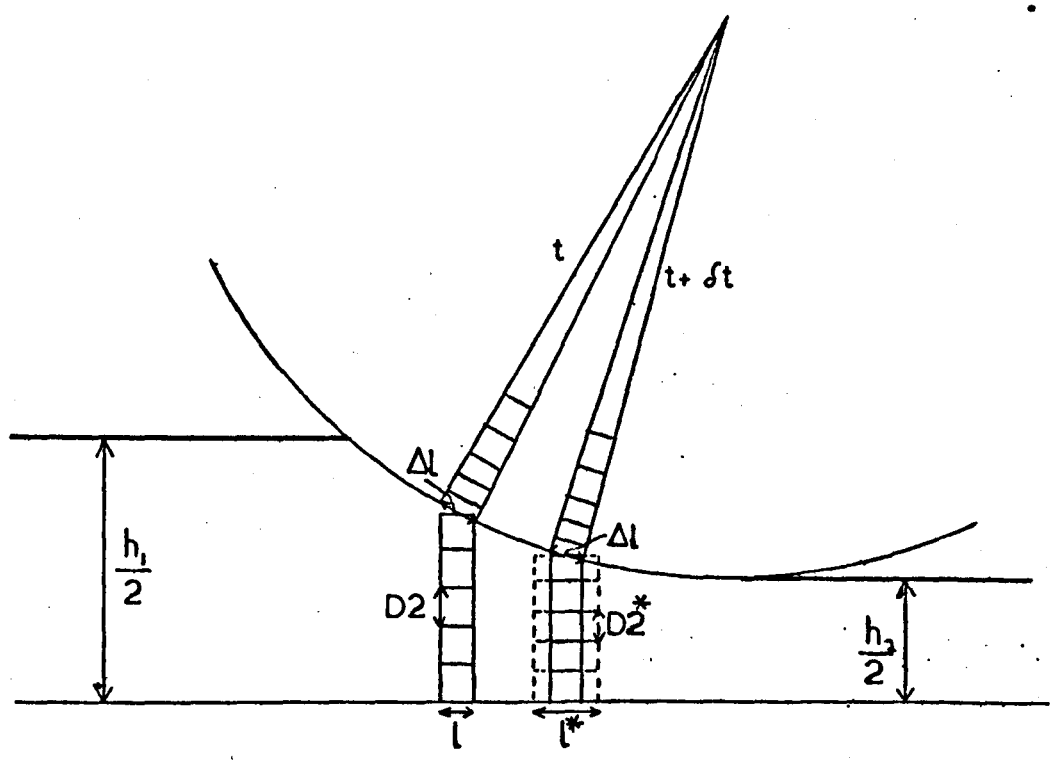

Fig.47 Slab dimensional changes during rolling.

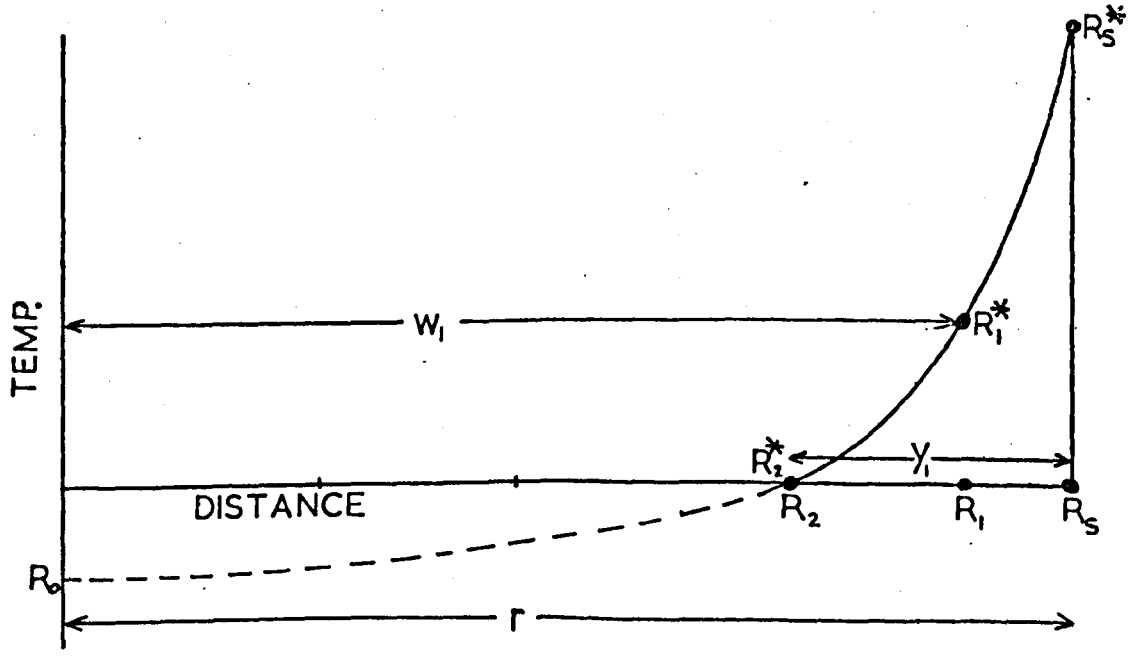

Fig.48 Basis of stability criterion for roll.

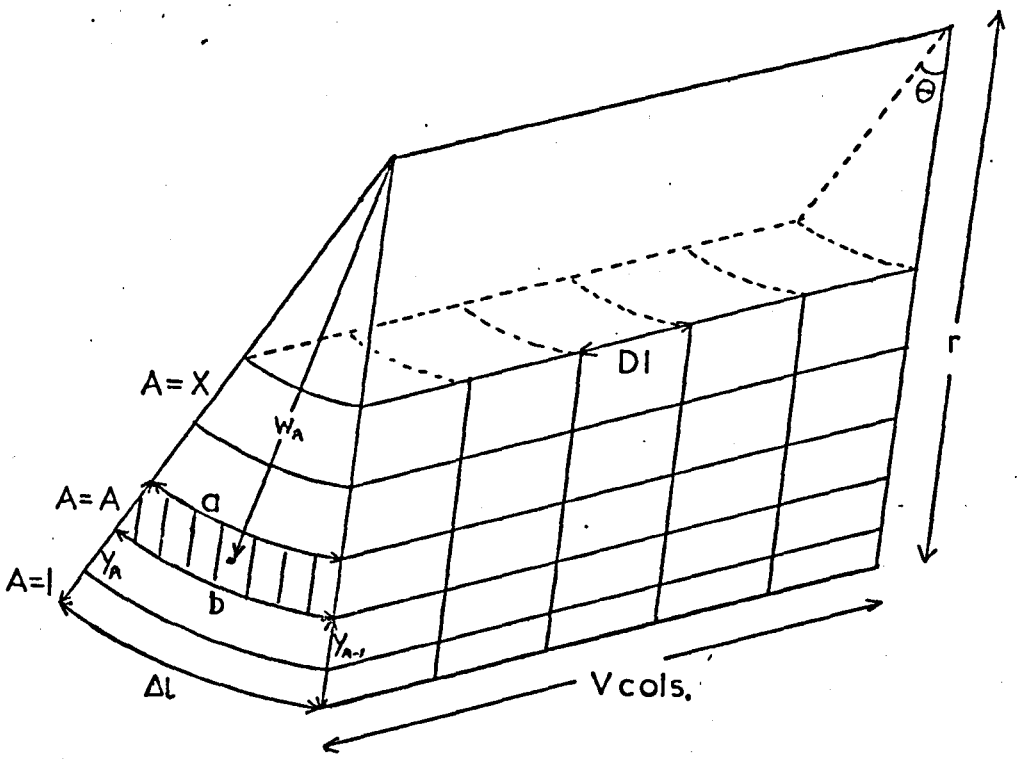

Fig.49 Representation of 'slice' of roll.

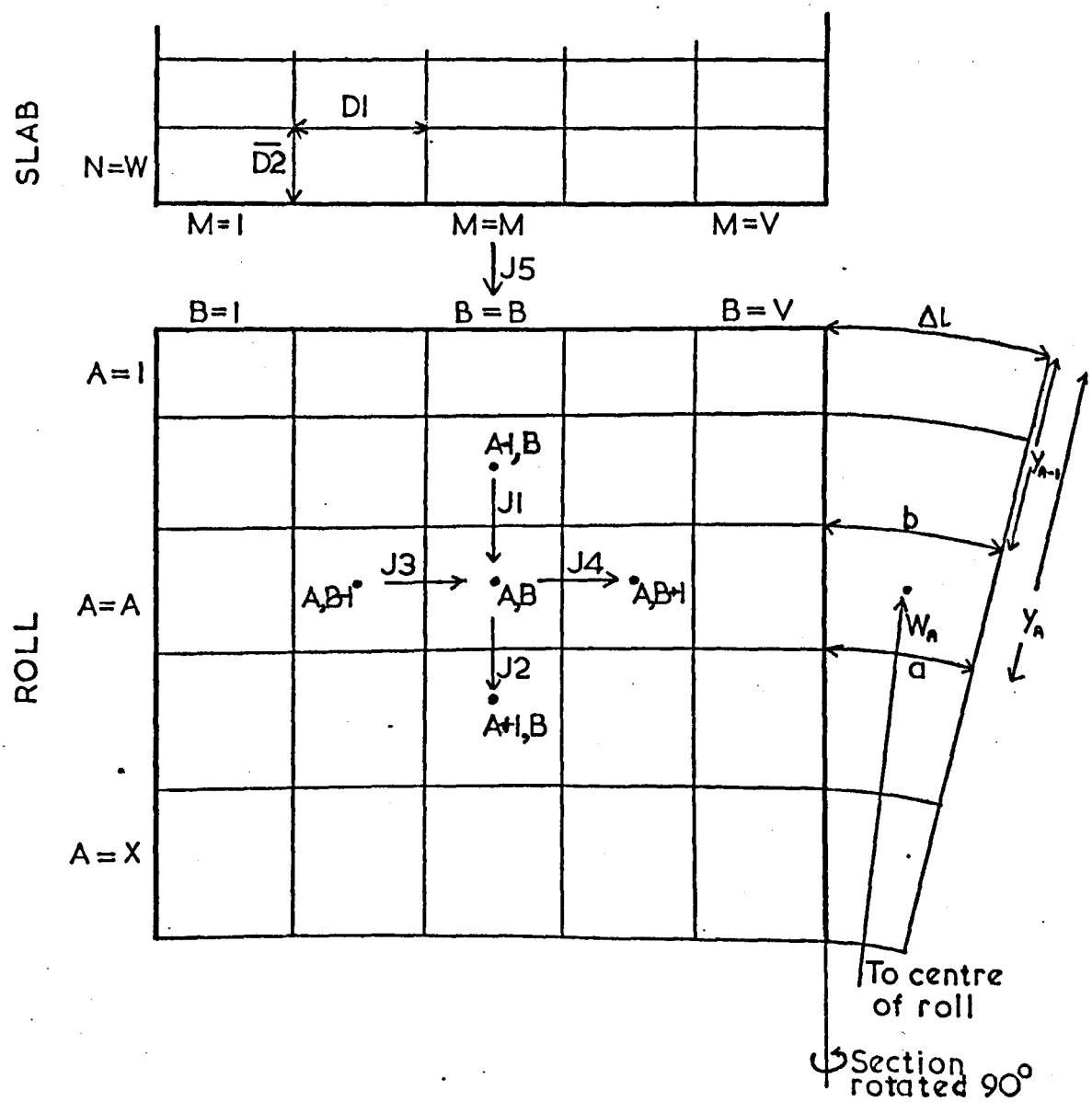

Fig.50 Heat flow within roll.

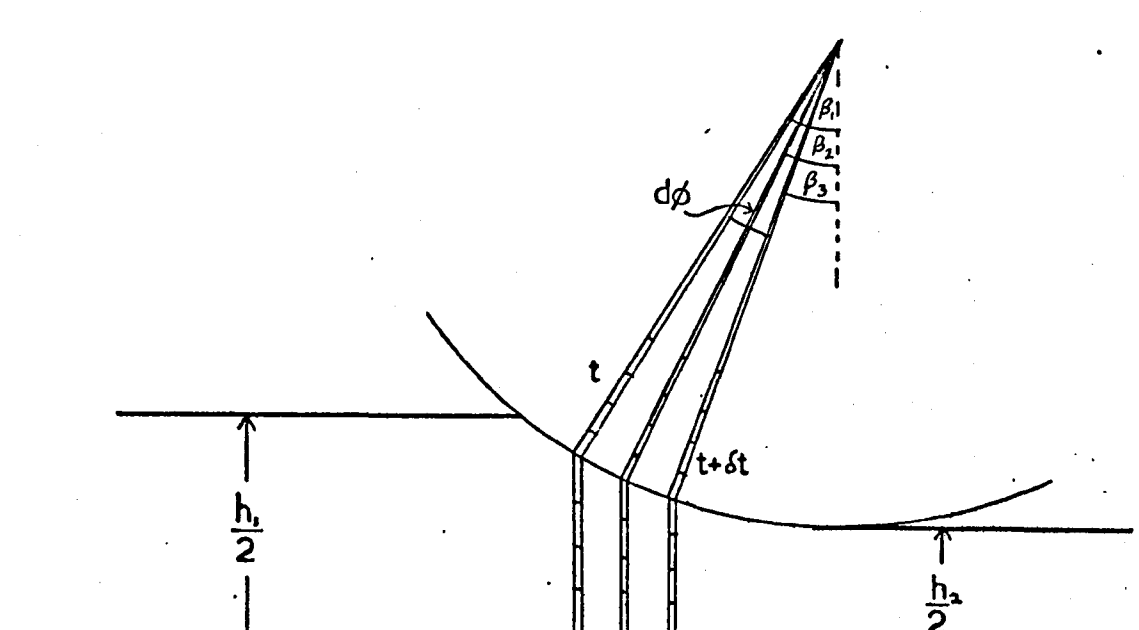

Fig.51 Change in slab element height with time and β.

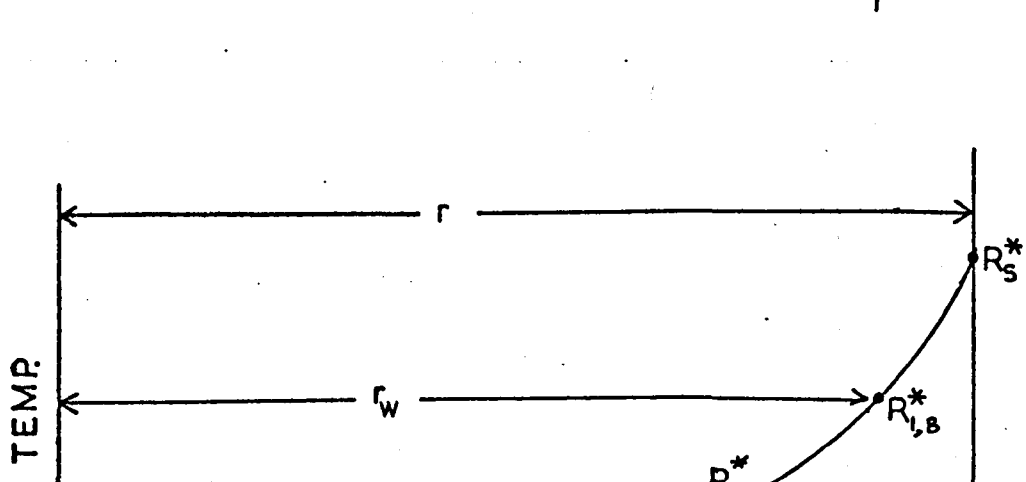

Fig.52 Extrapolation to obtain the true roll surface temperature.

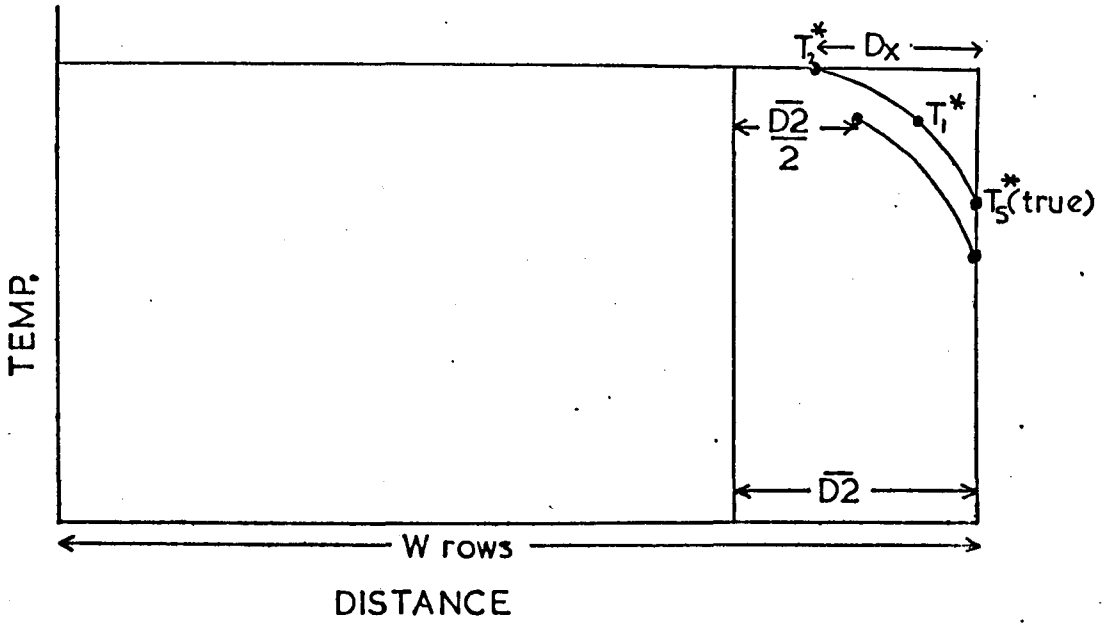

Fig.53 Penetration of temperature gradient into surface of slab.

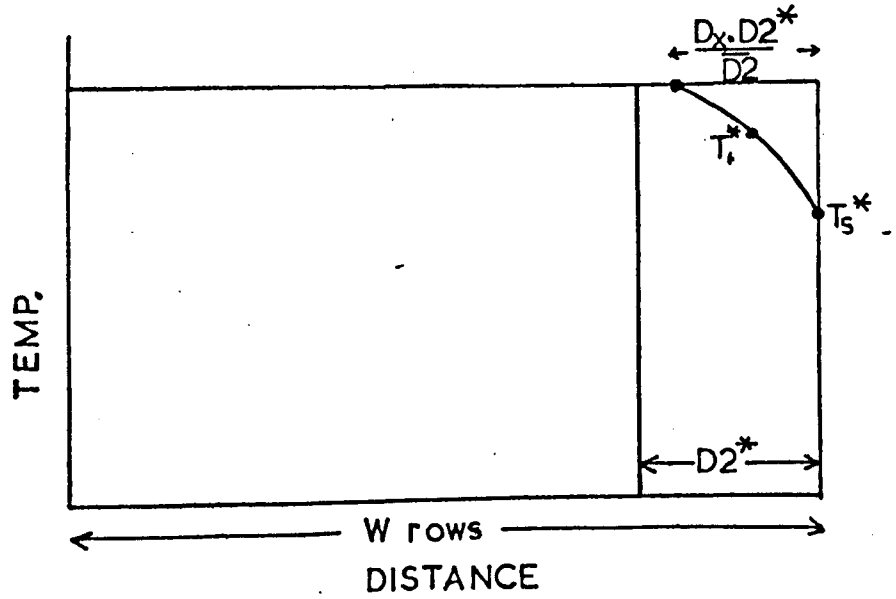

Fig.54 Extrapolation to obtain the true slab surface temperature during rolling.

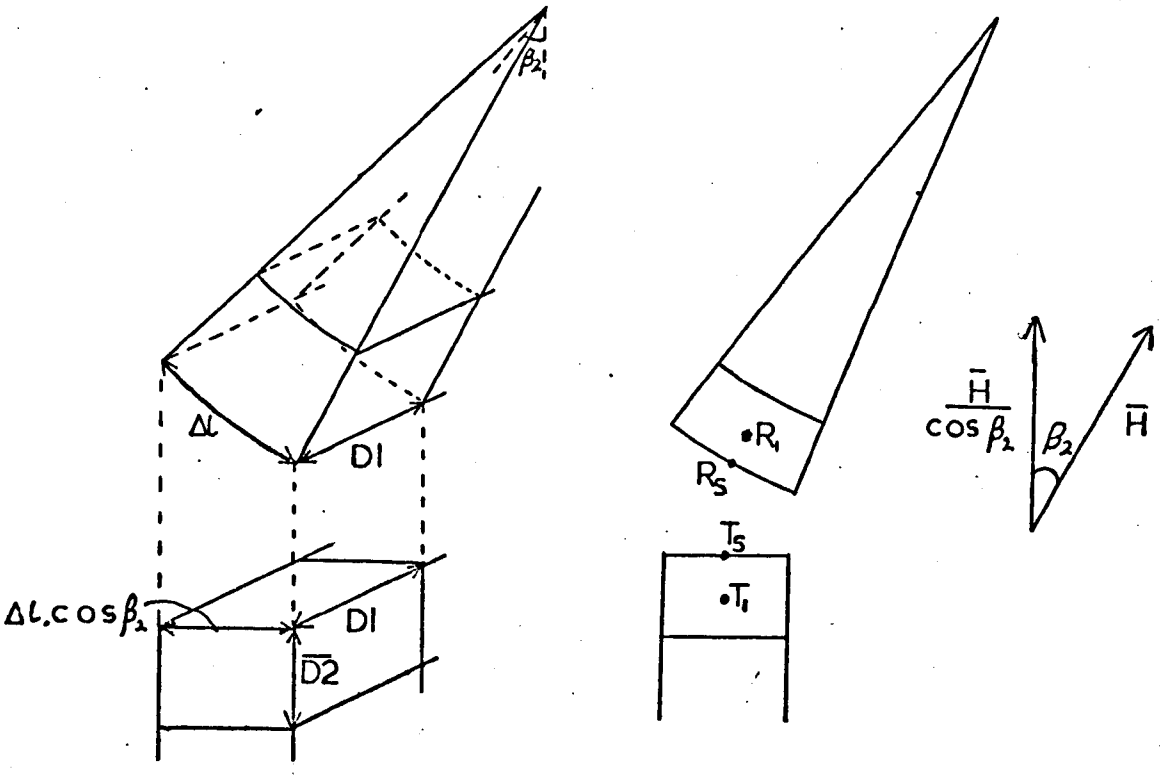

Fig.55 Heat transfer between the surface elements of slab and roll.

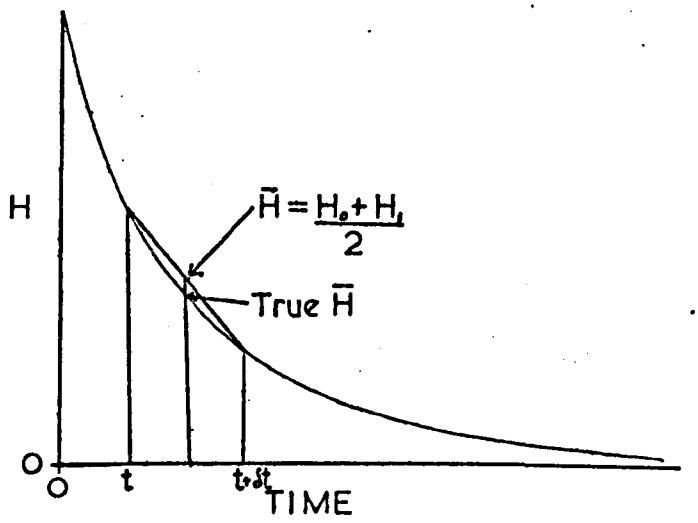

Fig.56 Estimation of mean heat transfer coefficient between slab and roll for the time interval δt.

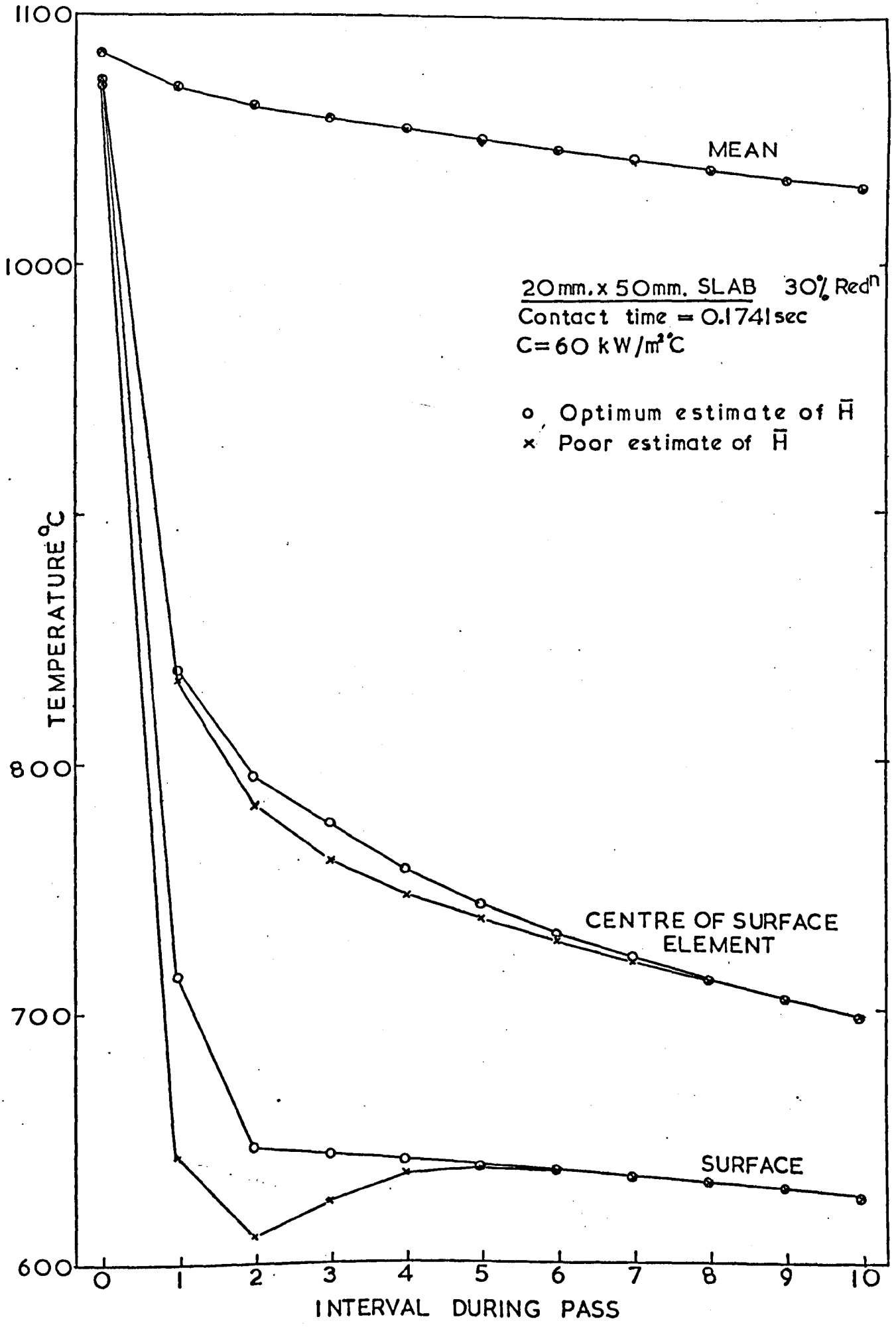

Fig.57 Effect of method of estimating $\bar{H}$ on the temperatures during a pass: low value of C.

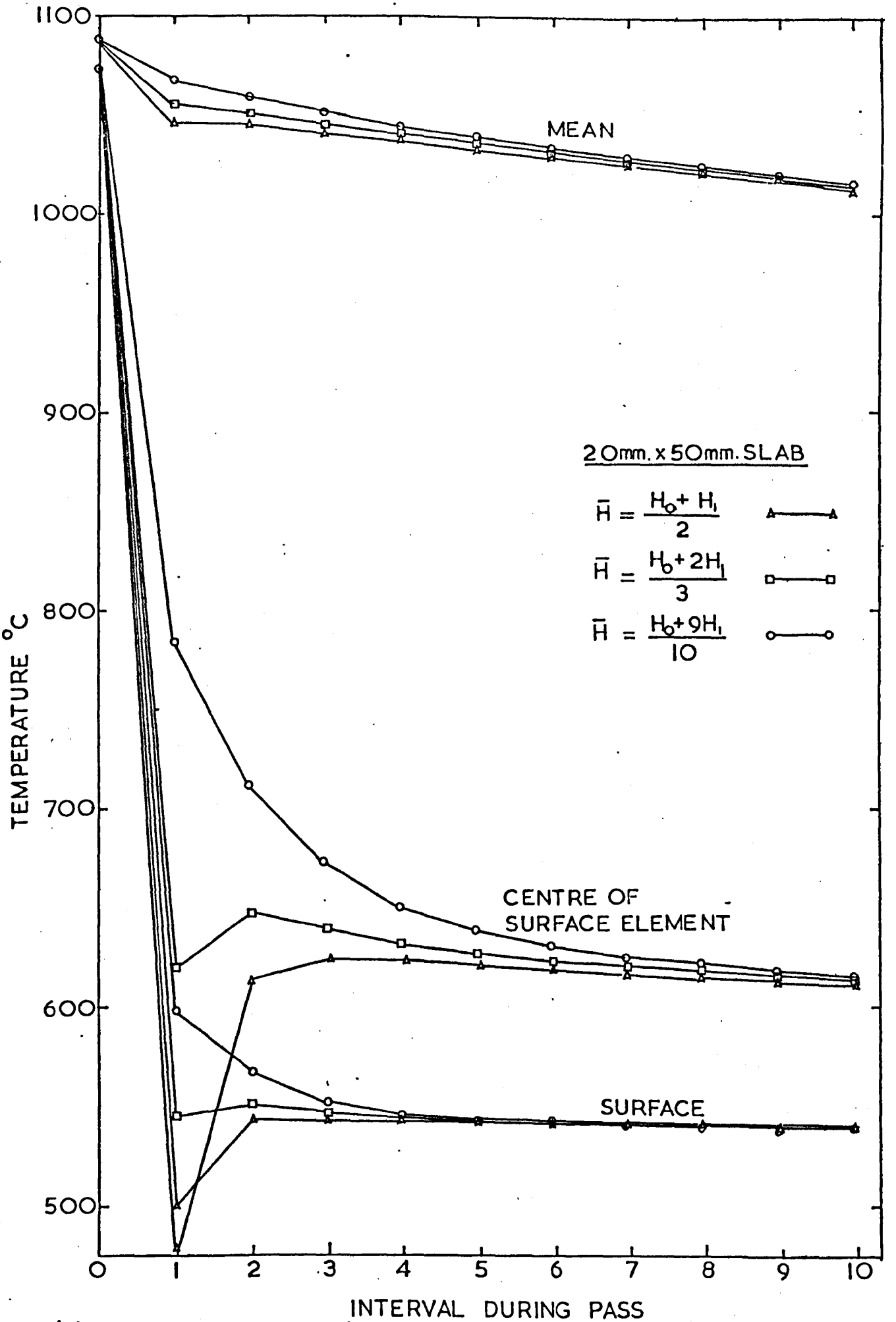

Fig.58 Effect of method of estimating $\bar{H}$ on the temperatures during a pass:high value of C.

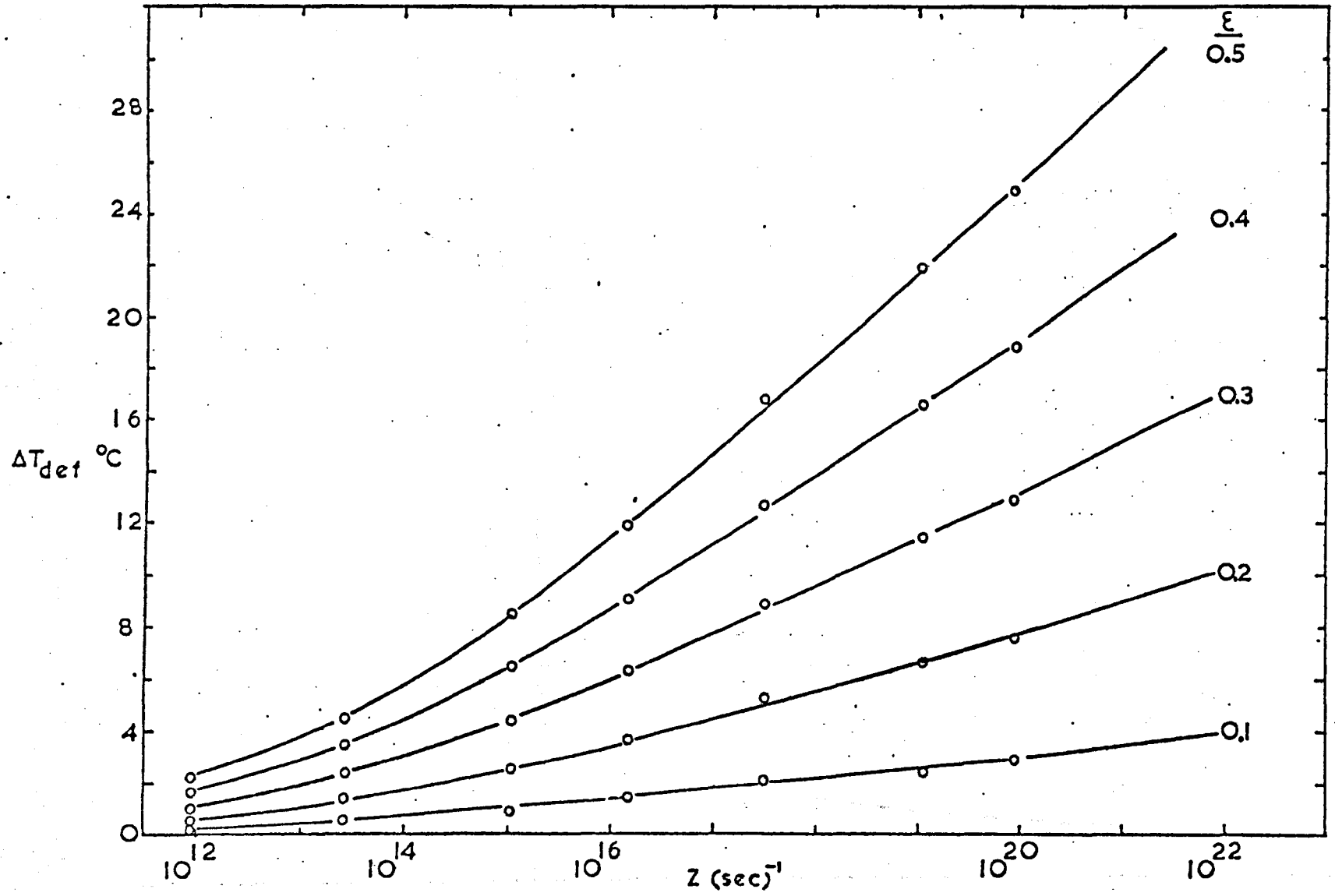

Fig.59 Predicted deformational heating effect as a function of Z (data from Barraclough 1974).

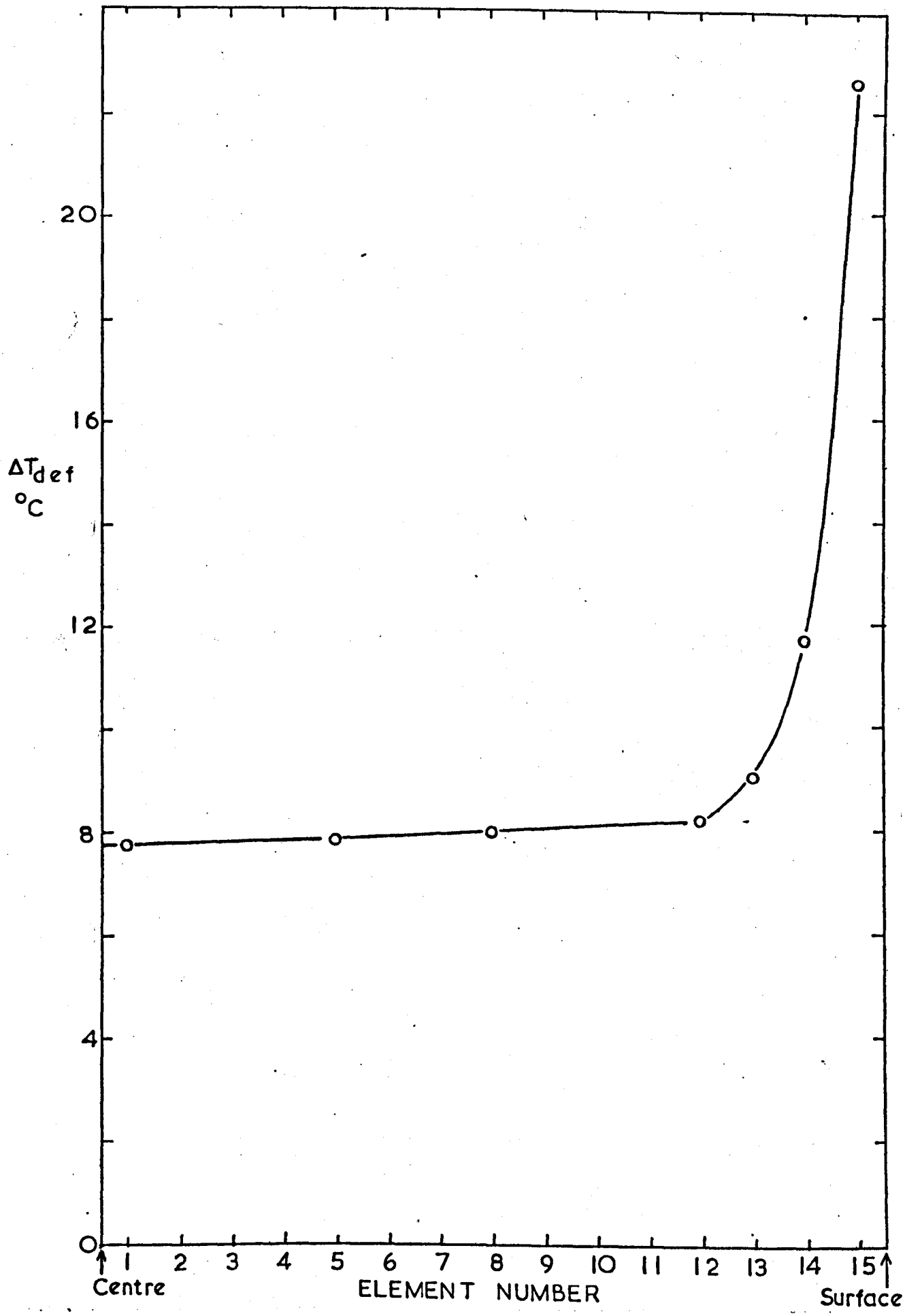

Fig.60 Predicted distribution of deformational temperature rise through the slab thickness during a 30% pass.

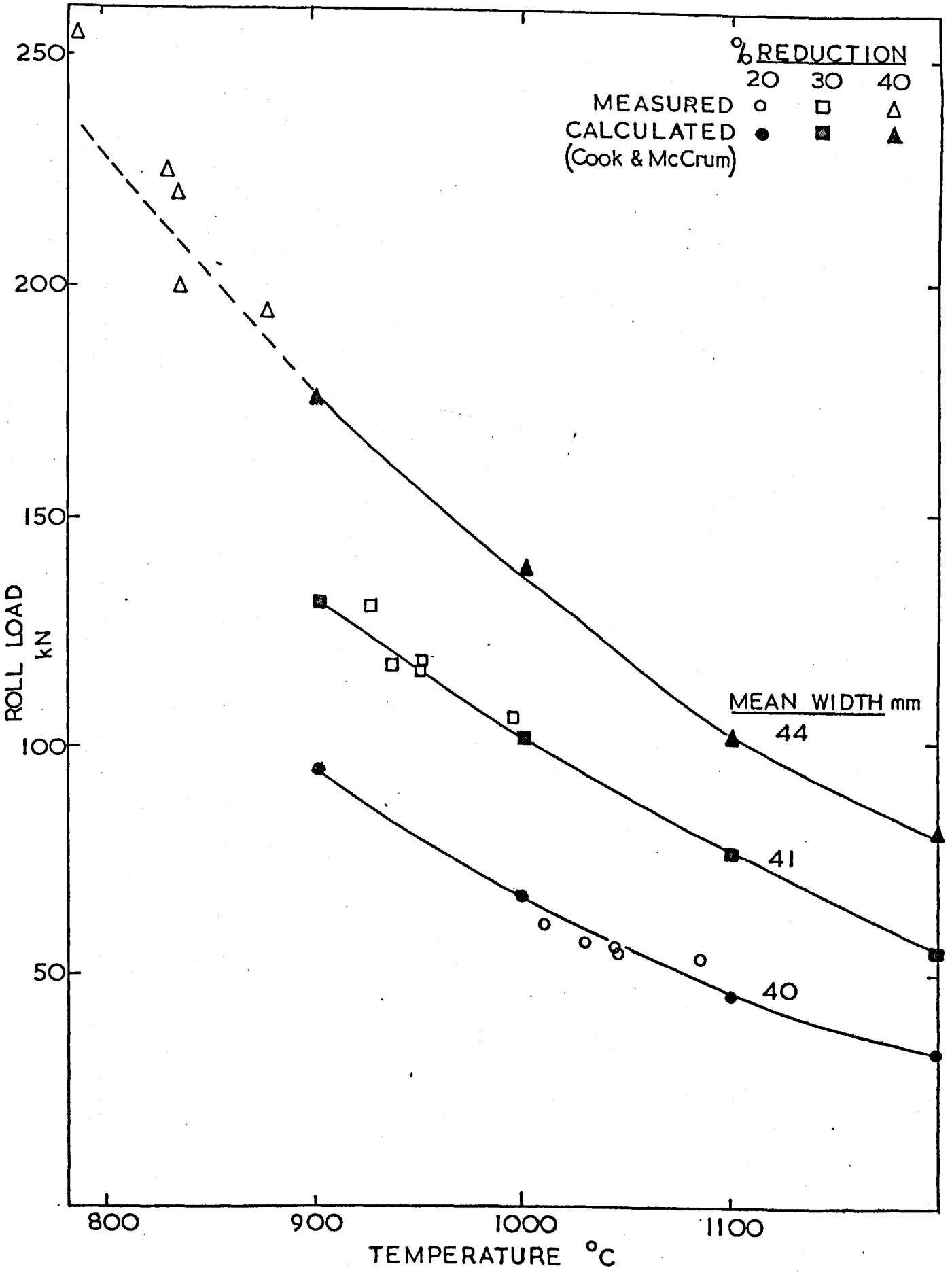

Fig.61 Roll load as a function of temperature (at the centre of slabs at entry to the rolls)for the hot rolling of mild steel;comparison with the data of Cook and McCrum.

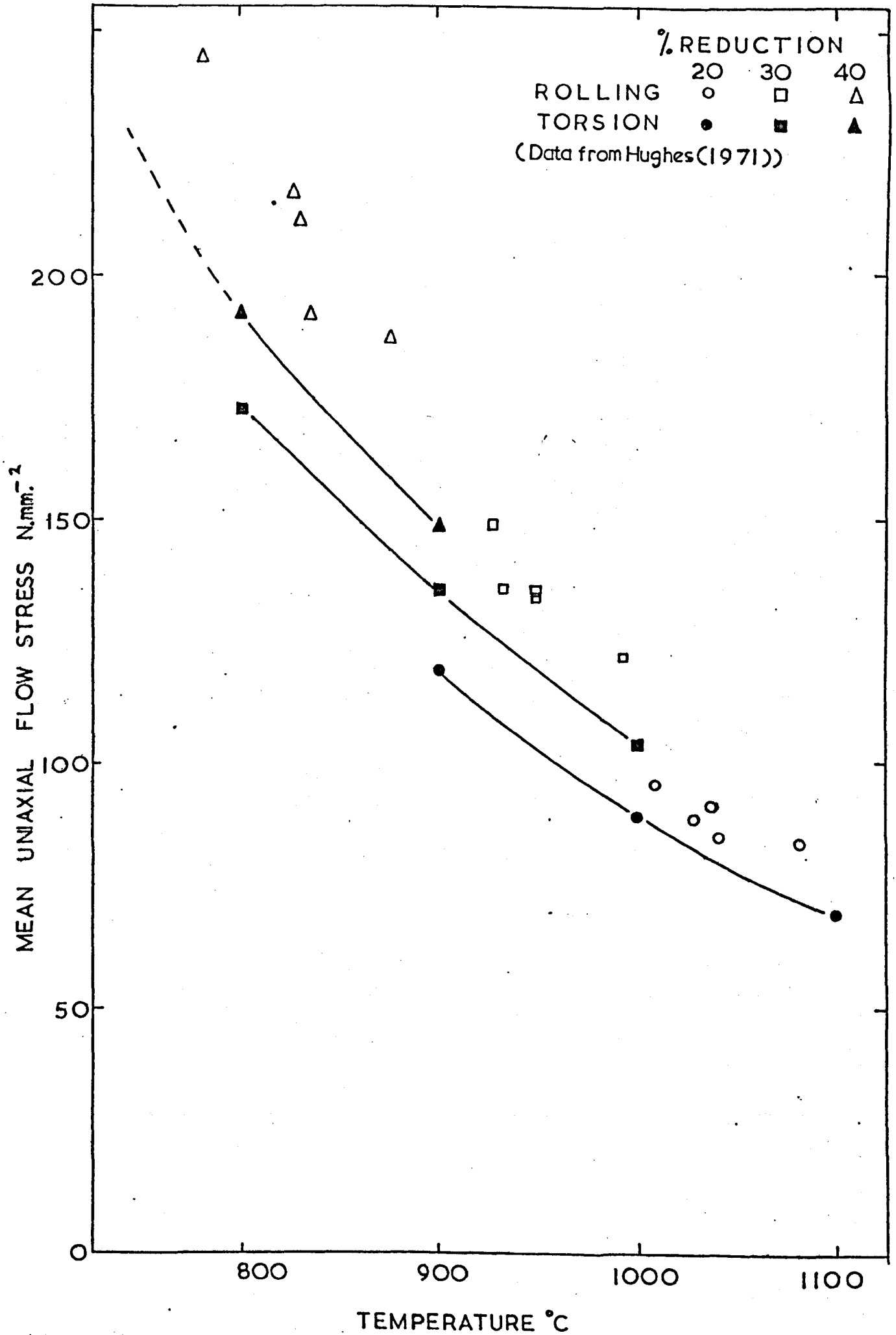

Fig.62 Mean uniaxial flow stresses derived from measured roll loads during mild steel rolling schedules; comparison with the torsional data of Hughes (1971).

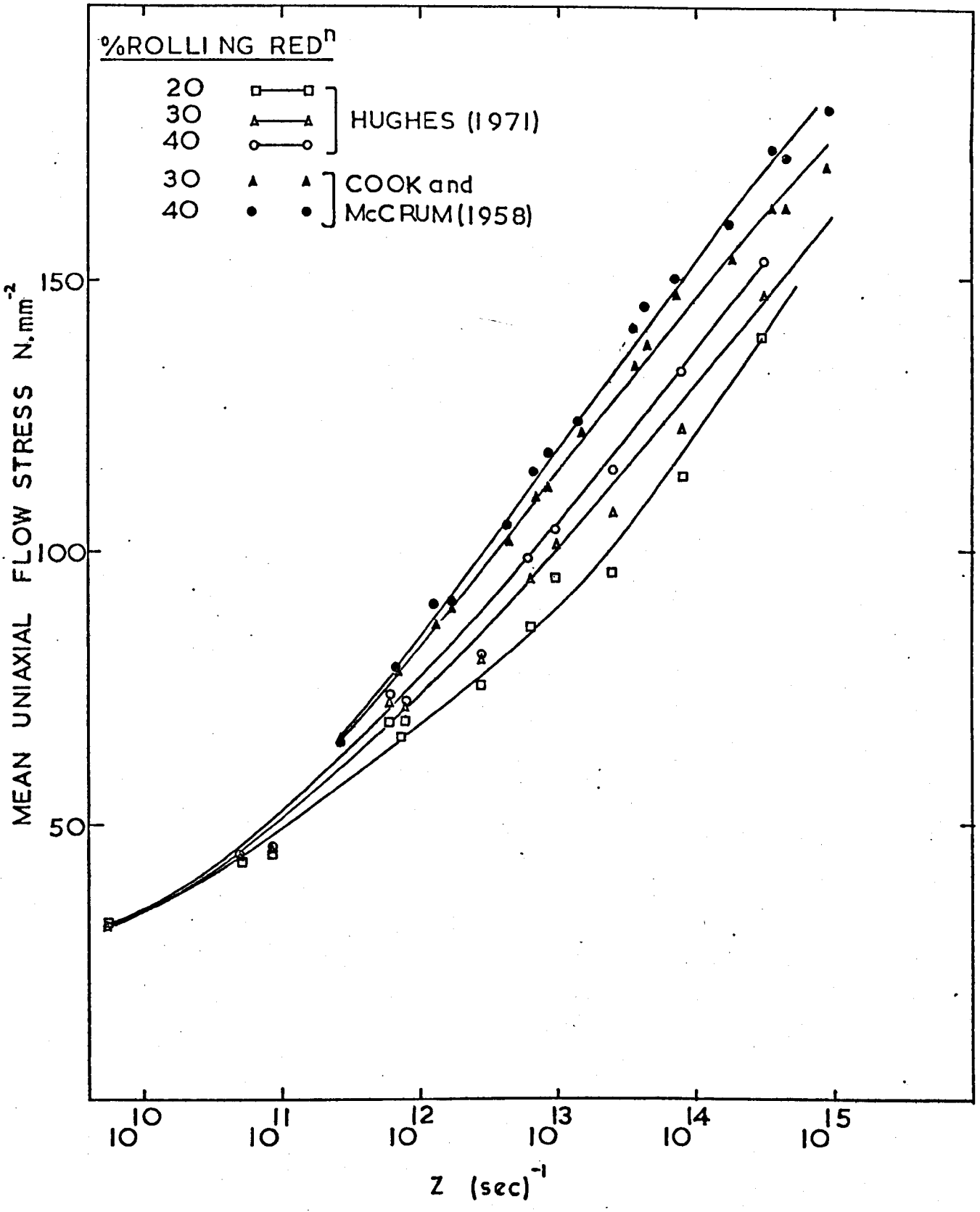

Fig.63 Comparison of mean uniaxial flow stresses for mild steel derived from the data of Cook and McCrum(1958) and Hughes(1971).

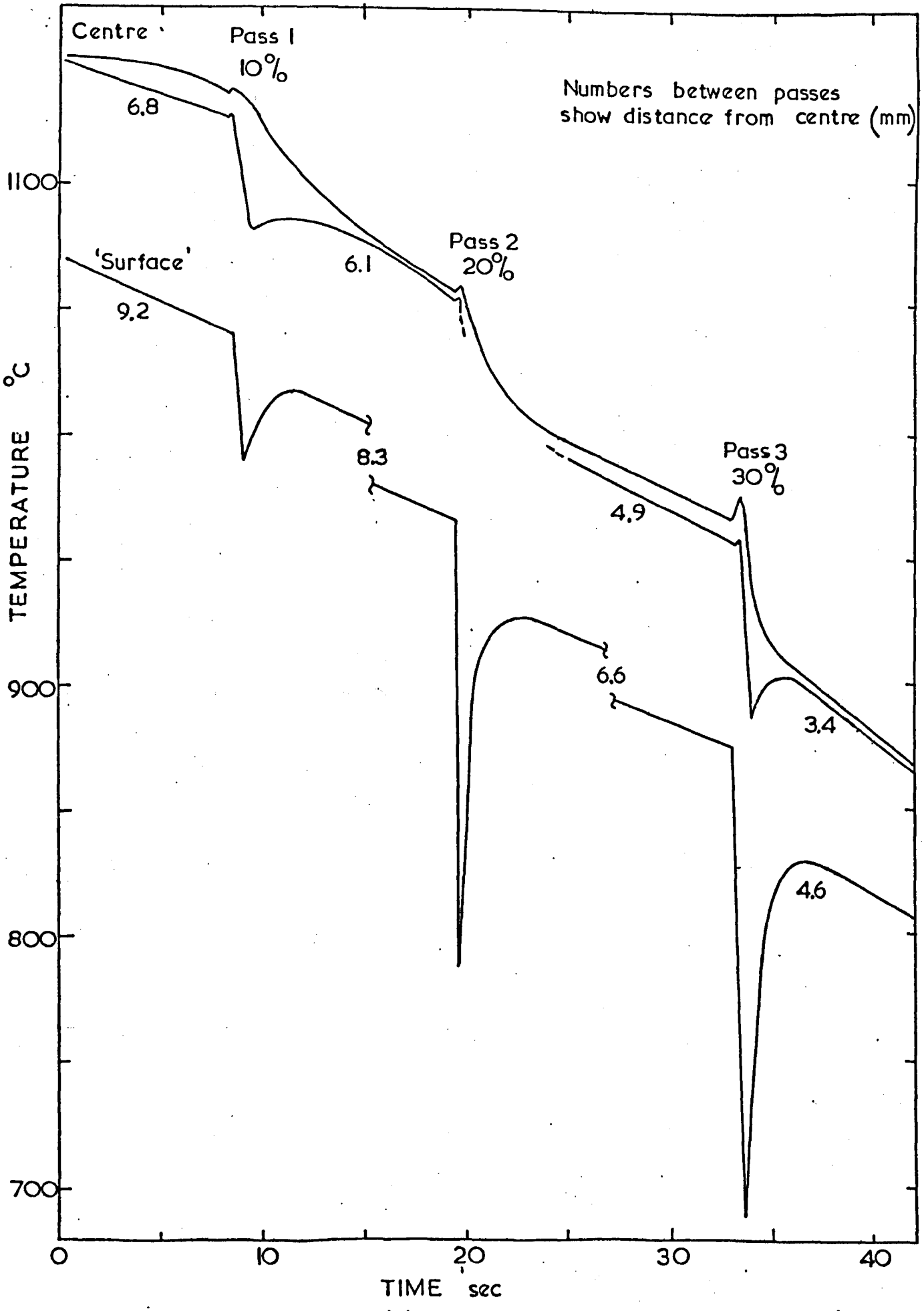

Fig.64 Typical temperature-time curves for mild steel hot rolling schedules.

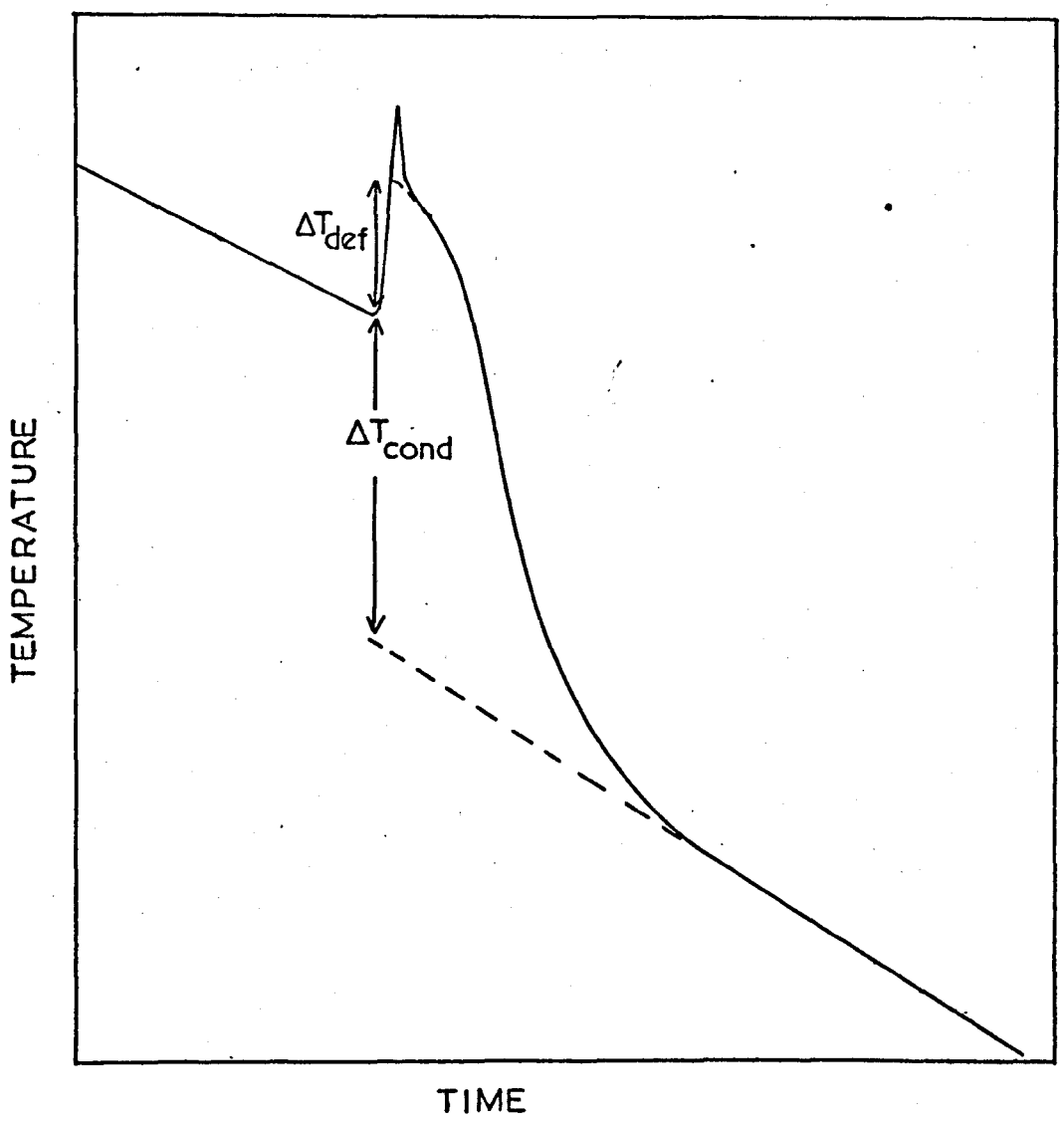

Fig.65 Extrapolation to obtain the temperature at the centre of the slab on exit from the rolls and the temperature drop due to conduction.

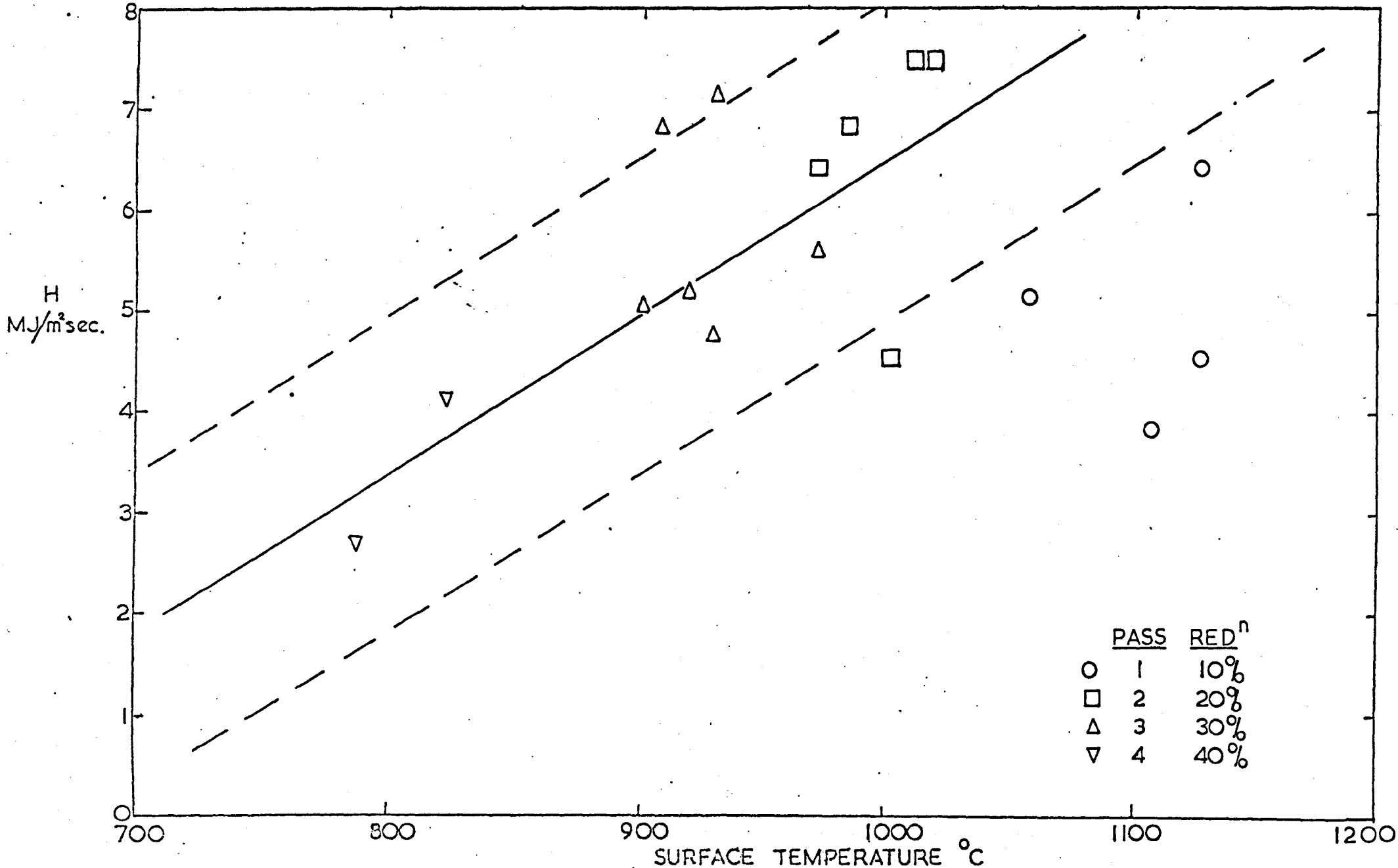

Fig.66 Heat conducted from mild steel slabs to the rolls/unit area/sec as a function of the maximum surface temperature on entry to the rolls.

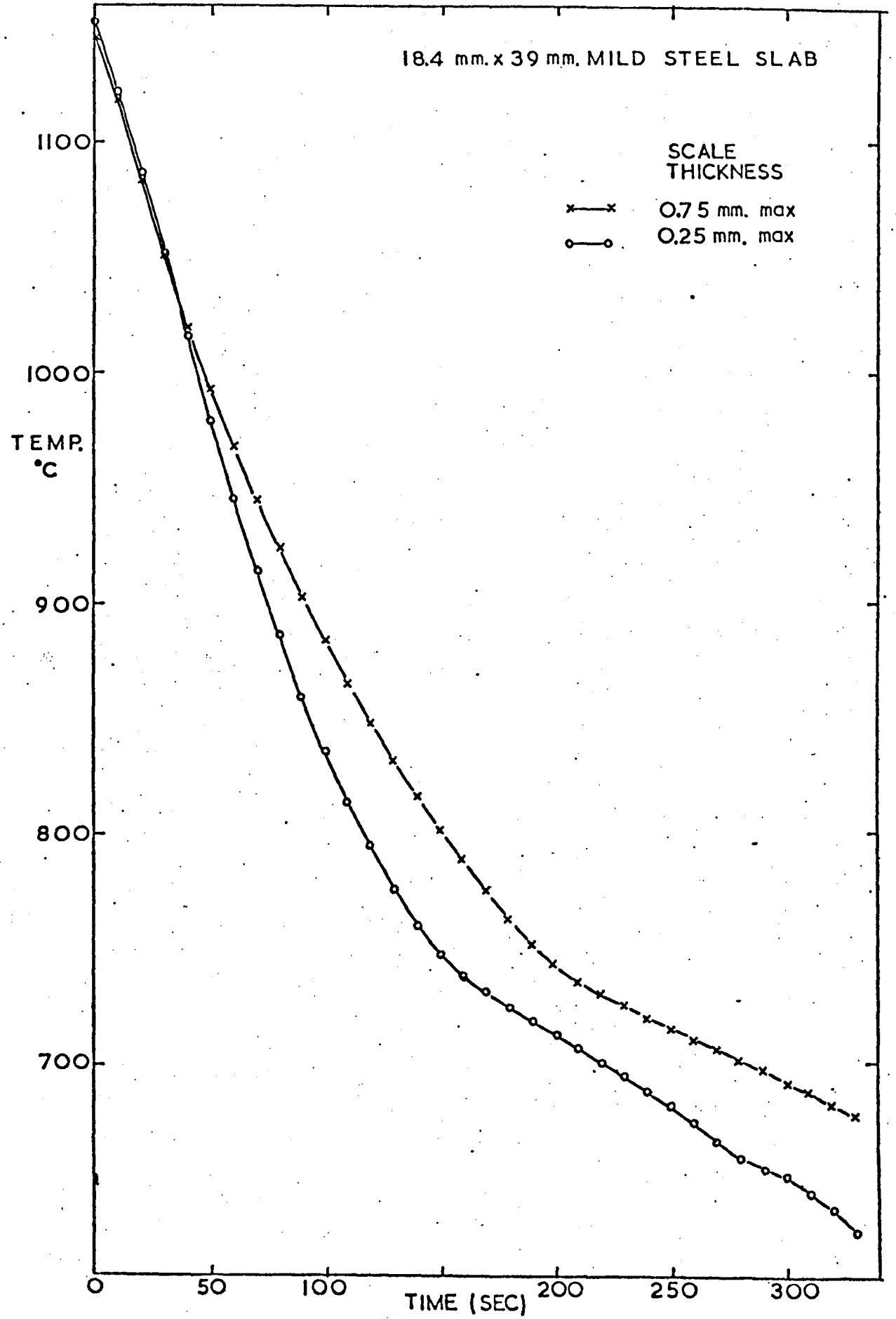

Fig.67 Effect of scale thickness on the air cooling curves of mild steel slabs.

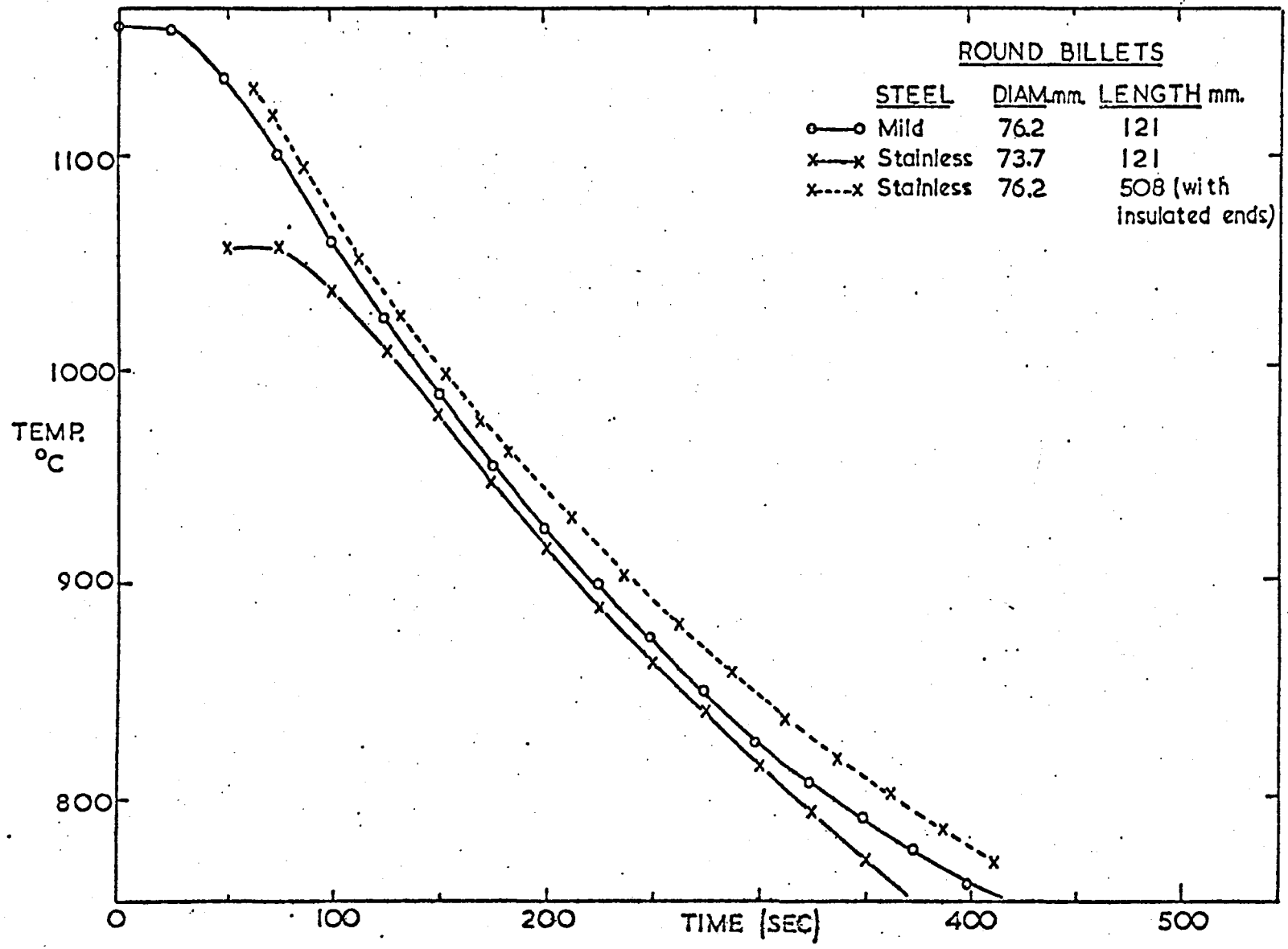

Fig.68 Comparison of the air cooling curves of mild and stainless steel round billets

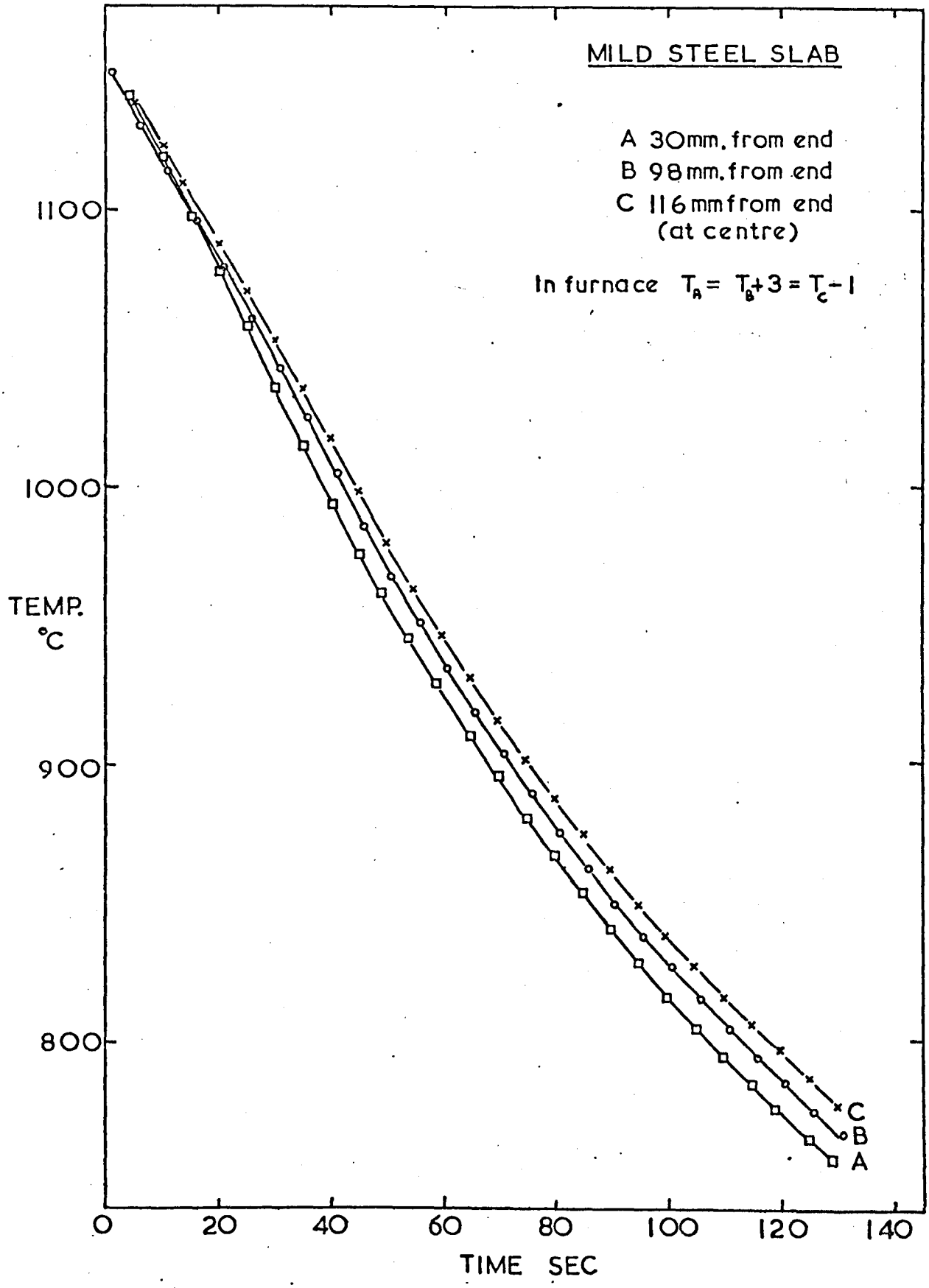

Fig.69 Development of a longitudinal temperature gradient in a 230 mm long mild steel slab during air cooling.

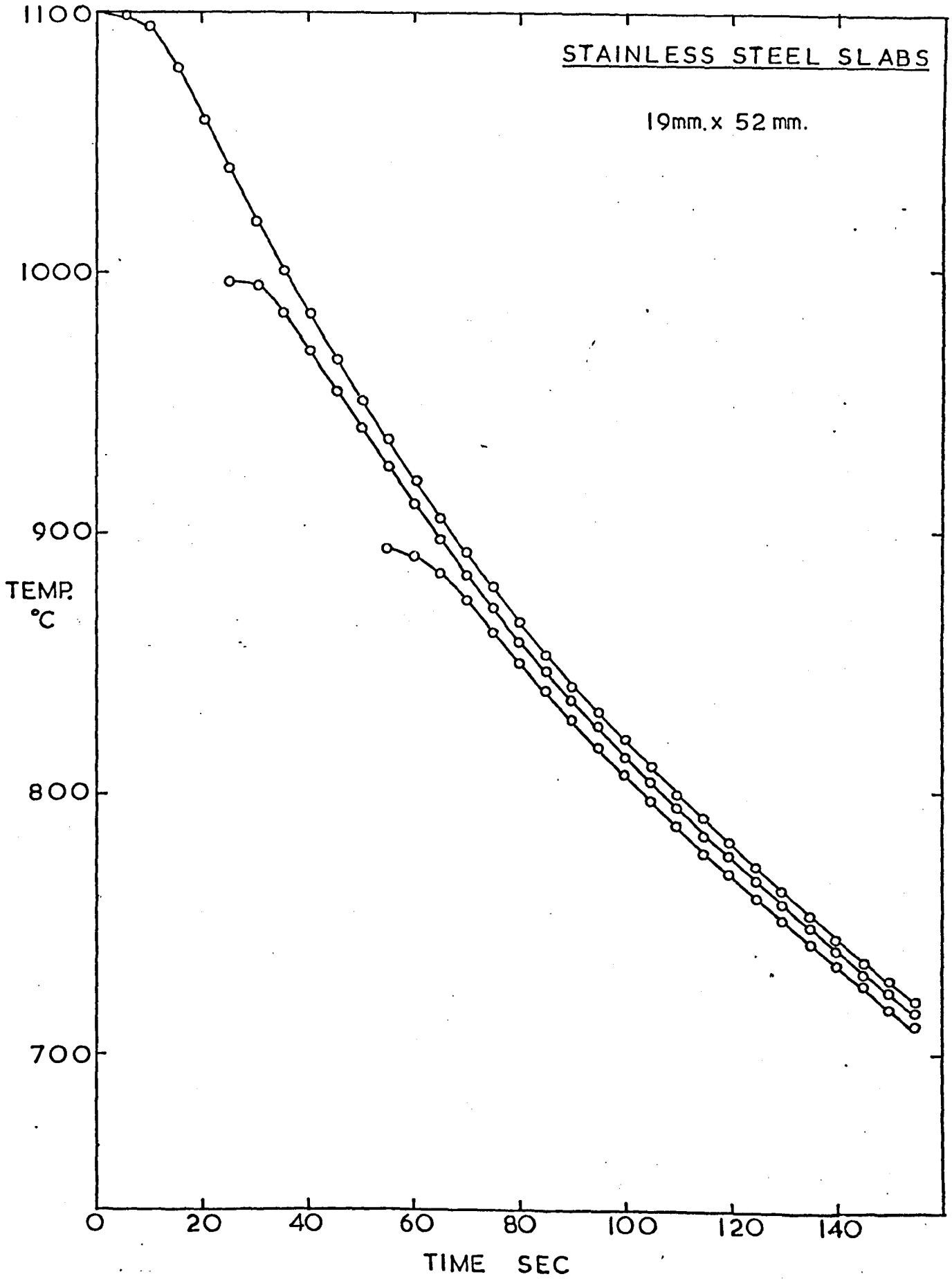

Fig.70 Air cooling curves of a stainless steel slab from 900, 1000 and 1100°C.

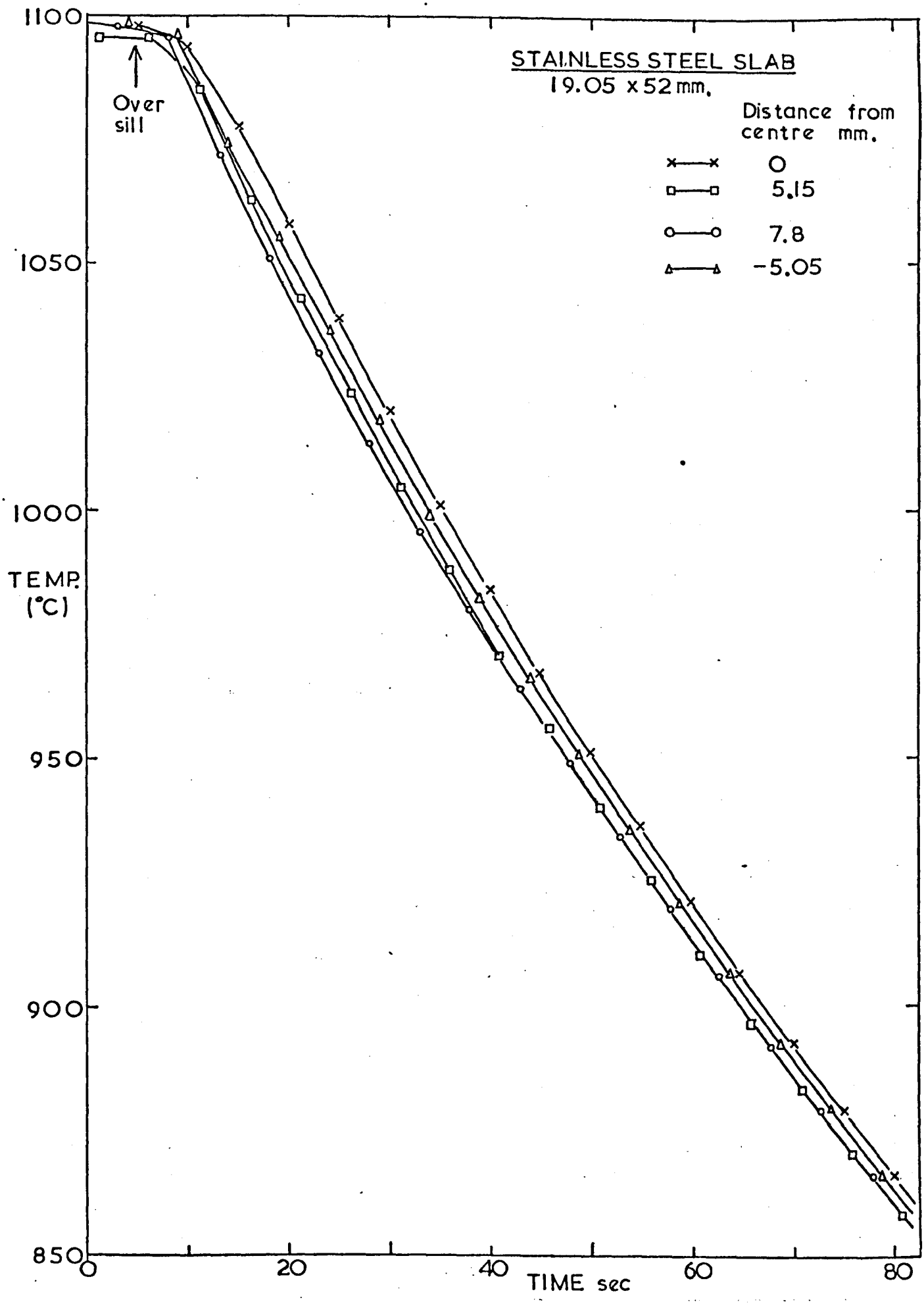

Fig.71 Development of the through thickness temperature gradient in a stainless steel slab during air cooling from 1100°C.

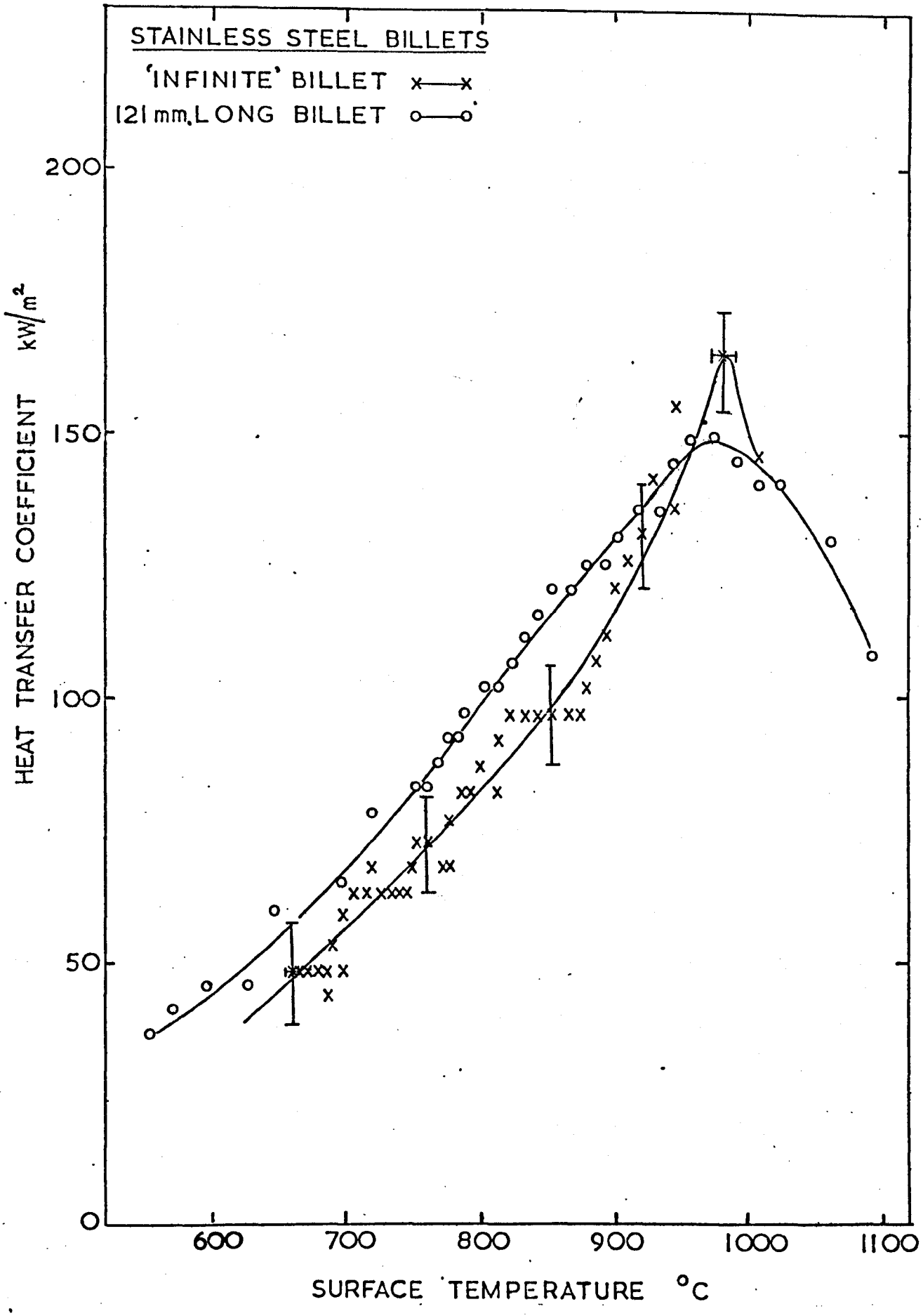

Fig.72 The air cooling heat transfer coefficient of stainless round billets as a function of surface temperature.

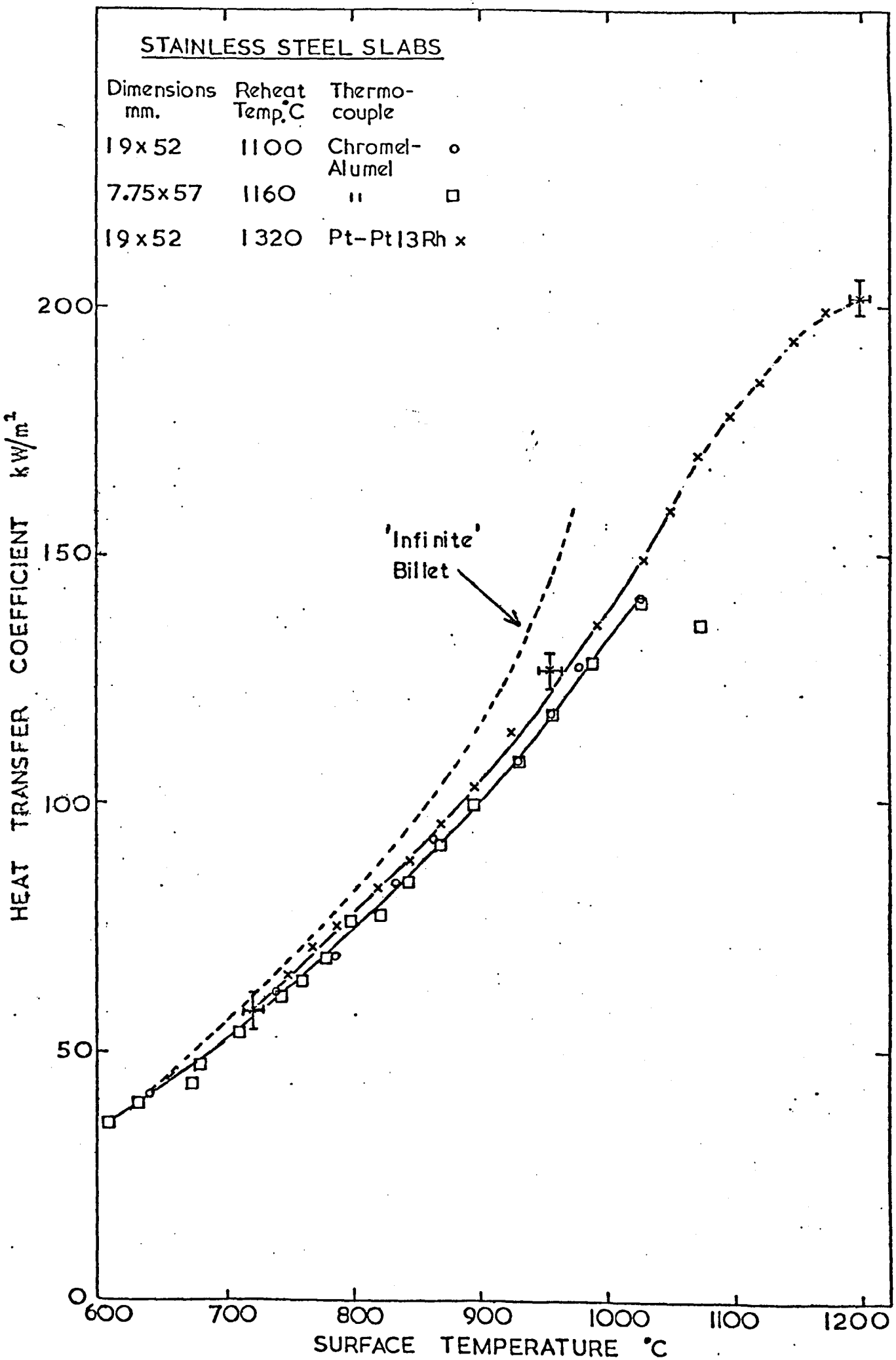

Fig.73 The air cooling heat transfer coefficient of stainless steel slabs as a function of the maximum surface temperature.

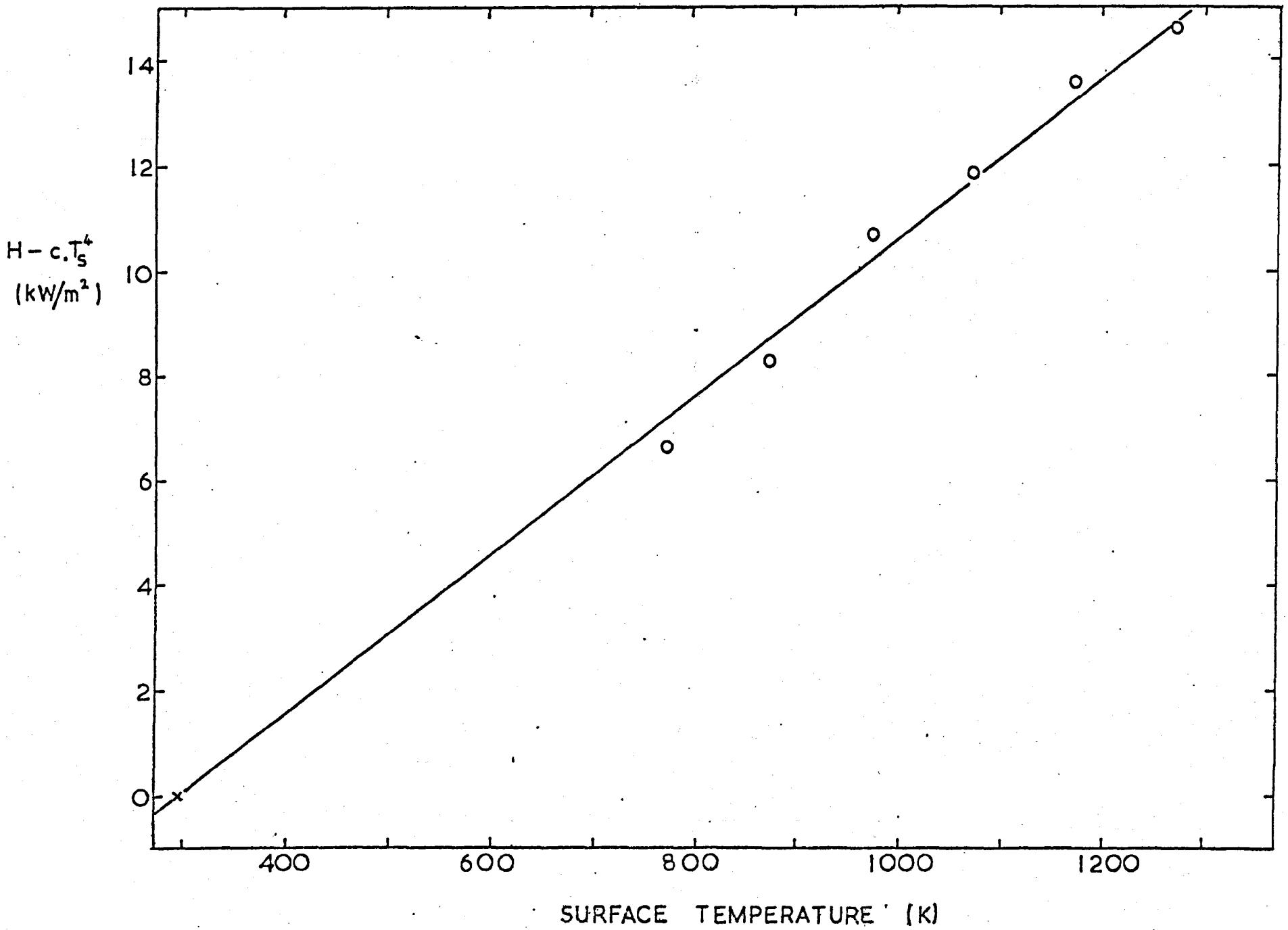

Fig.74 Fitting the experimental air cooling results to a Stefan Boltzmann equation.

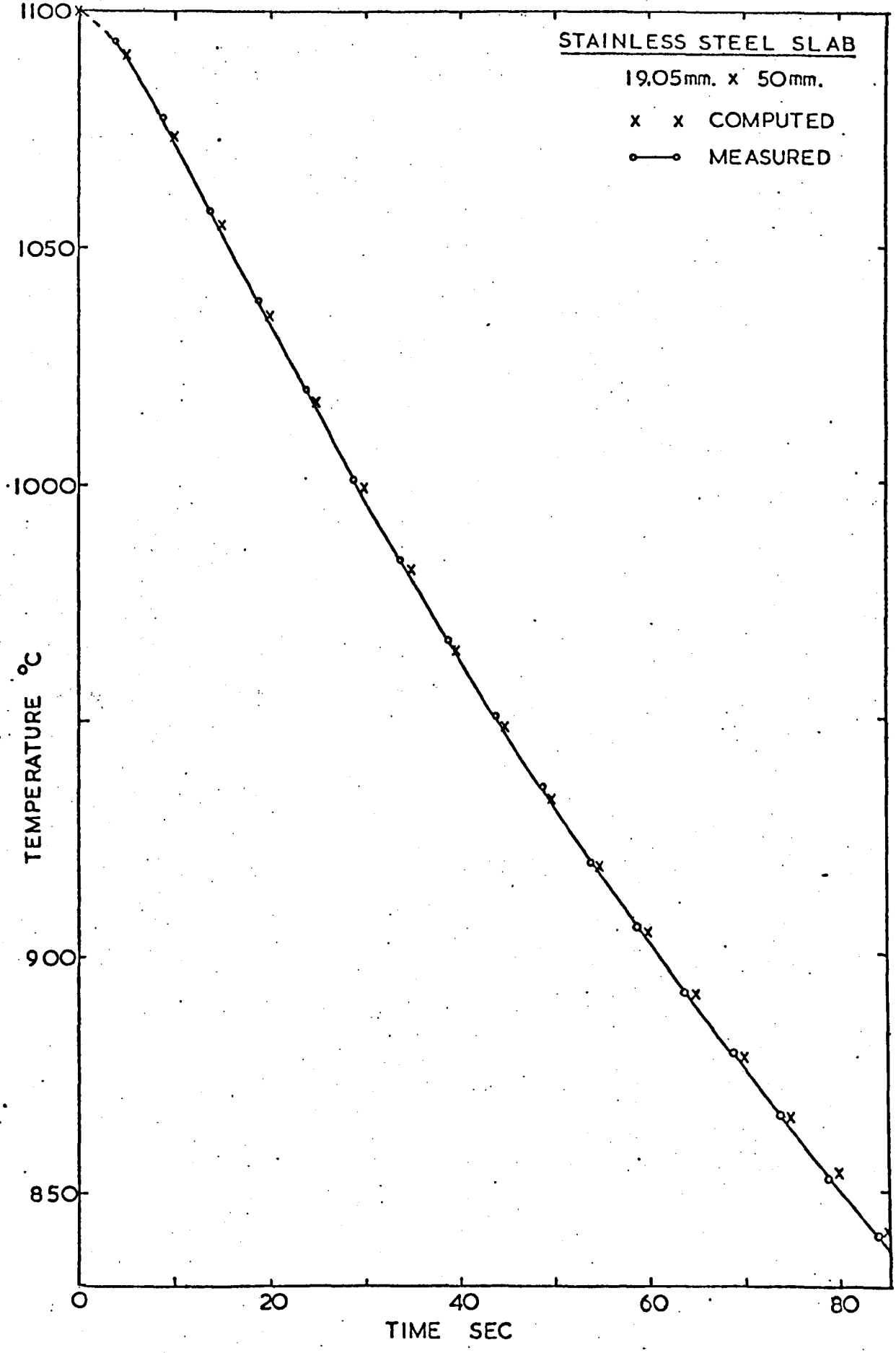

Fig.75 Comparison of measured and computed air cooling curves for a 19mm.x50mm. stainless steel slab.

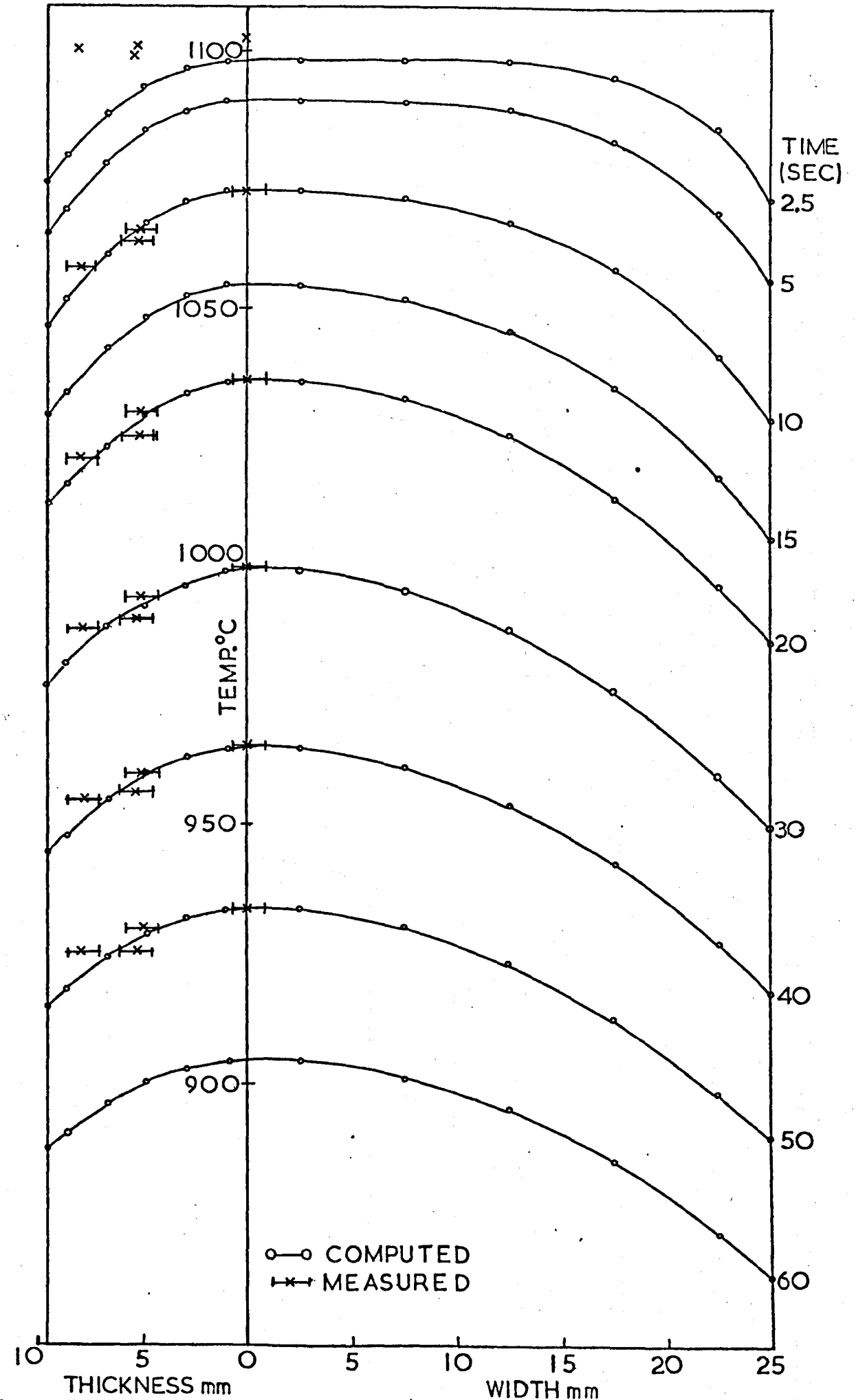

Fig.76 Computed temperature gradients through the thickness and width of a 19mm.x50mm.stainless steel slab;comparison with measured values.

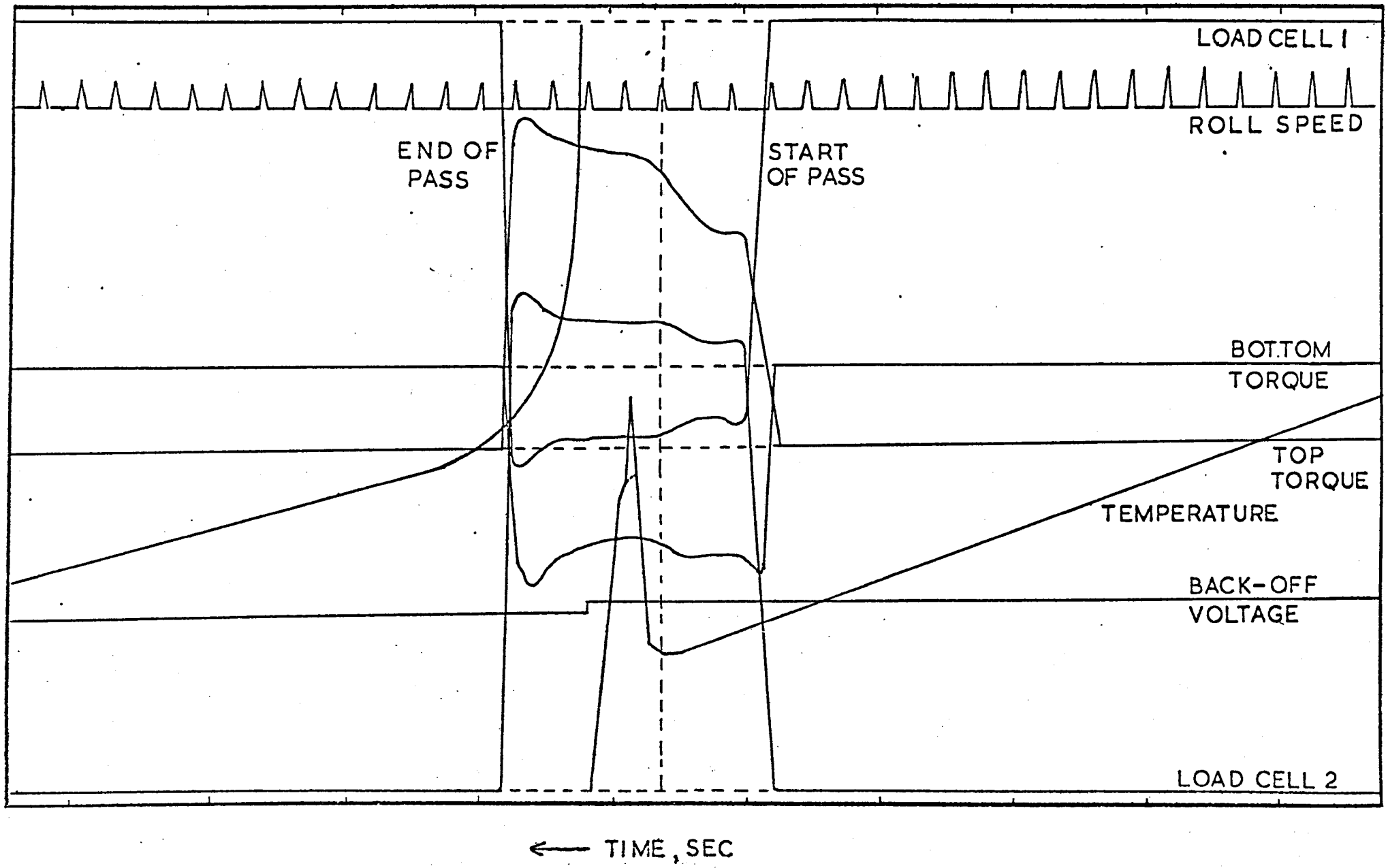

Fig.77 Typical section of U.V. chart record. Solid lines show experimental traces.

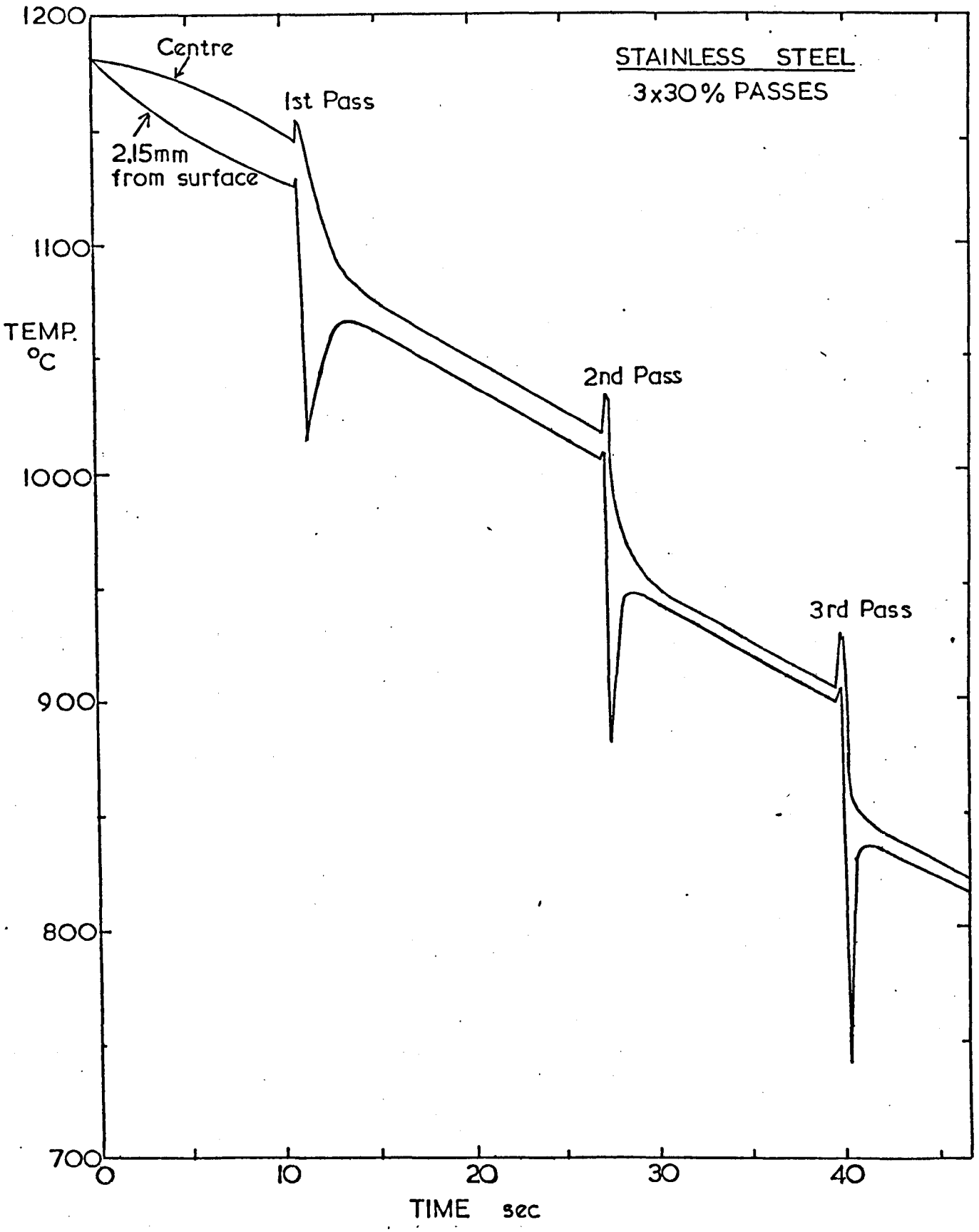

Fig.78 Measured temperature-time curves for the hot rolling of stainless steel slabs.

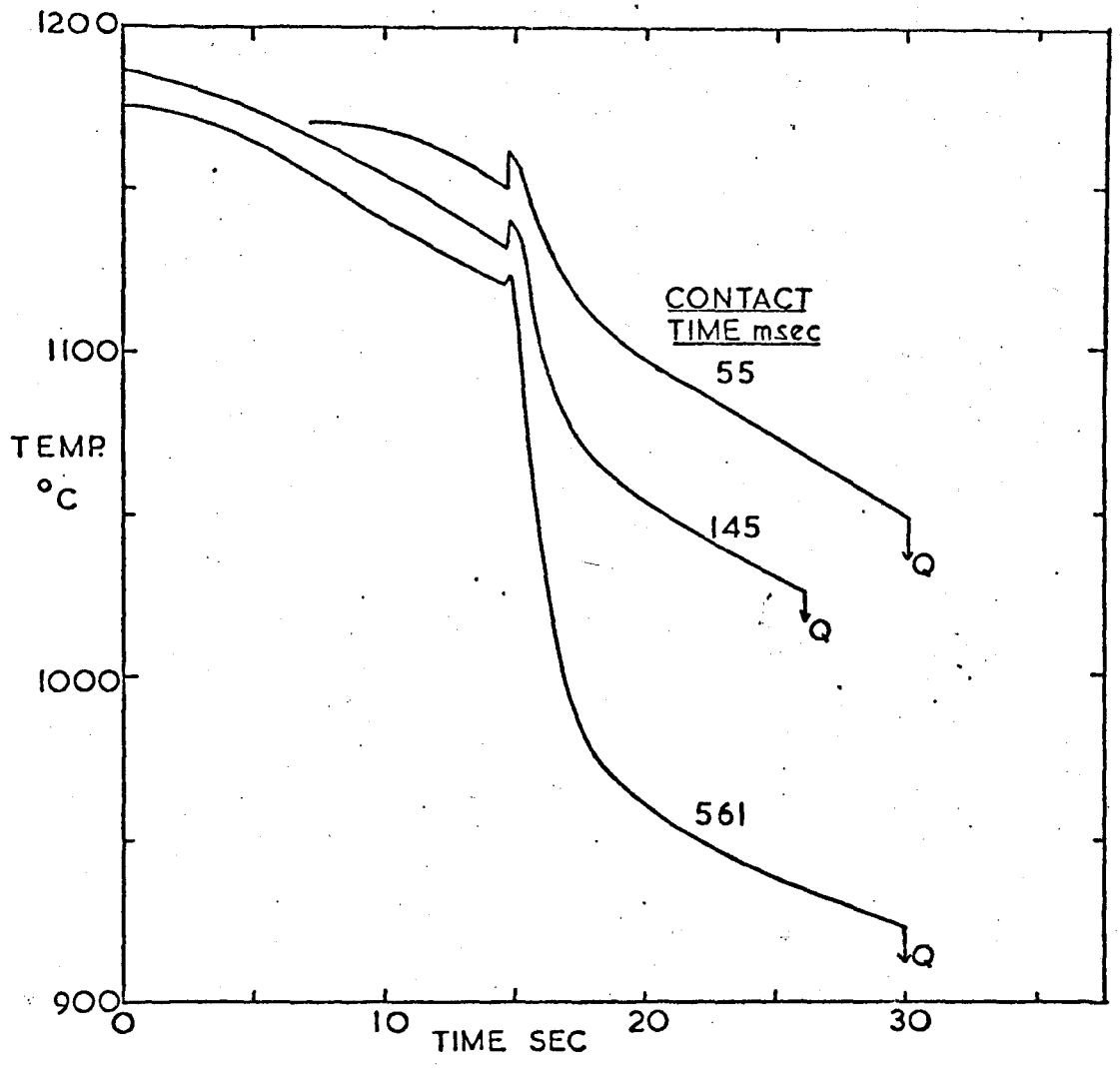

Fig.79 Effect of roll speed on the temperature changes for a 30% pass

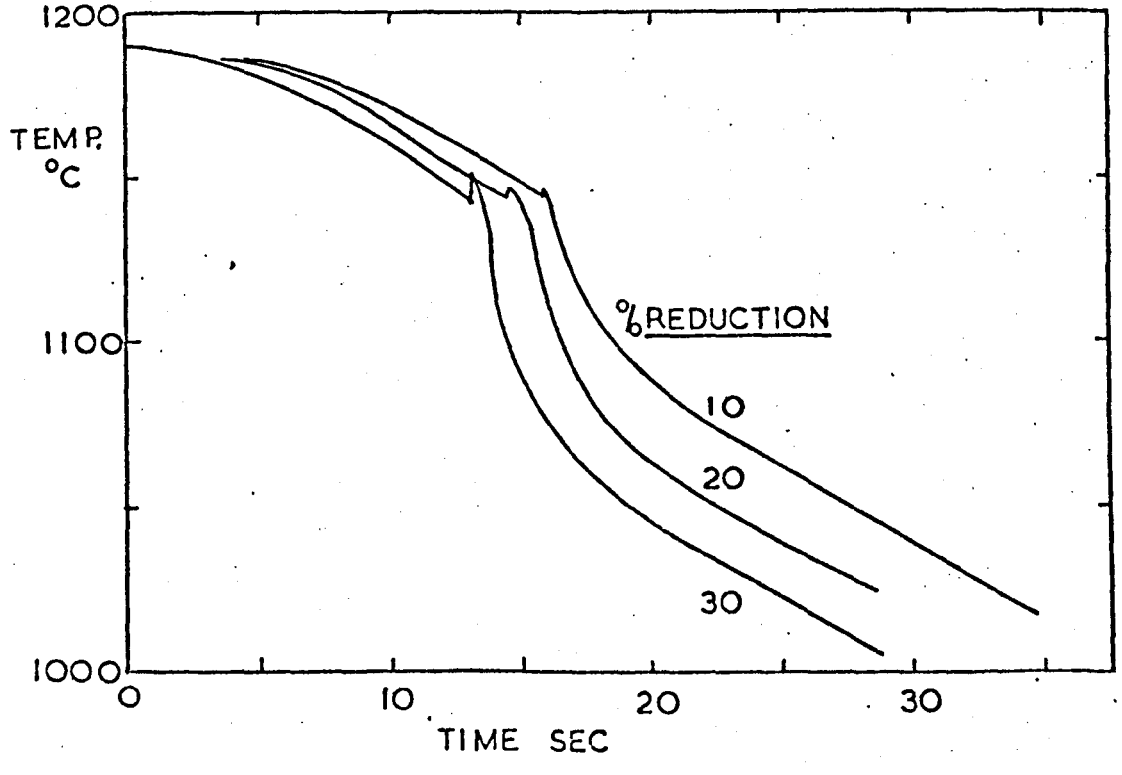

Fig.80 Effect of %reduction on the temperature changes for a constant peripheral roll speed.

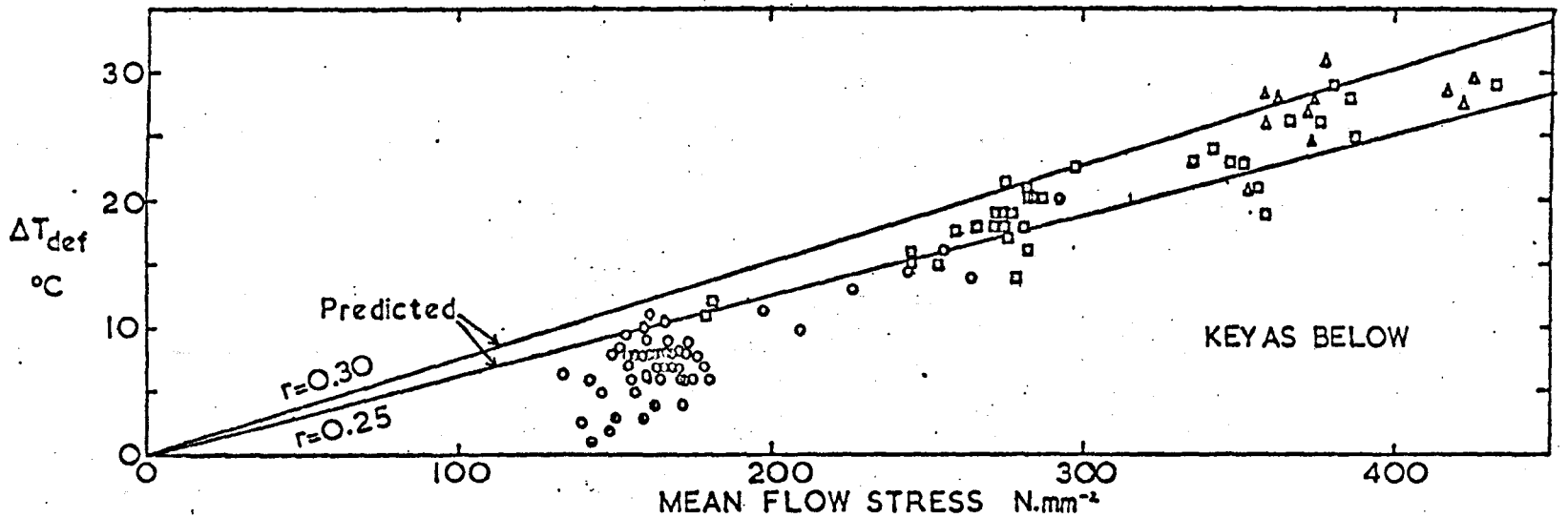

Fig.81b Correlation of the deformational temperature rise with the uniaxial mean flow stress.

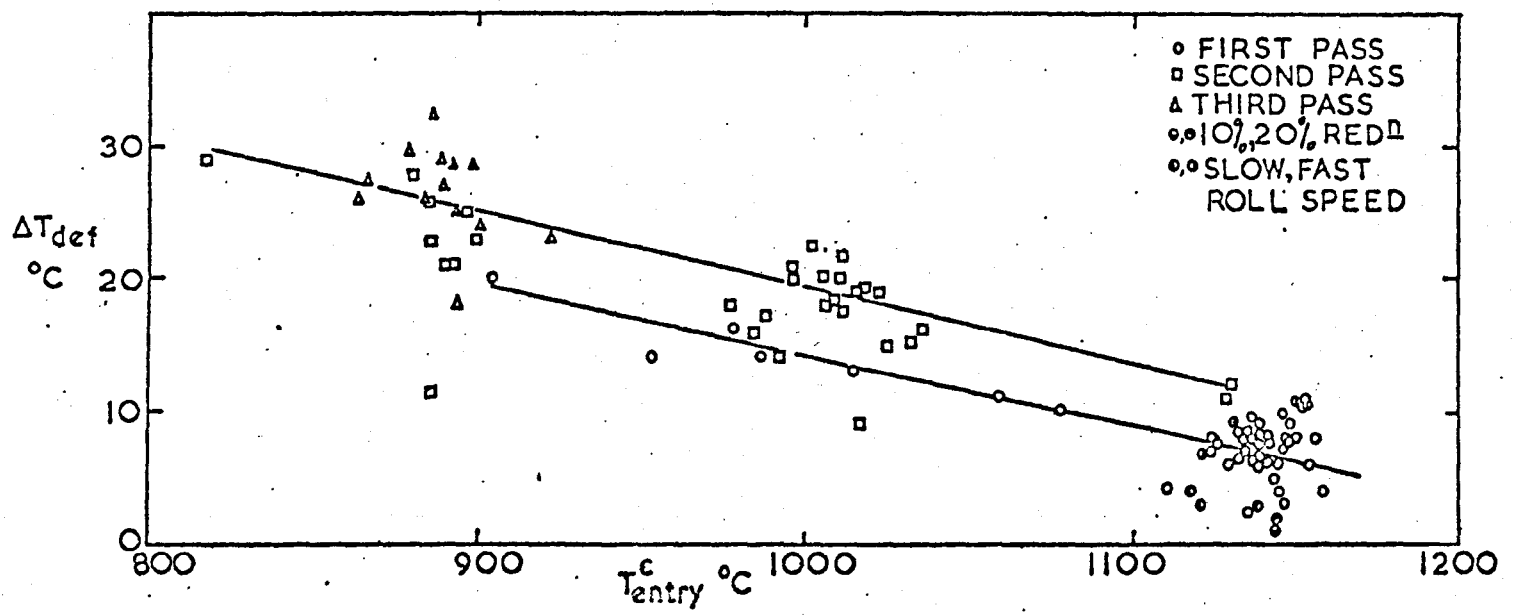

Fig.81a The effect of the temperature at the centre of the slab on entry to the rolls on the deformational temperature rise.

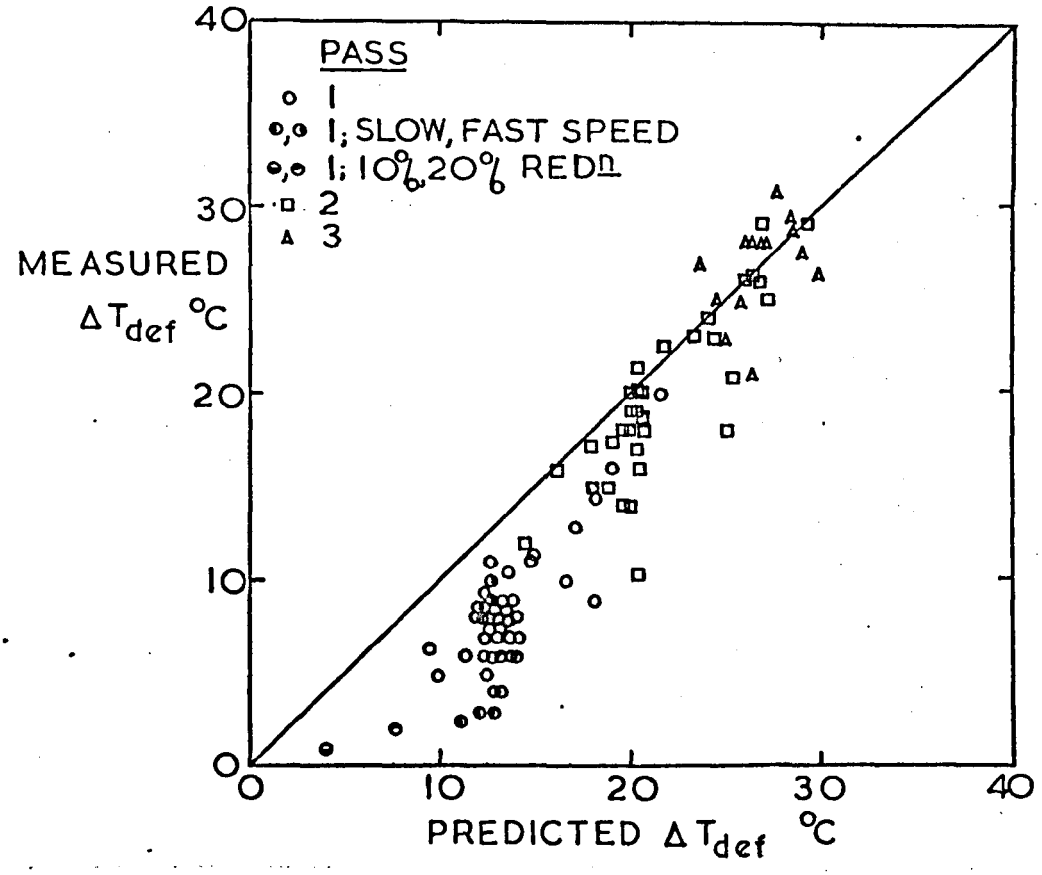

Fig.82 Comparison of measured deformational temperature rises with those predicted from mean flow stresses derived from roll loads.

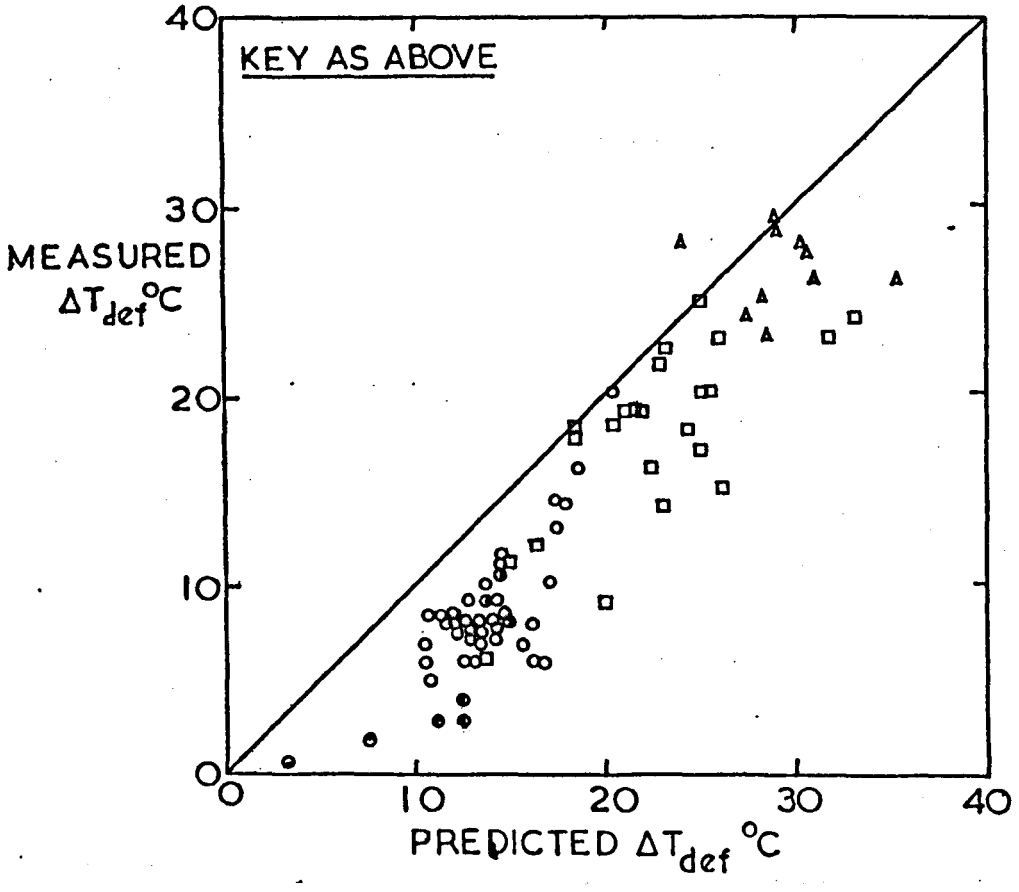

Fig.83 Comparison of measured deformational temperature rises with those predicted from measured roll torques.

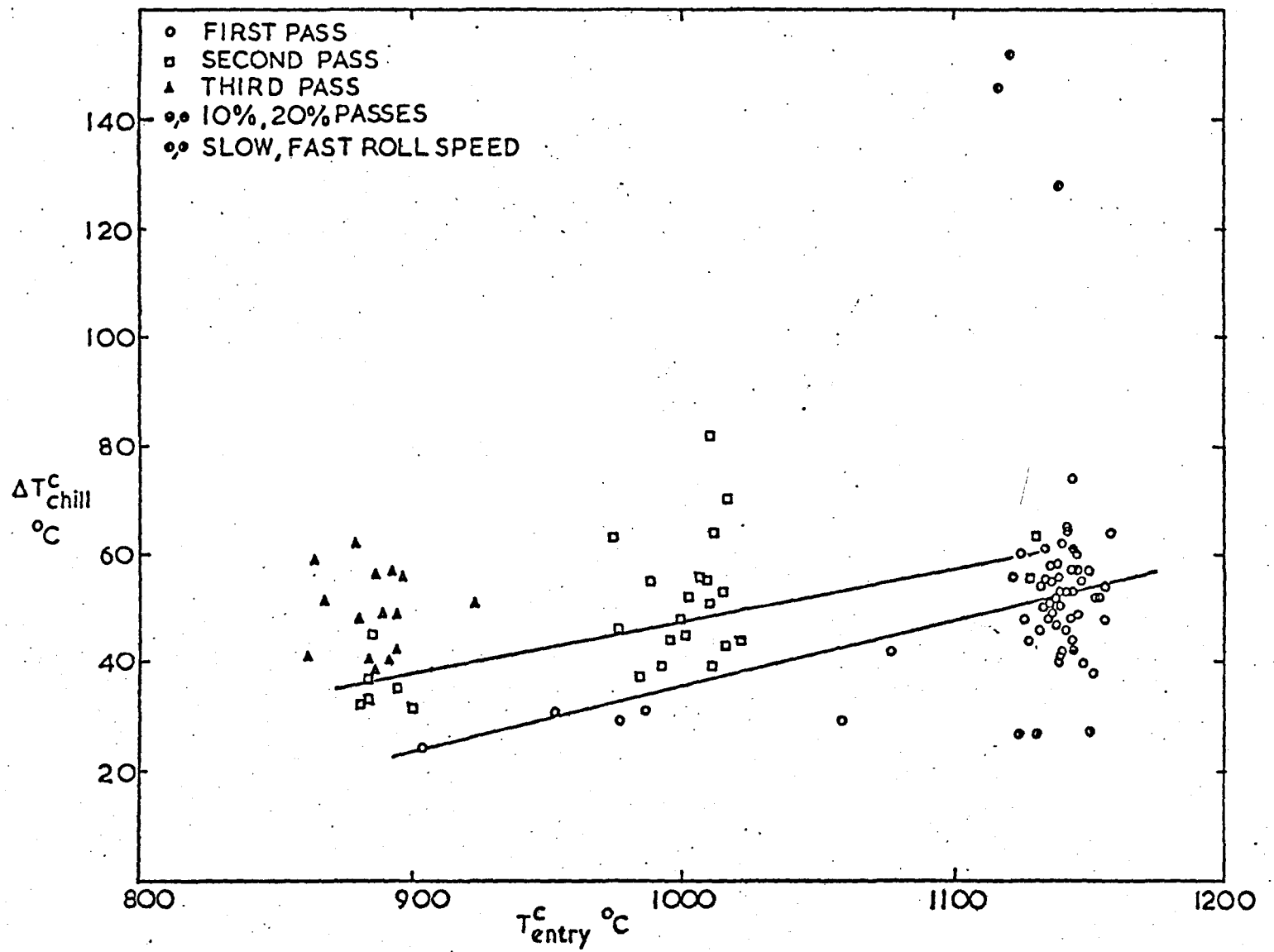

Fig.84 The dependence of the conductive temperature drop on the temperature at the centre of the slab at entry to the rolls.

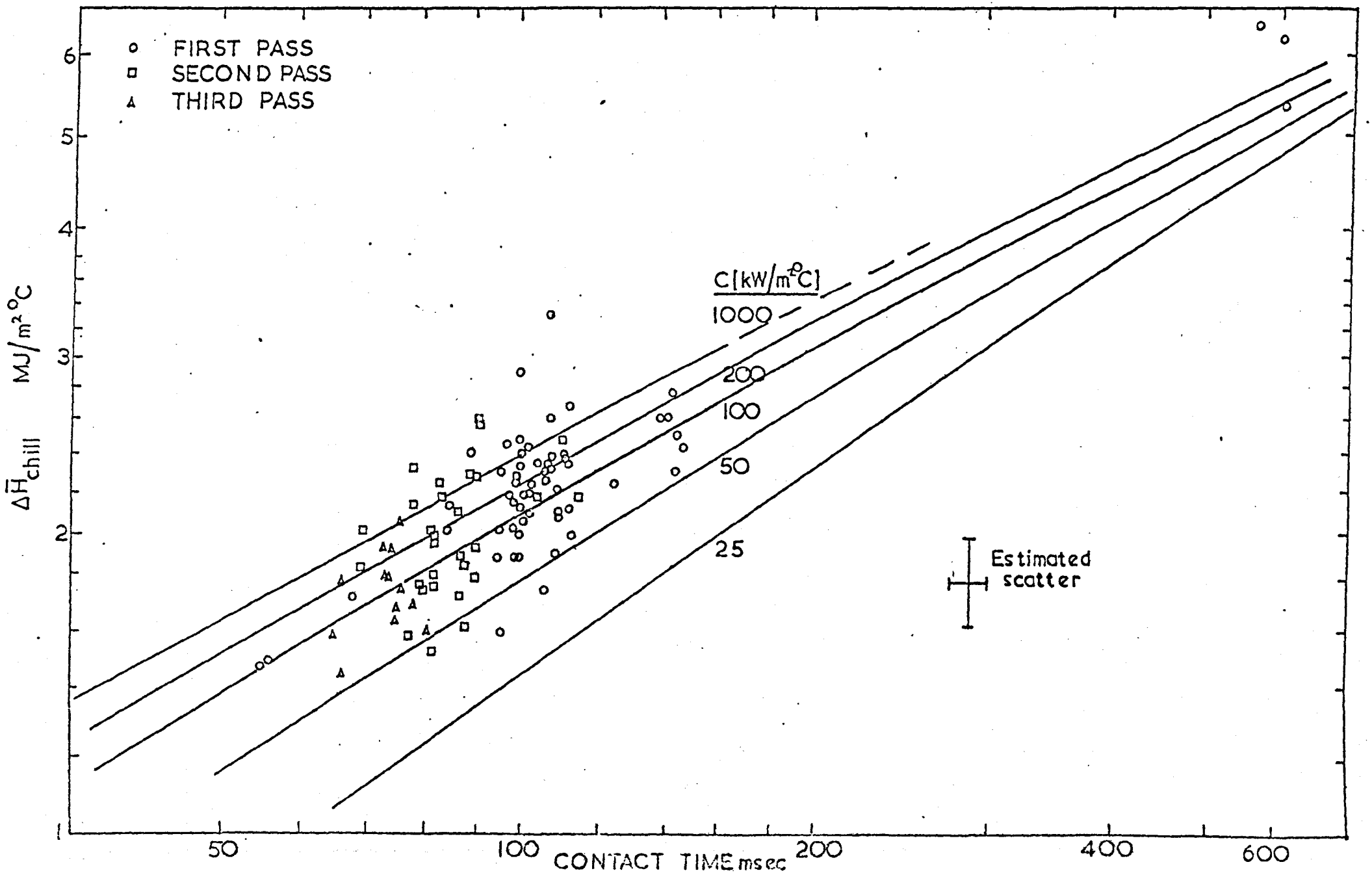

Fig.85 The effect of contact time on the measured mean heat loss/unit area/°C during hot rolling of stainless steel; correlation with computed values.

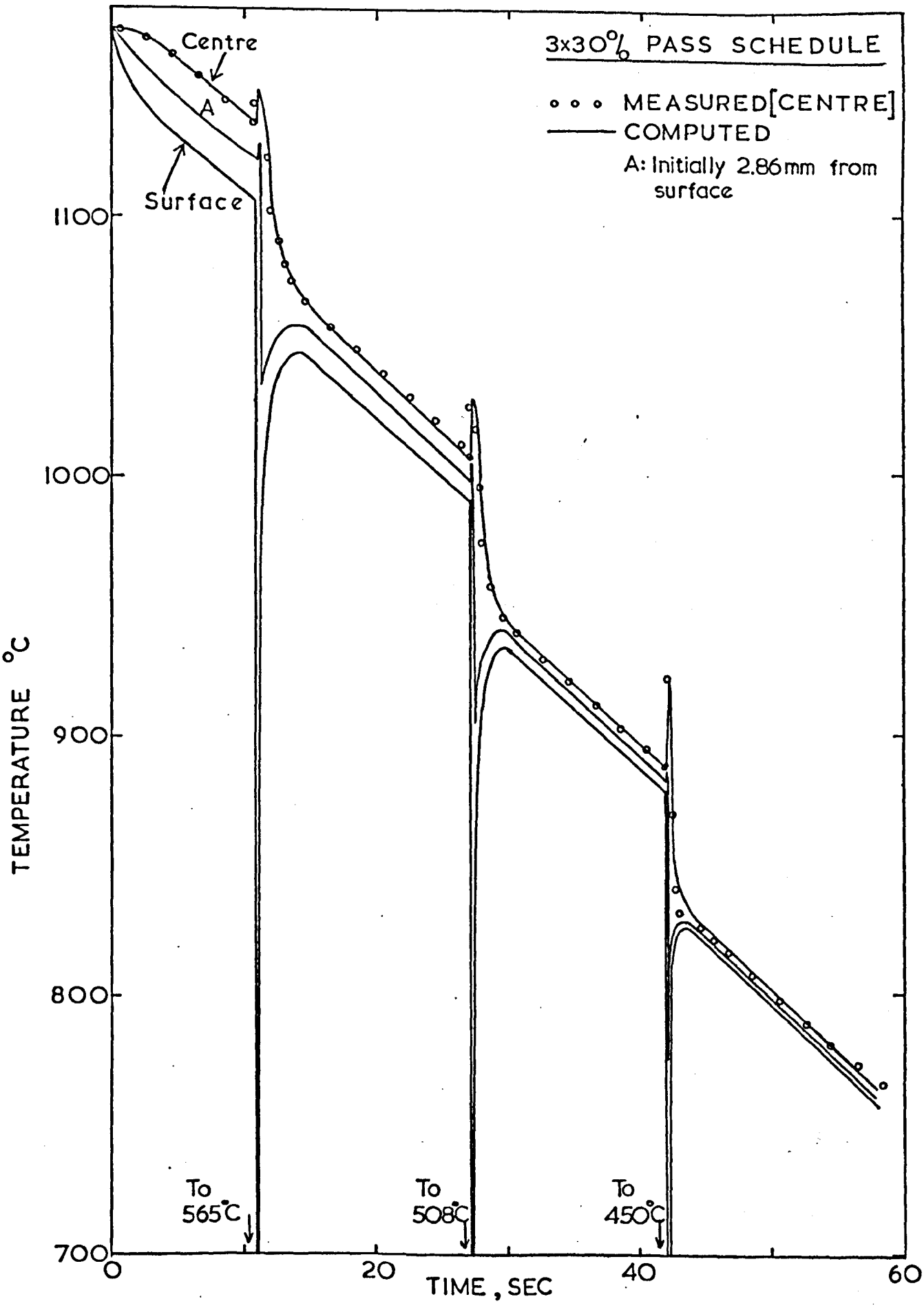

Fig.86 Comparison of measured (run 9) and computed temperature-time curves for a 3x30% stainless steel rolling schedule. Computed curve with C_{init}= 200 kW/m^2°C.

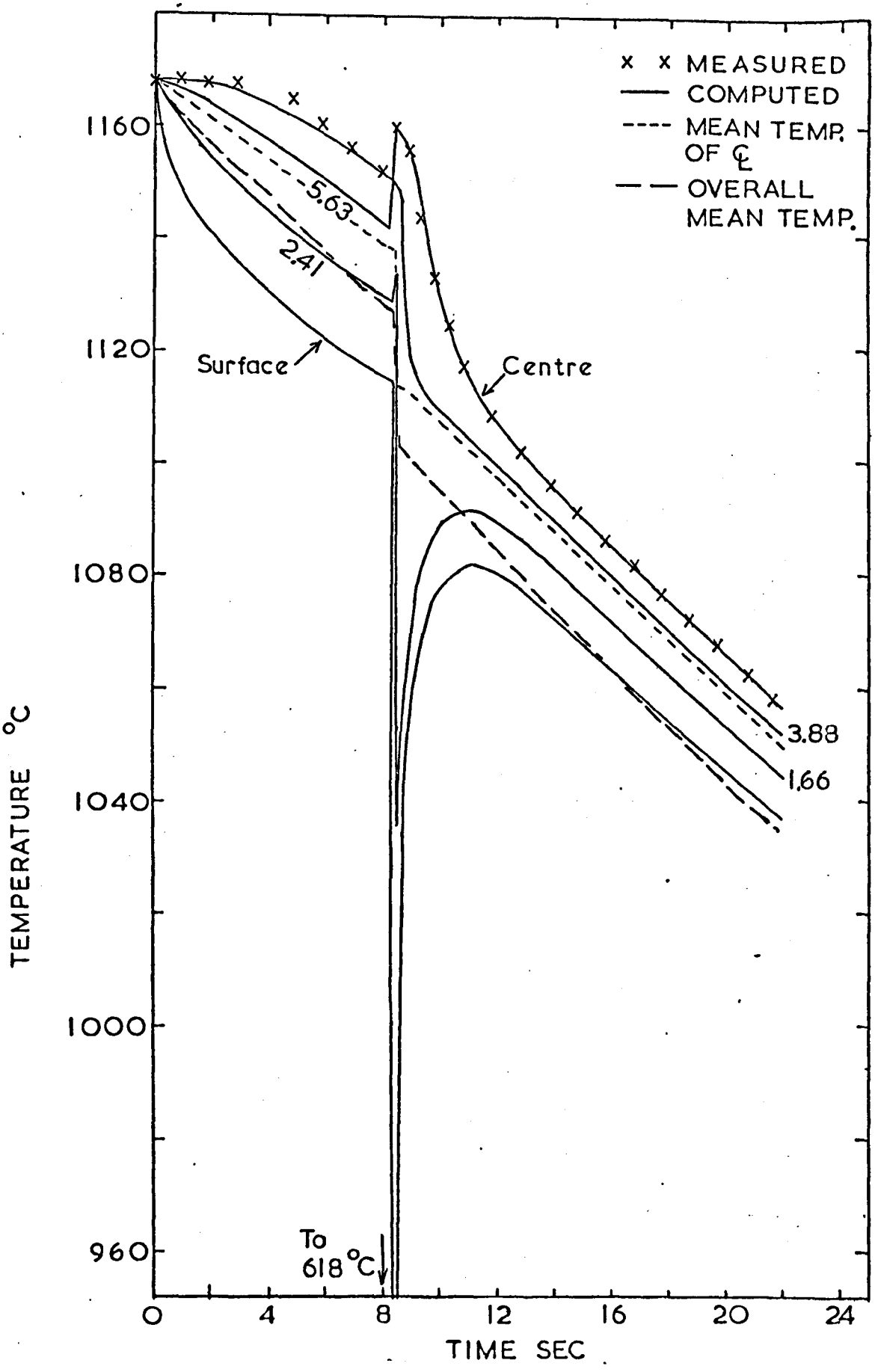

Fig.87 Simulation of run 71 (31.1%reduction at the maximum roll speed). Stainless steel slab initially 49.94mm.x 22.51mm.; t_{cont}= 54 msec.; C= 80 kW/m^2 °C.

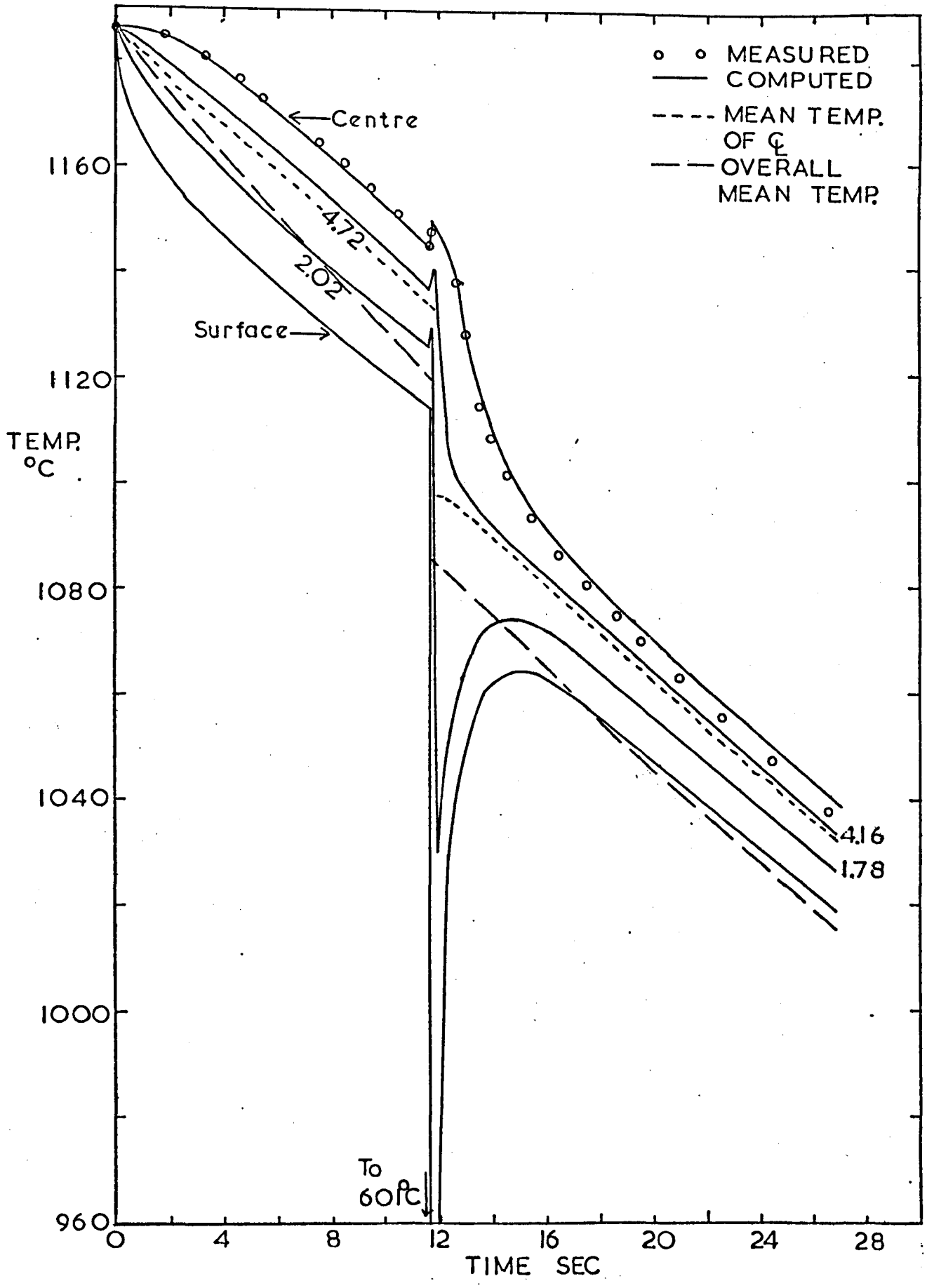

Fig.88 Simulation of run 17 (11.9% reduction at the normal roll speed). Stainless steel slab initially 51.5mm.x 18.88mm.; t_{cont} = 67.7 msec.; C = 100 kW/m^2 °C.

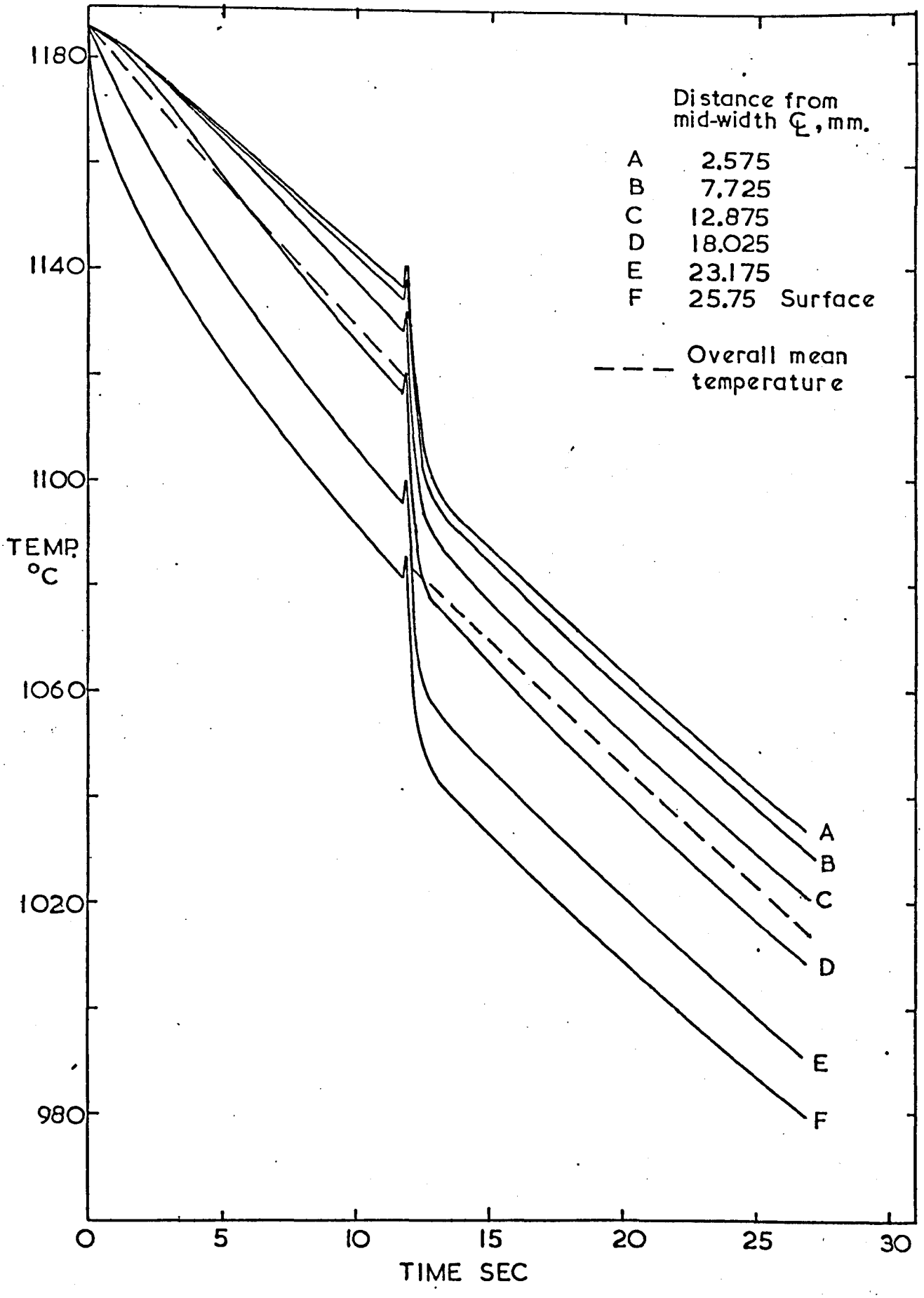

Fig.89 Computed temperature changes across the width of a slab (at the mid-thickness centre line) for the same run as Fig.88.

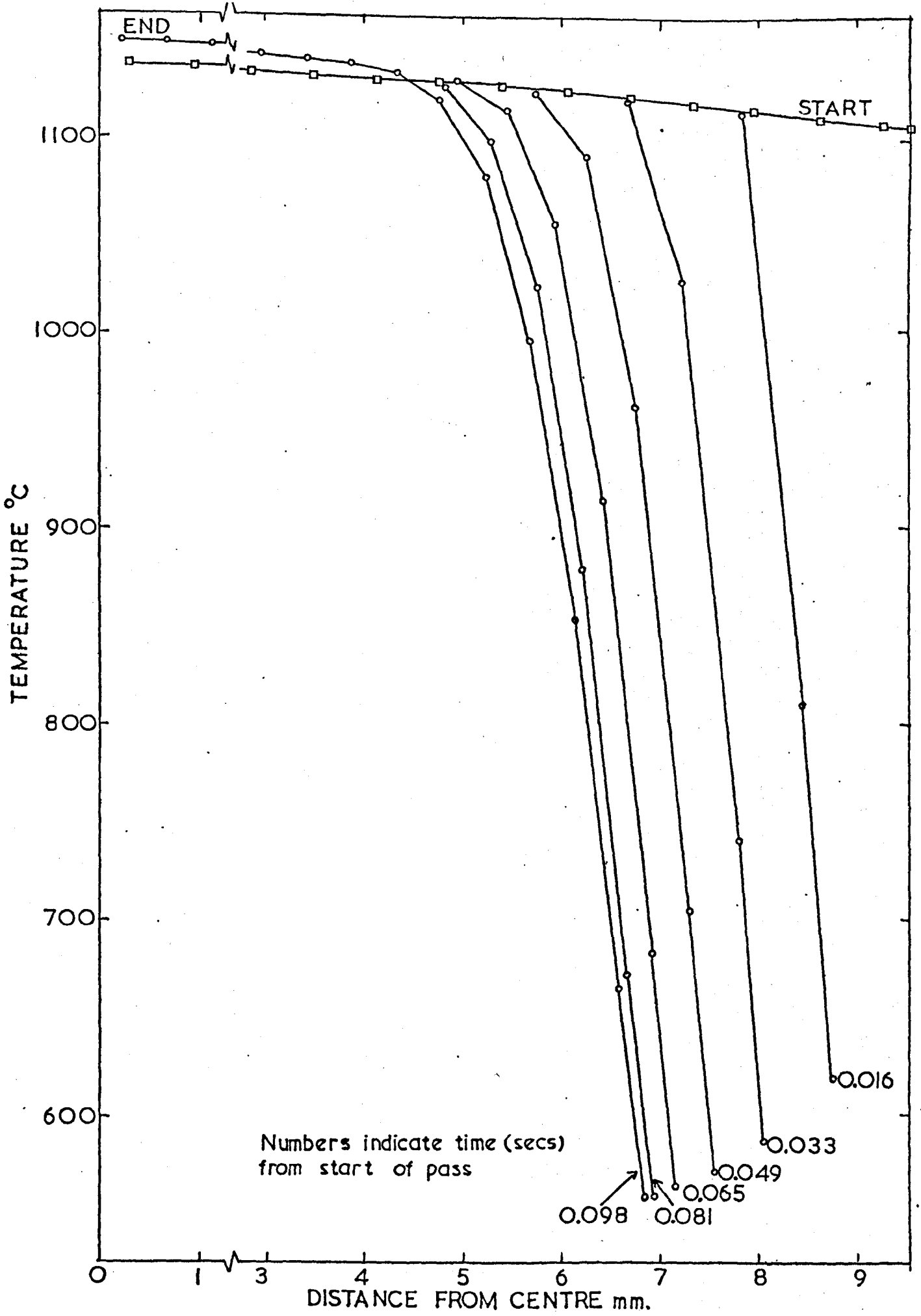

Fig.90 The development of the through thickness temperature gradient (along the centre line) during a 30% pass; corresponds to the first pass of Fig.86.

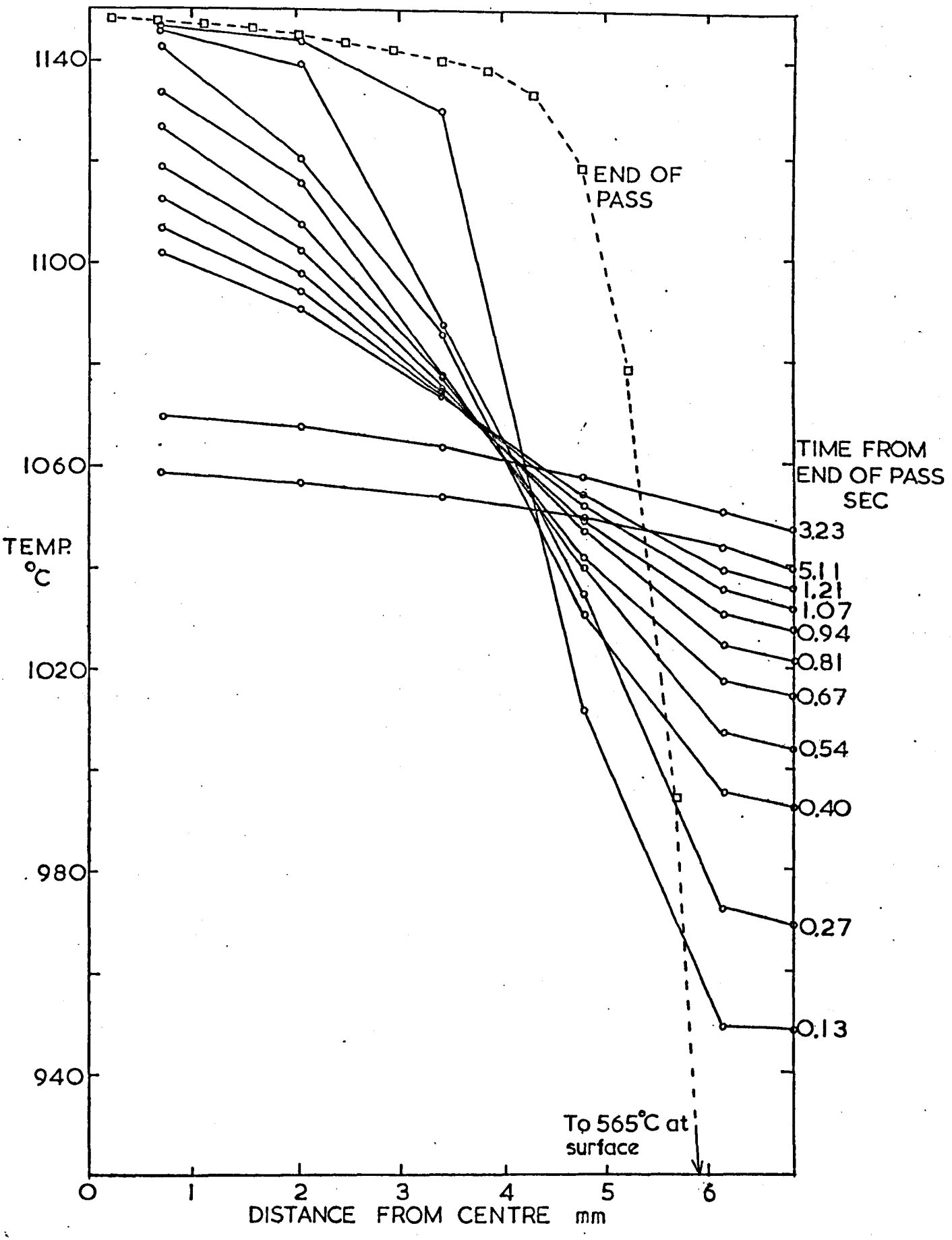

Fig.91 The changing through thickness temperature gradient following exit from the rolls; corresponds to the first pass of Fig.86.

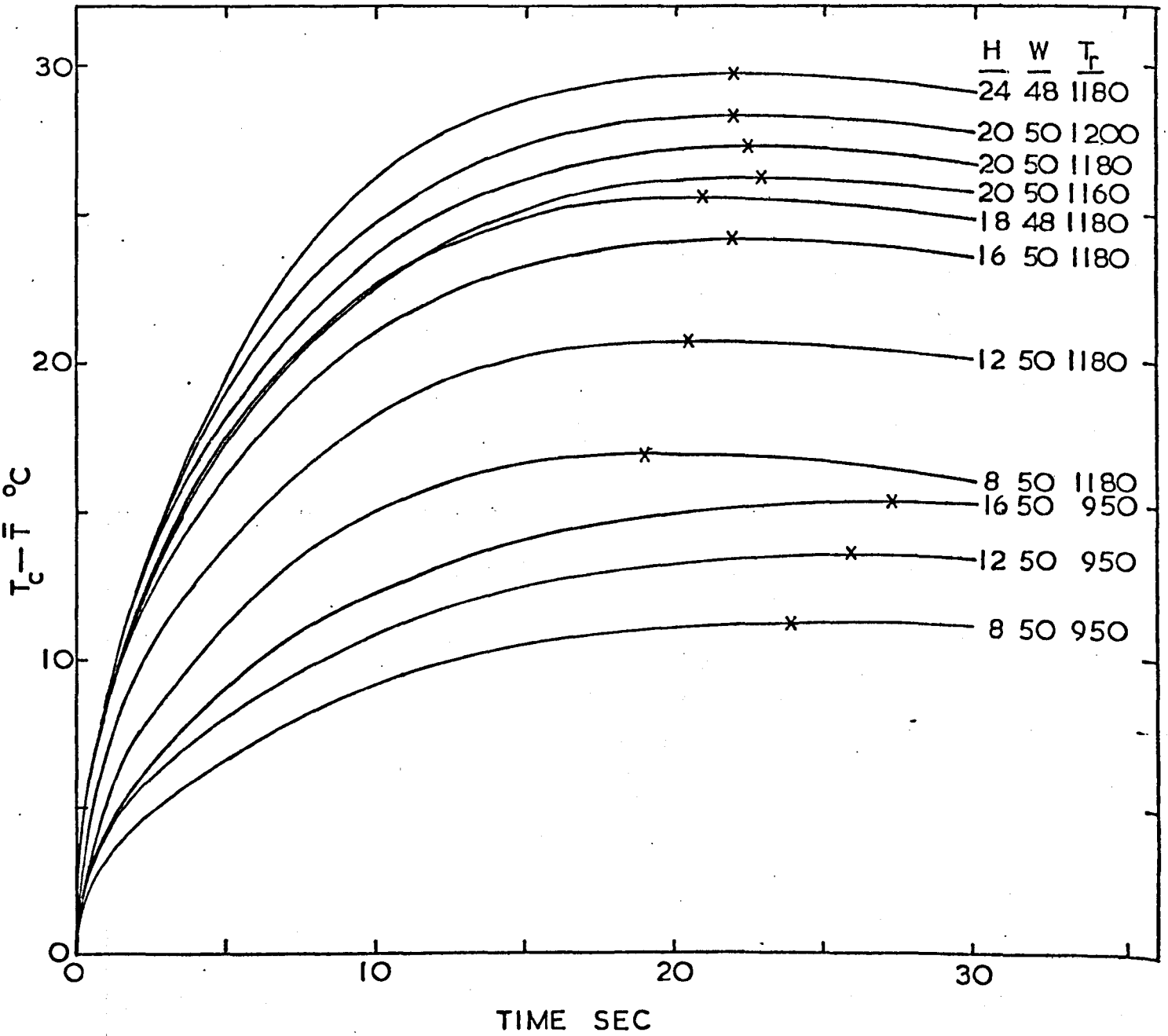

Fig.92 Computed values of $T_c - \bar{T}$ as a function of cooling time for a variety of slab dimensions and reheating temperatures.

H = thickness, mm.
W = width, mm.
T_r = reheating temperature, °C.
X = maximum.

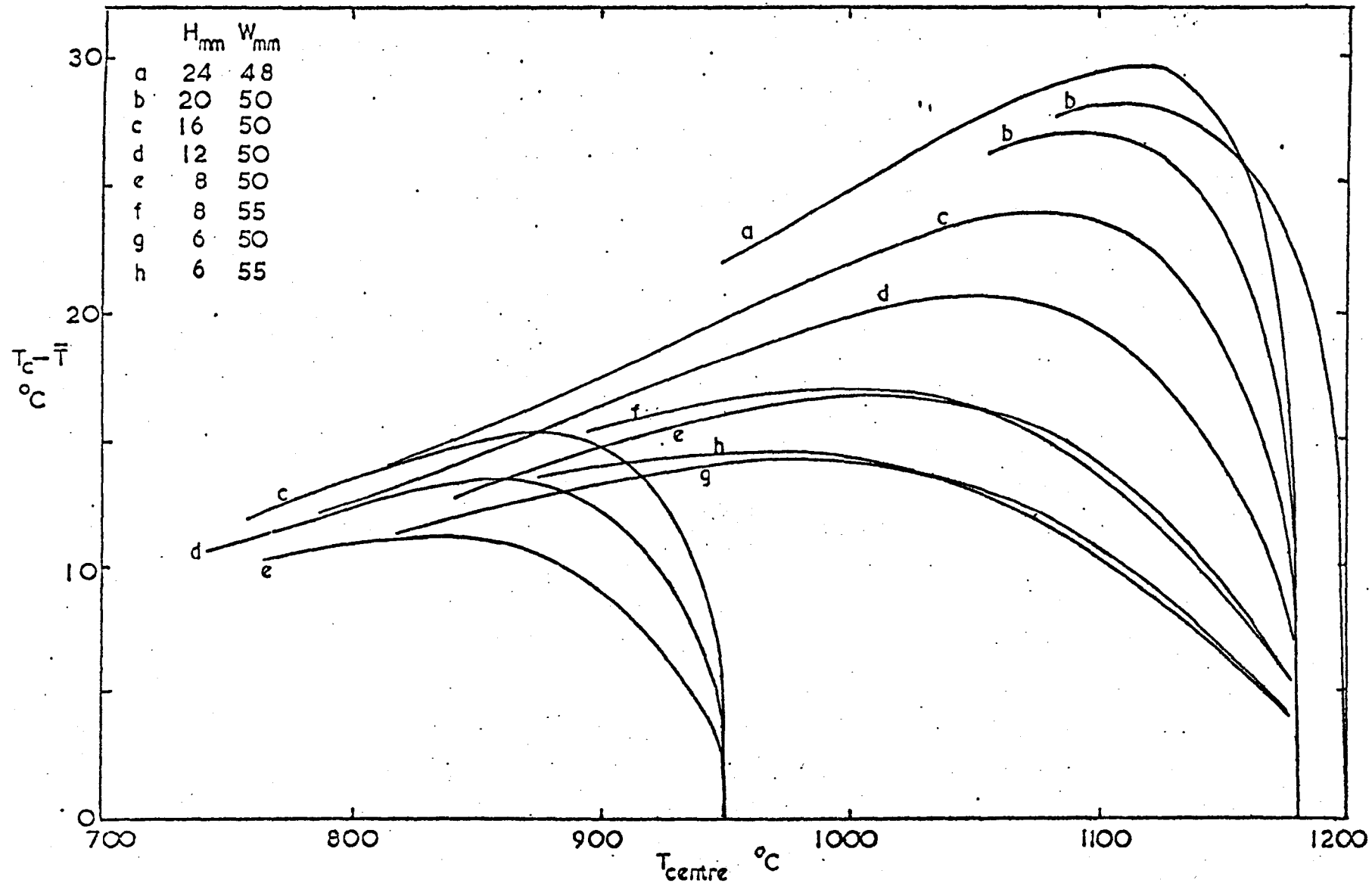

Fig.93 Computed values of $T_c - \bar{T}$ as a function of T_c for a variety of slab dimensions.

Fig.94 Longitudinal sections of stainless steel slabs after reheating.

(a) Surface x 76

(b) Centre x 76

(c) Centre x 200

(d) Centre x 76
With Magnetite
suspension

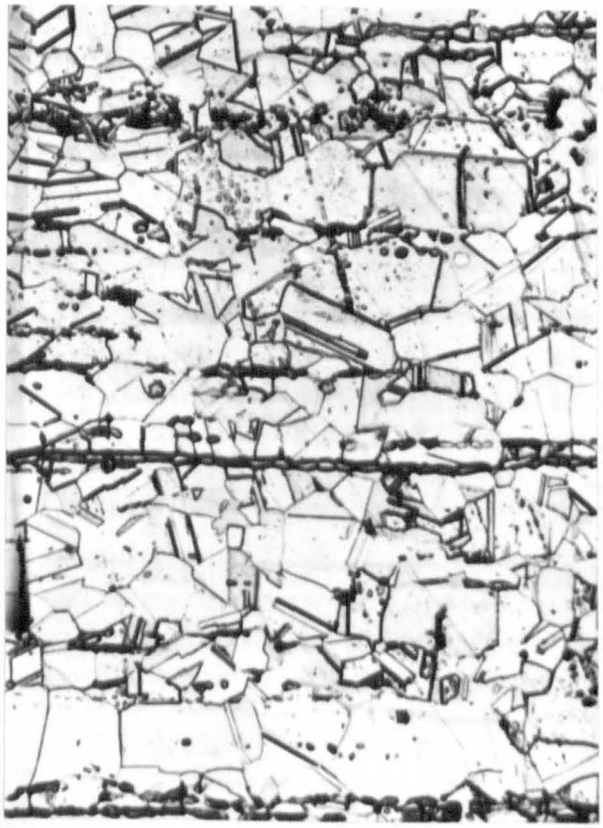

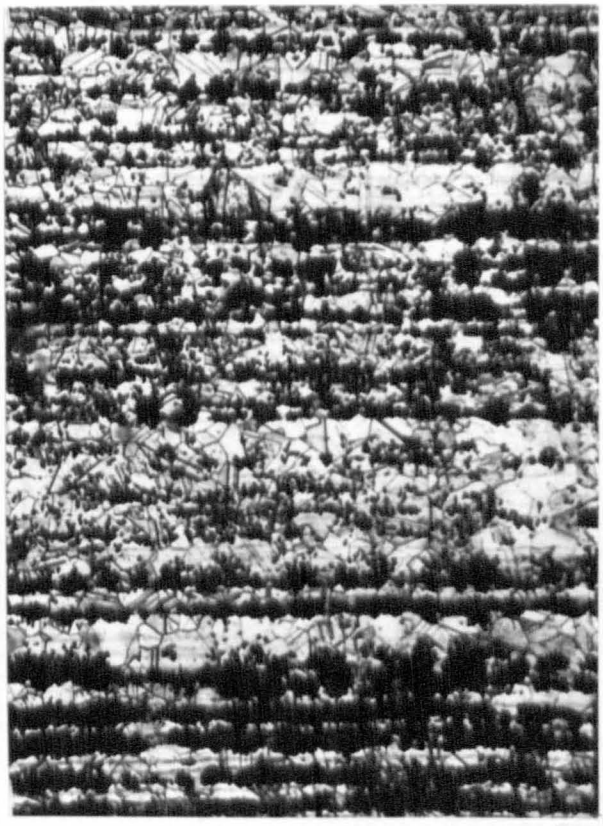

Fig.95 Longitudinal sections immediately below surface of as-rolled stainless steel slabs quenched at various times after the first pass.

(a) Quenched after 2 secs. x 50 (b) Quenched after 6 secs x 50

(c) Quenched after 12 secs.x 50 (d) Quenched after 20 secs x 50

Fig.96 Longitudinal sections at the centre of as-rolled stainless steel slabs quenched at various times after the first pass.

(a) Quenched after 2 seconds x 100

(b) Quenched after 12 seconds x 100

(c) Quenched after 20 seconds x 100

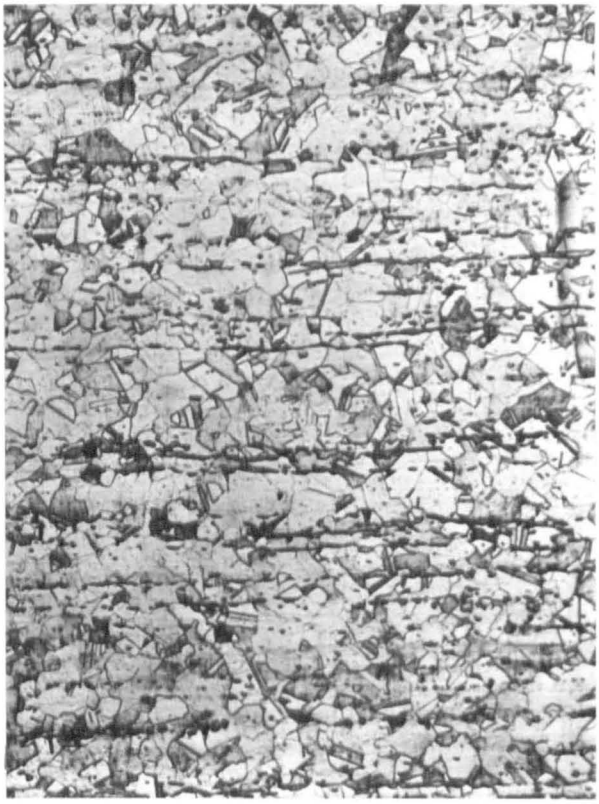

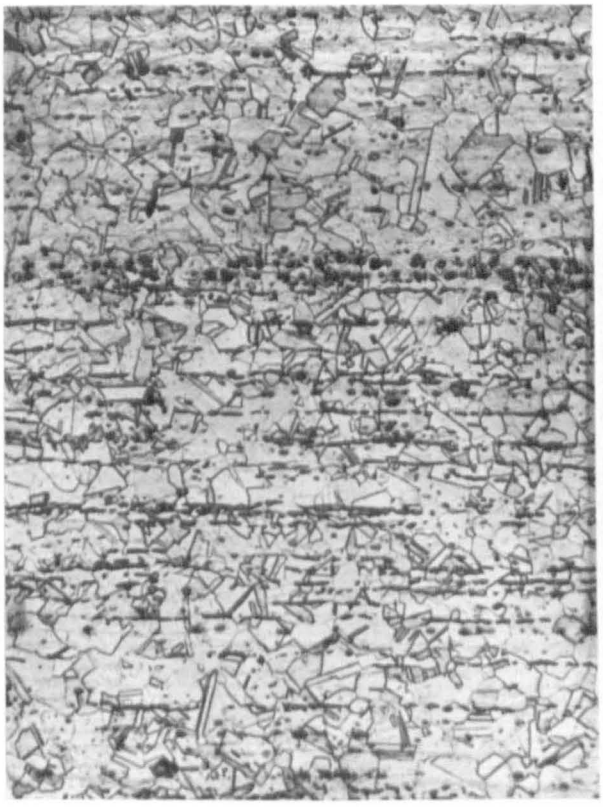

Fig.97 Longitudinal sections of as-rolled stainless steel slabs quenched after the second pass.

(a) Surface x 100

(b) Surface x 240

(c) Centre x 100

(d) Centre x 240

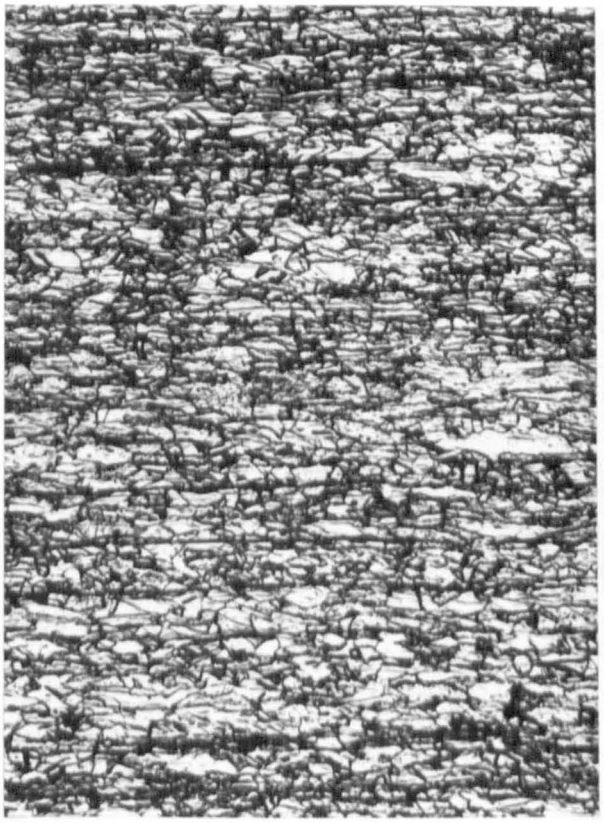

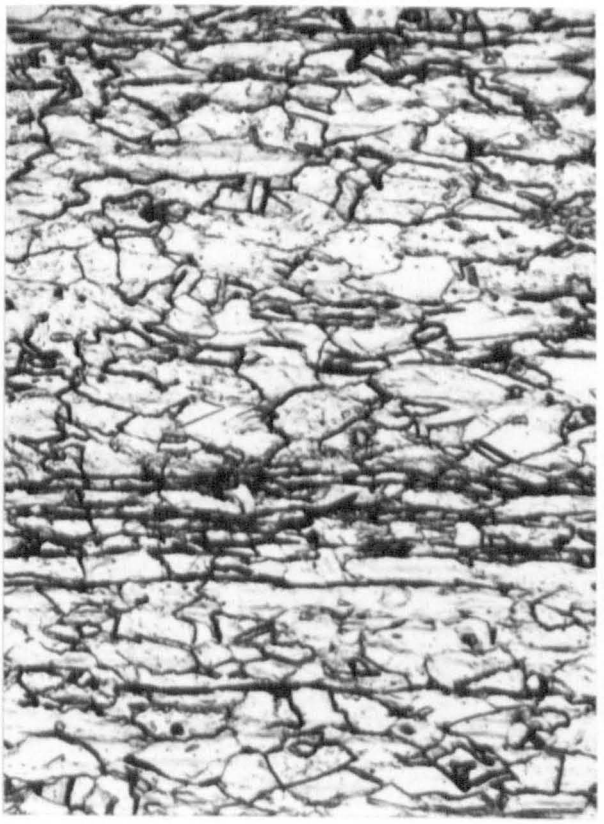

Fig.98 Longitudinal section of an as-rolled stainless steel slab quenched after the third pass x 210

Fig.99 Transverse sections of as-rolled stainless steel slabs.

(a) Quenched 2 seconds after first pass
Centre x 600

(b) Air cooled after a 30% at T_1, reheat at 1040°C, 30% at T_2, 30% at T_3 schedule.
Centre x 520.

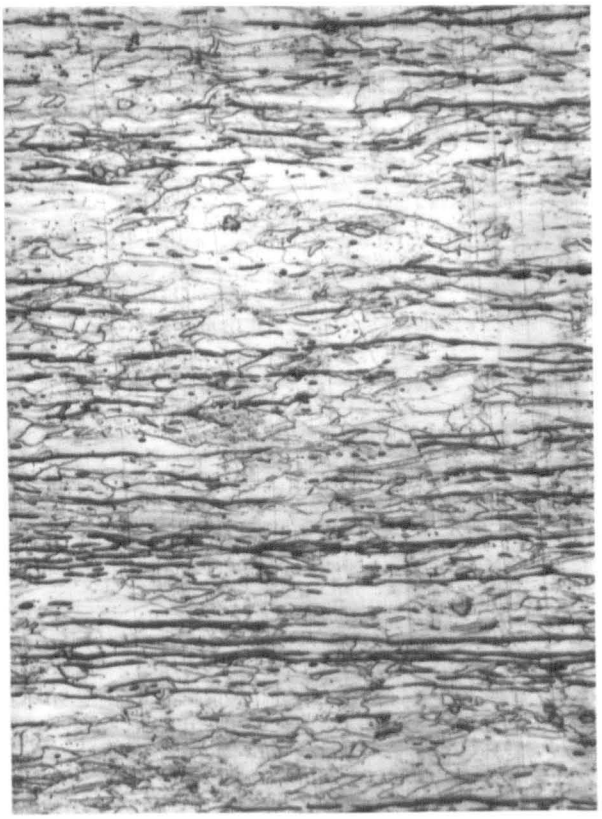

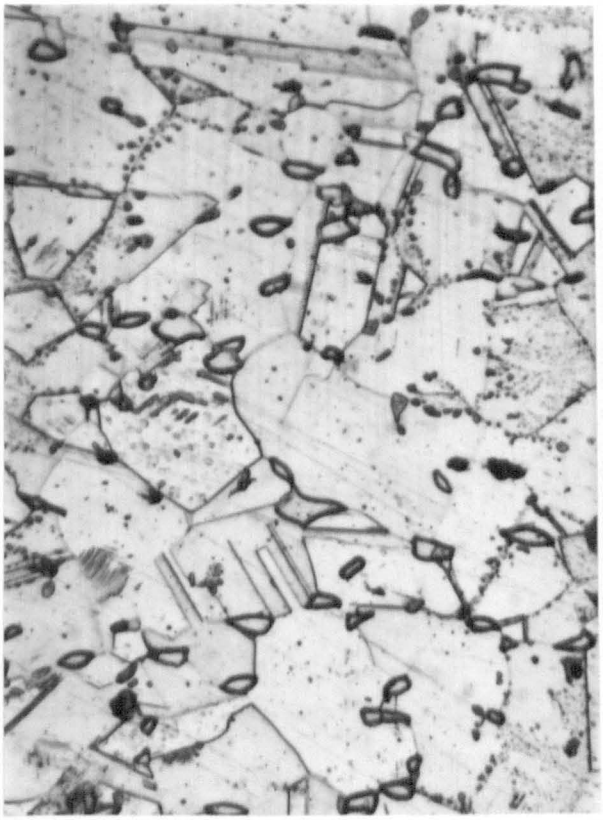

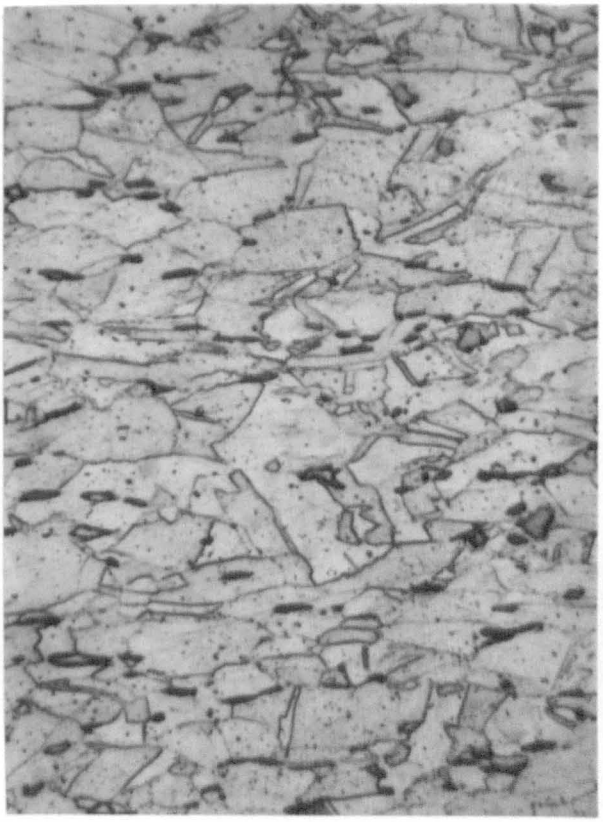

Fig.100 Longitudinal sections of as-rolled stainless steel slabs following a T_1, reheat at 1040°C for 20 minutes, T_2, T_3 schedule.

(a) Centre x 210

(b) Centre x 480

Fig.101 Structural changes in slabs given a T_1, T_3 schedule and reheated at 1000°C; longitudinal sections.

(a) Annealed for 600 sec. Centre x 144

(b) Annealed for 600 sec. Surface x 144

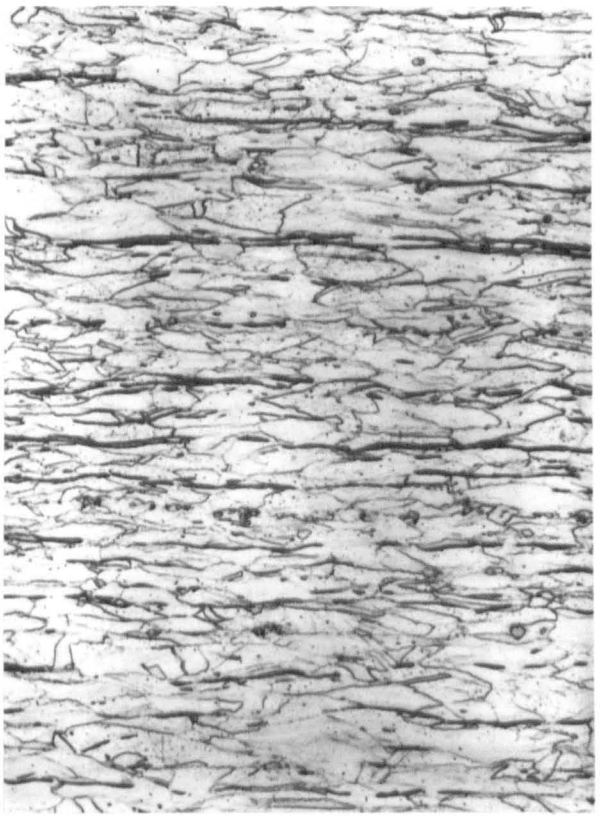

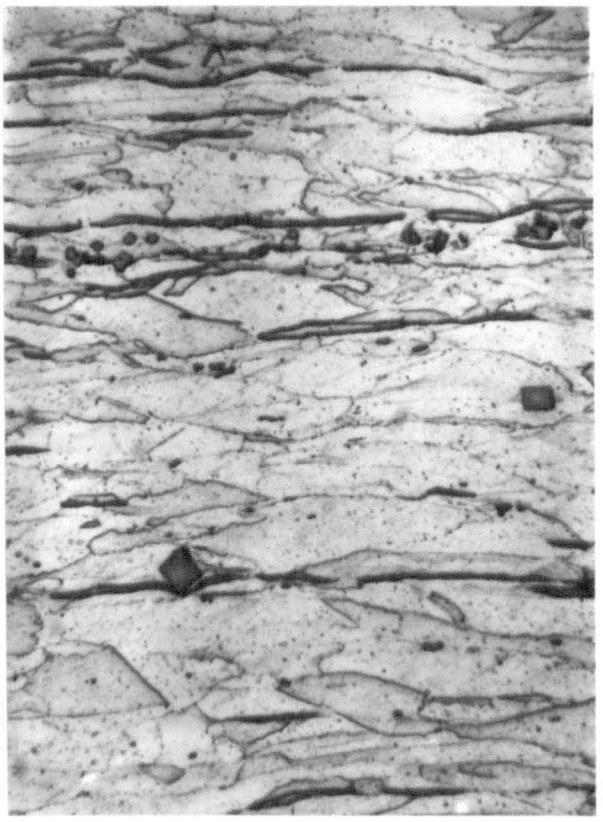

Fig.101 contd.

(c) Annealed for 1200 secs. Centre x 144

(d) Annealed for 1200 secs. Surface x 144

(e) Annealed for 2400 secs. Centre x 144

(f) Annealed for 2400 secs. Surface x 144

(g) Annealed for 19200 secs. Centre x 144

(h) Annealed for 19200 secs. Surface x 144

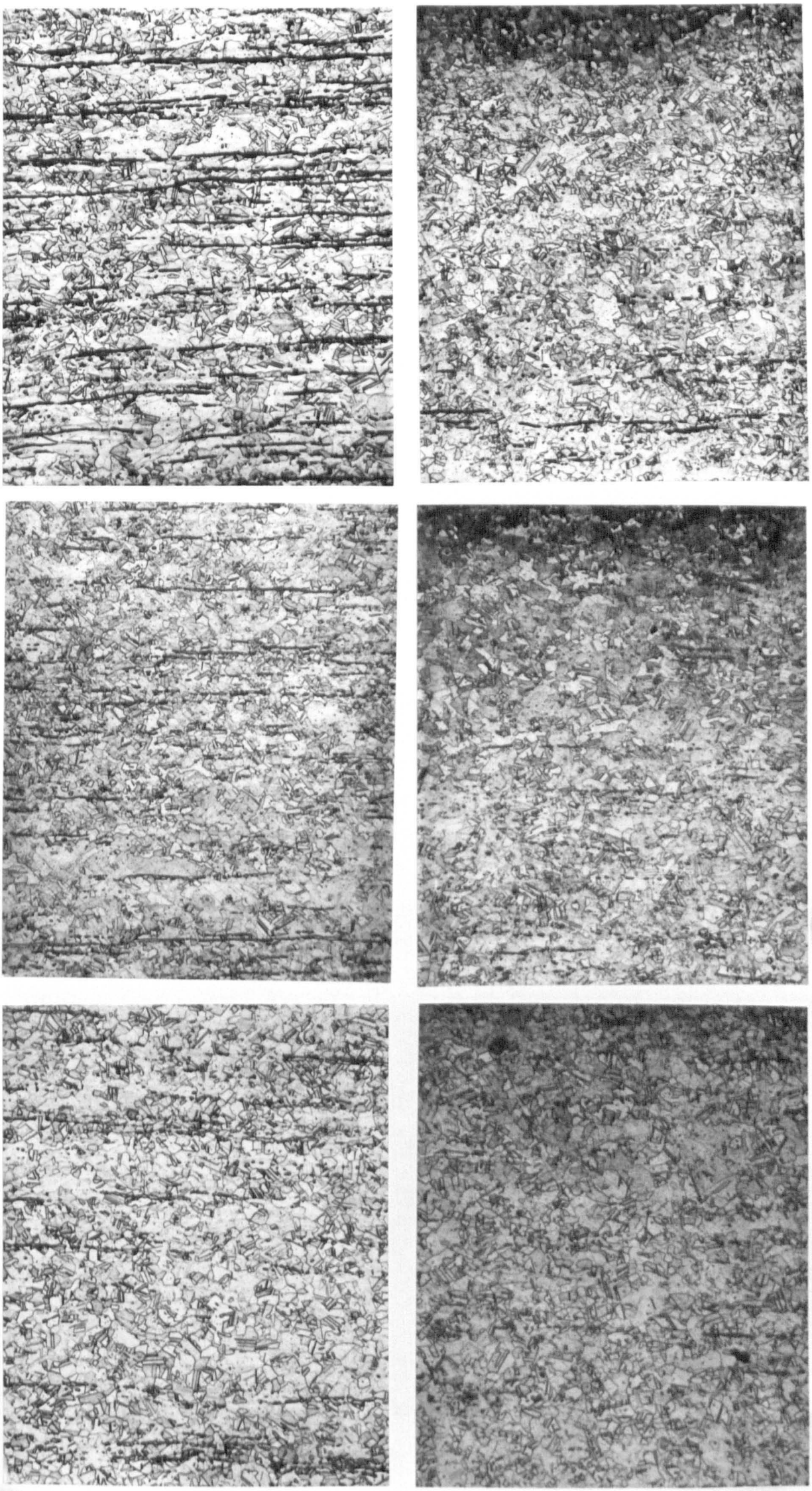

Fig.102 Initial (undeformed head) structures of stainless steel torsion specimens

(a) Reheated at 800°C
Longitudinal section
x 130

(b) Reheated at 1100°C
Longitudinal section
x 130

(c) Reheated at 800°C
Transverse section
x 130

(d) Reheated at 1100°C
Transverse section
x 130

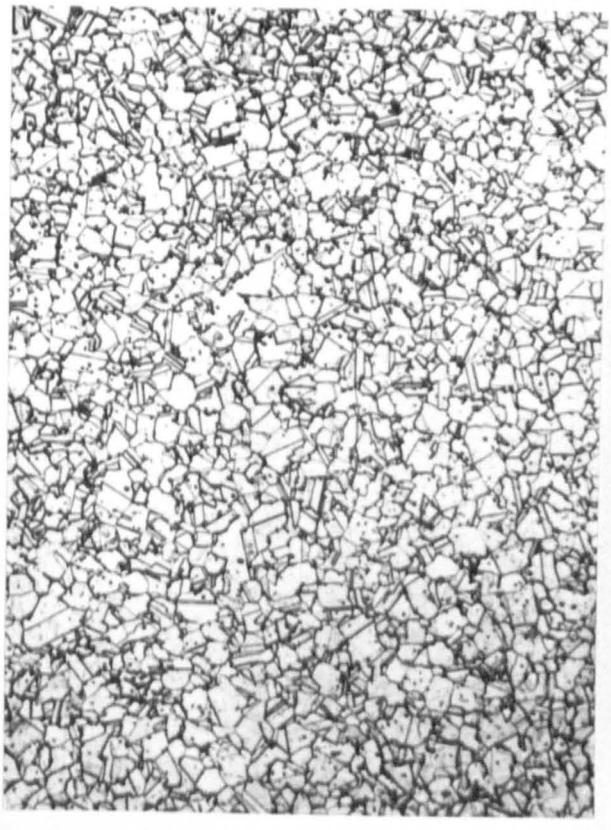

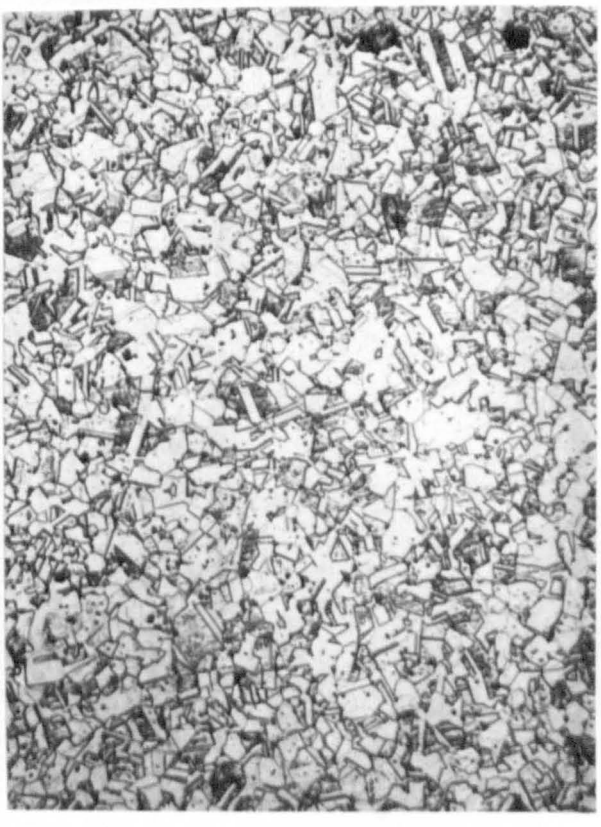

Fig.102 (contd)

(e) Reheated at 800°C
Transverse section
x 400

(f) Reheated at 1100°C
Transverse section
x 400

(g) Reheated at 1180°C prior to cooling to 900°C and testing
Transverse section x 130.

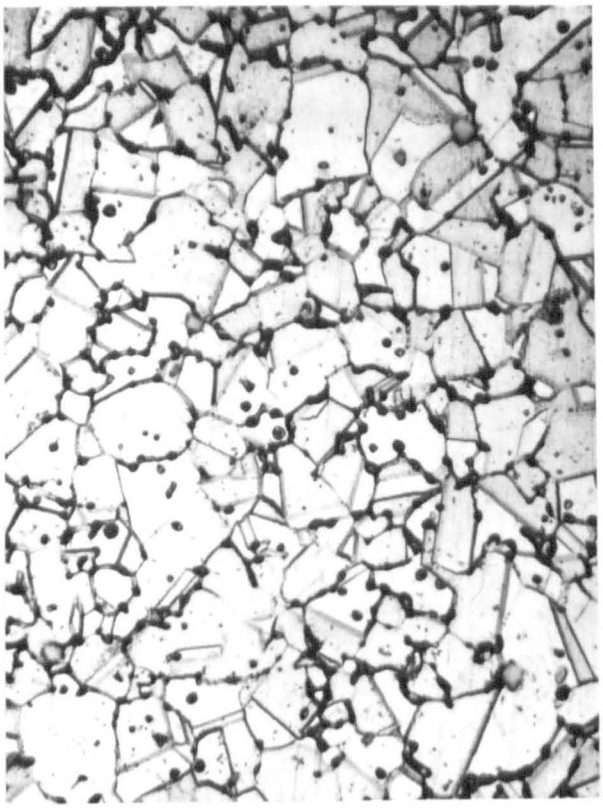

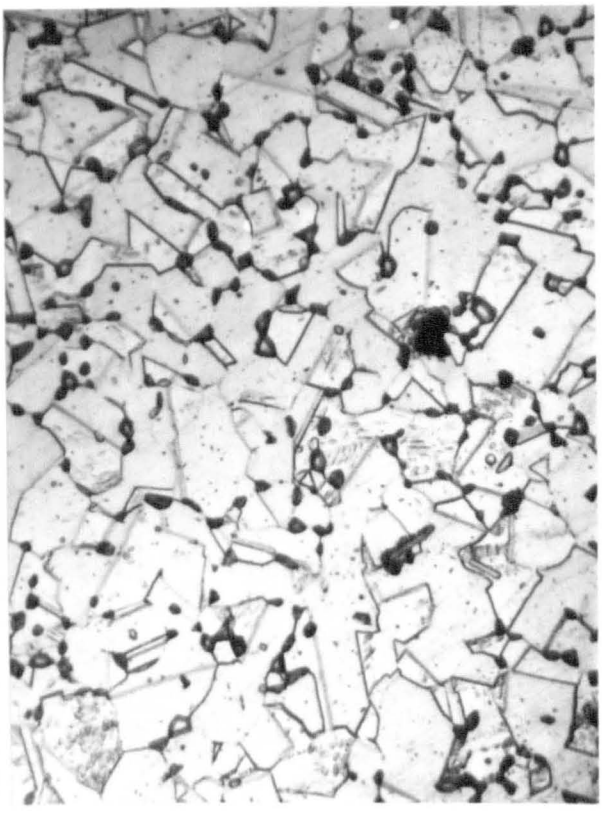

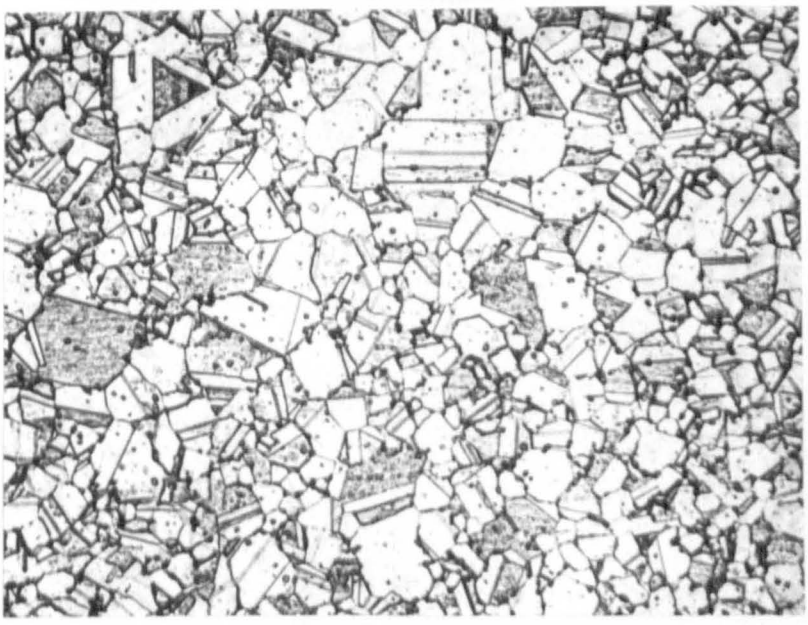

Fig.103 Thin foil electron microscopy to show effect of annealing treatments on as-extruded stainless steel bar.

(a) Annealed at 800°C
x 25,000

(b) Annealed at 1100°C
x 25,000

(c) Annealed at 800°C
x 55,000

(c) Annealed at 1100°C
x 55,000

(e) Annealed at 800°C
x 95,000

(f) Annealed at 1100°C
x 95,000

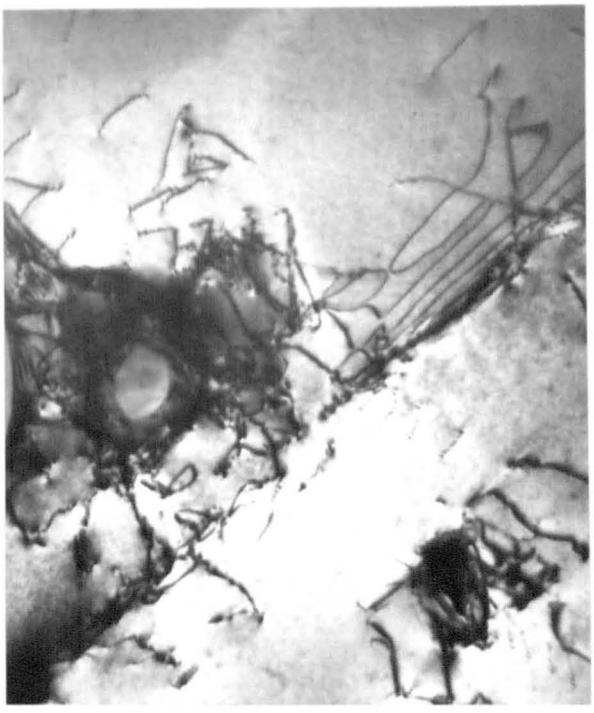

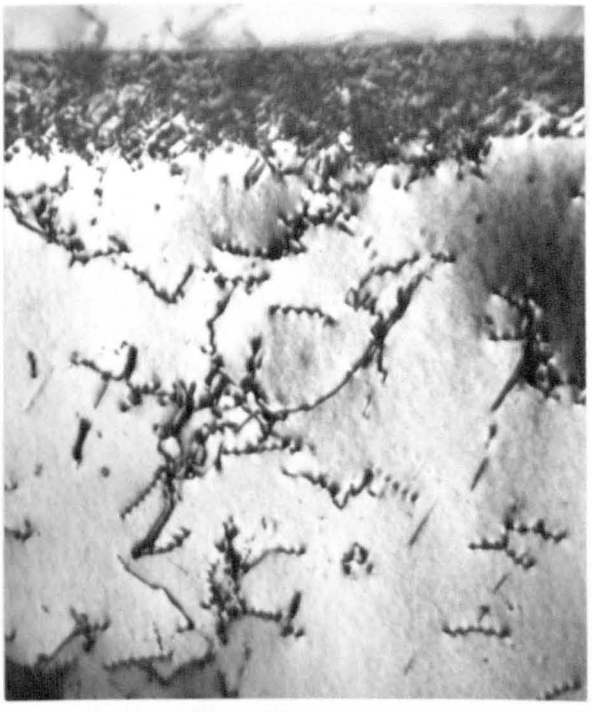

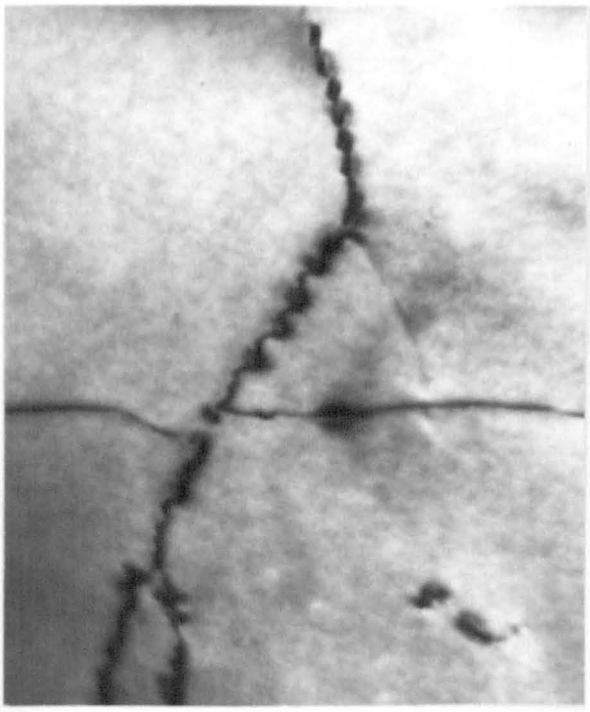

Fig.104 Thin foil electron microscopy of annealed, as-extruded stainless steel bar.

(a) Annealed at 800°C

Stacking fault tetrahedron x 104,000

(b) Annealed at 1100°C

Stacking faults x 65,000.

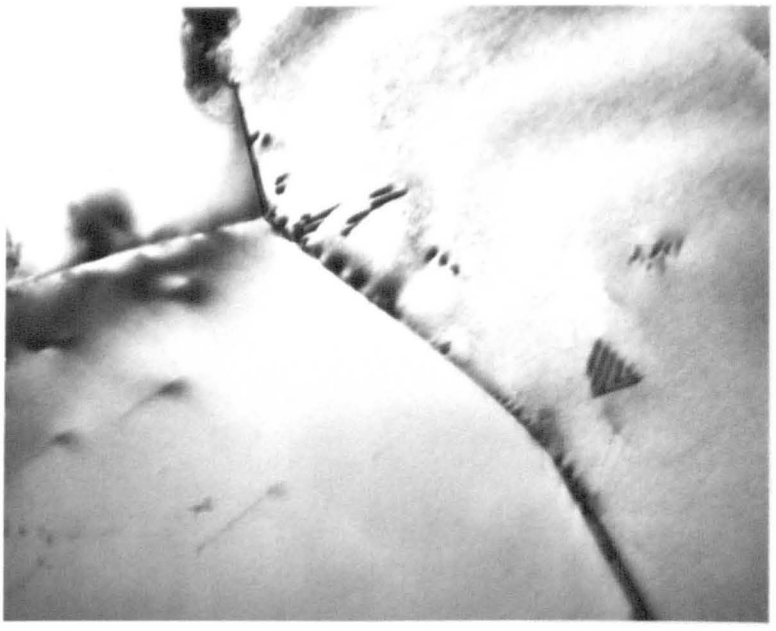

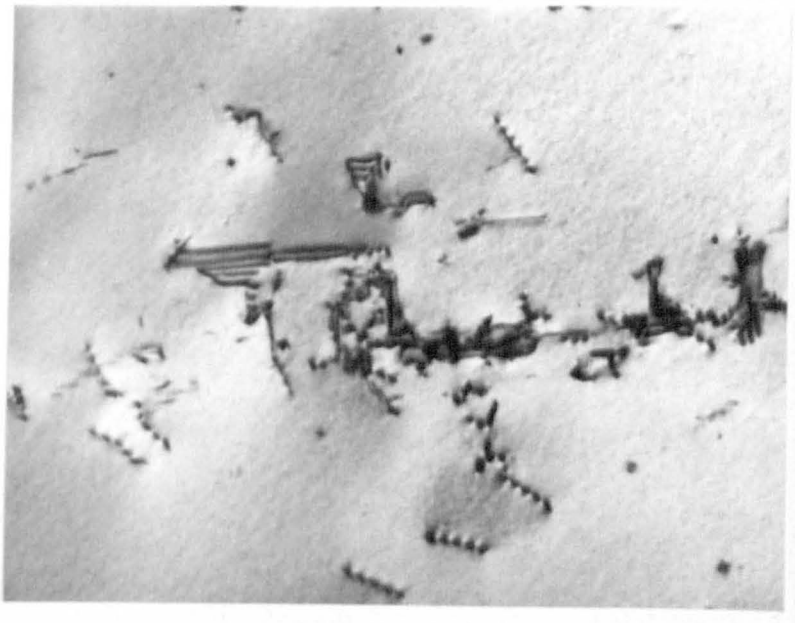

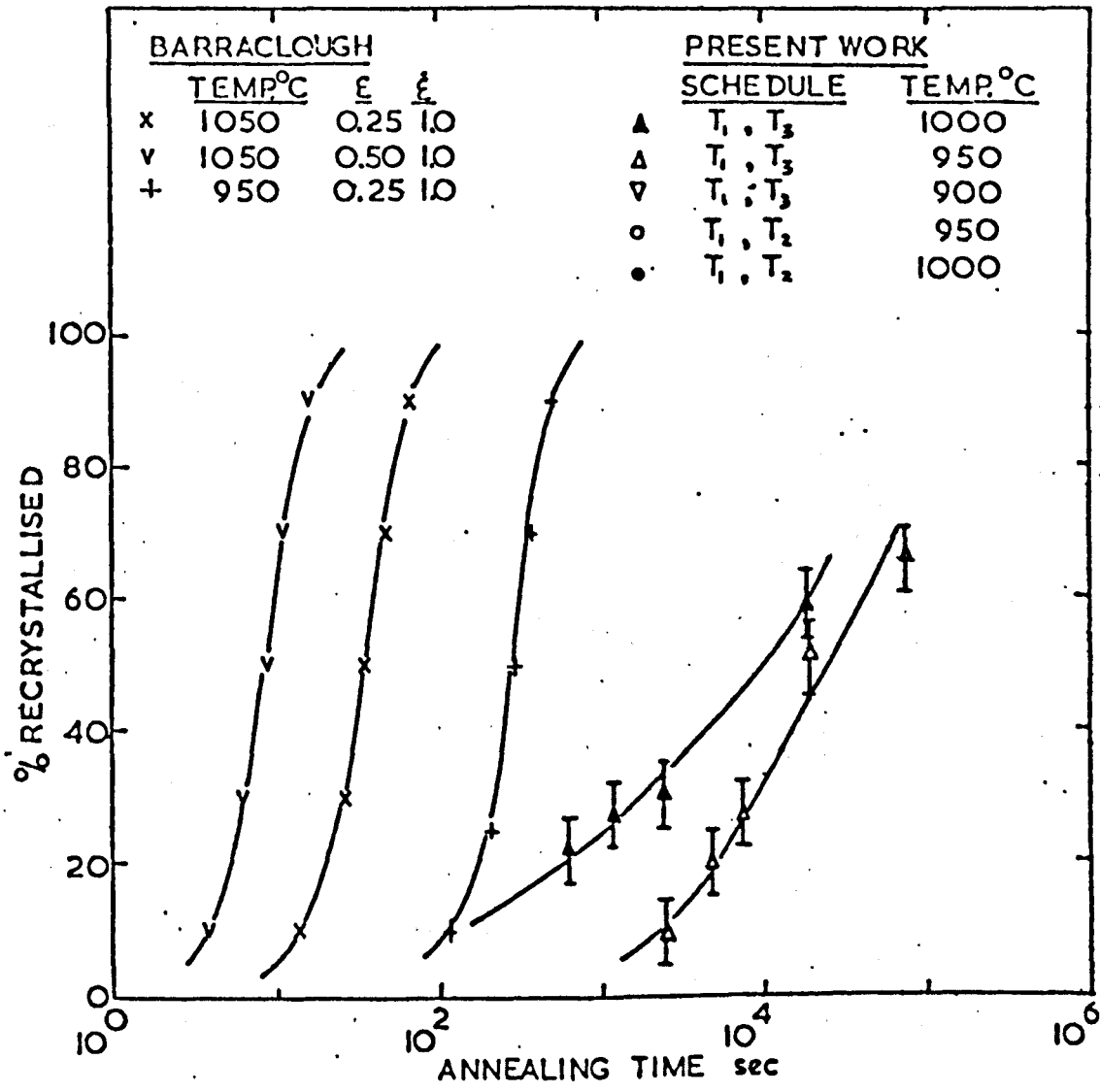

Fig.105 Progress of recrystallisation in stainless steel slabs given different rolling schedules and annealed at temperatures between 900°C and 1000°C.

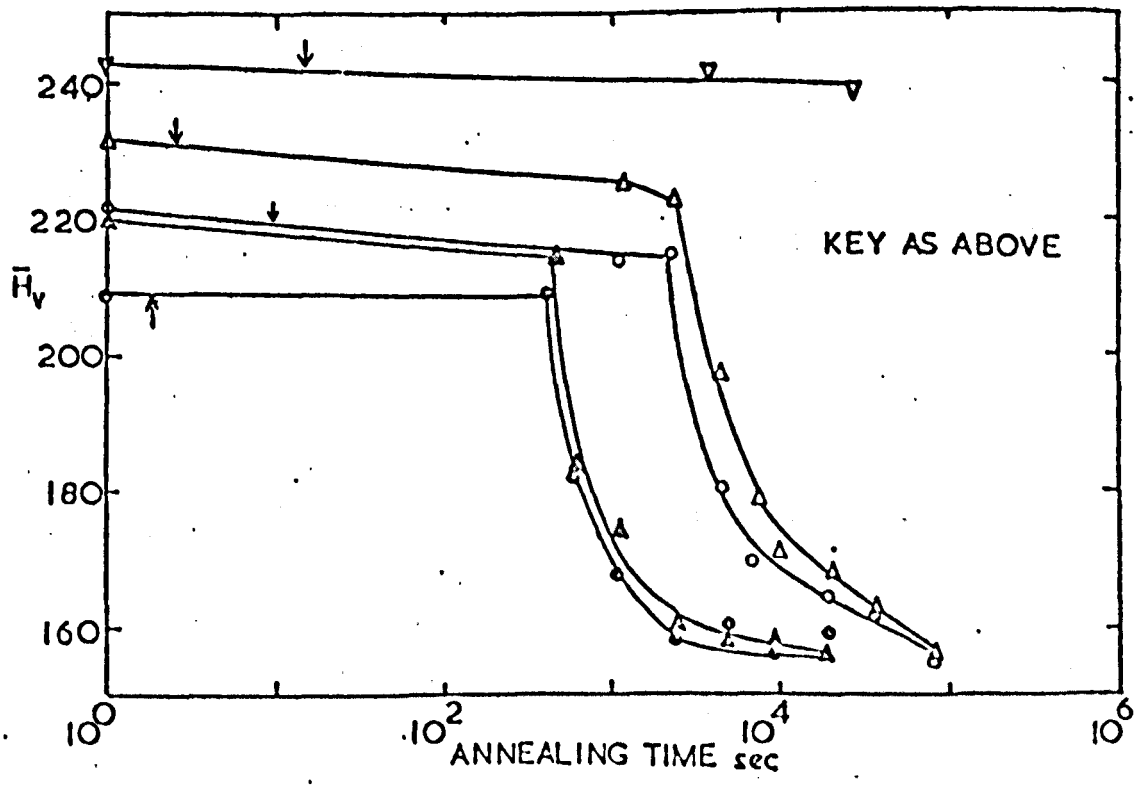

Fig.106 Change in Vickers hardness during annealing treatments. Arrows indicate time for 10% recrystallisation predicted from Barraclough (1974).

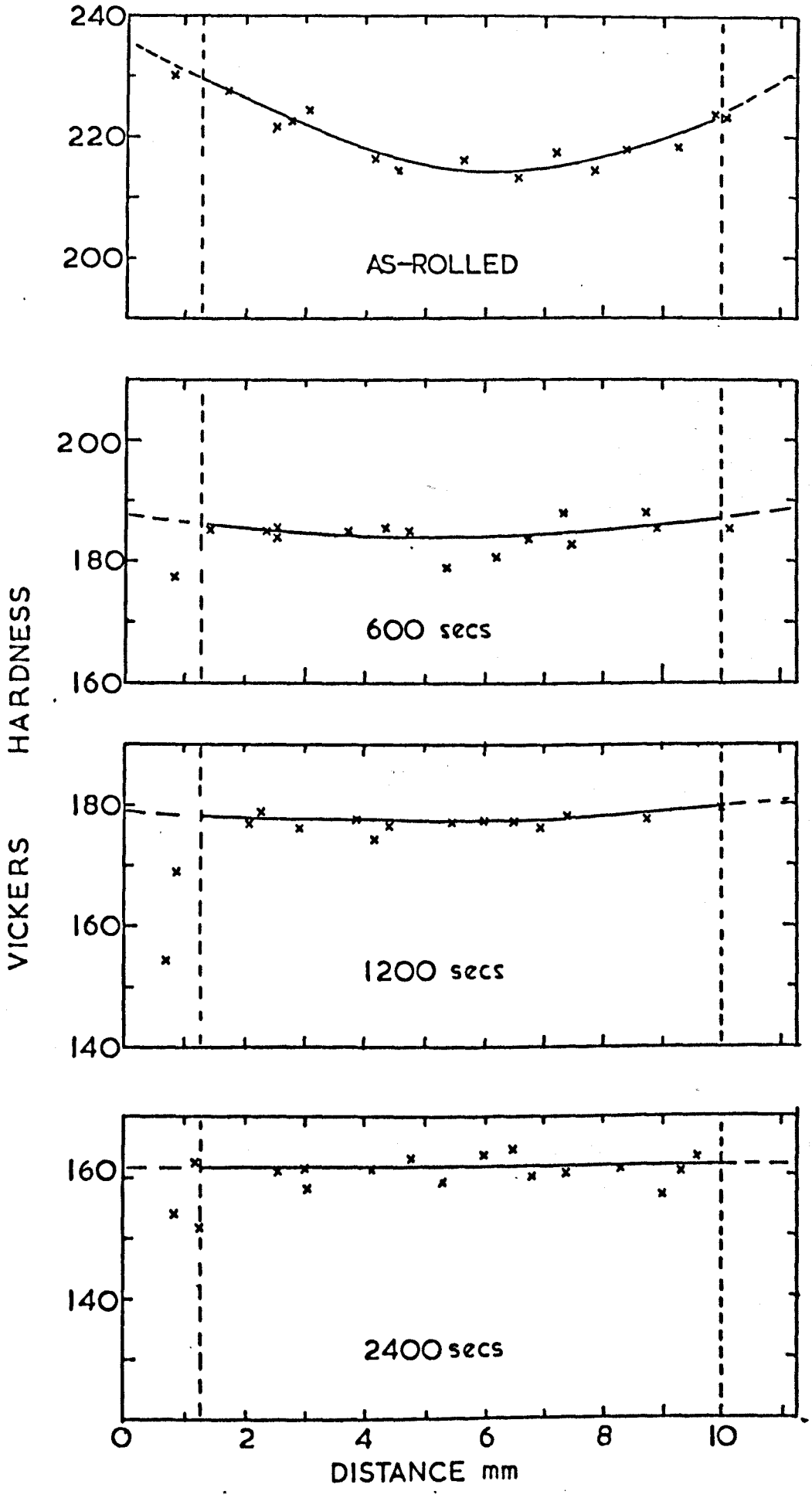

Fig.107 Changes in through thickness hardness profile of stainless slabs given a T_1, T_3 schedule and annealed at 1000°C. Broken lines indicate areas outside which hardness measurements not valid due to proximity of surface.

Fig.108 Structural and Compositional Changes at surface of slabs.

(a) Retarded recrystallisation at the surface (L.H. edge) of a slab given a T_1, T_3 schedule and annealed for 81900 seconds at 950°C. Mag.x 500.

(b) Corresponding Cr distribution

(c) Corresponding Ni distribution

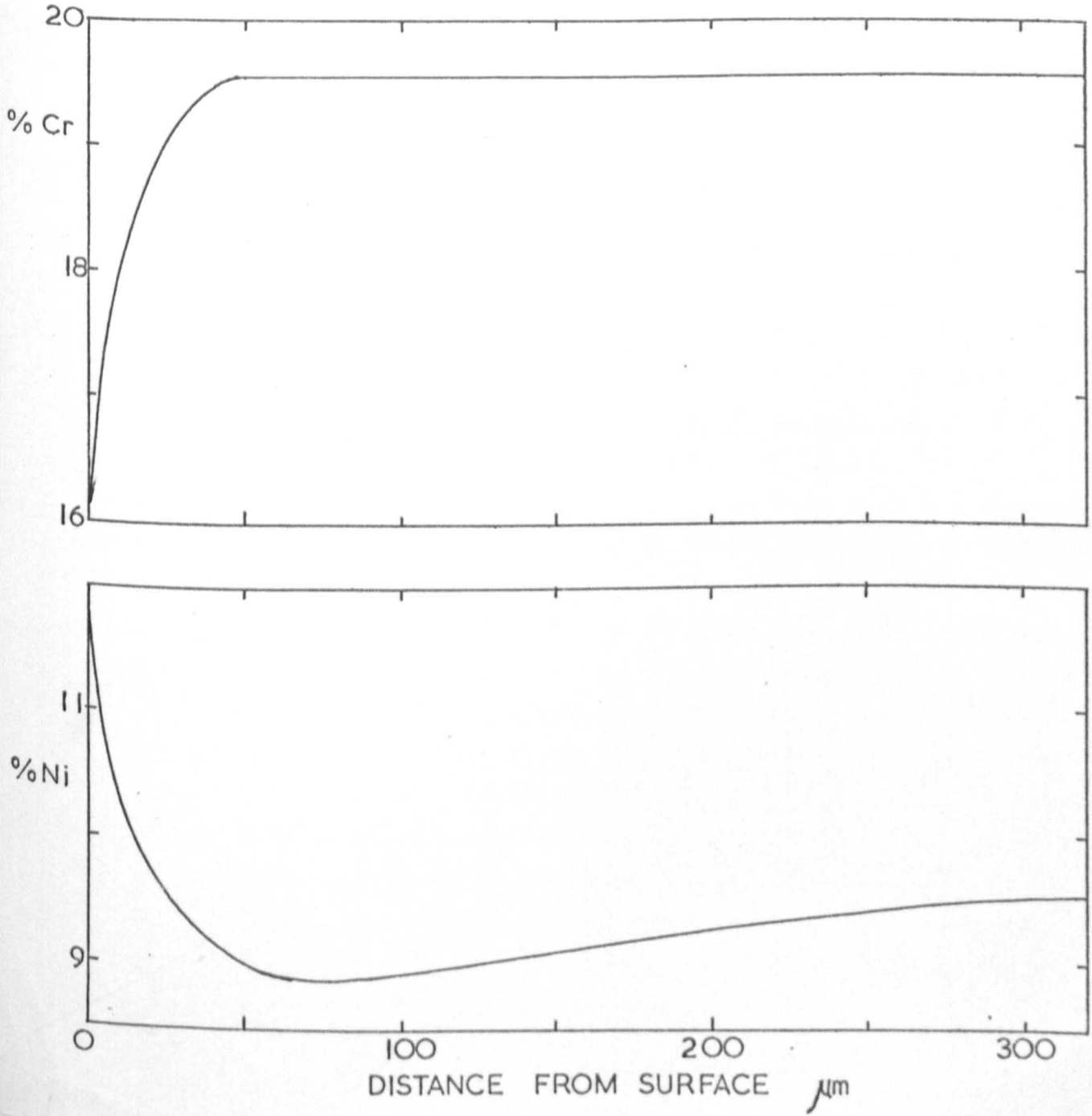
20
% Cr
18
16
11
%Ni
9
0
100
200
300
DISTANCE FROM SURFACE μm

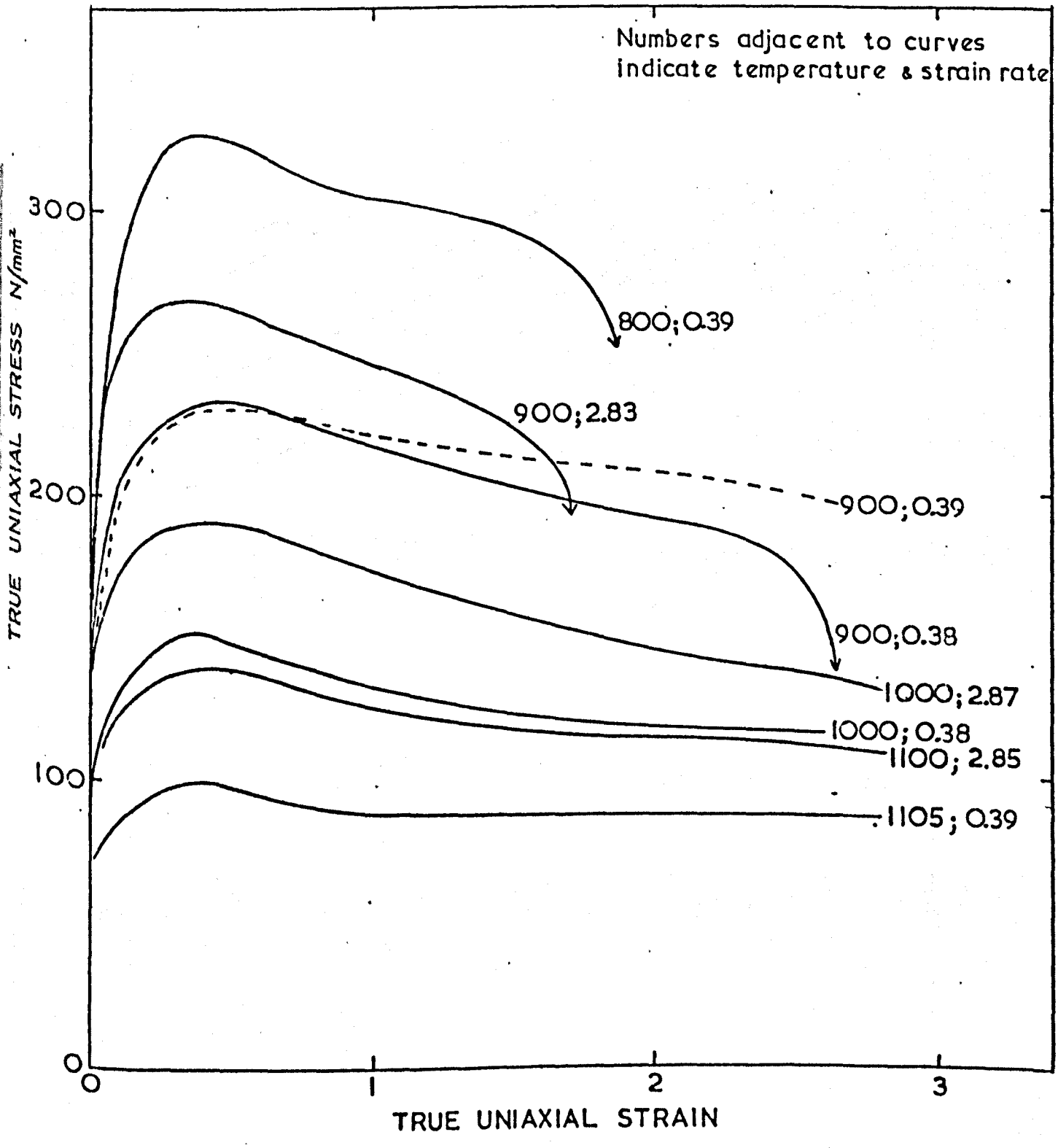

Fig.109 Stress-strain curves for stainless steel derived from torsion tests. The broken line indicates the specimen heated to 1180°C prior to testing at 900°C. All other specimens heated directly to test temperature.

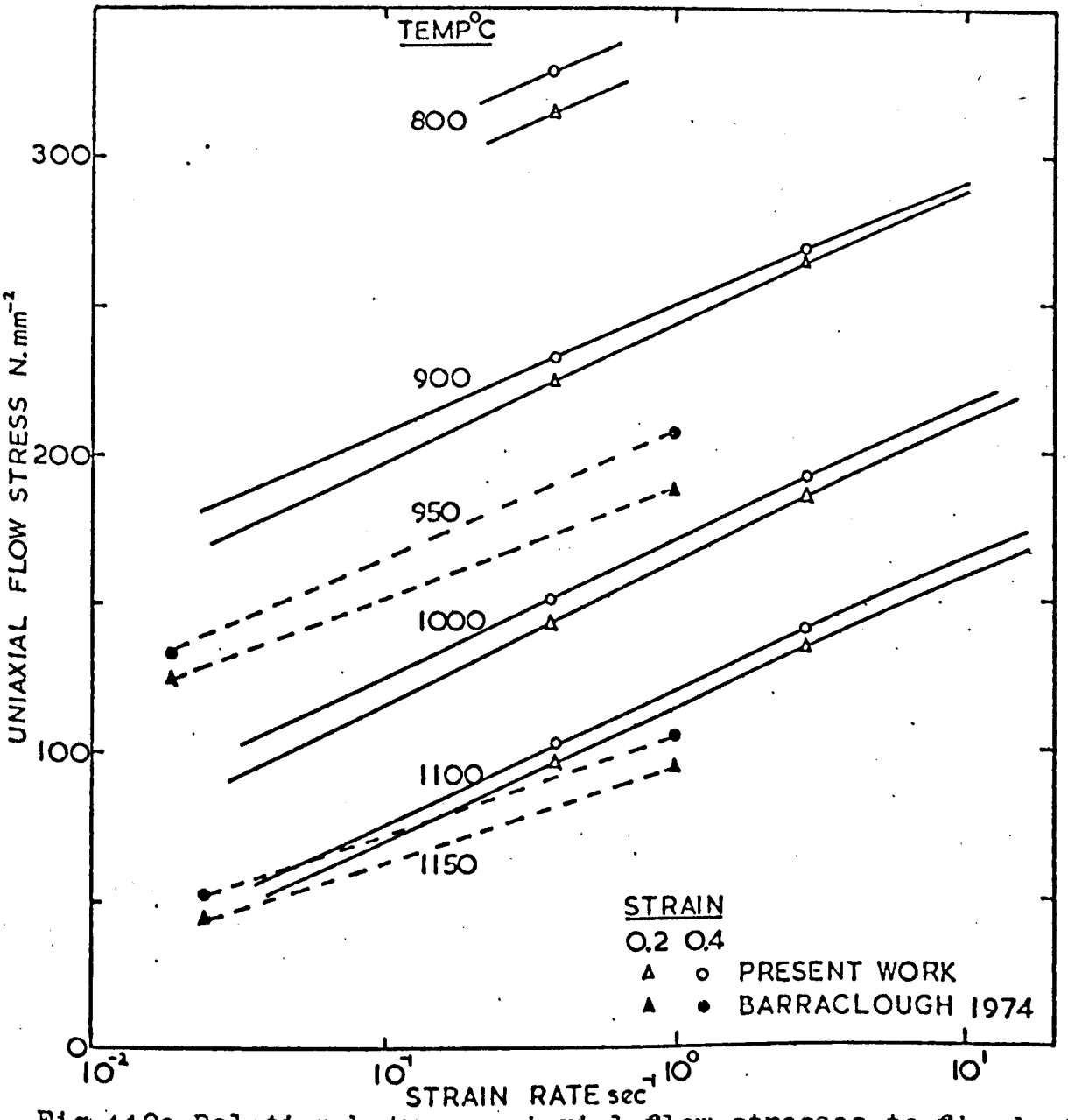

Fig.110a Relation between uniaxial flow stresses to fixed strains and strain rate at different test temperatures.

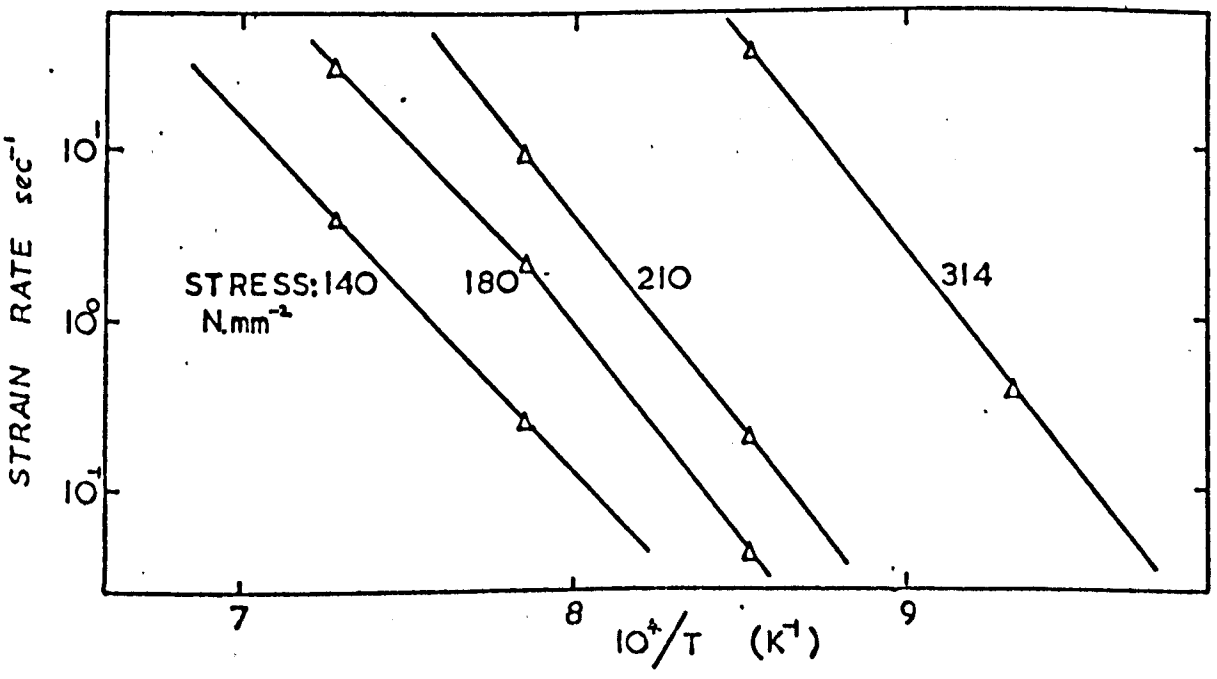

Fig.110b Correlation of the strain rate at a constant stress with temperature for stainless steel.

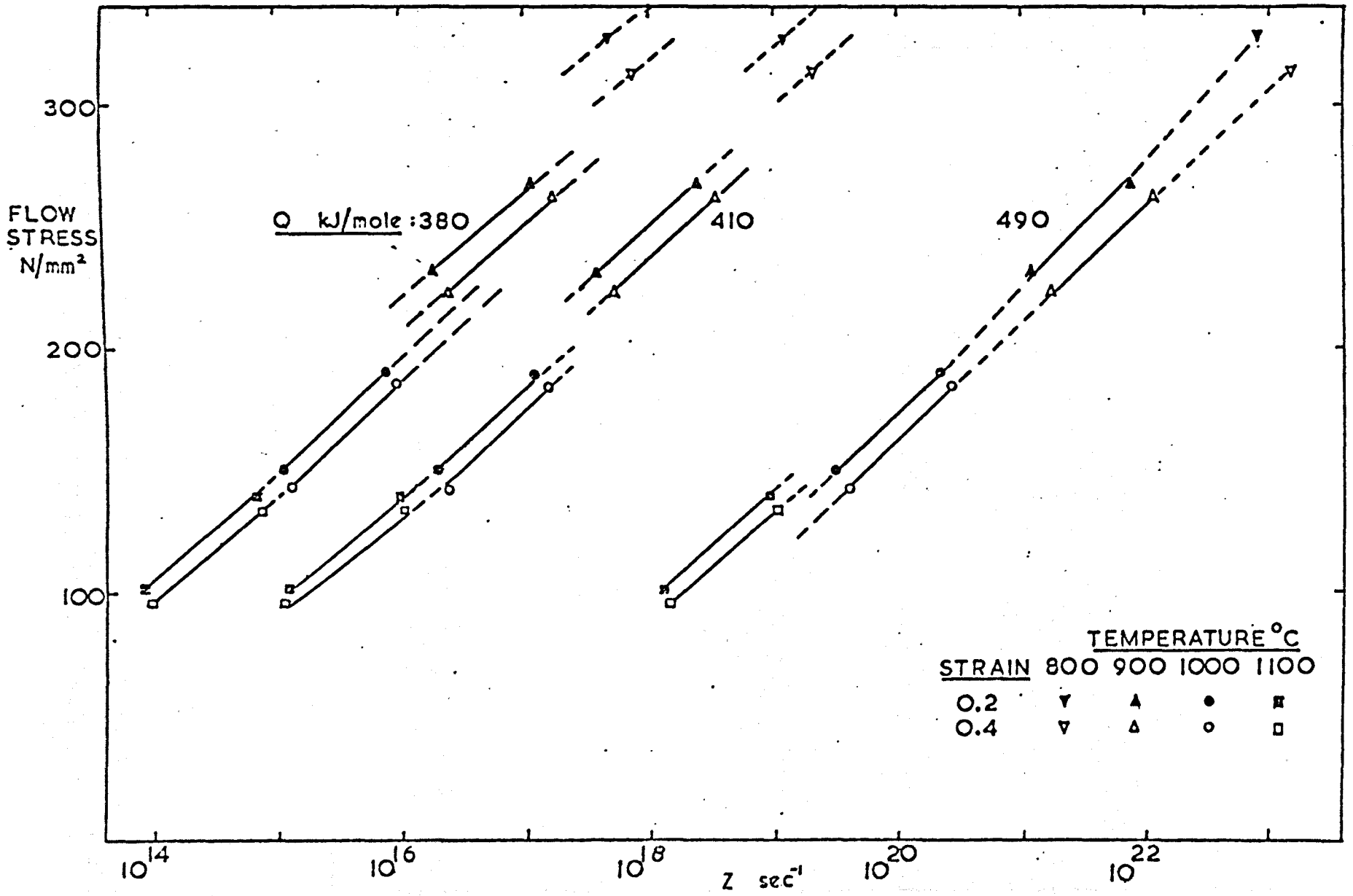

Fig.111 Correlation of uniaxial flow stresses (derived from torsion tests) with Z.

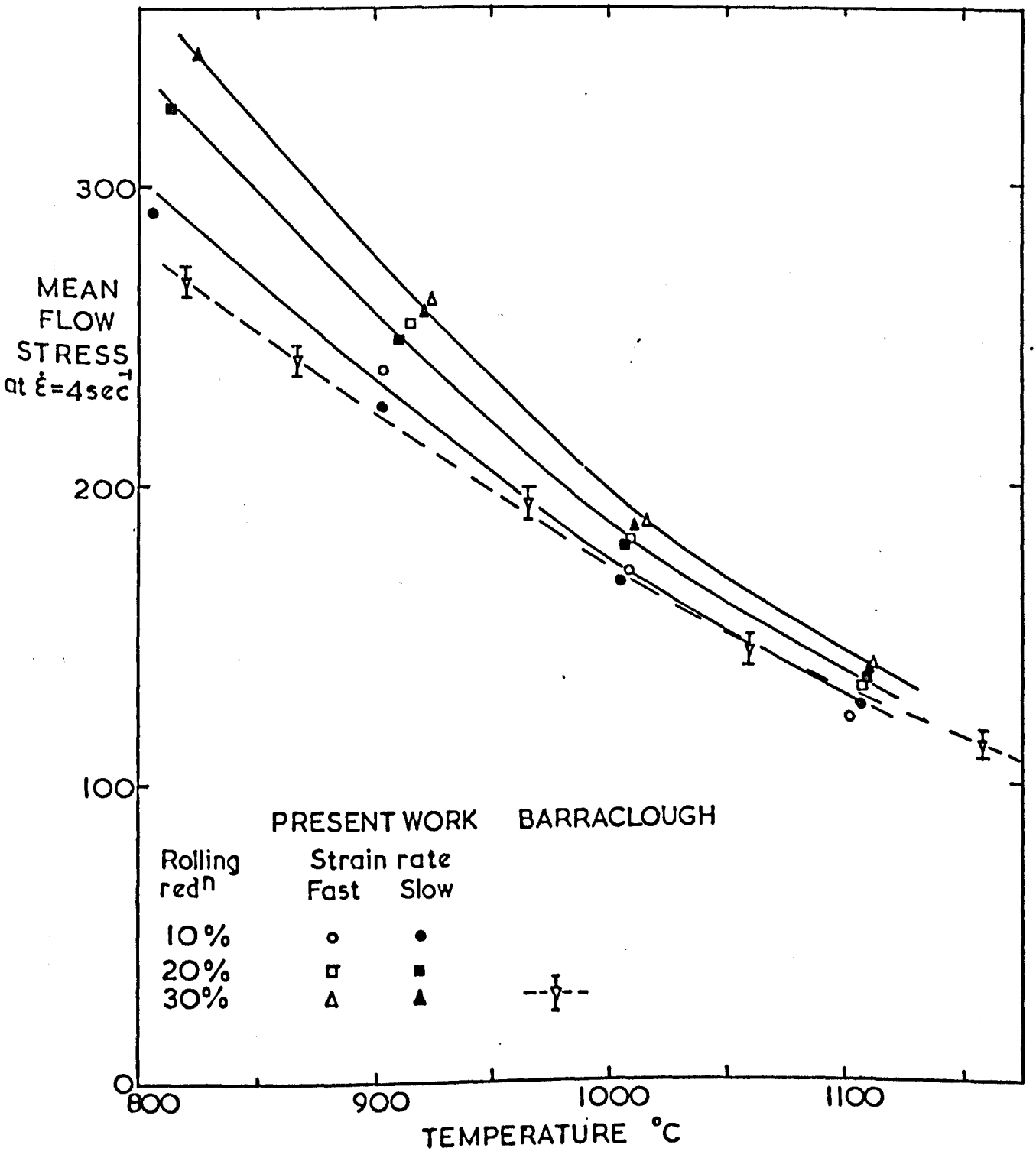

Fig.112 Mean uniaxial flow stresses, $\bar{\sigma}_g$, derived from torsion tests (corrected to a mean strain rate of 4 sec^{-1}) as a function of temperature for three rolling reductions.

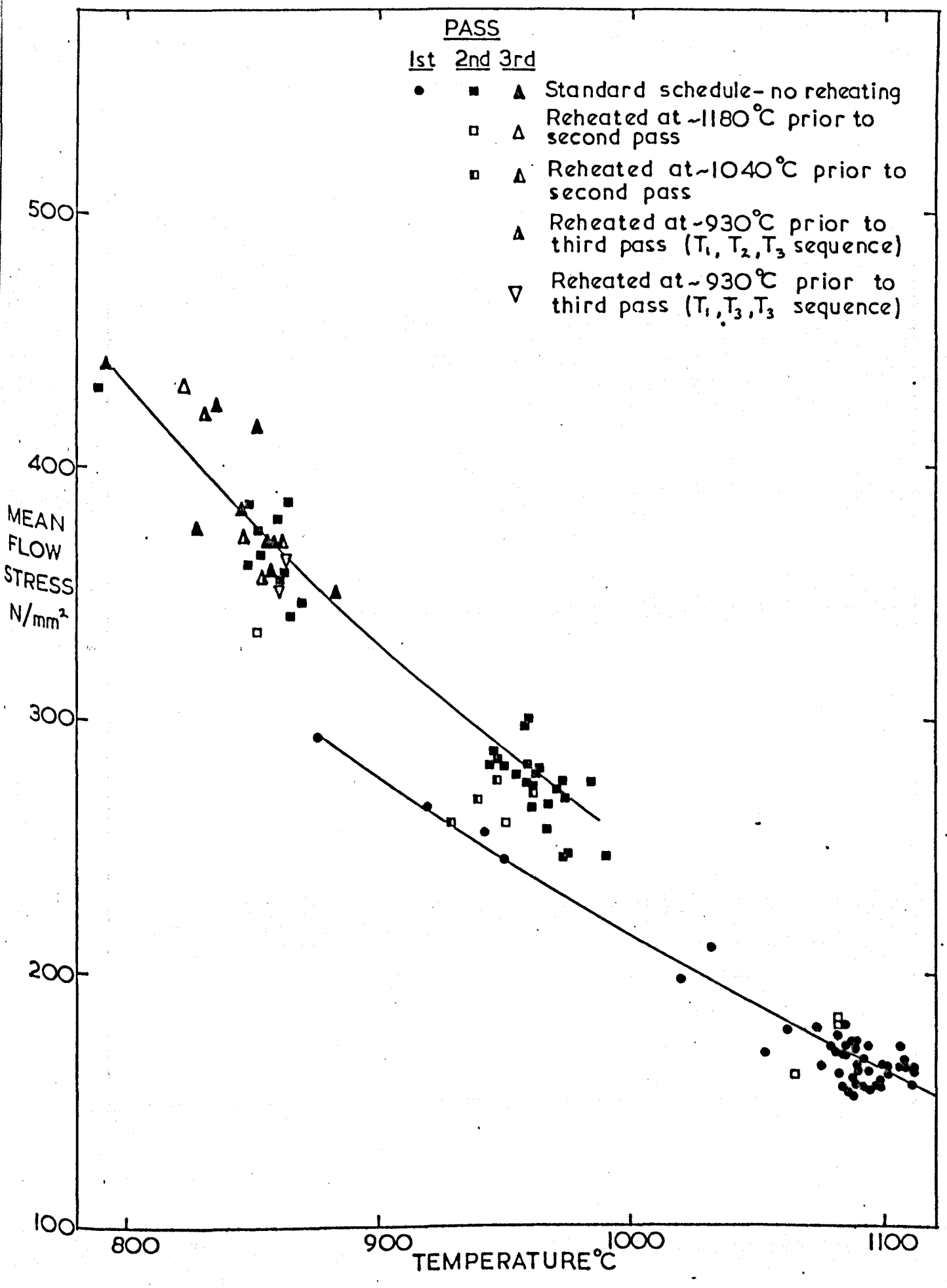

Fig.113 Mean uniaxial flow stresses derived from roll load measurements as a function of mean pass temperature. All nominally 30% passes.

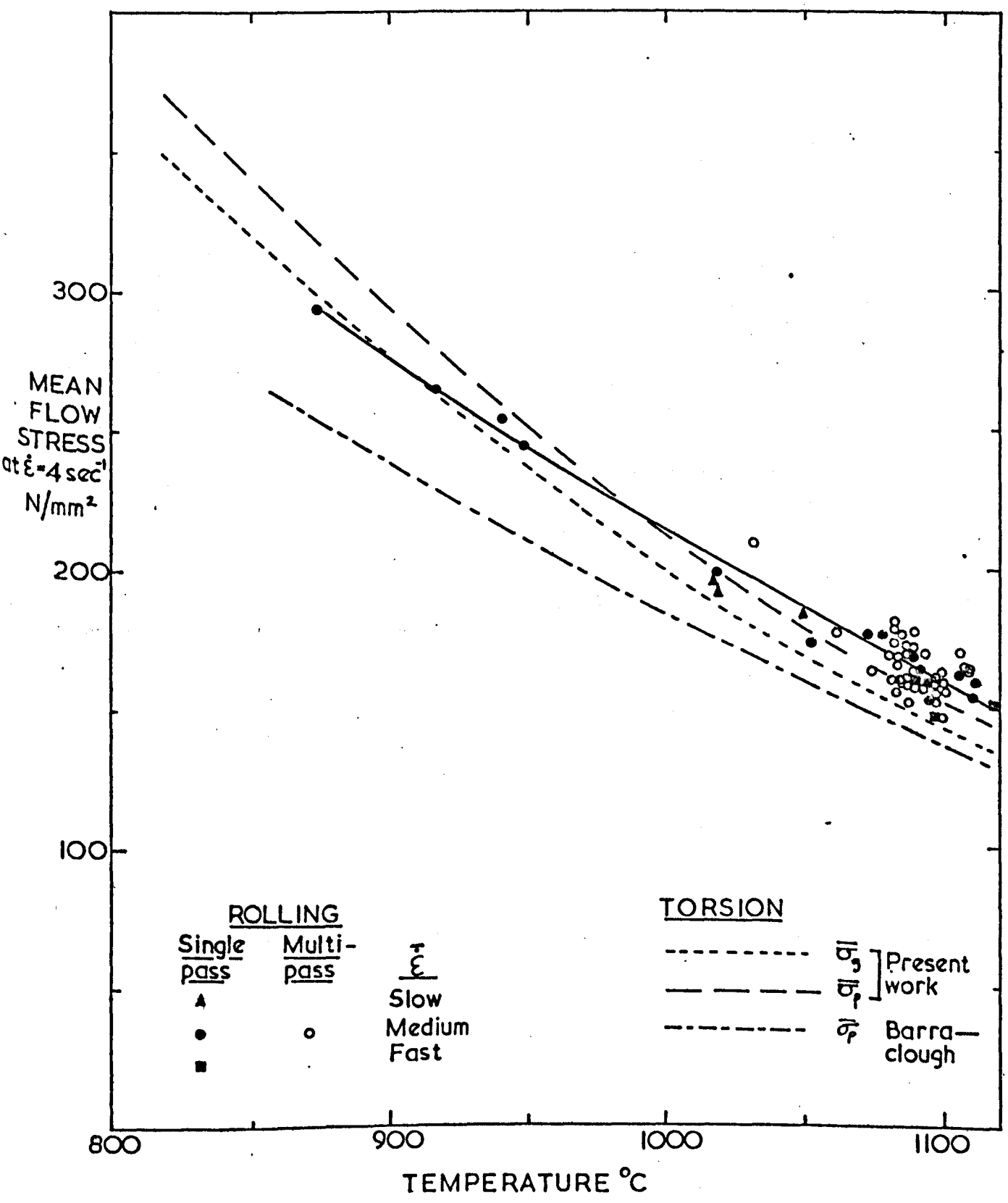

Fig.114 Comparison of mean uniaxial flow stresses derived from rolling and torsion tests and corrected to a mean uniaxial strain rate of 4 sec^{-1}. All nominally 30% passes carried out on recrystallised stainless steel.

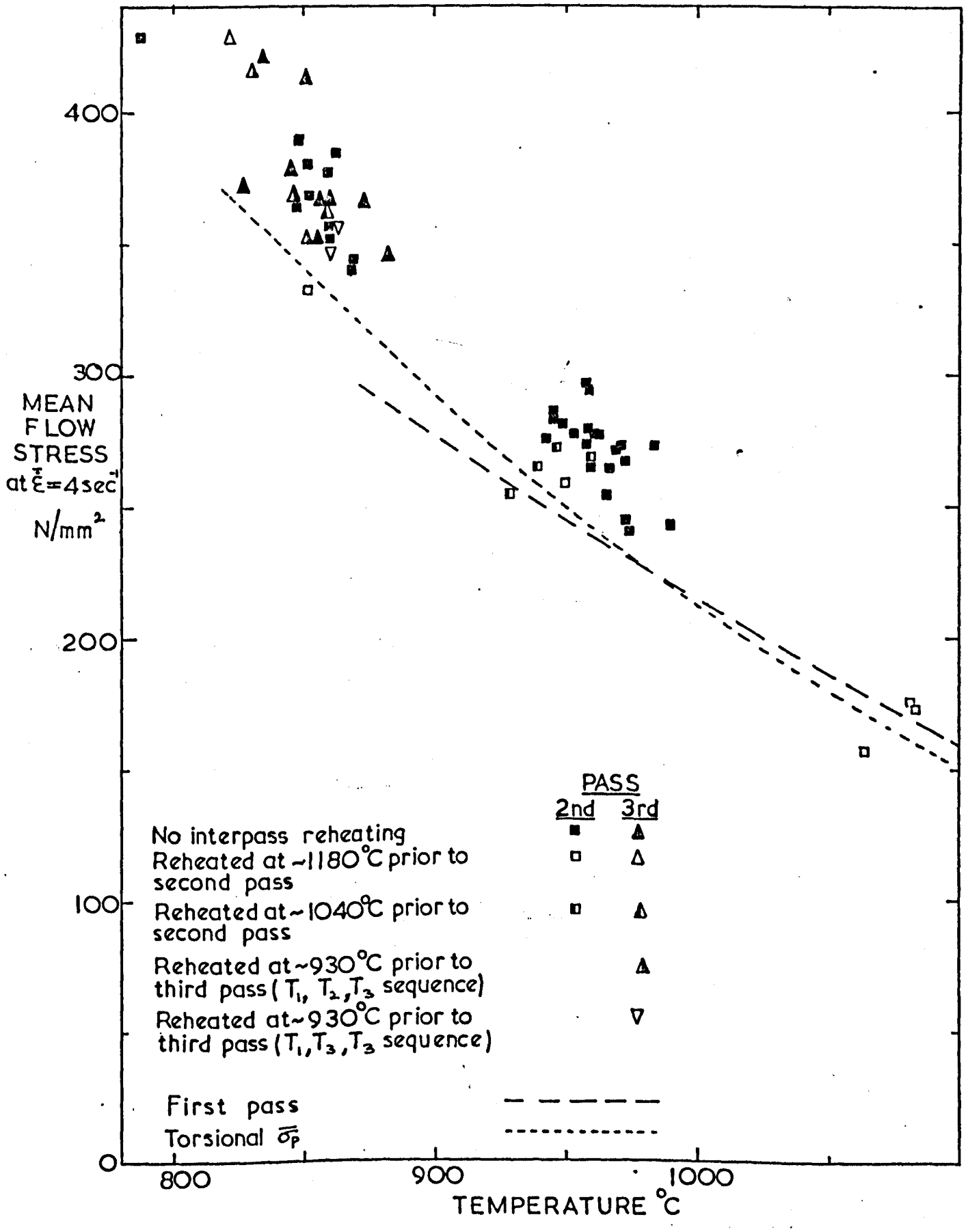

Fig.115 Mean uniaxial flow stresses (corrected to a mean uniaxial strain rate of 4 sec^{-1}) derived from the roll loads for the second and third 30% passes as a function of the mean pass temperature.

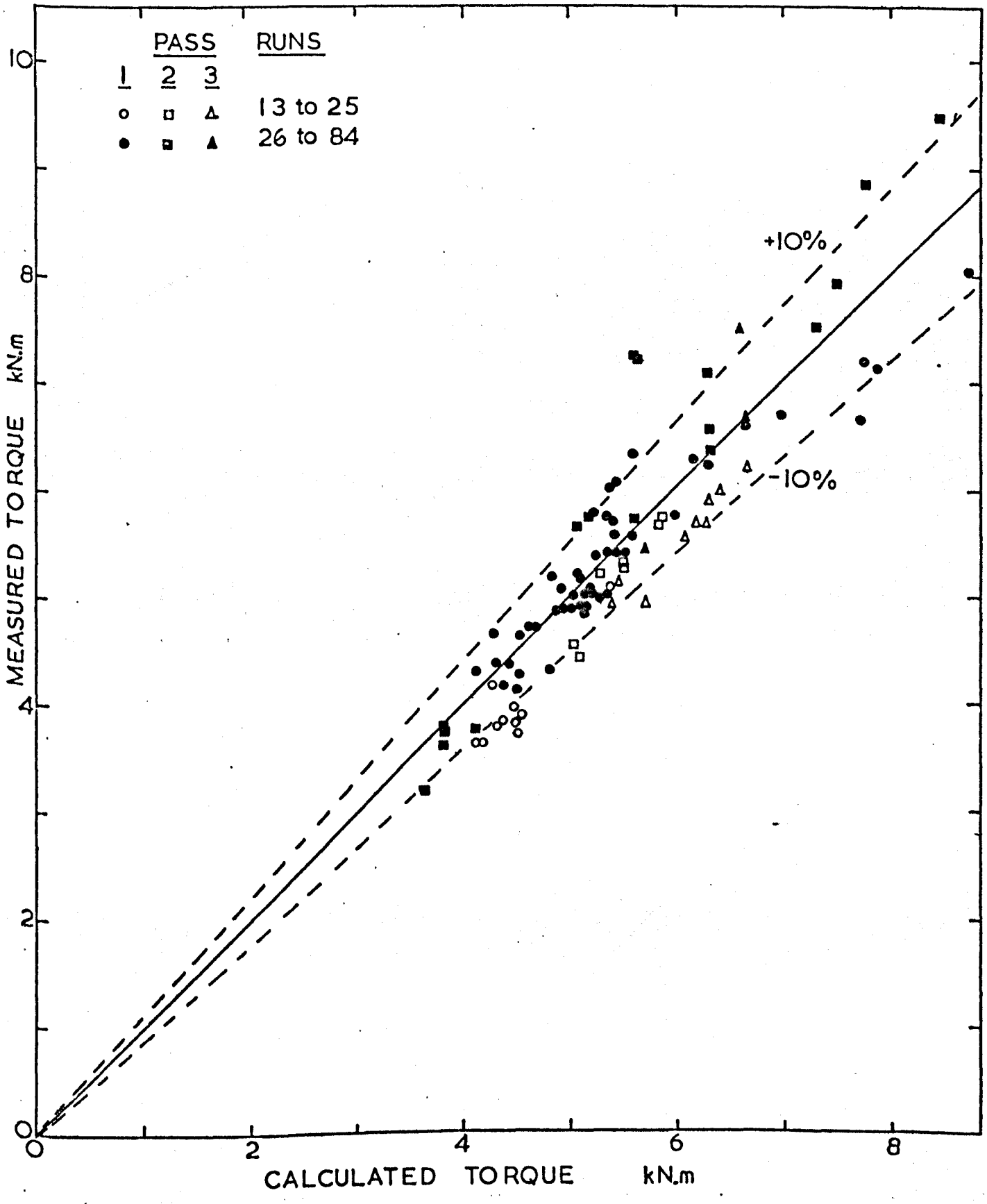

Fig.116 Comparison of total measured torques with total torques calculated from roll loads assuming a coefficient of roll neck friction of 0.03.

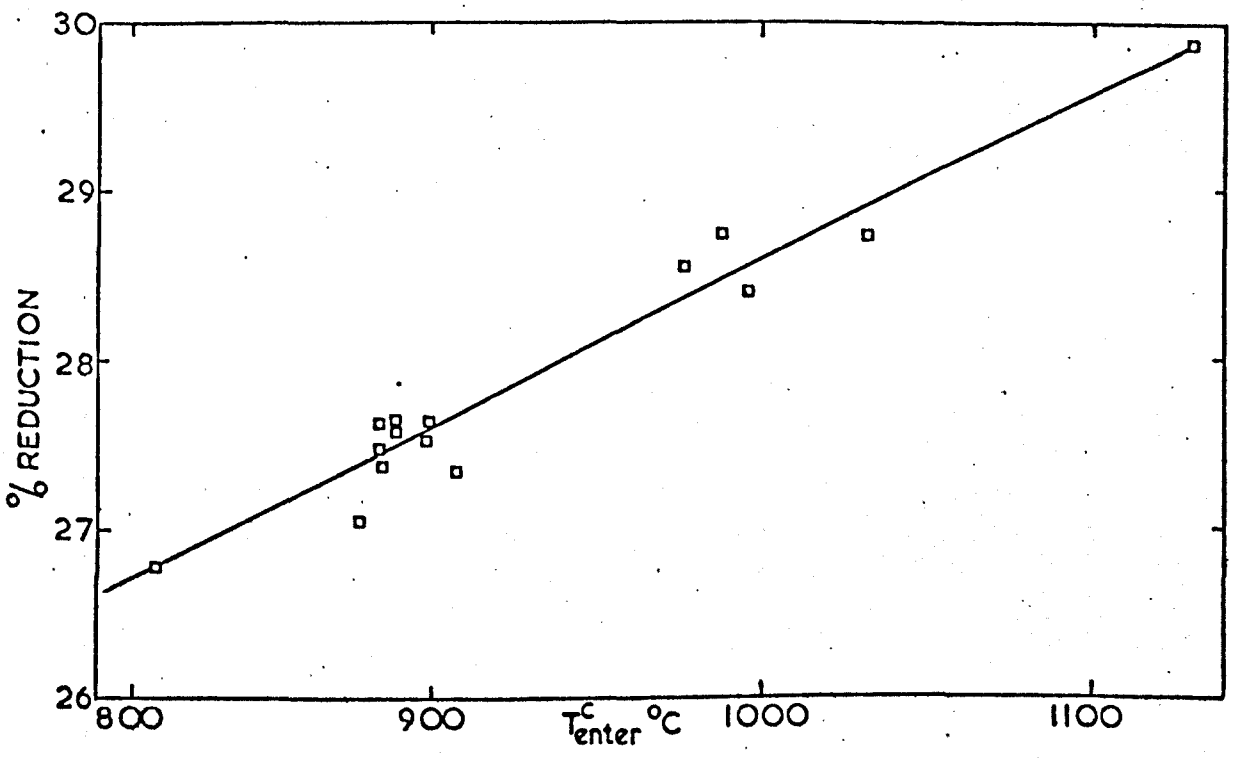

Fig.117a %Reduction obtained during the second pass (nominally 30%) of the stainless steel rolling schedules as a function of entry temperature.

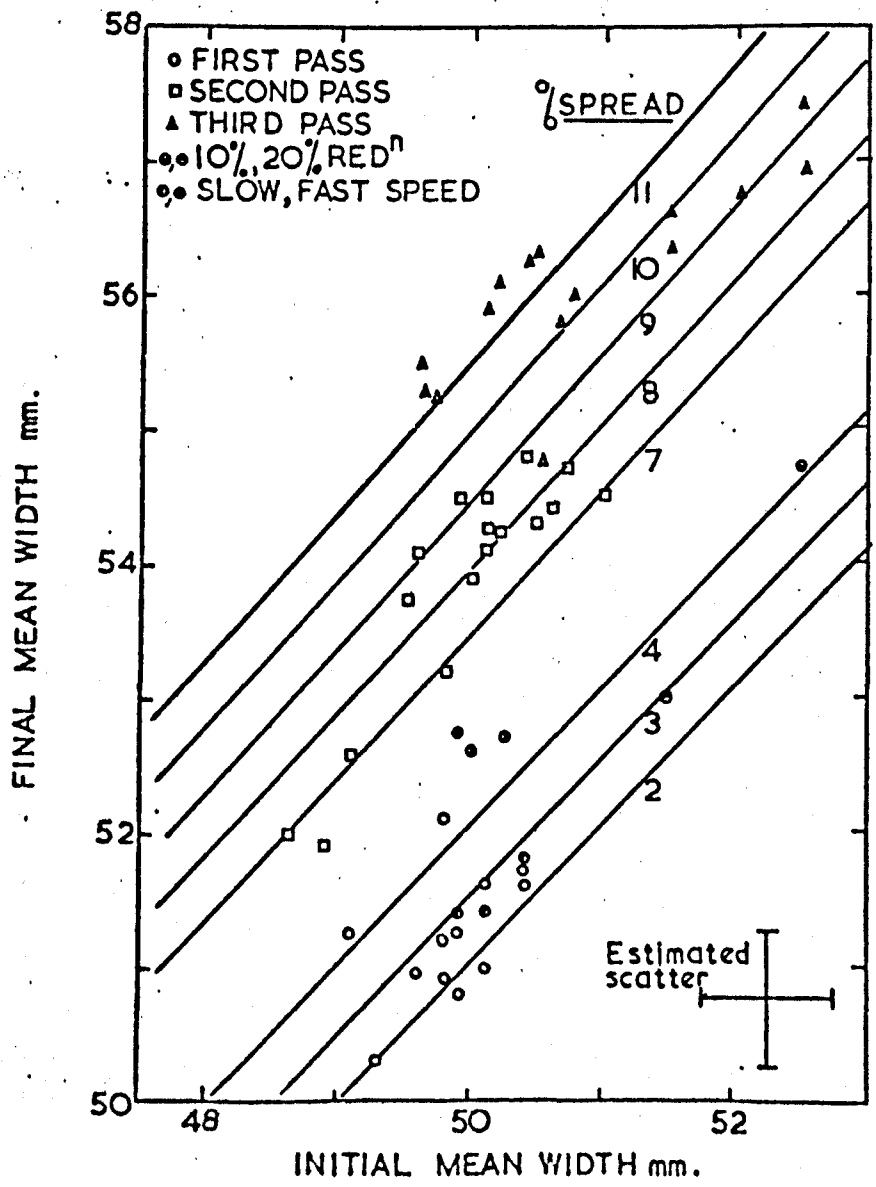

Fig.117b Spread during hot rolling of stainless steel.

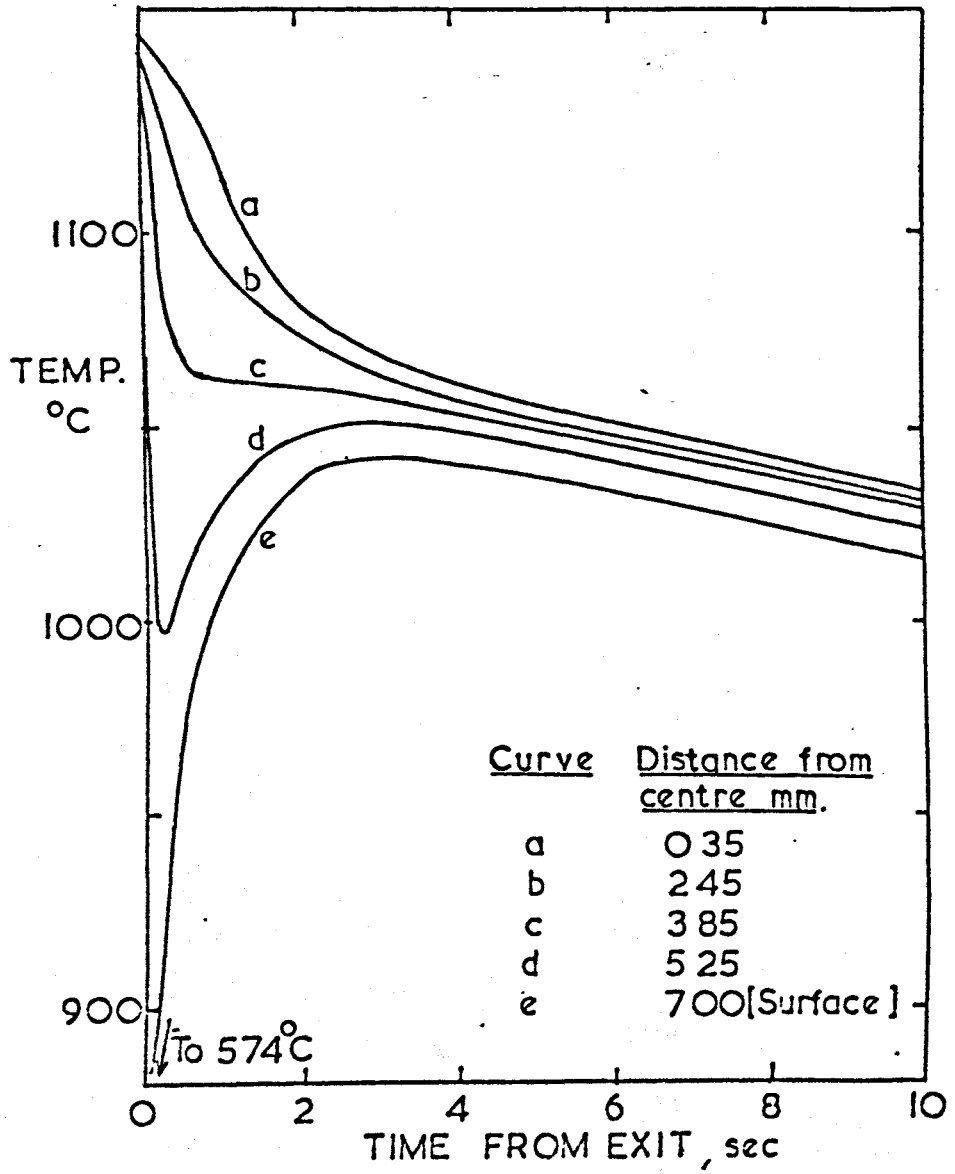

Fig.118a Temperature changes following exit from rolls for a typical first 30% pass.

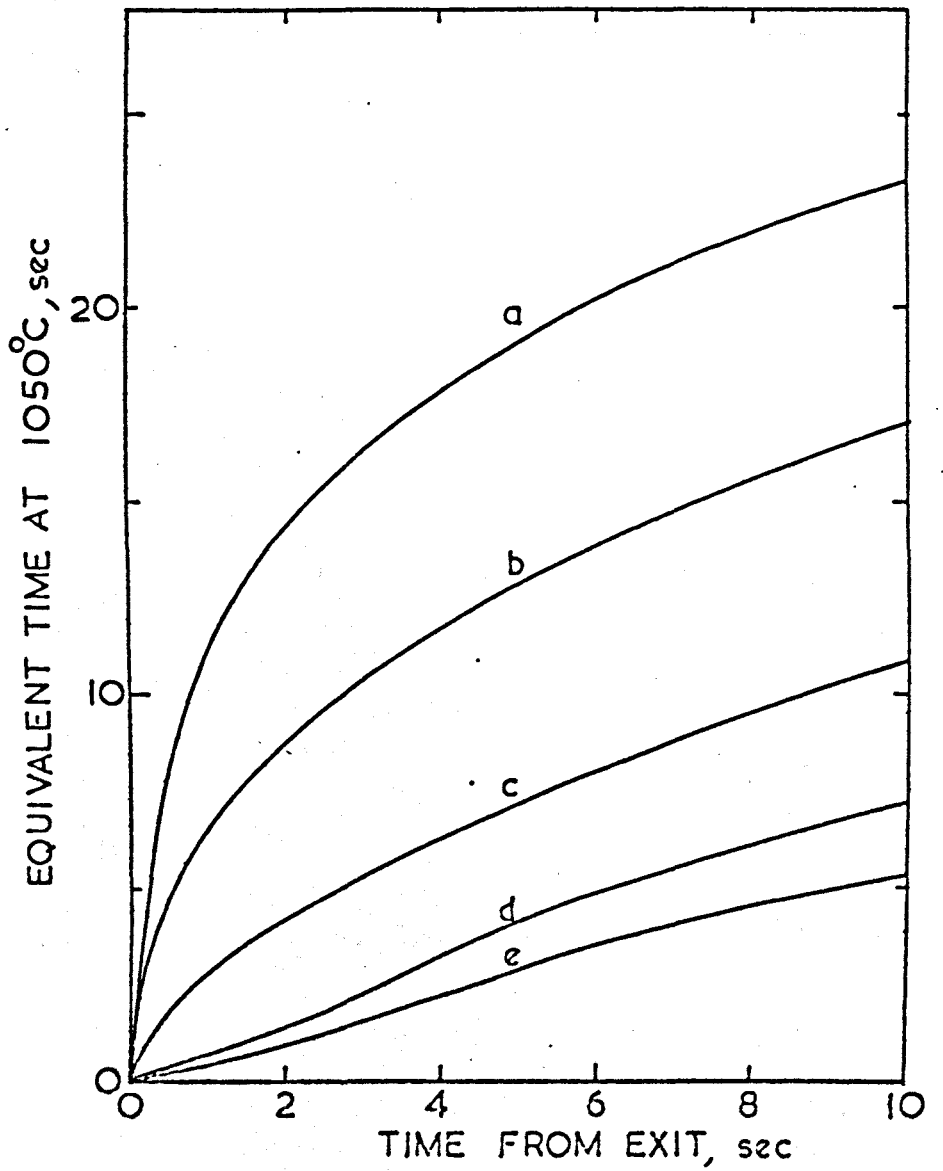

Fig.118b Equivalent recrystallisation time at 1050°C as a function of time following the pass for the same positions as in Fig.118a.

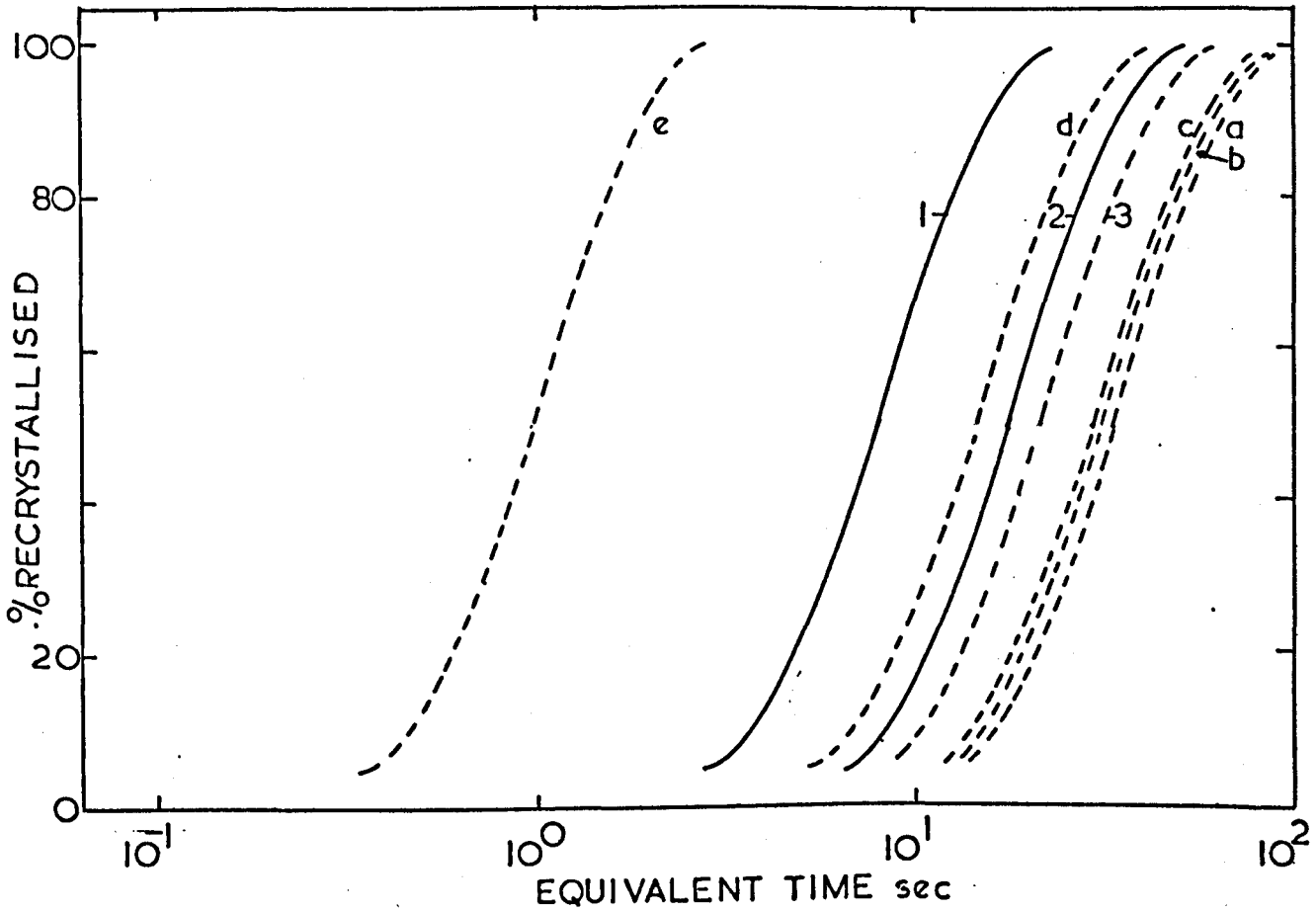

Fig.118c Recrystallisation data for use with Fig.118b.
Curve 1: T = 1050°C, $\bar{\dot{\varepsilon}}$ = 1 sec^{-1}, ε = 0.5 (After Barraclough)
Curve 2: Curve 1 corrected to ε = 0.4119.
Curve 3: Curve 2 corrected for mean strain rate and temperature for pass (i.e.uniform stored energy).
Curves a to e:Data for positions within slab as in Fig.118a (i.e. stored energy distribution).

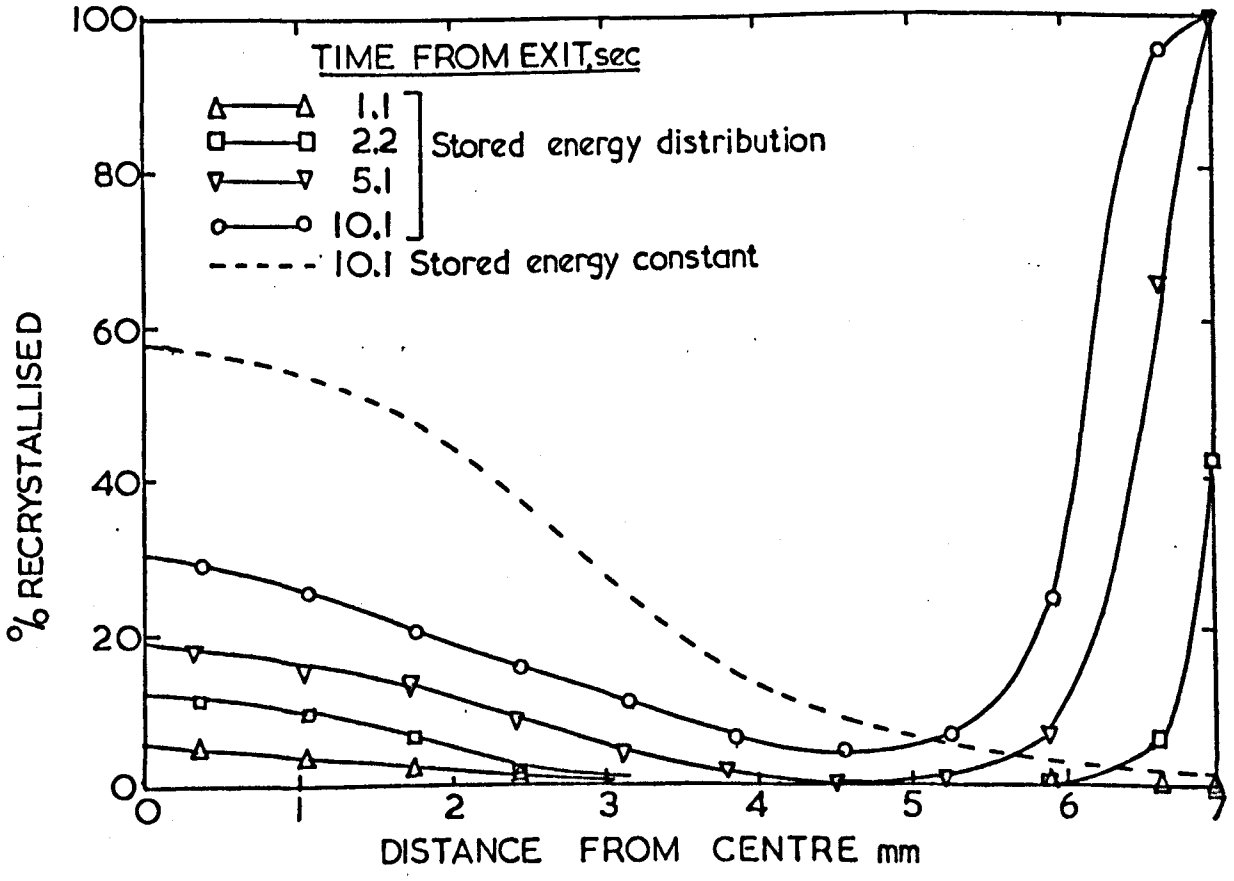

Fig.118d %Recrystallised through slab thickness as a function of time from end of pass;effect of stored energy distribution.

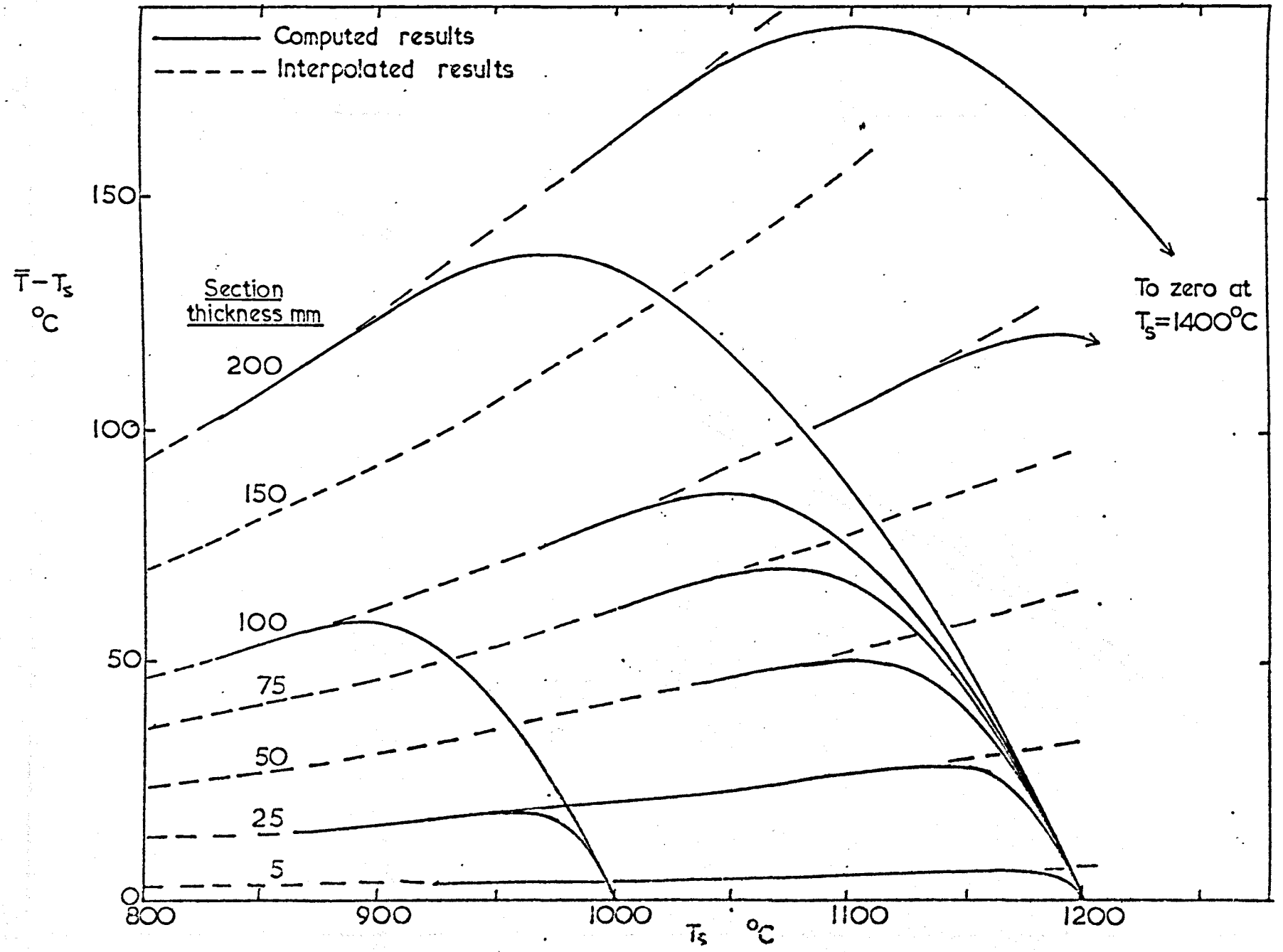

Fig.119 Relation between $\bar{T} - T_s$ and T_s for different section thicknesses (1D heat flow).

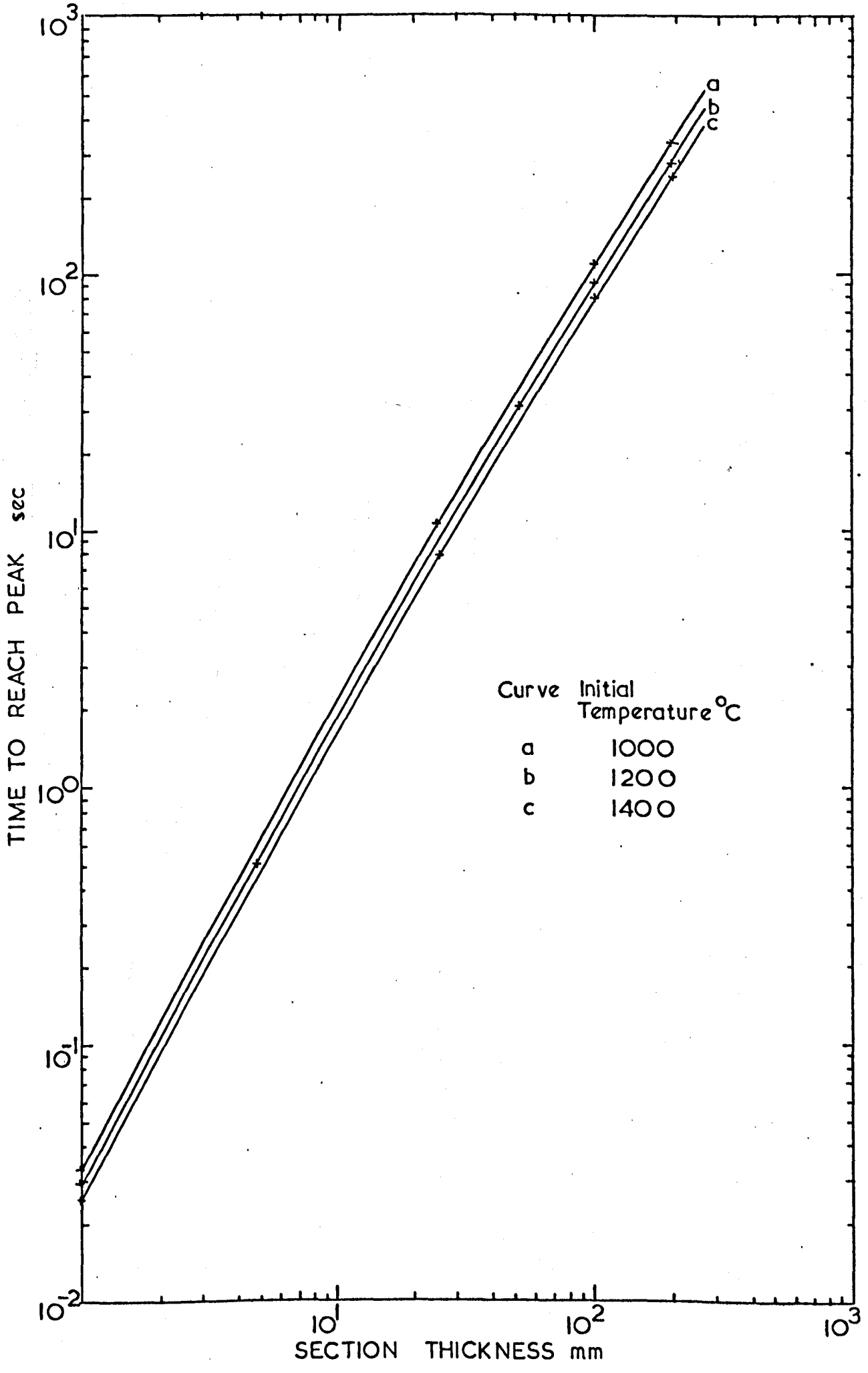

Fig.120 Time to establish equlibrium air cooling as a function of section thickness (1D heat flow).

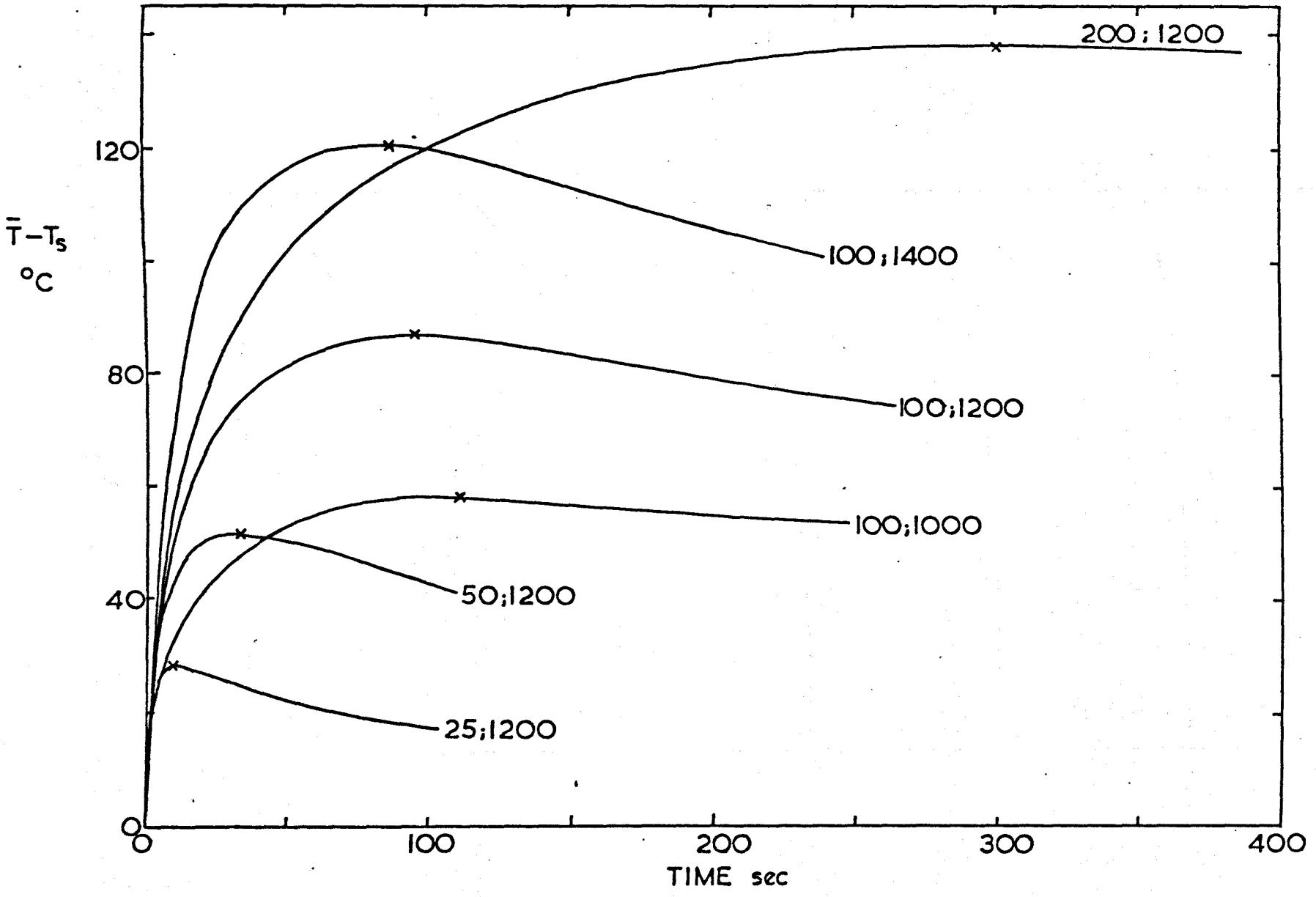

Fig.121 Computed values of $\bar{T} - T_s$ as a function of time. The numbers adjacent to each curve indicate the total section thickness (mm) and reheating temperature.

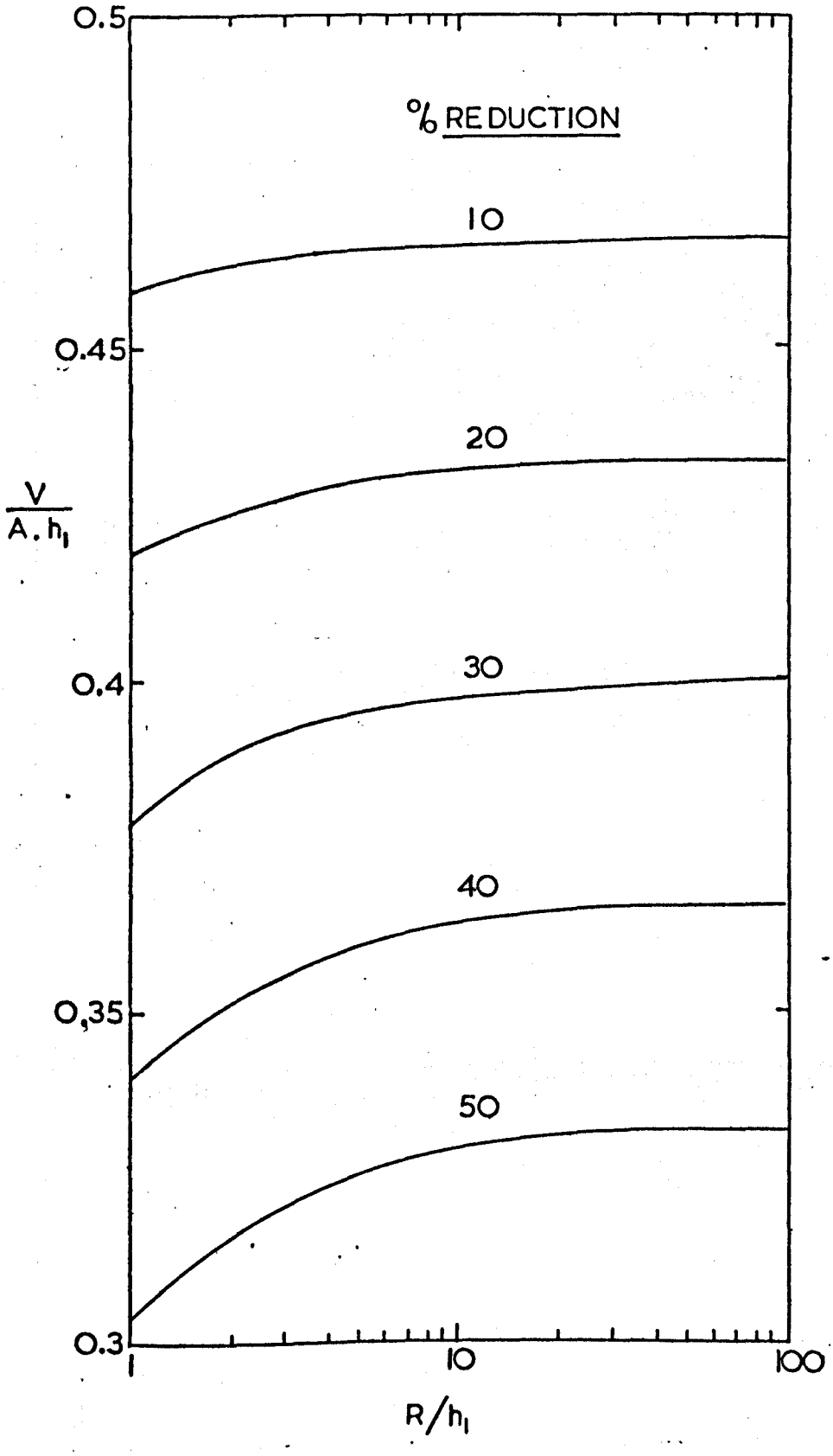

Fig.122 The V/Ah_1 ratio as a function of the R/h_1 ratio and % reduction.

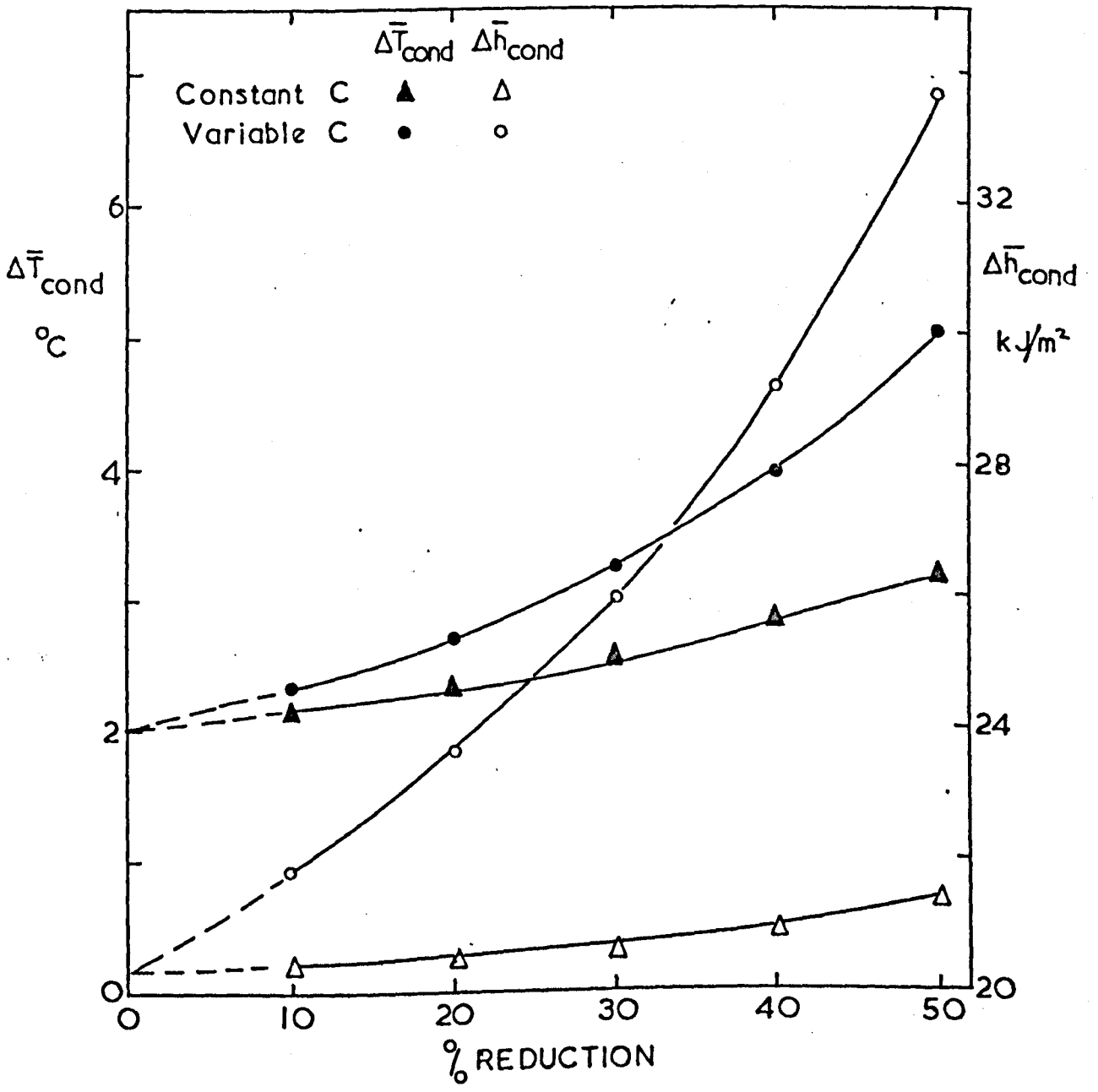

Fig.123 Computed mean temperature drop and mean heat loss as a function of % reduction. $\Delta T_s^{init} = 1000^{\circ}C$, $C = 12.5$ kW/m^2 °C, $t_c = 1.73$ msec., $h_1 = 4$ mm., $R/h_1 = 10$.

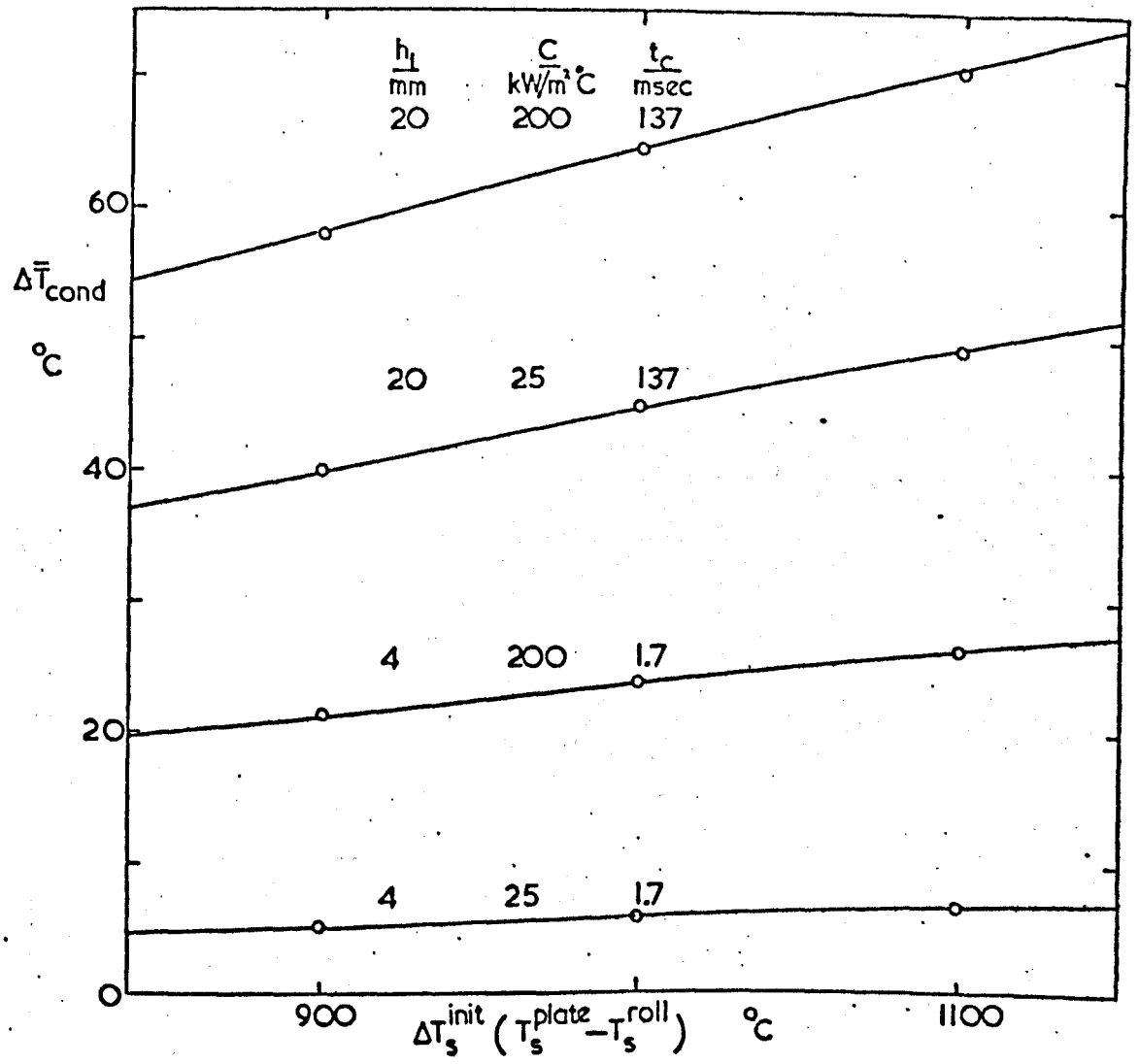

Fig.124 Computed mean temperature drop as a function of initial difference in plate and roll surface temperatures. (30% reduction).

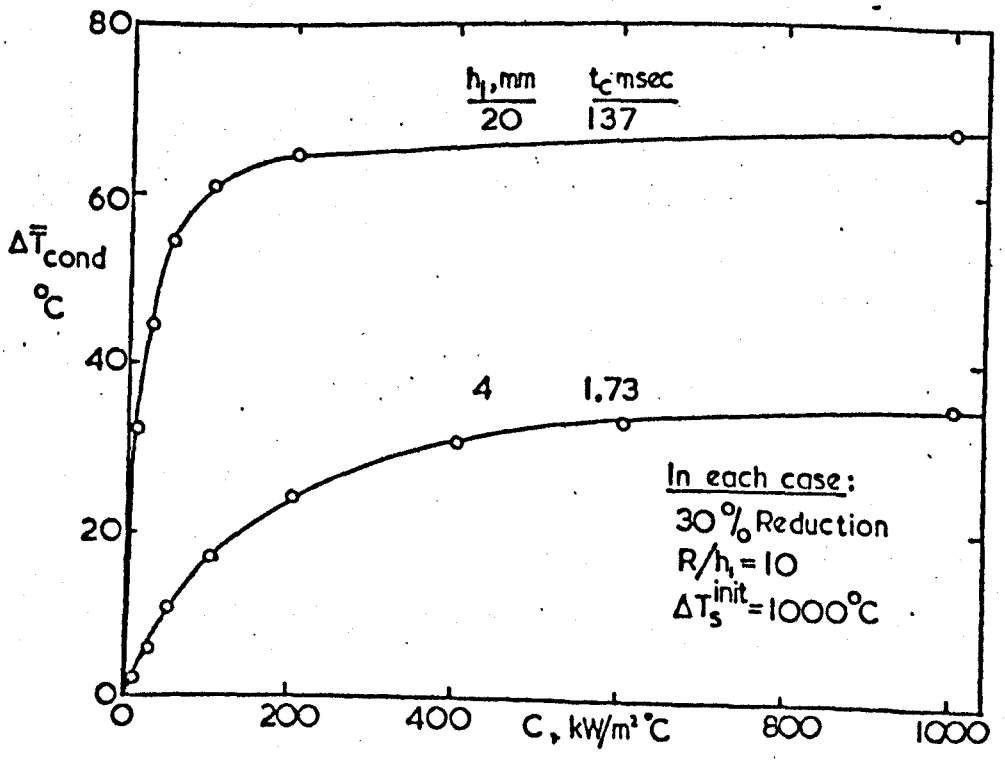

Fig.125 Computed mean temperature drop as a function of C.

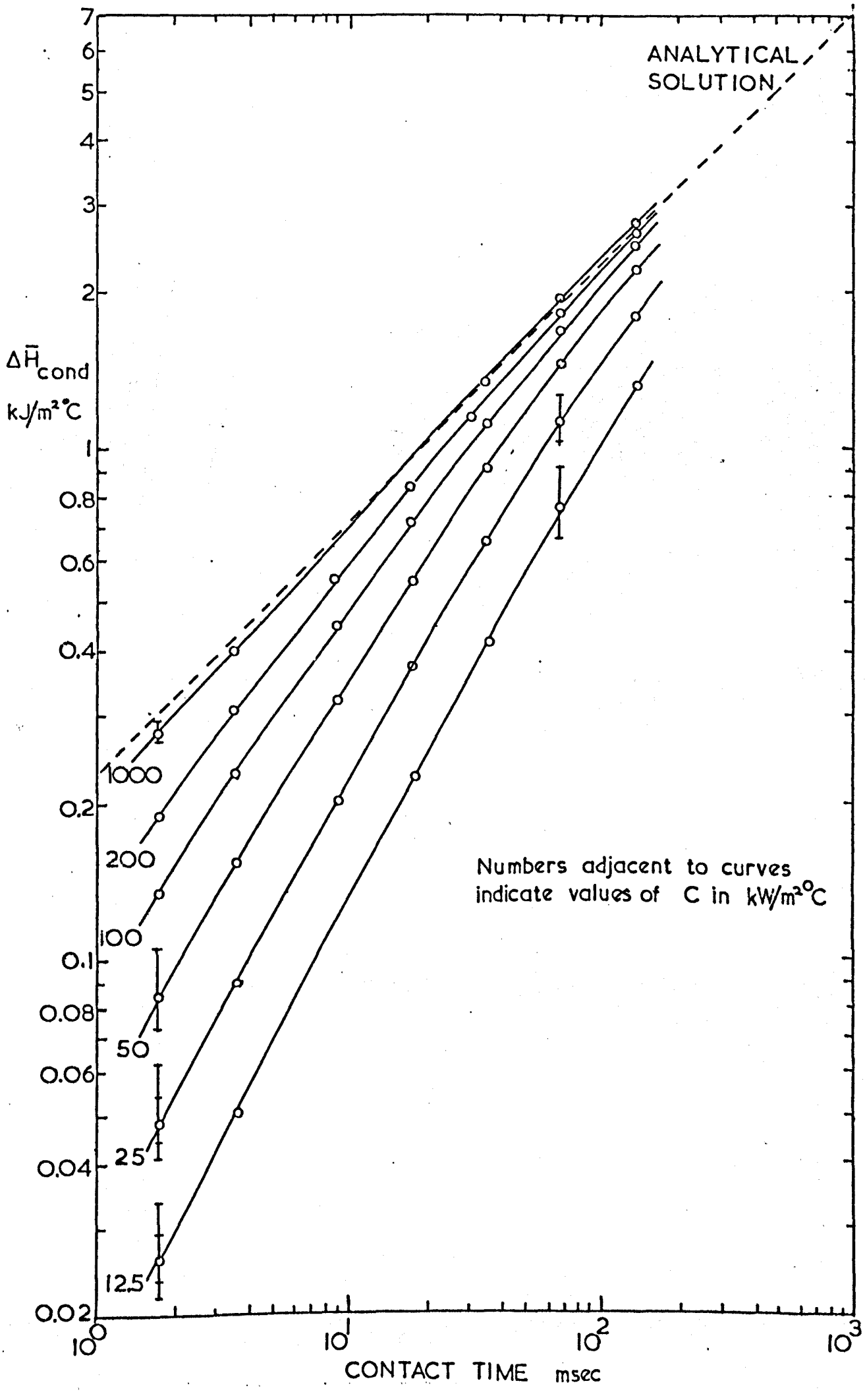

Fig.126 Computed values of $\Delta\bar{H}_{cond}$ as a function of contact time for different values of C.

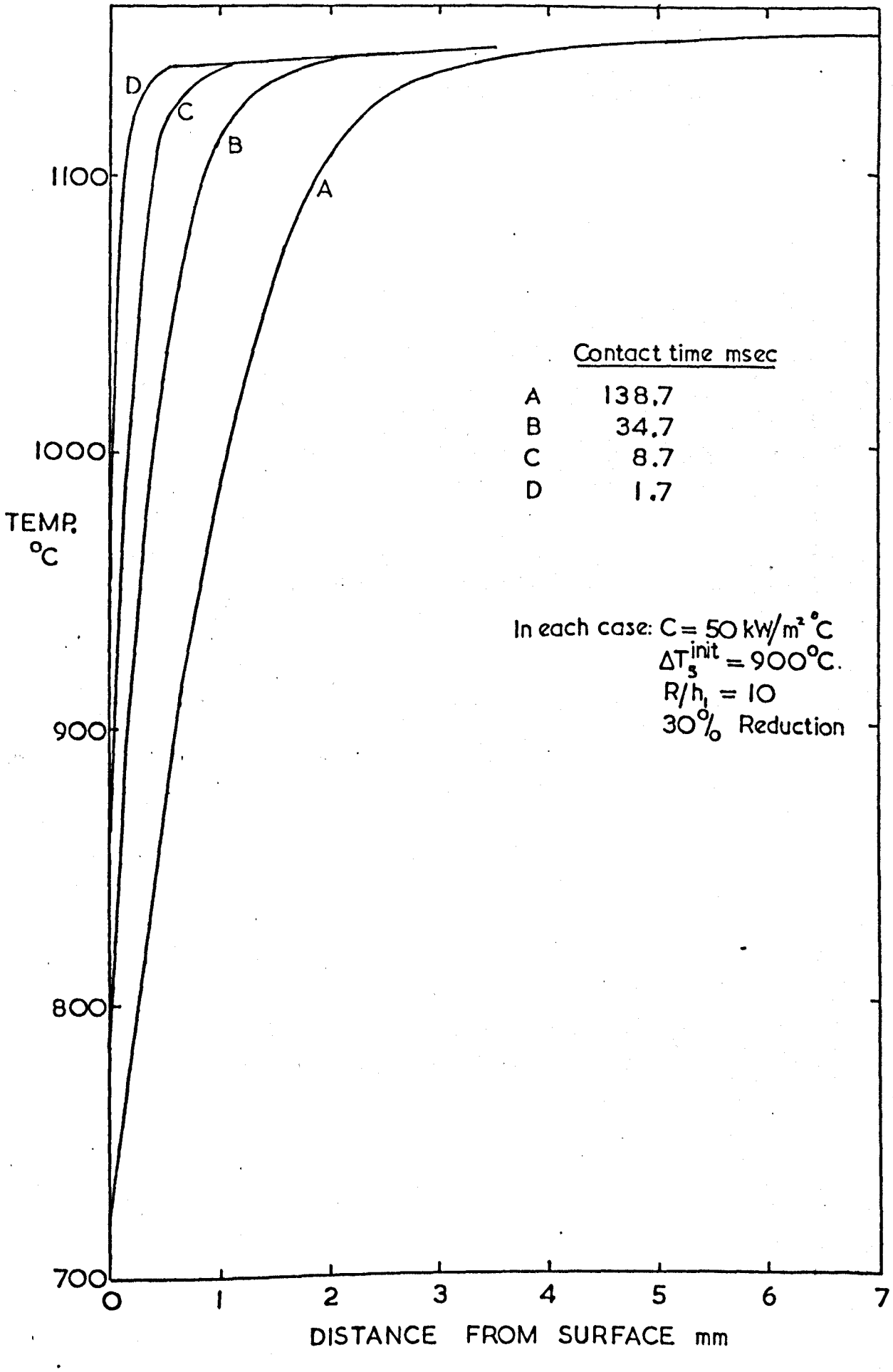

Fig.127 Temperature gradient through the plate thickness as a function of contact time.

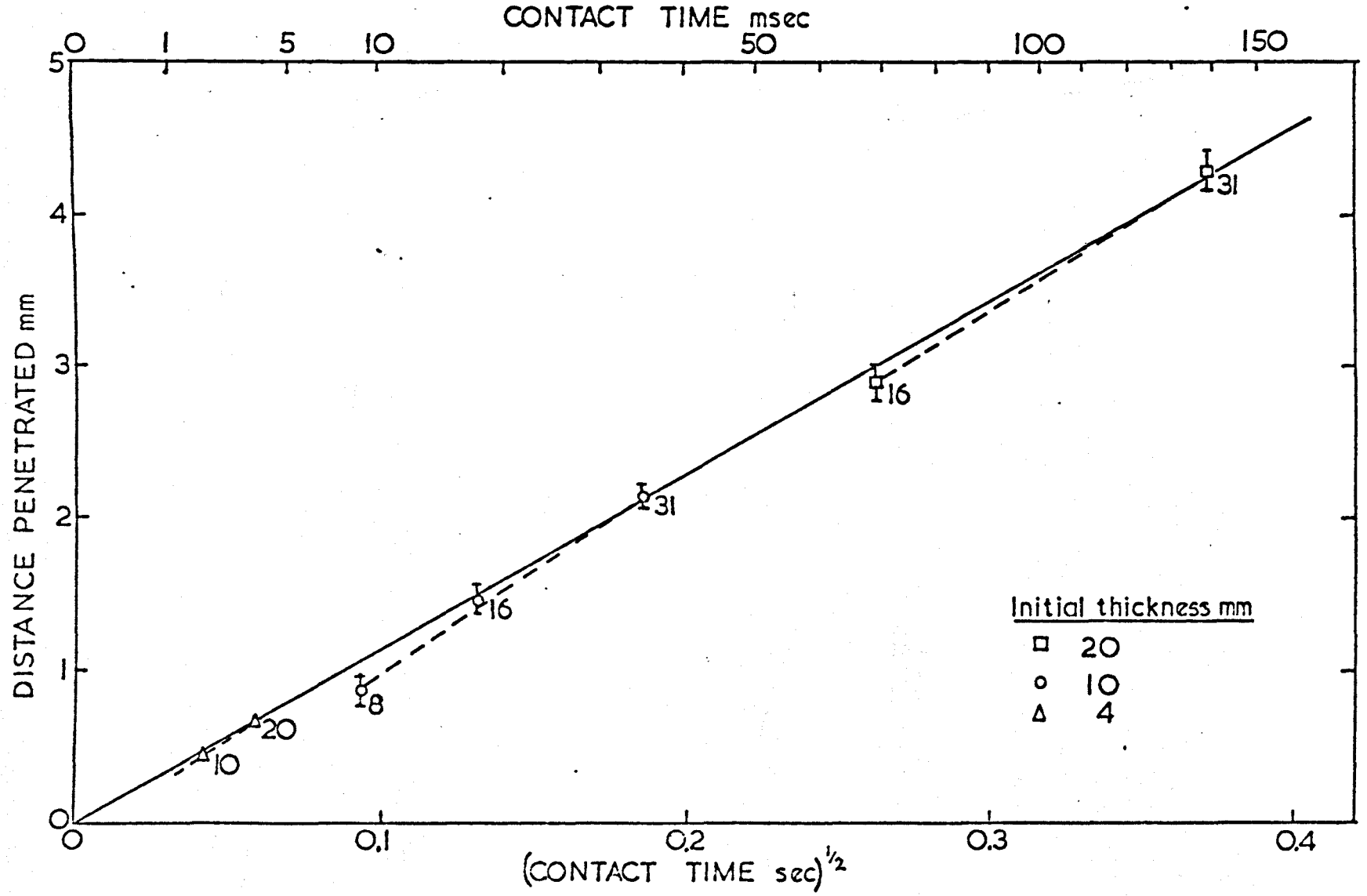

Fig.128 The effect of contact time on the distance penetrated by the temperature gradient. Numbers adjacent to points indicate number of computational time intervals during pass.

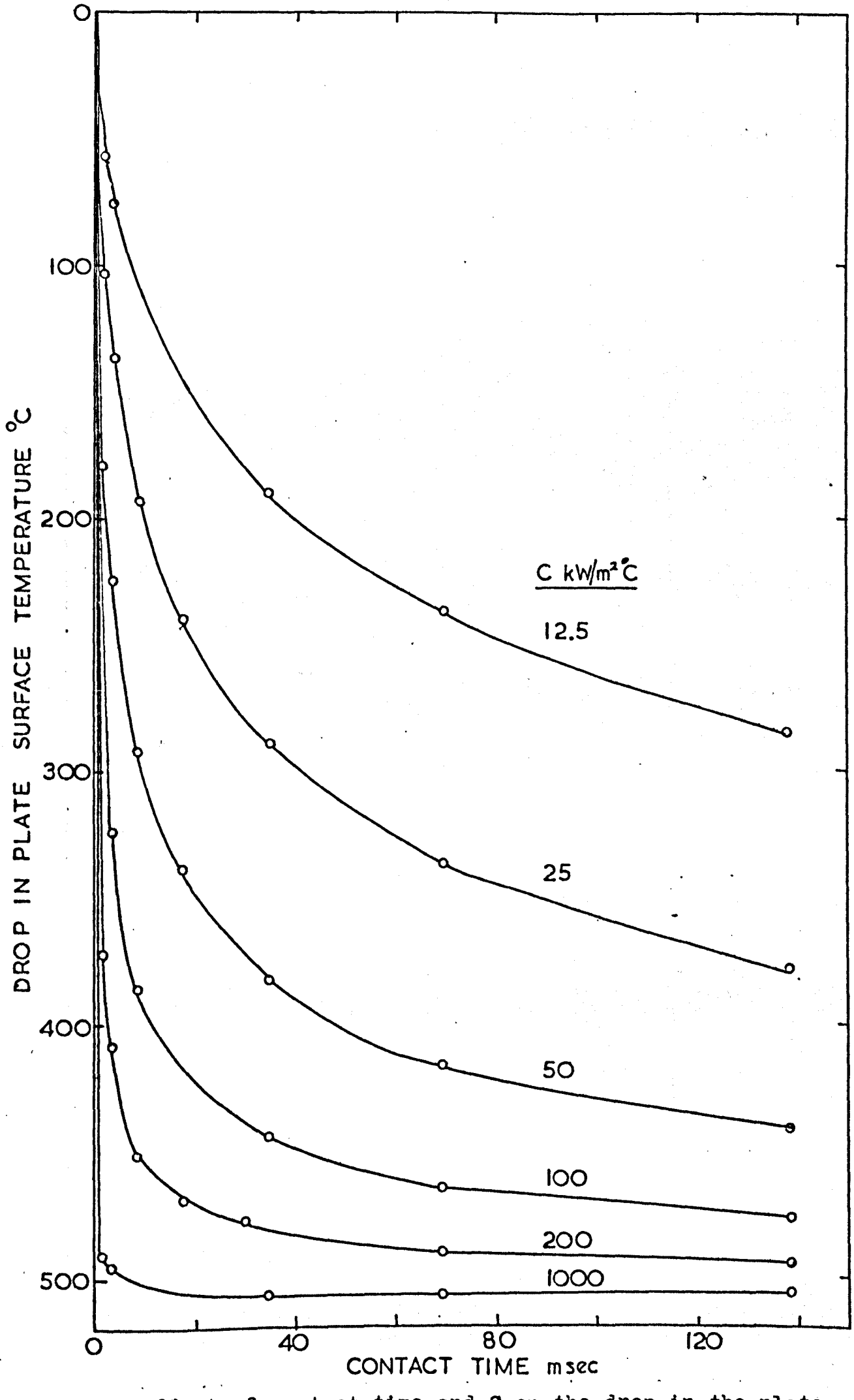

Fig.129 The effect of contact time and C on the drop in the plate surface temperature. All values for $\Delta T_s^{init} = 1000^{\circ}C$.

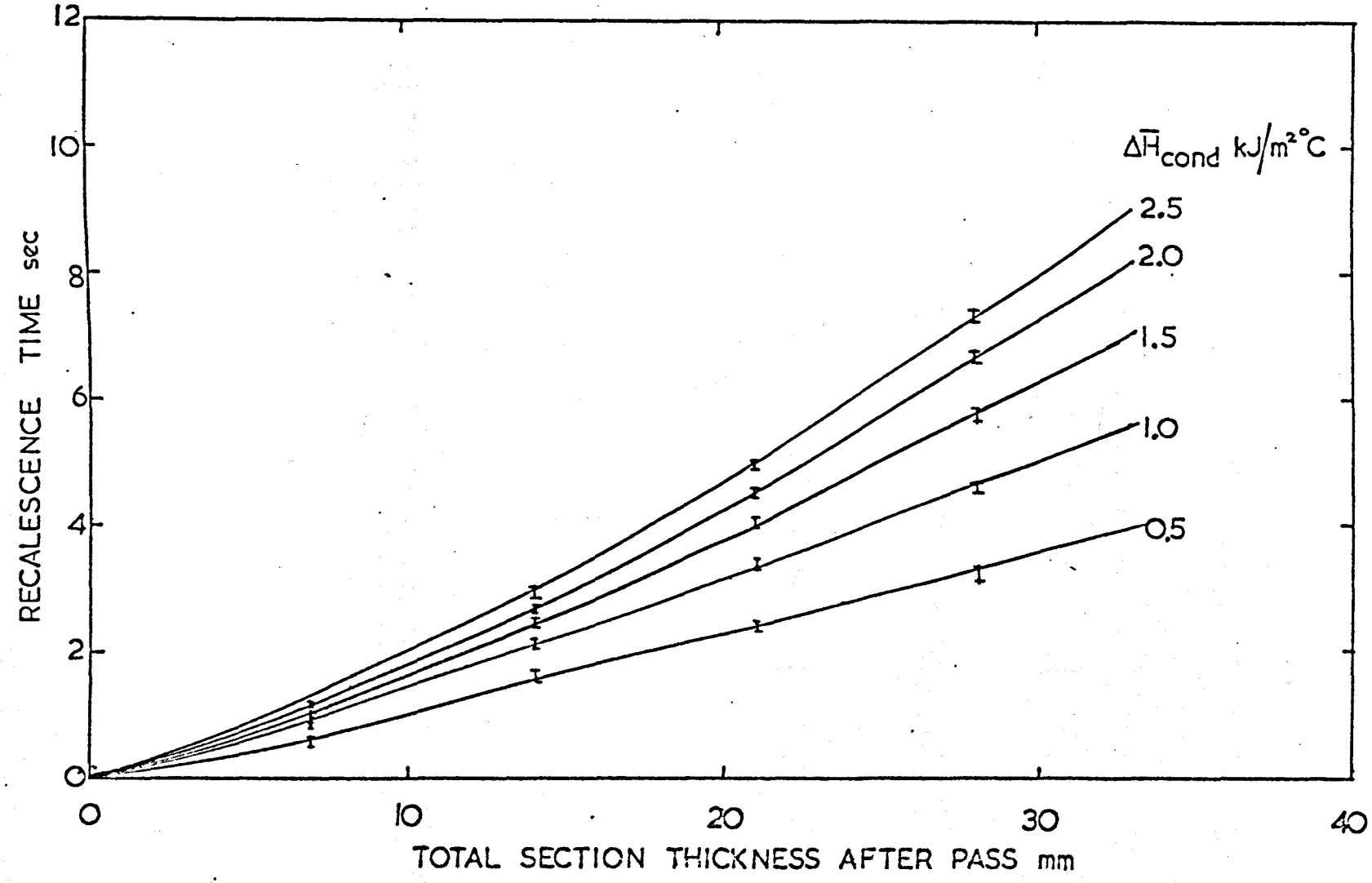

Fig.130 Effect of section thickness and heat loss during a pass on the recaleccence time.

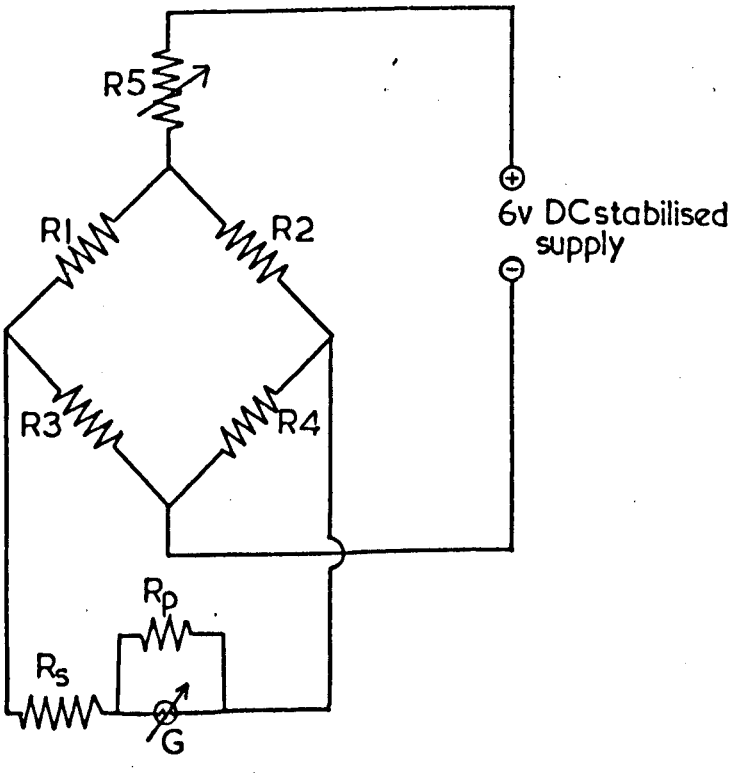

Fig.131 The strain gauge arrangement for roll torque measurement.
R1 to 4: Resistance of strain gauges.
R5 : Bridge balancing resistance.
R_s : Series attenuating resistance.
R_p : Parallel resistance.
G : B100 Galvanometer.

Fig.132 Cross-sections of thermocouples following deformation.

(a) 2 x 30% passes

(b) 3 x 30% passes

Fig.133 Schematic representation of thermocouple hot junctions

(a) Insulated hot junction

(b) Bonded hot junction

(c) Exposed hot junction

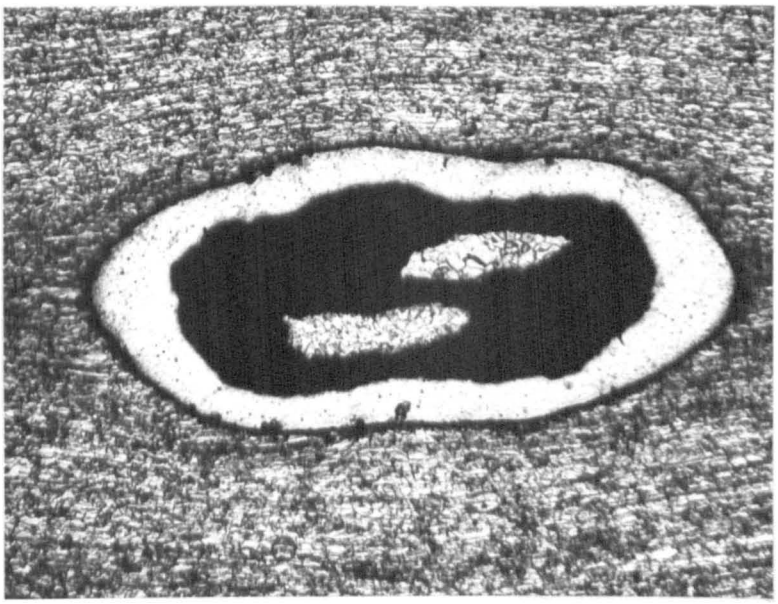

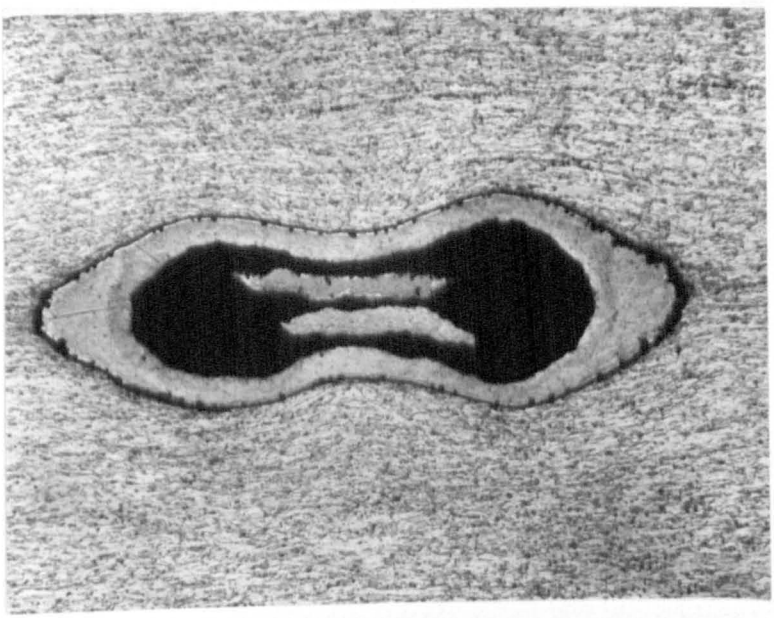

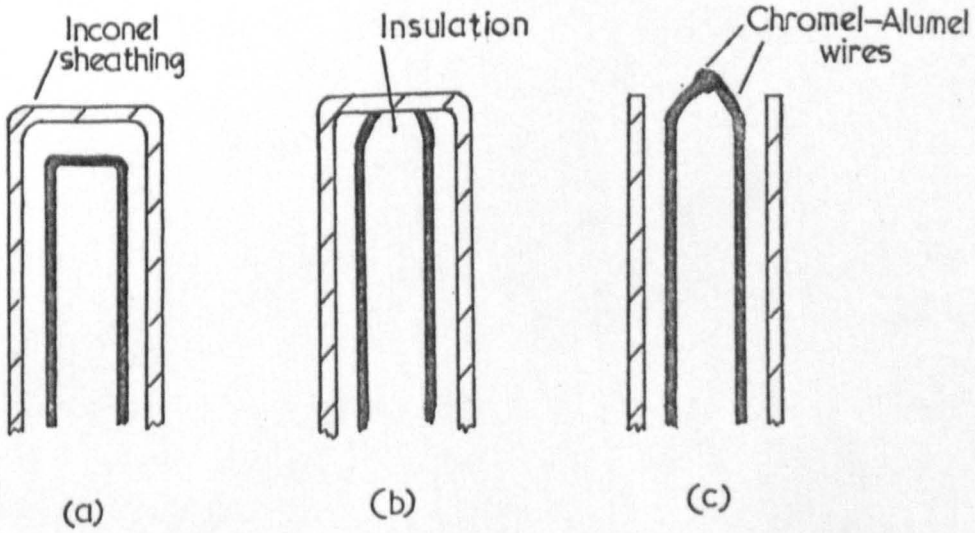
Inconel sheathing
Insulation
Chromel–Alumel wires
(a)
(b)
(c)

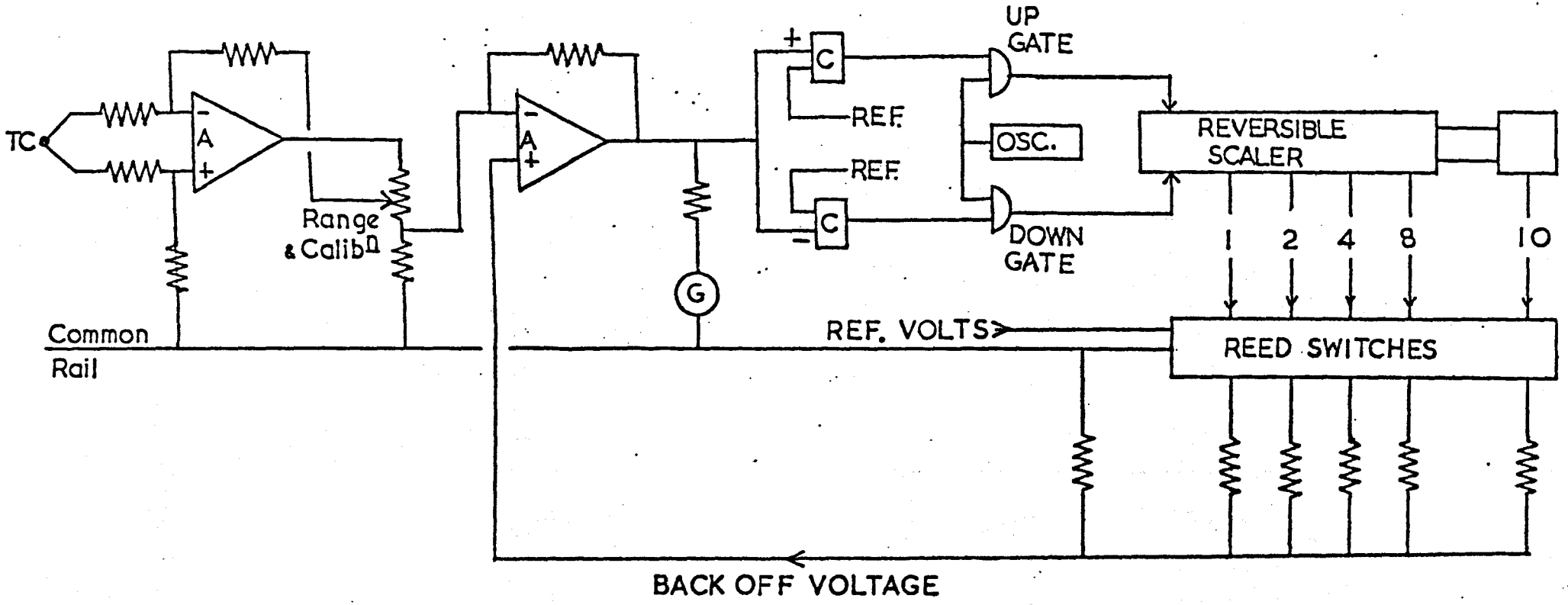

KEY:
- A Amplifiers
- C Comparators
- G U.V.Galvanometer
- TC Thermocouple

Fig.134 Schematic arrangement of automatic back-off system.

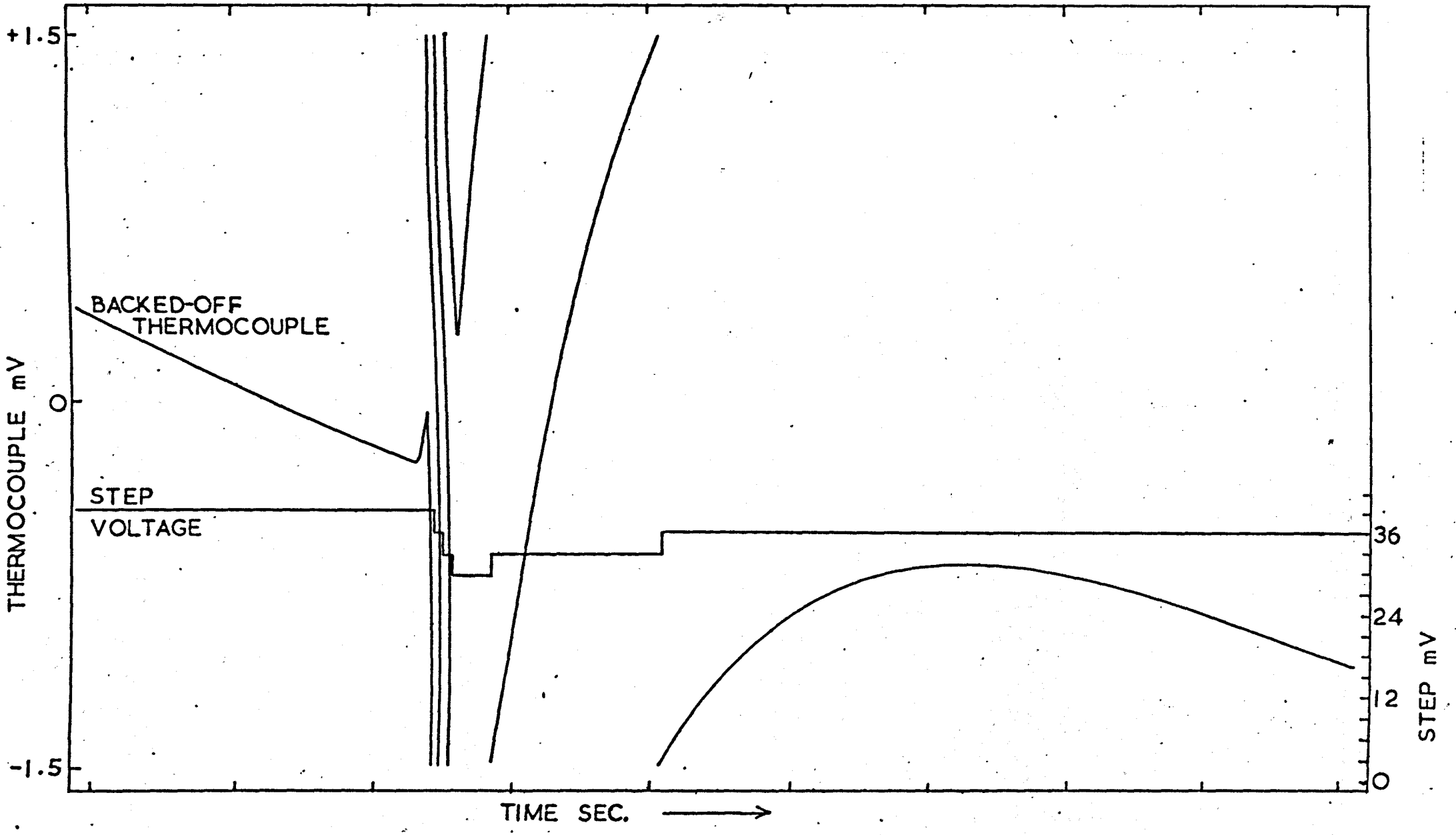

Fig.135 Typical U.V. chart record for subsurface thermocouple.(time scale reversed).

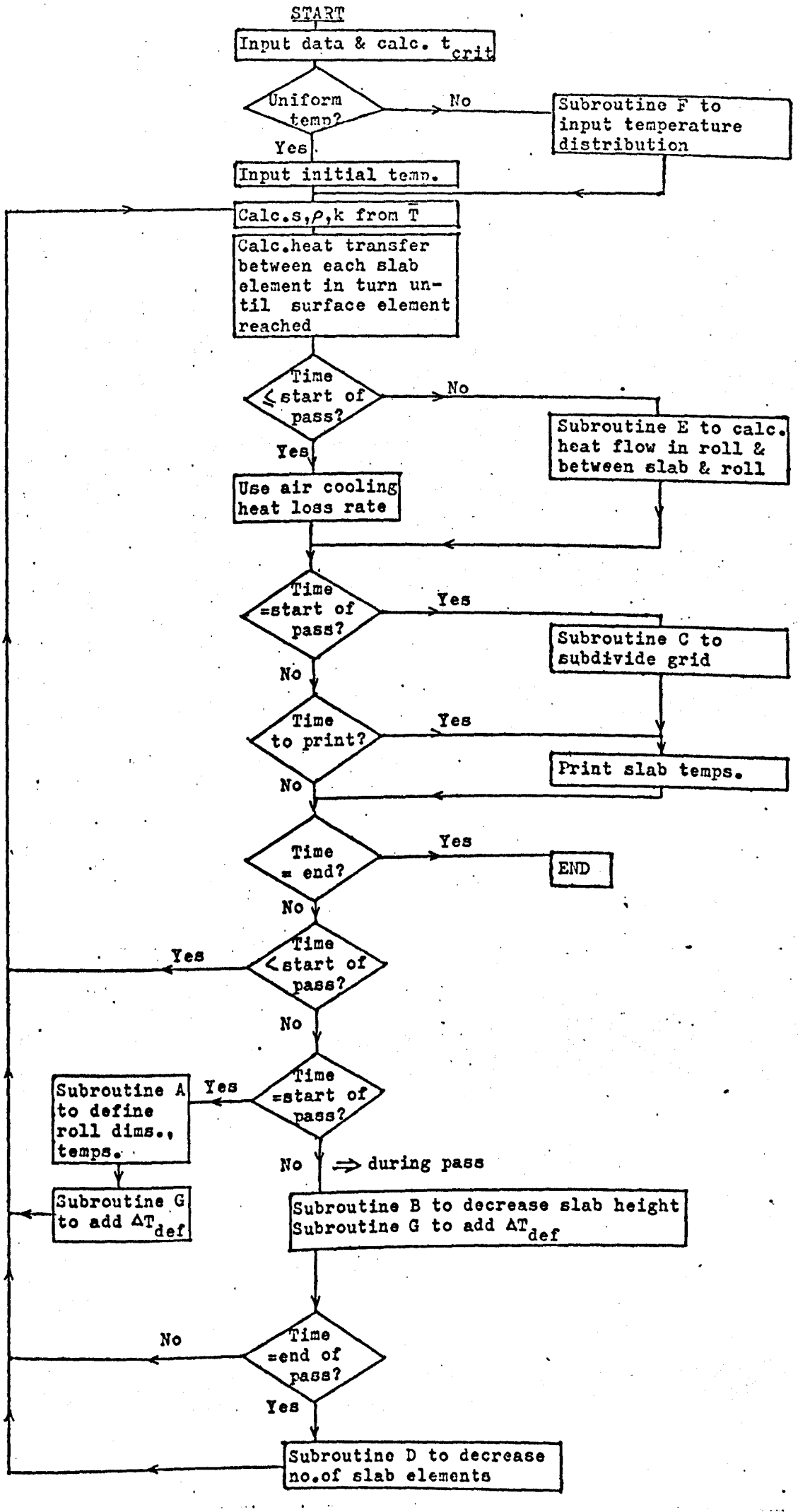

Fig.136 Flow chart showing access to subroutines.

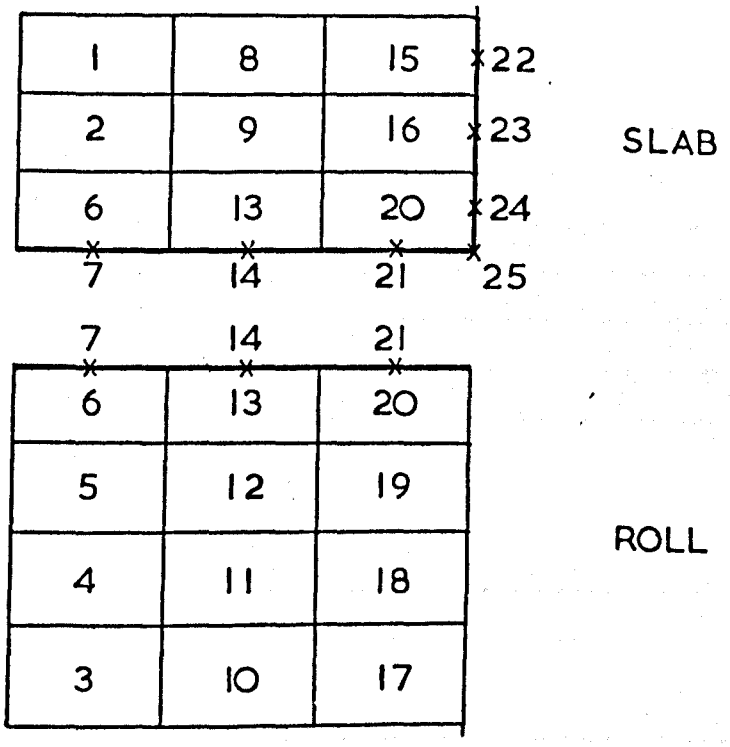

Fig.137 Order of computation during roll contact period (two dimensional model).

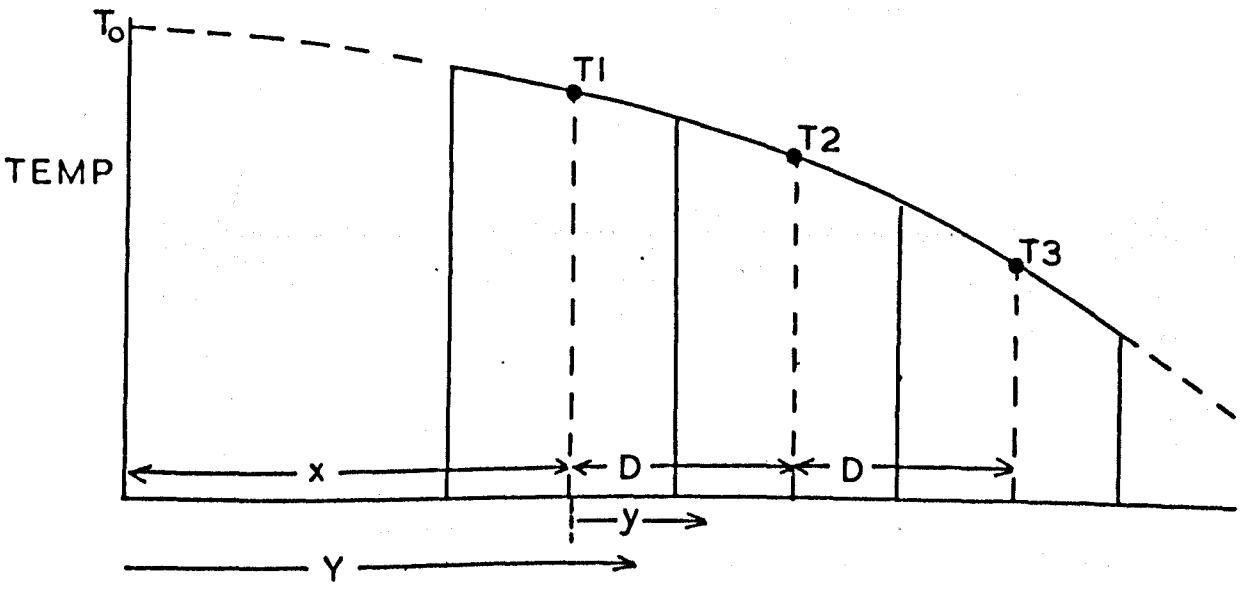

Fig.138a Fitting a parabolic equation to a portion of a temperature gradient.

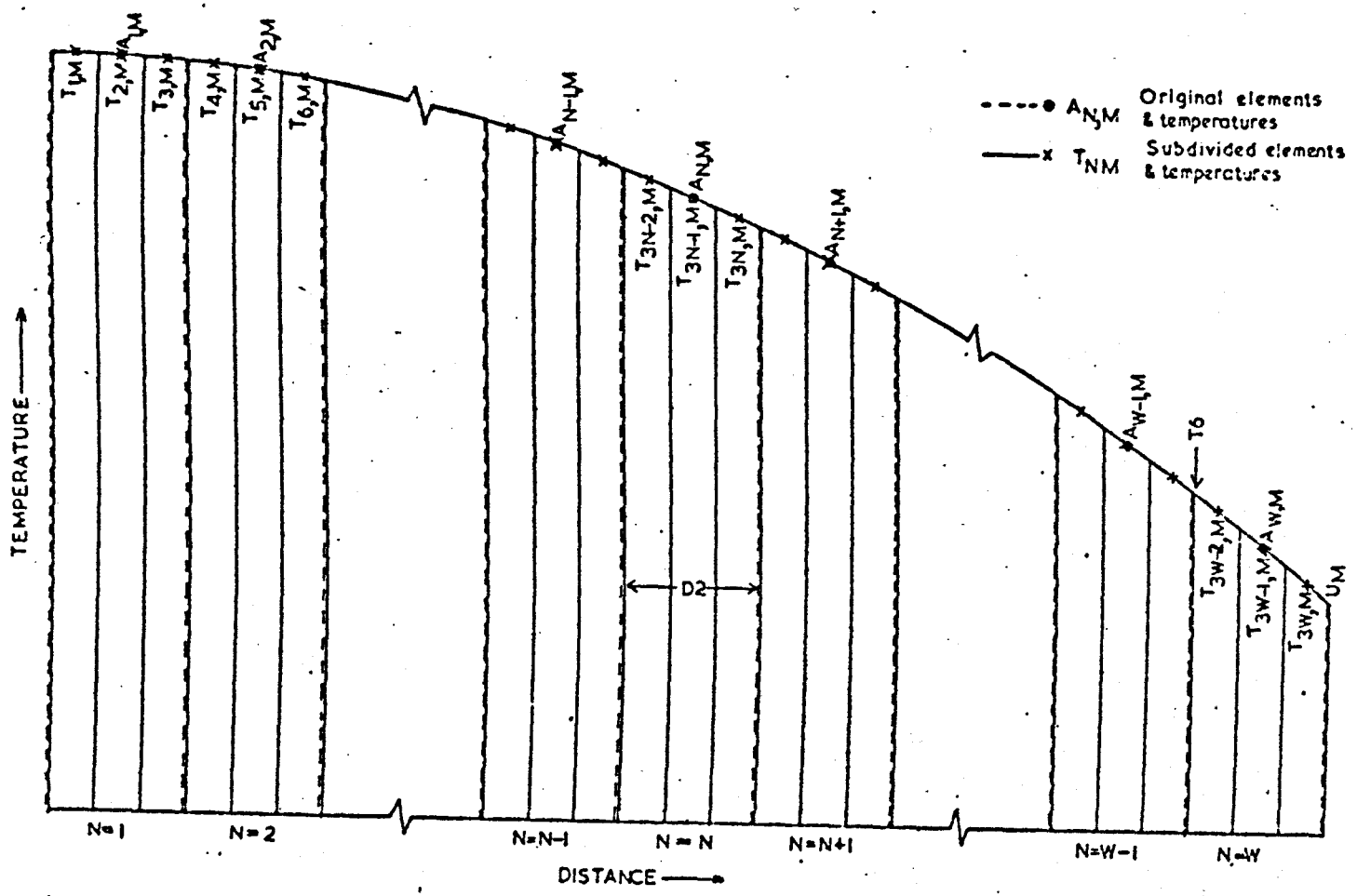

Fig.138b Notation for subdivision of slab matrices prior to pass.